

Topics in Current Chemistry 318

Carsten Tschierske *Editor*

Liquid Crystals

Materials Design and Self-Assembly

 Springer

318

Topics in Current Chemistry

Editorial Board:

K.N. Houk • C.A. Hunter • M.J. Krische • J.-M. Lehn

S.V. Ley • M. Olivucci • J. Thiem • M. Venturi • P. Vogel

C.-H. Wong • H. Wong • H. Yamamoto

Topics in Current Chemistry

Recently Published and Forthcoming Volumes

Liquid Crystals: Materials Design and Self-Assembly

Volume Editor: Carsten Tschierske
Vol. 318, 2012

Fragment-Based Drug Discovery and X-Ray Crystallography

Volume Editors: Thomas G. Davies,
Marko Hyvönen
Vol. 317, 2012

Novel Sampling Approaches in Higher Dimensional NMR

Volume Editors: Martin Billeter,
Vladislav Orekhov
Vol. 316, 2012

Advanced X-Ray Crystallography

Volume Editor: Kari Rissanen
Vol. 315, 2012

Pyrethroids: From Chrysanthemum to Modern Industrial Insecticide

Volume Editors: Noritada Matsuo, Tatsuya Mori
Vol. 314, 2012

Unimolecular and Supramolecular Electronics II

Volume Editor: Robert M. Metzger
Vol. 313, 2012

Unimolecular and Supramolecular Electronics I

Volume Editor: Robert M. Metzger
Vol. 312, 2012

Bismuth-Mediated Organic Reactions

Volume Editor: Thierry Ollevier
Vol. 311, 2012

Peptide-Based Materials

Volume Editor: Timothy Deming
Vol. 310, 2012

Alkaloid Synthesis

Volume Editor: Hans-Joachim Knölker
Vol. 309, 2012

Fluorous Chemistry

Volume Editor: István T. Horváth
Vol. 308, 2012

Multiscale Molecular Methods in Applied Chemistry

Volume Editors: Barbara Kirchner, Jadran Vrabec
Vol. 307, 2012

Solid State NMR

Volume Editor: Jerry C. C. Chan
Vol. 306, 2012

Prion Proteins

Volume Editor: Jörg Tatzelt
Vol. 305, 2011

Microfluidics: Technologies and Applications

Volume Editor: Bingcheng Lin
Vol. 304, 2011

Photocatalysis

Volume Editor: Carlo Alberto Bignozzi
Vol. 303, 2011

Computational Mechanisms of Au and Pt Catalyzed Reactions

Volume Editors: Elena Soriano,
José Marco-Contelles
Vol. 302, 2011

Reactivity Tuning in Oligosaccharide Assembly

Volume Editors: Bert Fraser-Reid,
J. Cristóbal López
Vol. 301, 2011

Luminescence Applied in Sensor Science

Volume Editors: Luca Prodi, Marco Montalti,
Nelsi Zaccheroni
Vol. 300, 2011

Liquid Crystals

Materials Design and Self-Assembly

Volume Editor: Carsten Tschierske

With Contributions by

T. Bellini · R. Cerbino · X. Feng · E. Gorecka · T. Hegmann ·
M. Kaller · T. Kato · S. Laschat · M. Lehmann · J. Mirzaei ·
D. Pocięcha · Y. Sagara · O. Stamatoiu · H. Takezoe · K. Tanabe ·
C. Tschierske · N. Vaupotič · S. Yamane · G. Zanchetta

 Springer

Editor

Prof. Carsten Tschierske
Institute of Chemistry
Organic Chemistry
Martin Luther University Halle-Wittenberg
Kurt-Mothes Str. 2
06120 Halle/Saale
Germany
carsten.tschierske@chemie.uni-halle.de

ISSN 0340-1022 e-ISSN 1436-5049
ISBN 978-3-642-27590-6 e-ISBN 978-3-642-27591-3
DOI 10.1007/978-3-642-27591-3
Springer Heidelberg Dordrecht London New York

Library of Congress Control Number: 2011945782

© Springer-Verlag Berlin Heidelberg 2012

This work is subject to copyright. All rights are reserved, whether the whole or part of the material is concerned, specifically the rights of translation, reprinting, reuse of illustrations, recitation, broadcasting, reproduction on microfilm or in any other way, and storage in data banks. Duplication of this publication or parts thereof is permitted only under the provisions of the German Copyright Law of September 9, 1965, in its current version, and permission for use must always be obtained from Springer. Violations are liable to prosecution under the German Copyright Law.

The use of general descriptive names, registered names, trademarks, etc. in this publication does not imply, even in the absence of a specific statement, that such names are exempt from the relevant protective laws and regulations and therefore free for general use.

Printed on acid-free paper

Springer is part of Springer Science+Business Media (www.springer.com)

Volume Editor

Prof. Carsten Tschierske

Institute of Chemistry
Organic Chemistry
Martin Luther University Halle-Wittenberg
Kurt-Mothes Str. 2
06120 Halle/Saale
Germany
carsten.tschierske@chemie.uni-halle.de

Editorial Board

Prof. Dr. Kendall N. Houk

University of California
Department of Chemistry and Biochemistry
405 Hilgard Avenue
Los Angeles, CA 90024-1589, USA
houk@chem.ucla.edu

Prof. Dr. Christopher A. Hunter

Department of Chemistry
University of Sheffield
Sheffield S3 7HF, United Kingdom
c.hunter@sheffield.ac.uk

Prof. Michael J. Krische

University of Texas at Austin
Chemistry & Biochemistry Department
1 University Station A5300
Austin TX, 78712-0165, USA
mkrische@mail.utexas.edu

Prof. Dr. Jean-Marie Lehn

ISIS
8, allée Gaspard Monge
BP 70028
67083 Strasbourg Cedex, France
lehn@isis.u-strasbg.fr

Prof. Dr. Steven V. Ley

University Chemical Laboratory
Lensfield Road
Cambridge CB2 1EW
Great Britain
Svl1000@cus.cam.ac.uk

Prof. Dr. Massimo Olivucci

Università di Siena
Dipartimento di Chimica
Via A De Gasperi 2
53100 Siena, Italy
olivucci@unisi.it

Prof. Dr. Joachim Thiem

Institut für Organische Chemie
Universität Hamburg
Martin-Luther-King-Platz 6
20146 Hamburg, Germany
thiem@chemie.uni-hamburg.de

Prof. Dr. Margherita Venturi

Dipartimento di Chimica
Università di Bologna
via Selmi 2
40126 Bologna, Italy
margherita.venturi@unibo.it

Prof. Dr. Pierre Vogel

Laboratory of Glycochemistry
and Asymmetric Synthesis
EPFL – Ecole polytechnique fédérale
de Lausanne
EPFL SB ISIC LGSA
BCH 5307 (Bat.BCH)
1015 Lausanne, Switzerland
pierre.vogel@epfl.ch

Prof. Dr. Chi-Huey Wong

Professor of Chemistry, Scripps Research
Institute
President of Academia Sinica
Academia Sinica
128 Academia Road
Section 2, Nankang
Taipei 115
Taiwan
chwong@gate.sinica.edu.tw

Prof. Dr. Henry Wong

The Chinese University of Hong Kong
University Science Centre
Department of Chemistry
Shatin, New Territories
hncwong@cuhk.edu.hk

Prof. Dr. Hisashi Yamamoto

Arthur Holly Compton Distinguished
Professor
Department of Chemistry
The University of Chicago
5735 South Ellis Avenue
Chicago, IL 60637
773-702-5059
USA
yamamoto@uchicago.edu

Topics in Current Chemistry Also Available Electronically

Topics in Current Chemistry is included in Springer's eBook package *Chemistry and Materials Science*. If a library does not opt for the whole package the book series may be bought on a subscription basis. Also, all back volumes are available electronically.

For all customers with a print standing order we offer free access to the electronic volumes of the series published in the current year.

If you do not have access, you can still view the table of contents of each volume and the abstract of each article by going to the SpringerLink homepage, clicking on "Chemistry and Materials Science," under Subject Collection, then "Book Series," under Content Type and finally by selecting *Topics in Current Chemistry*.

You will find information about the

- Editorial Board
- Aims and Scope
- Instructions for Authors
- Sample Contribution

at springer.com using the search function by typing in *Topics in Current Chemistry*.

Color figures are published in full color in the electronic version on SpringerLink.

Aims and Scope

The series *Topics in Current Chemistry* presents critical reviews of the present and future trends in modern chemical research. The scope includes all areas of chemical science, including the interfaces with related disciplines such as biology, medicine, and materials science.

The objective of each thematic volume is to give the non-specialist reader, whether at the university or in industry, a comprehensive overview of an area where new insights of interest to a larger scientific audience are emerging.

Thus each review within the volume critically surveys one aspect of that topic and places it within the context of the volume as a whole. The most significant developments of the last 5–10 years are presented, using selected examples to illustrate the principles discussed. A description of the laboratory procedures involved is often useful to the reader. The coverage is not exhaustive in data, but rather conceptual, concentrating on the methodological thinking that will allow the non-specialist reader to understand the information presented.

Discussion of possible future research directions in the area is welcome.

Review articles for the individual volumes are invited by the volume editors.

In references *Topics in Current Chemistry* is abbreviated *Top Curr Chem* and is cited as a journal.

Impact Factor 2010: 2.067; Section “Chemistry, Multidisciplinary”: Rank 44 of 144

Preface

Since their discovery in 1888, liquid crystals (LCs) have developed from a scientific curiosity to an interdisciplinary research field with broad commercial applications. LC displays (LCD) represent the most obvious and successful example for the practical application of LC, well known to a broad community. The light, flat and low power-consuming LCD is one of the key components of present mobile communication and data processing devices, which have changed our lives considerably. Nowadays, even the TV-market is dominated by LCD which allows incredible screen sizes and resolutions. However, beside the well known display technology there are many other applications of liquid crystals, for example polarized light reflecting and photonic band gap materials and light modulators. Liquid crystalline polymers are presently used for high strength fibres, for the encapsulation of microelectronic circuits and the construction of micro-electromechanical and micro-fluidic devices. Numerous new applications of LC are also approaching, such as organic light emitting diodes, photovoltaic devices, organic field effect transistors, tuneable lasers and many others. Besides the numerous technical applications there are also an increasing number of biomedical applications for drug delivery, gene delivery, sensors and as promising materials for artificial bones, tissues and actuators. In a more general sense, the combination of order and mobility in the LC state provides unique properties and is a basic requirement for self-assembly and structure formation in technical and bio-systems.

However, the LC displays are still based on the simplest mode of LC organization, the nematic phase, which comprises only an orientational order of the molecules, new applications, as for example in organic electronics also require the directed design of positional order in one, two or three dimensions as provided by smectic, columnar and cubic phases, respectively. In this way, through molecular design and synthesis of new LC molecules, the complexity of LC phases can be increased and this is the basis for the emergence of new materials properties, paving the way to new future applications. One recent example is provided by the so-called bent-core molecules, where ferroelectricity and spontaneous achiral symmetry breaking emerge in well ordered, but still fluid systems.

A number of fundamental aspects of liquid crystals chemistry were presented in volumes 94 and 95 of *Structure and Bonding*, edited by D. M. P. Mingos and published in 1999 and also in volume 128 of the same series, edited by T. Kato and published in 2008. Another monograph was published by Springer in 2007 (*Thermotropic Liquid Crystals*, edited by A. Ramamoorthy) and deals more with physical aspects of LC self assembly and methods of their investigation. This volume intends to shed light on a selection of different aspects of contemporary liquid crystal chemistry, focussing on molecular design carried out in order to influence the self-assembly behaviour of LC-forming molecules in a specific way.

The editor has intended to avoid duplications with subjects occurring in the previous volumes of the series *Structure and Bonding* and to provide the reader with most update information on design and self-assembly of LC materials. This volume in the *Topics in Current Chemistry* series combines eight chapters from different areas, starting with reviews on the current state in the fields of LCs with perfluorinated segments and LCs based on crown ether structures. The first one is focussed on nano-segregation as a basic tool for LC-design, leading to specific properties and new modes of self-assembly in liquid crystals. The second one provides a link to host-guest chemistry, a major area of supramolecular chemistry. The first chapter also gives a short introduction into the field of LC self-assembly and offers a brief description of the most important fundamental LC phase structures. LC phases formed by unusual molecules, namely three-arm-star molecules are reviewed in the third chapter. This is followed by a chapter presenting an overview of soft DNA-based structures, not only covering LC phases but also including other soft structures based on DNA nanotechnology, which provides some examples for the importance of LC self assembly in bio-systems and for the origin of life. As already mentioned above, another contemporary field of research is related to so-called bent-core mesogens. Two chapters are devoted to this subject, one reviewing complex phases with two-dimensional order and the other one focussing on spontaneous achiral symmetry breaking in bent-core LC and also in other LC phases. Another current research field deals with the combination of nano-particles and LCs. Nano-particles can either be combined with units promoting their mesogeneity and enabling them to organize into well defined periodic LC structures, or the self assembly of nano-particles can be mediated by a LC host matrix. Finally, there is also an influence of the nano-particles on the phase structure of the LC host. The last chapter is devoted to the directed molecular design of photo-luminescent LC.

It is obvious that this volume cannot be fully comprehensive, but at least it should provide a rough overview, covering some of the important subjects in the field of liquid crystal design and self-assembly. Nevertheless, I hope the present volume will be highly informative and inspiring for chemists and physicists who are interested in developing new materials based on the unique combination of order and mobility provided by the LC state.

Contents

Fluorinated Liquid Crystals: Design of Soft Nanostructures and Increased Complexity of Self-Assembly by Perfluorinated Segments	1
Carsten Tschierske	
Liquid Crystalline Crown Ethers	109
Martin Kaller and Sabine Laschat	
Star-Shaped Mesogens – Hekates: The Most Basic Star Structure with Three Branches	193
Matthias Lehmann	
DNA-Based Soft Phases	225
Tommaso Bellini, Roberto Cerbino, and Giuliano Zanchetta	
Polar and Apolar Columnar Phases Made of Bent-Core Mesogens	281
N. Vaupotič, D. Pocięcha, and E. Gorecka	
Spontaneous Achiral Symmetry Breaking in Liquid Crystalline Phases	303
H. Takezoe	
Nanoparticles in Liquid Crystals and Liquid Crystalline Nanoparticles	331
Oana Stamatiou, Javad Mirzaei, Xiang Feng, and Torsten Hegmann	
Stimuli-Responsive Photoluminescent Liquid Crystals	395
Shogo Yamane, Kana Tanabe, Yoshimitsu Sagara, and Takashi Kato	
Index	407

Fluorinated Liquid Crystals: Design of Soft Nanostructures and Increased Complexity of Self-Assembly by Perfluorinated Segments

Carsten Tschierske

Abstract The effects of perfluorinated and semiperfluorinated hydrocarbon units on the self-assembly of rod-like, disc-like, polycatenar, taper- and star-shaped, dendritic, and bent-core liquid crystalline (LC) materials is reviewed. The influence of fluorinated segments is analyzed on the basis of their contributions to the cohesive energy density, molecular shape, conformational flexibility, micro-segregation, space filling, and interface curvature. Though the focus is on recent progress in the last decade, previous main contributions, general aspects of perfluorinated organic molecules, and the basics of LC self-assembly are also briefly discussed to provide a complete overall picture. The main focus is on structure-property-relations and the use of micro-segregation to tailor mesophase morphologies. Especially polyphilic molecules with perfluorinated segments provide new modes of LC self-assembly, leading to ordered fluids with periodic multi-compartment structures and enhanced complexity compared to previously known systems.

Keywords Columnar mesophase · Cubic mesophase · Dendrimer · Liquid crystal · Metallomesogen · Micro-segregation · Organic semiconductor · Perfluorinated molecule · Polyphilic molecule · Self-assembly

Contents

1	Introduction	3
1.1	Liquid Crystal Self-Assembly	3
1.2	Fluorinated Liquid Crystals	10
1.3	Special Properties of Perfluorinated Organic Compounds	11

C. Tschierske

Institute of Chemistry, Organic Chemistry, Martin-Luther University Halle-Wittenberg,
Kurt-Mothes Str. 2, 06120 Halle/Saale, Germany
e-mail: carsten.tschierske@chemie.uni-halle.de

2	R _F -R _H -Diblocks: The Simplest Apolar Thermotropic LC	17
2.1	Semiperfluorinated <i>n</i> -Alkanes	17
2.2	R _F -R _H -Diblocks with an Additional Linking Unit	20
3	Linear, Taper-Shaped, and Dendritic Molecules with R _F -Chains	22
3.1	Smectic Phases of Liquid Crystals with One Aromatic Ring and One R _F -Chain ..	22
3.2	Taper Shaped and Dendritic Molecules Leading to Curved Aggregates	25
4	Rod-Like Liquid Crystals with Fluorinated Chains	36
4.1	Rod-Like Liquid Crystals with One (Semi)Perfluorinated Chain: Double Layer Smectic Phases	37
4.2	Rod-Like Liquid Crystals Combining R _H - and R _F -Chains: Monolayer Smectic Phases	40
4.3	Chiral SmC _A * Phases and de Vries Phases	44
4.4	Rod-Like Liquid Crystals with Two Fluorinated Chains at Opposite Ends: Layer Frustration	46
4.5	Polycatenar Liquid Crystals	51
5	Discotic Liquid Crystals	53
6	Metallomesogens	56
7	Polyphilic Liquid Crystals	60
7.1	Ternary Amphiphiles with Star-Like Shape	61
7.2	Liquid Crystal Honeycombs and Other Complex Phase Structures of T-Shaped Ternary Amphiphiles	64
7.3	Polyphiles with Bent Aromatic Cores: Trigonal Columnar Phases	74
7.4	X-Shaped Polyphiles: Liquid Crystalline Honeycombs with Single Molecule Walls	75
7.5	X-Shaped Tetraphiles: Liquid Crystalline Multicolor Tilings	75
8	Bent-Core Mesogens with Perfluorinated Segments	81
9	Dimesogens, Oligomesogens, Dendrimers, and Polymers	83
9.1	Dimesogens	83
9.2	Oligomesogens	85
9.3	Dendrimers	86
9.4	Polymers	89
10	Attractive Interactions Induced by Fluorination	92
10.1	Perfluorinated Aromatics	92
10.2	Partially Fluorinated Aliphatic Units	94
10.3	Supramolecular LC by Halogen Bonding	94
11	Synthetic Aspects	95
12	Summary and Conclusions	96
	References	98

Abbreviations

1D/2D/3D	One- two-, three-dimensional
a_{hex}	Hexagonal lattice parameter
CED	Cohesive energy density
Col	Columnar phase
Col _{hex}	Hexagonal columnar phase
Col _{ob}	Oblique columnar phase
Col _{ortho}	Orthorhombic “columnar” phase
Col _{rec}	Rectangular columnar Phase
Col _{squ}	Square columnar phase

Cr	Crystalline solid
Cub _I	Spheroidic (micellar) cubic phase
Cub _V	Bicontinuous cubic phase
<i>d</i>	Layer periodicity
E	Crystalline E phase
G	Glassy state
HT	High temperature phase
Iso	Isotropic liquid
Iso _{re}	Re-entrant isotropic phase
<i>l</i>	Molecular length
Lam _N	Laminated nematic phase
Lam _{Sm/cor}	Correlated laminated smectic phase
Lam _{Sm/dis}	Non-correlated laminated smectic phase
LC	Liquid crystal/Liquid crystalline
LT	Low temperature phase
M	Unknown mesophase
N/N*	Nematic phase/Chiral nematic Phase
R _F	Perfluoroalkyl chain
R _H	Alkyl chain
R _{Si}	Carbosilane chain
SmA	Smectic A phase (nontilted smectic phase)
SmA _d /SmC _d	Double layer SmA/SmC phase
SmB	Smectic B phase
SmC	Smectic C phase (synclinc tilted smectic C phase)
SmC*	Chiral (synclinc tilted) smectic C phase
SmC _A *	Chiral anticlinc tilted (antiferroelectric switching) SmC phase
SmCP _A	Antiferroelectric switching polar smectic C phase
SmCP _F	Ferroelectric switching polar smectic C phase
SmC _α *	Chiral smectic C alpha phase
SmI _A *	Chiral antiferroelectric switching smectic I phase
SmX	Smectic phase with unknown structure
UCST	Upper critical solution temperature
XRD	X-ray diffraction

1 Introduction

1.1 Liquid Crystal Self-Assembly

Liquid crystals (LC) represent truly fascinating materials in terms of their properties, their importance for the fundamental understanding of molecular self-assembly, and their tremendous success in commercial applications [1, 2]. Liquid crystals can be considered as a state of matter which in a unique way combines order and mobility [3–8]. The constituent molecules of LC phases are sufficiently

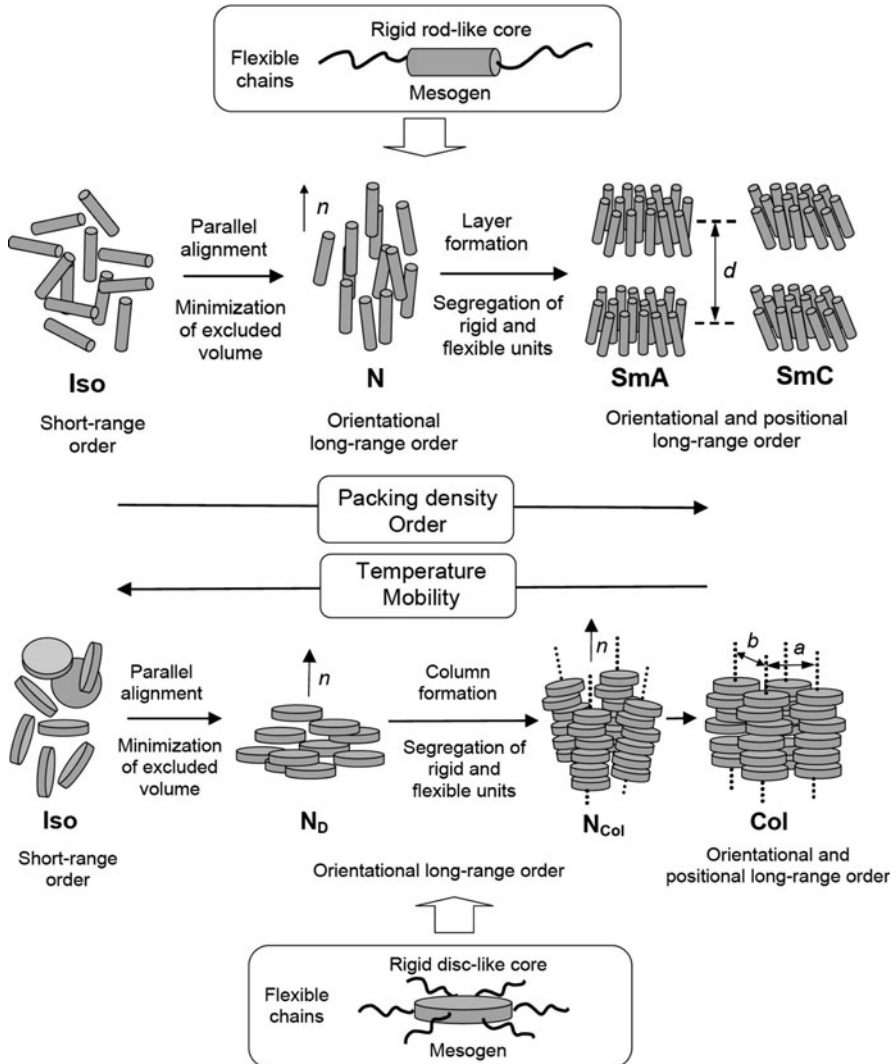


Fig. 1 Organization of rod-like molecules (*top*) and disc-like molecules (*bottom*) in LC phases (for clarity the alkyl chains are not shown in the models of the phase structures). Abbreviations: *Iso* isotropic liquid state; *N* nematic LC phase; *SmA* smectic A phase, *SmC* smectic C phase (tilted), *Col* columnar phase [8]

disordered to generate softness and even flow properties, yet comprising varying degrees of ordering depending on the actual type of liquid crystal phase (Fig. 1). Hence, depending on the rheological properties, liquid crystals can be considered as anisotropic soft matter or anisotropic fluids with interesting application properties. Liquid crystalline phases usually occur in a distinct temperature range between the

crystalline solid state (Cr) and the isotropic liquid state (Iso). Therefore, such phases are also called mesophases, and the compounds that exhibit such behavior are called mesogens or liquid crystals.

The *nematic* phase (N) is the least ordered, and hence the most fluid liquid crystal phase. The order in this type of LC phases is based on a rigid and anisometric (in most cases rod-shaped or disc-shaped) molecular architecture. Such molecules tend to minimize the excluded volume between them, and this leads to long range orientational order. For rod-like molecules the ratio between molecular length and its broadness determines the stability of the nematic phase with respect to the isotropic liquid state and the stability rises with increase of this ratio. In most cases the rigid cores are combined with flexible chains, typically alkyl chains, which hinder crystallization and in this way retain fluidity despite of the onset of order.

The combination of rigid and flexible segments in one molecule can lead to *amphiphilicity* if these chains are sufficiently long. This gives rise to nano-scale *segregation* of the rigid cores and flexible chains which is an important route to positional long range order, providing layer-like LC structures for rod-like molecules and columnar aggregates for disc-like molecules; see Fig. 1 [3, 4, 9, 10].

Layer structures (*smectic phases*, Sm) have a periodicity in only one direction (the distance d between the layers) and these phases can be further classified according to the order in the layers. If there is no order or rod-like anisometric units which adopt an orientation with the director n on average perpendicular to the layer planes, then the phase is assigned as SmA (Fig. 1). If anisometric units adopt a uniformly tilted configuration, the phase is assigned as SmC. With increasing order in the layers additional types of higher ordered smectic phases can arise (e.g., SmB, E, G. . .) [11]. Columnar aggregates assemble on a periodic 2D lattice, leading to *columnar phases* (Col) [12, 13].

Amphiphilicity is a very general driving force for molecular self-assembly and, besides the rigid-flexible amphiphiles [14] mentioned above, any other type of incompatibility can generate long range positional order. The most important are the polar/apolar incompatibility, leading to polar amphiphilic LC [15–18], and the incompatibility between hydrocarbons and fluorocarbons (“apolar” amphiphiles), but the combination of segments with a distinct shape, for example rod-like and disc-like can also lead to an amphiphilic structure (shape amphiphiles [19, 20]). Due to the very different kinds of amphiphilicity occurring in LC systems, which are often combined, it is difficult to describe them theoretically and to make precise quantitative predictions such as, for example, developed for lyotropic systems [21, 22] and block copolymers [23].

The concept of *micro-segregation*, (*nano-segregation* is used synonymously) developed for these thermotropic LC systems, is based on the approximation that micro-segregation of the two incompatible components of a binary amphiphile into two distinct nano-spaces can be related to the ability of macroscopic segregation (demixing) of two immiscible liquids with molecular structures similar to the two segments forming the amphiphile [6, 9, 10, 24, 25]. The Gibbs free energy of mixing of two liquids (ΔG_{mix}) must be positive (endergonic) for demixing. The free

energy term can be split into an enthalpic and an entropic contribution according to $\Delta G_{\text{mix}} = \Delta H_{\text{mix}} - T\Delta S_{\text{mix}}$. The mixing enthalpy (ΔH_{mix}) is related to the difference in cohesive energy density (CED, c) of the two components (A, B), i.e., $\Delta H_{\text{mix}} \sim (c_A - c_B)$. The CED can be calculated from the vaporization enthalpy (ΔH_V) and the molar volume (V_m) according to $c = (\Delta H_V - RT)/V_m$ or, alternatively, from the surface tension (γ) and the molar volume by $c = \gamma/V_m^{1/3}$. The Hildebrand solubility parameter (δ) [26] is the square root of the cohesive energy density $\delta = c^{1/2}$ and hence these parameters, which are tabulated [27, 28], can be used to estimate whether two molecules would mix or not. If these two molecules are interconnected in an amphiphile the degree of incompatibility of the two segments decides whether nano-scale segregation could take place. The larger the difference $\delta_A - \delta_B$ the larger the incompatibility and the higher the mesophase stability.¹ Segregation works against the entropy of mixing and hence segregation is favored for larger molecules because there are less molecules per volume unit and therefore in this case the influence of the mixing entropy to the entropy term ($-T\Delta S_{\text{mix}}$) is smaller than for small molecules. As ΔS_{mix} is positive and coupled with temperature ($-T$) it becomes more important at higher temperature. This reduces ΔG_{mix} and, as soon as it approaches zero and becomes negative, segregation is lost at the order-disorder transition temperature, also assigned as clearing temperature in LCs. It should be pointed out that the mesophase stability is independent from the total value of the cohesive energy density of the components; this only influences the transition from the liquid to the gaseous state, i.e., the complete isolation of the molecules (vaporization). Segregation is the reverse of mixing which is the separation of molecules by other molecules and this is driven by the *difference* in cohesive energy density between the two types of molecules (macroscopic demixing) or the distinct segments forming an amphiphilic mesogens (micro-segregation). Therefore, the stability of a positional ordered mesophase increases with growing *difference* of solubility parameters ($\Delta\delta$) of the two components which is equivalent to the difference in CED (Δc). Because it is the difference between the CEDs of the distinct segments of an amphiphilic mesogens which determines the mesophase stability and not their absolute values, an increase of mesophase stability can also be achieved by *reducing* the CED of one of the incompatible segments of an amphiphile. This is important for understanding mesophase stabilization by the

¹ More detailed analysis is possible with the Hansen solubility parameters where the total solubility parameter (δ_t), which corresponds to the Hildebrand parameter (δ) is split into contributions by dispersion (δ_d), dipolar interactions (δ_p) and hydrogen bonding (δ_h) [28].; for complex molecules the solubility parameters can be estimated from segmental group contributions. Estimation of the incompatibility of segments in LC molecules is also possible by means of the Flory interaction parameter $\chi = (\delta_A - \delta_B)^2 V_r (RT)^{-1}$ (V_r = relative volume = average volume of the repeat units), used for polymer solutions and allows direct the calculation of the Gibbs free energy. χN (N = number of repeat units, related to the size of the molecule) expresses the enthalpy-entropy balance and the larger the value, the stronger the segregation [23]. The disadvantages of these estimations are that they refer only to room temperature and do not consider the rigid flexible incompatibility, which is present in most LC molecules (rod-like, disc-like).

Table 1 Phase transitions, Flory interaction parameters (χ), free energies (ΔG) and differences of Hildebrand solubility parameters ($\Delta\delta$) depending on the molecular structure (fluorination of the alkyl chain) [25]

Formula	Phase transitions (°C)	χ	ΔG (kJ mol ⁻¹)	$\Delta\delta^a$
Ph-Ph-CH=N-C ₆ H ₁₃	Non-LC	2.5	-0.07	7.2
Ph-Ph-CH=N-CH ₂ CH ₂ -C ₄ F ₉	Cr 48 Sm 68 Iso	6.0	+0.44	10.3

^a δ -parameters used: Ph-Ph-CH=N: $\delta = 23.3$; C₆H₁₃: $\delta = 16.1$; CH₂-CH₂C₄F₉: 13.0

fluorophobic effect, as the CED of fluorinated alkyl chain is usually the lowest of all possible LC building blocks (see Sect. 1.3). Despite the total CED being reduced (i.e., the attractive forces between the molecules are reduced!) by perfluorination of the alkyl chains of the mesogens, the difference of the cohesive energy densities between the segments is increased. Therefore, fluorination usually leads to mesophase stabilization, as shown in Table 1 for a representative example. Though these considerations are simplified, they provide a fundamental understanding of the structure-property relations in nano-segregated LC systems and allow a comparison of related molecules and the effect of structural variations on the mesophase stability.

Segregation of the incompatible molecular segments takes place with formation of distinct nano-compartments organized on a one-dimensional (1D), two-dimensional (2D), or three-dimensional (3D) periodic lattice, separated by interfaces. These interfaces tend to be minimal in order to reduce the interfacial energy stored in the system. For amphiphilic molecules without anisometric segments (flexible amphiphiles) the mesophase type is mainly determined by the relative volume of the two incompatible segments, as shown in Fig. 2.

Lamellar phases (= smectic phases, Sm), composed of stacks of alternating layers, have flat interfaces between the micro-segregated regions (layers) and these structures are formed by molecules for which the incompatible segments have comparable sizes and hence require comparable cross section areas at the interfaces. If the size of one segment is increased the layers become unstable and a curvature of the interfaces arises. In this case the layers are replaced by columns, followed by spheroidic aggregates with increasing interface curvature (Fig. 2) [21]. Self-assembly of circular columns takes place on a hexagonal lattice, leading to hexagonal columnar phases (Col_{hex}) providing minimized interfaces compared to non-circular columns forming square (Col_{sq}), rectangular (Col_{rec}), or oblique (Col_{ob}) 2D lattices [29]. Formation of these non-hexagonal columnar phases requires additional contribution from the molecular shape.

Self assembly of spheroidic aggregates leads in most cases to *micellar cubic phases* (Cub_I) [30–35], where closed spheroidic aggregates are organized on a cubic 3D lattice (Fig. 2d,e).²

²Common cubic space groups in thermotropic LC systems: Cub_V: *Ia3d*, *Im3m* (*Pn3m*); Cub_I: *Pm3n*, *Im3m*.

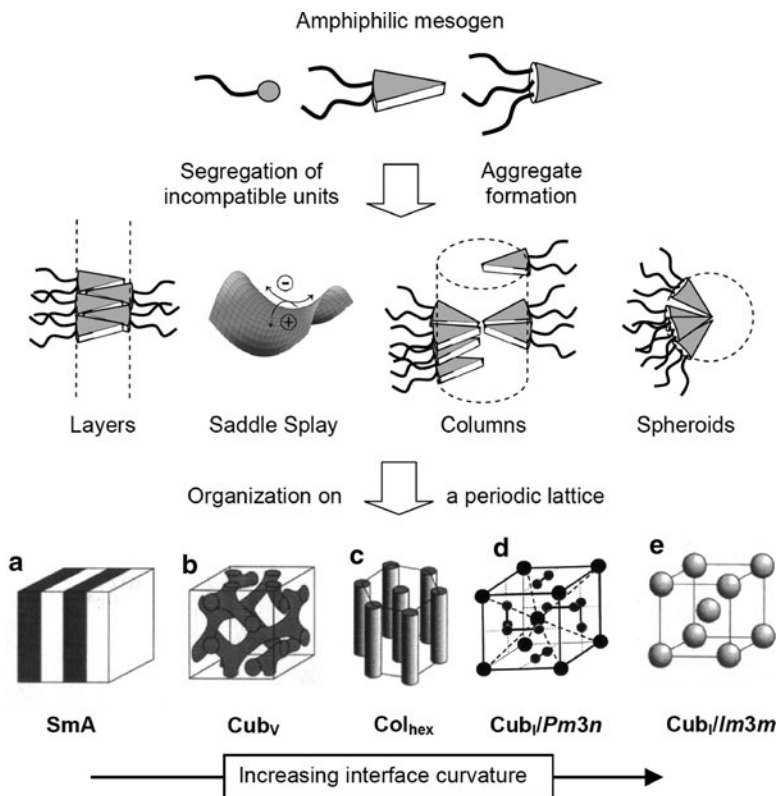


Fig. 2 Fundamental modes of self assembly of binary amphiphiles depending on the volume ratio of the two incompatible units

There is a second kind of cubic phases, assigned as *bicontinuous cubic phases* (abbreviated as Cub_V) which can occur at the transition between lamellar and columnar organization [35, 36]. In these cubic phases the layers develop saddle splay curvature (see Fig. 2) and adopt the shape of infinite minimal surfaces. Alternatively, these bicontinuous cubic phases could be considered as resulting from a branching of columns; these branched columns are interconnected at distinct nodes to give rise to two interwoven continuous networks (Fig. 2b) [32, 37, 38]. Both descriptions can be regarded as equivalent, one considering the regions of the alkyl chains and the other the segregated mesogenic cores. Depending on the shape of the infinite minimal surfaces and on the number of columns interconnected at each branching point, respectively, quite distinct structures could result which are again classified according to space group symmetry [29].² Although there is 3D-long range order in density fluctuations, cubic and other 3D mesophases are still regarded as liquid crystalline as long as there is no preferred position for individual molecules, i.e., as long as there is a diffuse wide-angle X-ray scattering.

Whereas formation of nematic phases usually requires a specific rod-like or disc-like molecular shape, this is not the case for mesophases based on nano-segregation [9, 10]. Any amphiphilic molecule can adopt the mesophase morphologies shown in Fig. 2a–e, depending on the size ratio of the incompatible units. However, a specific molecular shape can lead to a preference for a distinct type of self assembly. Generally, rod-like molecules prefer to be organized in layers as they tend to avoid the splay occurring in curved aggregates. Disc-like molecules provide curvature in their molecular structure and therefore preferably form columnar LC phases. Taper-shaped or cone-like molecules tend to form columnar and micellar cubic phases with strong interface curvature [31, 35, 39]. However, it is not always the case that self-assembly of anisometric units and amphiphilic self-assembly enhance each other. These two modes of self assembly can also be in competition and this can modify the mesophase morphology. For example, disc-like molecules can, under certain conditions, organize in layers (lamello-columnar phases) and rod-like molecules can form ribbons organized on a 2D lattice (assigned as modulated smectic phases or ribbon phases). Similarly, taper shaped molecules can arrange antiparallel and form layers (Fig. 2). If this competition provides significantly strong frustration, it can either lead to disorder (occurrence of isotropic or nematic phases) [40, 41] or, alternatively, to completely new LC structures [8]. Hence, competition is a way to new LC phases. Another alternative way to increased mesophase complexity consists in the combination of more than two incompatible units, leading to *polyphilic LC* (see Sect. 7) [8, 10, 42].

Depending on temperature, transitions between distinct types of LC phases can occur.³ All transitions between various liquid crystal phases with 0D, 1D, or 2D periodicity (nematic, smectic, and columnar phases) and between these liquid crystal phases and the isotropic liquid state are reversible with nearly no hysteresis. However, due to the kinetic nature of crystallization, strong hysteresis can occur for the transition to solid crystalline phases (overcooling), which allows liquid crystal phases to be observed below the melting point, and these phases are termed monotropic (monotropic phases are shown in parenthesis). Some overcooling could also be found for mesophases with 3D order, namely cubic phases. The order–disorder transition from the liquid crystalline phases to the isotropic liquid state (assigned as clearing temperature) is used as a measure of the stability of the LC phase considered.⁴

Besides molecular shapes and amphiphilicity, chirality also has a large influence on LC self assembly, leading to series of LC phases with helical superstructures, reduced symmetry, and chirality induced frustration [43–46].

Also mesogens with more complex shapes, such as, for example, those with bent aromatic cores (bent-core mesogens [47]), star mesogens [48], or cone-like

³ Phase transitions can also take place depending on the concentration of a solvent [37, 38]. These lyotropic phases will not be considered here.

⁴ This should not be mixed up with the existence range of a mesophase which also depends on the stability of an adjacent crystalline or other LC phases.

molecules are of contemporary interest, together with LC states formed by biomolecules [49–51], polymers, dendrimers, or network structures (gels, elastomers) [52–54]. The huge number of possible molecular and supramolecular structures and the complex relations between molecular shape, nano-scale segregation, and symmetry of molecular packing leads to a large number of self assembled LC structures, which is continuously growing.

Due to inherent fluidity these self-organized LC structures have the ability to change their configuration under the influence of *external stimuli* (surfaces, electric, magnetic, and mechanical fields) and to eliminate defects by *self-healing*. Therefore, this special state of matter is not only of interest for displays, adaptive optics, information storage, and nano-patterning – it provides a very general way to assemble functional molecules/materials into well defined superstructures. This can be used in technology, and it is an important concept of molecular self assembly in biosystems [55].

1.2 Fluorinated Liquid Crystals

Fluorination of LC provides a powerful tool for the design of new LC materials with unusual and practically important properties. The specific effects of F in organic molecules result from a unique combination of high polarity and low polarizability, as well as steric and conformational effects (see next section).

Fluorination of the rigid (in most cases rod-like) core of LC molecules provides LC materials with high positive (terminal substitution) or negative (lateral substitution) dielectric anisotropy ($\Delta\epsilon$), due to the high polarity of the C–F bond. It also leads to LC materials with low ion-solvation capability, due to the low polarizability and hence low Lewis basicity of covalently bound F. High $\Delta\epsilon$ and low ion conductivity are key requirements of all commercial LC mixtures used for LC display applications [56]. Small fluorinated substituents (CF_3) and segments (OCF_2) are also incorporated in these materials to reduce the elastic constants and to increase the dielectric anisotropy. In addition, F-substituents attached to alkyl chains or alicycles can affect molecular conformations due to stereoelectronic effects, such as the *gauche* effect and the *anomeric* effect [57, 58]. Representative examples of core fluorinated LC are shown in Fig. 3. This field has recently been reviewed by Hird [59, 61, 62] and others [63–65] and therefore will not be considered here. Focus of this review will be on LCs incorporating larger perfluorinated segments, specifically on molecules incorporating perfluoroalkyl chains with a special focus on molecular structures capable of providing new LC phases and an enhanced complexity in LC self assembly.

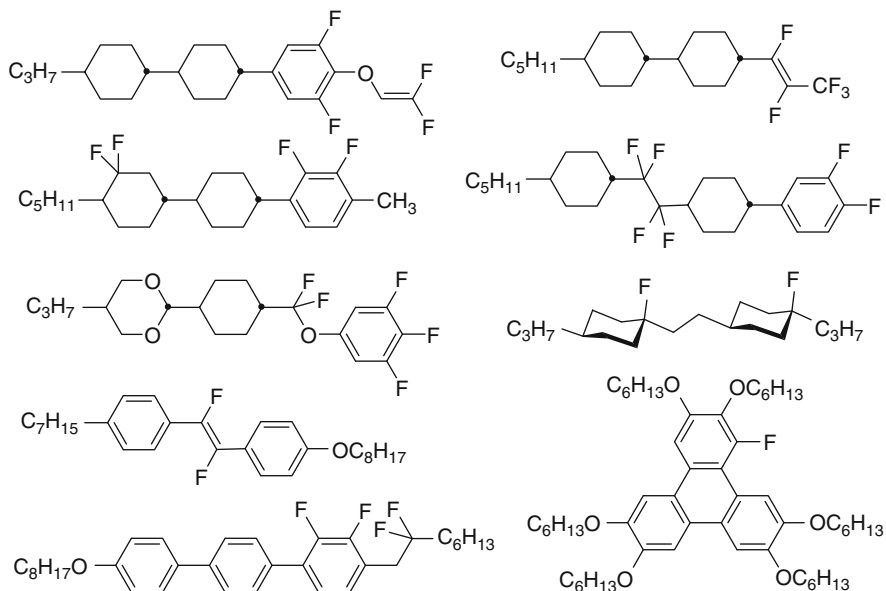


Fig. 3 Examples of LC with fluorinated core units (examples selected from [59] and [60])

1.3 Special Properties of Perfluorinated Organic Compounds

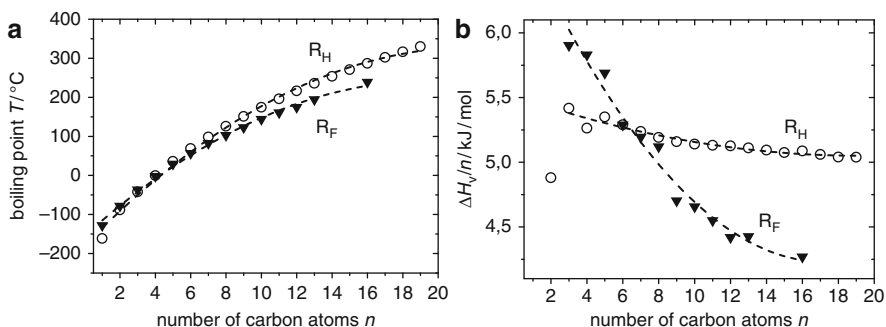
In order to provide a background of knowledge and understanding of the effects of polyfluorination on self-assembly, the fascinating and unusual properties of polyfluorinated organic compounds are briefly discussed [66–73]. There are two major effects which determine the specific properties of perfluorinated alkanes compared to analogous nonfluorinated alkanes, namely the high electronegativity of fluorine, leading to reduced polarizability and reduced intermolecular interactions, and the increased size of F compared to H which increases the molecular volume and surface area (Table 2). The distinct size also influences the molecular conformations and reduces the flexibility of linear fluorocarbon chains.

The intermolecular interactions in fluorocarbons are strongly chain length dependent. This is evident from Fig. 4a,b comparing the chain-length dependence of boiling points and vaporization enthalpy values for alkanes and perfluoroalkanes [75]. The shorter perfluoroalkanes have higher boiling points and higher vaporization enthalpies than the related hydrocarbons. However, for $n > 4$ the boiling points and for $n > 5$ the vaporization enthalpies of the fluorinated hydrocarbons become lower than those of the hydrocarbons and the difference becomes larger with increasing chain length. Also high level ab initio calculations show that for small molecules (CH_4/CF_4 and $\text{C}_2\text{H}_6/\text{C}_2\text{F}_6$) the intermolecular interactions between fluorocarbons are stronger than between hydrocarbons [76], whereas for $\text{C}_3\text{H}_8/\text{C}_3\text{F}_8$ it is reversed [77]. A main effect influencing the intermolecular interactions is the intermolecular separation (C...C distance), which is similar for CF_4 and CH_4 (0.40

Table 2 Comparison of common parameters of H- and F-substituents in organic compounds [59, 66]

	H	F
Electronegativity (Pauling)	2.1	4.0
Polarizability/ 10^{-25} cm^{-3}	6.67	5.57
Van der Waals radius/nm	0.120	0.147
C-X Dipole moment/D	0.4	1.41
C-X Bond length/nm	0.11	0.14
CX ₂ cross sectional area/nm ²	0.18–0.21 ^a	0.27–0.30
CX ₂ volume/nm ³	0.027	0.038
CX ₃ volume/nm ³	0.054	0.092

^aThe cross sectional area of a biphenyl unit in the LC state is estimated as 0.20–0.22 nm² [74]

**Fig. 4** (a) Boiling points and (b) vaporization enthalpies, normalized to the chain length ($\Delta H_{v/n}$), for n -alkanes and n -perfluoroalkanes depending on the chain length n , based on values from [75]

and 0.38 nm, respectively [76]) and increases for C₃F₈ to 0.48 nm, whereas it remains nearly constant for longer n -alkanes (e.g., C₃H₈ 0.40 nm) [77]. Longer R_F-chains adopt a helical conformation (see below) which further increases the intermolecular distances. As a consequence, introduction of small fluorinated groups, especially CF₃, can have different effects compared to longer fluorinated chains. For example, CF₃ groups at the end of an alkyl chain reduce the lipophilicity and enhance hydrophilicity [67],⁵ whereas longer R_F-segments always increase lipophilicity and reduce hydrophilicity.

Typically, relatively long fluorinated segments (C_{*n*}F_{2*n*+1} with $n = 4$ –12 in most cases) were used in the LC molecules, and therefore we focus attention on these perfluoroalkanes. Perfluoro- n -hexane, as a representative example for this type of

⁵ However, this is mainly due to the relatively strong dipole moment provided by the CH₂-CF₃ linkage.

Table 3 Comparison of selected properties of hydrocarbons, perfluorinated and semiperfluorinated hydrocarbons [66]

	C ₆ H ₁₄	H ₇ C ₃ -C ₃ F ₇	C ₆ F ₁₄
<i>M</i> /g mol ⁻¹	86	212	338
<i>b.p.</i> /°C	69	64	57
Density ρ /g cm ⁻³ (25 °C)	0.67	1.27	1.67
Viscosity η /cP	0.29	0.48	0.66
Surface tension γ /dyn cm ⁻¹	17.9	14.3	11.4
Dielectric constant ϵ	1.9	6.0	1.7

molecules, has a 12 K lower boiling point than *n*-hexane despite a much higher molecular weight.⁶ The low polarizability of fluorine, as a consequence of its high electronegativity, is the main reason for the lower boiling point, reflecting the reduced cohesive energy density (CED)⁷ provided by the perfluorinated alkanes, despite their much higher electron density.⁸ The weak intermolecular forces between perfluoroalkanes result in very low surface tensions of perfluorinated liquids and very low surface energies of perfluorinated solids. Perfluorohexane is also less polar than hexane and has a lower dielectric constant (Table 3), which is unexpected, considering the highly polar nature of the C–F bond. However, the symmetry of completely perfluorinated hydrocarbons causes a cancellation of the local dipoles. For the same reason perfluoroalkyl compounds usually do not engage in hydrogen bonding [78].

The larger size of F compared to H (but comparable with that of oxygen) increases the cross sectional area of R_F-chains with respect to R_H-chains by about 30% and the volume by about 40–60%, depending on the chain length. The size difference between CH₃ and CF₃ is especially large, the CF₃ group actually being comparable in size with an isopropyl group and hence the size difference is larger for shorter R_F-chains. Due to this size difference R_F-chains also display larger surface areas than R_H-chains, which contributes to reduced CED and enhanced hydrophobicity leading to a higher incompatibility with polar molecules [79, 80].

The larger size of fluorine also influences the conformational flexibility of linear perfluorinated chains which is significantly reduced compared to R_H-chains [81] and changes the major conformation from *linear all-trans* for R_H to *helical all-trans* for long R_F-chains with a twisting of about 12–15° around each C–C bond [82–84]. Though the individual helices are chiral there is a fast helix inversion and the chirality is not fixed. This helix inversion significantly contributes to R_F-chain mobility which is more based on sliding and rotation instead on chain folding. A planar *all-trans* conformation can only be found for short R_F-chains [85] and could be promoted by

⁶ If the boiling points are correlated with the molecular volumes the difference appears much smaller.

⁷ The CED (*c*) is directly related to the vaporization enthalpy by the equation: $c = (\Delta H_V - RT)/V_m$, (V_m = molecular volume); ΔH_V is related to the boiling point.

⁸ In fact the boiling points of the perfluoroalkanes are only about 25–30 K higher than those of noble gases with similar molecular mass, i.e. the CEDs of perfluoroalkanes are comparable with gases and hence gases have a high solubility in perfluoroalkanes.

Table 4 Comparison of selected UCST of hydrocarbon (C_mH_{2m+2})+fluorocarbon (C_nF_{2n+2}) mixtures depending on the chain lengths m, n

$F_n + H_m$ [90]	$T/^\circ\text{C}$	$F7 + Hm$ [91]	$T/^\circ\text{C}$	$F_n + H6$ [92]	$T/^\circ\text{C}$
F5 + H5 [89]	-7	F7 + H5	9	F3 + H6	2
F6 + H6	22	F7 + H8	60	F4 + H6	8
F7 + H7	50	F7 + H10	104	F6 + H6	22
F8 + H8	77	F7 + H12	141	F7 + H6	30
		F7 + H15	194	F8 + H6	41

linkage to less bulky R_H -chains [86, 87]. The increased stiffness of the R_F -chains (reduced occurrence of gauche defects, *trans/gauche* interchange energy is 4.6 vs. 2.0 kJ mol⁻¹ for R_F - and R_H -chains, respectively [73, 81]) compared to alkyl chains is reflected in the higher viscosity of perfluorohexane compared to hexane and facilitates chain stacking and crystallization. The combination of reduced cohesive energy density and enhanced crystallization tendency narrows the liquid phase existence region of perfluoroalkanes with increasing chain length (e.g., $C_{12}H_{26}$: Cr -10 °C Liq 216 °C Gas vs. $C_{12}F_{26}$: Cr 77 °C Liq 178 °C Gas).

Besides being more hydrophobic R_F -chains are also lipophobic. For this reason fluorocarbons and hydrocarbons have a relatively large positive (endothermic) heat of mixing and tend to segregate. The energy needed to transfer one CH_2 group from a hydrocarbon to a fluorocarbon phase amounts to 1.4 kJ/mol which is only one third compared to the 3.7 kJ/mol required for the transfer of one CH_2 from a hydrocarbon to water [88]. Accordingly, the lipophobic effect of R_F -chains (or fluorophobic effect of alkyl chains) is only about one third of the hydrophobic effect. Hence, the demixing tendency of R_F and R_H is weaker than for hydrocarbons and water and is strongly chain length dependent.

The upper critical solution temperature (UCST) provides a measure for the tendency of liquids to demix and this rises with growing chain length [89, 90], as shown in Table 4 (left). Immiscibility over the complete liquid and solid state regions can be found for mixtures of alkanes and perfluoroalkanes with $n \geq 12$ [93]. It is quite interesting that the UCST strongly depends on the length of the hydrocarbon chain (middle columns in Table 4) [91], whereas it is much less sensitive to the R_F -chain length (Table 4 right columns) [92].

The reason for the experimentally proven lipophobicity, i.e., the tendency of fluorinated and hydrogenated chains to phase separate, is much less clear than the other effects of fluorination and is still under debate. Mostly it is assigned to the disparity of cohesive energy densities between perfluoroalkanes and alkanes. A reduction of ca. 10% in the interactions between unlike pairs of molecules was estimated by several methods [90]. However, there are also simulations suggesting slightly stronger attractive contributions to the interaction between R_F/R_H pairs compared to the like interactions under certain circumstances [94].⁹ However,

⁹As the main contribution to polarizability comes from the carbon frame and the dispersion interactions strongly decrease with the distance, the contribution of this interaction should be larger

Table 5 Comparison of the boiling points of linear and branched alkanes and perfluoroalkanes with the same number of carbon atoms [67]

	$T^{\circ}\text{C}$ (X=F)	$T^{\circ}\text{C}$ (X=H)
<i>n</i> -C ₄ X ₁₀	29	36
<i>iso</i> -C ₄ X ₁₀	30	28
<i>tert</i> -C ₄ X ₁₀	30	10

perfluoroalkanes and alkanes also have a large positive volume change on mixing with values up to $5.5\text{ cm}^3\text{ mol}^{-1}$, which belongs to the largest known for non-electrolyte systems. This indicates a different packing in hydrocarbons and fluorocarbons and this is in line with a weaker $R_{\text{F}}/R_{\text{H}}$ interaction compared to the $R_{\text{F}}/R_{\text{F}}$ and $R_{\text{H}}/R_{\text{H}}$ interactions [95]. It must also be considered that at least part of the incompatibility between R_{F} - and R_{H} -chains might arise from their distinct shape (shape incompatibility) and flexibility (rigid-flexible incompatibility), as a stretching of the flexible alkyl chains between the rigid R_{F} -chains leads to a considerable entropic penalty. This is also in line with the strong effect of the alkyl chain length on the $R_{\text{F}}/R_{\text{H}}$ miscibility (see above).

Overall, the $R_{\text{F}}/R_{\text{H}}$ incompatibility seems to be mainly an exclusion effect. In order to maximize the stronger like-interactions between the non-fluorinated moieties, the R_{F} -chains are expelled (similar to the hydrophobic effect where hydrophobic surfaces are excluded from water [22]). Therefore, the fluorophobic effect strongly depends on the strength and the kind of intermolecular interactions between the non-fluorinated moieties. As in hydrocarbons the intermolecular interactions are relatively weak and the $R_{\text{F}}/R_{\text{H}}$ incompatibility is also weak. Increasing the intermolecular interactions by dipole interactions and hydrogen bonding provides much stronger cohesive forces and hence the incompatibility with the R_{F} -chains also becomes stronger. It should be mentioned that the use of the term “fluorophobic effect” is often not restricted to the incompatibility of alkyl chains with perfluoroalkyl chains; it is frequently used in a broader sense and refers to the segregation of highly fluorinated molecules/molecular segments from polar as well as from hydrocarbon based (hydrophobic) molecules/molecular segments, i.e., it refers to the increased “polarophobicity” as well as to the lipophobicity of fluorinated molecules/molecular segments.

Also interesting is the dependence of the UCST on molecular structural variations. Branching of hydrocarbon chains strongly reduces the UCST (e.g., F7 + *n*-H8: $60\text{ }^{\circ}\text{C}$ vs. F7 + *iso*-H8: $24\text{ }^{\circ}\text{C}$), indicating a reduced incompatibility of perfluoroalkanes with branched hydrocarbons. This is in line with the trends shown in Table 5. For the perfluoroalkanes there is practically no influence of chain

for $R_{\text{F}}-R_{\text{H}}$ interaction which allows shorter distances between the carbon frames than $R_{\text{F}}-R_{\text{F}}$ interaction. Related arguments were used to explain the attractive interactions between aromatic hydrocarbons and aromatic fluorocarbons allowing a short 3.5 nm face-to-face distance (see Sect. 10.1). However, there are also electrostatic interactions between the partial charges ($\text{C}^{(-)}-\text{H}^{(+)}$ and $\text{C}^{(+)}-\text{F}^{(-)}$) where interactions between the charges of peripheral atoms of one molecule and the carbon frame of the other provide a destabilizing contribution to the interaction between R_{F} and R_{H} chains [78].

branching on the boiling point, whereas for hydrocarbons there is a strong decrease of the boiling point upon chain branching [67]. The lower CED of branched alkyl chains makes them more compatible with perfluoroalkanes.⁷

Mixtures of perfluoroalkanes with cyclic hydrocarbons, especially benzene, lead to much higher UCSTs compared to linear hydrocarbons (e.g.: F7 + *n*-C6: 29 °C; F7 + *cyclo*-C6: 68 °C; F7 + C₆H₆: 99 °C), indicating an especially strong incompatibility [96]. This is of importance as most mesogens incorporate at least one benzene ring and these units provide an important source of incompatibility with R_F-chains.

Any increase of polarity of the hydrocarbon, for example by substitution with chlorine or by replacing CH₂ groups by ether oxygens, also increases incompatibility with perfluoroalkanes as polar interactions become more important [89, 96]. Polar groups are fundamental constituents of the mesogenic cores, especially as linking units and as substituents at aromatic moieties, and these groups increase the incompatibility between the aromatic cores and R_F-chains.

The influence of ether oxygens is very different for perfluorinated and non-fluorinated hydrocarbons. Here, the discussion is mainly focused on oligo(ethylene oxides) and their fluorinated analogs in comparison with related fluorinated and non-fluorinated alkanes. The presence of ether oxygens in alkanes usually leads to chain polarity and hydrophilicity due to the polarity of the C–O bonds and the Lewis basicity of the ether oxygens, capable of acting as proton acceptor in hydrogen bonding. Though there are additional polar interactions, the polarizability is reduced by the electronegative ether oxygens, leading to boiling points very similar to those of related *n*-alkanes (Table 6), suggesting that the total CED is similar to the *n*-alkanes and that in the absence of additional proton donors segregation of *n*-alkanes and relatively short oligo(ethylene oxides) is difficult to achieve. The ether oxygens also have a strong effect on molecular conformational equilibria (*gauche* effect, anomeric effect) and the absence of additional substituents at the oxygens increases the flexibility of the chains.

In contrast, the presence of oxygen in a fluorinated chain strongly decreases the boiling points (and hence the CED)⁷ and this effect increases dramatically with increasing oxygen content and chain length (Table 6). This is mainly due to the electron withdrawing effect of the CF₂-groups which reduce the polarity of the O–CF₂ bond compared to the O–CH₂ bond and reduces the polarizability of the electrons at the ether oxygens, effectively leading to a reduction of the

Table 6 Comparison of the boiling points (*T*/°C) of fluorinated and non-fluorinated ethers (C₃X₇ = *n*-C₃X₇), polyethers and related fluorinated and non-fluorinated alkanes [75, 97].

	Z=O		Z=CX ₂	
	X=F	X=H	X=F	X=H
X ₇ C ₃ -Z-C ₃ X ₇	56	90	82	98
X ₃ C-Z-CX ₂ CX ₂ -Z-CX ₃	17	85	57	69
X ₃ C-Z-(CX ₂ CX ₂ -Z) ₂ -CX ₃	61	162	123	151
X ₃ C-Z-(CX ₂ CX ₂ -Z) ₃ -CX ₃	105	216	175	216
X ₃ C-Z-(CX ₂ CX ₂ -Z) ₄ -CX ₃	138	276	228 [98]	271

electrostatic interactions, giving rise to reduced CED and removing the Lewis basicity [75]; i.e., the ether oxygens become similar to CF_2 , but with a much smaller size than CF_2 . This means that the R_F -chains remain hydrophobic by introduction of oxygen and it can be assumed that their hydrophobicity is even increased due to the reduced CED compared to perfluoroalkanes (compare $Z = \text{O}$, CH_2 for $X = \text{F}$ in Table 6).

As the steric interaction between the F atoms is significantly reduced by the free space around the ether oxygens of perfluoroethers, the chain flexibility is strongly increased [99] which leads to low melting points and (combined with the low CED) to low glass transition temperatures (T_g) of fluorinated polyethers which are even lower than those of the corresponding hydrocarbon based polyethers (e.g., poly(trimethylene oxide): $T_\text{g} = -78\text{ }^\circ\text{C}$ vs. poly(perfluorotrimethylene oxide): $T_\text{g} = -101\text{ }^\circ\text{C}$) [75]. Even lower melting points down to $-150\text{ }^\circ\text{C}$ can be achieved with oligo(perfluoromethylene oxides) due to the nearly free rotation around the $\text{O}-\text{CF}_2$ bonds [100]. These are the lowest melting temperatures observed for any organic compounds with comparable molecular weight. Hence, perfluorinated polyethers units could provide very interesting properties, combining low melting points with a strong fluorophobic effect, potentially leading to high mesophase stabilities and broad LC phase ranges. Though perfluoropolyethers could be expected to be advantageous over perfluorinated alkyl chains as building blocks of LC, they have rarely been used and mostly described in patents, mainly due to their limited availability and their difficult synthesis requiring reactions with elemental fluorine [97, 100, 101].

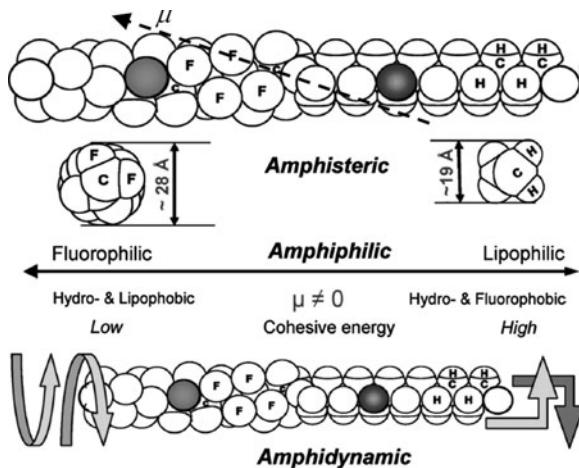
Overall, it seems that self assembly in LC structures is strongly affected by two major effects of perfluorinated segments, namely incompatibility (leading to positional order) and size effects which tend to favor curvature. In the case of linear perfluoroalkyl chains, which are used most often, there is in addition the effect of increased chain rigidity, leading to rigid-flexible incompatibility with R_H -chains and also favoring orientational order and layer formation. As the $\text{R}_\text{F}/\text{R}_\text{H}$ incompatibility is relatively weak it is often suppressed in order to optimize overall molecular packing. The incompatibility of R_F -chains with polar and aromatic molecular segments (core-structures) is much stronger than for R_H -chains and this incompatibility generally stabilizes LC phases (see Sect. 1.1).

2 R_F - R_H -Diblocks: The Simplest Apolar Thermotropic LC

2.1 *Semiperfluorinated n-Alkanes*

Combining perfluorinated (R_F) and non-fluorinated hydrocarbon chains (R_H) with a distinct minimum length leads to amphiphilicity despite the molecules being “apolar”. Incompatibility of the two segments results from shape- and packing amphiphilicity (combination of rigid linear R_F -segments with the conformationally more disordered alkyl chains), the distinct cohesive energy densities, and the

Fig. 5 Linear R_F - R_H diblocks are amphisteric (different cross sections of the F - and H -blocks), amphiphilic (distinct cohesive energy density), and amphidynamic (distinct flexibility, conformations). The *dashed arrow* indicates the direction of the dipole moment arising at the CH_2 - CF_2 connection. Reproduced with permission [66], copyright 2009, American Chemical Society (ACS)



distinct chain mobilities. Hence, these diblock molecules are not only amphiphilic, but also amphisteric and amphidynamic (see Fig. 5) [66].

R_F - R_H diblocks form layered liquid crystals with the molecules arranged in stacks of lamellae with their long axis parallel to each other and either perpendicular (SmB-like) or tilted (SmI/F-like) to the layer planes. Hence, R_F - R_H diblocks can be regarded as the most simple “apolar” liquid crystals. Typically there are temperature dependent transitions from true LC phases at higher temperature to plastic crystalline phases at lower temperature. Order in the LC phases results from the long range orientational and 1D positional order of the R_F -segments in layers and the mobility is provided by the conformationally disordered alkyl segments and rotational disorder of the R_F -segments. In the lamella the molecular packing is however frustrated due to the difference in cross section of the R_F - and R_H -chains. This mismatch can be reduced by increased conformational disorder of the flexible R_H -segments (chain melting), tilting and *interdigitation* (overlapping of similar molecular parts) or *intercalation* (overlapping of different parts) (see Fig. 6a–c). These distinct effects can be combined and give rise to a variety of possible structures, thereby retaining the flat lamellar organization. On the other hand, escape from this frustration can also be achieved by layer curvature leading to cylinder formation [105] or layer undulation/modulation [104] (see Fig. 6e,f).

Despite intensive research, the structural arrangements of R_F - R_H diblock molecules in their solid state and LC structures remain largely hypothetical as XRD patterns provide too small a number of reflections to prove unambiguously the proposed structures [66]. The present state of knowledge in this field was recently reviewed by Krafft and Riess [66] and therefore will not be discussed in detail here. Only four representative examples of non-modulated lamellar structures are shown in Fig. 6a–d; the two models on top were proposed for the LC1 (high temperature phase = HT) and LC2 (low temperature phase = LT) phases of $C_{10}H_{21}$ - $C_{10}F_{21}$ [102] and those shown in Fig. 6c,d were obtained by Monte-Carlo

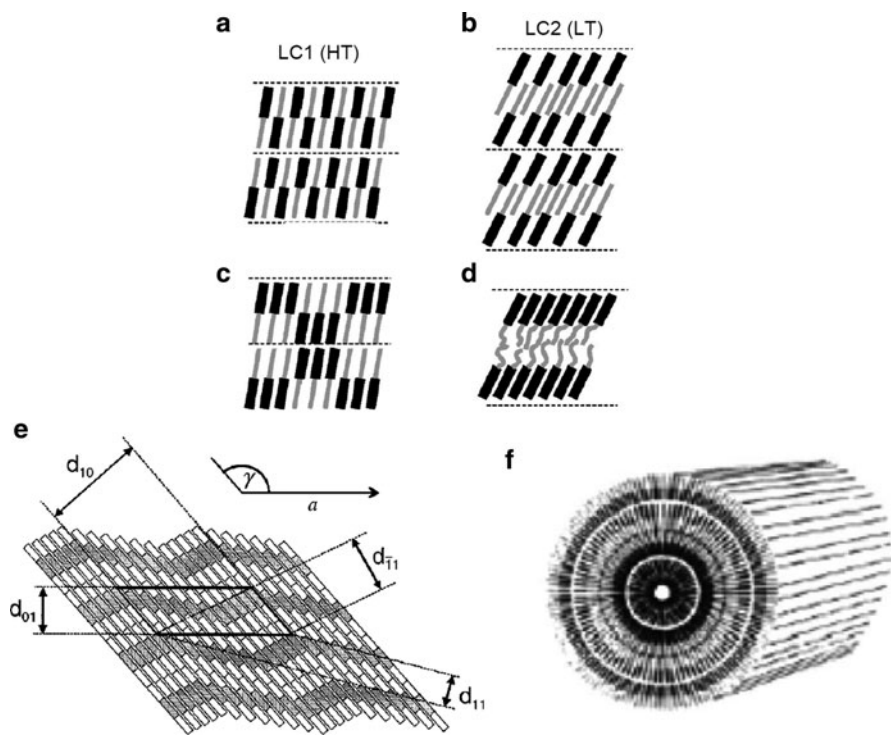


Fig. 6 Structures of mesophases of semiperfluoroalkanes: (a,c) LC1 and (b,d) LC2 phases; (a,b) as suggested for $C_{10}H_{21}-C_{10}F_{21}$ based on experimental data [102] and (c,d) as found in simulation; $R_F = \text{black}$, $R_H = \text{gray}$ [103]; (e,f) examples of non-lamellar modes of self assembly of R_F-R_H diblocks: (e) “ripple phase” proposed for the low-temperature solid phase of $C_{12}H_{25}-C_{12}F_{25}$ [104] and (f) model of a cylinder morphology encountered for $C_{12}H_{25}-C_{20}F_{41}$ as obtained under certain conditions [105]. (a–d) Reproduced with permission [103], copyright 2004, American Institute of Physics (AIP); (e,f) reproduced with permission [104, 105], copyright 1992, 1998, American Chemical Society (ACS)

simulation with a coarse-grained model of this compound [103]. These four structures illustrate the major possible ways for escaping from steric frustration by retaining a lamellar organization.

In diblock molecules combining R_F - and R_H -segments the C–F dipoles do not all cancel. This creates a dipole of 2.3–3.4 D at the R_F-R_H junction (arrow in Fig. 5) [66], leading to an increased dielectric constant of R_F-R_H diblocks compared to alkanes and perfluoroalkanes (see Table 2). This dipole increases the polar intermolecular interactions and should have an influence on the mode of self-assembly.

In homologous series liquid crystalline behavior is found for molecules with comparable length of R_H - and R_F -segments, whereas compounds with very different block size are usually crystalline [106, 107]. Substituents at the end of the aliphatic blocks have a significant effect on self assembly. Branching of the

R_F -chain, for example, removes LC phases [107] and, if the terminal hydrogen in the R_H -block is replaced by a bulky bromine, a structure with alternating tilt in adjacent layers. (anticlinic tilt) is formed [86]. Besides the R_F - R_H diblocks, different types of R_F - R_H multiblocks, such as R_F - R_H - R_F triblocks [66] and laterally coupled R_F - R_H -diblocks, have also been investigated [66, 108].

2.2 R_F - R_H -Diblocks with an Additional Linking Unit

Additional linking units can be introduced between the two segments of R_F - R_H -diblocks. No LC phases were reported for compounds with a *trans*-cyclohexane ring as linking unit [109], but LC phases were observed if a 1,4-disubstituted benzene ring was used. Compounds **1/n** (see Fig. 7), for example, form monotropic SmA phases if the alkyl segments (n) are short ($n < 5$) or long ($n > 11$), but not for the middle numbers ($n = 5-11$) [110, 111]. The layer distance in the SmA phases decreases with rising alkyl chain length giving ratios of the layer thickness d to molecular length l (d/l ratio) of 1.36 for $n = 1$ and 1.08 for $n = 4$. Further increasing chain length leads to disappearance of the SmA phase and for the long chain compound with $n = 12$ the SmA phase emerges again with a d/l ratio of 1.72. This indicates significant structural modifications occurring in the SmA phases depending on the R_H -chain length.

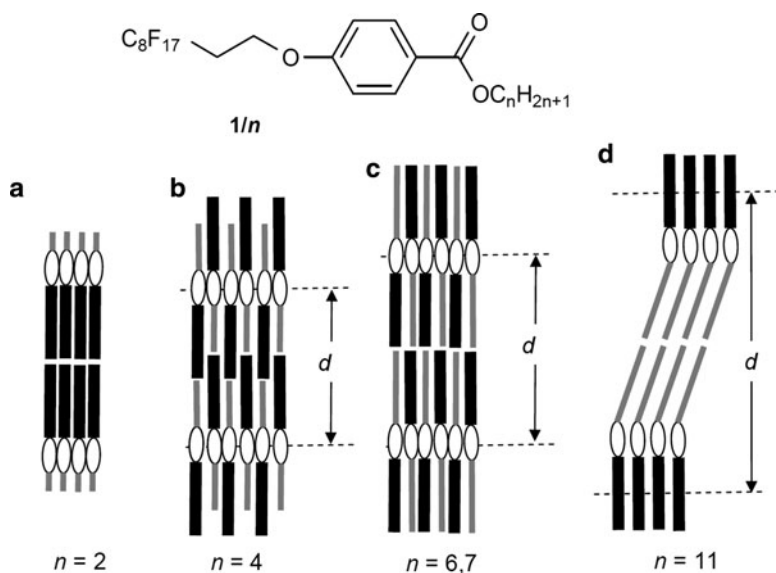


Fig. 7 Compounds **1/n** and schematics of their fundamental organization in distinct crystal structures depending on alkyl chain length; $R_F = \text{black}$, $R_H = \text{gray}$, additionally, there is the possibility of tilting which is not considered in all cases [94]

Hori et al. have investigated the crystal structures of compounds **1/n** and found four distinct modes of organization depending on the alkyl chain length [94, 112]. Though crystal structures are not directly related to the LC structures, they can show fundamental trends in the self assembly of these molecules. The organization of compounds **1/n** in the crystal state is dominated by the strongest intermolecular interaction between the aromatics in the middle of the molecules, i.e. the side-by-side packing of the aromatics is retained in all crystal structures. For the ethylester **1/2** there is a segregated packing of R_F and R_H in a separate layer (see Fig. 7a; there is an end-to-end arrangement of the R_F -chains in the crystal structure, but in the LC structure of **1/1** the R_F -chains are interdigitated as shown in Fig. 11a). For molecules with a medium alkyl chain length, there is an antiparallel packing of the molecules which reduces the contact area between like segments and increases the contacts between unlike chains, as shown in Fig. 7b. This indicates that the significant steric frustration due to the different cross sections of R_F and R_H can suppress their segregation. The contact area between the R_F -chains decreases with growing alkyl chain length and mesophase stability becomes lowest if R_F and R_H have the same length when the like contacts are completely lost (Fig. 7c). As segregation of R_H and R_F is relatively weak the steric effects, leading to a mixed packing are dominating for compounds with medium alkyl chain length. For longer alkyl chains R_H - R_F -segregation is stronger and becomes dominant over the steric effects. This suppresses the mixing of unlike chains, leading to a double layer structure with segregated R_F - and R_H -chains for compound **1/12**. In this structure

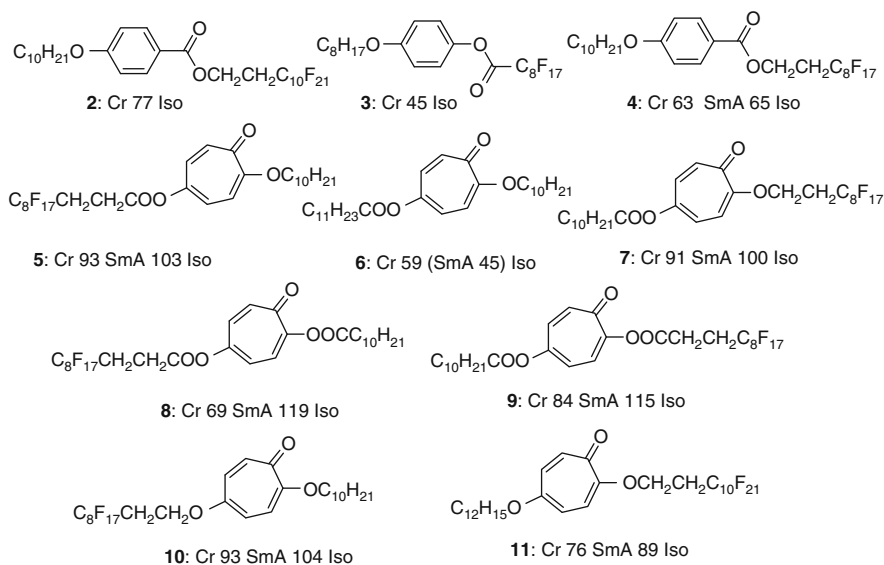


Fig. 8 Examples of mesogenic and potentially mesogenic molecules incorporating only one ring (T_C) [115, 116]

steric frustration is removed either by tilting (crystal structure, Fig. 7d) or by a significant folding and partial interdigitation of the thinner R_H -chains in the LC phase. The increased flexibility of longer alkyl chains not only disfavors their packing between the rigid R_F -chains (entropic penalty), but also allows efficient space filling by chain folding. A similar competition between space filling and segregation is also responsible for the distinct packing modes of molecules incorporating longer aromatic rod-like cores, which will be discussed in Sect. 4.2.

In addition to the derivatives of 4-hydroxybenzoic acid discussed above related compounds with reversed position of R_F - and R_H -chains (compound **2**), an additional nitro group or bromine at the benzene ring [109], with reversed direction of the COO group (compound **3**), 4-hydroxythiobenzoates (e.g., compound **4**) [115], tropolones **5–11** [116], and other similar compounds have been investigated; Fig. 8 shows a selection of these single ring mesogenic compounds.

3 Linear, Taper-Shaped, and Dendritic Molecules with R_F -Chains

Beside these compounds which combine alkyl chains and perfluorinated chains at opposite ends of a cyclic unit, there are several examples of liquid crystalline materials combining a single aromatic ring with a single semiperfluorinated alkyl chain or with two or three R_F -chains in close proximity.

3.1 *Smectic Phases of Liquid Crystals with One Aromatic Ring and One R_F -Chain*

Compounds combining only one benzene ring with an R_F -chain led to significant interest as they have shown that apolar thermotropic LC forming materials are possible without rod-like anisometric units. However, it is worth noting that not every combination of an aromatic unit with a perfluorinated chain automatically leads to LC properties. Careful choice of the connector binding the R_F -chain to the core as well as the presence of additional substituents at the benzene ring can affect the mesophase stability considerably [113, 117–120]. In general, polar linking groups ($-O-$, $-COO-$) and polar substituents (CN, NO_2) are preferable for mesophase formation as they enhance the amphiphilicity of these molecules (see compounds **12–27** in Figs. 9 and 10).

For these compounds the packing of the molecules also depends strongly on the details of the molecular structure (see Fig. 9) and on the delicate balance between segregation and optimized space filling. For example, for the SmA phases of the 4-substituted ethers **15b** (4- NO_2) and **16b** (4-CN) the $d//l$ ratio is around 1.7 and an antiparallel partial bilayer arrangement with interdigitated aromatics was proposed (see Fig. 11b) [113]. However, for the SmA phases of the 1,3-substituted ethers **15a**

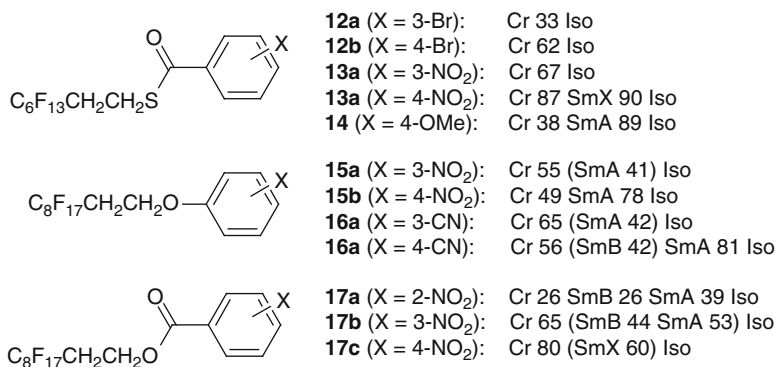


Fig. 9 Comparison of selected examples of compounds combining one semiperfluorinated chain with a benzene ring, showing the effects of substituent type and position ($T/^\circ\text{C}$) [113, 115, 117, 120]

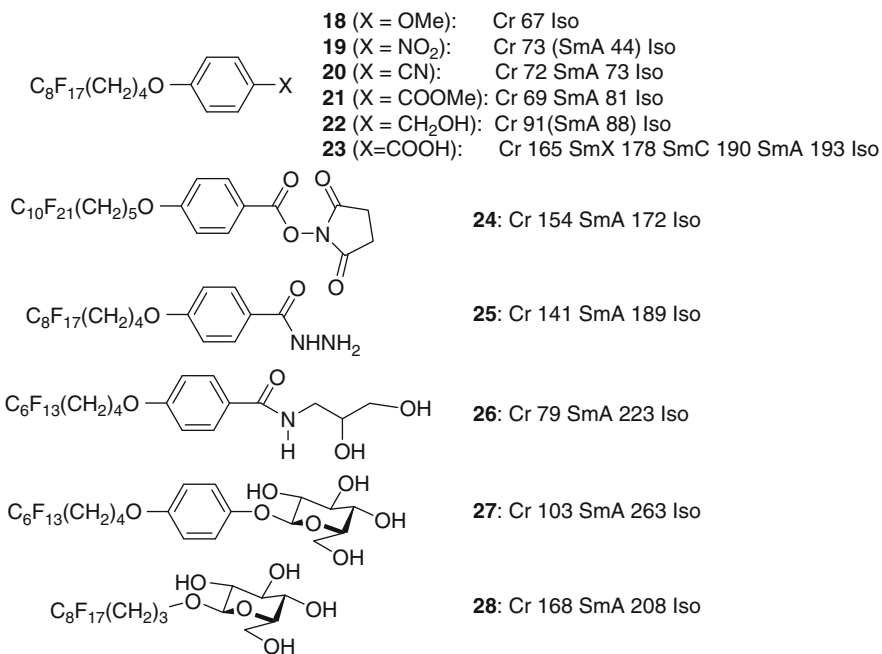


Fig. 10 Comparison of selected examples of thermotropic LC compounds combining one semiperfluorinated chain with a six-membered ring, showing the effect of increasing polarity of the *p*-substituent ($T/^\circ\text{C}$) [119, 121–125]

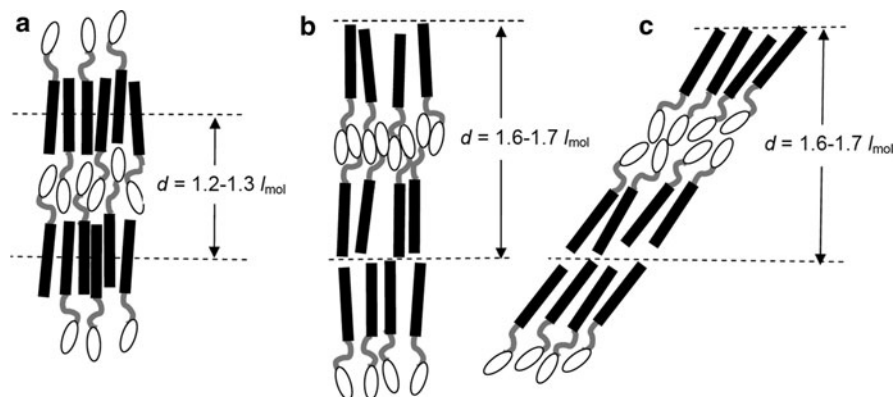


Fig. 11 Modes of self assembly of aromatics with a single semiperfluorinated chain depending on the kind and position of substituent at the aromatic core [113, 114]

(3-NO₂) and **16a** (3-CN) the d/l ratio is much smaller, only 1.2, and in this case a complete interdigitation of the R_F-chains, as shown in Fig. 11a, is assumed [113]. Similar d/l ratios of around 1.2–1.3 were also reported for 4-substituted methyl benzoates like compound **21** (Fig. 10) [119]. Detailed XRD studies of this compound confirmed a phase structure with layers of completely overlapping R_F-chains [114] and separate layers of the aromatics (see Fig. 11a).

The same study has shown that the organization completely changes for the corresponding benzoic acid **23** (Fig. 10) where the COOH groups form cyclic dimers with a linear shape.¹⁰ In this case there is no interdigitation of the R_F-chains and a (tilted) double layer structure is formed (see Fig. 11c), which is in line with the d/l ratio of 1.6–1.7 observed for these benzoic acids. Related types of LC structures have been discussed for other partly fluorinated 4-alkoxybenzoic acids [126], and succinimidyl benzoates **24** [121].

In Fig. 10 the effect of increasing polarity of the substituent at the aromatic ring is shown, also including strongly polar hydrogen bonding groups, such as hydrazides (**25**) [122], diols (**26**) [125] and carbohydrates (**27**, **28**) [123, 124]. The strong stabilization of the LC phases from **25** to **27** is due to the increasing CED as the number of hydrogen bonding between the polar groups grows. This rises the intramolecular CED difference which stabilizes the LC phases. Compounds like **28** can also form aggregates in water and behave as detergents. Perfluorinated amphiphiles of this type, together with fluorosurfactants and fluorolipids, represent a distinct field of its own which has been previously reviewed [66, 73, 127–131] and therefore will not be treated here in more detail; only amphiphiles incorporating at least one ring will be considered.

¹⁰ Hence, benzoic acids can be more appropriately considered as self-assembled rod-like mesogens with two fluorinated terminal chains (see Sect. 4.4).

3.2 *Taper Shaped and Dendritic Molecules Leading to Curved Aggregates*

3.2.1 The Influence of Fluorophobic Effect and Size Effects on Self-Assembly

Increasing the number of R_F -chains attached to one end of a benzene ring leads to an overcrowding of the periphery, providing a transition from lamellar (smectic) phases to liquid crystalline phases composed of curved aggregates, in most cases columns. The linking groups and additional polar substituents form the inner core of the columns which is surrounded by the “apolar” shell of the semiperfluorinated chains. Self assembly of these columns leads to a packing of the column cores on a hexagonal lattice. The disordered chains partially interdigitate and form a continuum embedding this lattice of cores. Percec et al. have shown that hexagonal columnar phases can be stabilized or induced if the alkyl chains in taper shaped crown ethers or linear polyethers were replaced by semiperfluorinated chains (compounds **29–34**, see Fig. 12, [133, 134, 136, 137]), and that the mesophases can be further stabilized by increasing the length of the perfluorinated segments; however, bicontinuous cubic phases have rarely been observed [135].

Tschierske et al. have shown for a variety of different molecular structures (see Figs. 13 and 14) that the whole series of mesophase morphologies with distinct interface curvature, starting from lamellar via bicontinuous cubic and columnar phases to micellar cubic phases composed of closed spheroidic aggregates, can be produced by systematic increase of the number and length of semiperfluorinated chains [9, 10, 125, 138–141]. This is the same sequence of LC phases as previously found by the same authors for related non-fluorinated alkylsubstituted diol-based and carbohydrate based taper shaped molecules [30, 35, 36]. In addition, due to the larger volume of perfluorinated chains, in some cases only two chains are sufficient for the formation of spheroidic aggregates instead of the three alkyl chains usually required for related non-fluorinated molecules (see compound **42** in Fig. 14). Interestingly, the sequence $SmA-Cub_V-Col_{hex}-Cub_I$ can also be found in mixtures between compounds carrying only one and two or three R_F -chains, as shown in Fig. 15a.

As a result of the mesophase stabilizing fluorophobic effect this phase sequence is also found for the star shaped blockmolecules **35–37** shown in Fig. 13 [24, 142]. These molecules are unique as they neither have an anisometric shape nor represent typical amphiphiles with a strongly polar headgroup or have an especially high molecular mass like block-copolymers. Moreover, compound **35** can be regarded as a tetramer of the simplest “apolar” LCs with only a single R_F -substituted aromatic ring, (discussed in Sect. 3.1). Compounds **36** and **37** can be considered as the smallest possible LC dendrimer structures (first generation dendrimers) with R_F -chains at the periphery, in this way unifying distinct areas of research (see also Sect. 9.3). As shown in Fig. 15b, mixing of the two molecules **35** and **37** with a very different number of R_F -chains in distinct ratios provides the whole sequence of phase structures from SmA to Cub_I , depending on the concentration of the two

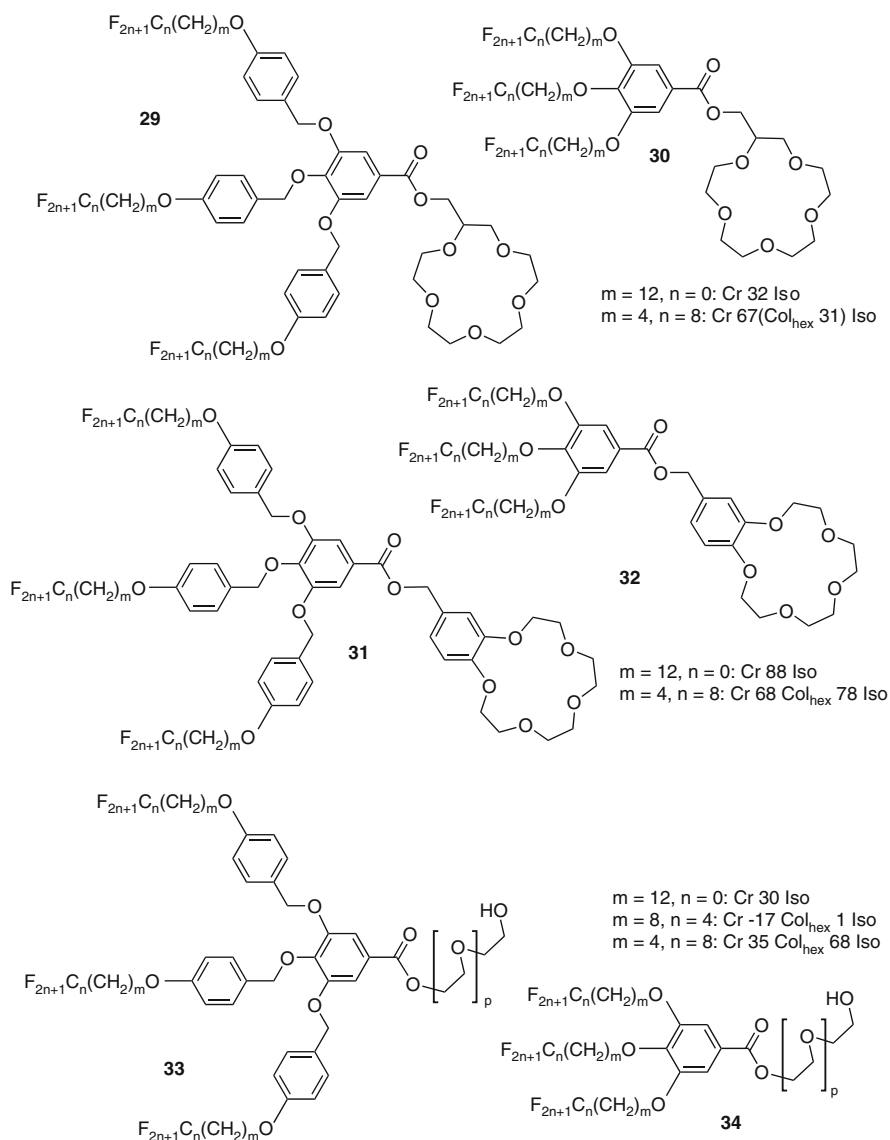


Fig. 12 Selected examples of taper shaped crown ethers and polyethers with three fluorinated chains (T/C); data refer to compounds **30**, **32** and **34** [132–135]

compounds (Fig. 15b). This indicates that in mixed systems the effect of the individual molecules is averaged and the “mean field” of the system as a whole determines the morphology of the self-assembled superstructure.

Whereas the mesophase morphologies of compounds **35–37** depend on the size ratio of polar and apolar segments, the mesophase stabilities are mainly influenced

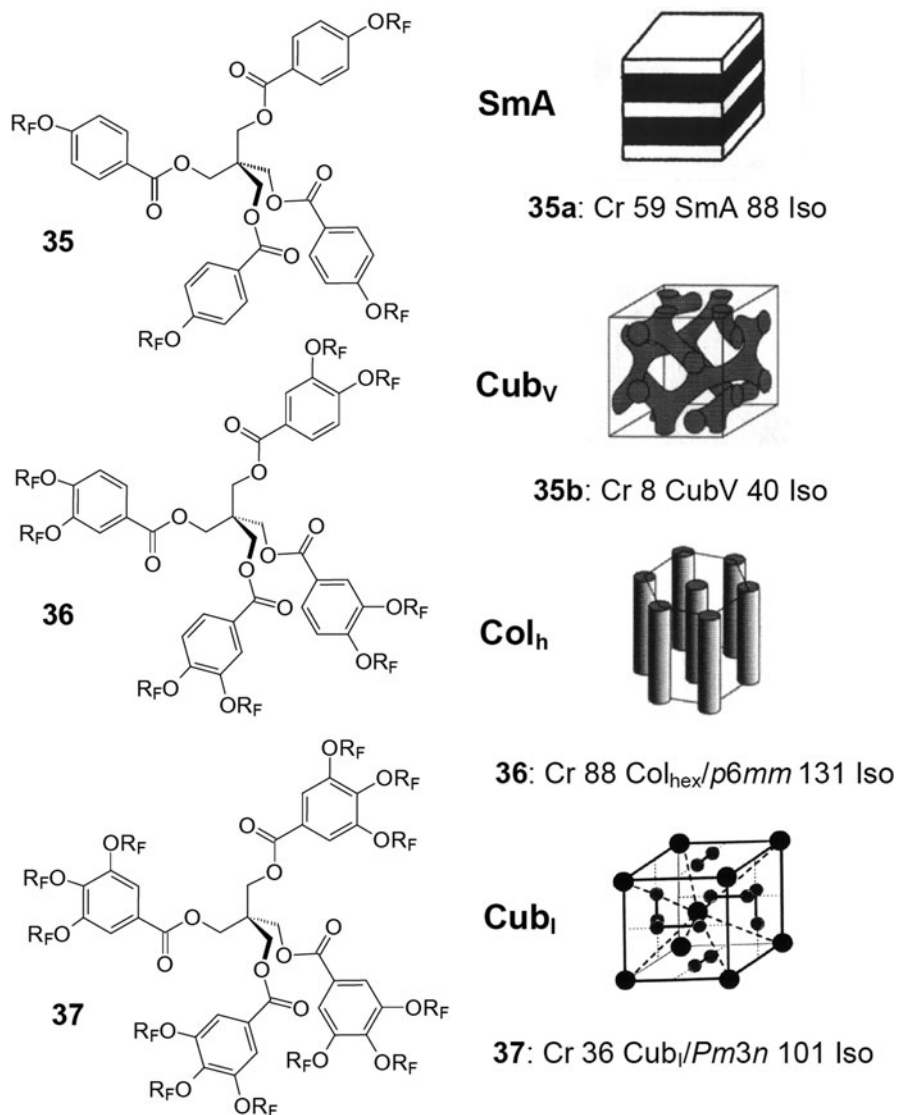


Fig. 13 Comparison of the LC phases of pentaerythritol tetrabenzoates depending on the number of fluorinated chains (**35a**, **36**, **37**: $R_F = (CH_2)_4C_6F_{13}$) [138]; **35b**: $R_F = (CH_2)_6C_4F_9$ ($T/^\circ C$) [125]

by the degree of incompatibility between the segments and by the molecular weight [24], similar to how the Flory-Huggins parameter and the degree of polymerization ($N\chi$) determine the order–disorder transition temperature of block copolymers [9, 10, 23]. Hence, these compounds provide a link between the modes of soft self assembly in thermotropic LC phases and in block copolymers.

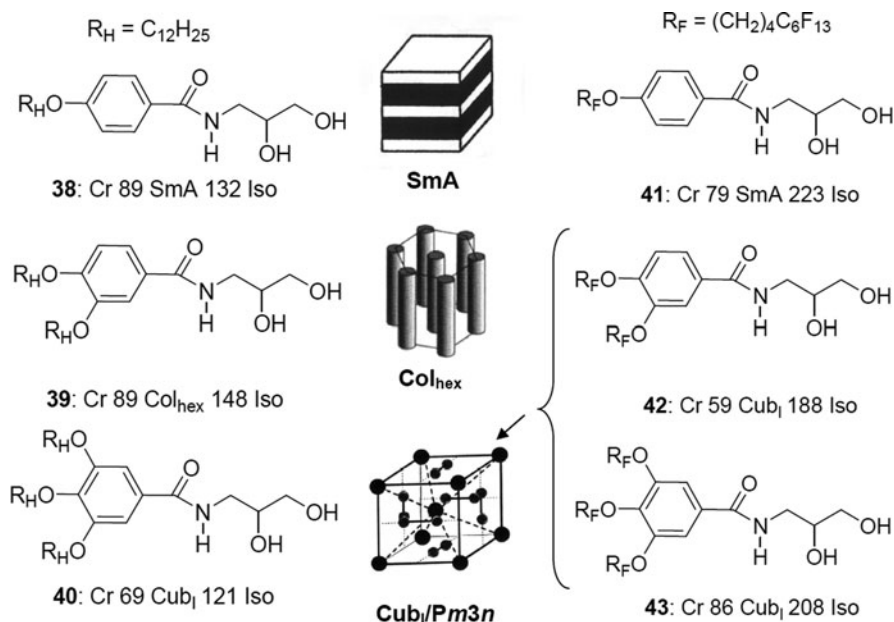


Fig. 14 Comparison of the LC phases of fluorinated (*right*) and nonfluorinated (*left*) amphiphilic diol derivatives depending on chain length (*dark areas* = polar groups, *white areas* = non-polar chains, $T/^\circ\text{C}$) [35, 139]

It should also be noted that the stability of the distinct mesophases can be quite different. It seems that there is a significant effect of molecular shape and topology, stabilizing SmA phases in the system **41/43** and Col_{hex} phases in the system **35/37**. In addition, the mesophase stability is often reduced close to the transition to another mesophase (see Fig. 15). Hence, the order–disorder temperatures can only be roughly estimated based on segmental solubility parameters [24, 25].

Dendritic molecules, forming predominately hexagonal columnar and micellar cubic phases, have been introduced and intensively investigated by Percec et al. and this field has recently been reviewed [143]. The mesophases of these dendrons can also be stabilized and modified by replacing alkyl chains by fluorinated chains; selected examples will be discussed in the next sections.

3.2.2 R_F-Substituted Benzoic Acids

R_F-substituted benzoic acids (compounds **44–49** in Fig. 16) are somewhat distinct from the other taper shaped amphiphiles as they tend to form discrete cyclic hydrogen bonded dimers, which provide some rigidity to the core region [126]. This gives rise to some interesting effects on mesophase structure. For example, the single

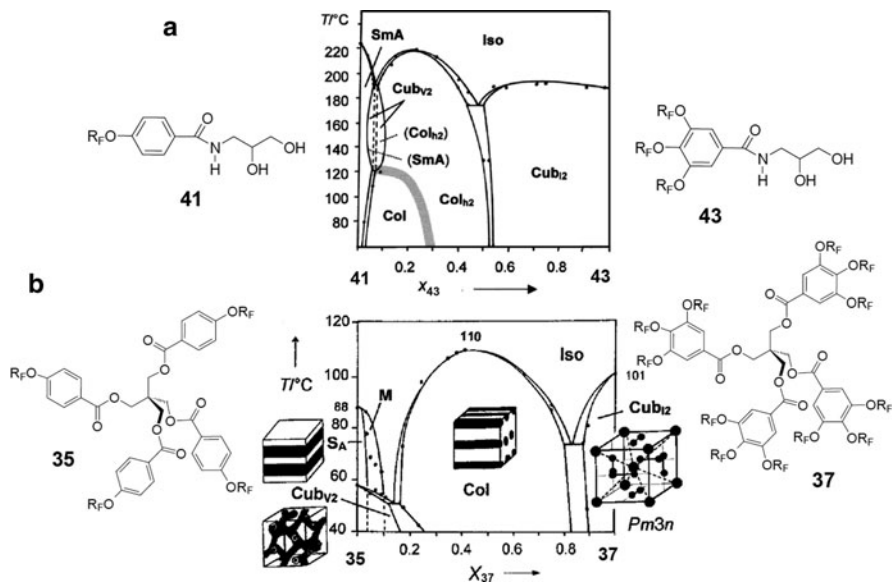


Fig. 15 Binary phase diagrams showing the change of the mesophase structure depending on the ratio of single-chain to three-chain compounds; (a) amphiphiles **41/43** [139] and (b) pentaerythritol tertbenzoates **35/37**; $R_F = (\text{CH}_2)_4\text{C}_6\text{F}_{13}$ for all compounds ($T/^\circ\text{C}$) [138]. Reproduced with permission (a) [139] copyright 2002, American Chemical Society (ACS); (b) [138] copyright 2000, Wiley-VCH

chain compound **44** forms a tilted smectic phase (SmC), which is absent for related R_F -substituted amphiphiles with other polar substituents, incapable of forming discrete rodlike dimers (see Fig. 10).

Due to the dimer structure it is also more difficult to obtain strongly curved aggregates as required for formation of micellar cubic phases (Cub_1). As shown in Fig. 16, even the three chain benzoic acids **46** form only a hexagonal columnar phase, whereas the fluorinated diol based amphiphiles **42** and **43** (Fig. 14) form exclusively micellar cubic phases, even if they have only two chains. For the benzoic acids a micellar cubic phase with $Pm3n$ lattice was only obtained after dendritic branching (compound **48**, Fig. 16) [144]. More recently, a cubic phase with a body centered $Im3m$ lattice and lattice parameter in the same range as the hexagonal parameter of the adjacent Col_{hex} phase (at lower temperature) was observed for a three chain semiperfluorinated benzoic acid **46** with decamethylene spacers and C_6F_{13} end-groups ($n = 6$, $m = 10$) [147]. Based on the observed phase sequence $\text{Col}_{\text{hex}}\text{-Cub-Iso}$ and the calculated lattice parameter it is likely that the cubic phase is a micellar one (Cub_1). It is interesting to note that exclusively Col_{hex} phases were reported for related compounds with $n = 6$ and $m = 8$, 11 [146]. This calls for more systematic investigations of the effects of spacer length and parity on the LC self assembly of this class of compounds.

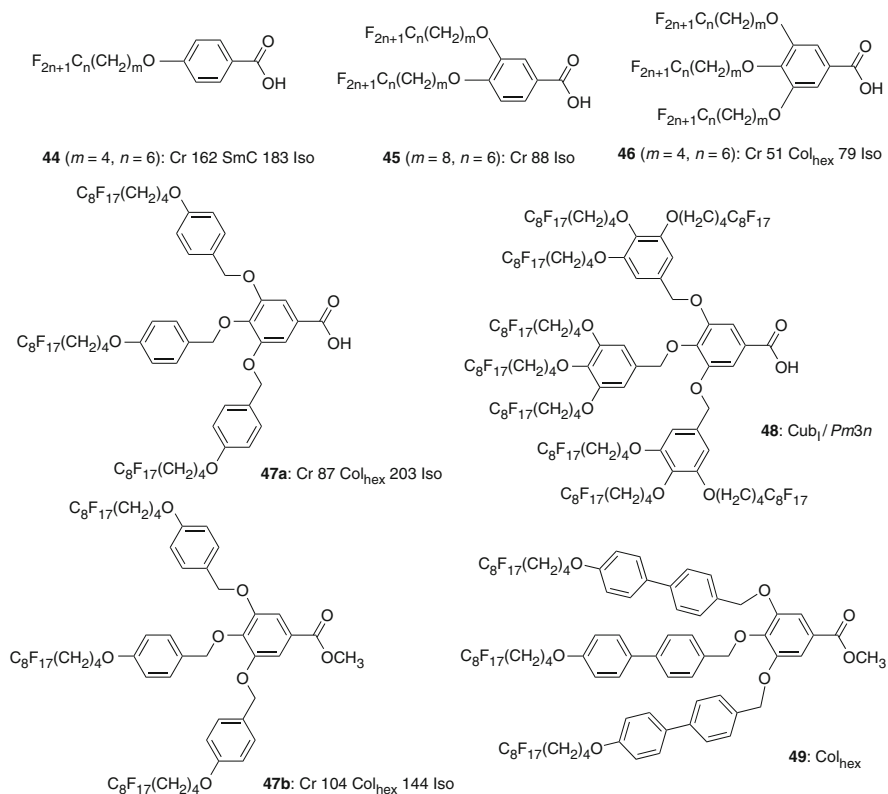


Fig. 16 Representative examples of semiperfluorinated benzoic acids and methyl benzoates with fluorinated chains (T_f^C) [126, 133, 134, 136, 144–146]

3.2.3 Taper-Shaped and Dendritic Molecules with Enlarged Apex

In general, the mesophase stabilizing effect of R_F -segments allows the formation of columnar superstructures for a wide variety of different taper-shaped molecules with quite large functional units at the apex, such as for example π -acceptor and π -donor aromatics (compounds **50–55**, Fig. 17) as required for molecular electronics applications [148–153, 156, 347]. Remarkably, the perylene diimide units of compound **50** are organized with their main axes parallel to the column long axis, whereas the aromatic units are usually aligned predominately perpendicular to the column long axis. This quite unusual orientation of the aromatics was recently also found in another class of fluorinated molecules which will be discussed in Sect. 7.2.4. In the case of the oligonucleotide **56** the focus was not on self-assembly; instead, the perfluorinated dendritic unit of this compound was used as a lipophilic anchor to improve oligonucleotide synthesis [151].

Additional recent examples of taper shaped molecules incorporating elongated rod-like units at the apex and two or three semiperfluorinated chains at the periphery

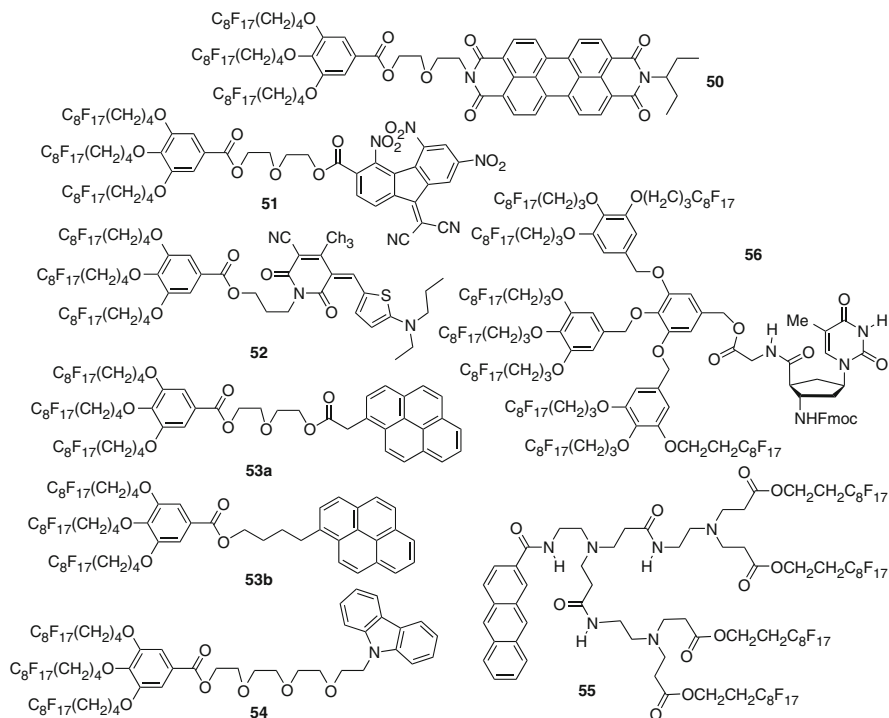


Fig. 17 Representative examples for semiperfluorinated taper shaped molecules bearing large functional units at their apex [143, 148–151]

are collated in Fig. 18 (compounds **57–78**). In all cases these fluorinated molecules form hexagonal columnar phases instead of spheroidal cubic phases because the taper angle, and hence the interfacial curvature, is reduced by the elongated rod-units. The methyl benzoate **49** (Fig. 16) has three rod-like biphenyl units in the periphery. Interestingly, this compound also shows a hexagonal columnar phase [145] and these anisometric biphenyl units seem to allow the alignment of the Col_{hex} phases under a magnetic field which is of importance for the directed and uniform alignment of columnar LC, as required for their use as charge carrier materials [145].

3.2.4 Effects of R_F-R_H-Segregation

Besides the simple effects of mesophase stabilization by increased polar-apolar incompatibility and modification of mesophase morphology due to size effects, there are additional specific effects based on the *lipophobicity* (R_F-R_H incompatibility) and *rigidity* of perfluorinated segments. In this respect it is important to

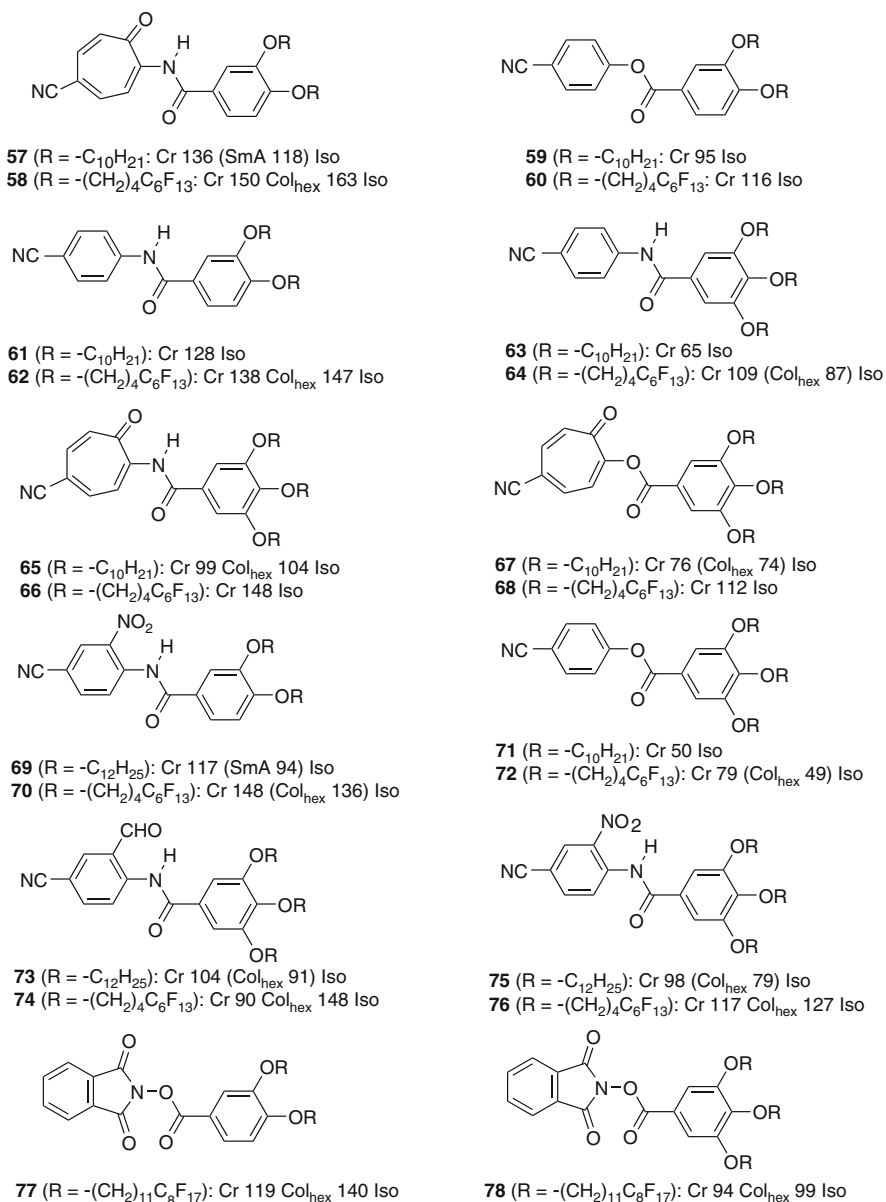


Fig. 18 Examples of short rod-like molecule with two or three semiperfluorinated chains (T° C). [121, 152]

note that in all reported cases the fluorinated chains were not directly attached to the aromatics; rather they are decoupled by aliphatic spacer units of different length, which are usually at least three methylene groups long (see Figs. 13–18). These

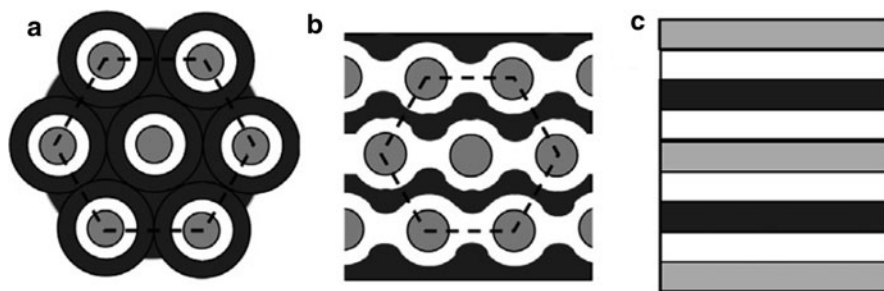


Fig. 19 (a) Core-shell columns, (b) “hexagonal-columns-in-lamellae” morphology and (c) segregated trilayers; *gray* = aromatic cores, *white* = aliphatic spacers and *dark* = R_F -chains [146]

aliphatic spacer units provide additional flexibility as the 30% smaller cross section area of the R_H -chains compared to R_F -chains leads to conformational disordering of sufficiently long aliphatic spacers and this reduces the melting points. In this way the melting points can occasionally become even lower than those of the related alkyl derivatives. Most importantly, however, these spacer units represent a distinct part which is incompatible with the aromatic core and the polar groups as well as with the R_F -segments of the chains, providing *polyphilicity*. For compounds with relatively long R_H -spacers the side-by-side preorganization of the aliphatic and fluorinated segments at the periphery of the 3,4- or 3,4,5-substituted aromatics favors the segregation of the R_H -spacers and R_F end-segments into distinct shells around the cores, leading to core-shell structures, as shown in Fig. 19a. [121, 146, 154–156]. In these core-shell structures the aromatics form the cores, the aliphatic spacers form the shells, and these core-shell columns are arranged on a hexagonal lattice in the continuum of by the R_F -segments.

3.2.5 Effects of R_F -Chain Rigidity

The rigidity of relatively long R_F -segments can provide a certain layer stabilizing effect. As shown in Fig. 13, compound **35a** with a larger fluorinated segment forms a lamellar phase whereas compound **35b** with a smaller R_F -segment forms a bicontinuous cubic phase. This sequence is reversed to that usually observed on increasing chain volume (see Fig. 2) and can be explained by the stronger tendency of longer R_F -chains to align parallel to one another in order to reduce the excluded volume. This preference for parallel alignment makes the curvature of the interfaces more difficult and therefore stabilizes the lamellar organization with respect to the bicontinuous cubic phase.

Due to the rigidity of R_F -chains, in fluorinated LCs the transition from smectic to columnar organization often takes place via modulated smectic phases (ribbon phases, $c2mm$, $p2gg$, and Col_{ob} ; see Fig. 20, left) which completely or partly replace the bicontinuous cubic phases at the Sm-to-Col cross-over. Similarly, in columnar phases the circular columns can be deformed to an elliptic, rectangular, or square

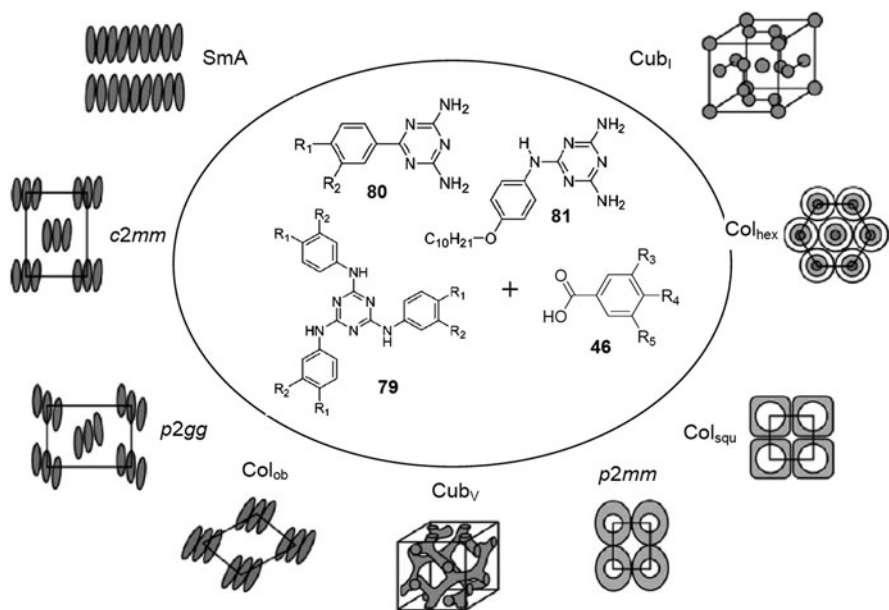


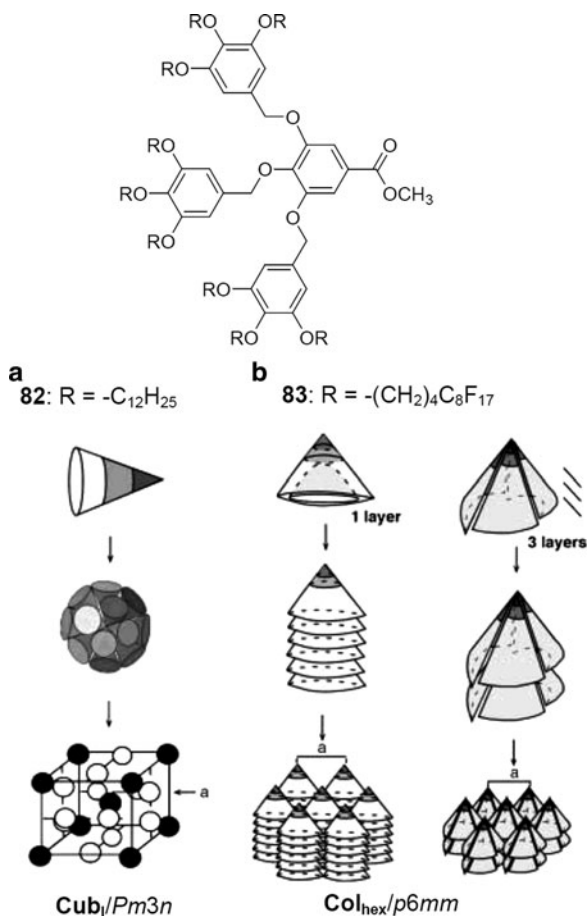
Fig. 20 Sequence of LC phases formed by hydrogen bonded complexes between substituted 1,3,5-triazines with complimentary benzoic acids depending on the number of chains and degree of fluorination (R_1 - $R_5 = \text{OR}_F, \text{OR}_H, \text{H}$) [153]

cross section, leading to replacement of hexagonal columnar phases by lower symmetry phases, as rectangular and square columnar phases (Fig. 20, right). This was, for example, demonstrated by Janietz et al. in a series of hydrogen bonded complexes of R_F -substituted benzoic acids **46** with different types of amino-1,3,5-triazines **79–81** which differ in the numbers of chains and the degree of fluorination [153, 157–160].

For some three chain benzoic acids **46** with long aliphatic spacers and R_F -chains ($m = 8, 11; n = 10$) an unusual phase structure, assigned as “hexagonal-columns-in-lamellae morphology” was proposed based on the analysis of powder XRD scattering intensities (Fig. 19b) [146]. In the proposed phase structure the aromatic columns are arranged on a hexagonal lattice which lies parallel to a (wavy deformed) lamellar structure resulting from parallel organization of the R_F -segments in distinct layers, but no direct proof of the proposed structure was given.

Another effect of chain stiffening and R_F -segregation occurs at the transition from columnar to micellar cubic self assembly (see Fig. 21). As shown by Percec et al. the non-fluorinated dendron **82** forms a micellar cubic phase composed of spheroidal aggregates ($\text{Cub}_1/Pm3n$). Unexpectedly, and in contrast to the trends shown for taper shaped diols (see Fig. 13) where fluorination favors formation of micellar aggregates, in the case of dendron **83** fluorination has removed the cubic phase which is replaced by a hexagonal columnar LC phase [161]. XRD analysis of this columnar phase indicates a π - π stacking of the aromatics along the column

Fig. 21 Self-assembly of two second generation dendrons (a) with alkyl chains and (b) semiperfluorinated chains in the periphery [161]. Reproduced with permission [161], copyright 2003, Wiley-VCH



axis with a distance of 3.9 nm and a tilted arrangement of the molecules with a tilt of about 42° with respect to the normal to the column long axis. It was concluded that the dendrons **83** adopt a crown-like or cone-like overall shape and stack on each other with a distinct shift (Fig. 21b). Tilting of the aromatics in the column stratum seems to be a way to reduce the curvature of the interfaces and to retain a columnar organization instead forming spheres, similarly, as in smectic phases, where tilting of the rod-like aromatic cores (SmC) can avoid transition from flat layers to bicontinuous cubic and columnar phases. These pyramidal columnar phases seem to represent a rather general organization of several different types of taper shaped and dendritic molecules comprising either rigid perfluorinated segments or rod-like biphenyl cores at the periphery [148, 156], or, alternatively, a cone shaped central unit [39, 143, 162]. It is also worth noting that the carboxylic acid **48** (Fig. 16), related to the methyl benzoate **82**, shows a micellar cubic phase instead of the pyramidal columnar phase. It seems that the formation of linear hydrogen bonded

dimers leads to increased rigidity of the core region which disfavors the formation of pyramidal columns and, hence, the organization in micellar aggregates is retained.

4 Rod-Like Liquid Crystals with Fluorinated Chains

There are numerous examples of rod-like molecules with perfluorinated chains and the field has been reviewed previously [56, 59, 61, 63, 64]; hence only some selected examples and major general trends will be discussed here. A large group of these compounds has a perfluorinated or semiperfluorinated chain at one end of the rod-like core and no or only a small polar group at the other end (Fig. 22a). This type of molecules is derived from the polar-apolar amphiphiles discussed in Sect. 3.1 by extension of the single benzene ring to a rod-like unit, which stabilizes lamellar self-assembly. The second type of compounds can be considered as linear polyphilics, composed of three distinct building blocks, the fluorinated chain, the central rod-like aromatic core, and the flexible alkyl chain at the opposite end (Fig. 22b), which all tend to segregate in their own domains (ABC triblock molecules). These molecules can be considered as derived from the R_F - R_H diblock molecules (Sects 2.1 and 2.2) by linear extension of the aromatic linking unit between the unlike blocks. A third type of molecules has perfluorinated chains at both ends and therefore represents ABA type amphiphiles (see Fig. 22c). In all cases additional spacer units can be used to decouple rod-like cores and fluorinated chains (Fig. 22e–g). If these are long aliphatic spacers they represent incompatible units of their own and might be able to form their own domains or mix with terminal alkyl chains of adjacent molecules.

In all cases of these rod-like molecules the fluorination of terminal chains leads to mesophase stabilization and to stabilization of smectic phases with respect to nematic phases. In most cases an increase of the melting temperatures¹¹ and a stabilization

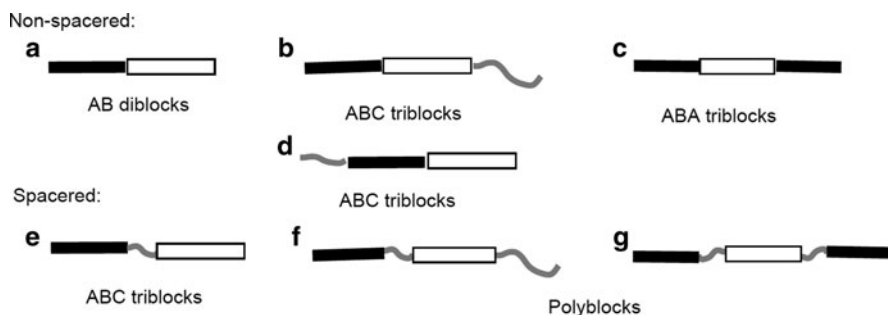


Fig. 22 Distinct types of rod-like molecules with perfluorinated segments; R_F = dark, R_H = gray, aromatic core = white box

¹¹ Strongly enhanced melting temperatures can hide LC phases in some cases.

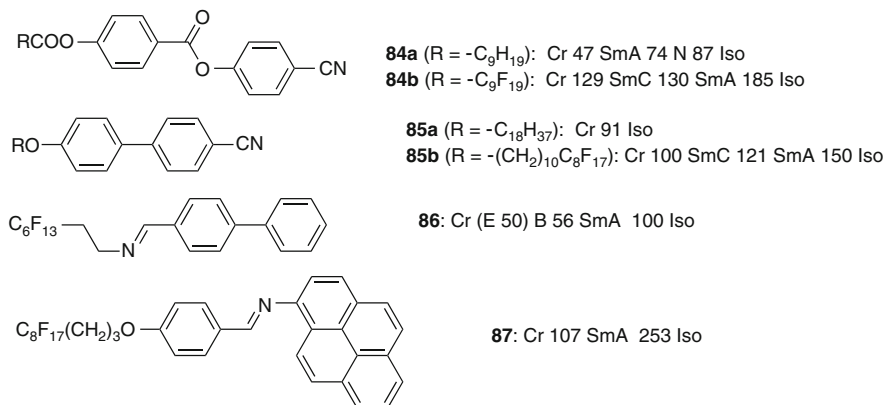


Fig. 23 Selected examples of rod-like molecules with one linear semiperfluorinated chain ($T/^\circ\text{C}$) [163–165]

of tilted smectic phases (SmC) with respect to non-tilted phases (SmA) were also found as indicated by the couples **84a/b** and **85a/b** in Fig. 23 [163]. Once again, melting and crystallization temperatures can be reduced by decoupling the semirigid fluorinated segments from the rigid mesogenic cores by elongated alkyl spacers or, alternatively, by replacing the rigid perfluoroalkyl chains by the more flexible fluorinated polyethers [99]; see compounds **92–97** in Figs. 26 and 27).

4.1 Rod-Like Liquid Crystals with One (Semi)Perfluorinated Chain: Double Layer Smectic Phases

LC biphenyl derivatives like compound **86** [63] and related compounds with other linking units [171], as well as compounds with additional small substituents such as CN [164], OMe [172, 173], OCF₃ [74], and COOEt [63] at the other end (see Fig. 23), represent well investigated examples of this type. However molecules comprising large groups like pyrene can also form a broad SmA phase region if combined with an R_F-chain (compound **87**) [165]. In most cases the layer spacing is larger than the molecular length but smaller than twice the molecular length (double layers).

Compound **86**, as an example, was investigated in more detail by XRD [174, 175]. It shows three distinct LC phases, namely SmA, B, and E. The layer spacing in all three phases is larger than the molecular length and the difference increases with growing length of the perfluorinated segment. This can be explained by a structure where the biphenyls overlap and the disordered R_F-chains are organized in separate layers between the layers of the aromatics (Fig. 24b). At high temperature, in the SmA phase, both segregated layers are liquid-like disordered as indicated in the XRD patterns by the presence of two diffuse scatterings, one at $d = 0.55$ nm

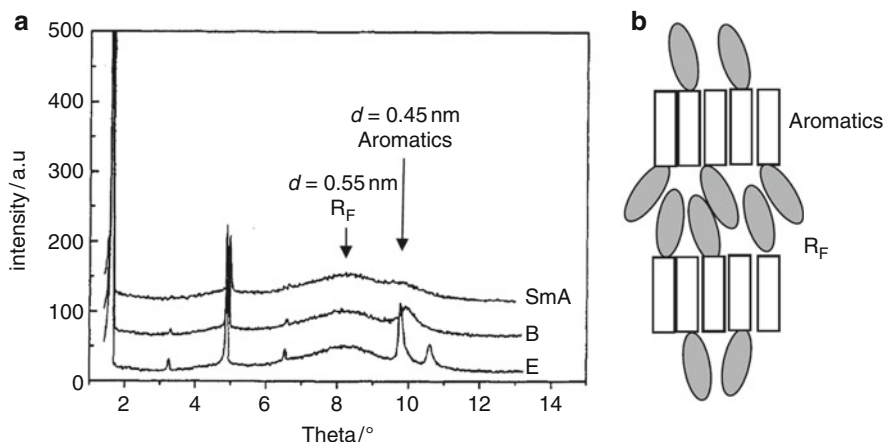


Fig. 24 XRD patterns of compound **86** in the three distinct mesophases [175]. Reproduced with permission [175], copyright 1997, Wiley-VCH

corresponding to the typical mean distance between fluid R_F -chains and a second one at $d = 0.45$ nm corresponding to the smaller mean distance between the biphenyls (see Fig. 24a). At the transition to the B phase the scattering at $d = 0.45$ nm becomes sharp and in the E phase it splits into a pattern which can be indexed to an orthorhombic lattice (Fig. 24a). However, the diffuse scattering related to the R_F -chains remains diffuse in all three phases. This indicates that in the B and E phases the aromatic cores are ordered on a hexagonal or orthorhombic cell, respectively, but the R_F -chains remain liquid-like disordered. This decoupling of core packing and chain packing is usually not observed for classical rod-like LCs with linear alkyl chains, as for these compounds core-ordering is coupled with alkyl chain-ordering as both units have approximately the same cross sectional area. The significant mismatch of the cross sectional areas of aromatics (~ 0.2 nm²) and R_F -chains (~ 0.3 nm²) leads to interdigitation of the aromatics, this provides additional space for the R_F -chains and in this way favors disorder of these chains. Hence, though the R_F -chains are more rigid than alkyl chains, steric effects lead to increased mobility of the R_F -chains, providing a unique decoupling of core packing and chain packing. Polar substituents at the end of the rod-like core and polar linking units can further modify the core packing due to polar interactions.

Quite generally, steric mismatch requires partial intercalation/interdigitation of some of the segments of the molecules [164] leading to partly intercalated/interdigitated smectic phases (SmA_d , SmC_d), which is illustrated by the following examples.

Compounds like **88** (Fig. 25a), in which the R_F -segments are decoupled from the rod-like core by longer aliphatic spacers, can be regarded as polyphilic ABC molecules which are expected to lead to triply segregated smectic phases as shown in Fig. 19c. However, in compound **88**, for example, the SmA -phase is composed of only two sets of distinct sublayers, though there are three mutually incompatible

segments. The reason is that in the smectic phases the aliphatic and aromatic segments are completely intercalated and form a common layer, and only the fluorinated segments form their own layers (Fig. 25a). Obviously the antiparallel packing with mixing of aromatic and aliphatic segments provides an optimized packing of the R_F -units. A similar structure with intercalated aliphatic spacers and aromatic cores was also proposed for the SmA phase of compound **93** (Fig. 26) [166].

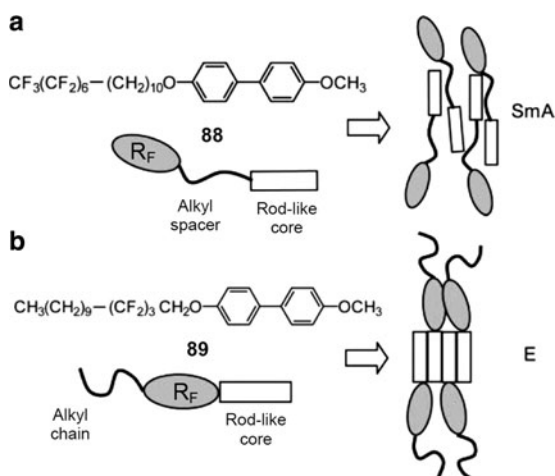


Fig. 25 Influence of the block sequence on the packing behavior of the linear ABC triblock molecules [172]; phase sequences **88**: M 123 SmA 145 Iso; **89**: Cr 60 E 87 Iso ($T^\circ\text{C}$) [10]

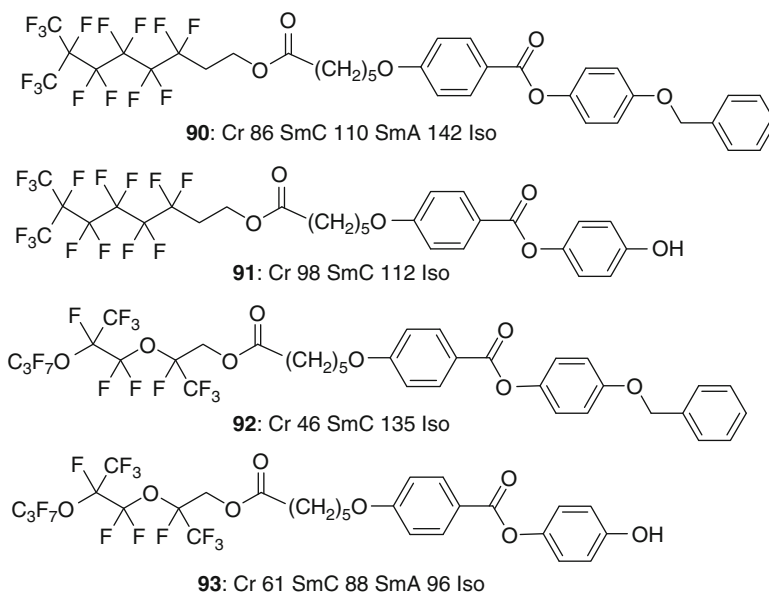


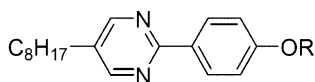
Fig. 26 Selected examples of rod-like molecules with one branched semiperfluorinated chain ($T^\circ\text{C}$) [166]

Compound **89** (Fig. 25b) represents the only known semiperfluorinated LC molecule which has an inverted sequence of R_F - and R_H -segments. Here the fluorinated segment is not at the end of the terminal alkyl chain but between alkyl chain and aromatic core (Fig. 24b) [172]. Though the fluorinated segment is only short, the E phase of this compound is characterized by the coexistence of three distinct sublayers, the layers of the crystallized and interdigitated biphenyl cores, the liquid-like layers of the aliphatic chains, and those of the perfluorinated segments. This molecular topology obviously favors segregation of all segments into their own layers, which is rarely observed.

Examples of rod-like molecules with a branched fluorinated chain at one end (compounds **90–93**) are collated in Fig. 26 [166]. It is interesting that smectic phases are retained despite the significant size of these chains. This is mainly a result of the intercalation of the aromatic cores and aliphatic spacers of these molecules, which can compensate this steric distortion. These branched chains remove the B and E phases with crystalline layers and replace them by fluid smectic phases, including SmC phases. The comparison in this figure also shows that the bulky and flexible bis(perfluoropropylene oxide) derived chains (compounds **92**, **93**) can provide LC materials with especially low melting points and broad mesophase ranges due to the higher conformational flexibility of perfluoroethers compared to linear perfluoroalkyl chains [99, 176].

4.2 Rod-Like Liquid Crystals Combining R_H - and R_F -Chains: Monolayer Smectic Phases

Monolayer phases with d/l ratios around 1 and mixed organization of R_F - and R_H -chains were found quite generally for compounds having alkyl and perfluoroalkyl chains at opposite ends of a rod-like core (compounds **94–97** in Fig. 27 and **100–106** in Fig. 29) [167, 177, 184–193], even for molecules with relatively long R_F -segments [167]. It seems that R_F/R_H segregation is reduced or suppressed because antiparallel packing of the molecules is in this case an efficient way to avoid steric mismatch between R_H - and R_F -chains and to avoid curvature of the interfaces, whereas parallel (segregated) packing would produce a higher energy



94: R = -C ₈ H ₁₇	Iso 68 N 62 SmA 56 SmC 29 Cr ^a
95: R = -CH ₂ C ₇ F ₁₅	Iso 117 SmA 85 SmC 71 M
96: R = -CH ₂ CF ₂ OCF ₂ CF ₂ OC ₄ F ₉	Iso 70 SmA 49 SmC -8 Cr
97: R = -CH ₂ CHF*CH ₂ CF ₂ OCF ₂ CF ₂ OC ₄ F ₉	Iso 88 SmA 62 SmC* < 20 Cr

Fig. 27 Comparison of phenylpyrimidine based rod-like mesogens with an alkyl chain at one end and different types of fluorinated chains at the other end ($T/^\circ\text{C}$); ^a observed on heating, all other transitions were observed on cooling [167–170]

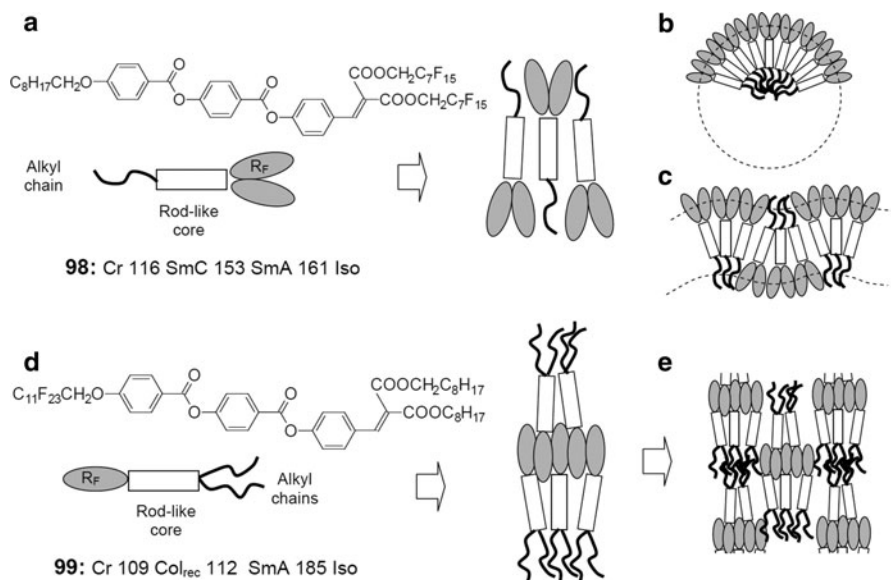


Fig. 28 (a,d) Influence of the position of the fluorinated chain(s) and the hydrocarbon chain(s) on the packing behavior of the tricatener compounds **98** and **99** ($T^{\circ}\text{C}$) and (b,c,e) different possible packing modes [194]

structure due to a local splay of neighboring molecules, associated with a bend of the smectic layers [74].

An extreme case, clearly demonstrating the competing effects of segregation and steric frustration, is provided by compound **98** (Fig. 28a) combining a linear alkyl chain at one end (cross sectional area $0.18\text{--}0.21\text{ nm}^2$) with a branched semiperfluorinated chains at the other end (total cross sectional area $0.54\text{--}0.60\text{ nm}^2$). Due to the relatively weak incompatibility between R_{F} - and R_{H} -chains this steric mismatch can remove segregation. By intercalation of the rather slim aliphatic and the bulky branched perfluorinated segments curvature (as shown in Fig. 28b,c) can be avoided which leads to formation of SmA and SmC phases. In the case of compound **99** (Fig. 28d), in which the aliphatic chain is branched and the semiperfluorinated chain is linear, the difference in cross sectional areas at both ends of the molecule is reduced ($0.36\text{--}0.42\text{ nm}^2$ vs. $0.27\text{--}0.30\text{ nm}^2$). In this case, segregation of the incompatible end-chains takes place more easily, also favored by the elongated fluorinated segment. As the mismatch of cross section area is retained in this case, the monolayer SmA phase of this compound is more related to a short range ordered checkerboard structure built up of ribbons, each composed of three distinct sub-layers (Fig. 28e). At reduced temperature they can adopt long range order, leading to a rectangular columnar phase (Col_{rec}) [194].

Hence, there are two options for molecules with unlike end-chains; either the incompatible chains mix which retains the lamellar structure, or these chains segregate and layer modulation with formation of ribbon phases (columnar phases)

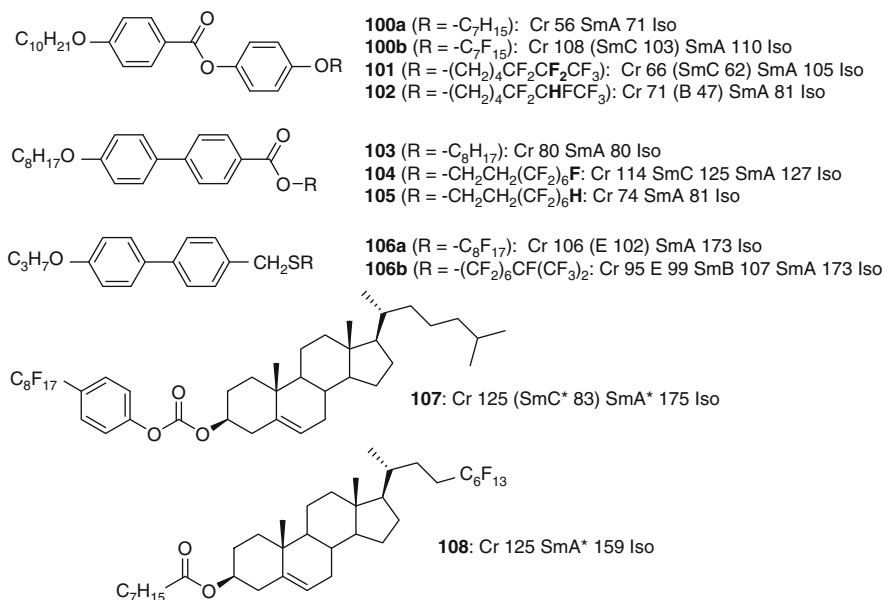
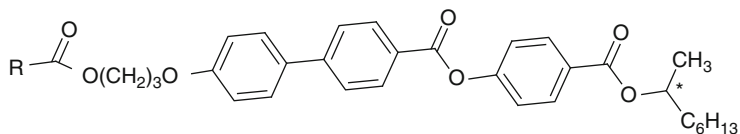


Fig. 29 Comparison of selected examples of rod-like mesogens combining hydrocarbon chains and semiperfluorinated chains ($T^\circ\text{C}$) indicating the effect of replacing one F by H (**101/102**; **105/106**) and the effect of R_F -chain branching (**106a,b**) [163, 177–183]

occurs if the layer modulation adopts a long range periodicity. In the first case sharp layer reflections with higher orders can be found in the XRD patterns and in this case SmC phases are often observed as low temperature phases.¹² It seems that this is observed for most of the rod-like molecules with one R_F - and one R_H -chain. It is not necessary that the molecular organization is strictly antiparallel; neighboring molecules can also be locally organized in small clusters comprising parallel aligned molecules. However, as soon as this local segregation becomes more dominating in the SmA phases, the layer reflection becomes weaker and higher order reflections disappear. If a low temperature phase is formed below these distorted SmA phases, it is a columnar ribbon-type phase. Interestingly, fluorination of the alkyl chains and increasing extent of fluorination [195] always stabilizes the smectic LC phases even if a complete mixing of the unlike chains takes place. Therefore, it seems that the major effect contributing to LC phase stabilization by R_F -chains comes from the reduced overall CED in the mixed $\text{R}_\text{H}/\text{R}_\text{F}$ -chain regions, providing improved segregation from the polar regions of the polar and aromatic core units with higher CED.

¹² As the cross sectional area of the mixed R_H and R_F chains is still larger than that of the aromatic cores random tilt (de Vries-like SmA) or uniform tilt (SmC) can compensate this remaining mismatch.



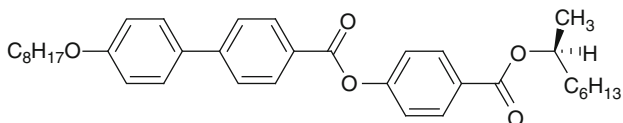
109a ($R = -C_3H_7$): Cr 67 SmI_A* 43 SmC_A* 92 SmA* 117 Iso

109b ($R = -C_3F_7$): Cr 83 SmI_A* (54 SmC_A*) 121 SmC* 124 SmA* 129 Iso

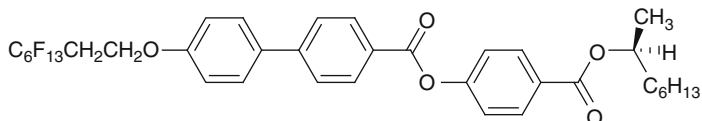
110a ($R = -C_7H_{15}$): Cr 50 (SmI_A* 25) SmC_A* 90 SmC* 92 SmA* 105 Iso

110b ($R = -C_7F_{15}$): Cr 69 SmCA* 98 SmC* 124 SmA* 156 Iso

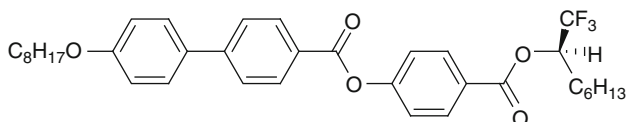
111 ($R = -(CH_2)_3CF(CF_3)_2$): Cr 52 SmC_A* 99 SmC* 117 SmA* 129 Iso



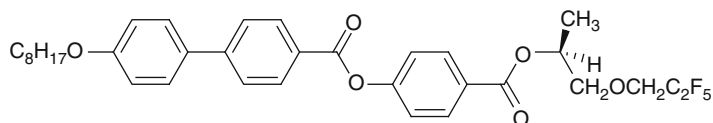
112a: Cr 74 SmC_A* 119 SmC_{FI}* 120 SmC* 122 SmC_α* 123 SmA* 148 Iso



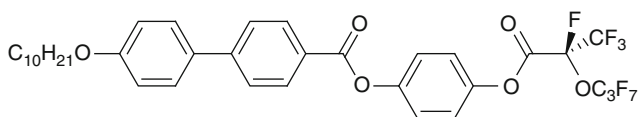
112b: Cr 98 SmC* 138 SmC_α* 148 SmA* 184 Iso



112c: Cr 84 SmCA* 108 SmC* 109 SmA* 121 Iso



112d: Cr 121 SmC_A* 154 SmC* 158 SmA* 173 Iso



112e: Cr 93 Iso

Fig. 30 Selected examples of chiral rod-like mesogens with one fluorinated chain (I^*C); one enantiomer is shown as example (SmC_A* = antiferroelectric SmC phase; SmC* = “ferroelectric” SmC phase; SmC_{FI}* = ferrielectric SmC phase; SmC_α* = helical SmC phase; SmI* = chiral tilted low temperature phase) [197–199]

End-branching of the R_F -chain has apparently no strong effect on the LC phase stability as shown in the examples of compounds **106a,b** with the same length as the (semi)fluorinated chain in Fig. 29 [177, 196] and for compounds **109b/111** with the same number of fluorinated carbon atoms as in the chain (Fig. 30) [198a]. This is surprising, considering the significant size of the perfluoroisopropyl group, but in line with the idea that nano-scale segregation instead of the rod-like shape of the R_F -chains provides a major contribution to mesophase stabilization. The effect of perfluorocyclohexyl end groups was also investigated recently [198b].

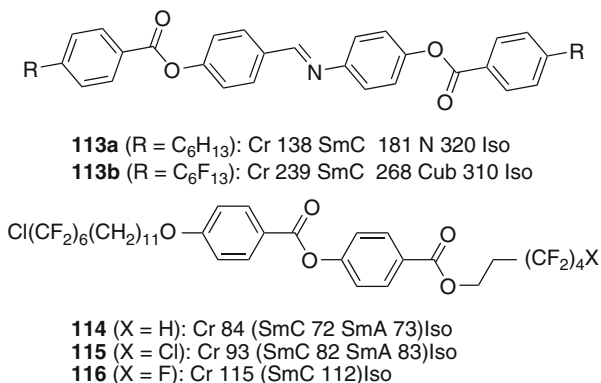
In addition to mesophase stabilization, R_F -chains also stabilize tilted smectic phases (SmC) with respect to non-tilted phases (SmA) – see, for example, compounds **100a,b**, **103**, and **104** in Fig. 29. Tilt can be caused by the specific interactions between the rod-like aromatic cores (dipolar, quadrupolar interaction and π -stacking) [200] or by adjustment of the average interfacial area required by the non-polar terminal chains and the aromatic cores at the aromatic-fluoroaliphatic interlayer interfaces. As the average cross section area of the terminal chains is increased by incorporation of R_F -chains the cross sectional area of the aromatic cores can be adjusted by increasing the tilt of these cores, as the projection of the cross section on the smectic plane rises with increasing tilt. For R_F -substituted rod-like molecules, tilting appears to be nearly independent of the core structure; even the cholesteryl benzoate **107**, incorporating only a single benzene ring, can form an SmC* phase [179, 180, 201]. Hence, the steric effect seems to be mainly responsible for SmC phase formation of fluorinated mesogens.

Surprising is the fact that replacement of only a single fluorine atom in the R_F -segment by a hydrogen atom leads to a dramatic reduction of mesophase stability, independent if the H is at the end of the R_F -segment [109, 181, 182] or in the middle [183] (see compounds **101/102** and **104/105** in Fig. 29). Probably, the induced dipole (less C–F dipoles are cancelled) and the polarization of the C–H bond increase the CED which reduces the incompatibility between the rod-like cores and the R_F chains and therefore distorts segregation. Replacement of one F by Cl also reduces mesophase stability but to a smaller extent (see, for example, compounds **114–116** in Fig. 31) [202, 204, 205]. Replacing only one H at the end of an alkyl chain by F also leads to a mesophase destabilization (see compounds **123**, **124** in Fig. 33 [206], as in this case the single fluorine decreases chain lipophilicity [67]. In all the above mentioned cases of substitution of a single F by H or H by F, it removes the tilt or reduces the SmC–SmA transition temperature. Only the introduction of one F in the middle of an alkyl chain has almost no effect on mesophase stability and tilt [195, 207].

4.3 Chiral SmC_A* Phases and de Vries Phases

Recently, fluorinated chiral LC with highly tilted smectic C phases and opposite tilt direction in adjacent layers (anticlinic tilt, SmC_A*) became of significant interest, as Lagerwall et al. proposed an application of 90° tilted anticlinic and

Fig. 31 Selected examples of rod-like mesogens with semiperfluorinated chains at both ends and the effect of modification of one chain end (T_f °C) [202, 203]



antiferroelectric smectics in display devices (orthoconic switching) [208]. Dabrowski et al. [197, 209–218] and several other groups [198a, 219–226] observed that LC with a chiral 2-octyloxy chain at one end and an alkyl chain with a relatively short fluorinated end-segments at the other end (e.g., compounds **109b**, **110b** and **111** in Fig. 30, and also related compounds with a reversed sequence of phenyl and biphenyl units or with other aromatic cores) can form anticlinic and antiferroelectric switching SmC phases (SmC_A^{*}) with a very high optical tilt of 40–45° and high values of the spontaneous polarization up to 500 nC/cm², whereas related nonfluorinated molecules have a significantly smaller tilt (20–35°) and much smaller polarization values.

There is experimental evidence that the optical tilt (40–45°) is much larger than the XRD tilt (around 20°), which suggests that the aromatic cores are much more tilted than the chains [198a, 212, 213, 227]. XRD and optical investigations indicate that the strong tilt in the SmC phases of semiperfluorinated LC is often retained in the SmA phases, but the tilt direction becomes randomized at the SmC-to-SmA transition, leading to so-called de Vries type smectic phases [228] (compounds **109b**, **110b** and **111** in Fig. 30 and also the pyrimidines **95–97** in Fig. 27) [213]. This type of randomly tilted smectic phases is formed if layer formation in smectic phases is mainly due to nano-segregation and not to molecular ordering of the rod-like segments (consequently in no case of de Vries phases an N-Sm transition was observed). In this case uniform tilt arises due to the transition from short range to long range tilt correlation and not by tilting of orthogonal aligned molecules, as usually observed for the SmA–SmC transitions. Such compounds show nearly no layer shrinkage at the SmA–SmC transition which is of importance for display applications.

Compounds **109–111** are related to MHPOBC (compound **112a**) which has a remarkable sequence of four distinct SmC^{*} subtypes and hence is one of the most carefully investigated LC materials [229]. Fluorination of this compound at the achiral chain (compound **112b**) leads to a material with broad regions of a synclitic tilted SmC^{*} and a helical SmC_α^{*} phase, but without anticlinic SmC_A^{*}. The sequence SmC_A^{*}–SmC^{*}–SmA^{*} is obtained if either the methyl group [229] or the other alkyl(oxy) group at the stereogenic center of **112a** was fluorinated

(compounds **112c** and **112d**, respectively) [230]. Comparison of the non-fluorinated compound **112a** with the CF_3 substituted compound **112c** indicates a significant mesophase destabilization by replacing the relatively small CH_3 group at the stereogenic center by a more bulky CF_3 group. No LC phases or strongly diminished mesophase stabilities were observed for molecules, like compound **112e**, combining the CF_3 -group with an additional perfluorinated chain at the stereogenic center [189, 199, 231]. Though end-branching of R_F -groups is tolerated (see compounds **90–93** in Fig. 26 and compound **106b** in Fig. 29), the close proximity of the branched R_F -group to the aromatic core strongly distorts the packing of these cores in the case of compound **112e** (Fig. 30).

4.4 Rod-Like Liquid Crystals with Two Fluorinated Chains at Opposite Ends: Layer Frustration

No escape from the steric mismatch between the cross sectional areas of the aromatic cores and the R_F -chains is possible for molecules with R_F -chains at both ends of a rod-like core. Therefore, there are nearly no LCs with two fluorinated chains directly attached to the aromatic core [74, 120]. Only if the aromatic core is sufficiently long to provide strong core–core interactions, is formation of mesophases possible, but in this case the direct connection of rigid core and rigid R_F -chains leads to very high melting points and therefore LC phases often cannot be observed (e.g., for the benzoic acid dimer **124b** in Fig. 33). Moreover, due to the mismatch of the cross sectional areas, there is an inherent tendency to form curved aggregates; for example, the fluorinated compound **113b** (Fig. 31) forms a bicontinuous cubic phase beside the SmC phase [203, 232–234]. Melting temperatures and interface curvature can be reduced by decoupling the R_F -segments by long alkylene spacers [202, 235, 236]. In compounds **114–116**, (Fig. 31), for example, the mixing of R_F -segments with the long C_{11} spacers by intercalation can effectively reduce the steric frustration occurring during layer formation, leading to SmA and SmC phases.

Another interesting aspect was worked out by Pugh et al., who have shown that rod-like compounds with fluorinated chains at both ends can accommodate large lateral substituents without distortion of the smectic phases (see compounds **118–121** in Fig. 32) [237, 238, 240, 241]. In contrast, the analogous hydrocarbon terminated molecules (e.g. compounds **117a,b**) form exclusively nematic phases and their mesophases are strongly destabilized by increasing the size of lateral substituents [239]. The mesophase destabilization in the case of the hydrocarbon analogs is due to a steric distortion of parallel packing of the rod-like cores and, for lateral alkyl chains, also due to the mixing of the lateral substituents with the terminal R_H -chains, in this way removing core–chain segregation. In the case of the fluorinated compounds the aliphatic and aromatic lateral substituents are incompatible with the R_F end-chains and hence organization in layers is retained. Moreover, the lateral groups can fill the excess space in the core region, in this way

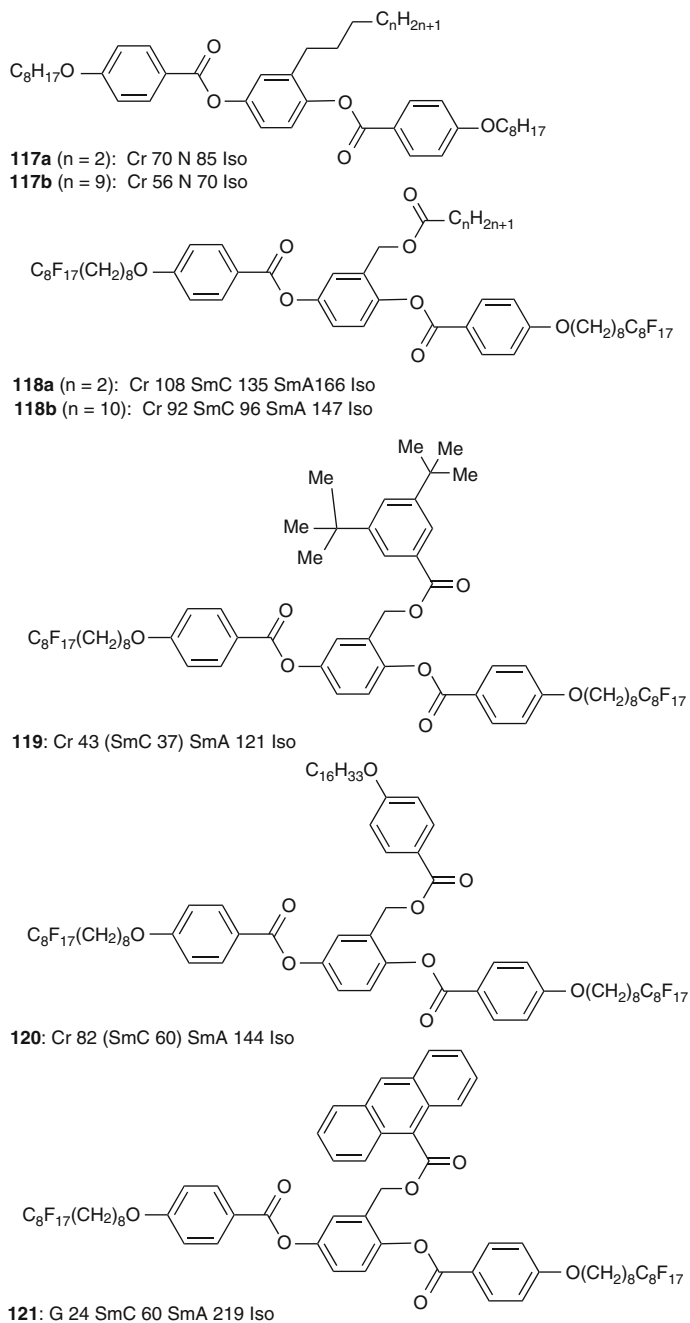


Fig. 32 Selected examples of rod-like mesogens with semiperfluorinated chains at both ends and additional bulky lateral substituents (T° C) [237–239]

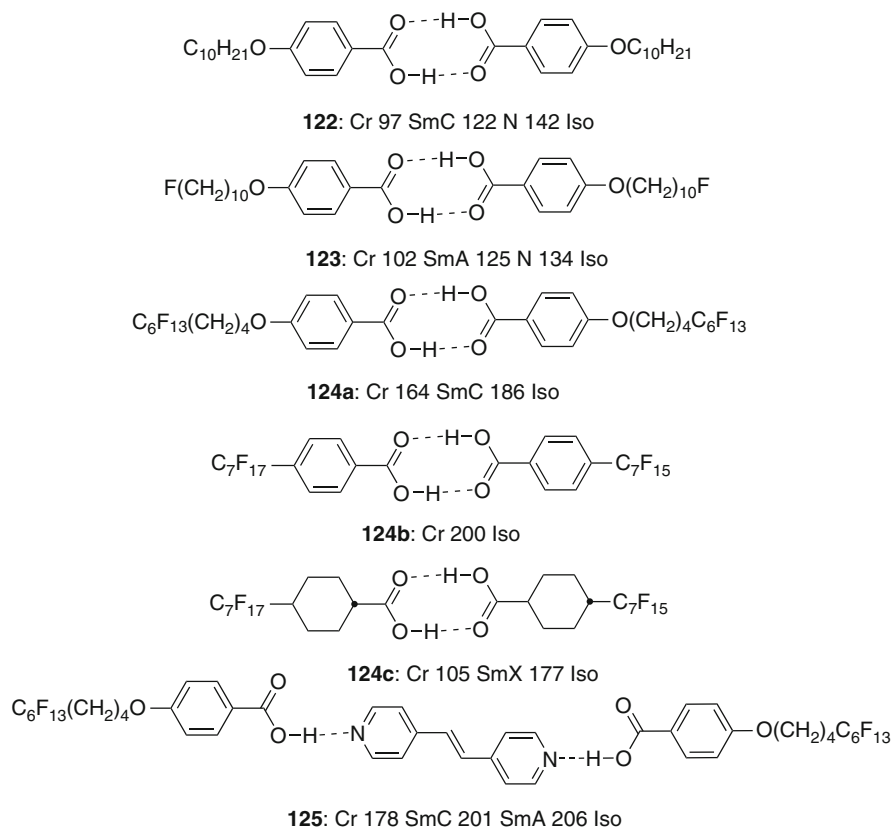


Fig. 33 Examples of supramolecular rod-like mesogens formed by self assembly of fluorinated benzoic acid and a *trans*-4- R_F -cyclohexane carboxylic acid ($T/^\circ\text{C}$) [120, 122]

increasing the average cross sectional area of the cores and reducing the difference to the cross sectional area of the R_F -chains, which reduces steric frustration for the packing in layers. This retains the layers, increases the SmA phase region, and reduces the stability of SmC phases. Interdigitation of the bulky R_F -chains could provide even more space, allowing the accommodation of extremely large lateral substituents. Related, but smaller effects of lateral substitution have also been observed for molecules with only one fluorinated tail [242].

Hydrogen bonded dimers of 4- R_F -substituted benzoic acids [119, 120, 122, 126], *trans*-4- R_F -substituted cyclohexane carboxylic acids [120], and hydrogen bonded complexes of benzoic acids with 4,4'-bipyridine and stilbazole [166, 243–246] can be regarded as supramolecular rod-like mesogens with two fluorinated chains. Figures 33 and 34 show comparisons of selected benzoic acid dimers and their bipyridine and stilbazole complexes. Comparison of the benzoic acid dimers **122** and **123** with *n*-alkyl chains and F-terminated *n*-alkyl chains, respectively, indicates that a single F-atom at the end of the alkyl chain reduces the mesophase stability

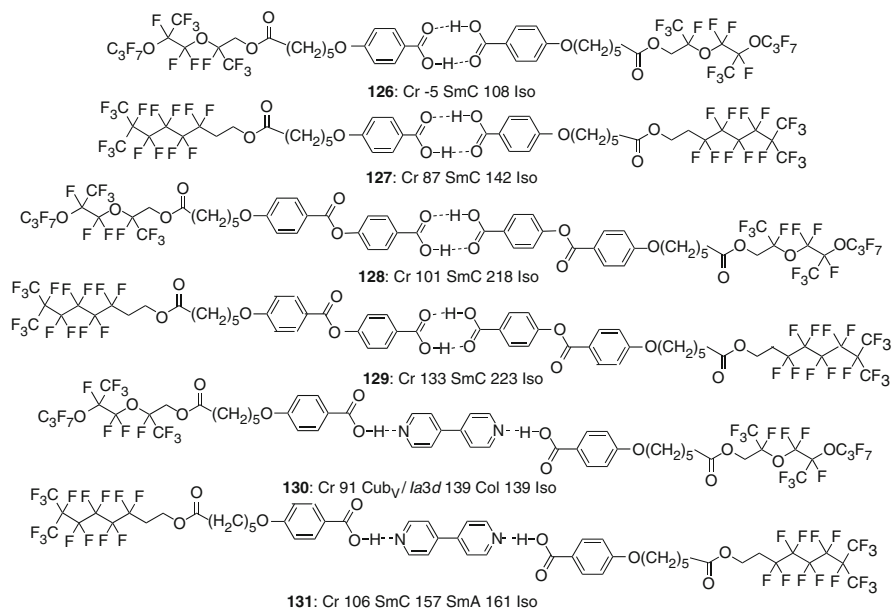


Fig. 34 Examples of supramolecular rod-like mesogens formed by self assembly of branched fluorinated benzoic acid into dimers and their 4,4'-bipyridine complexes (T° C) [166]

(see discussion in Sects. 1.3 and 4.2) and removes SmC phases whereas poly-fluorination of a longer segment (compound **124a**) gives rise to strong mesophase stabilization, favors tilt, and removes the nematic phase. Comparison of the benzoic acids **124a** and **124b** indicates the importance of the aliphatic spacers for the reduction of melting points; interestingly, a similar melting point depression is also observed by replacing the benzene rings of **124b** by a cyclohexane rings (**124c**). However, cyclohexane has rarely been used in combination with R_F -chains [120].

Whereas the hydrogen bonded complexes **124a,b** and **125** with linear R_F -chains have very high melting temperatures [246], much lower melting points were obtained with the complexes **126–131** comprising branched R_F -chains (Fig. 34) [166]. It is clear that the bis(perfluoropropylene oxide) chains are the most bulky R_F -groups in this series of compounds which leads to a bicontinuous cubic phase with *Ia3d* symmetry and a columnar phase for the bipyridine complex **130**. However, the benzoic acid dimers **126** and **128**, having the same bulky R_F -groups as **130**, do not form cubic and columnar phases. Probably, the increased polarity of the bipyridine complex compared with the benzoic acid dimers raises the polar-apolar incompatibility and increases the cohesive intermolecular forces between the self assembled rod-like cores. The dense packing combined with segregation of the bulky R_F -chains leads to the formation of curved aggregates.

It is also interesting to note that the bipyridine complex **131** with a slightly smaller end-branched fluorocarbon chain forms only SmA and SmC phases. In the SmA phase the layer distance ($d = 4.8$ nm) is significantly shorter than the length

of the complex (6.5 nm). This was explained by an intercalation of the R_F -segments with the relatively long aliphatic spacer units [166]. This provides another example of how suppression of segregation can reduce the steric frustration and retain lamellar organization. However, at reduced temperature, segregation of aliphatic spacers and R_F -chains appears (probably associated with a conformational change), now requiring a tilt of the molecules to compensate the different cross sectional areas of cores and R_F -chains. This leads to an unusual first order type transition to the SmC phase [166]. The improved segregation in the SmC phase leads to sharp layer interfaces which is evident from the XRD patterns as, for the segregated SmC phase, second and third order layer reflections can clearly be detected, while these reflections are absent in the SmA phase with mixed R_F -chains and spacers [166].

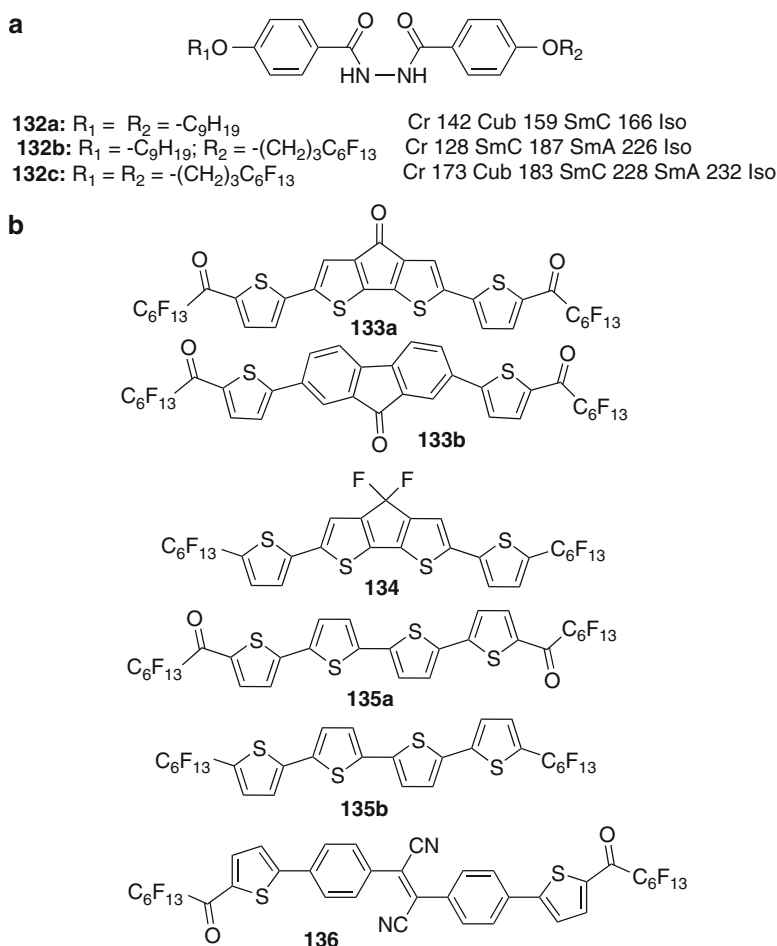


Fig. 35 Examples of (a) mesogenic dibenzoylhydrazines **132a–c** (T° C) [122] and (b) thiophene based π -conjugated aromatics [250–255]

An example of a special kind of mesogenic compound is provided by *N,N'*-bis(4-alkoxybenzoylhydrazines) (e.g., compound **132a**), known to form bicontinuous cubic phases [247–249]. It is interesting that fluorination of only one chain of these compounds (compound **132b**) removes the cubic phase which is restored if the second alkyl chain is also fluorinated (compound **132c**, see Fig. 35a) [122].

A main recent application of perfluorinated rod-like molecules is in organic electronics where π -conjugated rods were functionalized with R_F -chains in order to produce electron transport materials (n-type semiconductors) with 2D conduction pathways [256] and enhanced stability against oxidation. Some examples (compounds **133–136**) are collated in Fig. 35b, but their liquid crystalline phase behavior (if present) was in most cases not reported in detail [250–255].

4.5 Polycatenar Liquid Crystals

An even stronger effect of fluorination, producing layer modulation and transition from lamellar via bicontinuous cubic to columnar organization, could be expected for molecules with more than two terminal chains, so-called polycatenar mesogens [257–260]. In hydrocarbon based polycatenars the increasing mismatch between chain and core cross section area with rising chain number leads at first to nematic phases at higher temperature and SmC phase at lower temperature, completely replacing SmA phases. Further increase of the number of the chains and chain length gives rise to the phase sequence SmC-Cub_v-Col. The first polycatenar materials with perfluorinated chains were reported in 1991 [192]. Other compounds were reported by Nguyen et al. [258], Nishikawa et al. [261–264], and the Halle group (see compounds **98** and **99** in Fig. 28) [175, 194].

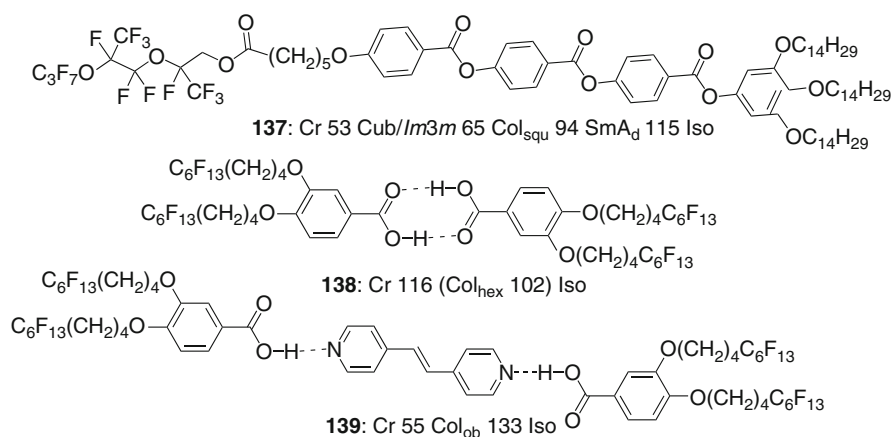


Fig. 36 Examples of molecular [262] and supramolecular [246] polycatenar mesogens with two fluorinated ends (**138**, **139**) and combining a fluorinated with a nonfluorinated end (**137**) (T° C)

For polycatenar hydrogen bonded complexes with fluorinated chains at both ends (e.g., **138**, **139**, see Fig. 36) formation of columnar phases was observed [246]. However, compound **137**, having a branched R_F -chain at one end and three R_H -chains at the other has a sequence of three distinct phases in the unusual sequence Cub-Col-SmA-Iso. For the SmA phase of compound **137** a structure with intercalated aromatic cores and R_F -chains and separated layers of the hydrocarbon chains was proposed. At lower temperature, when incompatibility rises and the aromatics and R_F -chains disintegrate, all three components form their own layers. However, this produces interface curvature and a columnar phase with square lattice is formed. On further cooling a transition to a cubic phase with $Im3m$ lattice takes place which is most likely of the bicontinuous type [262]. This leads to the unusual phase sequence Cub_V-Col-SmA where the positions of the Cub_V and Col phases are exchanged with respect to the usually observed phase sequences. The Col-Cub transition at lower temperature could be the result of the decreased conformational disorder of the terminal chains which reduces the steric frustration and hence reduces the interface curvature.

A systematic study concerning the effect of the number of R_F -chains on the LC phase type was carried out by Bilgin-Eran et al. for a series of Schiff base and salicylideneimine based LCs with relatively short rod-like cores combining R_F -chains with alkyl or oligo(ethylene oxide) chains [154]. Depending on the number of chains, SmA, SmC, and Col_{hex} phases were found. Core-shell columns and triple layer structures were discussed for some of the mesophases; selected examples (compounds **140–142**) are shown in Fig. 37. It is remarkable that phase stabilization by chain fluorination allows formation of LC phases even for polycatenar mesogens with relatively short rod-like cores. For non-fluorinated polycatenars the minimum number of rings in the core structure required to obtain

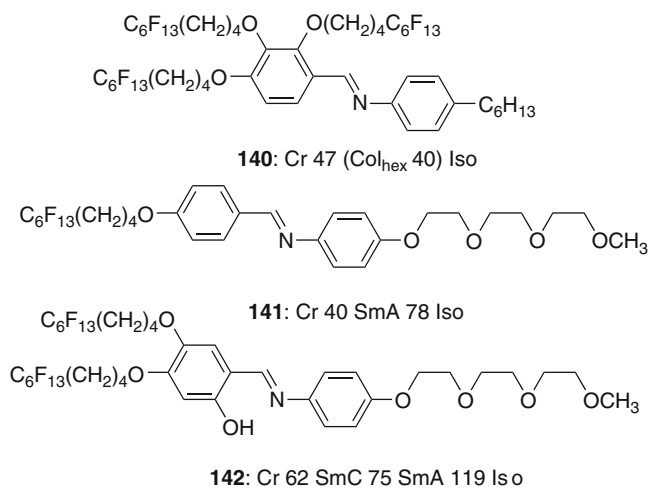


Fig. 37 Selected examples of polycatenar molecules based on Schiff base and salicylideneimine rod-like cores (T° C) [154]

LC phases usually corresponds to at least the number of attached chains [258]. Moreover, no SmA phases were observed for non-fluorinated polycatenar mesogens, whereas chain fluorination obviously enables the formation of SmA phases, which are most probably of the de Vries type. It seems that non-fluorinated polycatenars are mainly stabilized by core–core interactions, whereas the mesophase stabilization by the fluorophobic effect retains the layer structure even if core–core interactions are relatively weak.

5 Discotic Liquid Crystals

Disc-like molecules represent the second important group of liquid crystalline materials for which mesomorphism is based on the molecular shape [12, 13]. Due to the disc-like shape, these molecules have a natural tendency to organize in columns and to form columnar LC phases. Depending on the resulting 2D lattice hexagonal ($p6mm$), square ($p4mm$ or $p4gm$), different types of rectangular ($c2mm$, $p2mm$, $p2gg$, $p2mg$), and oblique lattices ($p2$) can be distinguished [29] (see Fig. 38). Distortion of the hexagonal symmetry could be due to the presence of an elliptical or board-like molecular shape or, alternatively, due to a uniform tilt of the disc-like molecules in the columns. However, reduced flexibility of R_F -chain and segregation of the R_F -segments could also lead to a transition from hexagonal to lower symmetry, or even to the organization of the columns in lamellae (lamello-

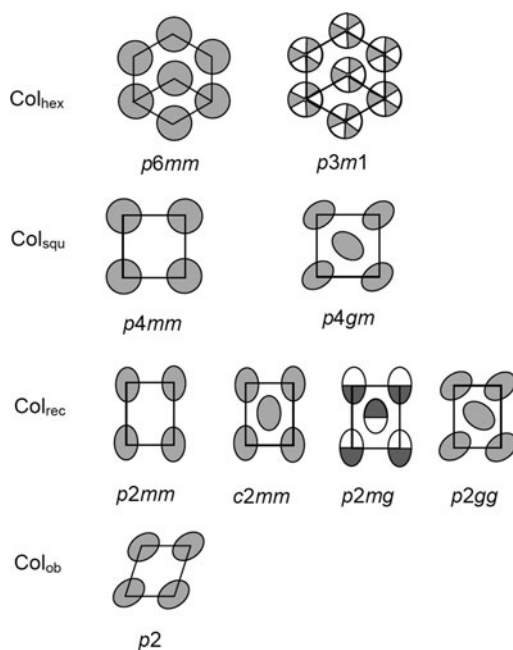


Fig. 38 2D-lattices of columnar mesophases (cuts perpendicular to the column long axes) and their plane groups

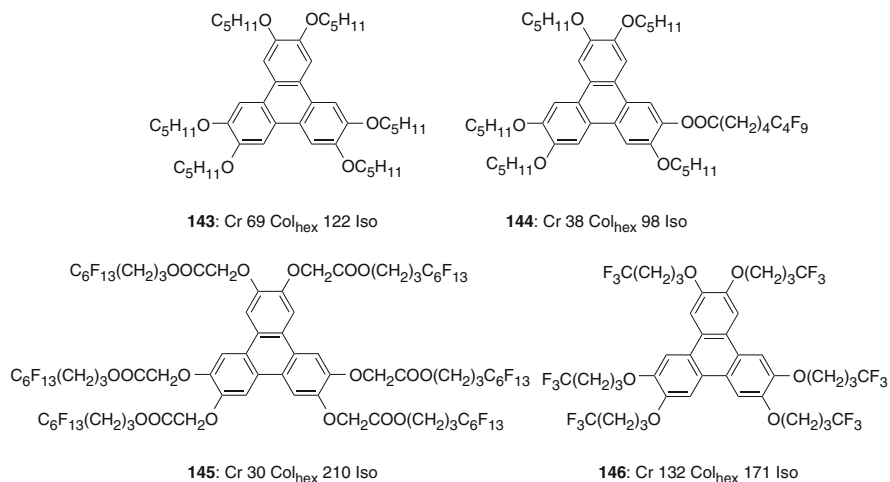


Fig. 39 Examples of triphenylene based disc-like molecules incorporating fluorinated segments in their peripheral chains (T° C) [267, 268]

columnar phases). It should also be noted that hexagonal symmetry often results from time and space averaging, i.e., the actual local symmetry could be lower, but on a larger scale it averages to give a hexagonal overall symmetry.

Present interest in disc-like aromatic molecules results mainly from their application as 1D charge carrier materials for use in photoconductors, light emitting devices, organic transistors, and photovoltaic applications [265].

Fluorinated disc-like molecules were first synthesized and investigated by Ringsdorff et al. [266, 267]. The use of a single fluorinated peripheral chain (compound **144**) has surprisingly reduced the columnar phase stability when compared with the parent hydrocarbon compound **143** (see Fig. 39) [267]. However, compound **145** with six fluorinated chains shows extremely high columnar phase stability, indicating a similar stabilizing effect of chain fluorination on LC phase stability as for rod-like mesogens [267]. Related triphenylenes with six R_F-chains have been reported by Shimizu et al. and these compounds have a high tendency for a homeotropic orientation (columns aligned perpendicular to the surface) on a variety of substrates, which allows controlled alignment of the (semi)conducting columns [268–270]. Even a single trifluoromethyl group at the end of each chain (compound **146**) provides a significant phase stabilizing effect (see Fig. 39) [268, 271].

Investigation of symmetric and non-symmetric triphenylenes combining three fluorinated and three non-fluorinated chains (compounds **149** and **150** in Fig. 40) has shown that these compounds can possess a higher stability of the columnar phases compared to those with all chains semiperfluorinated (compound **148**), whereas the distribution of the fluorinated chains (symmetric vs. non-symmetric) does not play a significant role [272].

Disc-like molecules with a pentakis(phenylethynyl)phenoxy core commonly form nematic phases which can be strongly stabilized by the presence of only one

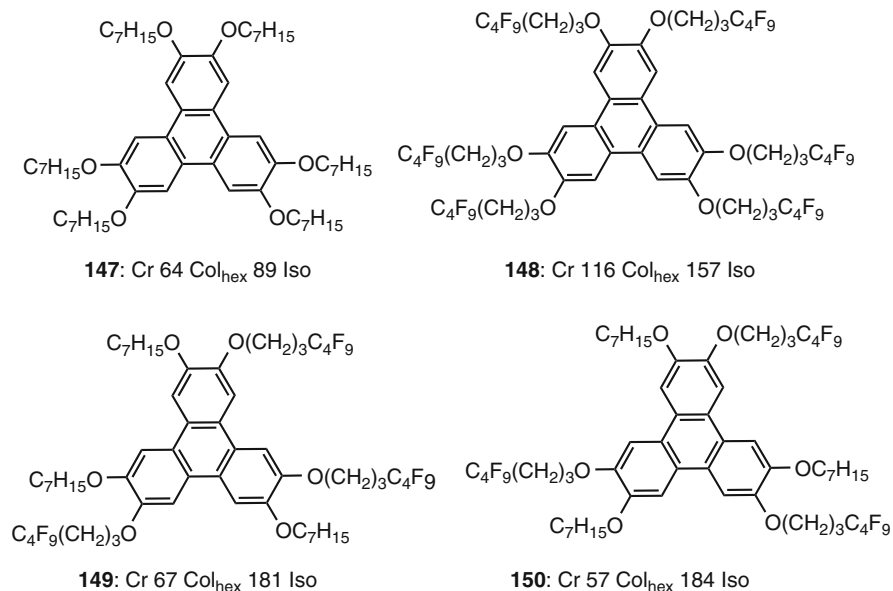


Fig. 40 Comparison of the effects of the number and distribution of the fluorinated chains in disc-like triphenylene mesogens (T° C) [272]

fluorinated chain (see compound **151** in Fig. 41). XRD studies indicate a nematic phase composed of a cybotactic cluster with local lamellar structure [273]. In this case the R_F-chains induce a local lamellar organization due to their segregation and tendency to align parallel with other R_F-chains; however, the fluorophobic effect of only one chain per molecule seems not to be strong enough to induce a long range smectic organization.

Hexa-*peri*-hexabenzocoronenes (see Fig. 42, e.g., compound **152**) were prepared with fluorinated chains at the periphery (e.g., compound **153**) to act as an insulating shield around the columns in order to reduce lateral conduction, and hence to improve one-dimensional charge carrier mobility [274, 275, 278]. Surprisingly, branching of the R_F-chains (compound **154**) leads to a loss of columnar order, giving rise to amorphous material [276]. Insertion of a *p*-substituted phenyl ring between disc-like core and semiperfluorinated chain (compound **155a**) switches the mesophase structure from columnar to smectic [274]. This seems to be an effect of the increased rigidity and linearity of the R_F-chains (see Sect. 3.2.5) which becomes more dominant if it is combined with a rigid and linear *p*-substituted benzene ring. Accordingly, the SmA phase is removed again and replaced by a hexagonal columnar phase if the rigid R_F-chain is shortened and the flexible alkyl spacer is elongated as in compound **155b**.

Introduction of perfluorinated chains into the periphery of other disc-like or board-like π -conjugated aromatics [251, 252], such as coronene diimides [279], perylene diimides [280–282], naphthalene tetracarboxylic diimides [283–286],

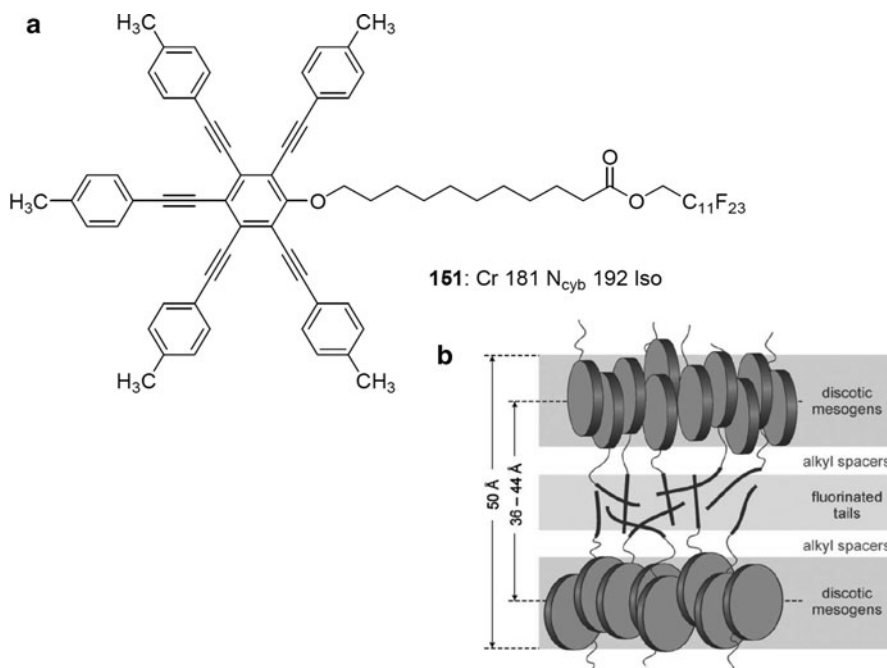


Fig. 41 Structure of a disc-like molecule with one R_F-chain and (b) the organization in the cybotactic clusters of the nematic phases (N_{cyb} = cybotactic nematic phase) (*T*/°C) [273]. Reproduced with permission [273], copyright 2007, The Royal Society of Chemistry (RSC)

pyromellitic diimides [287], and porphyrins (see for example compound **156**) [277, 288], was used to stabilize and modify self assembly by the fluorophobic and by the steric effects of R_F-chains, to improve alignment properties by tailoring the surface tension, and also to adjust the HOMO-LUMO gap by using the electron-withdrawing effect of the R_F-chains (if directly coupled to the π -system) [289, 290]. As for the rod-like π -conjugated aromatics, in this case n-type semiconductors can also be achieved due to the electron-withdrawing effect of R_F-chains and air stable organic semiconductors were also reported [256]. Though all these compounds have the potential to form LC phases, the main focus was on their solid state properties and charge carrier mobilities.

6 Metallomesogens

There are only relatively few metallomesogens [291a] incorporating semiperfluorinated segments, which are collated in Figs. 43–45. For example the rhenium(I) imine complex **157** (Fig. 43) shows an SmA phase instead of the nematic phase of the analogous alkyl substituted compound (Cr 129 N 167 Iso (°C)), again indicating the mesophase stabilizing and positional order inducing effect of perfluorinated

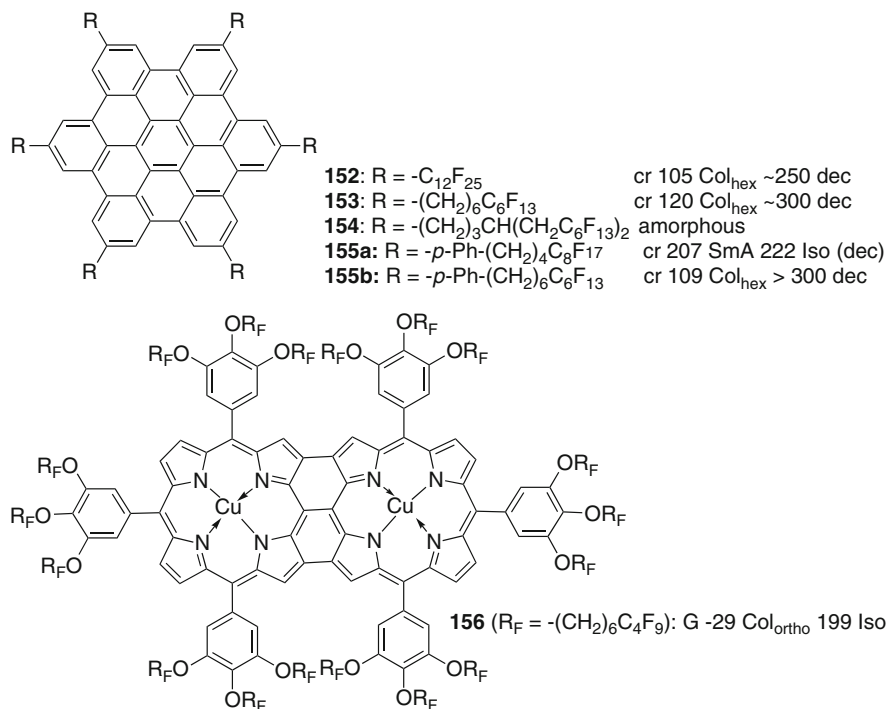


Fig. 42 Effect of chain fluorination on the LC phases of peri-hexabenzocoronene based mesogens (compounds **152–155**) [274–276] and the fused metalloporphyrin dimer **156** ($T^\circ\text{C}$); G = glassy state, $\text{Col}_{\text{ortho}}$ = orthorhombic phase [277]

chains [203, 232]. This rod-like metallomesogen is derived from compound **113b** (see Fig. 31) which forms a bicontinuous cubic phase. The introduction of the bulky $\text{Re}(\text{CO})_4$ unit increases the average cross section area of the core units which leads to removal of interface curvature and formation of an SmA phase, replacing the bicontinuous cubic phase. SmC* phases were reported for salicylideneimine-VO complexes [291b].

Other rod-like metallomesogens, based on Ag, Au, Cu, Fe, Pd, and Pt isocyanide complexes, forming SmA phases, have recently been reported by Espinet et al. [292] and examples are collated in Fig. 43. The isocyanide **158** and its complexes **159–162** can be regarded as mesogenic materials with only one aromatic ring as discussed in Sect. 3.1, some of them (**159**, **160**) additionally stabilized by interactions between the metal centers and ligands. Complexes **162** and **163** represent rod-like supramolecular (metallo)mesogens with R_F -chains at both ends (see Sect. 4.4). The counterions and iodo-ligands, respectively, fill the free space in the core region and therefore allow formation of SmA phases for these compounds.

Most other fluorinated metallomesogens represent disc-like or board-like molecules (Fig. 44). The focus of these studies was on the cross-over between lamellar and columnar self-assembly for molecules with a disc-like core. Stabilization of SmA

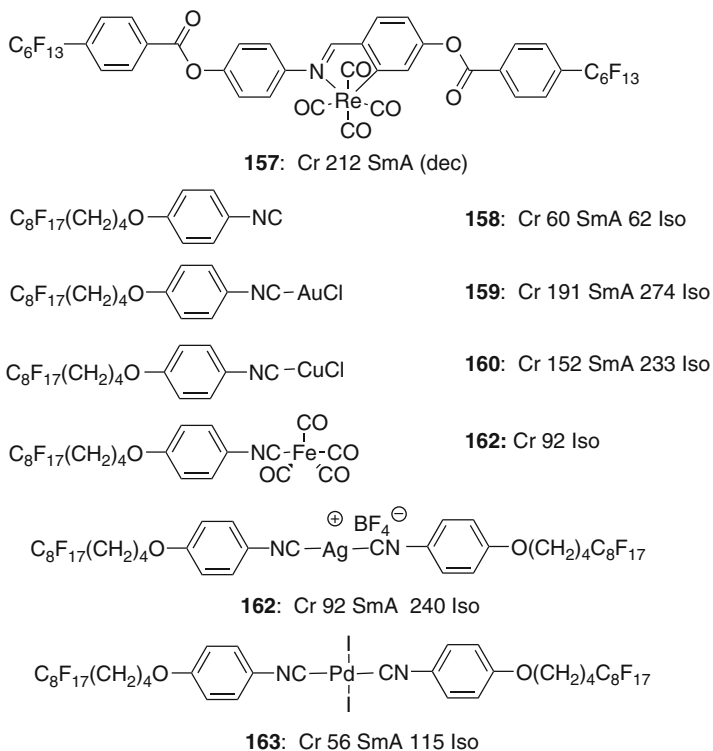


Fig. 43 Representative fluorinated metallomesogens forming SmA phases (T° C) [203, 292]

phases by chain fluorination was observed for the salicylaldimato Cu(II) and Pt(II) complexes **165** with only four chains [154]. A transition from lamellar to hexagonal columnar phases was reported by Szydłowska et al. for chain fluorination of enaminoketone Ni(II)-, Cu(II)-, and VO(II)-complexes (e.g., compound **164**) [294].

The perfluorinated Pd- and Pt-organyls **166–169**, carrying up to eight chains, (Figs. 44 and 45) have been synthesized by Bilgin-Eran et al. [40, 293]. In compound **168** the discotic nematic phase of the related hydrocarbon derivative was replaced by a hexagonal columnar phase with strongly increased phase transition temperature. A columnar phase was also formed by compound **166** with seven peripheral chains, whereas compound **167** and **169** with a smaller number of peripheral chains form SmA and SmC phases (see Figs. 44 and 45a) [40, 293]. Remarkably, in mixtures between the smectic six-chain compound **169** (SmA, SmC) and the hexagonal columnar eight-chain compound **168** (Col_{hex}), a nematic phase was induced (see Fig. 45a) at the columnar-smectic cross-over [293].

A unique temperature dependent phase sequence hexagonal columnar - re-entrant isotropic (Iso_{re}) - smectic A was observed by Szydłowska et al. for some *cis*-enaminoketone Ni(II) and Cu(II) complexes combining two fluorinated and two hydrocarbon chains (compound **171**). Related complexes with only one R_{F} -chain

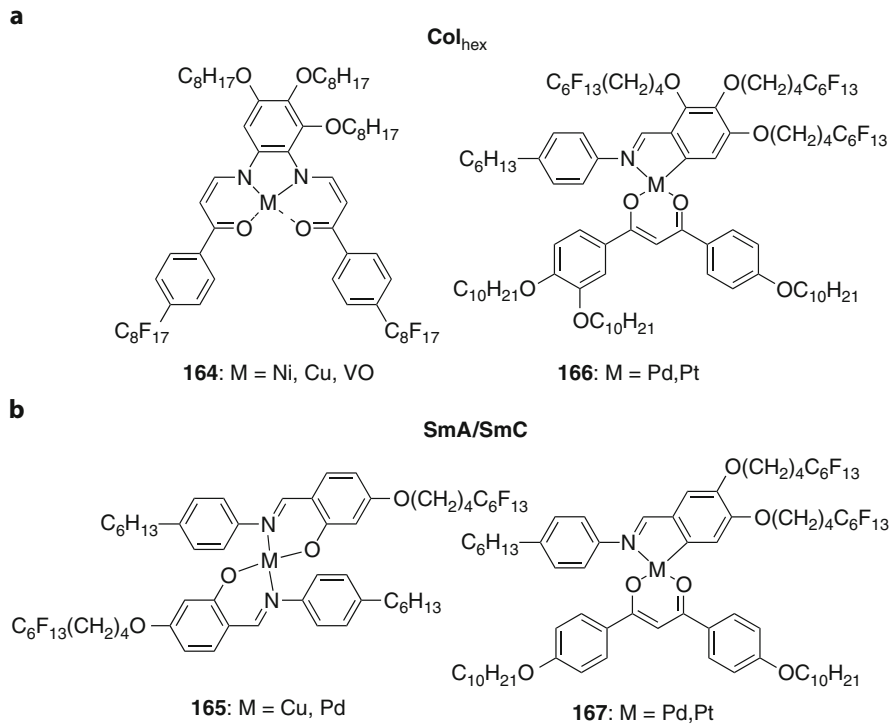
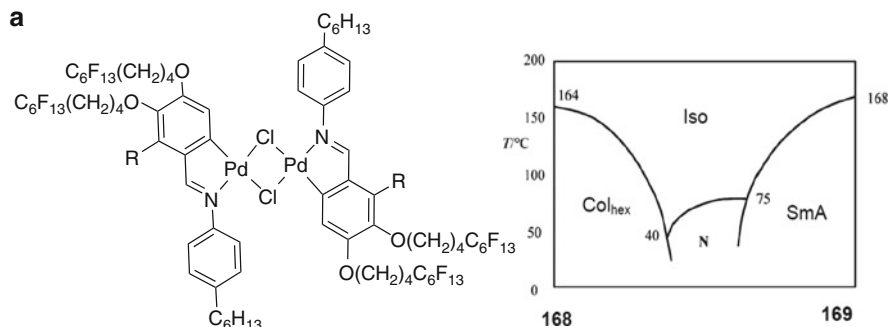


Fig. 44 Representative fluorous metallomesogens with disc-like and board-like shape (T° C) [40, 41, 294]

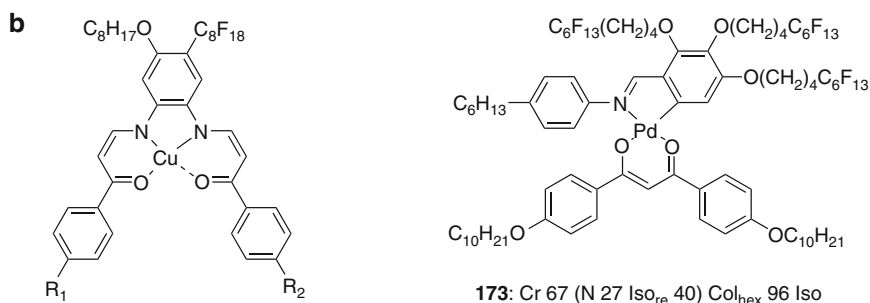
and three R_H -chains (compound **170**) form SmA phases and for complexes with three bulky R_F -chains and only one R_H -chain (compound **172**) hexagonal columnar phases were observed (see Fig. 45b) [41]. For the intermediate compound **171** with two R_F - and two R_H -chains the competing tendency to form columnar or lamellar structures leads to a complete loss of long range order with formation of a re-entrant isotropic phase (Iso_{re}) in a distinct temperature range between the Col_{hex} and the SmA phases [41]. This temperature dependent behavior is analogous to the observations made by mixing metallomesogens **168** and **169** (Fig. 45a) [293], but in these mixtures order is not completely removed at the Sm-Col transition as orientational order is retained in the induced nematic phase. A phase sequence N- Iso_{re} -Col combining the nematic and the re-entrant isotropic phase was observed for the Pd-diketonate complex **173** (Fig. 45c) [40]. Hence, it seems that for disc-like and board-like molecules disorder is generated at the lamellar-columnar cross-over instead of the formation of 3D ordered bicontinuous cubic phases as typically observed for flexible and also rod-like amphiphiles.

Fused copper porphyrin dimers (compounds **156** and **177**, see Figs. 42 and 47) with an orthorhombic phase and a rectangular column phase, respectively, were recently reported by Aida et al. [277]. Interestingly, the partly R_F -substituted



168 (R = O(CH₂)₆C₄H₉): Cr 101 Col_{hex} 165 Iso

169 (R = H): Cr 129 (SmC 107) SmA 168 Iso



170 (R₁ = R₂ = OC₈H₁₇): Cr 142 (SmA 115) Iso

171 (R₁ = OC₈H₁₇, R₂ = C₈F₁₇): Cr 121 (SmA 64 Iso_{re} 102 Col_{hex} 290 Iso)

172 (R₁ = R₂ = C₈F₁₇): Cr 120 Col_{hex} 270 Iso

Fig. 45 Fluorous metallomesogens at the lamellar-columnar cross-over: (a) induction of a nematic phase by mixing metallomesogens with smectic and columnar phases, (b) metallomesogens showing re-entrant isotropic mesophases (Iso_{re}) (*T*/°C) [40, 41, 293]

porphyrin **177** is an n-type semiconductor whereas the fully R_F-substituted porphyrin **156** is a p-type semiconductor, due to the changed stacking geometry in the two different LC phases (see Fig. 47d).

7 Polyphilic Liquid Crystals

Molecules composed of more than two distinct incompatible units can be regarded as polyphilic if polyphilicity is manifested by formation of a periodic LC structure where the distinct molecular segments are organized in at least three distinct nano-compartments. Some examples of polyphilic LCs were already included in the

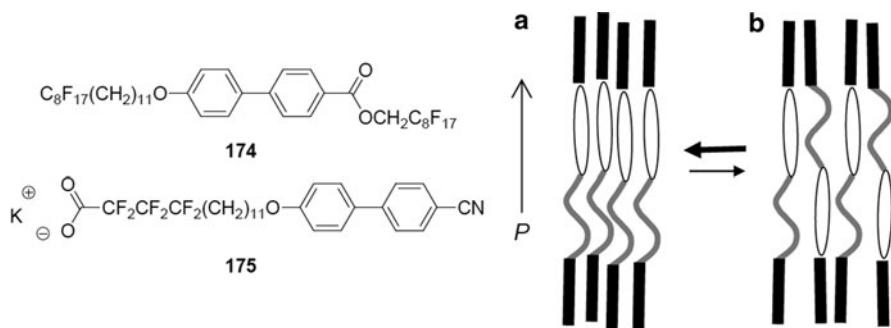


Fig. 46 Examples of polyphilic rod-like compounds and possible modes of self-assembly of compound **174**; (a) segregated non-centrosymmetric layer which would lead to longitudinal ferroelectricity if adjacent layers would organize with the same direction and (b) non-segregated centrosymmetric layer [297]

previous sections. For example, each rod-like or disc-like molecule combined with semiperfluorinated chains composed of two sufficiently large R_H - and R_F -segments could be regarded as polyphilic if polyphilicity is expressed by formation of a segregated trilayer structure in smectic phases or core-shell structures in columnar and micellar cubic phases [143, 146, 156].

In this Section, the focus will be on new modes of polyphilic self-assembly, leading to mesophase morphologies with reduced phase symmetry and increased complexity. First attempts in this direction were made by Tournilhac et al., who designed polyphilic rod-like molecules by combining more than two incompatible units. In compound **175**, for example, an aromatic core, an R_F -segment, and an aliphatic spacer were combined with an ionic group [296]. In compound **174** a biphenyl moiety, R_F -segments, and an aliphatic chain were interconnected in such a way that a non-centrosymmetric lamellar structure should be favored due to segregation of the R_F -segments from the aliphatic and aromatic units (see Fig. 46) [297]. This non-centrosymmetric lamellar organization can lead to longitudinal ferroelectricity in achiral LC phases, i.e., polar order perpendicular to the layer planes. Though ferroelectricity in LC phases of achiral molecules was later more easily achieved with bent-core mesogens (but in this case with the polar direction parallel to the layer planes) [298], this work has inspired attempts to achieve complexity in mesogenic systems by using molecular polyphilicity. Escape from simple layer structures is possible by changing the molecular topology of the polyphiles from linear to star-shaped, T-shaped, and X-shaped as discussed in the following sections.

7.1 Ternary Amphiphiles with Star-Like Shape

Lehmann et al. developed the concept of star-shaped molecules composed of three phenylbenzoate based rod-like cores directly connected by ester groups to a central

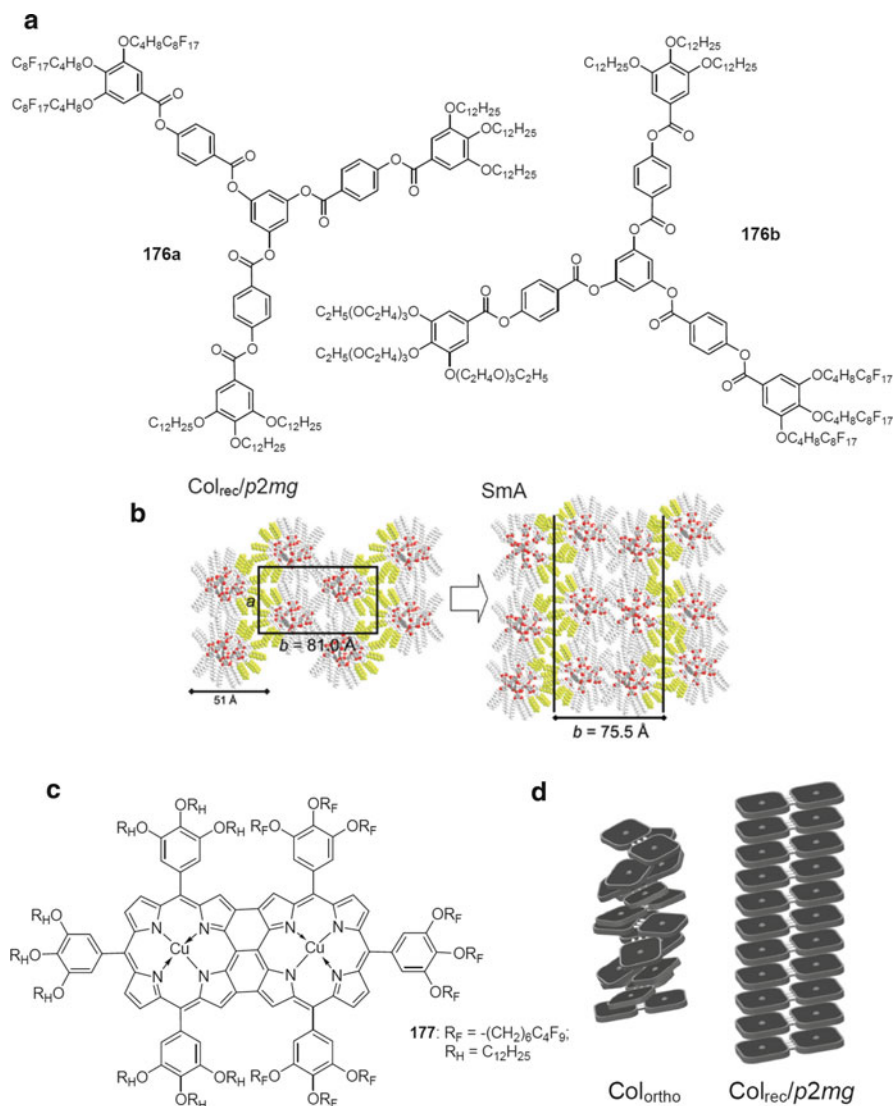


Fig. 47 (a) Examples of polyphilic molecules with star shaped molecular topologies and (b) their mesophase morphologies [295]. (c) Janus-type porphyrin **177** [277] and (d) modes of self assembly of the completely R_F -substituted porphyrin **156** (left, for structure see Fig. 42, Col_{ortho} ; G -29 °C Col_{ortho} , 199 °C Iso) and the partly fluorinated porphyrin **177** (right, $Col_{rec}/p2mg$, Cr -22 °C $Col_{rec}/p2mg$, 163 °C Iso); Col_{ortho} = orthorhombic columnar 3D phases; (b) reproduced with permission [295], copyright 2008, The Royal Society of Chemistry (RSC); (d) reproduced with permission [277], copyright 2011, American Chemical Society (ACS)

phloroglucinol core [48, 295]. In some of the star branched oligobenzoates, two (R_F , R_H) or even three different and incompatible types of chains (R_F , R_H , EO) were attached to the C_3 -symmetric aromatic core (Fig. 47). Compounds **176a,b**, for

example, show complex columnar mesophases at low temperature and lamellar phases (SmA) at higher temperature [295, 299].¹³ The SmA phase results from the segregation of the fluorinated chains into distinct layers, separate from the layers formed by the hydrocarbon parts of the molecules. The aromatic columns in the hydrocarbon layers adopt only short range correlation and hence a long range positional correlation of the columns in adjacent layers is not achieved. Only at reduced temperature is long range order of the aromatic columns established, which in the case of compound **176a** leads to a 2D lattice with the unusual plane group symmetry $p2mg$ ($Col_{rec}/p2mg$). The same type of $p2mg$ phase was observed for the Janus type porphyrin dimer **177** (Fig. 47) [277].

Janietz et al. reported several series of hydrogen bonded complexes between benzoic acids with two or three semi-perfluorinated chains and alkyl substituted melamine derivatives (see Fig. 18) [153]. For the complex **178** the R_F -chains segregate in distinct columns with adoption of long range positional order [153, 300]. As the periodicity of the positions of the R_F -columns is larger than the periodicity of the main columns formed by the aromatic cores, a larger super-lattice was observed (see Fig. 48). Related super-lattice structures were also reported for polyphiles incorporating oligosiloxane segments [301], polar groups [302], or incompatible polymer chains [303, 304].

Percec et al. described the self-assembly of R_F -substituted bis-dendritic benzamides, such as compounds **179a** and **179b**, combining a “dendron” decorated with perfluorinated chains and a “dendron” with alkyl chains. In the hexagonal columnar LC phases of these molecules the smaller alkyl chains form the centers of the columns, the aromatics are arranged in cylindrical shells surrounding the aliphatic columns, while the larger fluorinated chains form a fluororous continuum

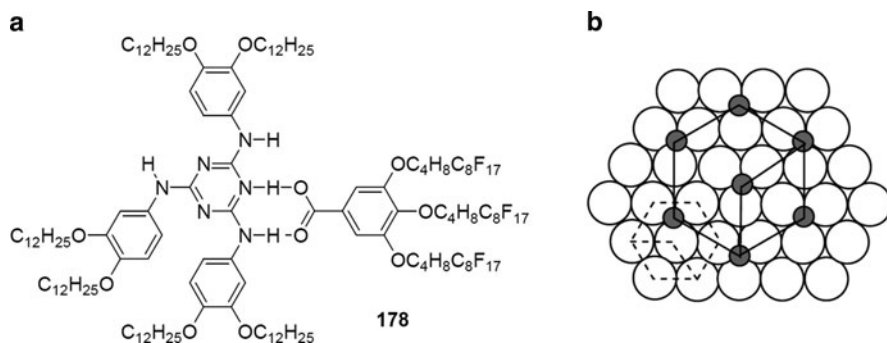


Fig. 48 (a) Janus-type discotic hydrogen bonded aggregate **178** and (b) possible hexagonal superlattice LC phase (cross section through the structure viewed along the column axis, gray = regions of the R_F -chains) [300]

¹³The mesophase stabilization by the fluorophobic effect is remarkably large for compound **176a** ($Col_{rec}/p2mg$ 144 °C SmA 174 °C Iso) [295] and compound **176b**: $Col_{rec}/p2mg$ 88 °C SmA 167 °C Iso [299] if compared to the related non-fluorinated compound (Col_{ortho} 53 °C Iso) [295]; (Fig. 47).

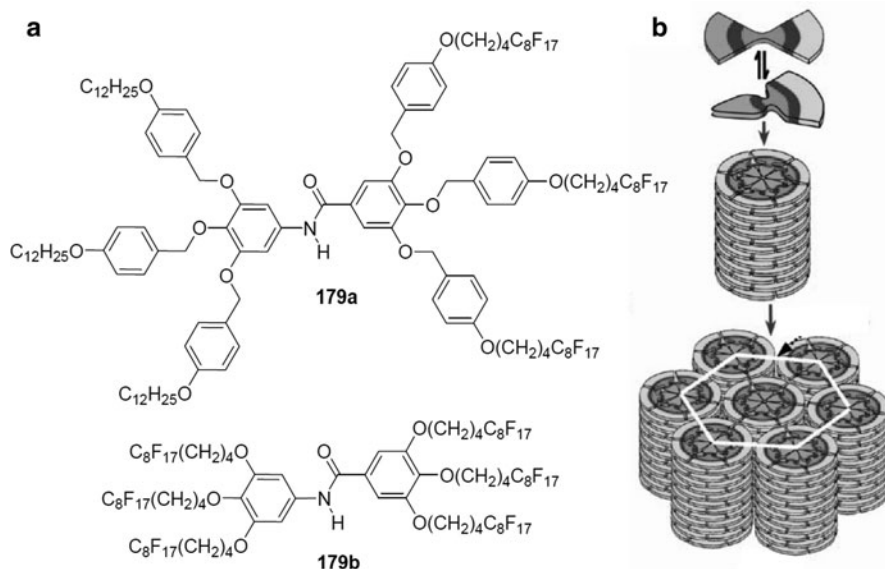


Fig. 49 (a) Examples of Janus-type bis-dendrons and (b) model of the self-assembly in a core-shell columnar LC structure [154]. Reproduced with permission [154, Bioinspired supra-molecular liquid crystals, Fig. 3], copyright 2006, The Royal Society

around the core-shell columns (see Fig. 49) [305]. With respect to the positions of aliphatic and aromatic units, this type of core-shell morphology can be regarded as inverted to those discussed in Sect. 3.2.4.

A very simple star polyphile with radial arrangement of hydrophilic, hydrocarbon and fluorocarbon chains linked to a central 1,3,5-substituted benzene ring (compound **180**) has recently been shown to form a hexagonal columnar LC structure when mixed with water. In this lyotropic LC phase all three units are separated, leading to a (12.6.4) tiling, as shown in Fig. 50 [306]. This tiling pattern is composed of hexagonally packed water channels embedded in a hydrophobic matrix which is split into oleophilic and fluorophilic prismatic domains. This tiling pattern is analogous to related tilings previously reported for the thermotropic LC phases of T-shaped polyphiles [8] and the morphologies of some ternary star polymers [307–309]. For compound **180** the added water enhances the polar interactions between the oligo (ethylene oxide) chains by providing hydrogen bondings, and therefore it is in this case required for micro-segregation and mesophase formation.

7.2 Liquid Crystal Honeycombs and Other Complex Phase Structures of T-Shaped Ternary Amphiphiles

A new direction in LC research is based on polyphilic molecules with a T-shaped molecular topology [8, 310–313]. Usually, in these molecules a rigid rod-like core

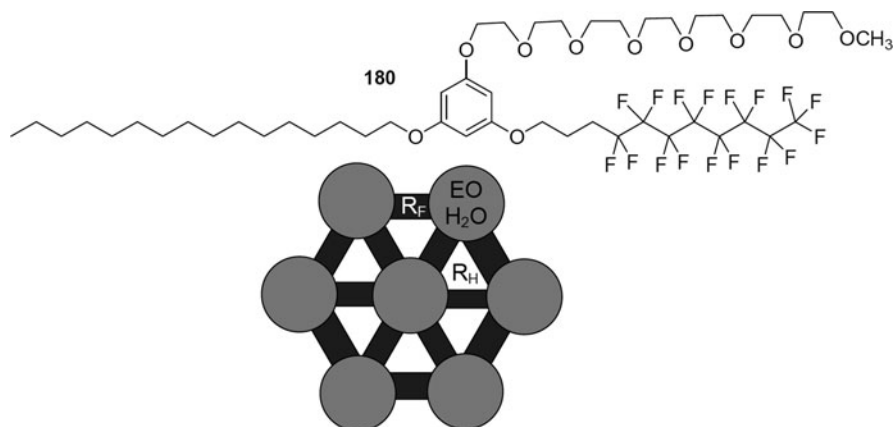


Fig. 50 Molecular structure of the star-polyphile **180** and schematic picture of the molecular arrangement in the (12.6.4) tiling of the lyotropic Col_{hex} phase [306]

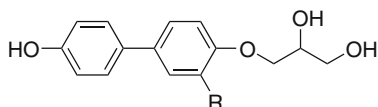
of specific length is combined with one or more polar groups at both ends, providing sufficiently strong intermolecular interaction, such as cooperative hydrogen bonding or ionic interactions [314, 315]. As a third incompatible unit a flexible and non-polar chain, incompatible with the polar groups as well as with the rigid aromatics is attached laterally to the rod-like moiety¹⁴.

Figure 51 shows selected examples of such T-shaped polyphiles with a bolaamphiphilic structure of the aromatic core (compounds **181–183**). Typically, semi-perfluoroalkyl chains were used as lateral chains [316, 317, 320–323], but also alkyl chains [318, 324], siloxanes, and carbosilanes can be used [325]. The advantage of the R_F -chains is again their increased incompatibility with the polar groups and aromatic unit, providing a considerably enhanced stability of the self-assembled structures. Moreover, as R_F -chains have a significantly larger volume compared with alkyl chains with the same length, space can be efficiently filled with shorter R_F -chains. In most cases the R_F -chains are attached via an aliphatic spacer unit to the rod-like core in order to achieve a decoupling of the relatively rigid R_F -chains from the aromatic cores. As shown in the comparison of the two compounds **182b** and **182c**, the additional spacer unit reduces the melting point, whereas the mesophase type (Col_{hex}) is not modified if the total chain volume is not changed [316].

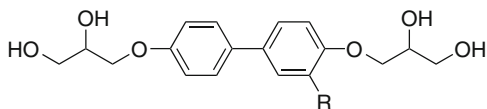
7.2.1 Liquid Crystal Honeycombs

In their LC phases these T-shaped block molecules, bearing three types of mutually incompatible groups, were found to form many different types of fluid self

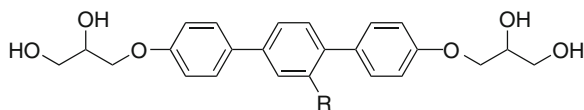
¹⁴ Besides the T-shaped bolaamphiphiles covered here, there are also T-shaped polyphiles with a reversed position of hydrophilic and lipophilic units, see [311–313].



181a (R = $-\text{C}_{11}\text{H}_{23}$): Cr 109 (Col_{hex} (hexagons) 102) Iso
181b (R = $-(\text{CH}_2)_3\text{C}_8\text{F}_{17}$): Cr 119 Lam_{Iso} 139 Iso



182a (R = $-\text{C}_9\text{H}_{19}$): Cr 67 Col_{rec}/*c2mm* (rhombs) 100 Iso
182b (R = $-(\text{CH}_2)_3\text{C}_6\text{F}_{13}$): Cr 47 Col_{hex} (hexagons) 171 Iso
182c: (R = $-\text{C}_8\text{F}_{17}$): Cr 97 M1 134 Col_{hex} (hexagons) 158 Iso



183a (R = $-\text{C}_{14}\text{H}_{29}$): Cr 77 Col_{rec}/*p2gg* (pentagons) 160 Iso
183b (R = $-(\text{CH}_2)_6\text{C}_8\text{F}_{17}$): Cr 47 Col_{hex} (hexagons) 229 Iso

Fig. 51 Examples of T-shaped bolaamphiphiles with non-polar lateral R_F/R_H-chains showing the effect of fluorination on mesophase types and transition temperatures ($T^\circ\text{C}$) [316–318, Lehmann A, Prehm M, Tschierske C, unpublished results, 319]

assembled structures, as shown in Fig. 52 for the series of biphenyl based bolaamphiphiles **182** with two terminal glycerol groups and one semiperfluorinated lateral chain. The most prominent are the honeycomb LC phases (also known as polygonal cylinder phases, see Fig. 52c–f) [8]. In these LC honeycomb phases (see Fig. 53), aromatic rod-like cores form cell walls connected at the “seams” by terminal hydrogen-bonding groups. The honeycomb cells of polygonal cross-section and infinite length are filled by the fluid lateral semiperfluorinated chains. Depending on the ratio of the volume of the chains to the length of the rod-like core, cells ranging from triangular via rhombic, square, and pentagonal to hexagonal were obtained [316]. The sequence of different honeycomb structures observed for biphenyl-based T-shaped bolaamphiphiles (compounds **182**) with increasing length of semiperfluorinated lateral chain is outlined in Fig. 52c–f. Projected on a Euclidian plane, most observed honeycombs are Archimedean tilings [326] (i.e., tilings in which all vertices, or nodes, are the same, Fig. 54a,b,d) or their duals (Laves tilings, where all tiles are the same, see Fig. 54c) [8, 311, 326].

Simulations using coarse grained methods and dissipative particle dynamics have confirmed the experimentally observed development of the polygonal honeycomb phases with different cylinder shape [327–329]. Though the sequences rhombs-squares-pentagons-hexagons and triangles-squares-pentagons-hexagons are quite

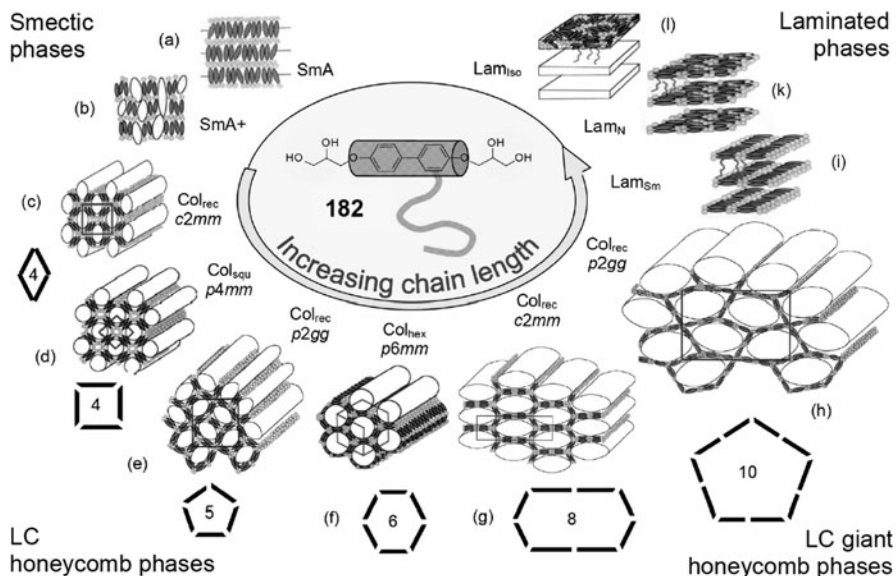


Fig. 52 Sequence of LC phases formed by self-assembly of T-shaped bolaamphiphiles (e.g. compounds **182**), depending on the size of the semiperfluorinated lateral chain: (a,b) smectic phases, (c–h) polygonal LC cylinder phases, and (i–l) Lam phases [8]

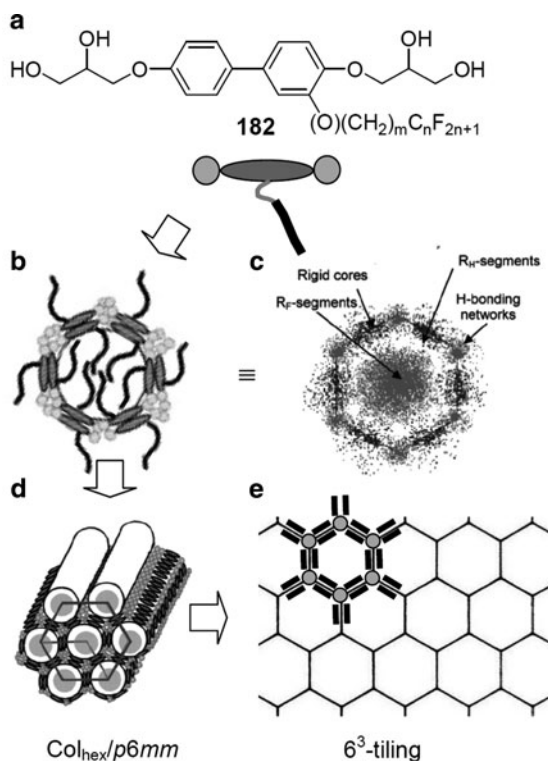


Fig. 53 Self assembly of T-shaped bolaamphiphiles (a) into hexagonal polygonal cylinders (b,c) which fuse to a honeycomb; (d,e)

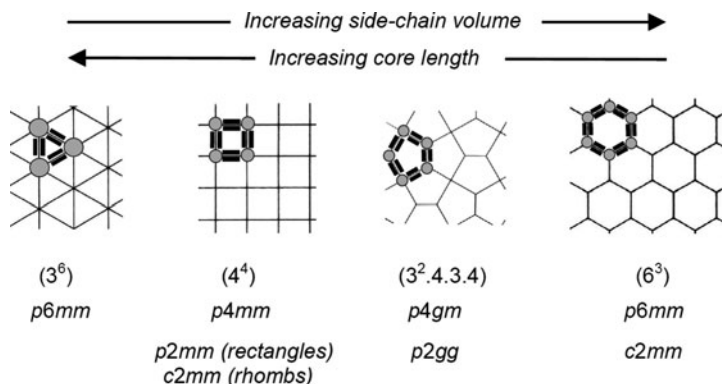
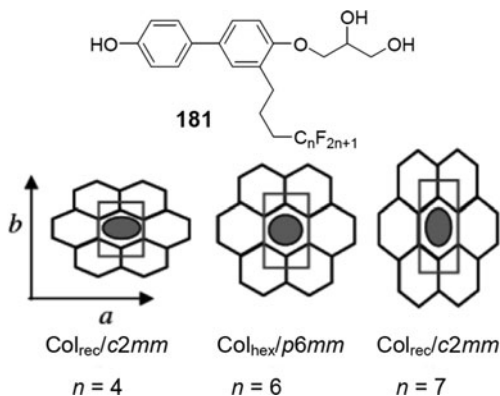


Fig. 54 Tiling patterns formed by self assembly of T-shaped bolaamphiphiles, their net-notations (*top line*) and plane group symmetries (highest symmetries, *middle line*) and reduced symmetries of their distorted variants (*bottom line*)

Fig. 55 Slight deformation of the hexagonal 1-1-1-honeycombs as observed for compounds **181** [317]



general for the development of the cylinder cross sectional shape with rising volume of the lateral chain, in some exceptional cases, the hexagonal cylinder structure seems to be relatively strongly favored, as for example, for the phenols **181** with a reduced density of hydrogen bonding. In this case, as shown in Fig. 55, a slight deformation of the hexagonal cylinders by a shrinkage or expansion along direction *b* seems to be possible which can adapt the space inside the hexagonal cylinders to the volume actually required by the lateral chains and this can lead to a reduced symmetry of the 2D lattice while retaining (distorted) hexagonal honeycombs (1-1-1-honeycombs) [317].

Deformation of the honeycomb cells is also observed for square and pentagonal honeycombs, leading to rhombic (*c2mm* lattice, Fig. 52c) and distorted pentagonal honeycombs (*p2gg* lattice, Fig. 52e). For the pentagonal honeycomb phases the cylinders are always deformed, because regular pentagons cannot tile a plane

periodically. Depending on the degree of deformation either a square ($p4gm$) or a rectangular ($p2gg$) lattice can be observed. Cylinder deformation can arise from an insufficient space filling of the cylinder cells by the lateral chains, but it also allows a larger number of lateral chains to adopt a dense parallel packing. However, cylinder deformation is more dependent on the chain position along the aromatic core (central vs. peripheral) [316] than on the type of chain, and there is obviously no significant effect of replacing R_H -chains by R_F -chains on the degree or deformation of the cylinders [316, 318].

Some T-shaped polyphiles display more than one thermotropic phase, and the general trend with increasing temperature is to undergo a phase transition from smaller to larger polygons, i.e., moving part of the way anticlockwise around the diagram in Fig. 52. This indicates that thermal expansion of the lateral chains is the main driving force for thermotropic phase transitions. Replacing R_H - by R_F -chain with equal number of C-atoms increases the size of the lateral chain and changes the phase type in counter clockwise direction. For example, compound **182a** forms rhombic cylinders whereas the fluorinated molecule **182b** forms hexagonal cylinders (see Fig. 51). Elongation of the rod-like cores at constant volume of the lateral chain has the opposite effect. As longer rods provide more space inside the cylinders the number of walls in the cross section of the cylinders must be reduced, i.e., moving clockwise around the diagram in Fig. 52 [330–332]. T-shaped polyphiles with extended π -conjugated rods, such as oligothiophenes [332–336] and oligo(*p*-phenylene ethylenes) [42, 337], are of significant interest for their luminescent and semiconducting properties and knowledge of the rules of their self assembly could be used to guide the assembly of luminescent and charge carrier materials in a predictable and well defined way [332].

7.2.2 Giant Cylinder Honeycombs

Further extension of the lateral R_F -chain gives rise to giant cylinder phases (Fig. 52 g,h) [316, 323]. In these giant cylinder phases, some or all cylinder walls have double lengths, being formed by two end-to-end connected molecules instead of just one molecule. For example, increasing the length of the fluorinated segment in the lateral chain of biphenyl based bolaamphiphiles **182** beyond the limits of hexagonal cylinders leads to two types of giant cylinder phases with $c2mm$ symmetry formed by elongated hexagons with, respectively, eight [316] and ten biphenyl cores [323, 338], arranged around the circumference of each core-shell-column (Fig. 56). Three adjacent sides of a 10-hexagon contain, respectively, 2, 2 and 1 molecules lengthwise, hence this structure is labeled 2-2-1. By analogy the 8-hexagons are labeled 2-1-1. Giant pentagonal cylinders, where each side contains two end-to-end molecules, represent another mode of organization of ten molecules in the circumference (see Fig. 52h) [316].

Another feature of the large honeycombs is the nano-phase segregation within the cylinders. The fluorinated segments congregate in the center while the alkyl spacers line the interior of the cylinder walls. This “core-shell-in-cylinder

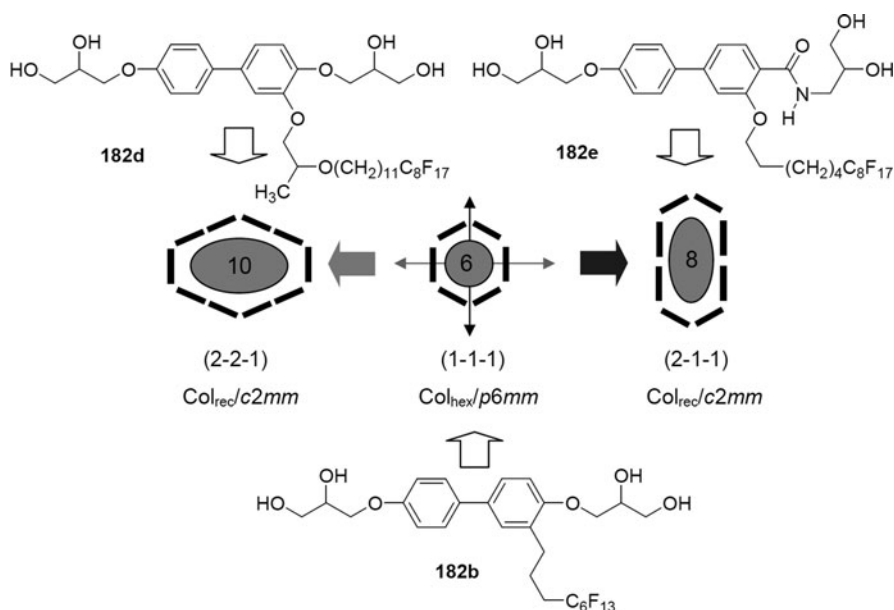


Fig. 56 Compounds **182d** and **182e**, showing two distinct types of rectangular columnar phases with giant hexagon cylinder structures, resulting from the stretching of regular hexagonal cylinders of the hexagonal honeycomb of compound **182b** either perpendicular to a side or along a diagonal; the gray cylinder cores are formed by the R_{F} -segments, around them is a shell of the R_{H} -spacers (white); only the aromatic cores (black) of one cylinder are shown for each structure and the hydrogen bondings at the edges and in the middle of the elongated walls are omitted [316, 323, 338]

structure” is a common feature of a number of honeycomb phases formed by molecules containing ≥ 6 perfluorinated carbons in the side-chain.

7.2.3 Laminated Phases

Increasing temperature or further enlargement of the lateral chain volume causes the cylinders to burst [323]; the side walls are removed leaving only disconnected layers, as shown in Figs. 52i–l and 57. Unlike the usual smectic phases (Fig. 52a), in these lamellar phases the π -conjugated rod-like cores are oriented parallel to the layer plane (denoted hereafter Lam phases) [8, 316, 317, 320–322, 339, 340]. For example, in the two lamellar phases of compound **128f** (Fig. 57a–c) occurring adjacent to the polygonal cylinder phases (Lam_{Sm} and Lam_{N}), the biphenyl cores remain parallel to the layer planes (Fig. 57b,c) before the in-plane molecular order is lost in the Lam_{Iso} phase occurring at higher temperature (see Fig. 57a) [316, 317, 320–322]. In the layers the rod-like molecular cores can adopt in-plane isotropic, nematic-like, and smectic-like order, respectively, giving the three dimensional

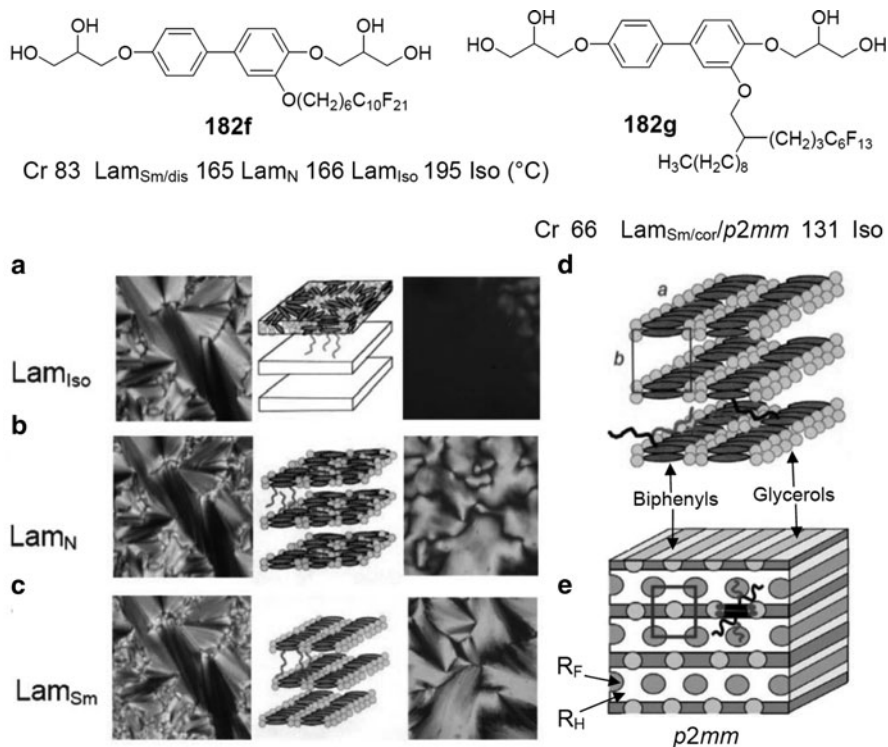


Fig. 57 Lam-phases (a–c) as formed by compound **182f** with a linear lateral R_F-chain and (d,e) Lam_{Sm/cor/p2mm} phase as formed by compound **182g** with a branched lateral chain: (a) Lam_{Iso} phase = lamellar phase without order in the layers; (b–d) in these Lam-phases the rod-like aromatic cores are organized on average parallel to the layer planes; (b) Lam_N (lamellar nematic phase) = lamellar phase with only orientational order in the layers and between layers; (c) Lam_{Sm/dis} (lamellar smectic phase) = lamellar phase with orientational and positional order in the layers and only orientational order between the layers, a sliding of the layers with respect to each other is possible; (d,e) in the correlated Lam_{Sm/cor} phase there is also positional order between the layers and a *p2mm*-lattice is formed [8, 316, 317, 320–322]. (a–c) Reproduced with permission [321], copyright 2002, American Chemical Society (ACS)

Lam_{Iso}, Lam_N, and Lam_{Sm} phases, where the layers of the rod-like molecular cores are separated by the layers formed by the disordered semiperfluorinated lateral chains. In the Lam_{Sm} and Lam_N phases there is orientational correlation of the aromatic cores in adjacent layers, leading to birefringence and typical optical textures. The absence of a long range positional correlation of the in-plane periodicity of the layers in the Lam_{Sm} phase (Lam_{Sm/dis} phase) indicates only a weak coupling of these layers by the layers of the fluid chains.

For bolaamphiphiles with a branched lateral chain, consisting of one alkyl and a perfluoroalkyl branch (e.g., compound **128g**) the coupling appears to be stronger

and in this case the occurrence of a positional correlation between adjacent layers leads to a 2D lattice with $p2mm$ plane group symmetry (Fig. 57d,e) [322]. It was assumed that the R_F -segments can form distinct columns within the non-polar sublayers of the lateral chains and these columns provide a stronger coupling between adjacent layers, allowing long range positional correlation ($Lam_{Sm/cor}$ phases). In the absence of segregated R_F -columns or if the R_F -segments form complete layers the correlation seems to be only short range, leading to non-correlated $Lam_{Sm/dis}$ phases. These Lam_{Sm} phases can be considered as a special type of columnar phases, but with a very different structure and melting behavior in the two ordering directions, offering the unique opportunity to investigate the transition between the sliding columnar phases ($Lam_{Sm/dis}$) and the columnar phases with long range 2D lattice ($Lam_{Sm/cor}$). More generally, the Lam phases also offer the possibility to investigate phase transitions in quasi 2D systems [341].

7.2.4 Rod-Bundle Phases

Further increasing the volume of the lateral chains by using two branched chains with at least one branch in each chain having a sufficiently long R_F -segment (e.g., compounds **184** and **185**) can lead to the break-up of the infinite rafts of bolaamphiphiles in the Lam phases into laterally isolated bundles [342, 343]. These pack on a hexagonal lattice, creating a unique type of columnar LC phase in which rod-like aromatics are arranged parallel to the column long axis, assigned as axial rod-bundle phases and shown in Fig. 58 [342]. This orientation of the aromatic cores contrasts the organization of the rod-like segments in the columnar phases of polycatenar compounds [258] and in the honeycomb structures of other T-shaped amphiphiles [8], where the aromatics are always organized perpendicular or slightly tilted to the column long axis. Also in columnar phases of disc-like molecules the aromatic planes are usually perpendicular or slightly tilted to the column long axis [12, 13]. Only the dendron **50** with a perylene diimide unit at the apex shows a similar alignment of the aromatics with the long axes of the π -system parallel to the columns (see Fig. 17) [148].

Also in the rod-bundle type LC phases the R_F -chains partly segregate from the R_H -chains and form regions with enhanced R_F concentration, which have a different shape depending on the size and distribution of the R_F -segments. As shown in Fig. 59, the R_F -chains could be localized in distinct columns located at the vertices of the hexagonal lattice (Fig. 59a), or they can be fused to a continuous honeycomb (Fig. 59b). The third type (Fig. 59c) with a helical structure of the R_F -regions arises upon reduction of the temperature for compounds **184** with branched chains having only one fluorinated branch in each lateral substituent. For these compounds, on lowering the temperature, a transition to a 3D ordered $R\bar{3}m$ phase with an intercolumnar long-range correlation is established [343], in which the bundles

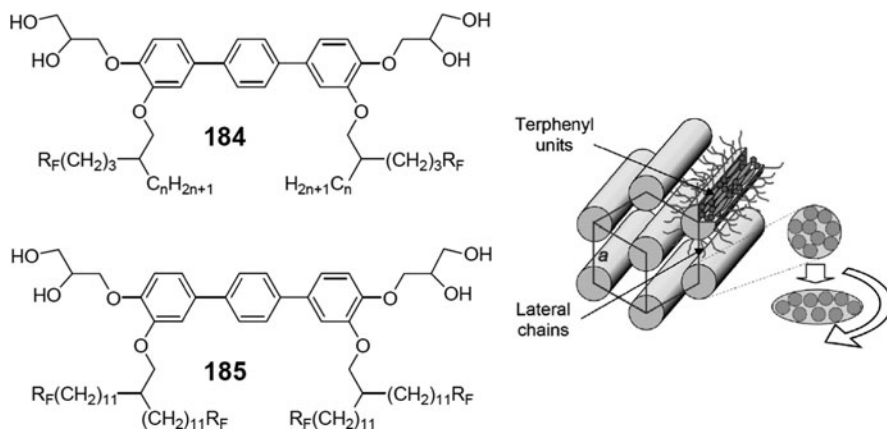


Fig. 58 Rod-bundle phase formed by compounds **184** and **185** with two branched and semiperfluorinated lateral chains and their organization in the LC rod-bundle phases; the local cross-section of the columns is thought to be elliptical, but circular when averaged over time and space, hence leading to 2D hexagonal symmetry [342, 343]. Reproduced with permission [342], copyright 2008, American Chemical Society (ACS)

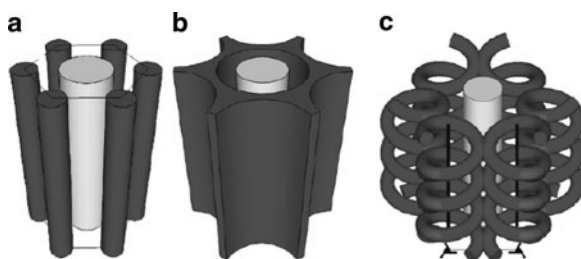


Fig. 59 Different modes of organization of the R_F -chains in the rod-bundle phases of compounds **184** and **185**; dark gray = R_F -rich regions; light gray = columns of the rod-bundles [343]. Reproduced with permission [343], copyright 2011, American Chemical Society (ACS)

are shifted by $\pm 1/3$ molecular length between adjacent columns. A helical structure of the R_F -domains (Fig. 59c) results from the 3_1 screw axes inherent to $R\bar{3}m$ symmetry and is linked to the $1/3$ shift of the individual columns.

In contrast to compounds **184** no transition to an $R\bar{3}m$ phase was observed for any of the compounds **185** with two R_F -branches in each swallow tail substituent. The reason might be that the side-by-side fixation of a fluorinated and a hydrocarbon chain in each of the swallow tail branches of compounds **184** may cause an increased tendency for segregation of R_F and R_H along the z -axis and not just in the x - y plane as in compounds **185**.

7.3 Polyphiles with Bent Aromatic Cores: Trigonal Columnar Phases

A 120° bend in the aromatic core of bolaamphiphiles, as in compounds **186a,b** [344], promotes the formation of hexagonal honeycombs and excludes other cylinder shapes. Only molecules with fluorinated lateral chains give enantiotropic (thermodynamically stable) LC phases whereas the mesophases of the alkyl substituted compounds are only monotropic. There are two different types of hexagons, 3-hexagons and 6-hexagons (with 3 or 6 molecules in the circumference), leading to LC honeycombs with $p3m1$ and $p6mm$ symmetry, respectively (Fig. 60b,c). Reducing the volume of the chains leads to a change from larger 6-hexagons to smaller 3-hexagons. The defining parameter is again the ratio between the length of the bent backbone and the volume of the attached chains, i.e., the circumference/area ratio of the polygon, similar to the cylinder phases formed by the linear T-shaped bolaamphiphiles **181** and **183**. It should be noted here, that the 3-hexagon honeycomb has broken symmetry, the plane group $p3m1$ not having a center of inversion; hence this is the first example of a trigonal columnar liquid crystalline phase which, due to the non-centrosymmetric structure, should have nonlinear optical properties [345].

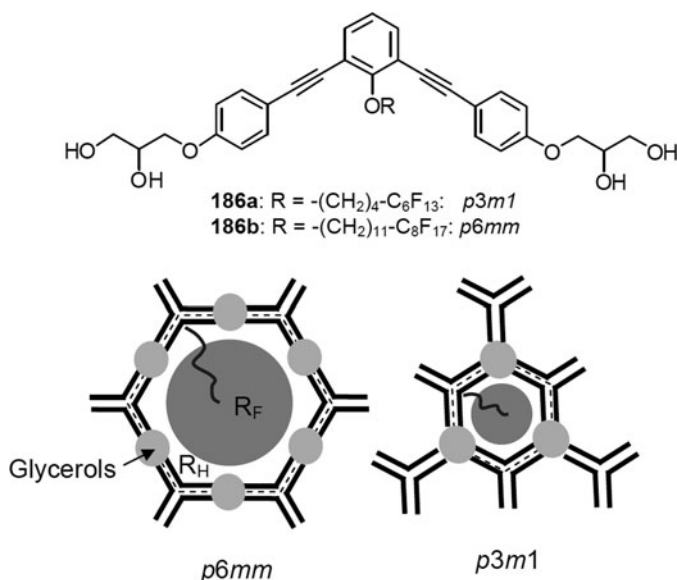
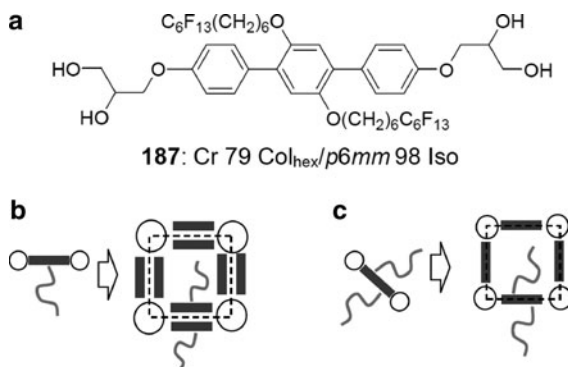


Fig. 60 Examples of anchor-shaped (bent-core) bolaamphiphiles and comparison of the hexagonal honeycombs: (a) 6-molecule hexagons ($p6mm$ symmetry) as formed by **186b**) and (b) 3-molecule hexagons ($p3m1$ symmetry) as formed by **186a** (dark gray = fluorinated cores, small light gray dots = glycerols) [344]

Fig. 61 (a) Example of an X-shaped molecules and (b,c) dependence of wall thickness on the number of lateral chains, shown for the case of a square cylinder phase; (b) double wall structure of T-shaped bolaamphiphiles; (c) single wall cylinders formed by X-shaped molecules [330]



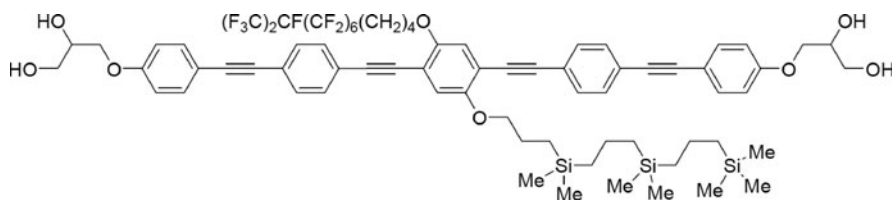
7.4 X-Shaped Polyphiles: Liquid Crystalline Honeycombs with Single Molecule Walls

Attaching only one lateral chain to the rod-like core (T-shaped amphiphiles **181–183**) gave rise to LC honeycomb phases where the cross-section of the honeycomb walls contains two rods arranged side-by-side, i.e., the honeycombs have double walls (Fig. 61a) [8]. However, attaching two lateral chains to opposite sides of the aromatic core (X-shaped polyphiles like compound **187**) generates polygonal honeycombs with walls that are only one molecule thick (Fig. 61b) [319]. As a consequence of the thinner walls, effectively more space is left available for the lateral chains inside the cells. Hence, honeycombs with smaller cells could be achieved by using two short lateral chains instead of only one chain with the same total volume [330].

7.5 X-Shaped Tetraphiles: Liquid Crystalline Multicolor Tilings

Attaching two different and incompatible chains, one an R_F -chain and at the opposite side an alkyl chain or any other chain which is incompatible with the R_F -chain (such as the carbosilane chain R_{Si} in compounds **188–190**, Figs. 62–64) offers the possibility of creating liquid crystalline honeycombs with cells of different composition. If projected on a Euclidian plane, such a structure can be described as tiling by two or even more different color tiles (multi-color tilings) [42].

Recently, polyphilic compounds have been reported, where an R_F -chain and a carbosilane chain were attached at opposite sides of a terphenyl or oligo (*p*-phenylene ethynylene) core [42]. Compound **188** with the longest oligo (*p*-phenylene ethynylene) core shows two hexagonal columnar phases separated by a thermoreversible continuous (second order) phase transition with critical behavior upon approaching the transition temperature. Based on XRD data it was



188: Cr 83 Col_{hex}/*p3m1* 85 Col_{hex}/*p3m1*_{dis} 189 Iso (°C)

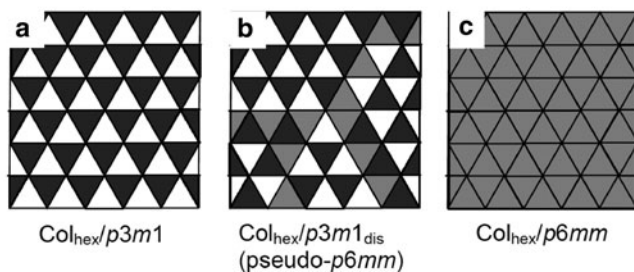


Fig. 62 X-shaped quaternary bolaamphiphile **188** forming triangular cylinder phases with models showing (a) the *p3m1* phase with long range order of the segregated two-color tiling, (b) the structure with only short range order of the two color tiling (Col_{hex}/*p3m1*_{dis}) and (c) the completely mixed *p6mm* structure; dark = R_F-chains; white = R_{Si}-chains; gray = mixed cells [42]

confirmed that in both Col_{hex} phases the molecules form honeycombs composed of triangular cylinders, hence the hexagonal lattice parameter a_{hex} corresponds to the molecular length (l). The Col_{hex} phase at low temperature is a periodic two-color tiling composed of two types of triangular cylinders with ratio 1:1; one type is filled with the R_F-chains the other one with the R_{Si}-chains (Fig. 62a). In this low temperature Col_{hex} phase the triangular cylinders are arranged on a long range *p3m1* lattice. Hence, this is a second type of polyphilic compounds forming non-centrosymmetric trigonal columnar LC phases. In the high temperature phase the correlation of the triangular cylinders forming the honeycomb is also long range, but the correlation of the “colors” of the honeycomb cells is only short range (see Fig. 62b), so that on a long range scale the 2D lattice has overall *p6mm* symmetry (Col_{hex}/*p3m1*_{dis} phase). This means that above the critical temperature there are local clusters of two-color tiling (Fig. 62b) that increase in size as the phase transition temperature is approached [42]. It seems that a *p6mm* type Col_{hex} phase with completely mixed cells (Fig. 62c) is not reached before the honeycomb structure breaks down at the Col_{hex}-to-Iso transition.

Compound **189** with a shorter terphenyl rod-like core also has two Col_{hex} phases, formed by cylinders, but with a hexagonal cross sectional area (Fig. 63). In this case a complete segregation of the R_F-chains from the R_{Si}-chains is impossible as it would lead to a packing frustration and therefore formation of cylinders incorporating mixed chains cannot be avoided. Based on simulation results [346], XRD data, and AFM results, the two color tiling with a *p6mm* superlattice

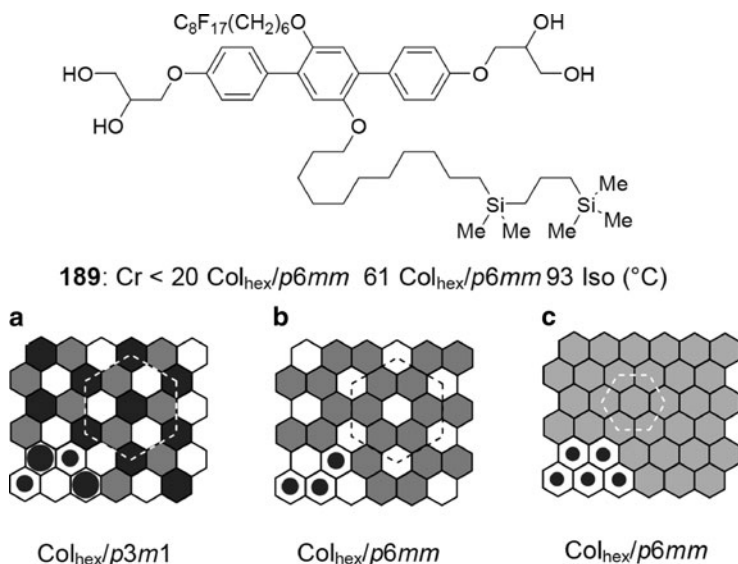


Fig. 63 X-shaped quaternary bolaamphiphile **189** forming hexagonal cylinder phases with models showing (a) the three-color, (b) two-color and (c) single color hexagon tiling patterns; in the left bottom corner the core-shell structure of the mixed cells is illustrated; *dark* = R_F -chains; *white* = R_{Si} -chains; *gray* = mixed cells [42]

($a_{hex} = 3l$, see Fig. 63b) was confirmed for the low temperature Col_{hex} phase [42]. In this hexagonal honeycomb phase the main columns on the hexagonal superlattice contain only R_{Si} and these chains are surrounded by hexagonal cylinders filled with a mixture of R_{Si} - and R_F -chains. Similar to the case of the triangular tiling there is a second order phase transition to a high temperature phase with only short range correlation of the positions of the main cylinders, leading to a loss of the $p6mm$ superlattice and only the smaller $p6mm$ lattice with a lattice parameter, corresponding to $a_{hex} = 3^{1/2}l$ is retained [42].

In the cylinders containing a mixture of R_{Si} - and R_F -chains, mixing is not homogeneous; instead, there is a core-shell structure in these columns with the R_F -chains forming the cores and the R_{Si} chains being mixed with the aliphatic spacers in the shell surrounding the R_F -cores. Hence, in these polygonal cylinder phases one has to distinguish two types of segregation, intercellular (intercolumnar) segregation, leading to multicolor tiling patterns, and intracellular (intracolumnar) segregation, leading to a multicompart structure inside the honeycomb cells. The competition between intracolumnar and intercolumnar segregation gives rise to new liquid crystalline phase structures with significantly enhanced complexity.

Complexity can be further increased by introducing geometric frustration. In the case of compound **190**, shown in Fig. 64, the size of the R_F -chain was further increased, compared to compound **188** (Fig. 62), so that organization in a triangular tiling pattern is no longer possible. Because of the large difference in area between equilateral triangles and squares the systems experiences a frustration with the

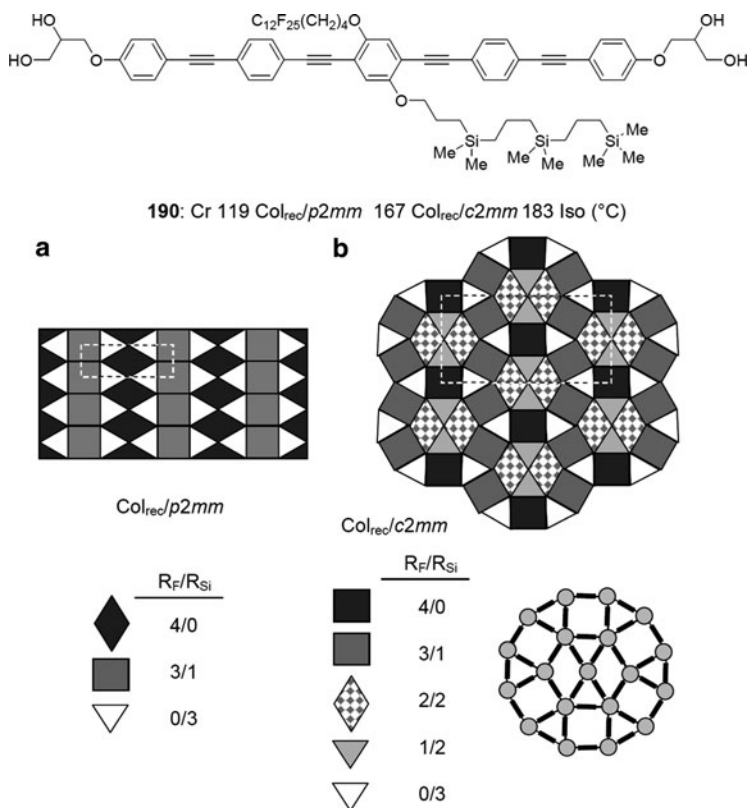


Fig. 64 (a) Three-color tiling and (b) five-color tiling of the LC phases formed by the quaternary X-shaped polyphile **190**; *dark* = R_F-chains; *white* = R_{Si}-chains; different *gray scales* = mixed cells with distinct mixing ratio as given below the models; the model at the right bottom shows the honeycomb framework of the bolaamphiphilic cores (*black rods* = aromatics, *dots* = glycerols) [42]

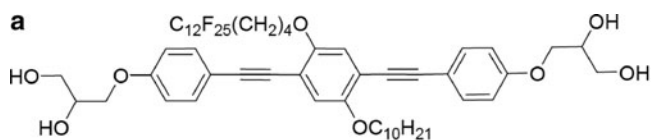
triangular cylinders being too small and square cylinders being too large. In addition to this purely steric frustration, compound **188** must simultaneously relieve the frustration due to the incompatibility of the side chains and their tendency to segregate into distinct cylinders, and to find a periodic tiling pattern that avoids mixing of the highly incompatible chains as much as possible. This is an extremely complex question and the outcome can presently not be predicted theoretically. The LC phases formed by compound **190** are shown in Fig. 64. This compound also has two distinct LC phases, although in this case separated by a first order phase transition at which the tiling pattern changes. In the low temperature phase with plane group symmetry *p2mm* (Fig. 64a) there are three distinct types of cylinders – triangular, rhombic, and square shaped which have different composition. The triangular cylinders are filled exclusively with the R_{Si} chains and the rhombs exclusively by the R_F-chains whereas the squares must be mixed in a ratio R_F:

$R_H = 3:1$, because the molecules between adjacent squares have to give their R_{Si} -chains into one of the adjacent R_F filled squares [42]. Note that in this structure the number of distinct columns is larger than the number of incompatible chains attached to the rod-like core. This means that mixing of the distinct chains gives rise to additional “colors” which further enhances the complexity of LC self-assembly.

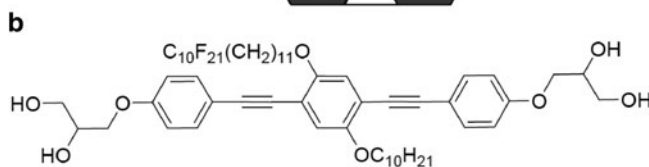
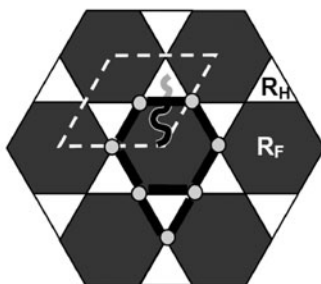
Upon increasing the temperature there seems to be a slight difference of the thermal expansion of the distinct molecular parts, and the miscibility of the incompatible chains (R_F and R_{Si}) can also increase. This leads to an even more complex tiling pattern, shown in Fig. 64b. It is composed of five distinct types of cylinders: triangles filled only by R_{Si} -chains, squares filled exclusively by the R_F -chains, and three types of cylinders with distinct shape, in which R_F - and R_{Si} -chains are mixed with different ratios. Hence, the number of colors can be further increased by distinct mixing ratios of the lateral chains inside the cylinders [42]. This represents a next step in increasing the complexity of LC self assembly. The complexity of this self assembled nano-scale soft matter structure is unprecedented, especially if it is considered that, beside the five-color tiling of the cylinder cells, the honeycomb framework represents also a segregated structure composed of cylinder walls formed by the π -conjugated cores and columns containing the glycerols at the edges. Thus, this $c2mm$ phase actually represents a periodic structure composed of in total seven distinct compartments. This illustrates that the fluorophobic effect can be used to achieve completely new LC structures with unprecedented complexity.

In the above reported tiling patterns polygonal cylinders with similar size were combined (triangles, rhombs, and squares), but it is also possible to combine cylinders of very different sizes, such as, for example, triangles and hexagons in the so-called Kagome pattern. This is obtained by adding two mutually incompatible lateral chains of very different length to an oligo(*p*-phenylene ethynylene) based bolaamphiphilic core of intermediate length [347]. In the resulting hexagonal columnar phase of compound **191a** ($Col_{hex}/p6mm$; $a_{hex} = 2 l$) the hexagons are filled by the larger semiperfluorinated chains, while the triangles are filled with the relatively short non-fluorinated alkyl chains, as shown in Fig. 65a [347].

In this case, segregation of R_F - and R_H -chains into distinct cylinders is favored by the very distinct volume in the cells and the possibility of a geometrically non-frustrated periodic tiling on a Kagome lattice. If however the aliphatic spacer connecting the R_F -segment to the aromatic core is enlarged, as in compound **191b**, a hexagonal columnar phase with much smaller lattice ($a_{hex} = 3^{1/2} l$) is found, consistent with a mixed organization of R_F - and R_H -chains in a single type of hexagonal cylinder (see Fig. 65b). In this case the intercolumnar segregation of the Kagome lattice is replaced by an intracolumnar segregation with formation of a core-shell structure inside the hexagonal cylinders. This becomes possible as the relatively long alkyl spacers can accommodate the relatively short R_H -chains. Hence antiparallel packing of the molecules along the cylinder walls allows the segregation of all hydrocarbons in the aliphatic shells and formation of fluorine cores in the centers of the cells.



191a: Cr 70 Col_X 88 Col_{hex}/p6mm 117 Iso (°C)



191b: Cr 93 Col_{hex}/p6mm 110 Iso (°C)

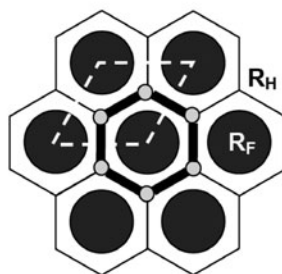


Fig. 65 (a) Kagome lattice formed by the quaternary X-shaped bolaamphiphile **191a** (intercellular segregation) and (b) hexagonal cylinder phase with core-shell morphology as formed by compound **191b** with a longer aliphatic spacer unit separating the aromatic core from the R_F-chain (intracellular segregation); *dark* = R_F-chains; *white* = R_H-chains [347]

Despite their complexity, the dynamics in these systems is fast with the molecules flipping and changing their positions. In fact these are ordered fluids composed of distinct compartments. There are no fixed positions of the molecules but distinct spaces with a maximum time averaged probability for each of the segregated units to be located and these “dynamic” compartments are arranged periodically in space. The structures are in thermodynamic equilibrium as indicated

by the absence or very small hysteresis in their phase transitions. In this respect the LC honeycombs differ from related cellular 2D structures in solid state materials and in morphologies of three arm star polymers [309].

8 Bent-Core Mesogens with Perfluorinated Segments

Another actual field of LC research is provided by so-called bent-core mesogens (banana mesogens) with a nonlinear bent shape of the rigid core units. Such molecules preferably pack with their apexes in a uniform direction, in this way generating the highest possible packing density and polar order in the layers. If the polar direction is opposite in adjacent layers then the smectic phase shows antiferroelectric switching and is assigned as SmP_A ; if the polar directions are parallel in adjacent layers the phase shows ferroelectric switching and the phase is assigned as SmP_F (see Fig. 66b). Tilted and orthogonal variants ($\text{SmCP}_A/\text{SmCP}_F$ or $\text{SmAP}_A/\text{SmAP}_F$), distinct modes of tilt correlation, layer intercalation, and layer undulation/modulation lead to an almost unlimited number of new LC phases, distinct from the classical mesophase types formed by rod-like and disc-like molecules [47]. Though there is a large number of core fluorinated bent-core molecules, there are only a few examples of bent-core mesogens carrying perfluorinated segments in the terminal chains (see Fig. 66a) [165b, 348–352]. In most cases R_F -segments were combined with sufficiently long alkylene spacers to avoid high transition temperatures [348, 350, 351], but in some cases shorter CH_2 and CH_2CH_2 spacer units were also used [349, 352]. Usually, replacing one or both terminal alkyl chains in bent-core mesogens by semiperfluorinated chains strongly stabilizes the polar smectic phases (SmCP_A phases, e.g., compounds **192–194**). As a consequence the naturally high transition temperatures of bent core mesogens are further increased [348]. Although, due to the mesophase stabilizing effect of the R_F -chains, the number of aromatic cores required to obtain LC properties with bent-core mesogens can be reduced from five to only three by replacing the terminal alkyl chains by semiperfluorinated chains, these 3-ring molecules do not show polar packing, and hence not the typical properties of bent-core mesogens [352]. This is most probably the result of the increased diameter of the R_F -chains which provides more space between the aromatic cores and in this way allows free rotation of the bent aromatic units.

In some cases (e.g., compounds **196**) a temperature dependent transition between a polar SmCP_A phase at low temperature and a nontilted and non-polar SmA phase at higher temperature was observed. At the transition from SmA to SmCP_A the layer thickness significantly increases which was interpreted as a transition from a single layer structure in the SmCP_A phase with a dense packing of the strongly tilted bent aromatic cores to a structure with interdigitated R_F -chains in the non-polar and non-tilted SmA phase. The interdigitation of the R_F -chains provides additional space between the aromatic cores and this leads to a loss of polar order at this phase transition [349].

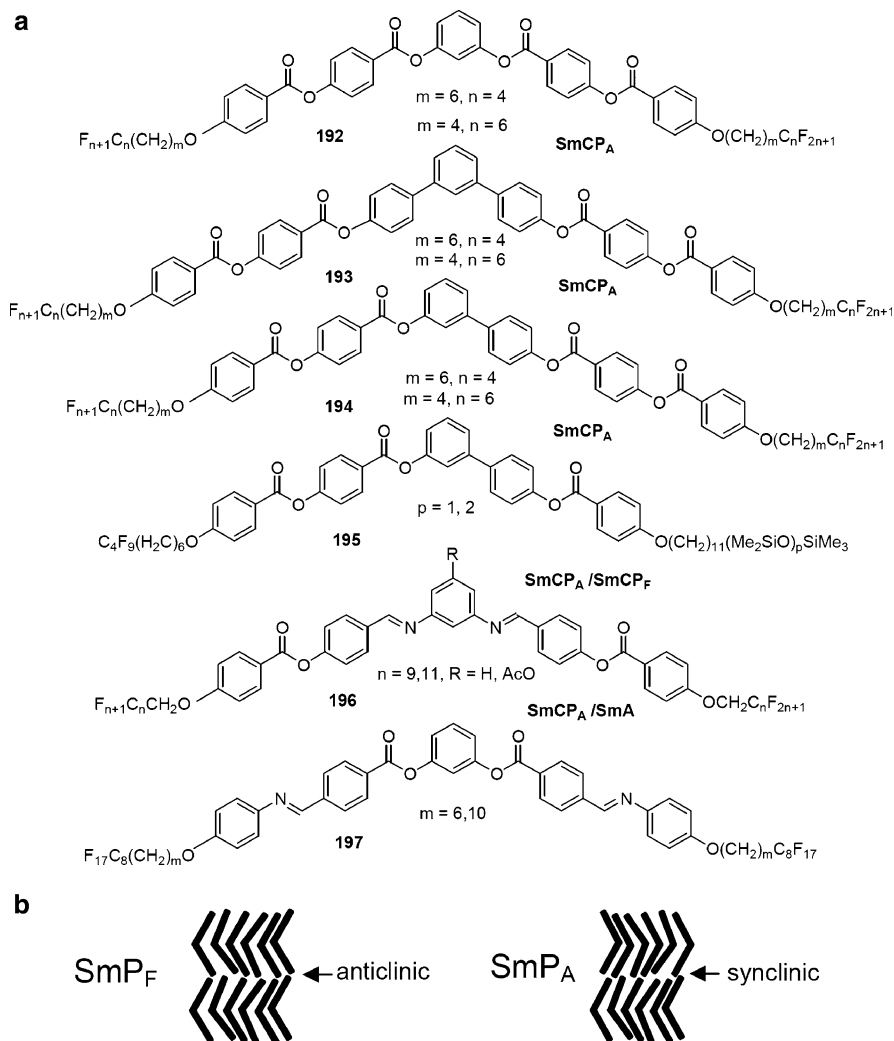


Fig. 66 (a) Examples of bent-core mesogens with semiperfluorinated terminal chains [348–351] and (b) models of the organization of the molecules in polar smectic phases

The bent-core mesogen **195** ($p = 1$) combining an oligosiloxane group and an R_F -chain represents a tetraphilic bent-core molecule for which an interesting change of switching behavior from ferroelectric ($SmCP_F$) at high temperature to antiferroelectric ($SmCP_A$) at low temperature was observed. This was attributed to the polyphilic structure; the increased stiffness of the R_F -chain favors synclinic layer correlation and hence stabilizes the antiferroelectric $SmCP_A$ structure of bent-core mesophases, whereas the oligosiloxane unit at the other end tends to decouple the layers, and hence favors anticlinic layer correlation which in bent-core

mesophases is favorable for the ferroelectric SmCP_F structure (see Fig. 66b) [350]. These two effects are temperature dependent and the competition between them changes the phase structure and switching behavior.

9 Dimesogens, Oligomesogens, Dendrimers, and Polymers

9.1 Dimesogens

Perfluorinated chains were used as end-chains and as spacer units for mesogenic dimers, as shown for selected examples in Fig. 67. In the simplest case two semiperfluorinated single ring mesogens were connected by alkylene spacers which stabilized their LC phases strongly, but without significant effect of the spacer parity on the phase stability (e.g., compound **198**) [353]. Biphenyl based dimesogens with R_F-units in the spacers or at the end chains are crystalline materials, except compound **199** which shows a nematic phase at very high temperature [354]. For dimesogens with Schiff base mesogenic cores, terminal R_F-chains, and odd-numbered aliphatic spacers (e.g., compound **201**), there is a transition between two distinct SmA phases associated with a relatively high transition enthalpy [355, 356]. It is proposed that this transition between SmA(LT) and SmA(HT) is associated with a change of the molecular conformation from U-shaped at low temperature to linear at high temperature. The dimesogen with a more rigid fluorinated spacer (compound **200**) shows only the SmA(HT) phase with stretched conformation whereas the dimesogen with a more flexible ether-based spacer (compound **202**, *gauche* effect) has exclusively the SmA(LT) phase with U-conformation [355]. This is in line with the proposed phase structures of compound **201**.

Biphenyl benzoate based dimesogens with R_F end-chains and oligo(ethylene oxide) spacers, like compound **203b**, show SmA and SmC phases, which can be modified by addition of lithium triflate which stabilizes and widens the SmA phases and at high concentration gives rise to a transition to a hexagonal columnar phase. The stabilization of the LC phases by the stronger lipophilicity and improved nano-segregation provided by the R_F-segments leads to removal of the N phase and to an increase of ion conductivity compared to related alkyl substituted compound **203a** [357]. The non-symmetric dimesogen **204**, incorporating a cholesterol unit and a terminal R_F-chain, forms an SmC* phase which exhibits very high spontaneous polarization (400–500 nC cm⁻²) and short response times [358, 359]. Komitov et al. reported SmC_A* phases with nearly 45° tilt and high spontaneous polarization for the chiral dimesogen **205** in which two chiral and partly fluorinated mesogens are interconnected by oligosiloxane spacers [360].

A combination of fluorinated segments and siloxane groups was used by Mehl et al. for the terminal-terminal and lateral-lateral interconnection of rod-like mesogens (e.g., compound **206**). In contrast to the usually observed smectic phases

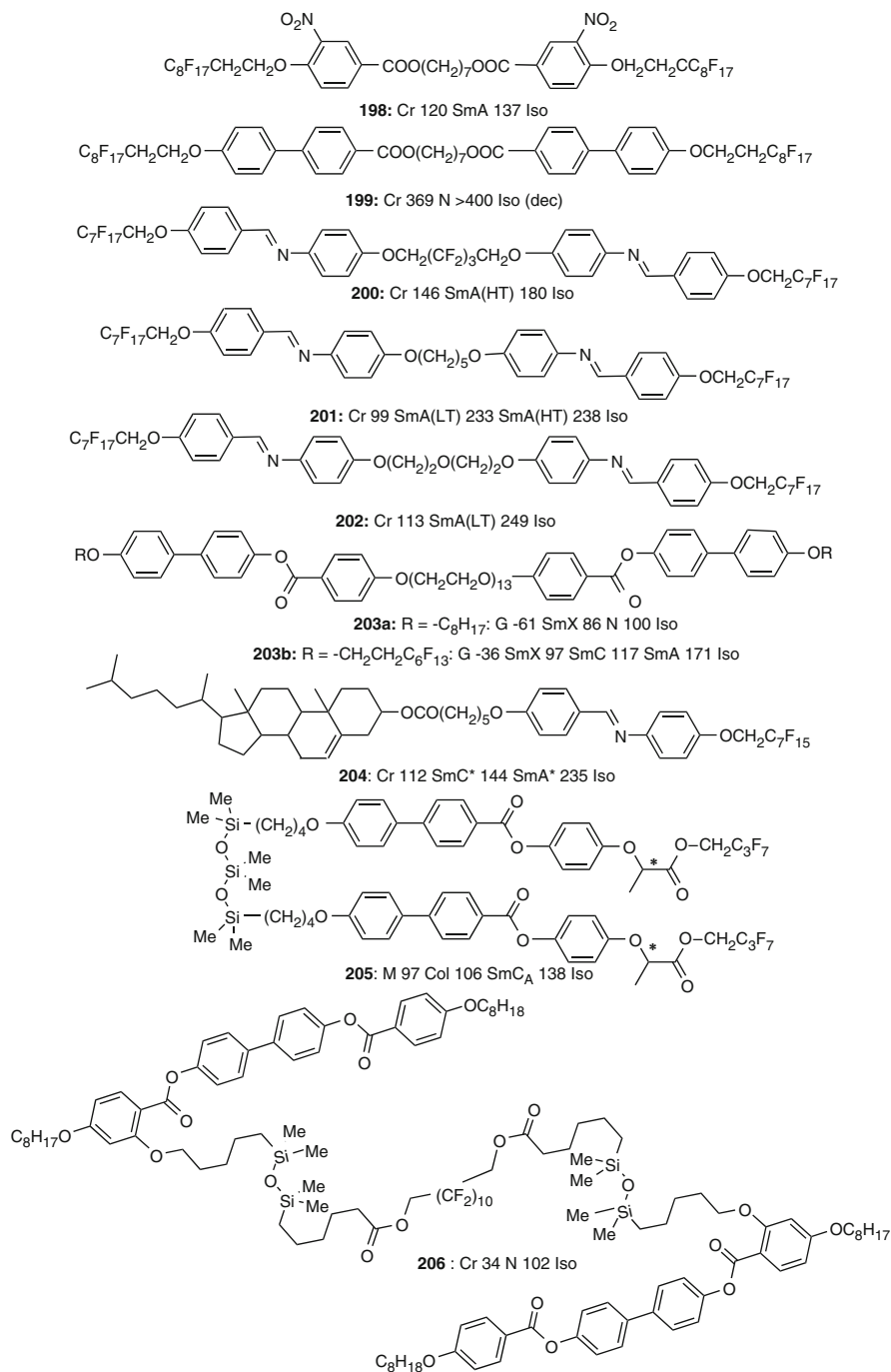
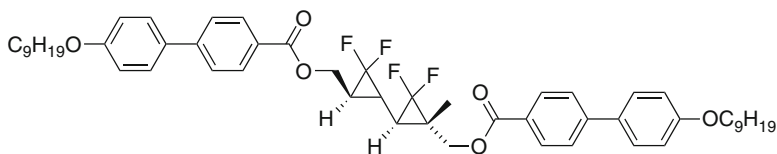


Fig. 67 Selected examples of rod-like dimesogens with fluorinated segments (T^p C) [353–362]



207: Cr 61 SmA 203 Iso

Fig. 68 Mesogenic dimer with a rigid *gem*-difluorocyclopropane based spacer unit (T° C) [363]

favoring effect of R_F -chains, nematic phase can be retained if the R_F -segments are located in a lateral spacer unit [361]. Spacer units containing R_F -segments were also used to interconnect two disc-like units; in this case nematic phases were also preserved [273, 362].

An unusual rigid spacer unit is provided by the chiral and relatively rigid bis (*gem*-difluoropropane) unit in compound **207** (Fig. 68) [363].

9.2 Oligomesogens

Yoshizawa et al. synthesized new types of taper shaped molecules by attaching two or three rod-like aromatic cores to the end of the alkyl chains of 3,4-dialkoxy benzoates and 3,4,5-trialkoxy benzoates, respectively, and having a perfluorinated chain at the apex; examples of such molecules are shown in Fig. 69.

Compared to the linear benzoate **208** which forms an SmC phase, increasing the number of cyanobiphenyl units leads to SmA phases and columnar phases (compounds **209** and **210**) as well as to bicontinuous cubic phases (compound **210**). This was attributed to a competition between the segregation of the R_F -chains providing amphiphilicity, and the steric effects due to a taper shape of these molecules [364–366]. In contrast to the phase sequence SmA-Cub_V-Col observed for polyhydroxy amphiphiles [30, 35, 36] and the phase sequence SmC-Cub_V-Col as typical for polycatenar molecules [257–260] in the series of compounds **208–210** the phase sequence on increasing the number of chains is SmC-Col_{hex}-Cub_V. This means that the interface curvature at first increases and then apparently decreases again. It seems that in this case the rigidity of the biphenyls, favoring organization in layers, plays an important role and this curvature reducing contribution rises from **208** to **210** with an increasing number of biphenyl units. However, in the same order the number of substituents attached to the benzoate core increases from only one to three which favor stronger interface curvature. From the phase sequence SmC-Col_{hex}-Cub_V and the presence of an SmA high temperature phase it can be concluded that there is a competition of these two effects; the parallel alignment of the biphenyls appears to become a bit stronger for compound **210** incorporating three biphenyls, and hence the interface curvature is reduced by going from **209** to **210** despite the three chains are more bulky than only two.

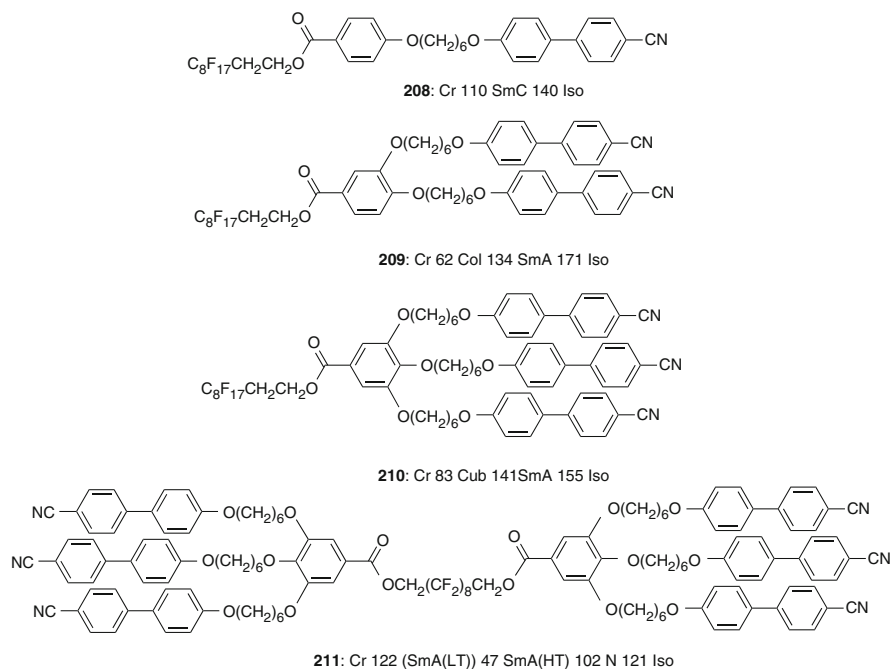


Fig. 69 Examples of oligomesogens incorporating semiperfluorinated chains (T^P C) [364–366]

In a related series of compounds with 5-heptyl-2-phenylpyrimidines replacing the 4'-cyanobiphenyls of compounds **208–210**, the sequence SmC-SmA-Col_{rec} was observed on increasing the number of phenylpyrimidine units [367]. This indicates an even stronger distortion of layer curvature by these rod-like units as hexagonal columnar and cubic phases are removed and replaced by a rectangular columnar ribbon phase.

End-to-end dimers of **210** incorporating a fluorinated spacer segment (compound **211**) form only a nematic and two different types of SmA phases, one with bilayer structure, the other an interdigitated one. This phase transition was attributed to a change of the molecular conformation from folded (bent), stabilized by segregation of the R_F-segments (SmA(HT)), to linear, favored by reduced conformational mobility and steric effects (SmA(LT)) [368].

9.3 Dendrimers

LC dendrimers represent an actual field in the search for new modes of organization in LC and for new applications [369, 370]. Dendrimers with perfluorinated chains at the periphery have been reviewed recently [371, 372], but there are only a few examples of LC dendrimers with R_F-chains (dendrons with R_F-chains have already

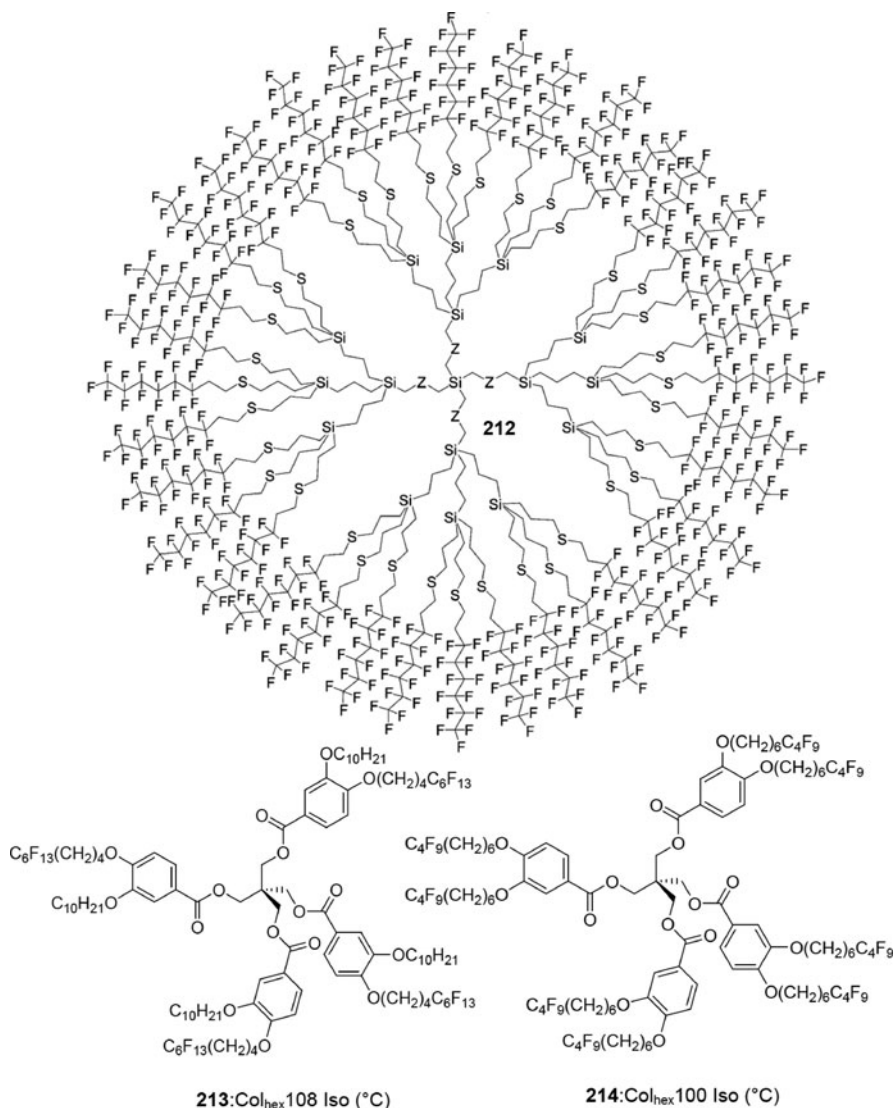


Fig. 70 Carbosilane based dendrimer (**212**, $Z = \text{CH}_2$) and pentaerythritol tetrabenzoates **213** and **214** with R_F -chains at the periphery [138, 141, 373]

been discussed in Sect. 3.2). Fluorinated carbosilane based dendrimers, like **212** (Fig. 70) with 4, 12, 36, and 108 R_F -chains (first to fourth generation) have been reported by Frey et al. [373–376]. The dendrimers with 12 and 36 R_F -chains form SmA phases whereas the compound with 108 chains forms a Col_{hex} phase. Mesomorphism clearly results from the nano-segregation of the R_F -shells from

the carbosilane cores. The transition SmA-to-Col_{hex} with increasing generation number is due to the increased packing density of the R_F-chains at the periphery.

As already discussed in Sect. 3.2.1, the tetrahedral molecules **35–37** (see Fig. 13) with a pentaerythritol core can be considered as the smallest molecules forming columnar LC phases only based on nano-segregation of a fluorinated periphery from a star branched fluorophobic core [140]. In this respect these star shaped molecules can be considered as the smallest dendrimers with fluorinated periphery and the whole sequence of mesophases SmA-Cub_V-Col_{hex}-Cub_I was achieved by increasing the number and the length of the R_F-chains. Remarkably, the columnar phase of the pentaerythritol tetrabenzoate **213** combining 4 alkyl chains and 4 semifluorinated chains (24 fluorinated carbons) has a higher stability of the Col_{hex} phase compared to **214** with 8 fluorinated chains and an in total larger number of 32 fluorinated carbons [141]. The reason for this unexpected behavior is not completely clear, especially as the R_F- and R_H-chains are fixed side by side in compound **213** and therefore a segregation of R_F- and R_H- chains is not favored. This parallels the observations made with partly R_F-substituted disc-like molecules (see Fig. 40) and the fact that rod-like molecules combining R_F- and R_H-chains almost always show higher mesophase stability than the related hydrocarbons even if no segregation of the R_F-chains can be detected. This is in line with the assumption that mesophase stabilization by R_F-chains mainly arises from the reduced average CED (enhanced “polarophobicity”) of the regions containing the mixed R_F/R_H-chains [94], as already discussed in Sects. 1.3 and 4.2. As mixing of R_H and R_F shows significant nonlinear effects it could be possible that segregation of a mixed R_F/R_H-shell from the aromatic core is more efficient than the combination of R_F/R_H-segregation and R_H-core segregation. It is also possible that for compound **213** with mixed chains the space filling in the periphery is closer to the optimal value required for phase stability maximum (see phase diagram in Fig. 15b).

Dendrimers with a polypropylene imine (PPI) core, decorated with a periphery of 3,4-dialkoxybenzamides with two semifluorinated chains (**215**, see Fig. 71), show a transition from a Col_{hex} phase for the third generation dendrimer (Cr 76 Col_{hex} 226 Iso) to a micellar cubic phase (Cr 78 Cub_I 235 Iso) for the fifth generation dendrimer [377].

Recently fluorinated chains were also attached to amine based dendrimers, like PPI and poly(amido amine) (PAMAM), by means of ionic self assembly with semiperfluorinated alkanic acids (Fig. 71, **216**, **217**). All dendrimer complexes **216** with perfluorinated alkanic acids show SmA phases except the fifth generation dendrimer which shows a Col_{rec} phase [378]. Also semiperfluorinated 4-alkoxybenzoic acids **217** [379] and mixed systems combining fluorinated and nonfluorinated alkanic or benzoic acids (**216**, **217**) have been reported [379–381]. In most cases layer structures (SmA) and for higher generation dendrimers also modulated SmA phases (Col_{rec} phases) were observed. The layer thickness of the SmA phases of the mixed complexes **216** depends on the ratio of fluorinated and non-fluorinated acids, where smaller *d* values were observed for dendrimers with low R_F-content; for R_F-rich dendrimers the more rigid R_F-chains provide

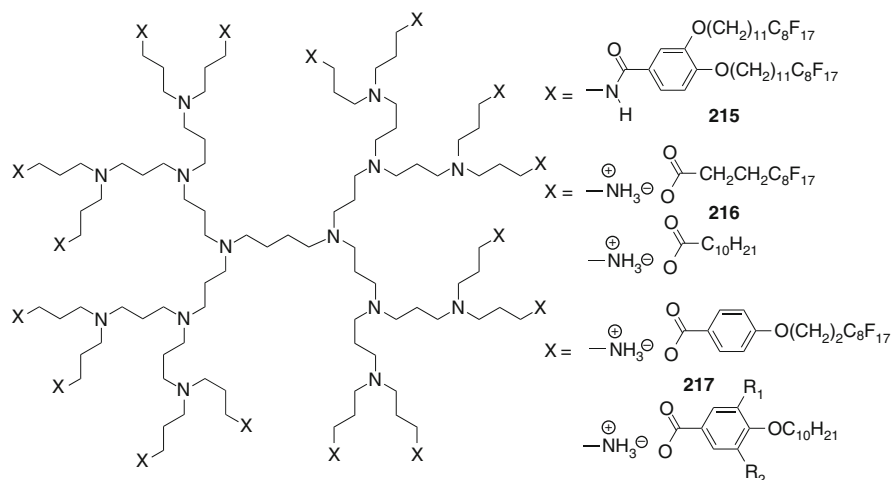


Fig. 71 Examples of PPI based molecular (**215**) and supramolecular third generation dendrimers (**216–217**) with fluorinated chains and mixed R_F/R_H -chains [377–381]

larger d -values. This behavior is found if one of the incompatible moieties exceeds 70%. For complexes with intermediate R_F -content between 30% and 70% frustrated SmA^+ phases [318] with a diffuse small angle scattering or the coexistence of two distinct SmA phases with different d -parameters was observed. In this case the SmA^+ phase seems to result from small domains with different layer spacing whereas larger domains lead to the coexistence of two distinct SmA phases [381]. There is a similarity to the binary mixtures of liquid alkanes and perfluoroalkanes, where R_F -rich and R_H -rich regions are separated by a miscibility gap in the medium concentration range [90–93]. For the ionic self assembled smectic phases of the dendrimers **216** R_F/R_H -mixing is additionally influenced by the restrictions provided by the polar layers. In this case mixing of R_F - and R_H -chains with different cross sectional areas is reinforced by the requirement for averaging the interfacial areas in order to retain flat interfaces. In this respect the situation is related to the smectic phases formed by rod-like molecules comprising a fluorinated and a nonfluorinated chain, as discussed in Sect. 4.2)

9.4 Polymers

Polymers with fluorinated segments represent a field on its own which is not considered here [382–384]. Polymer chains were also used to interconnect fluoruous mesogenic units, either comprising a single aromatic unit [385–389] or a rod-like units which can be attached either terminally [193, 390–394] or laterally [240, 395–397] to the polymer backbone. In most cases the termini of the mesogenic units

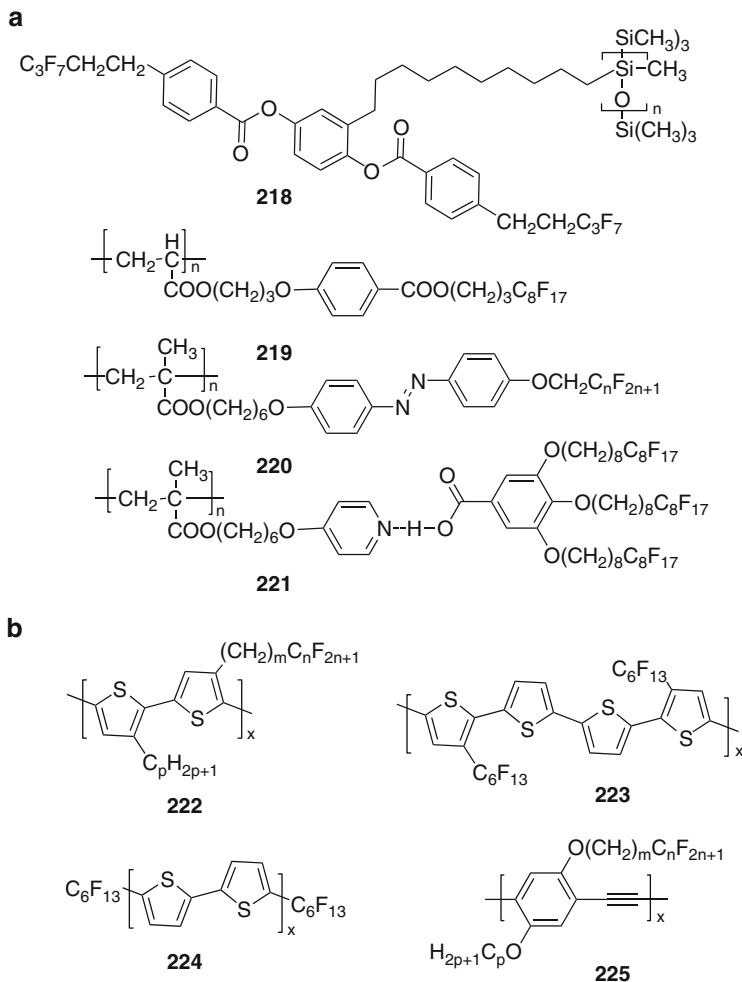


Fig. 72 Representative examples of (a) polymers with fluorinated mesogenic units [384, 390, 396, 399] and (b) π -conjugated polymers with fluorinated chains [400–404]

carry the R_F -chains, but fluorinated spacers based on perfluorinated oligoethers have also been used [398]. Selected examples are shown in Fig. 72.

In addition, taper-shaped and dendritic units were connected either covalently (at the apex or at the periphery) [133, 135, 383, 405] or by means of self assembly (e.g., hydrogen bonding [399]) to a polymer backbone. For example, polymers based on poly[4-(3-methacryloylpropyl)pyridine] form hydrogen bonded complexes with partially fluorinated mono-, di-, or trisubstituted benzoic acids (see complex **221** in Fig. 72). The type of mesophase formed by these complexes varies from smectic via columnar to cubic, most probably micellar cubic, with rising

numbers of R_F -chains attached to the benzoic acids [399]. Remarkably, for some two chain and all three chain benzoic acid dimers only hexagonal columnar phases were observed (Sect. 3.2.2), whereas their pyridine complexes show micellar cubic phases in most cases. This indicates that the binding of the fluorinated benzoic acid to the pyridine functionalized polymer increases the interface curvature compared to the mesogenic H-bonded dimers of the pure benzoic acids. This is opposite to the previously reported effect of covalent fixation of dendritic molecules at their apex which usually leads to a transition from spheroidal to columnar organization [143, 406].

Perfluorinated chains were also used for modifying self assembly, improving charge carrier mobility, and adjusting surface alignment and HOMO-LUMO band-gaps (by using the electron-withdrawing effect of the R_F -chains) of π -conjugated polymers, such as for example poly(thiophenes) **222–224** [400–403] and poly(phenylene ethylenes) like **225** (Fig. 72) [404].

Recently it has been demonstrated by Guittard et al. that the electrochemical polymerization of semifluorinated thiophenes (**226**) [407], 3,4-ethylenedioxythiophenes (**227**) [408], fluorenes [408], and 3,4-alkylenedioxyppyroles (**230**) [409] allowed the deposition of semiconducting polymer films with excellent antiwetting properties (superhydrophobic and lipophobic, see Fig. 73). Additional aromatics inserted between fluorinated tail and polymer chain (compounds **228**, **231**) improve mesogeneity and in this way decrease the mobility of the R_F -chains, preorganize the molecules, and thus improve the antiwetting properties [388, 410].

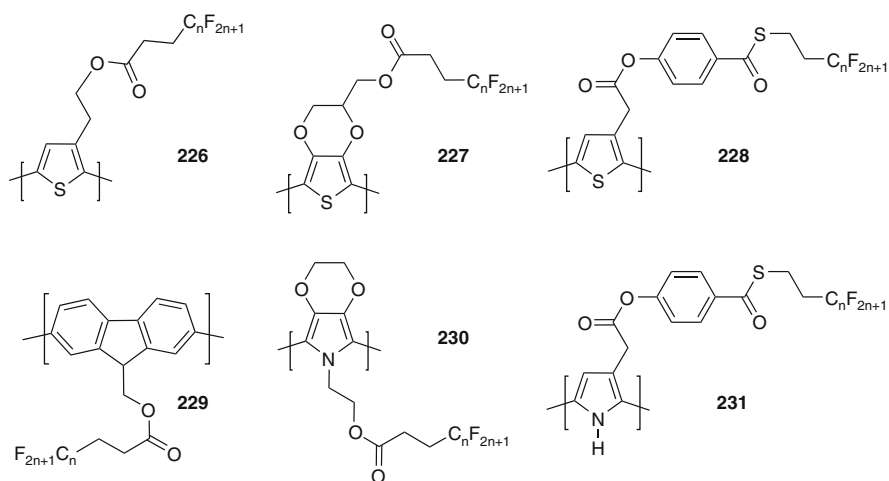


Fig. 73 Representative examples of electropolymerized LCs with fluorinated mesogenic units [388, 407–410]

10 Attractive Interactions Induced by Fluorination

10.1 Perfluorinated Aromatics

In contrast to perfluorinated alkyl chains, highly fluorinated aromatics behave differently in self assembling LC systems as such units are not incompatible with nonfluorinated aromatics; instead they favor attractive interactions with electron rich aromatics [78]. As an example, benzene and hexafluorobenzene form stable 1:1 complexes with a high degree of intermolecular attraction by π - π stacking between the electron rich benzene and the electron poor hexafluorobenzene [411–413].¹⁵ This concept was used to induce columnar self assembly by mixing fluorinated triphenylenes (compound **233**) and nonfluorinated triphenylenes, such as **232** or the polymer **234** [414], shown in Fig. 74. Columnar mesophases were also stabilized by introducing polyfluorinated aromatics into the periphery of disc-like triphenylenes (**237**) [415] and to the apex of taper shaped molecules (e.g., pentafluorophenylbenzoates like **238**) [416].

Smectic and nematic phases were induced in mixtures of non-mesogenic nonfluorinated and fluorinated rod-like 1,4-bis(phenylethynyl)benzenes (**235** and **236**, respectively) [417]. In the case of pentafluorophenyl substituted cyanobiphenyls **239** a significant part of mesophase stability could probably arise from attractive interactions between the electron rich biphenyl core and the electron poor pentafluorophenyl group [418] (Fig. 74). If pentafluorophenyl ester groups were added to both ends of the terminal alkyl chains of a rod-like LC molecule, then smectic phases were replaced by a nematic phase [235], probably due to the donor–acceptor interactions between the electron-rich core aromatics and the acceptor type end-aromatics, which distorts layer formation. Perfluoroarene–arene interactions were recently also used to induce phase biaxiality in SmA phases and cybotaxis in nematic phases of core fluorinated 4,4'-biphenyl bisbenzoates with different fluorination patterns [419]. As no chains were attached, layer formation is in this case induced by attractive core–core interactions and not by rigid-flexible or polar/apolar incompatibility as usually observed. Hence, attractive interactions between the aromatics can either remove smectic phases and induce nematic phases or remove nematic phases and induce smectic phases. This depends on the sequence of donor and acceptor aromatics along the molecule backbone, which either favors a staggered (leading to N) or a non-staggered (leading to Sm) parallel or antiparallel organization.

Special effects on mesogenic self-assembly have also been observed for highly core fluorinated bent-core mesogens [420].

¹⁵ See also Footnote 9 (Sect. 1.3) for an alternative discussion of the origin of attractive interactions between fluorinated and non-fluorinated aromatics.

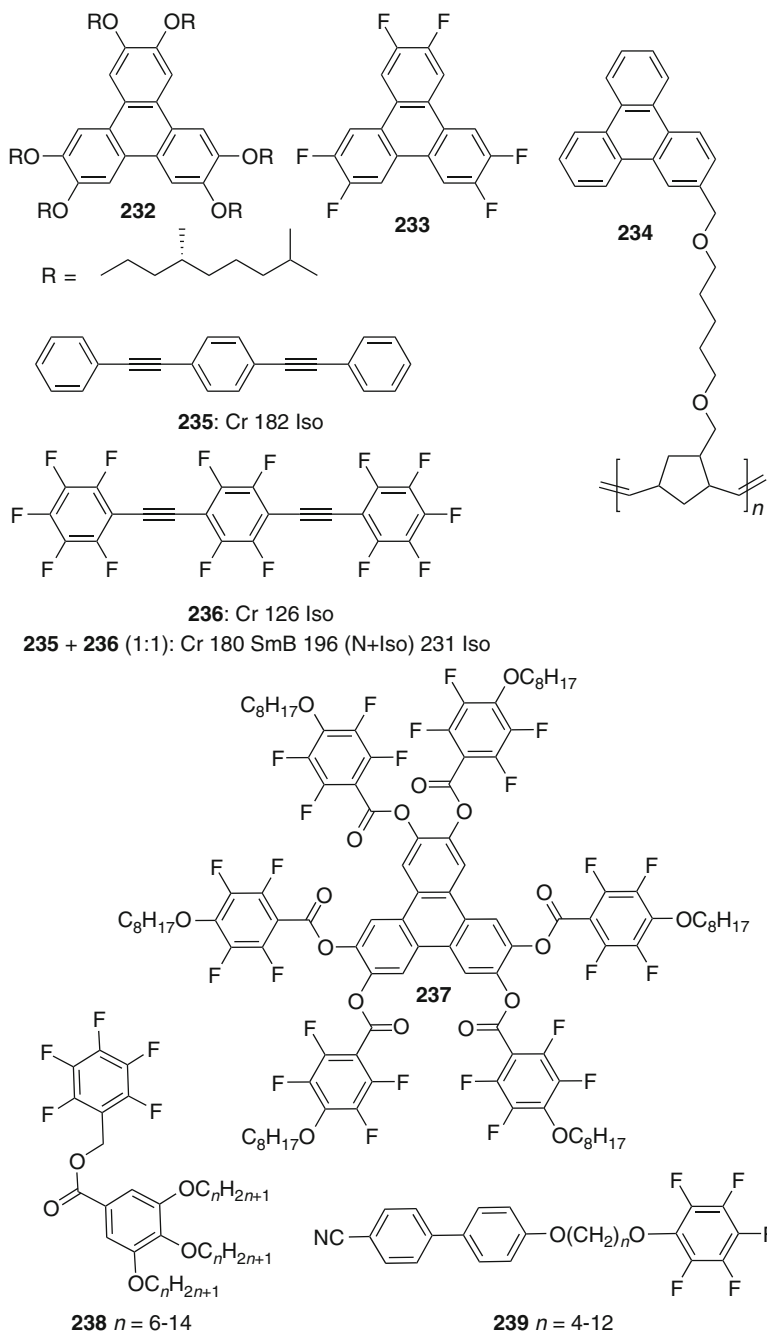


Fig. 74 Examples for mesophase induction and mesophase stabilization by perfluorinated aromatics (T° C) [414–418]; for the mixtures **235** + **236** there is a coexistence of nematic and isotropic phase (N+Iso)

10.2 Partially Fluorinated Aliphatic Units

Another possibility for achieving attractive interactions due to fluorination could be provided by partial fluorination of aliphatic hydrocarbons. If H and F are combined at one C atom the highly polar nature of the C–F bond can cause polarization of the C–H bond at the same carbon, thus enabling attractive interactions with fluorine atoms at neighboring molecules. For example, difluoromethane has a significantly higher boiling point (-52°C) than either methane (-161°C) or tetrafluoromethane (-128°C) [59, 421].

These polar interactions should affect the self assembly of molecules with polyfluorinated alkyl chains. Multi-*vicinal* polyfluoroalkanes represent a new type of polyfluorinated building blocks used in LC design, conceptually intermediate between alkyl chains and perfluoroalkyl chains. A $(\text{CHF})_6$ spacer with six vicinal F-atoms has been used to connect two *trans*-cyclohexane rings, leading to molecules **240** (Fig. 75). A distinguished feature of such compounds is their stereochemical complexity. The conformation of these compounds is governed by avoiding parallel 1,3-C–F-bonds (electrostatic repulsion 13 kJ mol^{-1}) and favoring *gauche* 1,2-C–F-bonds (3 kJ mol^{-1}). This can be used to tailor the molecular conformation, where an *all-syn* structure (**240a**) induces a helical arrangement and the *syn-anti-syn-anti-syn* fluorine pattern (**240b**) induces a zigzag conformation, leading to an overall linear molecular shape [57, 422, 423].

Poly(vinylidene fluoride) with the sequence $(\text{CF}_2\text{-CH}_2)_n$ is a well known ferroelectric polymer in the crystalline state where the chains adopt an *all-trans* conformation [424]. This structure could provide interesting properties if used as building block of LC.

10.3 Supramolecular LC by Halogen Bonding

Highly fluorinated molecules are also of significant interest for construction of supramolecular LC based on halogen bonding between perfluoroalkyl- or

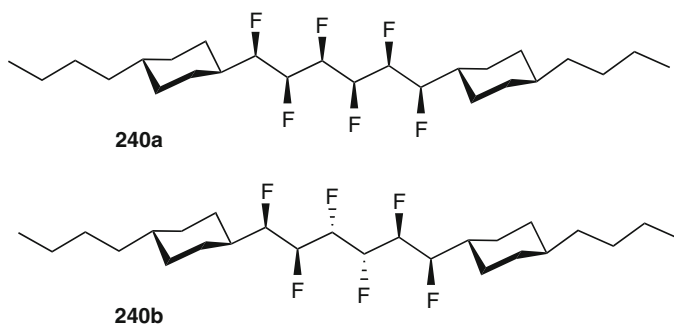


Fig. 75 Compounds incorporating a $(\text{CHF})_6$ chain as central unit [422]

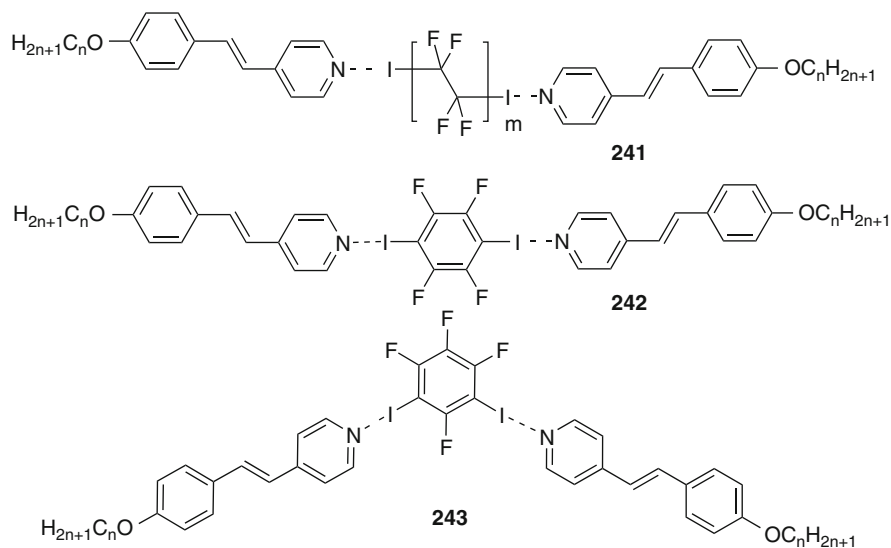


Fig. 76 (a) Supramolecular mesogens formed by halogen bonding [425, 426]

perfluoroaryl iodides and appropriately substituted pyridines (see Fig. 76). Here the electron-withdrawing effect of the perfluorinated alkyl chains (e.g., complex **241**) or perfluoroaryl groups (e.g., complex **242**) is required for the polarization of the C–iodine bond to be able to undergo electrostatic interactions with the substituted pyridines [425, 427]. Halogen bonding was also used to build supramolecular bent-core mesogens, for example complex **243** [426].

11 Synthetic Aspects

Generally the direct connection of R_F -chains to aromatics is rarely used due to the often unfavorable properties (high transition temperatures and strong steric frustration) of fluorinated compound with direct Ar- R_F linkages. The synthesis of these compounds usually requires Ullman-type coupling reactions of aryl iodides with iodoperfluoroalkanes and it is difficult to couple more than only one or two R_F -chains to an aromatic core by this method. In most cases the R_F -chains are decoupled from the core structure by aliphatic spacers with at least three CH_2 units, better with even longer alkylene spacers. These spacer units decouple rigid core and R_F -chain with respect to flexibility (reduces melting points, improves solubility) as well as electronically (reduced electron-withdrawing effect). The synthesis of these materials is usually based on the radical addition of perfluoroalkyl iodides to olefins, followed by reductive exchange of the iodide group by H. An often used method is the Pd^0 -catalyzed reaction, but also other methods can be applied

(dithionite, AIBN, etc.) for the radicalic addition. Allylsubstituted aromatics (e.g., allylphenols) as well as alcohols and alkanolic acids with a terminal double bond are commonly used as olefinic precursors to obtain semiperfluorinated alkyl aromatics, alcohols and carboxylic acids, respectively. The semiperfluorinated alcohols can be used for direct etherification (Mitsunobu) or esterification reactions with phenols and carboxylic acids, respectively. In most cases, however the alcohols are transformed to tosylates or halides (usually bromides) by different standard methods to use them in etherification reactions with phenolic OH groups under mild conditions with K_2CO_3 as base. Multiple functionalization of an aromatic core in a specific 3,4-, 3,5-, or 3,4,5-substitution pattern can in this way easily be achieved by etherification of the commercially available hydroxybenzoic acids. Semiperfluorinated carboxylic acids can be reduced to the corresponding alcohols or used in standard esterification reactions with aromatic or aliphatic OH groups.

Compounds with only one or two CH_2 groups between core unit and R_F -chain are more difficult to synthesize, though the corresponding alcohols and bromides are commercially available. This is due to the steric and electronic effects of the R_F -chains which are, in these compounds, not sufficiently decoupled from the functional groups. This changes the reactivity of these functional groups and also leads to solubility problems, often giving rise to low yields. Etherifications, for example, give the best yields with nonafluorobutanesulfonates as leaving groups. Further details concerning synthetic procedures can be found in the references cited throughout this chapter.

The electron-withdrawing properties of the R_F -chains also activate COO groups to the attack of nucleophiles so that perfluoroalkanoates, especially those with phenols, are sensitive to hydrolysis and there are long term stability problems [163]. The same problems arise for the relatively reactive esters of 1*H*,1*H*-perfluoroalkanoles. Hence such structures should be avoided if possible.

12 Summary and Conclusions

In summary, perfluorinated chains have a strong influence on mesophase stability and mesophase morphology due to hydrophobicity, lipophobicity, rigidity, and size of these chains. Generally, R_F -segments stabilize all LC phases, lamellar, columnar, and cubic, even if segregation of the R_F -chains from R_H -chains does not take place for packing and space filling reasons. Mesophase stabilization is mainly due to the reduced cohesive energy density (CED) of the R_F -chains or the regions with mixed R_F/R_H -chains. This increases the difference to other molecular segments with higher CED and hence the nonpolar chains are more efficiently excluded from these regions. This increased micro-segregation stabilizes all positionally ordered LC phases. The mesophase types are mainly influenced by the size of the R_F -chains, but the enhanced rigidity compared to R_H -chains can also contribute to modification of the mesophase structure to some extent.

The strongest effect on mesophase morphologies comes from the incompatibility of R_F -chains with all other units, especially from the incompatibility with R_H -chains. However, this incompatibility is relatively weak and can easily be removed if packing frustration occurs. Nevertheless, appropriate molecular design could lead to polyphilic molecules capable of forming multilayer structures, core-shell structures and also completely new types of LC phases. Such new mesophases can, for example, be generated in the polygonal honeycomb liquid crystals of T-shaped and X-shaped polyphiles, where segregation of R_F -chains from aliphatic chains can lead to multicompartiment structures composed of honeycombs filled by different material (multi-color tilings). The number of distinct compartments (colors) can exceed the number of incompatible units provided by the molecules themselves and is increased by the partial mixing of R_F - and R_H -chains in distinct fixed ratios. In this way complex LC structures incorporating up to seven distinct compartments have been achieved. The transition between uniform tiling and multicolor tilings turned out to be continuous in some cases, with critical behavior, and analogies to ferro- and antiferromagnetism could be drawn [42].

There are numerous properties which make fluorinated LC attractive for applications. Short R_F -segments lead to de Vries phases and to 90° tilted anti-ferroelectric SmC_A^* phases, useful for orthoconic switching in new display applications. Fluorination could also lead to enhanced polarization in ferroelectric and antiferroelectric LC phases.

R_F -chains can be used as insulating layers or shells separating charge carrier pathways, in this way enhancing the efficiency of devices based ion conduction or electron/hole transportation. The electron-withdrawing effect of R_F -chains, directly attached to conjugated π -systems, provides a way to n-type semiconductors with increased air stability. Self-assembly in the self-healing LC state can reduce defects and increase charge carrier mobilities; even a switching between p-type and n-type semiconductors is possible with the same core structure just by modifying the mode of LC self assembly [277].

Due to the low polarizability of the R_F -chains, LC materials with extended semiperfluorinated segments have a low surface energy density, leading to distinct surface and alignment properties. These can be used for the alignment of LCs and for controlled formation and suppression of surface relief gratings [428]. Fluorinated LCs can also form regular arrays of defects, which could be used for soft lithography [429], as optically addressable photo masks, and as micro lenses [430]. Further reduction of the size of regular patterns to molecular length scales can be achieved in the honeycomb cylinder phases of polyphilic mesogens [8, 310]. As in these honeycombs luminescent and semiconducting π -systems can be self-assembled in a defined way with periodicities in the range between 2 and 20 nm, there is potential for future applications of these materials to produce well defined functional nanostructures.

Hence, fluorous liquid crystal self assembly is an attractive area with importance for numerous practical applications and for the general understanding of the development of complexity in self-assembled systems. It is connected to other fields of soft matter research such as compartmentation of micelles and membranes

[431–433], self assembly of fluoros containers [434], to mention only a couple. In this way it is an actual field in fluoros chemistry in addition to other recent developments such as, for example, fluoros biphasic catalysis [435] and the use of fluoros anchors and linkers in chemical synthesis [436].

References

1. Pauluth D, Tarumi K (2004) *J Mater Chem* 14:1219
2. Kelly SM (2000) In: Connor JA (ed) *Flat panel displays - advanced organic materials*. Royal Society of Chemistry, Cambridge
3. Demus D, Goodby JW, Gray GW, Spiess H-W, Vill V (1998) *Handbook of liquid crystals*. Wiley-VCH, Weinheim
4. Collings PJ, Hird M (1997) *Introduction to liquid crystals chemistry and physics*. Taylor and Francis, London
5. Kato T, Mizoshita N, Kishimoto K (2006) *Angew Chem Int Ed* 45:38
6. Tschierske C (2001) *Ann Rep Progr Chem Ser C* 97:191
7. Goodby JW, Saez IM, Cowling SJ, Görtz V, Draper M, Hall AW, Sia S, Cosquer G, Lee SE, Raynes EP (2008) *Angew Chem Int Ed* 47:2754
8. Tschierske C (2007) *Chem Soc Rev* 36:1930
9. Tschierske C (1998) *J Mater Chem* 8:1485
10. Tschierske C (2001) *J Mater Chem* 11:2647
11. Gray GW, Goodby JW (1984) *Smectic liquid crystals – textures and structures*. Leonard Hill, Glasgow
12. Laschat S, Baro A, Steinke N, Giesselmann F, Hägele C, Scalia G, Judele J, Kapatsina E, Sauer S, Schreivogel A, Tosoni M (2007) *Angew Chem Int Ed* 46:4832
13. Kumar S (2010) *Chemistry of discotic liquid crystals*. CRC Press Inc, Boca Raton FL
14. Lee M, Cho BK, Zin WC (2001) *Chem Rev* 101:3869
15. Tschierske C (1996) *Progr Polym Sci* 21:775
16. Binnemans K (2005) *Chem Rev* 105:4148
17. Beginn U (2003) *Prog Polym Sci* 28:1049
18. Tschierske C (2002) *Cur Opin Coll Interf Sci* 7:355
19. Date RW, Bruce DW (2003) *J Am Chem Soc* 125:9012
20. Kouwer PHJ, Mehl GH (2009) *J Mater Chem* 19:1564
21. Israelachvili J (2010) *Intermolecular and surface forces*, 3rd edn. Academic, Burlington MA
22. Tanford C (1991) *The hydrophobic effect: formation of micelles and biological membranes*. Krieger Pun Comp, Malabar, FL
23. Hamley IW (1998) *The physics of block-copolymers*. Oxford University Press, Oxford
24. Pegenau A, Hegmann T, Tschierske C, Diele S (1999) *Chem Eur J* 5:1643
25. Bialecka-Florjanczyk E (2006) *J Phys Chem* 110:2582
26. Hildebrandt JL, Scott RL (1950) *The solubility of nonelectrolytes*, 3rd edn. Reinhold Pub Group, New York
27. Barton AFM (1991) *ORC handbook of solubility parameters and other cohesion parameters*, 2nd edn. CRC Press Inc, Boca Raton FL
28. Hansen C (2007) *Hansen solubility parameters: a user's handbook*, 2nd Ed. CRC Press Inc, Taylor & Francis Group, Boca Raton FL
29. Henry NM, Lonsdale K (1952) *International tables for X-ray crystallography*, vol 1. Kynoch Press, Birmingham, Symmetry Groups
30. Ungar G, Zeng XB (2005) *Soft Matter* 1:95
31. Borisch K, Diele S, Göring P, Tschierske C (1996) *J Chem Soc Chem Commun* 237
32. Diele S (2002) *Curr Opin Coll Interf Sci* 7:333

33. Imperor-Clerc M (2005) *Curr Opin Coll Interf Sci* 9:370
34. Kutsumizu S (2002) *Corr Opin Solid State Mater Sci* 6:537
35. Borisch K, Diele S, Göring P, Kresse H, Tschierske C (1998) *J Mater Chem* 8:529
36. Borisch K, Diele S, Göring P, Müller H, Tschierske D (1997) *Liq Cryst* 22:427
37. Hassan S, Rowe W, Tiddy, GJT (2002) In: Holmberg K (ed) *Handbook of applied surface and colloid chemistry*, vol. 1. Wiley-VCH, Chichester, p. 465
38. Seddon JM, Templer RH (1995). In: Lipowsky R, Sackmann E (ed) *Handbook of biological physics*, vol 1. Elsevier, Amsterdam, p 97
39. Percec V, Imam MR, Peterca M, Wilson DA, Heiney PA (2009) *J Am Chem Soc* 131:1294
40. Bilgin-Eran B, Tschierske C, Diele S, Baumeister U (2006) *J Mater Chem* 16:1145
41. Glebowska A, Przybylski P, Winek M, Krzyczkowska P, Krowczynski A, Szydłowska J, Pocięcha D, Gorecka E (2009) *J Mater Chem* 19:1395
42. Zeng XB, Kieffer R, Glettner B, Nürnberger C, Liu F, Pelz K, Prehm M, Baumeister U, Hahn H, Lang H, Gehring GA, Weber CHM, Hobbs JK, Tschierske C, Ungar G (2011) *Science* 331:1302
43. Kitzerow HS, Bahr C (2001) *Chirality in liquid crystals*. Springer, New York
44. Lagerwall ST (1999) *Ferroelectric and antiferroelectric liquid crystals*. Wiley-VCH, Weinheim
45. Lemieux R (2001) *Acc Chem Res* 34:845
46. Nishiyama I (2009) *Chem Rec* 9:340
47. Reddy RA, Tschierske C (2006) *J Mater Chem* 16:907
48. Lehmann M (2009) *Chem Eur J* 15:3638
49. Stewart GT (2004) *Liq Cryst* 31:403
50. Rey AD (2010) *Soft Matter* 6:3402
51. Hamley IW (2010) *Soft Matter* 6:1863
52. Mingos DMP (1999) *Liquid crystals II. Structure and Bonding*. Springer, Berlin, p 95
53. Kato T (2008) *Liquid crystalline functional assemblies and their supramolecular structures. Structure and Bonding*. Springer, Berlin, p 128
54. Ramamoorthy A (2007) *Thermotropic liquid crystals, recent advances*. Springer, Dordrecht
55. Zanchetta G, Bellini T, Nakata M, Clark NA (2008) *J Am Chem Soc* 130:12864
56. Kirsch P, Bremer M (2000) *Angew Chem Int Ed* 39:4216
57. Hunter L (2010) *Beilstein J Org Chem* 6:38
58. Kirsch P, Bremer M (2009) *ChemPhysChem* 11:357
59. Hird M (2007) *Chem Soc Rev* 36:2070
60. Kato T, Ushioda M, Shioda, Miyazawa K (2006) *Liq Cryst* 33:543
61. Hird M, Goodby JW, Lewis RA, Toyne KJ (2003) *Mol Cryst Liq Cryst* 401:1
62. Hird M, Toyne KJ (1998) *Mol Cryst Liq Cryst* 323:1
63. Guittard F, Taffin de Givenchy E, Geribaldi S, Cambon A (1999) *J Fluorine Chem* 100:85
64. Petrov VP (2010) *Mol Cryst Liq Cryst* 517:27
65. Goodby JW, Saez IM, Cowling SJ, Gasowska JS, MacDonald RA, Sia S, Watson P, Toyne KJ, Hird M, Lewis RA, Lee SE, Vaschenko V (2009) *Liq Cryst* 36:567
66. Krafft MP, Riess JG (2009) *Chem Rev* 109:1714
67. Smart BE (2001) *J Fluorine Chem* 109:3
68. Reed TM (1964) In: Simmons JH (ed) *Fluorine chemistry*, vol. 5. Academic Press, New York, p 133
69. Banks RE, Smart BE, Tatlow JC (1994) *Organofluorine chemistry: principles and commercial applications*. Plenum Press, New York
70. Kirsch P (2004) *Modern fluoroorganic chemistry*. Wiley-VCH, Weinheim
71. Uneyama K (2006) *Organofluorine chemistry*. Blackwell, Oxford
72. Smart BE (1995). In: Hudlicky M, Pavlath AE (eds) *Chemistry of organic fluorine compounds II*. American Chemical Society, Washington, DC, Chap 6, p 979
73. Riess JG (2002) *Tetrahedron* 58:4113
74. Lobko TA, Ostrovskii BI, Paluchenko AI, Sulianov SN (1993) *Liq Cryst* 15:361

75. Marchionni G, Ajroldi G, Righetti CM, Pezzin G (1993) *Macromolecules* 26:1751
76. Tsuzuki S, Uchimaru T, Mikami M (2002) *J Chem Phys* 116:3309
77. Tsuzuki S, Uchimaru T, Mikami M (2002) *J Chem Phys* 121:9917
78. Dunitz JD (2004) *Chem Bio Chem* 5:614
79. Mukerjee P (1994) *Colloids Surf A Physicochem Eng Aspects* 84:1
80. Mukerjee P, Handa T (1981) *J Phys Chem* 85:2298
81. Campos Vallette M, Rey Lafon M (1983) *J Mol Struct* 101:23
82. Albrecht T, Elben H, Jaeger R, Kimmig M, Steiner R, Strobl G, Stühn B, Schwickert H, Ritter C (1991) *J Chem Phys* 95:2807
83. Bunn CW, Howells ER (1954) *Nature* 174:549
84. Schwickert H, Strobl GR, Kimmig M (1991) *J Chem Phys* 95:2800
85. Piaggio P, Francese PG, Masetti G, Dellepiane G (1975) *J Mol Struct* 26:421
86. Wang J, Ober CK (1999) *Liq Cryst* 26:637
87. Knochenhauer G, Reiche J, Brehmer L, Barberka T, Woolley M, Tredgold R, Hodge P (1995) *J Chem Soc Chem Commun* 1619
88. Binks BP, Fletcher PDI, Kotsev SN, Thompson RL (1997) *Langmuir* 13:6669
89. Duce C, Tine MR, Lepori L, Matteoli E, Marongiu B, Piras A (2008) *J Therm Anal Cal* 92:145
90. Pratas de Melo MJ, Dias AMA, Blesic M, Rebelo LPN, Vega LF, Coputinho JAP, Marrucho IM (2006) *Fluid Phase Equilibria* 242:210
91. Young CL (1969) *Trans Faraday Soc* 65:2639
92. Binks BP, Fletcher PDI, Sager WFC, Thompson RL (1997) *J Mol Liq* 72:177
93. Dorset DL (1990) *Macromolecules* 23:894
94. Yano M, Taketsugu T, Hori K, Okamoto H, Takenaka S (2004) *Chem Eur J* 10:3991
95. Lepori L, Matteoli E, Spanedda A, Duce C, Tine R (2002) *Fluid Phase Equilibria* 201:119
96. Lo Nostro P, Scalise L, Baglioni P (2005) *J Chem Eng Data* 50:1148
97. Gerhardt GE, Lagow RJ (1977) *J Chem Soc Chem Commun* 259
98. http://www.chemicalbook.com/ChemicalProductProperty_DE_CB1696808.htm
99. Pacansky J, Miller M, Hatton W, Liu B, Scheiner A (1991) *J Am Chem Soc* 113:329
100. Sung K, Lagow RJ (1995) *J Am Chem Soc* 117:4276
101. Banks RE, Tatlow JC (1986) *J Fluorine Chem* 33:227
102. Viney C, Russell TP, Depero LE, Twieg RJ (1989) *Mol Cryst Liq Cryst* 168:63
103. Escobedo FA, Chen Z (2004) *J Chem Phys* 121:11463
104. Marczuk P, Lang P (1998) *Macromolecules* 31:9013
105. Höpken J, Möller M (1992) *Macromolecules* 25:2482
106. Broniatowski M, Dynarowicz-Latka P, Witko W (2005) *J Fluorine Chem* 126:79
107. Broniatowski M, Dynarowicz-Latka P, Witko W (2006) *Mol Cryst Liq Cryst* 460:63
108. Clark CG, Floudes GA, Lee YJ, Graf R, Spiess HW, Müllen K (2009) *J Am Chem Soc* 131:8537
109. Okamoto H, Yamada N, Takenaka S (1998) *J Fluorine Chem* 91:125
110. Okamoto H, Murai H, Takenaka S (1997) *Bull Chem Soc Jpn* 70:3163
111. Duan M, Okamoto H, Petrov VF, Takenaka S (1998) *Bull Chem Soc Jpn* 71:2735
112. Hori K, Maeda M, Yano M, Kunugi M (2011) *Liq Cryst* 38:287
113. Duan M, Okamoto H, Petrov VF, Takenaka S (1999) *Bull Chem Soc Jpn* 72:1637
114. Ungar G, Noble K, Percec V, Johansson G (2000) *J Mat Sci* 35:5241
115. Fornasieri G, Guittard F, Geribaldi S (2003) *Liq Cryst* 30:663
116. Mori A, Unio K, Takeshita H, Takematsu S (2005) *Liq Cryst* 32:107
117. Takenaka S (1992) *J Chem Soc Chem Commun* 1748
118. Fornasieri G, Guittard F, Geribaldi S (2004) *Liq Cryst* 31:491
119. Johansson G, Percec V, Ungar G, Smith K (1997) *Chem Mater* 9:164
120. Petrov VF, Duan M, Okamoto H, Takenaka S (2000) *Mol Cryst Liq Cryst* 350:187 and references therein
121. Schaz A, Valaityte E, Lattermann G (2005) *Liq Cryst* 32:513

122. Khairuddean M, Twieg RJ (2009) *Mol Cryst Liq Cryst* 503:3
123. Miethchen R, Hein M (2000) *Carbohydrate Res* 327:169
124. Nguyen HL, Dedier J, Nguyen HT, Rouillon JC, Sigaud G (1999) *Liq Cryst* 26:1637
125. Cheng XH (2001) PhD Thesis, Halle
126. Schaz A, Valaityte E, Lattermann G (2004) *Liq Cryst* 31:1311
127. Riess JG (2009) *Curr Opin Colloid Interf Sci* 14:294
128. Matsuoka K, Moroi Y (2003) *Curr Opin Colloid Interf Sci* 8:227
129. Guittard F, Geribaldi S (2001) *J Fluorine Chem* 107:363
130. Rico Lattes I, Guidetti B, Lattes A (2001) *J Fluorine Chem* 107:355
131. Vierling P, Santaella C, Greiner J (2001) *J Fluorine Chem* 107:337
132. Newkome GR, Lin X (1991) *Macromolecules* 24:443
133. Johansson G, Percec V, Ungar G, Zhou JP (1996) *Macromolecules* 29:646
134. Percec V, Schlueter D, Kwon YK, Blackwell J, Möller M, Slangen PJ (1995) *Macromolecules* 28:8807
135. Chvalun SN, Shcherbina MA, Yakunin AN, Blackwell J, Percec V (2007) *Polym Sci Ser A* 49:158
136. Percec V, Johansson G, Ungar G, Zhou J (1996) *J Am Chem Soc* 118:9855
137. Hudson SD, Jung HT, Percec V, Cho WD, Johansson G, Ungar G, Balagurusamy VSK (1997) *Science* 278:449
138. Cheng XH, Diele S, Tschierske C (2000) *Angew Chem Int Ed* 39:592
139. Cheng XH, Das K, Diele S, Tschierske C (2002) *Langmuir* 18:6521
140. Borisch K, Diele S, Göring P, Kresse H, Tschierske C (1997) *Angew Chem Int Ed Eng* 36:2087
141. Pegenau A, Cheng XH, Tschierske C, Göring P, Diele S (1999) *New J Chem* 23:465
142. Pegenau A, Göring P, Tschierske C (1996) *J Chem Soc Chem Commun* 2563
143. Rosen BM, Wilson CJ, Wilson DA, Peterca M, Imam MR, Percec V (2009) *Chem Rev* 109:6275
144. Dukeson DR, Ungar G, Balagurusamy VSK, Percec V, Johansson GA, Glodde M (2003) *J Am Chem Soc* 125:15974
145. Yoon DK, Lee SR, Kim YH, Choi SM, Jung HT (2006) *Adv Mater* 18:509
146. Schaz A, Lattermann G (2005) *Liq Cryst* 32:407
147. Zhou X, Narayanan T, Lin Q (2007) *Liq Cryst* 34:1243
148. Percec V, Aqad E, Peterca M, Imam MR, Glodde M, Bera TK, Miura Y, Balagurusamy VSK, Ewbank PC, Würthner F, Heiney PA (2007) *Chem Eur J* 13:3330
149. Yanagimoto Y, Takaguchi Y, Sako Y, Tsuboi S, Ichihara M, Ohta K (2006) *Tetrahedron* 62:8373
150. Kim YH, Yoon DK, Lee EH, Ko YK, Jung H-T (2006) *J Phys Chem B* 110:20836
151. Threlfall R, Cosstick R, Wada T (2008) *Nucleic Acids Symp Ser* 52:337
152. Mori A, Hashimoto M, Ujije S (2011) *Liq Cryst* 38:263
153. Janietz D, Kohlmeier A (2009) *Liq Cryst* 36:685
154. Bilgin Eran B, Yörür C, Tschierske C, Prehm M, Baumeister U (2007) *J Mater Chem* 17:2319
155. Percec V (2006) *Phil Trans R Soc A* 364:2709
156. Percec V, Glodde M, Peterca M, Rapp A, Schnell I, Spiess HW, Bera TK, Miura Y, Balagurusamy VSK, Aqad E, Heiney PA (2006) *Chem Eur J* 12:6298
157. Kohlmeier A, Janietz D (2010) *Chem Eur J* 16:10453
158. Janietz D, Kohlmeier A (2009) *Mol Cryst Liq Cryst* 509:39
159. Kohlmeier A, Nordsieck A, Janietz D (2009) *Chem Mater* 21:491
160. Kohlmeier A, Janietz D (2006) *Chem Mater* 18:59
161. Percec V, Glodde M, Johansson G, Balagurusamy VSK, Heiney PA (2003) *Angew Chem Int Ed* 42:4338
162. Peterca M, Percec V, Imam MR, Leonawat P, Morimitsu K, Heiney PA (2008) *J Am Chem Soc* 130:14840
163. Neubert ME, Keast SS, Law CC, Lohman MC, Bhatt JC (2005) *Liq Cryst* 32:781

164. Ostrovskii BI, Tournilhac FG, Blinov LM, Haase W (1995) *J Phys II France* 5:979
165. (a) Iwan A, Janeczak H, Jarzabek B, Domanski M, Rannou P (2009) *Liq Cryst* 36:873;
(b) Iwan A, Janeczak H, Hreniak A, Palewicz M, Pocięcha D (2010) *Liq Cryst* 37:1021
166. Nishikawa E, Yamamoto J, Yokoyama H (2003) *Liq Cryst* 30:785
167. Rieker TP, Janulis EP (1995) *Phys Rec E* 52:2688
168. Zaszke H (1977) PhD Thesis B, Halle
169. Radcliff MD, Brostrom ML, Epstein KA, Rappaport AG, Thomas BN, Shao R, Clark NA (1999) *Liq Cryst* 26:789
170. Ema K, Takekoshi K, Yao H, Wang ST, Huang CC (2005) *Phys Rev E* 71:031706
171. Taffin de Givenchy E, Guittard F, Bracon F, Cambon A (1999) *Liq Cryst* 26:1163
172. Pensec S, Tournilhac FG, Bassoul P, Durliat C (1998) *J Phys Chem B* 102:52
173. Pensec S, Tournilhac F-G, Bassoul P (1996) *J Phys II France* 6:1597
174. Diele S, Lose D, Kruth H, Pelzl G, Guittard F, Cambon A (1996) *Liq Cryst* 21:603
175. Pelzl G, Diele S, Lose D, Ostrovski BI, Weissflog W (1997) *Cryst Res Technol* 32:99
176. Chiang YH, Ames AE, Gaudiana RA, Adams TG (1991) *Mol Cryst Liq Cryst* 208:85
177. Abe K, Yang X, Yano S, Kato T, Takeuchi H (2000) *Liq Cryst* 27:839
178. Gray GW, Goodby JW (1976) *Mol Cryst Liq Cryst* 37:157
179. Shen Y, Wen J (2002) *J Fluorine Chem* 113:13
180. Qin C, Rong G, Wen J, Vajda A, Eber N (2004) *Liq Cryst* 31:1677
181. Koden M, Nakagawa K, Ishii Y, Funada F, Matsuura M, Awane K (1989) *Mol Cryst Liq Cryst Lett* 6:85
182. Chen BQ, Wen JX (1999) *Liq Cryst* 26:1135
183. Liu H, Nohira H (1998) *Ferroelectrics* 207:541
184. Fornasieri G, Guittard F, Geribaldi S (2003) *Liq Cryst* 30:251
185. Kromm P, Cotrait M, Nguyen HT (1996) *Liq Cryst* 21:95
186. Taffin de Givenchy E, Guittard F, Caillier L, Munuera J, Geribaldi S (2005) *Mol Cryst Liq Cryst* 436:237
187. Cumming WJ, Gaudiana RA (1996) *Liq Cryst* 20:283
188. Doi T, Sakurai Y, Tamatani A, Takenaka S, Kusabayashi S, Nishihata Y, Terauchi H (1991) *J Mater Chem* 1:169
189. Yang X, Abe K, Kato R, Yano S, Kato T, Miyazawa K, Takeuchi H (1999) *Liq Cryst* 26:1485
190. Yang YG, Chen H, Tang G, Wen JX (2002) *Mol Cryst Liq Cryst* 373:1
191. Yang Y, Li H, Wen J (2007) *Mol Cryst Liq Cryst* 469:23
192. Nguyen HT, Sigaud G, Achard MF, Hardouin F, Twieg RJ, Betterton K (1991) *Liq Cryst* 10:389
193. Laffitte JD, Mauzac M, Twieg RJ, Nguyen HT, Sigaud G (1994) *Liq Cryst* 16:223
194. Lose D, Diele S, Pelzl G, Dietzmann E, Weissflog W (1998) *Liq Cryst* 24:707
195. Liu H, Nohira H (1997) *Liq Cryst* 22:217
196. Misaki S, Takamatsu S, Suefuji M, Mitote T, Matsumura M (1981) *Mol Cryst Liq Cryst* 66:123
197. Drzewinski W, Dabrowski R, Czuprynski K (2002) *Pol J Chem* 76:273
198. (a) Cowling SJ, Hall AW, Goodby JW, Wang Y, Gleeson HF (2006) *J Mater Chem* 16:2181;
(b) Cowling SJ, Hall AW, Goodby JW (2011) *J Mat Chem* 21:9031
199. Doi T, Takenaka S, Kusabayashi S, Nishihata Y, Terauchi H (1991) *Mol Cryst Liq Cryst* 204:9
200. Emelyanenko AV, Osipov MA (2004) *Phys Rev E* 70:021704
201. Wen J, Chen H, Shen Y (1999) *Liq Cryst* 26:1833
202. Yang YG, Wen JX (2001) *Liq Cryst* 28:1735
203. Guillevic MA, Bruce DW (2000) *Liq Cryst* 27:153
204. Yang Y, Li H, Wen J (2007) *Liq Cryst* 34:1167
205. Li H, Wen J, Yang Y (2007) *Mol Cryst Liq Cryst* 473:15
206. Twieg R, Betterton K, DiPietro R, Gravert D, Nguyen C, Nguyen HT, Babeau A, Destrade C, Sigaud G (1992) *Mol Cryst Liq Cryst* 217:201

207. Liu H, Nohira H (1998) *Liq Cryst* 24:719
208. Lagerwall ST, Dahlgren A, Jagemalm P, Rudquist P, D'Have K, Pauwels H, Dabrowski R, Drzewinski W (2001) *Adv Funct Mater* 11:2
209. Dabrowski R (2000) *Ferroelectrics* 243:1
210. Fafara A, Gestblom B, Wrobel S, Dabrowski R, Drzewinski W, Kilian D, Haase W (1998) *Ferroelectrics* 212:79
211. Drzewinski W, Czuprynski K, Dabrowski R, Neubert M (1999) *Mol Cryst Liq Cryst* 328:401
212. Piecek W, Raszewski Z, Perkowski P, Kedzierski J, Ruthowska J, Zielinski J, Nowinowski-Kruszelnicki E, Dabrowski R, Tykarska M, Przedmojski J (2005) *Mol Cryst Liq Cryst* 436:149
213. Dabrowski R, Gasowska J, Filipowicz M, Przedmojski J, Tykarska M, Oton JM, Castillos PL, Bennis N (2005) *Phase Trans* 78:927
214. Kula P, Dabrowski R, Tykarska M (2007) *Phase Trans* 80:771
215. Dabrowski R, Kula P, Tykarska M, Przedmojski J, Piecek W (2007) *Mol Cryst Liq Cryst* 475:137
216. Zurowska M, Dabrowski R, Dziaduszek J, Rejmer W, Czuprynski K, Raszewski Z, Piecek W (2010) *Mol Cryst Liq Cryst* 525:219
217. Rejmer W, Zurowska M, Dabrowski R, Czuprynski K, Raszewski Z, Piecek W (2009) *Mol Cryst Liq Cryst* 509:195
218. Tykarska M, Dabrowski R, Przedmojski J, Piecek W, Skrzypek K, Donnio B, Guillon D (2008) *Liq Cryst* 35:1053
219. Stipetic AI, Goodby JW, Hird M, Raoul YM, Gleeson HF (2006) *Liq Cryst* 33:819
220. Chiang YH, Ames AE, Gaudiani RA, Adams TG (1991) *Mol Cryst Liq Cryst* 208:85
221. Nguyen HT, Rouillon JC, Babeau A, Marcerou JP, Sigaud G, Cotrait M, Allouchi H (1999) *Liq Cryst* 26:1007
222. Wu S-L, Lin C-Y (2005) *Liq Cryst* 32:663
223. Wu S-L, Lin C-Y (2007) *Liq Cryst* 34:25
224. Wu S-L, Lin C-Y (2006) *Liq Cryst* 33:953
225. Yang Y, Li H, Wen J (2007) *Mol Cryst Liq Cryst* 469:51
226. Perkowski P, Raszewski Z, Kedzierski J, Piecek W, Rutkowska J, Klosowicz S, Zielinski J (2004) *Mol Cryst Liq Cryst* 411:145
227. Lagerwall JPF, Saipa A, Giesselmann F, Dabrowski R (2004) *Liq Cryst* 31:1175
228. Lagerwall JPF, Giesselmann F (2006) *ChemPhysChem* 7:20
229. Fukuda A, Takanishi Y, Isozaki T, Ishikawa K, Takezoe H (1994) *J Mater Chem* 4:997
230. Wu S-L, Lin C-Y (2005) *Liq Cryst* 32:1053
231. Yang X, Abe K, Kato R, Yano S, Kato T, Miyazawa K, Takeuchi H (1998) *Liq Cryst* 25:639
232. Guillevic MA, Gelbrich T, Hursthouse MB, Bruce DW (2001) *Mol Cryst Liq Cryst* 362:147
233. Yoneya M, Nishikawa E, Yokoyama H (2004) *J Chem Phys* 121:7520
234. Schwäbisch D, Miethchen R (2003) *J Fluorine Chem* 120:8591
235. Nishiyama I, Yamamoto T, Yamamoto J, Yokoyama H, Goodby JW (2005) *Mol Cryst Liq Cryst* 439:55
236. Gorria P, Nguyen HT, Twieg RJ, Betterton K, Sigaud G (1996) *Liq Cryst* 21:523
237. Small AC, Hunt DK, Pugh C (1999) *Liq Cryst* 26:849
238. Pugh C, Small AC, Helfer CA, Mattice WL (2001) *Liq Cryst* 28:991
239. Weissflog W, Demus D (1984) *Cryst Res Technol* 19:55
240. Arehart SV, Pugh C (1997) *J Am Chem Soc* 119:3027
241. Small AC, Pugh C (2002) *Macromolecules* 35:2105
242. Dietzmann E, Weissflog W (1997) *Mol Cryst Liq Cryst* 299:419
243. Nishikawa E, Yamamoto J, Yokoyama H (2001) *Chem Lett* 94
244. Bernhardt H, Weissflog W, Kresse H (1997) *Chem Lett* 151
245. Nishikawa E, Yamamoto J, Yokoyama H (2004) *Mol Cryst Liq Cryst* 411:139
246. Kohlmeier A, Janietz D (2007) *Liq Cryst* 34:65

247. Demus D, Gloza A, Hartung H, Hauser A, Rapphel I, Wiegeleben A (1981) *Cryst Res Technol* 16:1445
248. Mori H, Kutsumizu S, Saito K, Yamamoto K, Sakurai S, Sakajiri K (2010) *Langmuir* 26:11605
249. Zeng X, Ungar G, Imperor-Clerc M (2005) *Nat Mater* 4:562
250. Facchetti A, Deng Y, Wang A, Koide Y, Sirringhaus H, Marks TJ, Friend RH (2000) *Angew Chem Int Ed* 39:4547
251. Jung BJ, Tremblay NJ, Yeh M-L, Katz HE (2011) *Chem Mater* 23:568
252. Tang ML, Bao Z (2011) *Chem Mater* 23:446
253. Yoon M-H, DiBenedetto SA, Russel MT, Facchetti A, Marks TJ (2007) *Chem Mater* 19:4864
254. Ie Y, Nitani M, Ishikawa M, Nakayama K, Tada H, Kaneda T, Aso Y (2007) *Org Lett* 9:2115
255. Facchetti A, Mushrush M, Katz HE, Marks TJ (2003) *Adv Mater* 15:33
256. Pisula W, Zorn M, Chang JY, Müllen K, Zentel R (2009) *Macromol Rapid Commun* 30:1179
257. Malthete J, Levelut AM, Nguyen HT (1985) *J Phys (Paris) Lett* 46:L875
258. Nguyen HT, Destrade C, Malthete J (1997) *Adv Mater* 9:375
259. Gharbia M, Gharbi A, Nguyen HT, Malthete J (2002) *Curr Opin Colloid Interf Sci* 7:312
260. Bruce DW (2000) *Acc Chem Res* 33:831
261. Nishikawa E, Yamamoto J, Yokoyama H (2003) *Chem Commun* 420
262. Nishikawa E, Yamamoto J, Yokoyama H (2003) *J Mater Chem* 13:1887
263. Nishikawa E, Yamamoto J, Yokoyama H (2005) *Liq Cryst* 32:585
264. Maeda Y, Nishikawa E, Yokoyama H (2006) *Liq Cryst* 33:865
265. Sergeev S, Pisula W, Geerts YH (2007) *Chem Soc Rev* 36:1902
266. Bengs H, Closs F, Frey T, Funhoff D, Ringsdorf H, Siemensmeyer K (1993) *Liq Cryst* 15:565
267. Dahn U, Erdelen C, Ringsdorf H, Festag R, Wendorff JH, Heiney PA, Maliszewskij NC (1995) *Liq Cryst* 19:759
268. Terasawa N, Monobe H, Kiyohara K, Shimizu Y (2003) *Chem Commun* 1678
269. Terasawa N, Monobe H (2007) *Liq Cryst* 34:4477
270. Yang GF, Zhao KQ, Yu WH, Hu P, Wang BQ (2009) *Sci China Ser B Chem* 52:1244
271. Terasawa N, Monobe H, Kiyohara K, Shimizu Y (2003) *Chem Lett* 32:214
272. Terasawa N, Monobe H, Kiyohara K (2007) *Liq Cryst* 34:311
273. Kowser PHJ, Picken SJ, Mehl GH (2007) *J Mater Chem* 17:4196
274. Alameddine B, Aebischer OF, Amrein W, Donnio B, Deschenaux R, Guillon D, Savary C, Scanu D, Scheidegger O, Jenny TA (2005) *Chem Mater* 17:4798
275. Aebischer OT, Alameddine B, Jenny TA (2008) *Chimia* 62:967
276. Aebischer A, Aebischer OF, Donnio B, Alameddine B, Dadras M, Güdel HU, Guillon D, Jenny TA (2007) *J Mater Chem* 17:1262
277. Sakurai T, Tashiro K, Honsho, Saeki A, Seki S, Osuka A, Muranaka A, Uchiyama M, Kim J, Ha S, Kato K, Takata M, Aida T (2011) *J Am Chem Soc* 133:6537
278. Miyake Y, Fuijii A, Ozaki M, Shimizu Y (2010) *Mol Cryst Liq Cryst* 516:246
279. An Z, Yu J, Domercq B, Jones SC, Barlow S, Kippelen B, Mader SR (2009) *J Mater Chem* 19:6688
280. De Luca G, Liscio A, Melucci M, Schnitzler T, Pisula W, Clark CG Jr, Scolaro LM, Palermo V, Müllen K, Samori P (2010) *J Mater Chem* 20:71
281. Li Y, Tan L, Wang Z, Qian H, Shi Y, Hu W (2008) *Org Lett* 10:529
282. Schmidt R, Ling MM, Oh JH, Winkler M, Konemann M, Bao ZN, Würthner F (2007) *Adv Mater* 19:3692
283. Katz HE, Lovinger AJ, Johnson J, Kloc C, Siegrist T, Li W, Lin YY, Dodabalapur A (2000) *Nature* 404:478
284. See KC, Landis C, Sarjeant A, Katz HE (2008) *Chem Mater* 20:3609
285. Katz HE, Johnson J, Lovinger AJ, Li WJ (2000) *J Am Chem Soc* 122:7787
286. Jung BJ, Lee K, Sun J, Andreou AG, Katz HE (2010) *Adv Funct Mater* 20:2930
287. Zheng QD, Huang J, Sarjeant A, Katz HE (2008) *J Am Chem Soc* 130:14410

288. Zhou X, Kang SW, Kumar S, Li Q (2009) *Liq Cryst* 36:269
289. Chikamatsu M, Itakura A, Yoshida Y, Azumi R, Yase K (2008) *Chem Mater* 20:7365
290. Wöbkenberg PH, Ball J, Bradley DDC, Anthopoulos TD, Kooistra F, Hummelen JC, de Leeuw DM (2008) *Appl Phys Lett* 92:143310
291. (a) Serrano JL. (1996) *Metallomesogens – synthesis properties applications*. VCH Weinheim;
(b) Pinol R, Ros, MB, Serrano JL, Sierra T, De La Fuente MR (2004) *Liq Cryst* 31:1293
292. Dembinski R, Espinet P, Lentijo S, Markowicz MW, Martin-Alvarez JM, Rheingold AL, Schmidt DJ, Sniady A (2008) *Eur J Inorg Chem* 1565
293. Bilgin-Eran B, Tschierske C, Diele S, Baumeister U (2006) *J Mater Chem* 16:1136
294. Szydłowska J, Krowczyński A, Pietrasik U, Rogowska A (2005) *Liq Cryst* 32:651
295. Lehmann M, Jahr M, Gutmann J (2008) *J Mater Chem* 18:2995
296. Pensec S, Tournilhac F-G (1997) *Chem Commun* 441
297. Tournilhac F, Blinov LM, Simon J, Yablonsky SV (1992) *Nature* 359:621
298. Niori T, Sekine T, Watanabe J, Furukawa T, Takezoe H (1996) *J Mater Chem* 6:1231
299. Jahr M (2011) PhD Thesis, Chemnitz
300. Kohlmeier A, Janietz D (2007) *Liq Cryst* 34:289
301. Zelcer A, Donnio B, Bourgogne C, Cukiernik FD, Guillon D (2007) *Chem Mater* 19:1992
302. Sauer S, Steinke N, Baro A, Laschat S, Giesselmann F, Kantlehner W (2008) *Chem Mater* 20:1909
303. Percec V, Bera TK, Glodde M, Fu Q, Balagurusamy VSK, Heiney PA (2003) *Chem Eur J* 9:921
304. Percec V, Ahn C-H, Bera TK, Ungar G, Yeardley DJP (1999) *Chem Eur J* 5:1070
305. Percec V, Imam MR, Bera TK, Balagurusamy VSK, Peterca M, Heiney PA (2005) *Angew Chem Int Ed* 44:4739
306. de Campo L, Varslot T, Moghaddam MJ, Kirkensgaard JJK, Mortensen K, Hyde ST (2011) *Phys Chem Chem Phys* 13:3139
307. Sioula S, Hadjichristidis N, Thomas EL (1998) *Macromolecules* 31:5272
308. Takano A, Kawashima W, Noro A, Isono Y, Tanaka N, Dotera T, Matsushita Y (2005) *J Polymer Sci B Polymer Phys* 43:2427
309. Matsushita Y, Hayashida K, Takano A (2010) *Macromol Rapid Commun* 31:1579
310. Ungar G, Tschierske C, Abetz V, Holyst R, Bates MA, Liu F, Prehm M, Kieffer R, Zeng XB, Walker M, Glettner B, Zywockinski A (2011) *Adv Funct Mater* 21:1296
311. Chen B, Zeng X, Baumeister U, Ungar G, Tschierske C (2005) *Science* 307:96
312. Chen B, Baumeister U, Pelzl G, Das MK, Zeng X, Ungar G, Tschierske C (2005) *J Am Chem Soc* 127:16578
313. Chen B, Baumeister U, Diele S, Das MK, Zeng X, Ungar G, Tschierske C (2004) *J Am Chem Soc* 126:8608
314. Chen B, Zeng XB, Baumeister U, Diele S, Ungar G, Tschierske C (2004) *Angew Chem Int Ed* 43:4621
315. Cook AG, Baumeister U, Tschierske C (2005) *J Mater Chem* 15:1708
316. Cheng X, Prehm M, Das MK, Kain J, Baumeister U, Diele S, Leine D, Blume A, Tschierske C (2003) *J Am Chem Soc* 125:10977
317. Cheng X, Das MK, Baumeister U, Diele S, Tschierske C (2004) *J Am Chem Soc* 126:12930
318. Kölbel M, Beyersdorff T, Cheng XH, Tschierske C, Kain J, Diele S (2001) *J Am Chem Soc* 123:6809
319. Kieffer R, Prehm M, Glettner B, Pelzl K, Baumeister U, Liu F, Zeng X, Ungar G, Tschierske C (2008) *Chem Commun* 3861
320. Cheng XH, Das MK, Diele S, Tschierske C (2002) *Angew Chem Int Ed* 41:4031
321. Prehm M, Cheng XH, Diele S, Das MK, Tschierske C (2002) *J Am Chem Soc* 124:12072
322. Prehm M, Diele S, Das MK, Tschierske C (2003) *J Am Chem Soc* 125:614
323. Prehm M, Liu F, Baumeister U, Zeng X, Ungar G, Tschierske C (2007) *Angew Chem Int Ed* 46:7972

324. Prehm M, Enders C, Anzahae MY, Glettner B, Baumeister U, Tschierske C (2008) *Chem Eur J* 14:6352
325. Kieffer R, Prehm M, Pelz K, Baumeister U, Liu F, Hahn H, Lang L, Ungar G, Tschierske C (2009) *Soft Matter* 5:1214
326. Grünbaum B, Shephard GC (1987) *Tilings and Patterns*. W.H. Freeman, New York
327. Bates M, Walker M (2009) *Soft Matter* 5:346
328. Bates MA, Walker M (2010) *Mol Cryst Liq Cryst* 525:204
329. Crane AJ, Martinez-Veracochea FJ, Escobedo FA, Müller EA (2008) *Soft Matter* 4:1820
330. Cheng X, Dong X, Wie G, Prehm M, Tschierske C (2009) *Angew Chem Int Ed* 48:8014
331. Cheng X, Dong X, Huang R, Zeng X, Ungar G, Prehm M, Tschierske C (2008) *Chem Mater* 20:4729
332. Prehm M, Götz G, Bäuerle P, Liu F, Zeng X, Ungar G, Tschierske C (2007) *Angew Chem Int Ed* 46:7856
333. Mishra A, Ma C-Q, Bäuerle P (2009) *Chem Rev* 109:1141
334. Melucci M, Favaretto L, Bettini C, Gazzano M, Camaioni N, Maccagnani P, Ostojica P, Monari M, Barbarella G (2007) *Chem Eur J* 13:10046
335. Yasuda T, Ooi H, Morita J, Akama Y, Minoura K, Funahashi M, Shimomura T, Kato T (2009) *Adv Funct Mater* 19:411
336. Leroy J, Boucher N, Sergeev S, Sferrazza M, Geerts YH (2007) *Eur J Org Chem* 1256
337. Bunz UHF (2009) *Macromol Rapid Commun* 30:772
338. Ungar G, Liu F, Zeng XB, Glettner B, Prehm M, Kieffer R, Tschierske C (2010) *J Phys Conf Series* 247:012032
339. Patel NM, Dodge MR, Zhu MH, Petschek RG, Rosenblatt C, Prehm M, Tschierske C (2004) *Phys Rev Lett* 92:015501
340. Patel NM, Rosenblatt C, Prehm M, Tschierske C (2005) *Liq Cryst* 32:55
341. Chattham N, Zhu C, Cheng X, Limtrakul J, Tschierske C, MacLennan JE, Clark NA (2011) *Soft Matter* 7:9978
342. Prehm M, Liu F, Zeng X, Ungar G, Tschierske C (2008) *J Am Chem Soc* 130:14922
343. Prehm M, Liu F, Zeng X, Ungar G, Tschierske C (2011) *J Am Chem Soc* 133:4906
344. Glettner B, Liu F, Zeng X, Prehm M, Baumeister U, Ungar G, Tschierske C (2008) *Angew Chem Int Ed* 47:6080
345. Hennrich G, Omenat A, Asselberghs I, Foerier S, Clays K, Verbiest T, Serrano JL (2006) *Angew Chem Int Ed* 45:4203
346. Bates MA, Walker M (2009) *Phys Chem Chem Phys* 11:1893
347. Glettner B, Liu F, Zeng X, Prehm M, Baumeister U, Walker M, Bates MA, Boesecke P, Ungar G, Tschierske C (2008) *Angew Chem Int Ed* 47:9063
348. Shen D, Pegenau A, Diele S, Wirth I, Tschierske C (2000) *J Am Chem Soc* 122:1593
349. Kovalenko L, Weissflog W, Grande S, Diele S, Pelzl G, Wirth I (2000) *Liq Cryst* 27:683
350. Reddy RA, Dantlgraber G, Baumeister U, Tschierske C (2006) *Angew Chem Int Ed* 45:1928
351. Choi EJ, Sim HS, Chien LC, Lee SM (2011) *Bull Korean Chem Soc* 32:725
352. Kovalenko L (2004) PhD Thesis, Halle
353. Okamoto H, Morita Y, Doi T, Takenaka S (2005) *Mol Cryst Liq Cryst* 439:2299
354. Weissflog W, Richter S, Dietzmann E, Risse J, Diele S, Schiller P, Pelzl G (1997) *Cryst Res Technol* 32:271
355. Eremin A, Diele S, Pelzl G, Kovalenko L, Pelz K, Weissflog W (2001) *Liq Cryst* 28:1451
356. Iwan A, Pocięcha D, Sikora A, Janecek H, Węgrzyn M (2010) *Liq Cryst* 37:1479
357. Hoshino K, Kanie K, Ohtake T, Mukai T, Yoshizawa M, Ujiiie S, Ohno H, Kato T (2002) *Macromol Chem Phys* 203:1547
358. Lee JW, Park Y, Jin JI, Achard MF, Hardouin F (2003) *J Mater Chem* 13:1367
359. Kim KN, Do ED, Kwon YW, Jin JI (2005) *Liq Cryst* 32:229
360. Olsson N, Schröder M, Diele S, Andersson G, Dahl I, Helgee B, Komitov L (2007) *J Mater Chem* 17:2517
361. Shepperson KJ, Meyer T, Mehl GH (2004) *Mol Cryst Liq Cryst* 411:185

362. Kouwer PHJ, Mehl GH, Pieken SJ (2004) *Mol Cryst Liq Cryst* 411:387
363. Itoh T, Ishida N, Ohashi M, Asep R, Nohira H (2003) *Chem Lett* 32:494
364. Yamaguchi A, Yoshizawa A (2007) *Mol Cryst Liq Cryst* 479:181
365. Yamaguchi A, Maeda Y, Yokoyama H, Yoshizawa A (2006) *Chem Mater* 18:5704
366. Yoshizawa A (2008) *J Mater Chem* 18:2877
367. Takeuchi K, Takanishi Y, Yamamoto J, Yoshizawa A (2010) *Liq Cryst* 37:507
368. Yamaguchi A, Uehara N, Yamamoto J, Yoshizawa A (2007) *Chem Mater* 19:6445
369. Donnio B, Guillon D (2006) *Adv Polym Sci* 201:45
370. Marcos M, Martin-Rapun R, Omenat A, Serrano JL (2007) *Chem Soc Rev* 36:1889
371. Caminade AM, Turrin CO, Sutra P, Majoral JP (2003) *Curr Opin Coll Interf Sci* 8:282
372. Hirao A, Sugiyama K, Yokoyama H (2007) *Prog Polym Sci* 32:1393
373. Lorenz K, Frey H, Stuehn B, Mühlhaupt R (1997) *Macromolecules* 30:6860
374. Stark B, Lach C, Frey H, Stühn B (1999) *Macromol Symp* 146:33
375. Stark B, Stühn B, Frey H, Lach C, Lorenz K, Frick B (1998) *Macromolecules* 31:5415
376. Trahasch B, Stühn B, Frey H, Lorenz K (1999) *Macromolecules* 32:1962
377. Facher A (2000) PhD Thesis, Bayreuth, p 129
378. Martin-Rapun R, Marcos M, Omenat A, Serrano JL, Taffin de Givenchy E, Guittard F (2007) *Liq Cryst* 34:395
379. Hernandez-Ainsa S, Barbera J, Marcos M, Serrano JL (2010) *Chem Mater* 22:4762
380. Hernandez-Ainsa S, Barbera J, Marcos M, Serrano JL (2010) *J Polym Sci A Polym Chem* 49:278
381. Hernandez-Ainsa S, Marcos M, Barbera J, Serrano JL (2010) *Angew Chem Int Ed* 49:1990
382. Hirao A, Sugiyama K, Yokoyama H (2007) *Prg Polym Sci* 32:1393
383. Xiang M, Li X, Ober CK, Char K, Genzer J, Sivaniah E, Kramer EJ, Fischer DA (2000) *Macromolecules* 33:6106
384. Krishnan S, Kwark YJ, Ober CK (2004) *Chem Rec* 4:315
385. Bao X, Dix LR (1997) *Mol Cryst Liq Cryst* 304:41
386. Martinelli E, Paoli F, Gallot B, Galli G (2010) *J Polym Sci A Polym Chem* 48:4128
387. Li X, Andruzzi L, Chiellini E, Galli G, Ober CK, Hexemer A, Kramer EJ, Fischer DA (2002) *Macromolecules* 35:8078
388. Darmanin T, Taffin de Givenchy E, Guittard F (2010) *Macromolecules* 43:9365
389. Caillier L, Taffin de Givenchy E, Geribaldi S, Guittard F (2008) *J Mater Chem* 18:5382
390. Ruhmann R, Thiele T, Wolff D, Prescher D, Springer J (1996) *Liq Cryst* 21:307
391. You F, Paik MY, Häckel M, Kador L, Kropp D, Schmidt HW, Ober CK (2006) *Adv Funct Mater* 16:1577
392. Andruzzi L, D'Apollo F, Galli G, Gallot B (2001) *Macromolecules* 34:7707
393. Hartmann P, Collet A, Viguier M (2006) *Macromolecules* 39:6975
394. Meng F-B, He X-Z, Zhang X-D, Ma Y, Han H-L, Lu H (2011) *Colloid Polym Sci* 289:955
395. Mu J, Okamoto H, Yanai T, Takenaka S, Feng X (2001) *Coll Surf A: Physicochem Eng Aspects* 181:303
396. Komp A, Finkelmann H (2007) *Macromol Rapid Commun* 28:55
397. Gopalan P, Andruzzi L, Li X, Ober CK (2002) *Macromol Chem Phys* 203:1573
398. Percec V, Tomazos D, Feiring AE (1991) *Polymer* 32:1897
399. Smirnova AI, Lattermann G (2007) *Polym Sci Ser A* 49:538
400. Yoon M-H, DiBenedetto SA, Facchetti A, Marks TJ (2005) *J Am Chem Soc* 127:1348
401. Wang B, Watt S, Hong M, Domercq B, Sun R, Kippelen B, Collard DM (2008) *Macromolecules* 41:5156
402. Facchetti A, Yoon M-H, Stern CL, Hutchison GR, Ratner MA, Marks TJ (2004) *J Am Chem Soc* 126:13480
403. Li L, Collard DM (2006) *Macromolecules* 39:6092
404. Woody KB, Nambiar R, Brizius GL, Collard DM (2009) *Macromolecules* 42:8102
405. Percec V, Bera TK (2002) *Tetrahedron* 58:4031
406. Percec V, Ahn CH, Ungar G, Yeardley DJP, Möller M, Sheiko SS (1998) *Nature* 391:161

407. Darmanin T, Guittard F (2009) *J Am Chem Soc* 131:7928
408. Darmanin T, Nicolas M, Guittard F (2008) *Langmuir* 24:9739
409. Nicolas M, Guittard F, Geribaldi S (2006) *Angew Chem Int Ed* 45:2251
410. Darmanin T, Taffin de Givenchy E, Amigoni S, Guittard F (2011) *J Fluorine Chem*, doi:10.1016/j.jfluchem.2011.04.014
411. Patrick CR, Prosser GS (1960) *Nature* 187:1021
412. West AP Jr, Mecozzi S, Dougherty D (1997) *J Phys Org Chem* 10:347
413. Williams JH (1993) *Acc Chem Res* 26:593
414. Weck M, Dunn AR, Matsumoto K, Coates GW, Lobkovsky EB, Grubbs RH (1999) *Angew Chem Int Ed* 38:2741
415. Sasada Y, Monobe H, Ueda Y, Shimizu Y (2010) *Mol Cryst Liq Cryst* 525:153
416. Kishikawa K, Oda K, Aikyo S, Kohmoto S (2007) *Angew Chem Int Ed* 46:764
417. Dai C, Nguyen P, Marder TB, Scott AJ, Clegg W, Viney C (1999) *Chem Commun* 2493
418. Itahara T (2005) *Liq Cryst* 32:115
419. Kishikawa K, Aikyo S, Akiyama S, Inoue T, Takahashi M, Yagai S, Aonuma H, Kohmoto S (2011) *Soft Matter* 7:5176
420. Fergusson KM, Hird M (2010) *J Mater Chem* 20:3069
421. Caminati W, Melandri S, Moreschini P, Favero PG (1999) *Angew Chem Int Ed* 38:2924
422. Hunter L, Kirsch P, Slawin AMZ, O'Hagan D (2009) *Angew Chem Int Ed* 48:5457
423. Nicoletti M, Bremer M, Kirsch P, O'Hagan D (2007) *Chem Commun* 5075
424. Lovinger AJ (1983) *Science* 220:1115
425. Bruce DW (2008) *Structure and Bonding*, 126. Springer, Berlin, 161
426. Präsang C, Whitwood AC, Bruce DW (2008) *Chem Commun* 2137
427. Bruce DW, Metrangolo P, Meyer F, Pilati T, Präsang C, Resnati G, Terraneo G, Wainwright SG, Whitwood AC (2010) *Chem Eur J* 16:9511
428. Kim YH, Yoon DK, Jeong HS, Lavrentovich OD, Jung H-T (2011) *Adv Funct Mater* 21:610
429. Kim YH, Yoon DK, Jeong HS, Jung HT (2010) *Soft Matter* 6:1426
430. Kim YH, Lee JO, Jeong HS, Kim JH, Yoon EK, Yoon DK, Yoon JB, Jung HT (2010) *Adv Mater* 22:2416
431. Li Z, Hillmyer MA, Lodge TP (2006) *Macromolecules* 39:765
432. Kubowicz S, Baussard J-F, Lutz, J-F Thönemann, AF, von Berlepsch H, Laschewsky A (2005) *Angew Chem Int Ed* 44:5262
433. Amado E, Kressler J (2011) *Soft Matter* 7:7144
434. Sato S, Iida J, Suzuki K, Kawano MT, Ozeki T, Fujita M (2006) *Science* 313:1273
435. Horvath IT (1998) *Acc Chem Res* 31:641
436. Zhang W (2009) *Chem Rev* 109:749
437. Percec V, Glodde M, Bera TK, Miura Y, Shiyankovskaya I, Singer KD, Balagurusamy VSK, Heiney PA, Schnell I, Rapp A, Spiess HW, Hudson SD, Duan H (2002) *Nature* 419:384

Liquid Crystalline Crown Ethers

Martin Kaller and Sabine Laschat

Abstract In this chapter, a comprehensive review over the entire research on liquid crystalline crown ethers since their discovery will be given. Monomeric and polymeric molecules containing crown ethers as well as aza crown ethers, thia crown ethers and crown ethers with several different heteroatoms will be presented. Liquid crystallinity is, in most cases, caused by the substituents attached to the crown ethers. The respective macrocycle can be surrounded by multiple substituents or attachment can take place terminally or laterally. Within the substituents, a variety of geometries, such as rods, discs or tapers have been reported, resulting in different types of mesophases. The effects of complexation will be discussed in detail as complexation has a varying influence on the properties, ranging from the induction or stabilization of a mesophase to the destabilization or even the complete loss of the mesophase, depending on the crown, the salt or the counterion of the salt. For selected examples, the synthesis of the materials will be discussed. Possible applications in sensor or membrane technology as well as in chromatography will be shown.

Keywords Crown compounds · Liquid crystals · Mesophases · Metallomesogens · Polymers · Salt effects · Self-assembly · Substituent effects · Supramolecular chemistry · Phthalocyanines · Cyclophanes

Contents

1	Introduction	110
2	Mesogenic Crown Ethers	111
2.1	Terminally Attached Crown Ethers with Rod-Like Substituents	111
2.2	Rod-Like Molecules with Laterally Attached Crown Ethers	125
2.3	Central Crown Ethers with Terminally Attached Rod-Like Substituents	130
2.4	Terminal Crown Ethers with One Taper-Shaped Substituent	144

M. Kaller and S. Laschat (✉)
Institut für Organische Chemie der Universität Stuttgart, Pfaffenwaldring 55, 70569 Stuttgart,
Germany
e-mail: sabine.laschat@oc.uni-stuttgart.de

2.5	Central Crown Ethers with More than One Peripheral Substituent	156
2.6	Crown Ethers with a Central Phthalocyanine	171
2.7	Crown-Like Cyclophanes	176
2.8	Metallomesogens	182
3	Concluding Remarks	188
	References	189

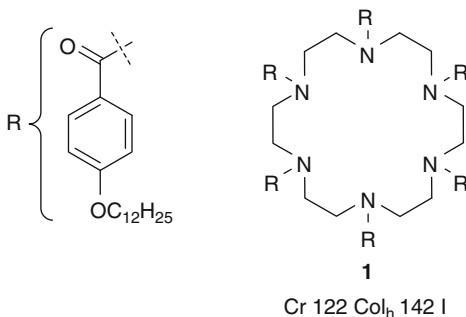
1 Introduction

Since the discovery of crown ethers, cryptands, and other macrocyclic ligands by Cram, Lehn, and Pedersen, who were awarded the 1987 Nobel Prize in chemistry “for their development and use of molecules with structure-specific interactions of high selectivity” [1], a completely new research field was opened: supramolecular chemistry [2–4]. Since then, this research field has been extended in many fields such as molecular recognition, organic sensing, and liquid crystals.

The combination of crown ethers with mesogenic groups is interesting because the resulting hybrid materials possess the properties of both constructive subunits, i.e., liquid crystalline order in the mesophase and the ability to complex specific cations selectively according to the crown ether cavity size.

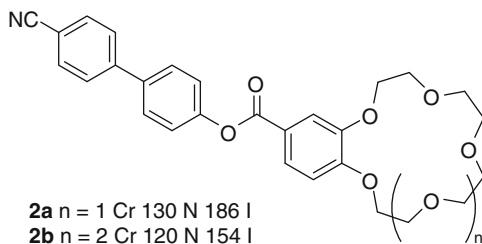
Since the first description of substituted aza crown ethers **1** (Scheme 1) by Lehn in 1985 [5], showing columnar hexagonal phases, many groups have entered the field and extended the knowledge on structure-property relations in these versatile hybrid systems.

Matsuda presented the first examples of liquid crystalline crown ethers **2** (Scheme 2) in 1987 [6]. In all subsequent studies, he wanted to answer two



Scheme 1 First liquid crystalline crown ether **1**

Scheme 2 First liquid crystalline crown ethers **2**



questions [7]: (1) what is the influence of a crown ether on the thermal properties of the liquid crystalline substituent and (2) how do complexed salts alter the thermal behavior? These fundamental questions must always be investigated when dealing with liquid crystalline crown ethers. This review discusses all substances with respect to these questions.

Until now, i.e., in 25 years of research, only two reviews on liquid crystalline crown ethers have been published [8, 9]. As both reviews cover the field only partially and, e.g., the fascinating polymeric crown ethers as well as taper-shaped liquid crystalline crown ethers are not discussed, we decided to give the first comprehensive review. The present chapter will be structured according to the molecular structure of the mesogens. The discussion of each type of crown ether mesogen will start with small molecules, continue with polymeric compounds, and conclude with possible applications (where applicable).

The present chapter will not deal with general topics of liquid crystals or crown ethers as this exceeds the scope of this volume. Interesting reviews and monographs on liquid crystals and their properties can be found in the literature [10–13]. The synthesis of crown ethers can be challenging. Most commonly, the synthetic routes are based on procedures established by Pedersen [14–17]. A review by Bradshaw [18] and a monograph edited by Patai [19] also cover the synthesis and properties of crown ethers. More recent reviews deal with the use of crown ethers as chemosensors [20, 21], potential antitumor agents [22], molecular wires [23], or carriers for the separation of metal ions in liquid membrane processes [24].

2 Mesogenic Crown Ethers

The schematic representations used to describe the molecular design of the discussed mesogens are depicted in Table 1.

For the mesophase ranges, we will use the following nomenclature:

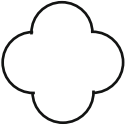



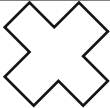


Phase ₁ xx °C Phase ₂ yy °C I	Phase transitions upon heating
I yy °C (Phase ₂ xx °C Phase ₁)	Phase transitions upon cooling (mostly used in the case of monotropic phases)
Phase ₁ yy °C (Phase ₂ xx °C) I	Monotropic phase upon cooling

All phase transition enthalpies will be omitted for reasons of clarity.

2.1 Terminally Attached Crown Ethers with Rod-Like Substituents

The general design of the following crown ether mesogens is a terminal crown ether connected to a calamitic unit carrying flexible side chains and optional functional groups (Fig. 1).

Table 1 Schematic representation of the building blocks of the discussed mesogens

Symbol	Explanation
	crown ether
	disk-like unit
	flexible chain
	functional or polymerizable group
	phthalocyanine
	rod-like unit
	spacer

**Fig. 1** Rod-like mesogen with terminal crown ether

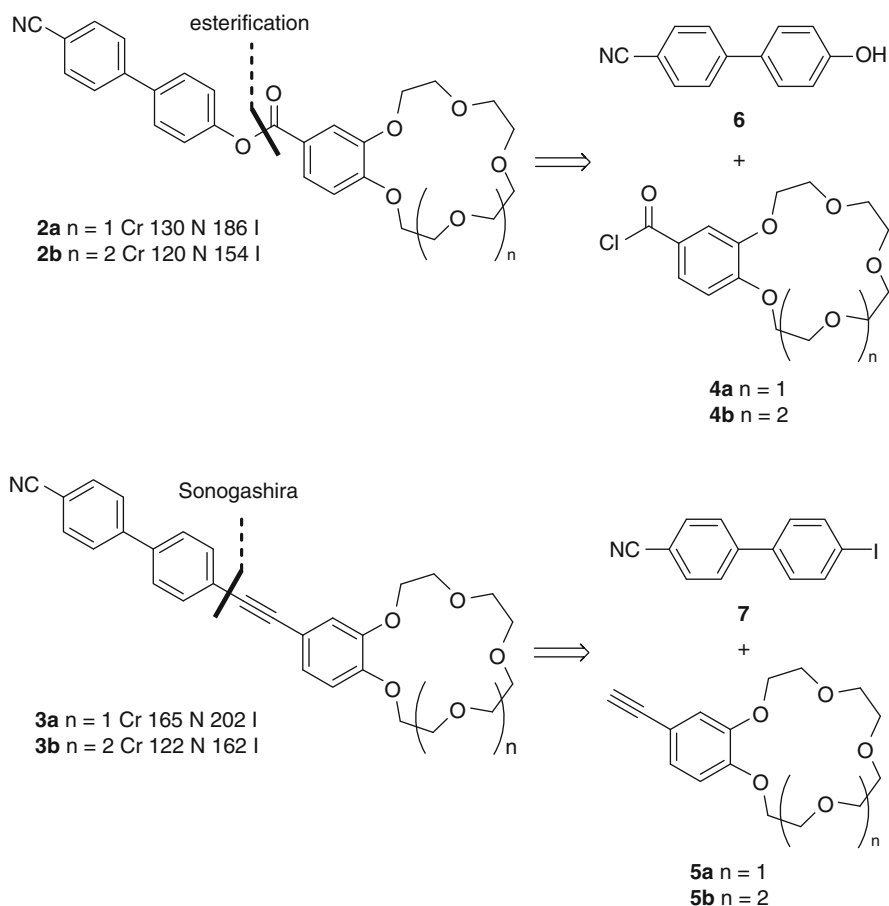
2.1.1 Monomeric Compounds

Matsuda [6, 7] was the first to synthesize liquid crystalline crown ethers of this type. Benzo[15]crown-5 and benzo[18]crown-6 were attached to a cyanobiphenyl moiety via an ester (**2a,b**) or an ethynylene (**3a,b**) linker group (Scheme 3). The synthesis was straightforward starting from the respective crown ethers carrying carboxylic acid chlorides (**4a,b**) or ethynylene (**5a,b**) functional groups. Linkage was achieved by esterification with hydroxy cyanobiphenyl **6** or by Sonogashira coupling with iodo-cyanobiphenyl **7**.

Matsuda and coworkers investigated (1) the effect of a crown unit on the mesomorphic properties and (2) the behavior after complexation with suitable salts. These issues are still relevant today in current investigations.

Upon addition of a terminal crown ether to the calamitic core unit, nematic phases were observed for **2**, **3** in agreement with previous studies on substituted cyano biphenyls [25, 26].

Ester-linked crown ether **2a** with a 15C5 substituent showed a nematic phase width of 56 K (Scheme 3). For the homolog with an 18C6 unit (**2b**) it could be noted that the transitions generally occurred at lower temperatures and the phases were less stable (a range of 34 K). Ethynylene-linked crowns **3** showed a similar behavior as their ester-linked homologs **2**. For 15C5 (**3a**), melting into the nematic phase was observed at 165 °C and clearing at 202 °C while **3b** with the larger 18C6 showed melting at and clearing at significantly lower temperatures (122 °C and 162 °C,



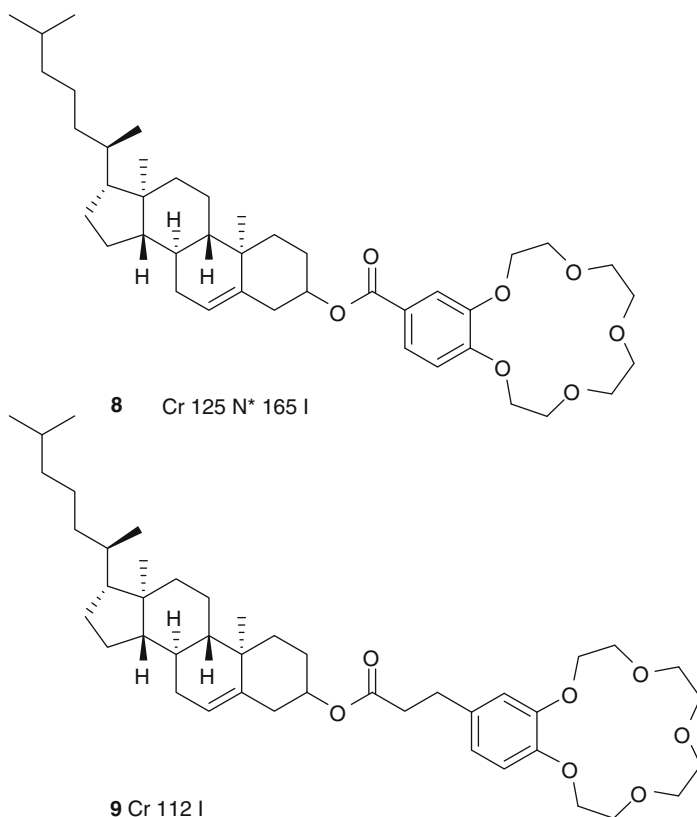
Scheme 3 Retrosynthesis of liquid crystalline crown ethers **2**, **3**

respectively). This behavior was attributed to the larger and more flexible crown in 18C6 derivatives leading to disorder and lower transition temperatures.

The complexation of ester-linked **2** with picrate salts was monitored by absorption and fluorescence spectroscopy [7, 27]. Sodium picrate doping of **2a** with a 15C5 moiety led to a red shift in UV measurements (in the mesophase) while potassium and tetramethylammonium picrate did not show this effect. This result was taken as evidence for the selective complexation of sodium cations by the crown mesogen. The uptake of sodium picrate had drastic effects on the nematic-isotropic transition which was lowered from 186 °C (without sodium picrate) to 120 °C upon complexation with 0.5 equiv. of sodium picrate. It was suggested that this result originates from the decreased anisotropy and polarizability of **2a** that leads to steric effects hindering molecular packing and thus lowering the clearing temperatures.

It is also possible to attach chiral peripheral groups to benzo[15]crown-5 as demonstrated by Shinkai [28]. In **8** (Scheme 4), a cholesteryl subunit was attached using an ester group as linker and a chiral nematic phase was observed.

For the liquid crystalline behavior, the position of the ester group was crucial. Introduction of an ethyl spacer in **9** led to the complete loss of the mesophase and



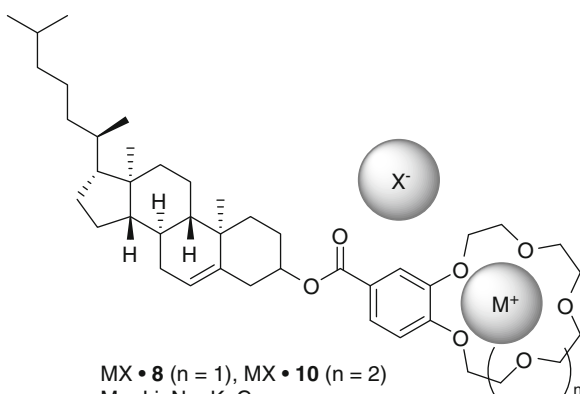
Scheme 4 Liquid crystalline crown ethers **8**, **9** with cholesteryl subunits

only melting to the isotropic phase was observed. Most interestingly, a 1:1 mixture of **8** and **9** exhibits a liquid crystalline phase between <0 and 108 °C. The **8/9** 1:1 mixture was used to produce an ion-permeable membrane[28]. Perylene[®], **8** and **9** were dissolved in CHCl_3 , spread on a glass plate, dried in high vacuum, and tempered at 140 °C. The resulting membrane was 70 μm thick and used for ion transport studies. It was shown that both NaSCN and KSCN could be transported across the membrane. Sodium cations were transported faster than potassium cations, which is due to the perfect recognition of Na^+ by **15C5**. The activation energy for the permeation of Na^+ is $E_A = 43.4$ kJ mol^{-1} , indicating an ion translocation process through the ion channels consisting of stacked crown moieties.

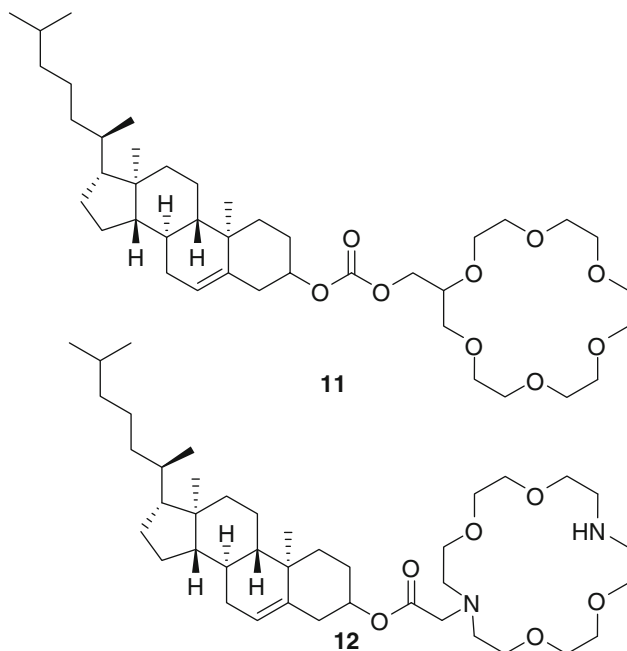
Subsequent studies on the chiral nematic phase of **8** and **10** showed the influence of complexed salts on the liquid crystalline properties. In the complexes (Scheme 5), the helical pitch was strongly affected by the complexed cation and the counterions [29].

For $\text{MSCN}\cdot\mathbf{8}$, the pitch increased with increasing radius of the cation in the order of $\text{Li}^+ < \text{Na}^+ < \text{Cs}^+ < \text{K}^+$ while the order changed for $\text{MSCN}\cdot\mathbf{10}$ with $\text{Li}^+ < \text{Na}^+ < \text{K}^+ < \text{Cs}^+$. On investigation of the helical pitch in complexes $\text{KX}\cdot\mathbf{10}$ it was found that the pitch increased with the size of the anion $\text{Cl}^- < \text{SCN}^- < \text{ClO}_4^- \ll \text{B}(\text{p-Cl-C}_6\text{H}_5)_4^-$. The authors proposed the use of **8**, **10** as promising host-guest sensory systems.

In a subsequent study [30], cholesteryl-substituted **18C6** derivative **11** and diaza [18]crown-6 **12** (Scheme 6) were used to create solid-supported bilayer lipids. The liquid crystalline crown derivatives **11**, **12** were dissolved in chloroform and mixed with squalene or squalene saturated with cholesterol. The solid-supported bilayers were prepared in freshly cut stainless steel wires. A 10^{-4} to 10^{-1} mol L^{-1} solution of MCl ($\text{M} = \text{Li, Na, K, Rb, Cs}$) or MgCl_2 was used as aqueous phase. Measurement of the membrane potential revealed a Nernst response to the concentration of M^+ in solution. It was possible to differentiate between the different cations which might be used for the preparation of new ion sensors. For the detection of K^+ and Rb^+ , aza crown derivative **12** proved to be the most selective. A problem was the presence of traces of $\text{Fe}^{2+/3+}$ that made the measurements difficult. It was also not



Scheme 5 Complexation of chiral liquid crystals **8** and **10** with alkaline metal salts

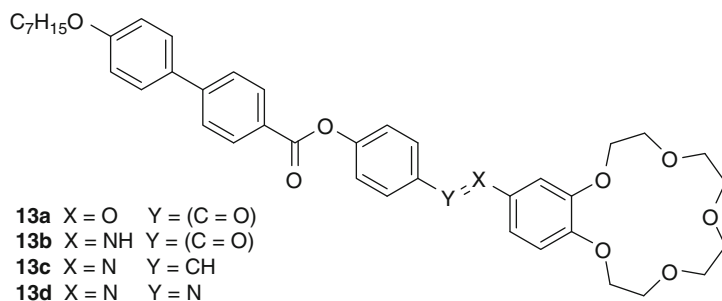


Scheme 6 Cholesteryl-substituted [18]crown-6 **11**, **12** and diaza[18]crown-6

possible to detect Li^+ and Mg^{2+} due to their low binding constants resulting from their small diameters, high charge density, and high hydration energy.

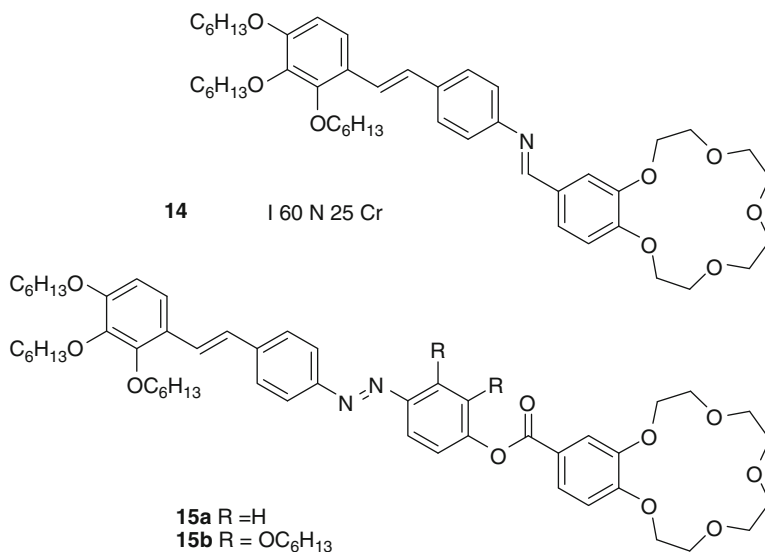
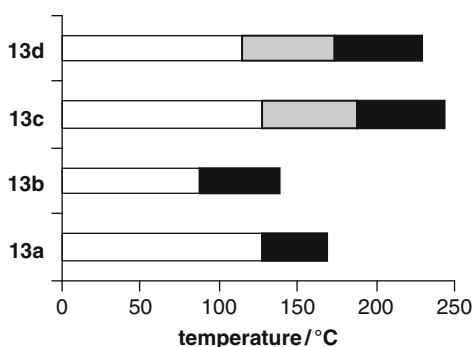
Jiang and co-workers presented a series of substituted crown ethers (Scheme 7) with the macrocycle being attached via an ester (**13a**), amide (**13b**), imine (**13c**), or aza (**13d**) spacer [31]. All compounds exhibit liquid crystalline phases (Fig. 2). The clearing points decrease in the order $-\text{N}=\text{CH}- > -\text{N}=\text{N}- > -\text{C}(\text{O})\text{O}- > -\text{C}(\text{O})\text{NH}-$. While **13a,b** with ester or amide linkers possess only nematic phases, smectic and nematic phases were observed for **13c,d** with imine or aza bridges. The reason why compounds **13c,d** with imine and aza spacers exhibit additional smectic phases and high clearing points is the presence of an additional double bond in the spacer. The electrons in this particular bond are delocalized into the two adjacent benzene rings leading to a large flat and conjugated system. The intermolecular attraction between **13c,d** is therefore higher than for **13a,b** where the conjugation is interrupted by the $\text{C}=\text{O}$ bond. Thus, **13a,b** show nematic phases only with low clearing points (Fig. 2).

Judeinstein found that crown ethers **14** (Scheme 8) with a nematogenic unit linked via an imine bond showed monotropic mesophases upon cooling that were stable until room temperature [32]. When the aromatic core was extended by an additional benzene ring in **15a**, the melting temperatures to the nematic phase were raised to ~ 150 °C and the clearing temperatures to ~ 200 °C. Lateral substitution of the additional ring in **15b** decreased the clearing temperatures to ~ 90 °C. The complexation of **15a** with NaOTf and LiBF_4 was also investigated [32]. It was found that the phase width of the nematic phase decreased with increasing amounts



Scheme 7 Liquid crystalline crown ethers **13** with different spacers

Fig. 2 Mesophases of **13a–d**; *white shade* crystalline, *grey shade* smectic, *black shade* nematic



Scheme 8 Liquid crystalline crown ethers with imine **14** and aza **15** spacers

of salt, having a minimum at 0.5 equiv. of added salt due to the formation of sandwich complexes. Upon further addition of salt, a smectic phase was induced that had the maximum phase width at 1.0 equiv. of added salt. Thus, the phase type and the phase stability could be tuned by an external stimulus.

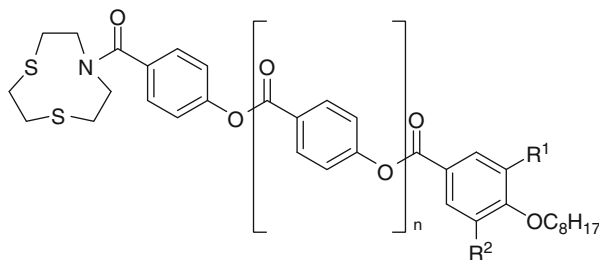
Most of the above liquid crystalline crown ethers contained a benzo[15]crown-5 unit or common [18]crown-6 as well as some aza derivatives. It was also possible to obtain liquid crystals **16** (Scheme 9) containing more unusual crown ethers such as 1,4-dithia-7-azacyclononane [33].

The dithiaazacrown was modified with a variety of rod- and disc-like substituents. With the shortest rod-like substituent carrying one terminal octyl chain (**16a**), direct melting into the isotropic state was observed. By adding an additional *p*-salicylic acid group (**16b**), a monotropic nematic phase was observed upon cooling. Attaching a second octyl chain gave **16c** but destroyed the mesomorphism and the only visible transition was isotropic melting. However, adding a third terminal alkyl chain in **16d** gave a material that exhibits a columnar hexagonal mesophase. There is a subtle relation between the molecular structure and the observed phases: clearly rod-like substituents as in **16b** exhibit a nematic phase and clearly discotic substituents as in **16d** give columnar phases. Molecules with a morphology in between (**16c** with two terminal chains) give no mesophase.

2.1.2 Polymeric Compounds

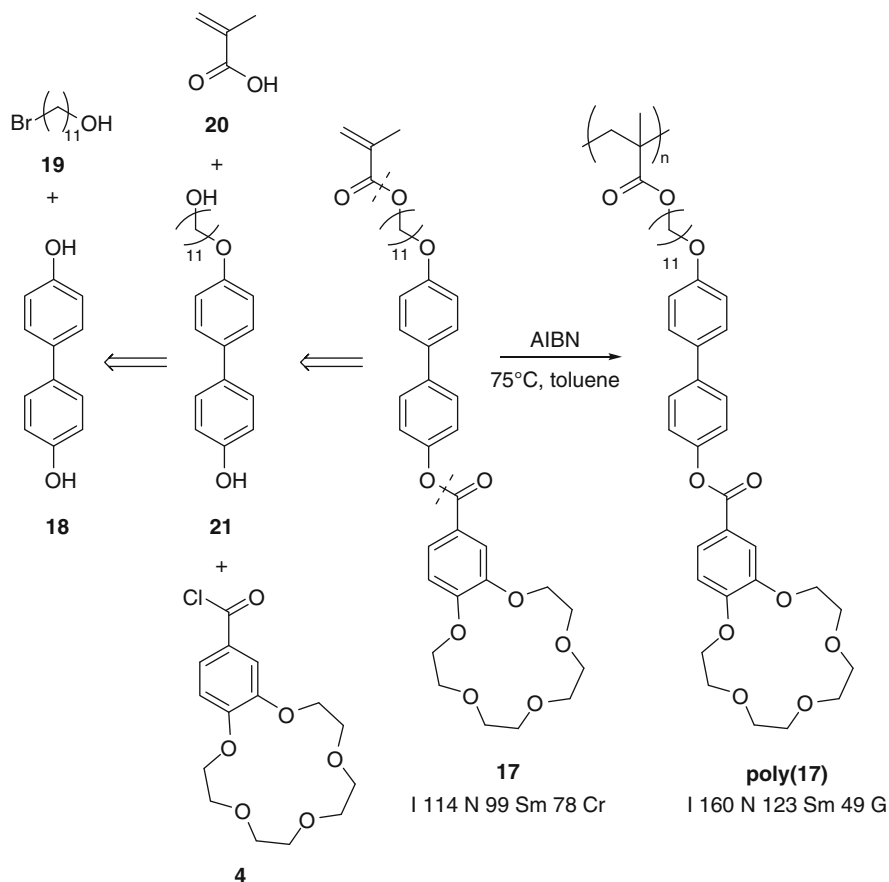
A variety of polymers containing liquid crystalline crown ethers of the molecular shape discussed in this section is known throughout the literature, most of which originate from Percec's laboratory.

One of the first published examples (Scheme 10) was the modified poly-methacrylate **poly(17)** obtained from monomer **17** containing a benzo[15]crown-5 unit and a biphenyl linked via an ester group [34]. The synthesis was



16a	$n = 0$	$R^1 = R^2 = H$	Cr 108 I
16b	$n = 1$	$R^1 = R^2 = H$	I 114 N 96 Cr
16c	$n = 1$	$R^1 = C_8H_{17}$ $R^2 = H$	Cr 90 I
16d	$n = 1$	$R^1 = R^2 = C_8H_{17}$	Cr 37 Col _h 48 I

Scheme 9 Liquid crystals **16** bearing thiaaza crown ethers

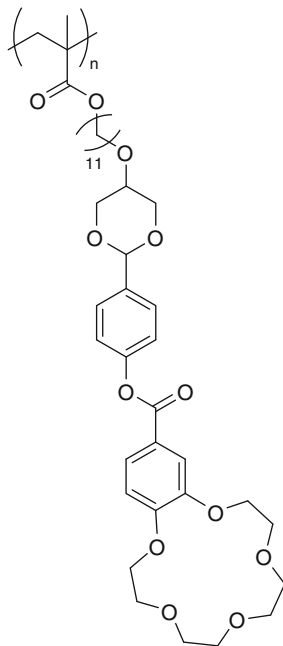


Scheme 10 Liquid crystalline polymer **poly(17)** and its precursors

straightforward starting from 4,4'-dihydroxybiphenyl **18** and 11-bromoundecan-1-ol **19**. Addition of a methacrylic acid moiety gave monomer **17**. Living radical polymerization was initiated with AIBN and carried out in toluene to give **poly(17)**. Monomer **17** and **poly(17)** display mesophases. Monomer **17** displays a monotropic nematic phase upon cooling which is stable for 15 K while **poly(17)** displays enantiotropic smectic and nematic mesophases stable for 111 K. Detailed X-ray scattering experiments [35] revealed the presence of SmA and SmC phases for **poly(17)**. It is remarkable that polymerization could turn a monotropic phase into an enantiotropic phase with a higher range of stable mesophases. The reason why the transition temperatures for the polymers are higher than for the monomers is a loss of degrees of freedom due to the limited free volume within the polymer.

When one of the phenyl groups in **poly(17)** was changed to a *trans*-1,3-dioxane ring (Scheme 11), the mesophase of the resulting **poly(22)** became smaller and the clearing transition was lowered by 33 K due to the loss of rigidity in the molecule [36].

Scheme 11 Liquid crystalline crown ether polymer **poly(22)**



poly(22)

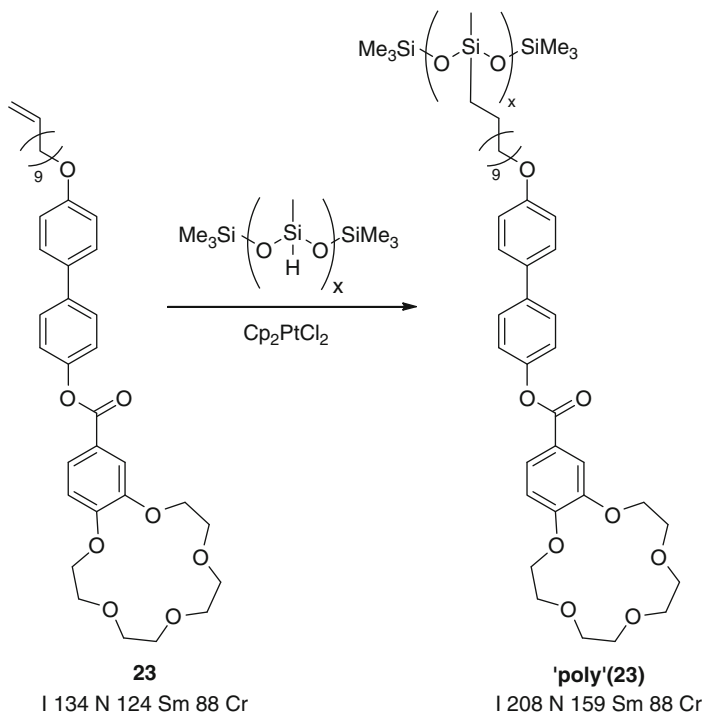
I 127 N 85 Cr

Percec and co-workers not only developed monomers suitable for radical polymerization but also presented systems suitable for the introduction into poly(methylsiloxane)s [34] via hydrosilylation (Scheme 12). Monomer **23** with a terminal double bond was added to the poly(methylsiloxane) using Cp_2PtCl_2 as a catalyst to give '**poly**'(**23**). The trends observed for '**poly**'(**23**) were also found for **poly**(**17**) as polymerization improves the mesophase stability significantly.

Another mechanism to obtain polymers is cationic polymerization. Monomeric **24** which already displays a broad nematic phase could be polymerized to **poly**(**24**) (Scheme 13) which displays an even broader phase [37]. Neither the triple bond nor the crown ether moiety in **24** was affected by the harsh conditions for polymerization (EtAlCl_2 , SMe_2).

A variety of other liquid crystalline crown ether containing polymers were synthesized, all possessing the same mesophase-stabilizing effect of polymerization (polymer effect) [38, 39].

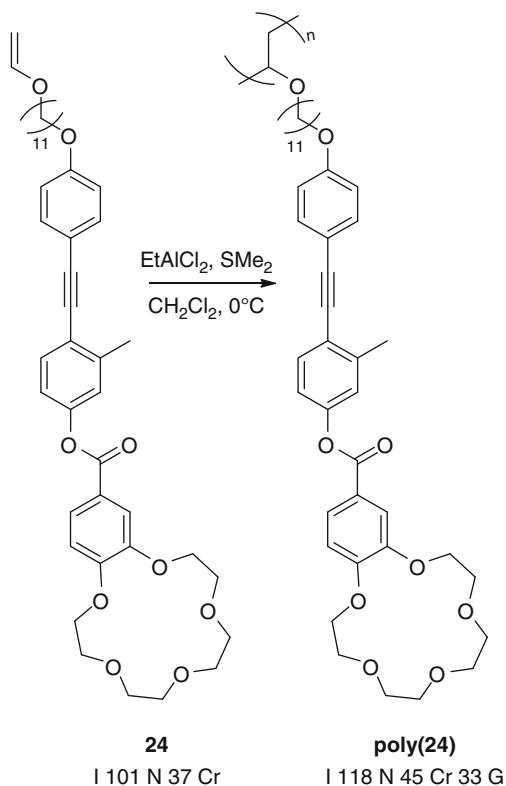
Most interesting are the effects of salt complexation on the mesomorphic behavior of liquid crystalline crown ethers and liquid crystalline crown ether polymers. Sodium triflate was added to **poly**(**17**) [34] and **poly**(**25**) (Scheme 14) [39]. The enantiotropic nematic and smectic phases of **poly**(**17**) were changed dramatically [40]. With increasing amounts of salt, the clearing temperatures are shifted to higher values while the melting transition increases only slightly.



Scheme 12 Synthesis of crown-containing liquid crystalline polysiloxane **'poly'(23)**

Additionally, the smectic phase is lost and only nematic phases are being observed. One of the reasons for the increase in the mesophase stabilities upon complexation is the increased polarity of the crown moiety leading to stronger microsegregation. Also, the complexed crown is more rigid than the neat crown. The more polar the crown ether fragment, the higher the isotropization temperature. Uncomplexed **poly(25)** with a triple bond instead of a biphenyl group is crystalline. Complexation induced a smectic phase. Further experiments on similar polymers could confirm the observations and also revealed the stabilizing effect of complexation [41].

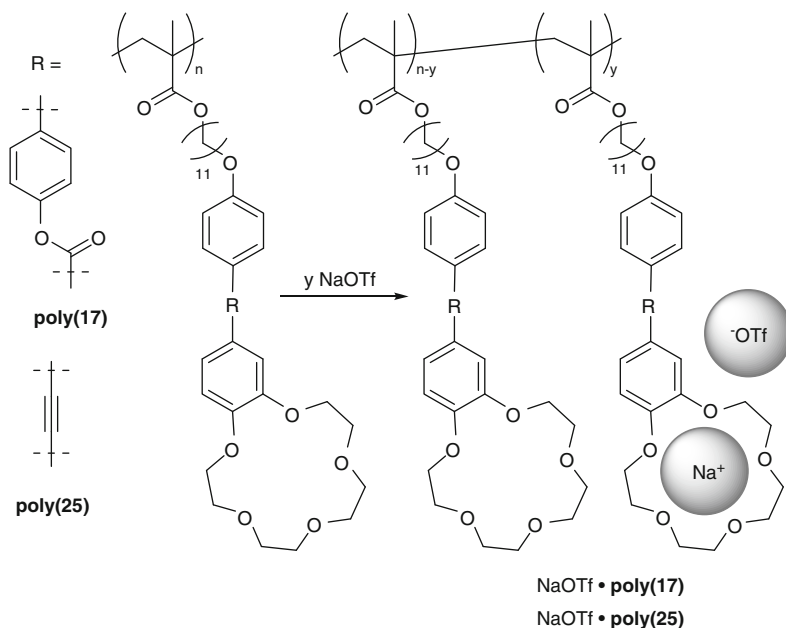
Bobrowsky prepared copolyacrylates **26–28** (Scheme 15) containing the nematogenic phenylmethoxybenzoate group as well as different crown ether substituted fragments [42]. The aim of the study was to obtain multifunctional materials. It is known that the incorporation of azobenzene groups into polymers leads to light-controllable films that might have uses in data recording and storage. In previous studies on crown ethers containing azobenzene groups, it could be shown that only the *Z*-isomer of the azobenzene group was able to form complexes with alkali metals whereas the *E*-isomer was unable to form complexes [43, 44]. Combination of both properties could yield novel polyfunctional materials. Unfortunately, the study revealed that the crown ether substituents are too bulky and prevent photoorientation of the azobenzene groups diminishing the photoinduced order. Another observation was the decrease in phase stability upon uptake of

Scheme 13 Cationic polymerization of **24**

potassium perchlorate. This was attributed to the reduction of the side group anisotropy, mainly due to the presence of the perchlorate anion. Taking Percec's results from complexation experiments using sodium triflate [40] into account, it would be interesting for further investigations how **26–28** behave upon complexation of other salts with smaller anions.

2.1.3 Applications

Crown ethers of the type discussed in this section have been used as sensors, membranes, or materials for chromatography. Shinkai used cholesterol-substituted crown ether **10** as a sensor for chirality in chiral ammonium compounds (Scheme 16). It was found that the pitch of the cholesteric phase exhibited by **10** was changed upon addition of the chiral salt. As the wavelength of reflection for incident light depends on the pitch, a color change was observed that was visible to the naked eye [45, 46]. Such chirality sensing systems were known before but chromophores had to be bound to the crown ether in order to observe color changes [47]. This problem could be overcome by **10**, which uses intrinsic properties of the chiral nematic phase.



Scheme 14 Complexation of liquid crystalline crown ether polymers **poly(17, 25)**

Kimura used the cholesterol-substituted [15]crown-5 **8** in ion sensing membranes. It was found that the addition of the crown ether affects the sensor properties, especially the ion specificity, and it was possible to obtain sensors with extremely high sensitivities [48]. The performance could be further increased by using perfluoroalkyl side chains instead of cholesterol [49].

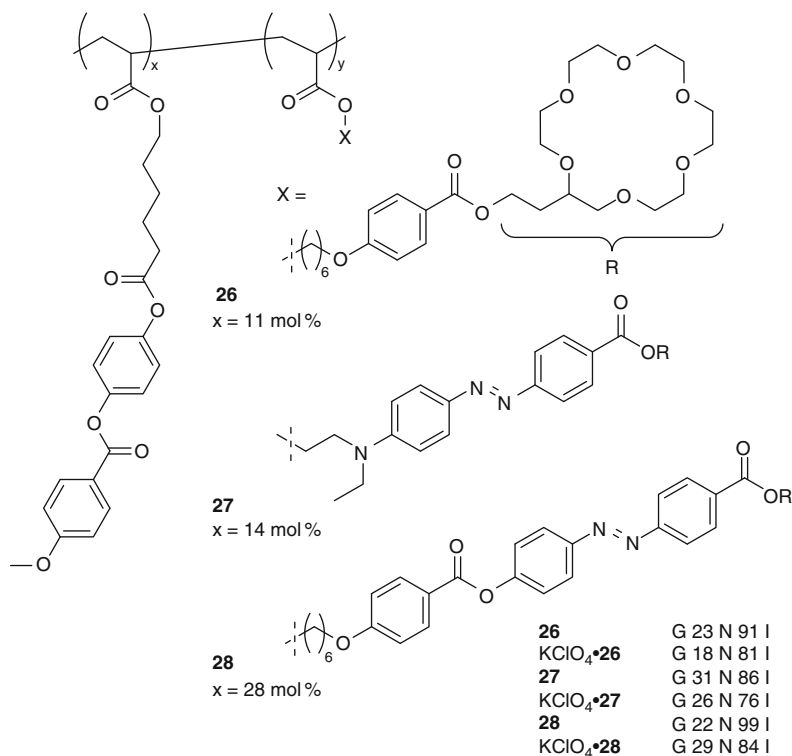
Zeng used a silica monolith modified with the liquid crystalline crown ether **29** as a column material in capillary electrochromatography (Scheme 17) [50]. Polycyclic aromatic compounds, benzenediols, pesticides, and steroids were successfully separated on the column. Introduction of the liquid crystalline crown ether led to a significant improve of the electrochromatographic performance.

2.1.4 Summary

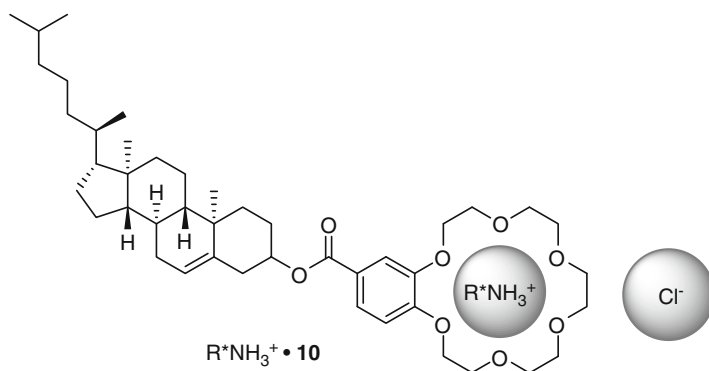
In most cases, the addition of a rod-shaped molecule to a crown ether leads to the formation of a nematic phase. In the case of addition of a chiral unit, such as cholesterol, chiral nematic phases can be observed. Some molecules can also show smectic phases when the attached rod shaped unit is long and inflexible.

Polymerization of liquid crystalline crown ethers leads to an increase in phase transition temperatures due to the loss of degrees of freedom.

Complexation can have different effects. In some cases, the phase widths were decreased upon complexation while stabilizing effects were observed in complexed



Scheme 15 Liquid crystalline polymethacrylates **26–28** containing [18]crown-6



Scheme 16 Liquid crystalline crown **10** as chiral sensor

polymeric crown ethers. An exception to this behavior was found when perchlorate was used as the counterion – due to the size, the anisotropy of the complexes was decreased and the phase width decreased, too.

Scheme 17 Novel material **29** for capillary electrophoresis

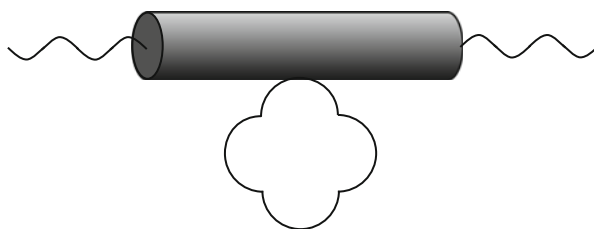
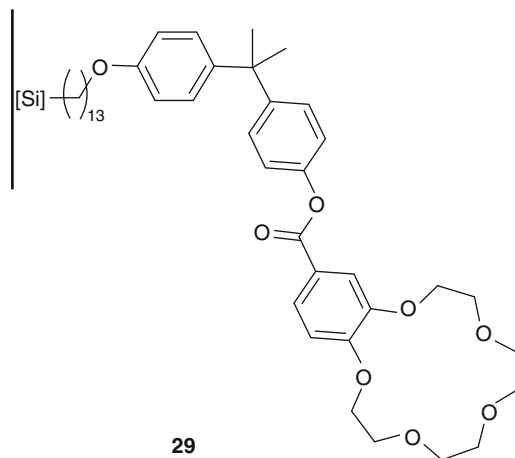


Fig. 3 Rod-like molecules with laterally attached crown ethers

2.2 Rod-Like Molecules with Laterally Attached Crown Ethers

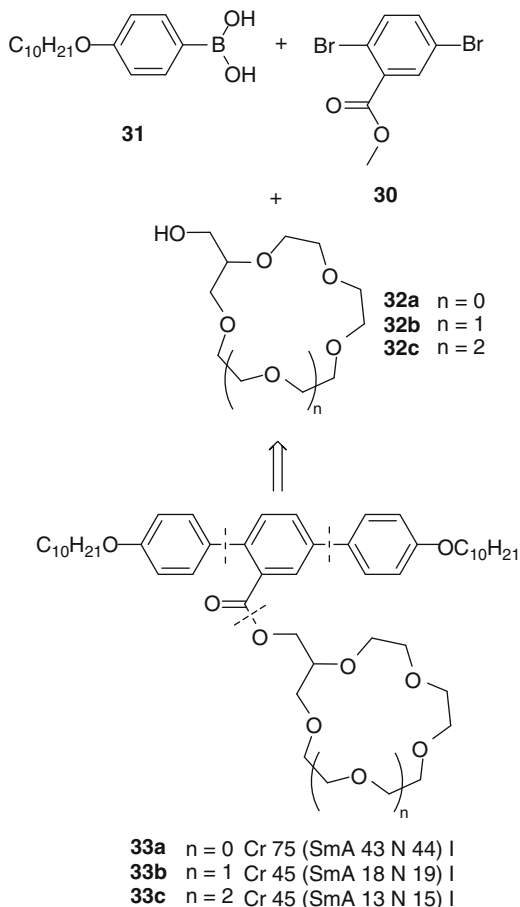
The general design concept for liquid crystalline crown ethers discussed in this section consists of a rigid core with terminal chains and a laterally attached crown ether unit (Fig. 3).

2.2.1 Monomeric Compounds

Tschierske developed a variety of molecules containing a *p*-terphenyl unit as backbone equipped with two terminal decyloxy chains and laterally attached crown ethers of different sizes [51–53]. The synthesis was straightforward starting from methyl-2,5-dibromobenzoate **30** that was coupled with [4-(decyloxy)phenyl]boronic acid **31** in a subsequent Pd⁰-catalyzed Suzuki reaction. The 2-hydroxymethyl crown ethers **32** were attached in the last step (Scheme 18) to yield mesogenic **33**.

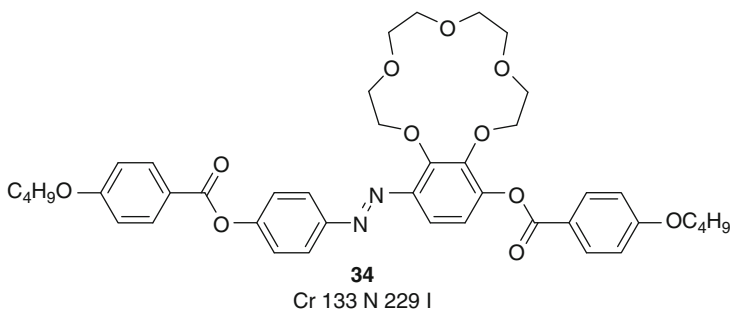
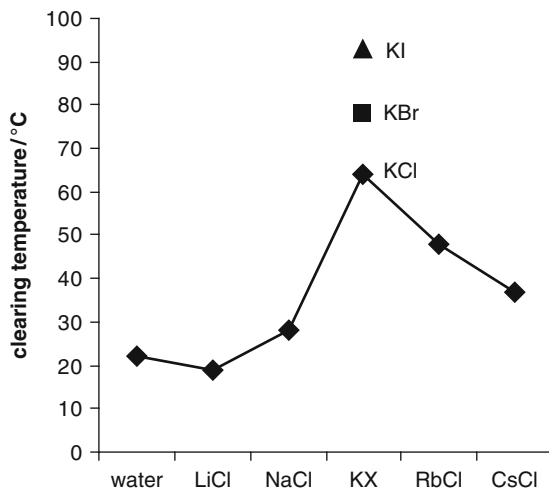
In the crown ether derivatives **33**, only monotropic phases were observed. All compounds exhibited a very small nematic phase with a relatively broad smectic phase. Decreasing the size of the crown ether unit resulted in higher clearing points

Scheme 18 Synthesis and mesogenic properties of crown ethers **33** with a lateral *p*-terphenyl group



and stability of the smectic phase. The bulky crown ether groups are normally prone to suppress smectic phases and induce nematic phases. It is likely that the crown ether units force micro-segregation between the rigid *p*-terphenyls and the alkyl chains. In conclusion, steric disturbance caused by the crown ether competes with layer-stabilizing micro-segregation and causes the observed phase behavior [54]. It is worth mentioning that crown ethers **33** form Langmuir films at the air-water interface. The properties of these films are strongly dependent on the nature of dissolved salt in the aqueous phase [53]. The most surprising and interesting effects of complexation on the mesophase behavior were observed in the system **33c** ($n = 2$)/water/MX [51]. First, it was observed that the lyotropic system MX/water/**33c** exhibits a columnar rectangular mesophase instead of a smectic phase for neat **33c**. Complexation with a salt can change the phase type. A ribbon-type model was proposed for the mesophase with the *p*-terphenyl units packed parallel to each other and separated by the complexed crown ether moiety with the solvent molecules. The space between the ribbons should be filled with the molten alkyl

Fig. 4 Mesomorphic properties of the lyotropic system **33c**/water/MX

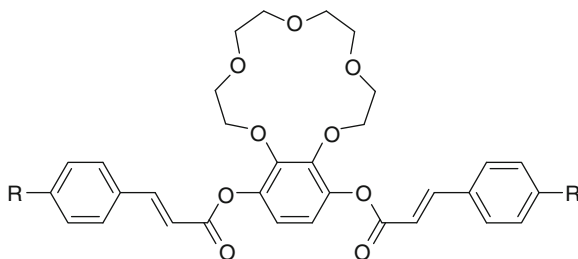


Scheme 19 Liquid crystalline properties of **34**

chains. The clearing points of the lyotropic columnar mesophases vary with the size of the cation. For cations which are smaller than the diameter of the [18]crown-6 unit (Li^+ , Na^+), low clearing points are exhibited (Fig. 4). The same issue arises for Rb^+ and Cs^+ , which are larger than the cavity. The highest clearing points were observed for K^+ , which fills the crown perfectly. Another observation was the dependence of the clearing point on the anion of the complexed salt. For potassium halides, T_{clear} increases with increasing size of the counterion with $\text{I}^- > \text{Br}^- > \text{Cl}^-$ (Fig. 4). Ion pairing could be a reason for the increase in thermostability [55].

Bayle presented liquid crystal **34** (Scheme 19) bearing four aromatic units linked by ester and azo functional groups [56]. Two butyloxy groups are attached at the ends of the molecule and the crown ether is bound at the side of the molecule. The nematic phase exhibited by **34** is quite broad ($\Delta T = 96$ K). Upon complexation with LiBF_4 , the nematic range diminishes with increasing amounts of added salt and disappears completely at 0.5 equiv. of added LiBF_4 which is most likely due to the formation of a 2:1 crown:lithium complex. From 0.2 equiv. of salt, a smectic

Scheme 20 Symmetric substitution on benzo[15] crown-5 and physical properties of **35**

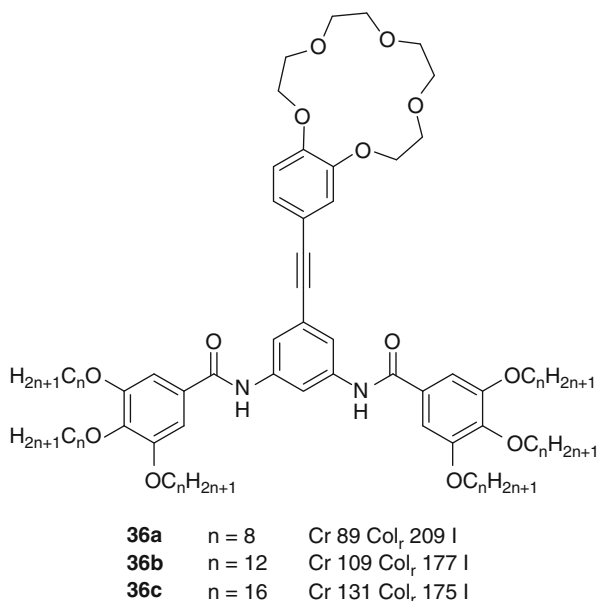


35a	R = O(CH ₂ CH ₂ O) ₁ CH ₃	Cr 127 N 141 I
35b	R = O(CH ₂ CH ₂ O) ₂ CH ₃	Cr 73 N 85 I
35c	R = O(CH ₂ CH ₂ O) ₃ CH ₃	Cr 32 I
35d	R = O(CH ₂ CH ₂ O) ₁ C ₄ H ₉	Cr 75 N 90 I
35e	R = O(CH ₂ CH ₂ O) ₂ C ₄ H ₉	Cr 65 I
35f	R = OC ₇ H ₁₅	Cr 122 N 147 I
35g	R = OC ₁₁ H ₂₃	Cr 102 N 125 I

phase appears which gains in stability upon further addition of LiBF₄. Upon further (>0.5 equiv.) addition of salt, the smectic range stays almost constant. This is another example of molecular recognition that can change the type of mesophases.

The symmetric derivatives **35a–g** with lateral crown ethers prepared by the same group (Scheme 20) were used for three purposes: (1) to find out about the geometry of the lateral ring in the mesophase, (2) to examine the effect of different side groups, e.g., poly(ethylene glycol) chains, and (3) the further elucidation of the effects of LiBF₄ complexation [57]. The molecules prepared possess a mirror plane in the molecule to ease the assignment of the NMR signals observed in the ¹³C 2D-SLF method used to elucidate the structure of the ring. The NMR experiments revealed that the crown ether moiety is far from being flat and the conformation changes significantly upon temperature changes. The most stable nematic phases were observed for **35f,g** with alkyloxy chains. When ethylene glycol fragments are included (**35a–e**) in the side chains, the clearing temperatures and nematic ranges decrease. If the number of –OCH₂CH₂– fragments is too high, the nematic phase is lost (**35c,e**). Most surprising and in contrast to what was observed for LiBF₄·**34** [56], the mesophase was lost in LiBF₄·**35a–g**. A possible reason for this behavior could be the presence of the two ester groups that might form a peculiar cavity together with the crown macrocycle that is unsuitable for the uptake of Li⁺. Another reason might be the presence of only three aromatic rings. This mesogenic unit is probably not powerful enough to overrule the geometry change upon complexation.

Ziessel and co-workers presented the “three block” crown ethers **36** (Scheme 21) [58] consisting of the aromatic part, the crown ether fragment, and the alkyl chains. Columnar rectangular mesophases were observed in X-ray experiments. The geometry of the phases is always *p2mm* and the columnar range is very broad ($\Delta T = 120$ K for **36a**) but decreases with increasing chain length as the melting points increase and the clearing points decrease. In the mesophase, microsegregation can be observed as the alkyl chains form a continuum while the molecules are disposed

Scheme 21 Liquid crystalline crown ethers **36**

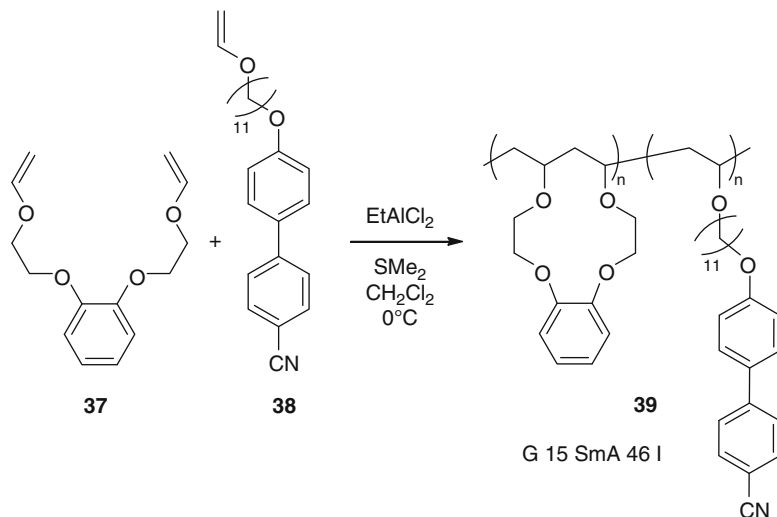
alternately within the $p2mm$ phase. In the third dimension, microsegregation will be maintained and the molecules are stacked over each other – probably in an alternating manner – allowing hydrogen bonds to stabilize the structure.

2.2.2 Polymeric Compounds

There is only one example that fits into this section and it uses a spectacular way to form the crown ether in the polymer that is worth noting (Scheme 22). In contrast to all other procedures that use crown ethers pre-formed in the monomers, this example by Percec forms the crown ether [13]crown-4 during the polymerization reaction [59]. Cationic cyclocopolymerization of 1,2-bis(2-ethenyloxyethoxy)benzene **37** with the mesogenic cyano biphenyl unit **38** gave copolymer **39** with a 1:1 ratio of **37:38** displaying a smectic phase.

2.2.3 Summary

There have been only a few reports on crown ethers laterally attached to rod-like molecules in the last few years. Nevertheless, very interesting compounds have been synthesized in the past. The general problem of this compound class is the flexible crown ether itself that can destroy the mesomorphic properties when attached laterally. Making the rigid rod longer can circumvent this problem. Another way to obtain stable mesophases is the complexation with suitable salts.



Scheme 22 Crown formation during polymerization

Examples were presented where the uptake of the salt led to a change of the mesophase geometry.

Future research in this field should concentrate on the effect of ion complexation and possible applications.

2.3 Central Crown Ethers with Terminally Attached Rod-Like Substituents

In this section, molecules will be discussed that have a crown ether in the center of the molecule which is substituted by two rigid rod substituents equipped with terminal flexible chains (Fig. 5). Attaching functional groups is also feasible.

2.3.1 Monomeric Compounds

Most of the liquid crystals discussed in this section bear a diaza[18]crown-6 **40**, a 4,4'-diaminodibenzo[18]crown-6 **41**, or a thia crown ether **42** in their center (Scheme 23). Substitution in **40** and **41** is conveniently feasible on the nitrogen atoms by formation of a Schiff base or an aza compound (in the case of **41**) or by N-alkylation or -acylation (in the case of **41**). *O*-Alkylation and -acylation of **42**, which are difficult to obtain, open a path to thia crown centered liquid crystals.

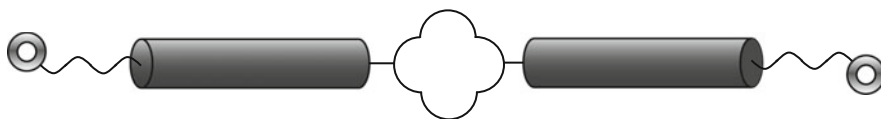
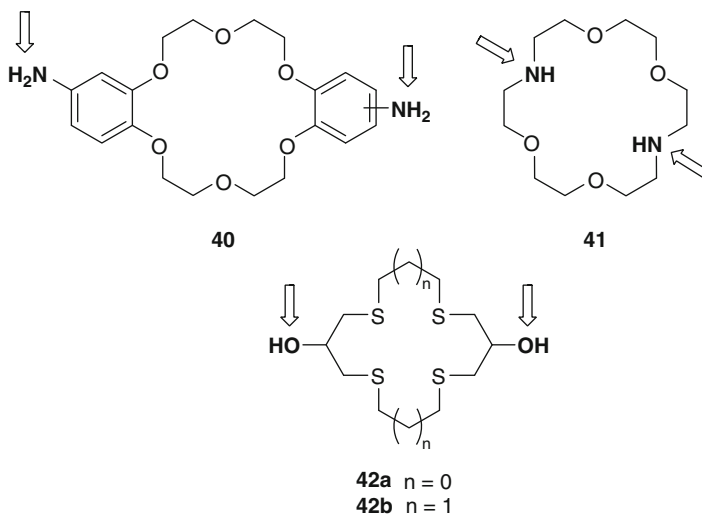


Fig. 5 Schematic representation of crown ethers with two rod-like substituents

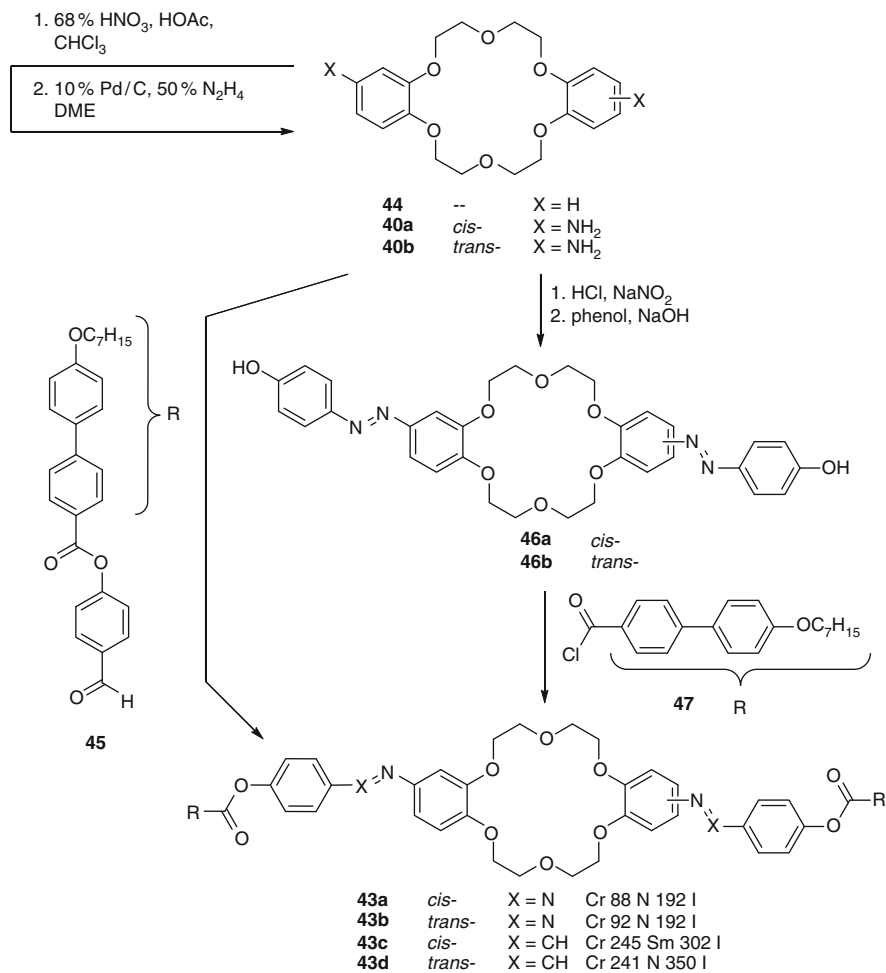


Scheme 23 Common precursors **40–42** for terminal attachment of mesogenic groups

Schiff Bases and Azo Compounds

The Schiff base (**43c,d**) and azo (**43a,b**) linked liquid crystalline crown ethers were synthesized (Scheme 24) by Xie [60] starting from dibenzo[18]crown-6 **44** which was nitrated with 68% nitric acid. Subsequent reduction with hydrazine and catalytic amounts of palladium gave 4,4'-diaminodibenzo[18]crown-6 **40**. The amino groups are either *cis* or *trans* and the products can be obtained separately according to literature procedures [61]. The Schiff bases **43c,d** were obtained by coupling **40a,b** with aldehyde **45**. In order to obtain the azo-linked compounds **43a,b**, **40a,b** (*cis* and *trans* refer to the positions relative to the crown ether, not to the geometry of the —N=N— double bond) was diazotized followed by azo coupling with phenol and intermediate **46a,b** was finally esterified with acid chloride **47**.

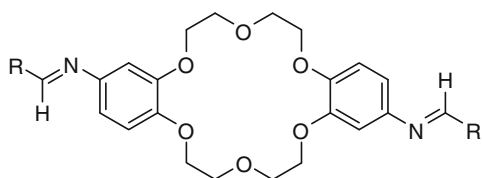
The liquid crystalline properties of **43a–d** were interesting as all derivatives showed very stable mesophases with phase widths of 57–109 K. It is remarkable that Schiff bases **43c,d** are stable at temperatures above 300 °C. It also strikes that, in contrast to conventional calamitic liquid crystals, the Schiff bases **43c,d** possess significantly higher phase transition temperatures compared to azo linked **43a,b**. Additionally, the *trans* compounds tend to possess higher clearing temperatures due to the elongated shape of the molecules.



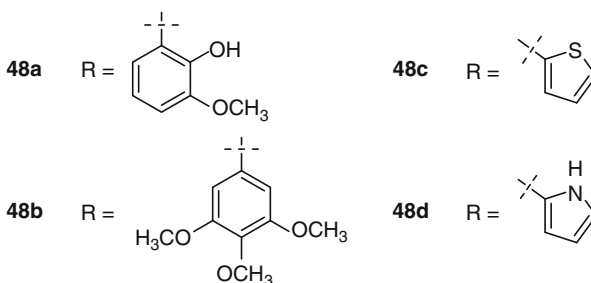
Scheme 24 Synthesis and properties of Schiff base and azo-linked liquid crystals **43**

Li and co-workers investigated derivatives of **43c,d** [62]. Instead of the terminal heptyl chains, chiral (*S*)-2-methylbutyl or dodecyl chains were used. For the methylbutane side chain, a chiral smectic and a chiral nematic phase were observed and the clearing points were higher than in **43c,d** due to the shorter chain while they were lower for the longer dodecyl side chains. It was also observed that the *trans*-compounds possess higher clearing temperatures compared to their *cis*-derivatives.

Menon presented a set of interesting liquid crystals **48** (Scheme 25) based on dibenzo[18]crown-6 modified with 2-hydroxy-3-methoxybenzene (**48a**), 3,4,5-trimethoxybenzene (**48b**), thiophene (**48c**), and pyrrole (**48d**) linked via a Schiff base [63]. All compounds are lacking long alkyl chains in the periphery. Nonetheless, broad mesophases with different geometries (SmC, SmA, N) were observed.



48a Cr 123 SmC 153 SmA 225 N 244 I
48b Cr 92 SmA 132 N 300 I
48c Cr 155 SmC 196 I
48d Cr 171 N 210 I



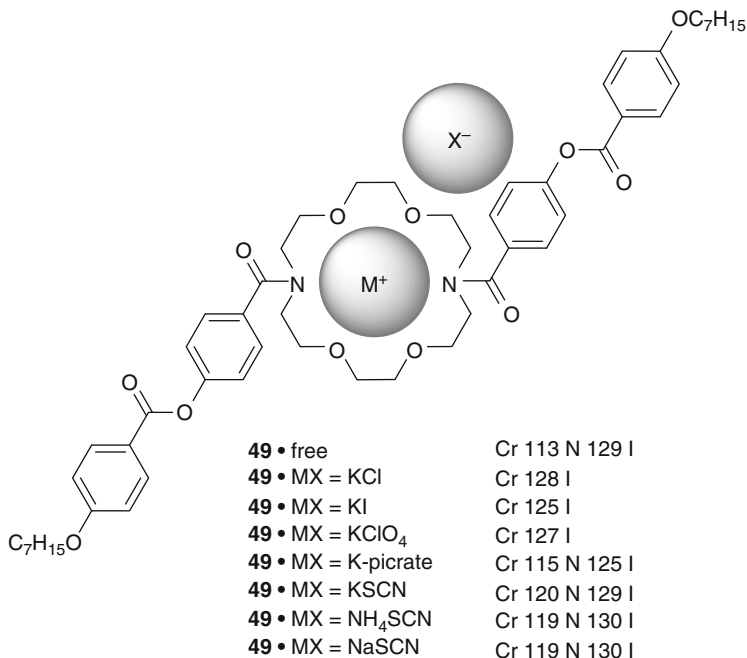
Scheme 25 Liquid crystals **48** devoid of peripheral chains

Diazacrowns

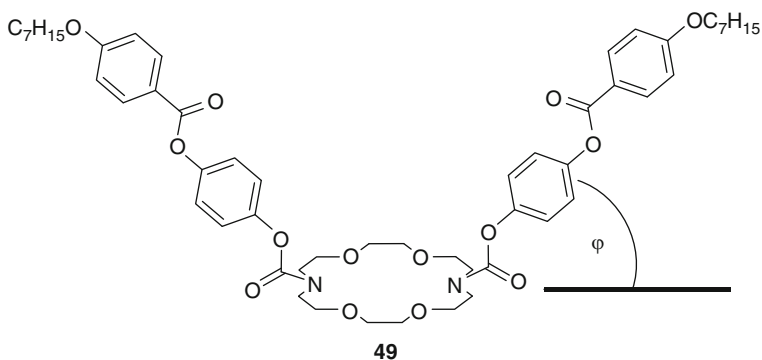
The first azacrowns with two mesogenic 4-[(4-(heptyloxy)benzyl)oxy]benzoic acid side groups bound to the crown ether *N*-atoms were presented by Xie [64] (Scheme 26). Neat **49** exhibits a nematic phase with a small ($\Delta T = 16$ K) range. Upon complexation with KCl, KI, and KClO_4 , the nematic phase is lost while the clearing temperature is almost constant. Upon complexation with potassium picrate, the clearing point is lowered while the melting point is increased, resulting in a smaller mesophase. Complexation with thiocyanates also results in smaller mesophases as the melting points are increased while the clearing points remain virtually unchanged. Once more, complexation decreases the tendency to form mesophases.

Heiney [65] investigated Langmuir films formed by Xie's liquid crystalline crown ether **49** and improved the synthesis towards higher purity of the final product. It was found that **49** self-assembles at the air-water interface as depicted in Scheme 27. The crown ether part of the molecule is located at the aqueous side while the arms of the molecule are bent by the angle φ , which is small but different from zero, and point into the air.

Xie [66] also investigated derivatives of diaza[12]crown-4 (**50a**) and diaza[18]crown-6 (**50b–d**) with terminal cholesterol moieties (Scheme 28). While **50a** with the smaller ring is not liquid crystalline, the derivatives **50b–d** with the larger diaza [18]crown-6 center show remarkably stable smectic phases as observed under the POM. Comparing **50b–d** with each other, no specific tendency is observed. Derivative **50b** with the side groups added via a urethane group has a smectic range



Scheme 26 Effect of complexation on **49**

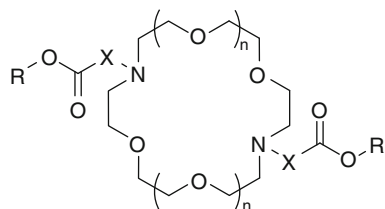


Scheme 27 Geometry of **49** at the air-water interface

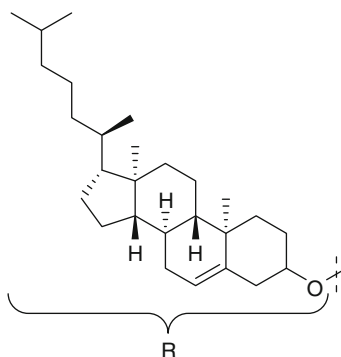
of 66 K while derivative **50c** with a CH₂ spacer between the ester and the amino group has a much broader phase (133 K) and **50d** with an ethyl spacer has the smallest phase (31 K).

Goodby presented a series of substituted diaza crown ethers **51–53** (Scheme 29, Table 2) containing three aromatic rings on each attached arm and studied the effects of different central ring sizes (6-, 12- and 18-membered rings), different

Scheme 28 Aza crown ethers **50** modified with cholesterol



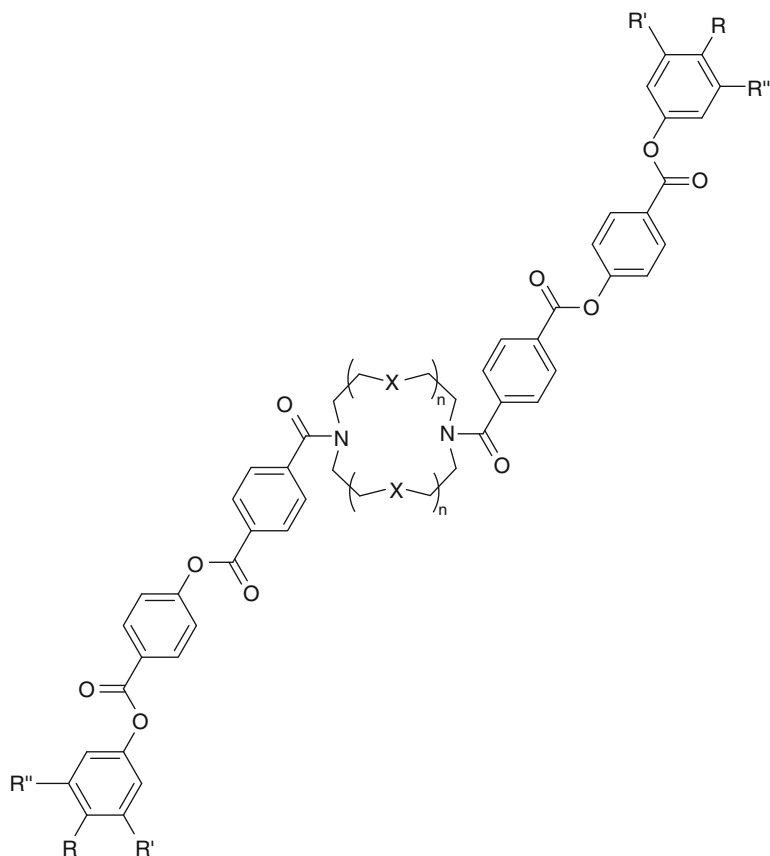
50a	n = 0	X = --	Cr 260 I
50b	n = 1	X = --	Cr 149 Sm 215 I
50c	n = 1	X = CH ₂	Cr 125 Sm 258 I
50d	n = 1	X = C ₂ H ₄	Cr 173 Sm 204 I



substitution patterns at the termini (dicatenar, tetracatenar, and hexacatenar), and different heteroatoms in the crown ether macrocycles (oxygen and sulfur) [67, 68].

First, the effects of different sized central rings and different heteroatoms in the crown ether of dicatenar compounds **51** with octyloxy chains in the periphery were investigated [67]. It was found that the mesomorphic behavior is strongly dependent on the size of the central ring (Table 3). While compound **51a** with a piperazine central unit possesses a clearing point at 322 °C (accompanied by decomposition), **51b** possessing a diaza[12]crown-4 central unit exhibits a clearing point which is 150 K lower. For **51c**, with the largest examined central unit (diaza [18]crown-6), the isotropization temperature is on a par with **51b**. The reason for the huge differences in the phase transition temperatures is the flexibility of the crown ethers: small rings behave like a rigid core while larger rings behave like a flexible linker of the two mesogenic side groups. Concerning the phase types, it was found that the larger the crown, the less probable is the occurrence of smectic phases. On replacing the oxygen atoms by sulfur (**51d**) the mesogeneity is almost lost, which is surprising as one would expect the opposite effect due to increased van-der-Waals interaction between the S-containing molecules.

For **51c**, temperature-dependent NMR experiments were carried out [67] that suggest the presence of a variety of conformers in solution. It was assumed that the same conformers will be present in the mesophase, too. The U- and zigzag-shaped



Scheme 29 Diaza crown ethers **51–53** of different sizes and with different terminal substituents

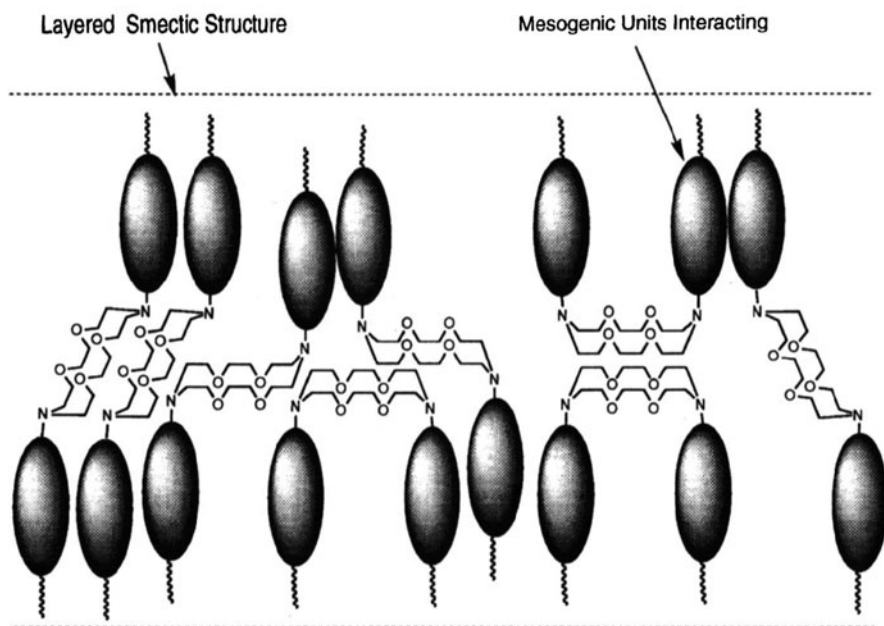
Table 2 Ring sizes and terminal substituents in **51–53**

Compound	X	<i>n</i>	R	R'	R''
51a	O	0	OC ₈ H ₁₇	H	H
51b	O	1	OC ₈ H ₁₇	H	H
51c	O	2	OC ₈ H ₁₇	H	H
51d	S	2	OC ₈ H ₁₇	H	H
52a	O	2	OC ₁₀ H ₂₁	OC ₁₀ H ₂₁	H
52b	O	2	OC ₁₄ H ₂₉	OC ₁₄ H ₂₉	H
52c	O	2	OC ₁₆ H ₃₃	OC ₁₆ H ₃₃	H
52d	O	2	OC ₁₈ H ₃₇	OC ₁₈ H ₃₇	H
53	O	2	OC ₁₀ H ₂₁	OC ₁₀ H ₂₁	OC ₁₀ H ₂₁

conformers were discussed to be the most stable ones and were used to explain packing within the smectic layers (Fig. 6). Folding of this type of molecules was also observed by Heiney [65].

Table 3 Mesomorphic properties of **51**–**53**

Compound	Transition temperatures (°C)
51a	Cr 205 SmX 211 N 322 I decomp
51b	Cr 156 N 157 SmA 175 I
51c	Cr 170 N 184 I
51d	Cr 172 N 173 I
52a	Cr 138 (SmC \approx 88) I
52b	Cr 134 (SmC 130) I
52c	Cr 120 (Col _h 90) I
52d	Cr 79 Col _h 86 I
53	G –6 Col _h 46 I

**Fig. 6** Proposed layered structure of **51c**. Reproduced by permission of The Royal Society of Chemistry from [67]

Further investigations revealed the dependence of the mesomorphic properties on the number of terminal alkyloxy substituents [68]. While **51** and **52** are not directly comparable due to the different lengths of the terminal chains, the trend is clear: with increasing number of alkyl chains, the clearing temperatures are shifted to lower temperatures. This becomes more obvious on comparing **52a** with four decyloxy chains that clears at 138 °C with **53** carrying six decyloxy chains which clears at 46 °C. Overall, all examined compounds do not possess broad mesophases. Interestingly, tetracatenar derivatives **52c,d** possess columnar phases instead of smectic phases in the case of **52a,b**. Compound **53** also possesses a columnar phase as deduced from POM (Fig. 7) which can be explained by the presence of the terminal gallic acid group.

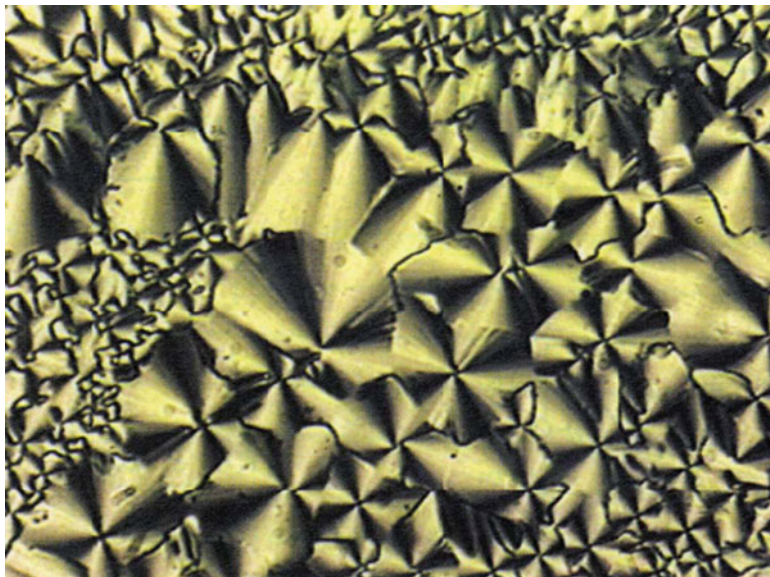


Fig. 7 Texture of **53** as observed under POM. Reproduced by permission of The Royal Society of Chemistry from [68]

The columnar order in **52a,b** was explained by molecular folding: the molecules are assumed to be in their U- (or wedge-) shaped conformation and six molecules self-assemble to a supramolecular disc. These discs are stacked in columns and arranged within a columnar hexagonal lattice (Fig. 8). Folding of similar mesogens was also seen by Heiney [65].

It has to be emphasized that all assumptions on the mesophase geometries and packing models made by Goodby are based on observations made under the POM; X-ray experiments were not carried out. Thus, the observations still have preliminary character [67, 68]. Similar compounds were also studied by Neve, also with respect to complexation. Copper [69] and palladium [70] complexes of derivatives of **51d** were found to form mesophases.

Lanthanide-containing mesophases are known with phthalocyanines and porphyrins [71–77] and possess interesting properties for bio-analyses and materials science due to their photochemical properties and the magnetic anisotropy of the complexed cations. It could be possible to obtain materials with properties that can be tuned by magnetic fields [78]. Bünzli investigated the first liquid crystalline crown ether complexes of lanthanide salts. The liquid crystalline and photoluminescence properties of **54** and its complexes with $\text{Eu}(\text{NO}_3)_3$ and $\text{Tb}(\text{NO}_3)_3$ [79, 80] (Scheme 30) were studied in detail. It was found that a broad Col_h mesophase ($\Delta T \approx 115$ K) could be induced by complexation of $\text{Ln}(\text{NO}_3)_3$ ($\text{Ln} = \text{Eu}, \text{Tb}$) with the non-mesomorphic host **54**. This is surprising as, up to now, mesophase induction and stabilization by complexation was only known for liquid crystalline polymers – not for low mass materials. The columnar hexagonal arrangement

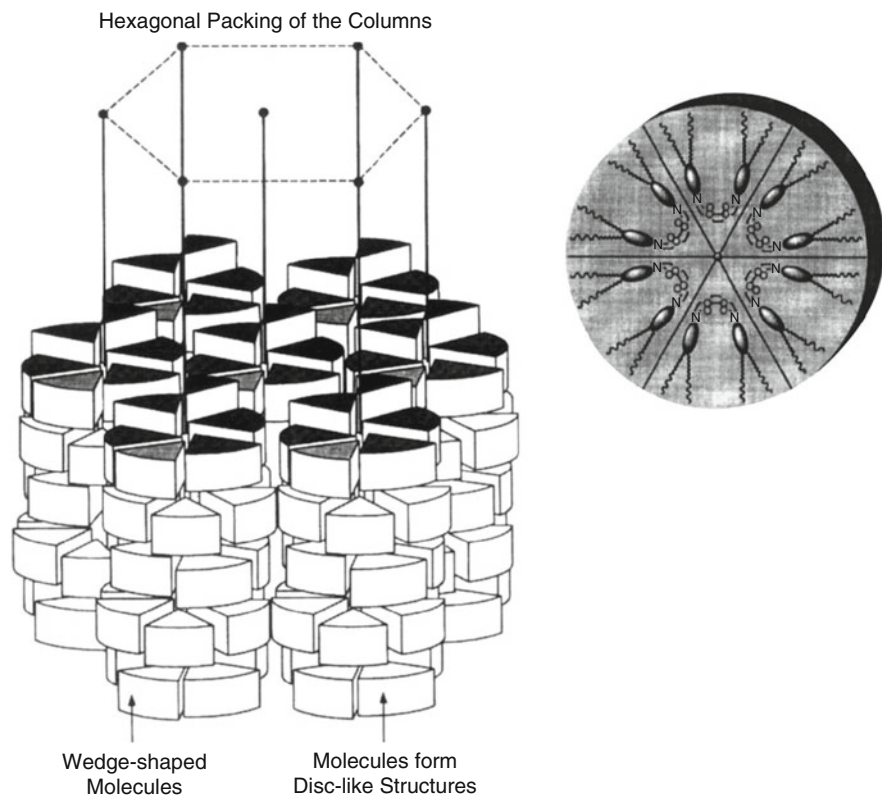


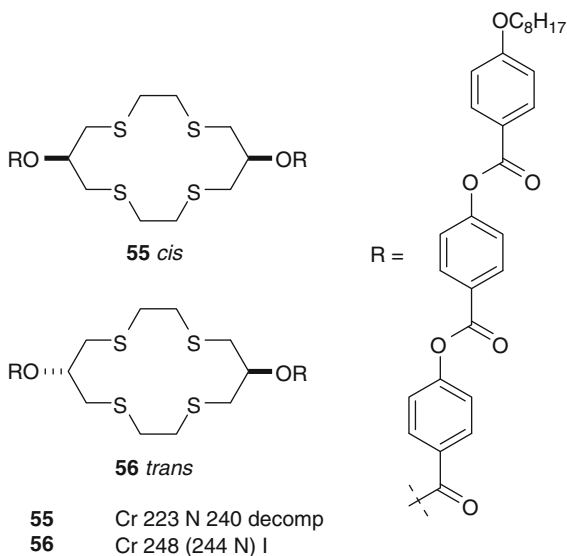
Fig. 8 Schematic representation of the formation of supramolecular discs from six molecules of **52** and their assembly into columnar phases. Reproduced by permission of The Royal Society of Chemistry from [68]

(as demonstrated by SAXS) is made possible through the increased microsegregation between the aliphatic chains and the polar crown upon complexation. The presence of the anions also disturbs the structure leading to mesomorphic behavior.

The complex with Eu^{3+} contained 0.25 equiv. of water while 1 equiv. of THF was included in the Tb^{3+} complex as deduced by elemental analyses. The ${}^5\text{D}_0 \rightarrow {}^7\text{F}_2$ emission for Eu^{3+} and the ${}^5\text{D}_4 \rightarrow {}^7\text{F}_5$ emission for Tb^{3+} were monitored. At the $\text{Cr} \rightarrow \text{Co}_\text{h}$ transition, both the lifetime and the intensity of both transitions were changed. Thus, it was possible to determine the melting point with a high level of accuracy using photoluminescence. The melting points observed in this way agree with the values obtained by conventional methods (DSC, POM), which further demonstrates the usefulness of this method.

In a further study, the effects of side chain length and lanthanide salt were investigated [78]. It was found that the chain length only plays a minor role and that the phase transition temperatures to the Co_h and the isotropic phase remain

Scheme 32 Liquid crystalline thia crown ethers **55**, **56**

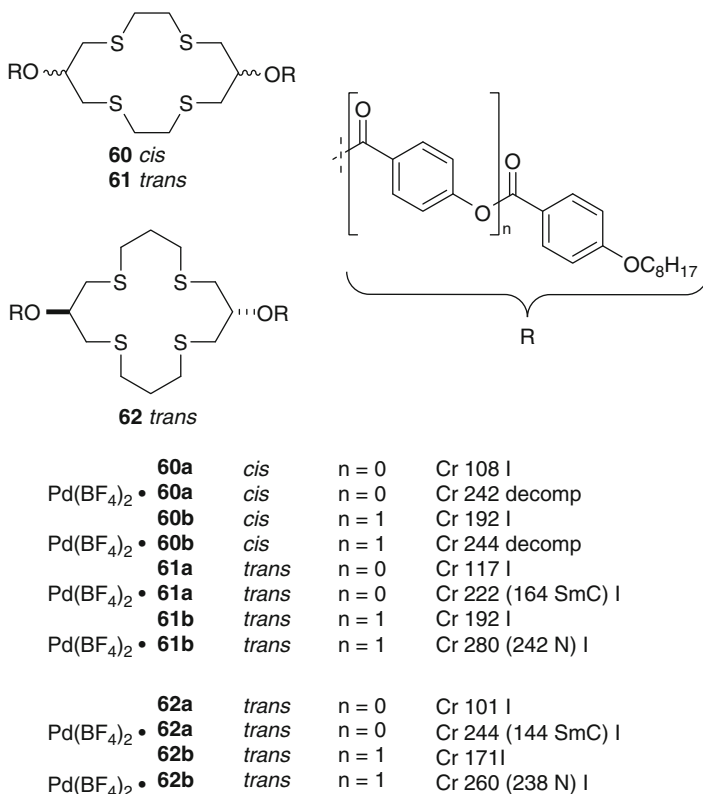


Crown Thioethers

The first examples of homoleptic thio crown ether liquid crystals (**55**, **56**) were presented by Bruce and Schröder [81] (Scheme 32). The synthesis and especially the separation of *cis*-(**42a**) and *trans*-(**42b**) forms of the macroheterocyclic diol were challenging. Reaction of (\pm)-epichlorohydrin **57** with 1,2-ethanedithiol **58** gave intermediate dichloride **59** that was finally reacted with 1,2-ethanedithiol **58** to give the *cis/trans* mixture of **42a** (Scheme 31). Separation of *cis*- and *trans*- and **42a** was carried out by flash chromatography followed by several recrystallization and fractional crystallization steps.

After DMAP-catalyzed esterification of **42a** with tri-benzoate esters, liquid crystals **55**, **56** (Scheme 32) were obtained, which both displayed narrow nematic phases as identified by their typical *Schlieren* texture. The melting and clearing points are high and, in the case of **55**, accompanied by decomposition. Compounds with shorter arms were also synthesized but found to be crystalline.

In a subsequent study, the influence of complexes with Pd²⁺ was examined in detail (Scheme 33) [82]. All uncomplexed crown ethers **60–62** only show a transition to the isotropic melt. For longer side arms ($n = 1$), transition temperatures are higher than for the related compounds with shorter ($n = 0$) substituents. Complexation changes this situation dramatically: upon uptake of Pd(BF₄)₂, all *cis*-complexes Pd(BF₄)₂-**60a,b** still showed isotropic melting as the only transition, while Pd(BF₄)₂-**61a,b** and Pd(BF₄)₂-**62a,b** showed monotropic smectic C ($n = 0$) phases or nematic ($n = 1$) phases. All phase transition temperatures were shifted to significantly higher temperatures. Still, longer substituents lead to higher phase transition temperatures.



Scheme 33 Effect of Pd(BF₄)₂ uptake by **60–62**

Mesophase induction by complexation was explained with the help of single crystal X-ray diffraction (Fig. 9). In the crystalline state, Pd(BF₄)₂·**61** and Pd(BF₄)₂·**62** adopt a zigzag conformation with the Pd²⁺ ion located in the inversion center of the molecule and hence in the exact center of the S₄ plane. Hereby, the crown ether loses some flexibility. It can now be considered as rigid core that interlocks the two attached substituents which promotes mesogeneity. Crystal structures of the corresponding Pd(BF₄)₂·**60** suggest the presence of a U-shaped conformation with the Pd²⁺ slightly out of the S₄ plane. This arrangement seems to disfavor the existence of liquid crystalline phases.

2.3.2 Polymeric Compounds

Percec and Rodenhouse presented the first main-chain liquid crystalline polymer with a crown ether moiety in the backbone of the polymer [83]. Liquid crystalline polyethers **63** were obtained by phase transfer catalyzed polyetherification of

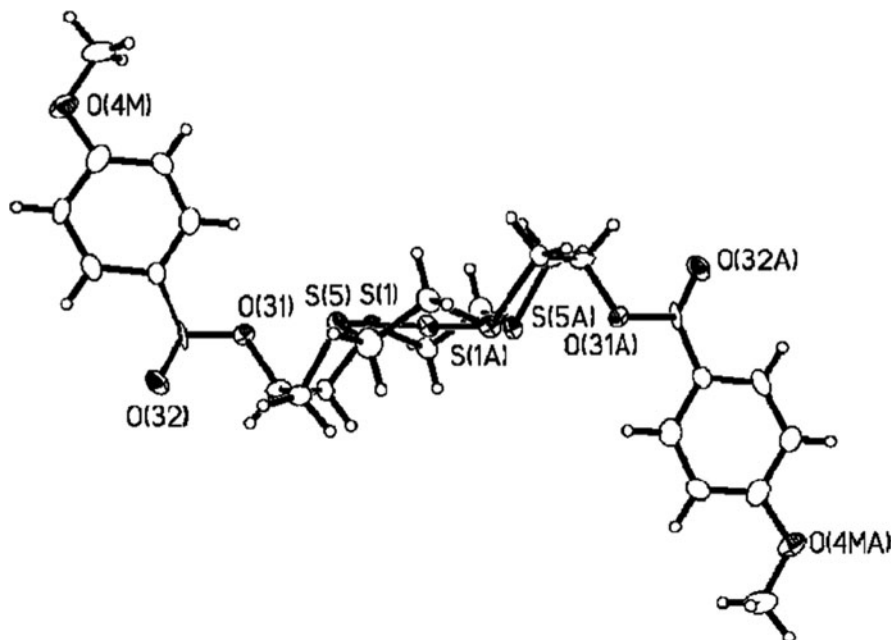
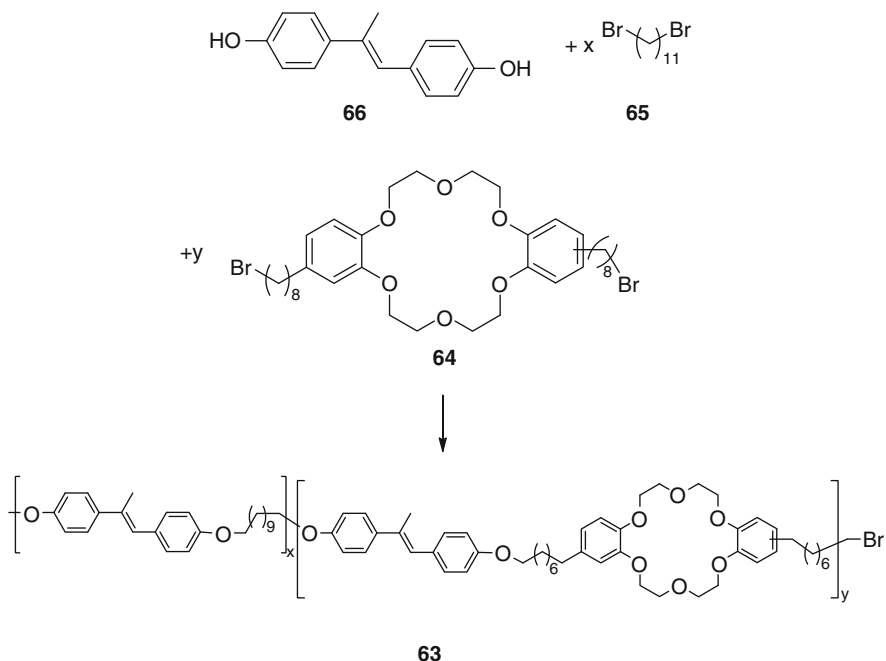


Fig. 9 Zigzag conformation of $\text{Pd}(\text{BF}_4)_2 \cdot \mathbf{61a}$ in the crystalline state. Reproduced by permission of The Royal Society of Chemistry from [82]

bis(8-bromooctyl)dibenzo[18]crown-6 **64** with 1,11-dibromoundecane **65** and the mesogenic unit 4,4'-dihydroxy- α -methylstilbene **66** (Scheme 34). The copolyethers **63** with ratios of **64/65** exhibit monotropic nematic phases for compositions between 80/20 to 40/60. The I \rightarrow N transition upon cooling was influenced by the amount of crown ether: for a molar ratio of 80/20, $T_{\text{I}\rightarrow\text{N}}$ was at 95 °C and decreased to 65 °C for a 40/60 ratio.

2.3.3 Summary

Liquid crystals with a central crown ether and lateral rod-like substituents are very versatile compounds. Plenty of possibilities for variation of the structure were presented. All materials exhibit a multitude of phase geometries, including nematic, smectic, and columnar. The mesomorphic properties can be tuned by complexation. Thia- and aza crown ethers offer the interesting possibility to complex transition or f-block metal salts. Due to their interesting magnetic or luminescence properties, novel light emitting or magneto-responsive liquid crystalline materials for analytics or material science could be obtained.



Scheme 34 Main chain liquid crystalline polymer **63**

2.4 Terminal Crown Ethers with One Taper-Shaped Substituent

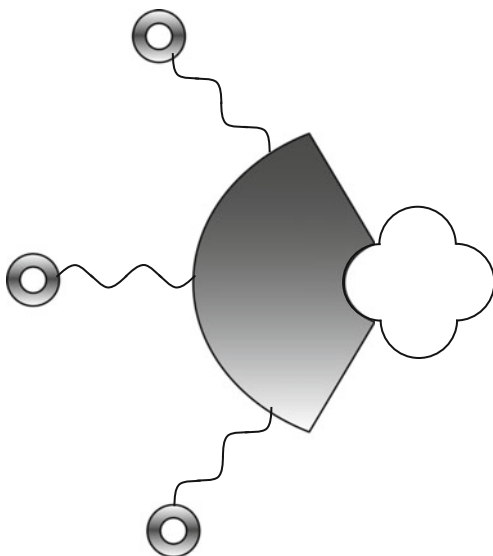
In this section, crown ethers will be discussed which are equipped with one taper-shaped substituent (Fig. 10). Columnar hexagonal mesophases are the most commonly observed phases in this kind of molecule.

2.4.1 Monomeric Compounds

Percec studied taper-shaped molecules like **67** and **68** (Scheme 35) and investigated their liquid crystalline properties upon complexation with NaOTf and KOTf [84, 85]. It was found that the neat materials exhibit only crystalline phases with **67** melting at 60 °C and **68** melting at 94 °C. The increased melting point in the latter system can be explained by the presence of an additional aromatic ring. Both **67** and **68** consist of an *endo*-receptor (the [15]crown-5 macrocycle) and an *exo*-receptor (the taper-shaped 3,4,5-tris(*p*-dodecyloxybenzoate)).

Upon addition of NaOTf, columnar hexagonal mesophases could be induced. For **68**, 0.4 equiv. of salt were needed while for **67**, only 0.2 equiv. of NaOTf were needed for mesophase induction. Upon complexation, the complexed crown ether moieties and the anions self-assemble within a supramolecular tube and the taper-shaped side groups stack over each other in the periphery. X-Ray scattering

Fig. 10 General design of liquid crystalline crown ethers with a taper-shaped substituent

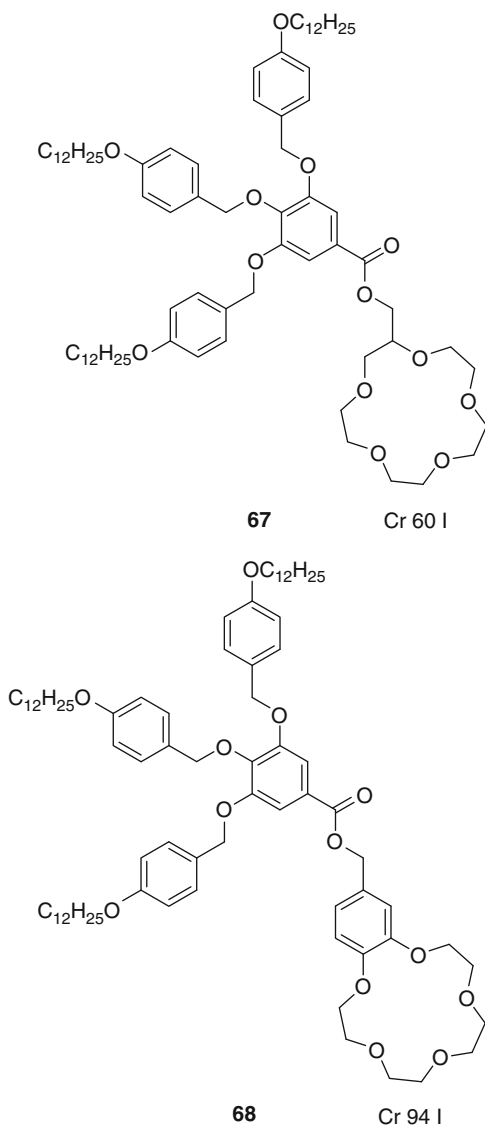


experiments were carried out to elucidate the structure of the mesophase. It was found that a supramolecular disc within the columns consists of approximately six molecules (Fig. 11). The interesting mechanism of this molecular recognition-mediated self-assembly is related to that observed in the tobacco mosaic virus [85].

Another finding was that, in contrast to the observations made for most crown ether modified rod-like molecules, the uptake of a salt led to an increase in the mesophase stability (Fig. 12). While neat crown ether **67** recrystallized at 12 °C, a transition from the isotropic melt to a columnar hexagonal phase was observed at 39 °C for 0.4 equiv. of NaOTf-**67**. At higher concentrations of salts, the clearing point was shifted to higher temperatures and reached its maximum at 2.0 equiv. of salt. Interestingly, the Col_h phases were stable far below room temperature upon cooling and maintained the columnar order even in the subsequently observed glassy or crystalline phases (Fig. 12).

The DC conductivity of NaOTf-**68** was measured to be in a range of 10^{-6} to 10^{-7} S cm⁻¹, a value typical for ionic conductors [84]. The authors proposed that the crown ethers stack over each other to form six parallel ion channels within the tube.

The electric conductivity was also measured for complexes of taper-shaped mesogens with oligo(ethylene oxide) central groups. The DC conductivity is in a range of 10^{-9} to 10^{-6} S cm⁻¹ and shows a step-like increase at the crystal-columnar phase transition [86]. It was also shown that taper-shaped molecules adjacent to different endo-receptors such as crown ethers or oligo(ethylene oxide) chains were miscible with a poly(methacrylate) matrix and formed isomorphic phases [87]. Applications as columnar reaction media for polymerizations were foreseen. Comprehensive summaries of Percec's taper-shaped molecules can be found in the literature [88, 89].

Scheme 35 Taper-shaped crown ethers **67**, **68**

The effects of fluorinated side chains were also investigated [90]. Replacing the dodecyloxy chains from **67** and **68** with heptafluorododecyloxy chains resulted in taper-shaped **69** and **70** (Scheme 36). While **69** exhibited an enantiotropic columnar hexagonal phase, **70** showed a cubic phase solely upon cooling. This shows impressively that fluorination enhanced the self-assembly of the materials as the corresponding alkyl-substituted derivatives **67** and **68** are non-mesomorphic. The geometry of the columnar hexagonal phase is the same as discussed above with the crown ethers side by side in the center of the column and the melted taper-shaped

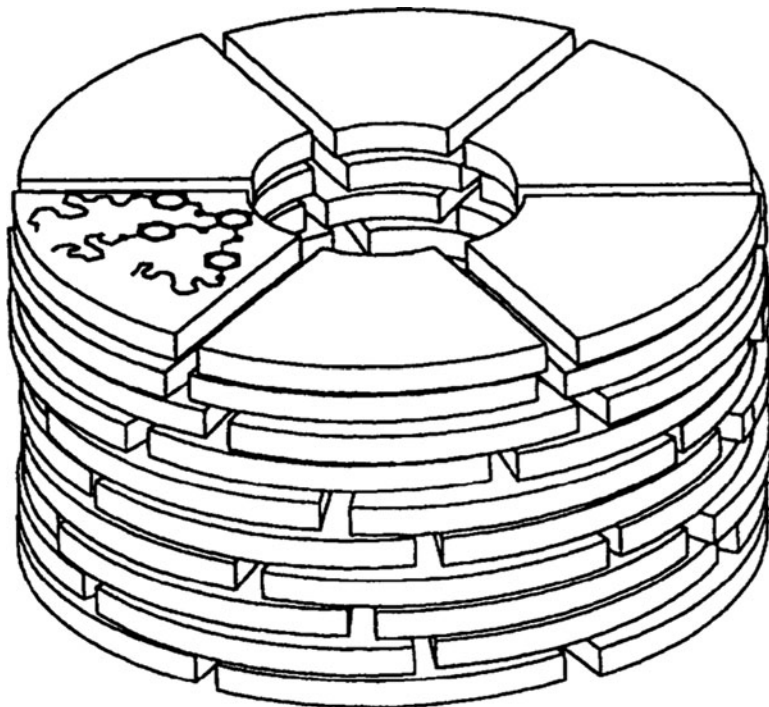


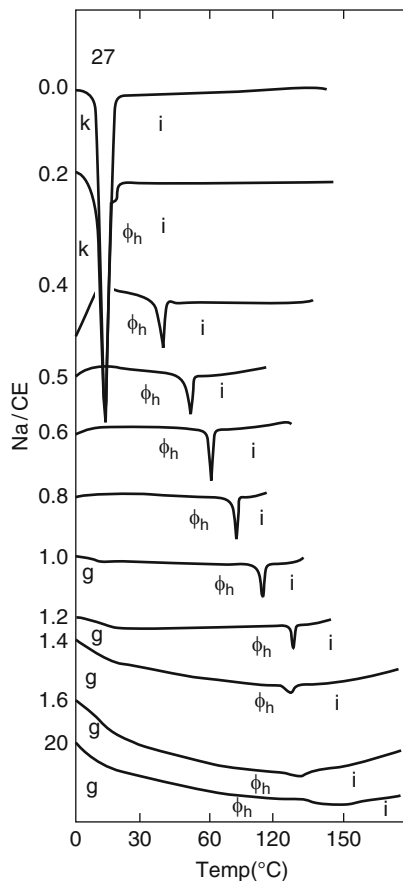
Fig. 11 Molecular recognition directed self-assembly of NaOTf-**67**, NaOTf-**68** to supramolecular discs which further self-assemble to supramolecular tubes. Reproduced by permission of The Royal Society of Chemistry from [85]

groups in the periphery. The fluorinated segments are microsegregated via the fluorophobic effect from the hydrogenated and aromatic units. More interestingly, the mesophase range and stability are higher for neat fluorinated **69** than for complexed hydrogenated NaOTf-**69**. This means that the fluorophobic effect overrules the ion-mediated self-assembly.

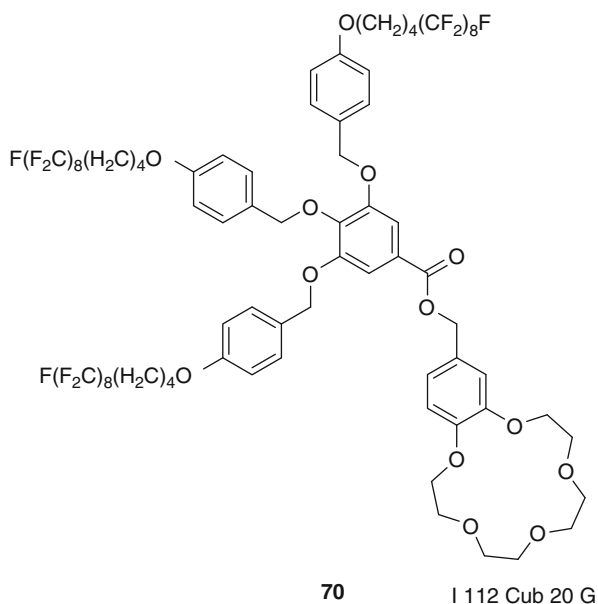
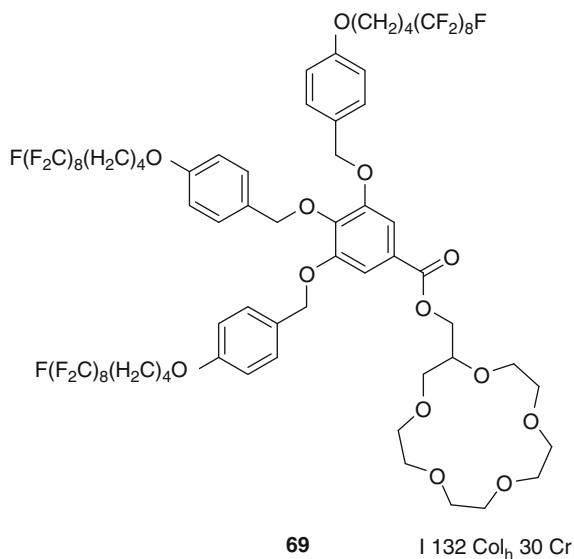
A detailed study on the elastic behavior of **69** based on the POM textures and observations under the TEM were carried out by Jung [91].

Percec published a detailed and elaborated study about monodendritic crown ethers based on benzo[15]crown-5 modified with parallelepiped (**71**), tapered (**72**), conic (**73**), and half-disc (**74**) shaped substituents [92] (Scheme 37) and the effects of complexation of NaOTf by these crown ethers (Scheme 38). Some general trends of NaOTf complexation were found. First, SmA phases formed by parallelepiped monodendrons (**71**) are stabilized upon complexation. While neat **71** exhibits an SmA phase range of only 7 K, 0.8 equiv. NaOTf-**71** leads to a smectic phase which is stable for 101 K (Table 4). This was explained by the interdigitated bilayer structure derived from X-ray measurements. The crown ether moieties are located in the middle of the bilayer and uptake of a salt leads to ionic interactions stabilizing the bilayer and hence increasing the clearing point and mesophase range.

Fig. 12 DSC traces of NaOTf·**67** upon cooling from the isotropic phase. *k* crystalline, *g* glass, ϕ_h columnar hexagonal, *I* isotropic, *CE* crown ether **67**. Reproduced by permission of The Royal Society of Chemistry from [85]

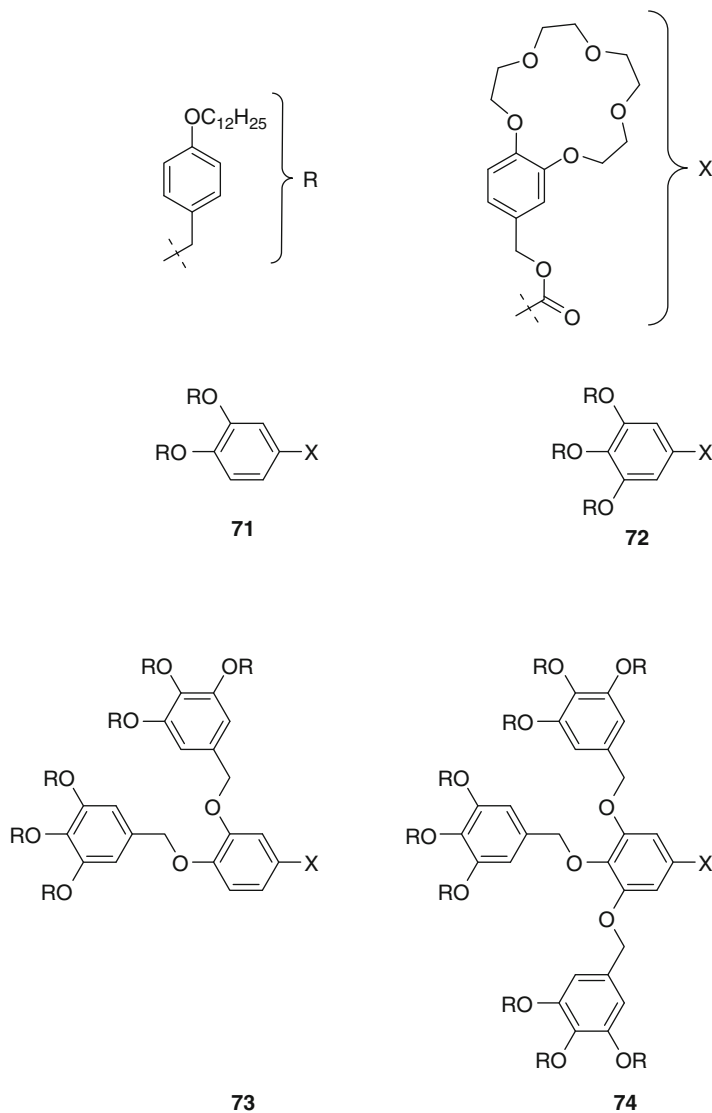


Second, the mesophase behavior observed for taper shaped monodendrons (**72**) is also significantly influenced by the complexation with NaOTf. While neat **72** is crystalline, the complex 1.0 equiv. NaOTf·**72** exhibits a columnar hexagonal phase which is stable for 67 K (Table 4). The possible reason for the induction of a mesophase and the mechanism of self-assembly of taper-shaped molecules has already been discussed above for **67**, **68** and is shown in Scheme 38. Third, cubic phases as observed in spherical monodendrons **73** are also stabilized by the presence of NaOTf. Uncomplexed **73** exhibits a cubic phase as broad as 39 K while 0.4 equiv. NaOTf·**73** possesses a cubic phase range of 141 K and is stable until -26 °C (Table 4). Conic monodendrons self-assemble to spheric dendrons that organize in cubic lattices (Scheme 38). As the crown ether is located at the center of the spheres, the uptake of NaOTf and the associated ionic interactions lead to the drastic improvement of the liquid crystalline properties. Fourth, the columnar hexagonal mesophases observed for half disc-shaped molecules **74** are being destabilized upon complexation. Neat **74** has a columnar phase range of 131 K.



Scheme 36 Liquid crystalline crowns **69**, **70** with fluorinated side chains

In contrast, complexation of **74** with 0.4 equiv. NaOTf yielded a phase which is only 110 K stable (Table 4). As complexation leads to a side by side arrangement of the crown ethers, induction of columnar phases is most effective for taper-shaped molecules that do not disturb each other when being placed close to each other.

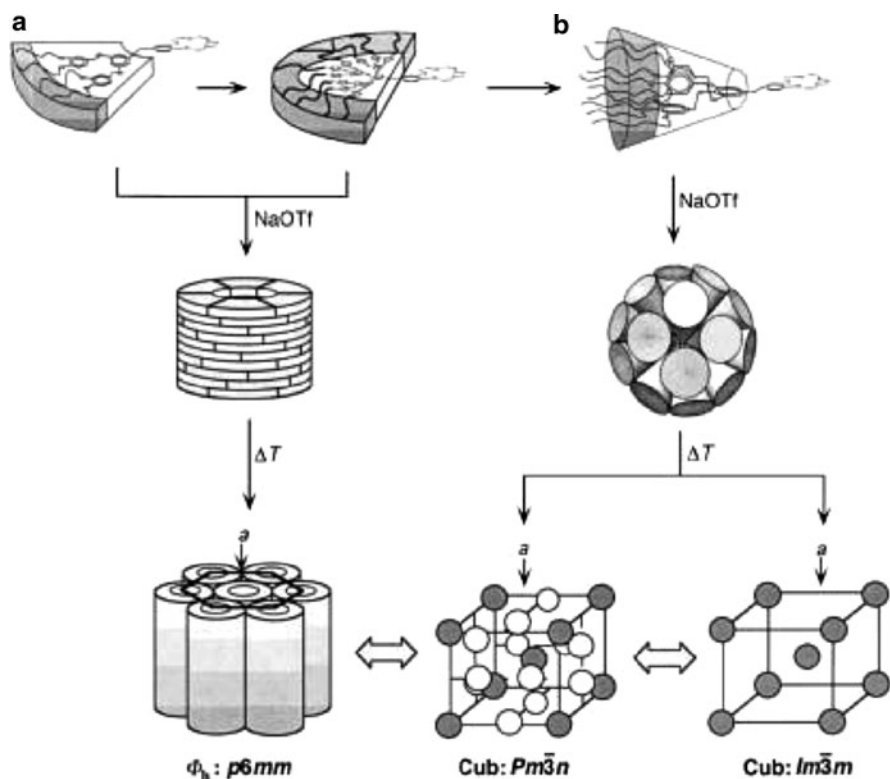


Scheme 37 Monodendritic crown ethers **71–74** with differently shaped substituents

Molecules possessing a half disc shape cannot be placed side by side to form a supramolecular disc as the half disc molecules disturb each other, which ultimately leads to smaller mesophase ranges.

Gitsov presented a series of poly(benzyl ether) monodendrimers capable of cation complexation lacking alkyloxy side chains which were non-mesomorphic [93].

Laschat followed a different route to obtain disk-like liquid crystals equipped with crown ether moieties. The crown ether was not attached to the mesogenic



Scheme 38 (a) Self-assembly of taper- and half disc-shaped molecules to form tubes that self-organize into Col_h (Φ_h) phases; (b) self-assembly of monodendrons of conic shape into spherical dendrimers that self-organize in Cub phases. Copyright Wiley-VCH Verlag GmbH & Co. KGaA. Reproduced with permission from [92]

Table 4 Mesomorphic properties of 71–74

Phase transition temperatures ($^{\circ}\text{C}$) of 71–74 and their complexes with NaOTf upon first cooling	
71	I 50 SmA 43 G
0.8 equiv. NaOTf-71	I 117 SmA 16 G
72	I 34 Cr
1.0 equiv. NaOTf-72	I 98 Col_h 31 G
73	I 78 Cub 40 Cr
0.4 equiv. NaOTf-73	I 115 Cub –26 Cr
74	I 107 Col_h –24 Cr
0.4 equiv. NaOTf-74	I 85 Col_h –25 Cr

group by a methylene linking group but was directly attached to the *o*-terphenyl side group [94–96]. The effects of different substituents adjacent to the *o*-terphenyl substituent (alkyloxy 75, acyloxy 76, or gallic esters 77, Scheme 39) as well as the influence of NaI complexation were studied.

Scheme 39 Liquid crystalline [15]crown-5 ethers **75–77** with differently substituted *o*-terphenyl units

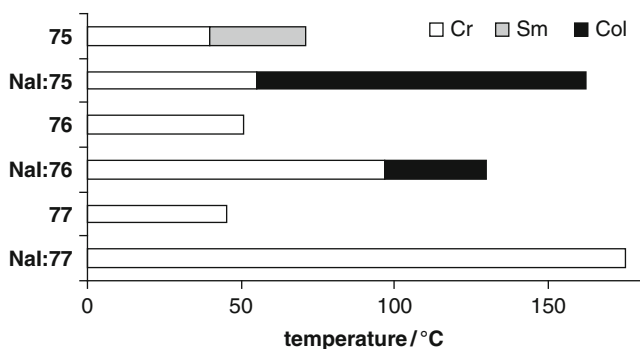
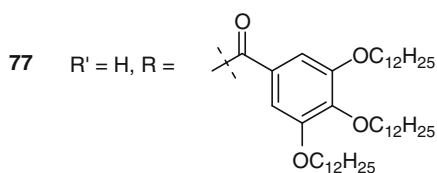
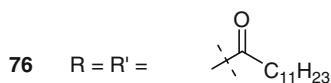
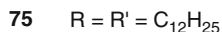
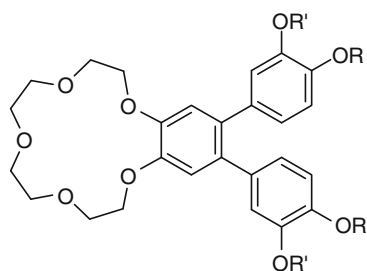


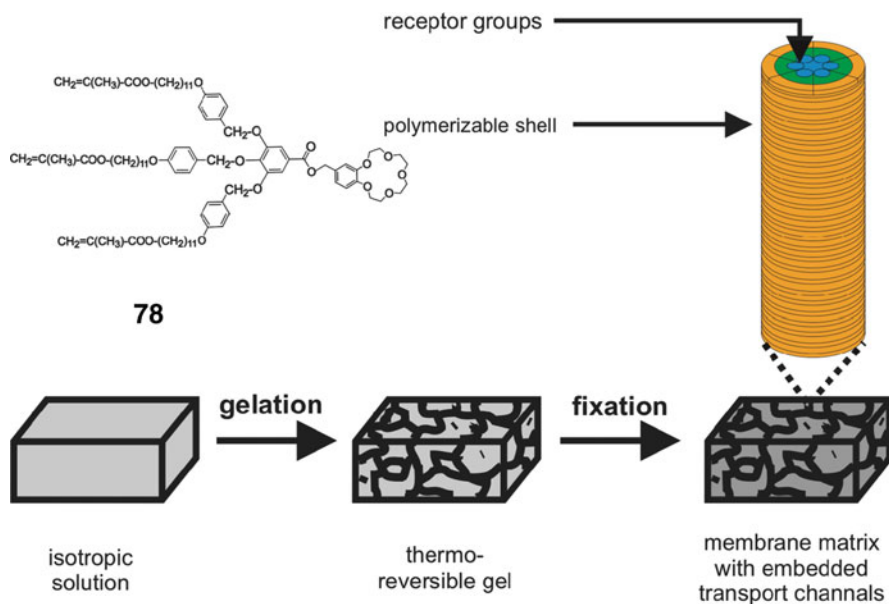
Fig. 13 Liquid crystalline properties of **75–77**

While alkyloxy-substituted **75** exhibits a smectic phase from 40–71 °C (Fig. 13), NaI induces a change in the phase geometry as complex NaI·**75** exhibits a columnar rectangular phase which is significantly more stable than the smectic phase of **75** [94, 96]. As deduced from single crystal X-ray analysis, ion channels form in the liquid crystalline state with the molecules being aligned antiparallel. The introduction of acyloxy groups in **76** changes the behavior [95, 96]. Neat compounds **76** are crystalline. Introduction of NaI leads to the presence of

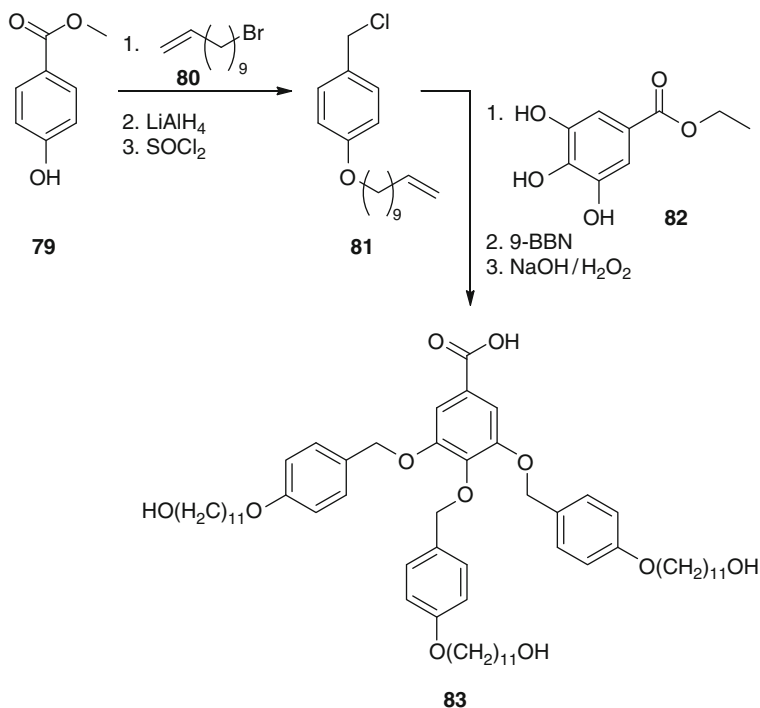
a columnar phase, which is smaller compared to NaI-75. The introduction of gallic esters in 77 finally results in disappearance of the liquid crystalline properties. Neither 77 nor NaI-77 show any mesophases. Nevertheless, complexation still leads to a drastic increase in the clearing point. The reason for the loss of mesomorphism might be the large number of alkyl chains. The tendency to nanosegregate is much lower for 77 because the polar crown ether plays a minor role as compared to the number of alkyl chains.

2.4.2 Polymeric Compounds and Possible Applications

Beginn developed Percec-type dendrimers, which are known to form supramolecular channels, with polymerizable acrylate groups in order to obtain ion-permeable membranes [97–99]. First, the dendron 78 (Scheme 40) was dissolved in a polymerizable acrylate mixture that does not shrink on polymerization. The second step was the thermo-reversible gelation of the acrylate mixture, which was followed by the last step, polymerization to fix the supramolecular channel structure (Scheme 40). In the first experiments, compounds with only one polymerizable group were used but it turned out that the gelating properties were not sufficient [100, 101] so threefold modified 78 had to be developed.



Scheme 40 Formation of membrane-fixed supramolecular channels from 78. Copyright Wiley-VCH Verlag GmbH & Co. KGaA. Reproduced with permission from [98]



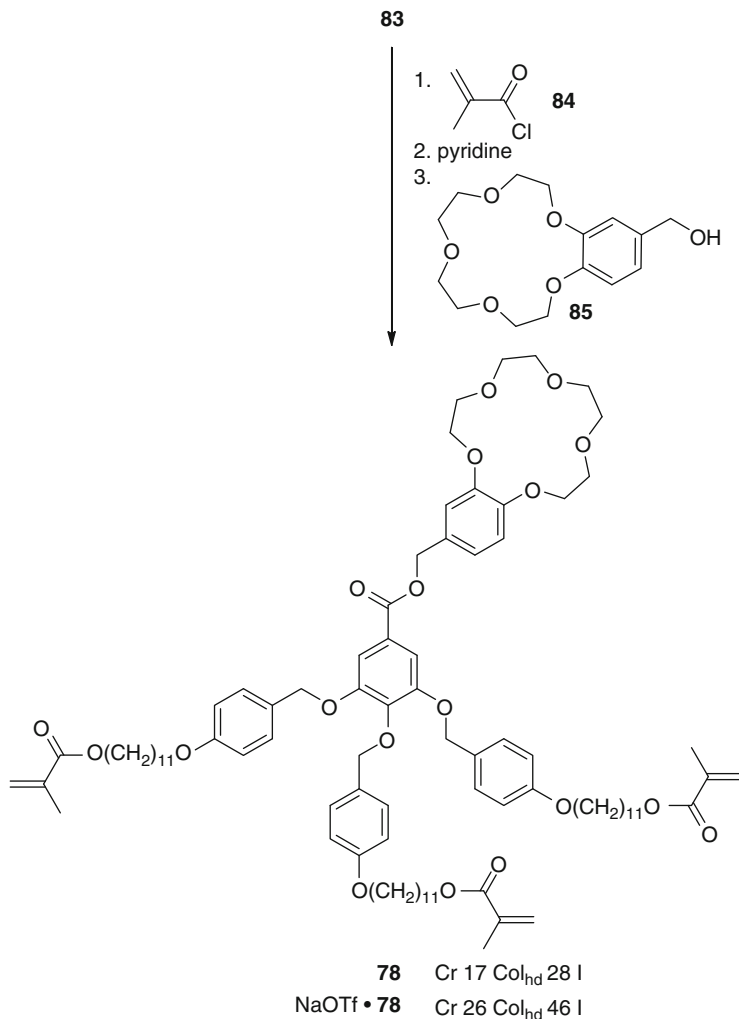
Scheme 41 Synthesis of precursor **83** for monodendritic crown ether **78**

The synthesis of **78** [97] started from methyl-4-hydroxybenzoate **79** that was alkylated with 11-bromoundec-1-ene **80**. The ester group was reduced with LiAlH_4 and the resulting alcohol was reacted to chloride **81** using SOCl_2 . Coupling with **82** followed by hydroboration of the terminal double bonds and oxidation accompanied by ester cleavage yielded monodendron **83** with three alcohol units (Scheme 41).

Reaction of **83** with methacryloyl chloride **84**, followed by cleavage of the intermediate acid anhydride with pyridine and subsequent coupling with crown fragment **85**, gave the desired final product **78** [97] (Scheme 42).

Compound **78** as well as the complex $\text{NaOTf}\cdot\mathbf{78}$ (Scheme 42) forms columnar hexagonal disordered mesophases [97]. While neat **78** exhibits a columnar phase range of 11 K, $\text{NaOTf}\cdot\mathbf{78}$ increases the clearing temperature and stabilizes the mesophase resulting in a phase range of 20 K. Furthermore, it was shown that the columnar phase of **78** accepts up to 10 wt% of polymerizable methacrylates while leading to gelation of the added methacrylates.

The properties of the gels were investigated in detail [102] and it was found that well-defined cylinders built up from **78** are present in the transparent gels offering the possibility of ion transport. Closer investigation of the membranes [98, 99] revealed that MNO_3 , MCl , and MClO_4 ($\text{M} = \text{Li}, \text{Na}, \text{K}$) can pass the membranes.



Scheme 42 Synthesis of polymerizable liquid crystalline crown ether **78**

The transport velocity of Li^+ is faster than that of Na^+ and K^+ due to the size of the cation. The data are consistent with a hopping transport mechanism of the cations accompanied by a non-specific co-transport of the anions. The transport rates for $\text{NO}_3^- > \text{Cl}^- > \text{ClO}_4^-$ are related to the adjacent hydrate shell and not yet fully understood. Anyway, a path in the center of the supramolecular tubes, where the crown ethers assemble, must exist and allow for the co-transport of the anions. By forming the membranes in the pores of track-etched membranes, the transport rates could be improved by an order of magnitude due to the orientation of the channels perpendicular to the membrane surface.

2.4.3 Summary

Terminal crown ethers with taper-shaped substituents often possess columnar phases. Sometimes, the columnar order is only observed after the complexation of specific salts. The uptake of salts often results in the crown ethers assembling side by side forming supramolecular cylinders with the crown moieties on the inside and the alkyl chains on the outside leading to possible ion-conducting arrangements within an insulating jacket. Indeed, it was shown that matrix-fixed tubular arrangements are ion conductors.

2.5 *Central Crown Ethers with More than One Peripheral Substituent*

Crown ethers discussed in this section possess rod-like substituents all around them or flat substituents at either end (Fig. 14). The former was the structure of the first liquid crystalline crown-like molecules and will be discussed first. The latter one comprises molecules with taper- or disk-shaped terminal groups.

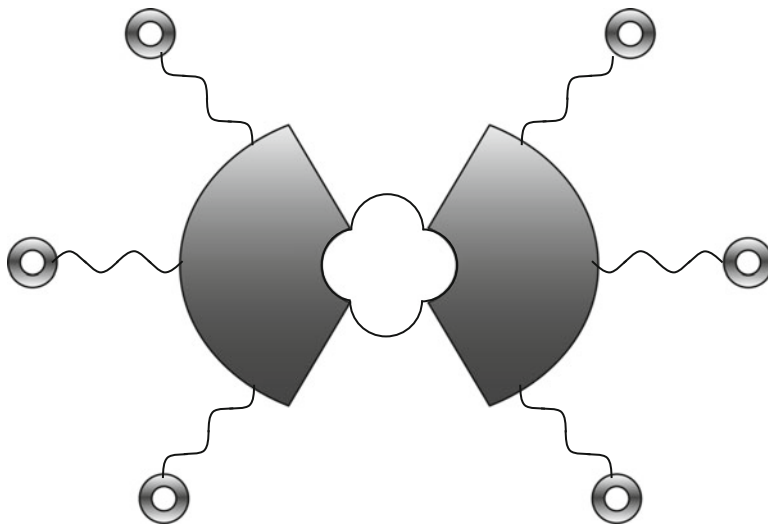
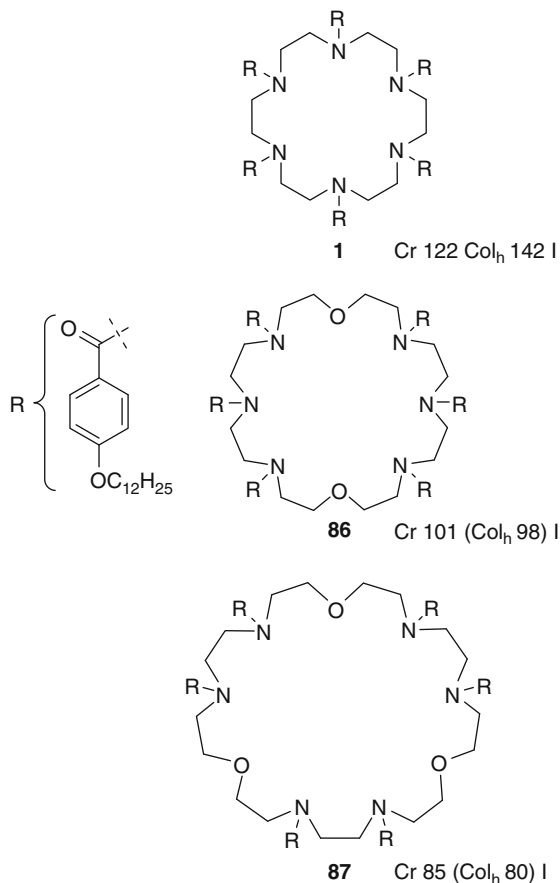


Fig. 14 Schematic representation of crown ethers with several taper- or disk-shaped substituents

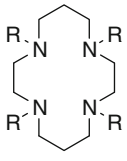
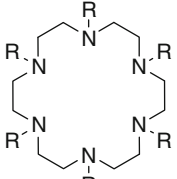
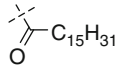
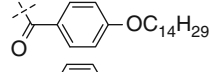
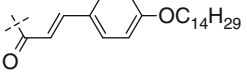
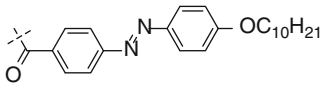
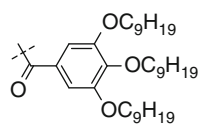
2.5.1 Polysubstituted Macrocylic Polyamines

Lehn presented the first crown-like liquid crystals (Scheme 43) in 1985 [5]. The core was built up from several polyamines, e.g., hexacyclen in **1** (termed [18]-N₆ due to the similarity to [18]crown-6). The larger [24]-N₆O₂ in **86** and [27]-N₆O₃ in **87** were also investigated. Substitution with *p*-dodecyloxybenzoyl (R) moieties was performed at all nitrogen atoms. All substances display columnar hexagonal mesophases as deduced from X-ray scattering, which were also termed “tubular” due to the hollow channels formed by the crown molecules upon stacking. While **1** exhibits an enantiotropic Col_h phase with a phase width of 20 K, **86** and **87** exhibit small (< 5 K) monotropic columnar phase widths. The reason for the reduced clearing points and phase stabilities for the larger macrocycles is probably due to the increased flexibility of the ring. For the 24- and 27-membered rings, the conformation is too far away from a disc-like arrangement to form stable mesophases.



Scheme 43 First liquid crystalline crown ethers **1**, **86**, **87**

Table 5 Phase transition temperatures (°C) of [14]-N₄ and [18]-N₆ derivatives **88**, **89**

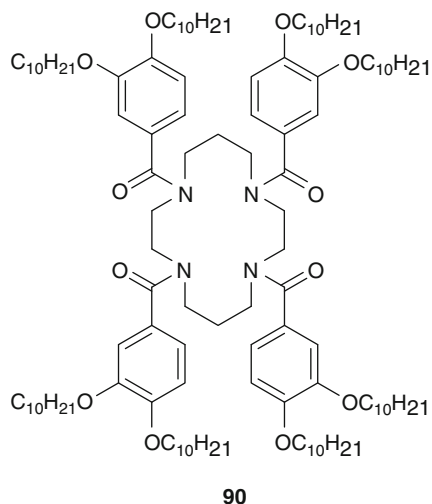
	R =	 88	 89
a		Cr 114 I	Cr 107 I
b		Cr 196 I	Cr 106 Col _{hd} 136 I
c		Cr 168 I	Cr 217 Col _{hd} 233 I
d		–	Cr 237 Col 245 I
e		glassy	glassy

Also, **86** forms monolayers at the air-water interface as deduced from surface pressure vs surface concentration measurements [103]. It was observed that the macrocycles and the amide linkage touch the water surface while the aromatic and aliphatic substituents are tilted upright and point towards the air.

Ringsdorf also investigated derivatives of [14]-N₄ and [18]-N₆ **88** and **89** with aliphatic (**a**), rod-like aromatic (**b–d**) or taper-shaped aromatic (**e**) substituents [104] (Table 5). While none of the smaller macroheterocycles **88** were found to be liquid crystalline, most of **89** exhibit enantiotropic columnar hexagonal mesophases as deduced from X-ray measurements¹ and optical textures. Exceptions are the hexadecanoic acid substituted **89a** as well as the gallic acid substituted **89e**. The observed mesophases of derivatives **89c,d** occur at far higher temperatures as compared to **89b** which might be due to the extended aromatic core in **89c,d** resulting in increased interactions between neighboring molecules. It was concluded that the sixfold symmetry and the presence of a rod-like substituent attached via an sp²-carbon are essential for the formation of stable columnar phases.

¹ It has to be noted that only the (001) reflection accompanied by a wide-angle halo was observed which would also account for a smectic phase. Yet, the textures indicate a columnar order.

Scheme 44 The first liquid crystalline [14]-N₄ derivative **90**



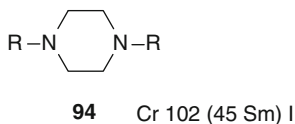
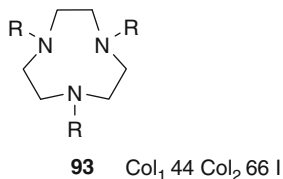
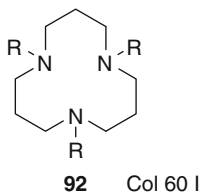
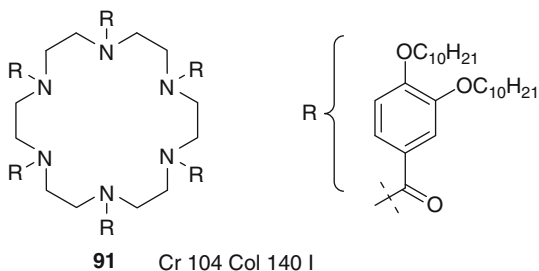
Lattermann found that the sixfold symmetry is not important for the presence of columnar mesophases in [14]-N₄ when appropriate peripheral groups are chosen [105]. As substituents with one terminal alkyl (**88a–d**) chain and with three terminal alkyl chains (**88e**) are not able to induce liquid crystalline behavior in **88** (Table 5) [104], a substituent with two alkyl chains, namely 3,4-bis(alkyloxy)benzoyl, was chosen since it has been known to induce liquid crystalline phases in other systems. A mesophase (most likely Col_h due to the texture) was observed between 96 and 132 °C for **90** (Scheme 44).

Based on the observations by Lehn that large polyamine rings do not exhibit stable mesophases [104] and the previous finding that 3,4-bis(alkyloxy)benzoyl substituted [14]-N₄ **90** shows columnar mesomorphism [105], Lattermann synthesized [18]-N₆, [12]-N₃, [9]-N₃ [106], and piperazine ([6]-N₂) [107] derivatives **91–94** with 3,4-bis(decyloxy)benzoyl substituents (Scheme 45). It was found that compounds **91–93** exhibit columnar mesophases while **94** exhibits a monotropic smectic phase. Derivatives **92**, **93** with 12- and 9-membered rings do not crystallize from the first cooling cycle onwards. The columnar phases (deduced from their POM textures) supercool and are stable even below room temperature. Interestingly, the clearing points decrease with decreasing ring size (with the exception of **94**).

Lattermann [106] and Ford [108] showed that the presence of water can change the properties of liquid crystalline polyamines like **91** and explained the different phase transition temperatures obtained by different groups by the presence of one to four water molecules in derivatives of [18]-N₆ as deduced from elemental analysis.

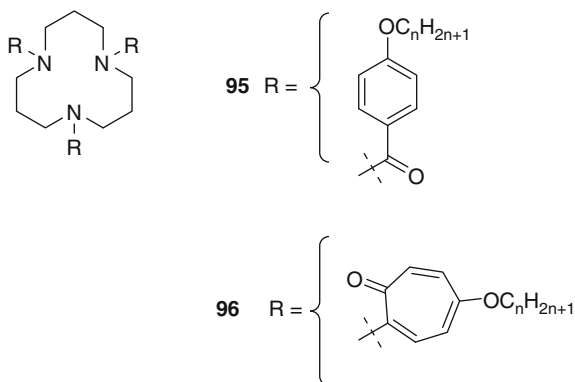
As all cyclic polyamines presented up to now were assigned to be columnar hexagonal based on their high viscosity, the typical texture or X-ray measurements devoid of the (110) or any higher reflection, Heiney and Smith [109] reinvestigated Lehn's [5] polyamine **1**. Scattering experiments were carried out using laboratory

Scheme 45 Liquid crystalline cyclic polyamines **91–94** with different ring sizes

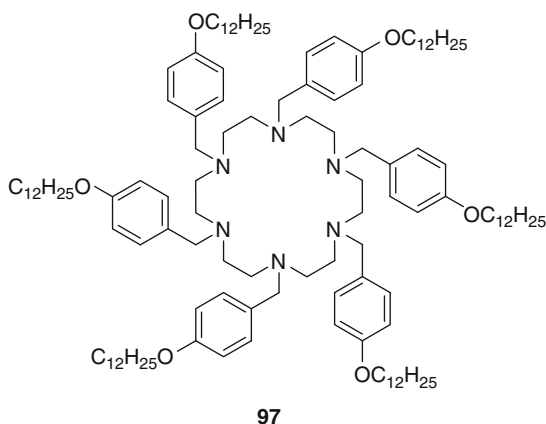


and synchrotron X-ray sources and were found to show only the (001) reflection accompanied by a broad wide-angle halo accounting for a smectic A or C phase. There are arguments for columnar as well as for smectic structures and neither of them could be ruled out. In a later study, Lehn [110] probed the columnar hexagonal structure of the mesophase based on X-ray and miscibility (with other Col_h mesogens) experiments.

Mori [111] removed one alkyl chain from derivative **92** to obtain **95** (Scheme 46). Removal of one side chain changed the mesophase type from columnar to smectic A with an interdigitated jellyfish-like arrangement of **95**. The addition of tropolone side arms in **96** led to the formation of cubic *Pn3m* phases as suggested by X-ray diffraction. In the cubic phase, the molecules are arranged in a disk-like conformation with overlapping cores. The columns are branched and undulated leading to the three-dimensional skeleton of the cubic phase with the alkyl chains arranged around the skeleton. It was interesting to observe that in **95** the mesophase stability increases with increasing chain length

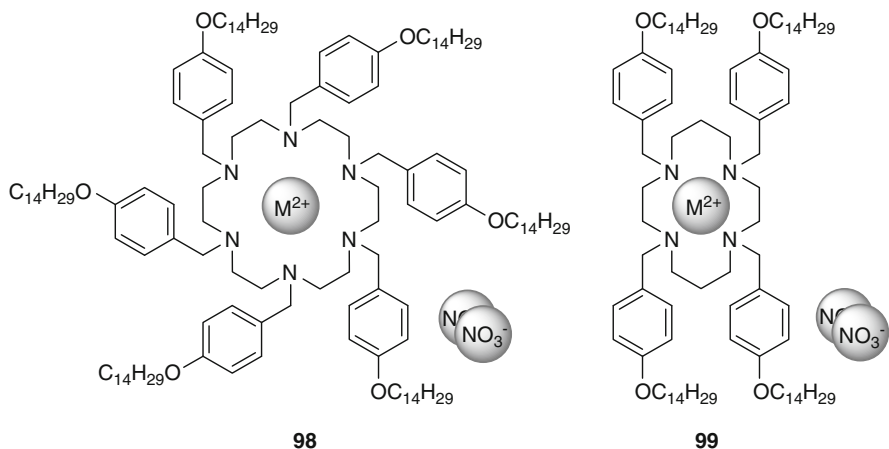
Scheme 46 Liquid crystalline [12]-N₃ **95**, **96****Table 6** Liquid crystalline properties of **95**, **96**

	<i>n</i>	Phase transitions		<i>n</i>	Phase transitions
95a	12	Cr 98 Cub 118 I	96a	12	Cr 63 I
95b	14	Cr 94 Cub 111 I	96b	14	Cr 64 SmA 79 I
95c	16	Cr 92 Cub 107 I	96c	16	Cr 70 SmA 81 I
95d	18	Cr 88 Cub 98 I	96d	18	Cr 69 SmA 87 I

Scheme 47 Non-mesomorphic amine-substituted cyclic [18]-N₆ **97**

while for **96** the mesophase stability decreases with increasing chain length (Table 6). The authors concluded that, for longer alkyl chains, a more efficient space filling is possible, destabilizing the cubic phase. It was proposed that for even longer chains, **96** should also exhibit smectic phases.

Heiney and Smith removed the carbonyl groups from Lehn's system **1** by reduction with LiAlH₄ in order to find out about the necessity of amide links for the presence of mesophases [109]. Compound **97** (Scheme 47) with amine instead of amide links show no mesomorphism.



Scheme 48 Complexation of transition metal nitrated by **98**, **99**

Table 7 Mesomorphic properties of complexes **98**, **99**

Complex	Ratio host/guest	Phase transition temperatures (°C)
Co(NO ₃) ₂ · 98	2:1	Cr 30 N _D 60 I
Ni(NO ₃) ₂ · 98	1:1	Cr 29 M _X 95 I
Cu(NO ₃) ₂ · 99	1:1	Cr 18 M _X 160 decomp

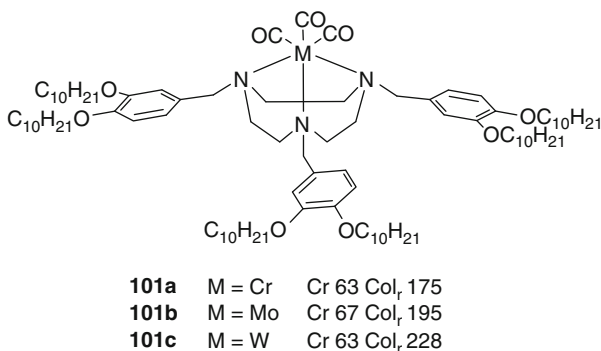
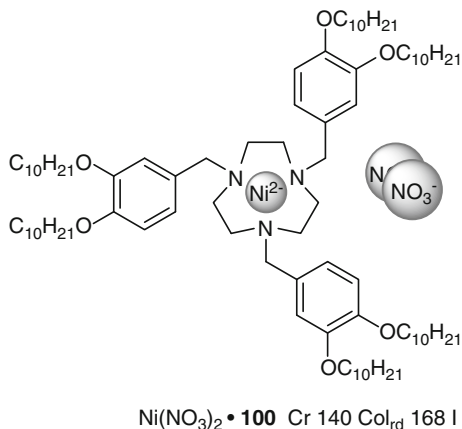
Ringsdorf investigated the complexation of Co(NO₃)₂, Ni(NO₃)₂, and Cu(NO₃)₂ on the mesomorphic behavior of amine-linked **98** and **99** [112] (Scheme 48). Complexation induced mesomorphism in both substrates (Table 7).

Cobalt(II) nitrate induces a columnar nematic phase in the 1:2 complex with **98** (Table 7) as deduced from X-ray scattering which is stable for 30 K. Also, nickel(II) nitrate turned **98** into a liquid crystal with an unknown phase. The complex between **99** and copper(II) nitrate showed the same unknown mesophase. The phase range was ~140 K but the samples decompose before clearing. A possible reason for the induction of a mesophase by complexation is the stiffening of the crown and the adjacent flexibly linked groups [112].

By reduction of **93** [106] with BH₃·THF, Lattermann was able to obtain tridentate [9]-N₃ derivative **100** [113] (Scheme 49). While the host system **100** is only crystalline, complexation with Ni(NO₃)₂ induced a columnar rectangular phase as confirmed by X-ray scattering experiments.

Complexation of **100** with carbonyl complexes of chromium, molybdenum, and tungsten yielded liquid crystalline complexes **101a–c** [114] (Scheme 50). All derivatives **101** melted at similar temperatures into the columnar rectangular mesophase (deduced from WAXS and SAXS measurements). However, the clearing points were strongly dependent on the metal center and increased with increasing atom number. Upon complexation, the aza crown macrocycle loses its flexibility, with the metal carbonyl fragment located above the crown leading to a cone-shaped

Scheme 49 Induction of columnar phases in **100** by complexation of $\text{Ni}(\text{NO}_3)_2$



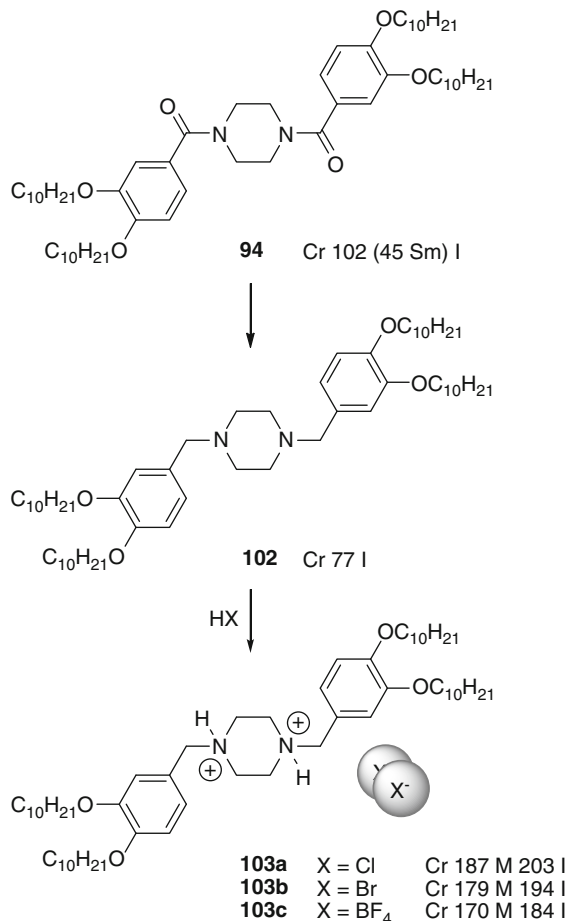
Scheme 50 Uptake of group six metal carbonyl complexes by **100**

molecule. The molecular cones can be stacked over each other and the resulting columns are comfortably accommodated within a rectangular phase.

Interesting effects were not only found upon complexation of amine substituted aza crowns, but also upon protonation. Lattermann reduced piperazine amide derivative **94** which showed a monotropic smectic phase to obtain crystalline **102** (Scheme 51). Subsequent protonation with various acids gave **103** [107] showing mesophases with broken focal-conic textures suggesting columnar phases (Scheme 51). Under the conditions of SAXS measurements, the compounds decomposed so that a clear assignment of the mesophase was not possible. Interestingly, with increasing size of the anion, the melting and clearing points decreased.

Ringsdorf investigated the photochemical properties of **89c** carrying six cinnamoyl substituents around the [18]-N₆ core [115]. Upon irradiation of *E*-**89c** in its liquid crystalline state with UV light, the mesomorphism was lost after a short time due to isomerization of the double bond (way A in Scheme 52). This showed

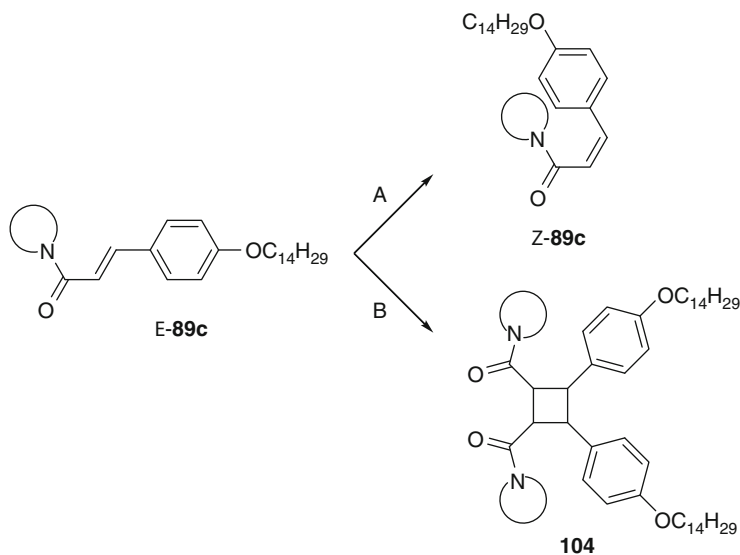
Scheme 51 Piperazine-based ionic liquid crystals **103** and the effects of anion exchange



that the *Z*-isomer of the side chain suppresses mesomorphism. Upon irradiation of *E*-**89c** in cyclohexane solution, *E/Z*-isomerization (way A in Scheme 52) was observed until a steady state was reached. Upon further irradiation, [2+2] photocycloaddition (way B in Scheme 52) was observed. GPC analysis showed the presence of dimers, trimers, and higher aggregates (up to 20-mer) of **89c** in a tube-like array. The cycloaddition reaction is strongly dependent on the solvent – in chloroform various unidentified side-reactions took place. The cycloaddition is another way to lock the columnar alignment of the molecules and feasible only in non-polar solvents.

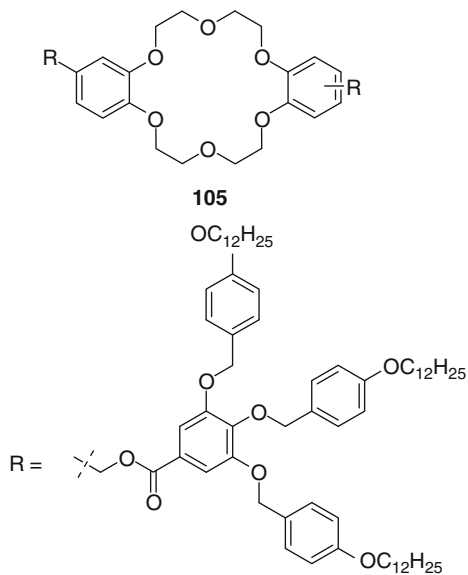
2.5.2 Crown Ethers with Several Taper- or Disc-Shaped Substituents

Hirose studied liquid crystal **105** consisting of a central dibenzo[18]crown-6 macrocycle and Percec-type side group dendrons (Scheme 53) [116].



Scheme 52 Possible reaction pathways of *E*-**89c** upon UV irradiation. A: *E/Z* isomerization, B: [2+2] cycloaddition

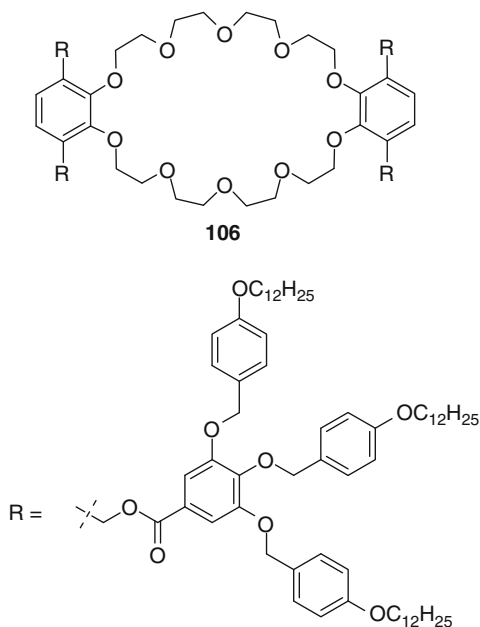
Scheme 53 Dibenzo[18] crown-6 **105** modified with Percec-type dendrons



The mesophase of **105** could not be clearly identified due to missing X-ray experiments but it was considered to be a columnar phase as deduced from polarizing optical microscopy. It was found that complexation with LiClO₄ and NaClO₄ leads to a decrease of the melting and clearing point but increasing the

Table 8 Phase transition temperatures of **105** and $\text{MClO}_4\cdot\mathbf{105}$

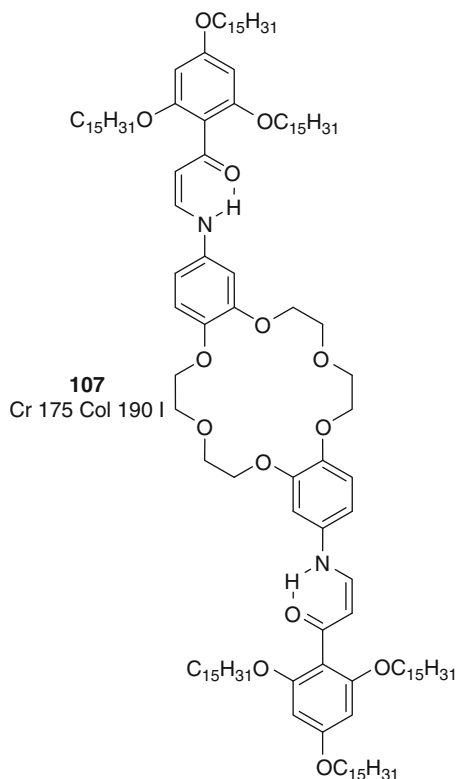
Compound	Phase transition temperatures ($^{\circ}\text{C}$)
105	Cr 125 M_{X1} 135 M_{X2} 145 I
$\text{LiClO}_4\cdot\mathbf{105}$	Cr 95 M_{X1} 102 M_{X2} 112 M_{X3} 117 I
$\text{NaClO}_4\cdot\mathbf{105}$	Cr 109 M_{X1} 121 M_{X2} 137 I
$\text{KClO}_4\cdot\mathbf{105}$	Cr 124 M_{X1} 129 M_{X2} 134 M_{X3} 144 I

Scheme 54 Dibenzo[30] crown-10 derivative **106** carrying four Percec-type dendrons

phase range slightly. Complexation with KClO_4 did not change the transition temperatures or the phase range (Table 8). The ionic conductivity of **105** and $\text{KClO}_4\cdot\mathbf{105}$ was measured and it was found that complexation increases the ionic conductivity by ~ 1.5 orders of magnitude to be $\sim 10^{-7} \text{ S m}^{-1}$.

Very recently, Chen published dibenzo[30]crown-10 fourfold substituted with first generation Percec-type dendrons **106** (Scheme 54) [117]. Liquid crystalline properties were not described for dry **106** but it was demonstrated that **106** is a powerful gelator of *n*-dodecane. For concentrations of **106** $> 0.1\%$ (w/v), a gel with columnar rectangular lattice (*c2mm*) was formed upon cooling from the isotropic solution. The authors gained a deeper understanding of the mechanism of gelation: in the first step, the molecules self-assemble into cylindrical micelles. Upon further cooling, the micelles grow and form fibers which entangle and lead to a solid-like gel. Furthermore, the authors accomplished the solubilization of the cationic dye rhodamine B in *n*-dodecane. The solvent, the dye, and **106** were heated until all constituents were dissolved. Upon cooling, a gel was formed with rhodamine B included in the crown ether cavities. Possible practical applications of such functional gels were seen in drug delivery, filtration, or separation.

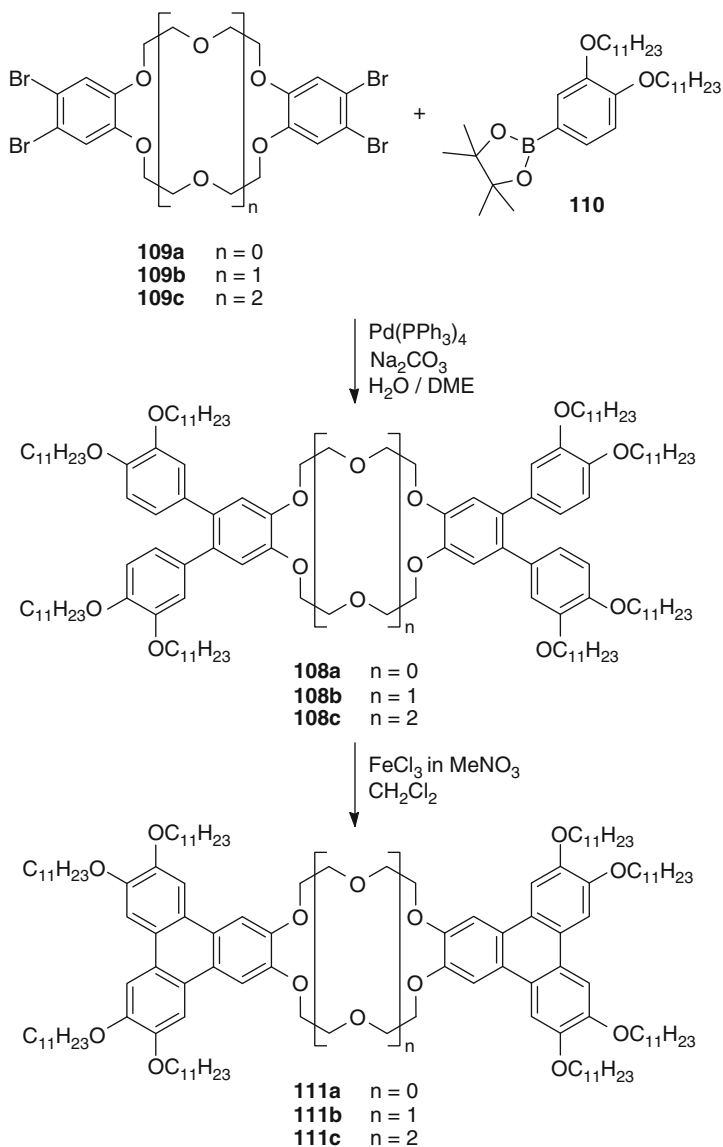
Scheme 55 Liquid crystalline derivative **107** of dibenzo[18]crown-6 stabilized by internal hydrogen bonds



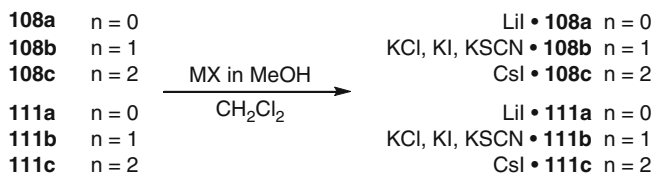
Akopova synthesized enamine ketone derivative **107** of dibenzo[18]crown-6 (Scheme 55) which exhibits columnar mesomorphism [8]. An interesting feature of compound **107** is the hydrogen-bond mediated stabilization within the side group.

Laschat developed a method by which a variety of liquid crystalline crown ethers of different ring sizes with two *o*-terphenyl or triphenylene substituents are conveniently accessible. Derivatives with *o*-terphenyl substituents of [12]crown-4 **108a** [118], [18]crown-6 **108b** [55, 119], and [24]crown-8 **108c** [118] were synthesized from the respective 4,4',5,5'-tetrabromodibenzo[18]crown-6 **109a–c** and boronic acid **110** in a Suzuki coupling reaction (Scheme 56). Oxidative cyclization using FeCl₃ as oxidant gave the corresponding triphenylene-substituted crown ethers **111a** [118], **111b** [120], and **111c** [118] (Scheme 56). Compounds **108** and **111** were studied with respect to their liquid crystalline properties.

An essential part of the studies was also to gain insight into the effects of complexation of salts on liquid crystalline phases. Crown ethers **108a**, **111a** with ring sizes of 12 atoms were complexed with LiI [118] (Scheme 57). The homologs **108b**, **111b** with central [18]crown-6 cores were complexed with a variety of potassium salts (e.g., KCl, KI, KSCN) [55, 120] in order to obtain information



Scheme 56 Synthesis of substituted crown ethers **108**, **111** with varying ring size



Scheme 57 Synthesis of crown ether complexes

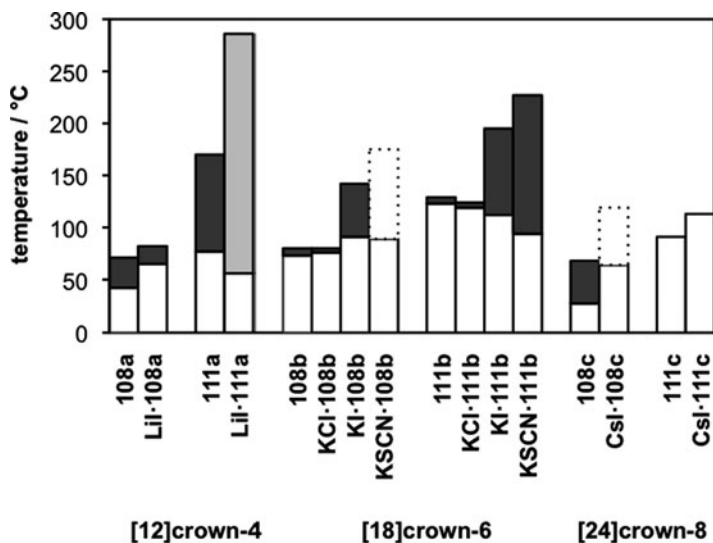
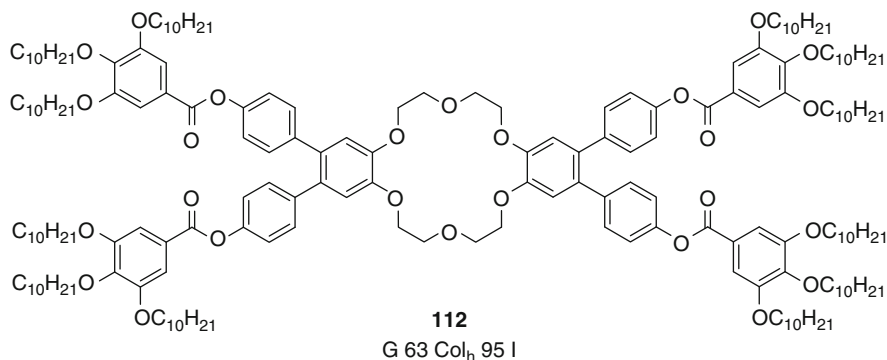


Fig. 15 Mesomorphic behavior of **108**, **111** and their metal complexes; *white shade* crystalline, *grey shade* columnar hexagonal ordered, *black shade* columnar, – plastic

about the influence of the different counterions (Scheme 57). Crown ethers **108c**, **111c** with a 24-membered macrocycle were complexed with CsI (Scheme 57) [118].

Several interesting trends were observed comparing the different compounds (Fig. 15²). First, triphenylene-substituted crown ethers **111** generally possess higher clearing temperatures compared with *o*-terphenyl-substituted **108**. The reason can be seen in π - π -stacking, which is stronger in **111** than in **108**. Second, the clearing temperatures and phase widths are dependent on the size of the macrocycle, especially for the series **111a-c**. While **111a** possesses a columnar hexagonal phase with a range of 93 K clearing at 170 °C, **111b** clears at 129 °C possessing a columnar rectangular range of 6 K. Finally, **111c** clears at 91 °C and is devoid of a mesophase. Third, complexation with salts possessing hard counterions (e.g., KCl) leaves the mesomorphic properties virtually unchanged (KCl·**108b** possesses a columnar rectangular phase range of 4 K compared with 7 K observed for **108b**) while salts with soft counterions (e.g., LiI, KI, and KSCN) lead to a significant increase in the mesophase range (51 K for KI·**108b**, 133 K for KSCN·**111b**). It was concluded from NMR experiments that tight ion pairs are present in these complexes and are responsible for the increase of the clearing points [55, 120].

² A variety of phase geometries (*p6mm*, *p2mg*, *p2gg*, *c2mm*) was observed depending on lateral substituent and complexed salt. Details can be found in [55, 118–120].



Scheme 58 Dibenzo[18]crown-6 **112** modified with four gallic acid groups

In the case of KSCN-**108b**, the interactions are too strong, leading to a plastic phase. In the case of LiI-**111a**, columnar hexagonal ordered phases were observed.

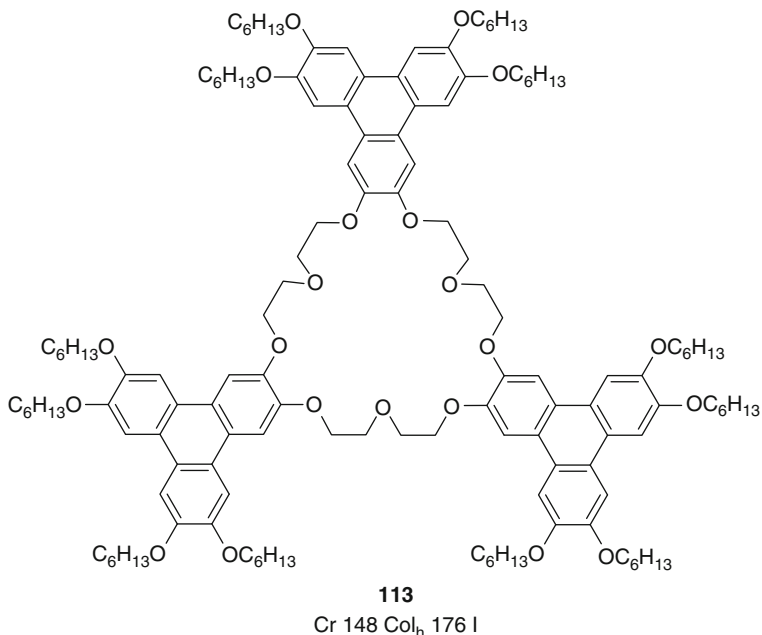
Summarizing, it can be stated that for the neat compounds, broad mesophases can be observed for small rings with rigid substituents (**111a**). If the ring is too large (**111c**), mesophases are absent. For complexation, a different picture emerges: as complexation can lead to the formation of ion pairs, the crown ether should be of medium size (**108b**, **111b**) in order to obtain broad mesophases. For smaller crowns, complexation rigidifies the crown too much leading to ordered phases (LiI-**111a**). If the crown is too large and flexible (**108c**, **111c**), complexation cannot induce mesophases.

When the lateral substituents were changed from ether to gallic ester groups, a columnar hexagonal phase was observed for **112**, while complexation with KI destroyed the mesomorphic behavior [121] (Scheme 58). The presence of ion pairs in the complex presumably leads to unfavorable interactions between neighboring molecules leading to non-mesogeneity.

He and Cammidge prepared liquid crystal **113** (Scheme 59) with a central [27] crown-9 moiety, three attached triphenylene units carrying a total of 12 hexyloxy chains and exhibiting a columnar hexagonal mesophase [122].

2.5.3 Summary

The compounds presented in this section possess, in most cases, columnar phases as expected from their molecular shape. Aza crown ethers and conventional crowns offer a multitude of possibilities to add functional groups. Possible applications can be seen in the field of sensors or functional channels. Unfortunately, no applications have been reported yet. Addition of polymerizable groups might lead to functional membranes as shown in Scheme 40.



Scheme 59 [27]crown-9 **113** with three triphenylene substituents

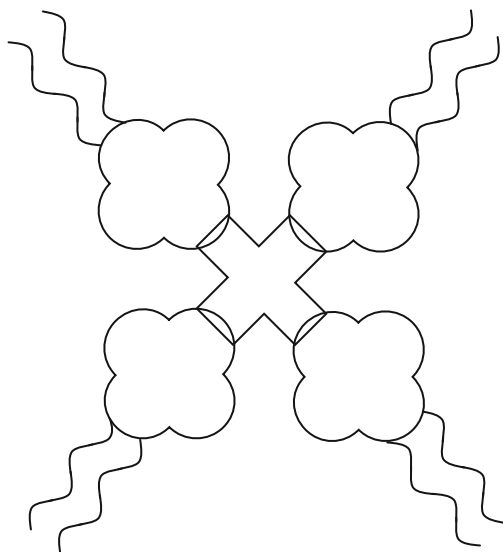
2.6 Crown Ethers with a Central Phthalocyanine

Possessing a flat shape, phthalocyanines are predestined to form columnar mesophases. The addition of crown ethers (Fig. 16) can yield interesting materials that can complex two different salts (one in the crown, one in the phthalocyanine) leading to interesting columnar channel structures.

Nolte synthesized the first liquid crystalline phthalocyanine **114a** bearing crown ether moieties in the periphery (Scheme 60). In total, eight decyloxy chains were present in the molecule [123]. The phthalocyanine was also equipped with a dihydroxy silicon group in the center in order to obtain polymerizable **114b** [124].

Compound **114a** showed a columnar hexagonal mesophase that was confirmed by X-ray scattering experiments [123]. The mesophase appeared at 170 °C while the isotropic phase could not be observed as **114a** decomposed above 320 °C. Despite the high number of alkyl chains, **114a** was insoluble in most organic solvents. Only boiling chloroform and toluene could dissolve it. Chloroform solutions of **114a** with a minimum concentration of 7 mg mL⁻¹ turned into a gel upon cooling. TEM photographs showed the presence of a network of fibers. The fibers were several micrometers in lengths and consist of bundles of strands. The strands themselves are of molecular thickness (~50–60 Å). Within one fiber, the surprisingly high number of approximately 10⁴ molecules is accommodated

Fig. 16 Schematic representation of liquid crystalline crown ethers with a central phthalocyanine core



[123]. Compound **114b** can be regarded as multifunctional molecular cable with the central electron conducting phthalocyanine surrounded by the ion channels formed by the crown ethers and isolated by the alkyl chains.

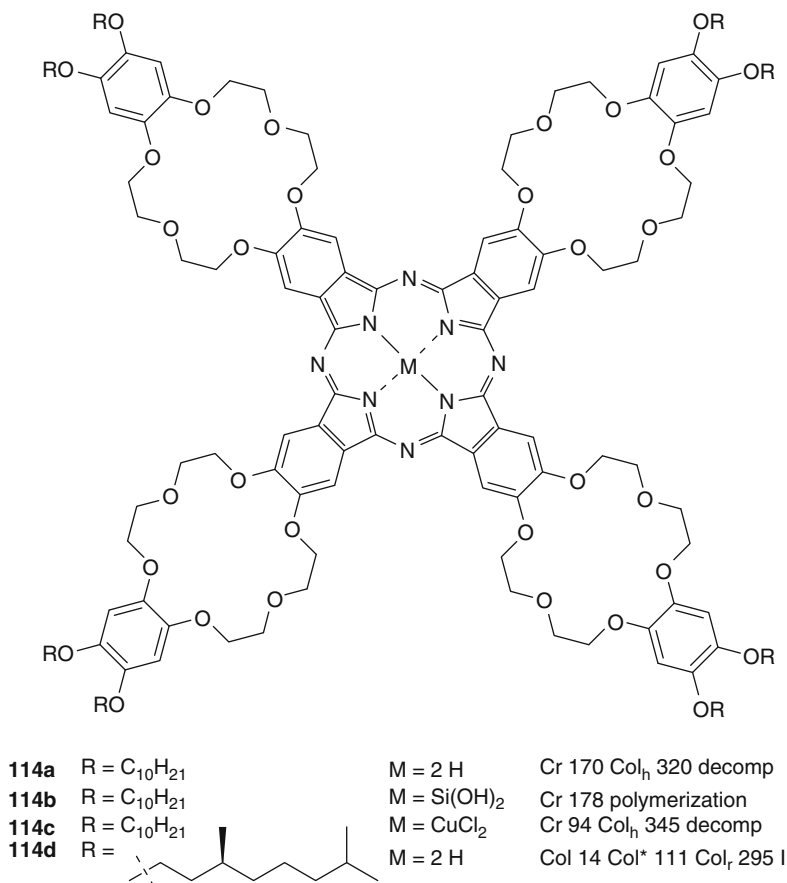
For **114b**, a completely different behavior was found [124]. This compound is crystalline, polymerizing at 178 °C. The axial hydroxy groups prevented stacking of the molecules within a columnar phase. The behavior of **114b** at the air-water interface was examined and it was found that monolayers are formed. The phthalocyanine entity is lying flat on the water while the crown ethers and the alkyl chains point into the air. Addition of KCl changed the shape of the molecule leading to the crown ethers also lying flat on the water. It was possible to join the monolayers onto a glass substrate in order to obtain a Langmuir–Blodgett film [124].

Copper complex **114c** also shows columnar hexagonal phases [125]. Copper leads to an increase in the columnar phase range. The melting point is lowered to 94 °C while the decomposition does not occur before 345 °C.

Compound **114d** possesses significantly lower transition temperatures (Scheme 60) due to the branched side chains [126]. A columnar phase is present even below room temperature. At 14 °C, a new chiral columnar phase was observed while above 111 °C, an achiral columnar rectangular phase was observed. The spiral-pattern texture of **114d** in the chiral Col* mesophase is shown in Fig. 17.

Three possible arrangements of **114d** leading to the Col* phase are shown in Fig. 18. The molecules are either in a spiral staircase arrangement (left), staggered against each other at constant staggering angles (middle), or tilted and gradually rotated (right) as the most likely arrangement.

Interesting aggregation behavior was found for **114d** [128]. In chloroform, gel formation was also observed. The gel consists of long, left-handedly twisted fibers of nanometer diameter and micrometer lengths (Fig. 19a, b). These fibers



Scheme 60 Crown ether phthalocyanines **114** with different substituents in the central core

themselves consist of up to 25 fibers possessing the diameter of a single **114d** (~60 Å) (Fig. 19a, b).

Addition of potassium ions to the fibers leaves the fibrous structure intact but destroys the helicity [128]. Sandwich complexes between the cation and **114d** are observed. With higher concentrations of potassium, the sandwich complexes break down and isolated $4K^+ \cdot 114d$ are observed (Scheme 61). In both complexed forms the salt blocks the chirality transfer from the side chains to the supramolecular assemblies. Such fibers with controllable chirality can be interesting materials for molecular switches or in sensors devices.

At the gel-graphite interface, **114d** forms hexagonal (side-on arrangement of **114d** on the surface) and lamellar (edge-on arrangement) phases [129]. It could also be shown that **114a** can be oriented in high magnetic fields [130].

Ahsen synthesized liquid crystalline phthalocyanine complexes **115** equipped with four monoaza[15]crown-5 moieties substituted with substituted gallic acids

Fig. 17 Spiral-pattern texture of **114d** in the Col* phase. Reproduced by permission of Taylor & Francis (www.informaworld.com) from [127]

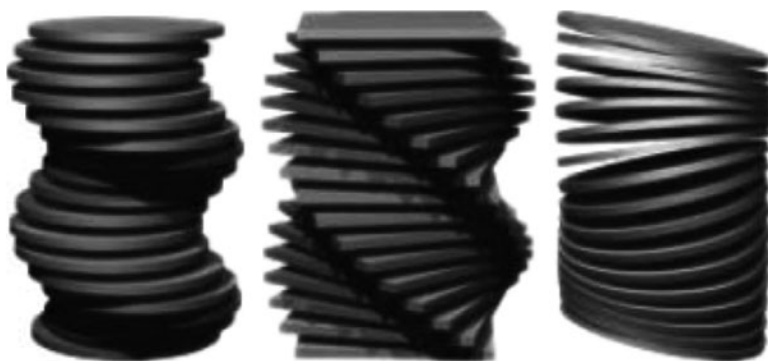
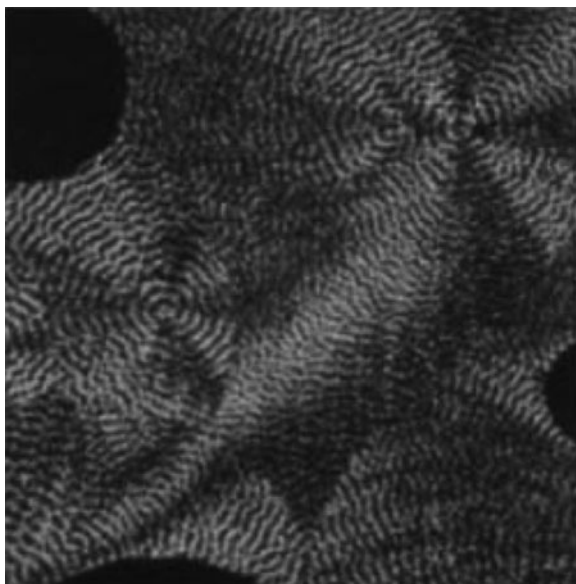
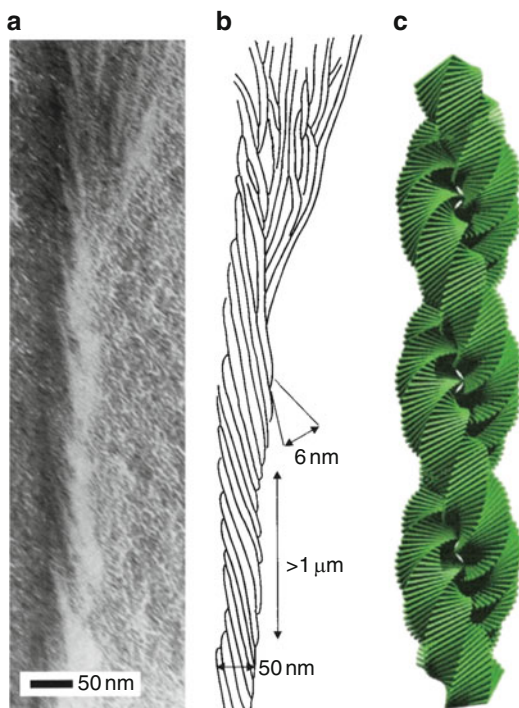


Fig. 18 Spiral staircase (*left*), staggered (*middle*), or tilted and rotated (*right*) arrangement of **114d** in the Col* phase. Reproduced by permission of AAAS from [128]

via amide linkages [131] (Scheme 62). From ~ 110 °C, both the zinc (**115a**) and the nickel complex (**115b**) exhibit a columnar hexagonal mesophase. Transition to the isotropic phase could not be observed as decomposition started at temperatures exceeding 320 °C.

Akopova reported liquid crystalline phthalocyanines **116a–c** (Scheme 63) with eight peripheral crown ethers devoid of alkyl chains [132]. Nonetheless, discotic nematic phases could be observed as derived from miscibility experiments with the discotic nematogen hexa(cyclohexanebenzoyloxy)triphenylene and optical textures. In the case of metal-free **116a**, a phase width of 43 K was found. Complexation with Zn(II) (**116b**) decreased the phase range to 35 K and with

Fig. 19 TEM micrographs of gels of **114d** in chloroform showing left-handed coiled-coil aggregates (a) and schematic representation thereof (b). (c) Calculated model of the coiled coils. Reproduced by permission of AAAS from [128]

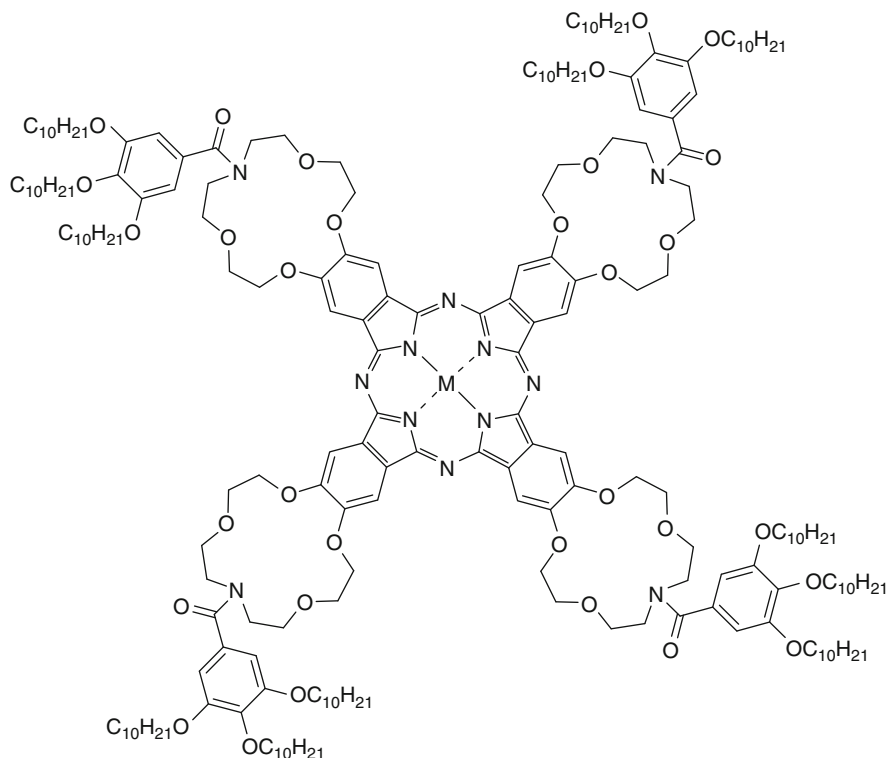


Scheme 61 Schematic representation of the formation and breakdown of sandwich complexes between K^+ and **114d**. Reproduced by permission of AAAS from [128]

Ni(II) (**116c**) displayed a mesophase for only 5 K. Complexation of the phthalocyanine seems to increase the interaction between the molecules leading to higher ordered systems with high melting points into the subsequently small mesophases.

The combination of a phthalocyanine ring with crown ether moieties and redox-active tetrathiafulvalenes gave compound **117** (Scheme 64) and was described by Zou as a good candidate for a redox-active Na^+ sensor [133].

Crown ether-phthalocyanines **118** ($n = 0, 1, 2$) (Scheme 65) were used as gas sensors for NO_2 . They were found to be superior to the previously used materials



115a M = Zn(II) Cr 117 Col_h >320 decomp
115b M = Ni(II) Cr 109 Col_h >320 decomp

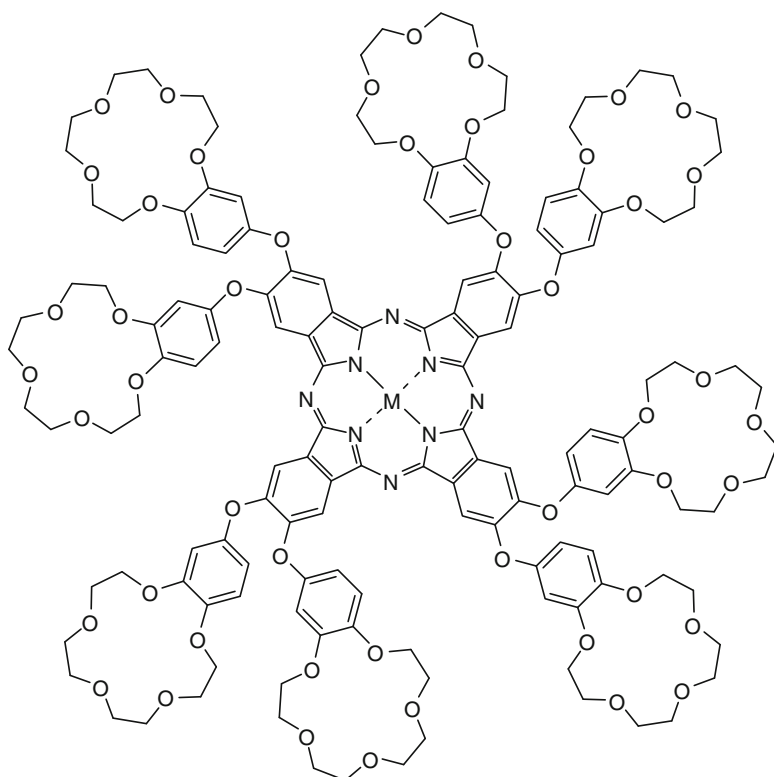
Scheme 62 Zn(II) and Ni(II) complexes of crown ether-modified phthalocyanine **115**

based on phthalocyanines without crown ethers. They offer faster responses and reversal times and can sense NO₂ even at ppb levels [134].

In summary, phthalocyanines modified with crown ethers are interesting synthetic targets as they are prone to form columnar phases. Their electron conductivity and complexation properties make them interesting candidates for the design of sensor materials or supramolecular switches.

2.7 Crown-Like Cyclophanes

Stoddart synthesized biphenylophane derivatives **119** depicted in Scheme 66 [135]. Compared with conventional biphenyl derivatives, the series of **119a–e** exhibits high melting and clearing temperatures. The incorporation of two mesogenic units into a macrocycle seems to be a powerful approach towards mesophase induction

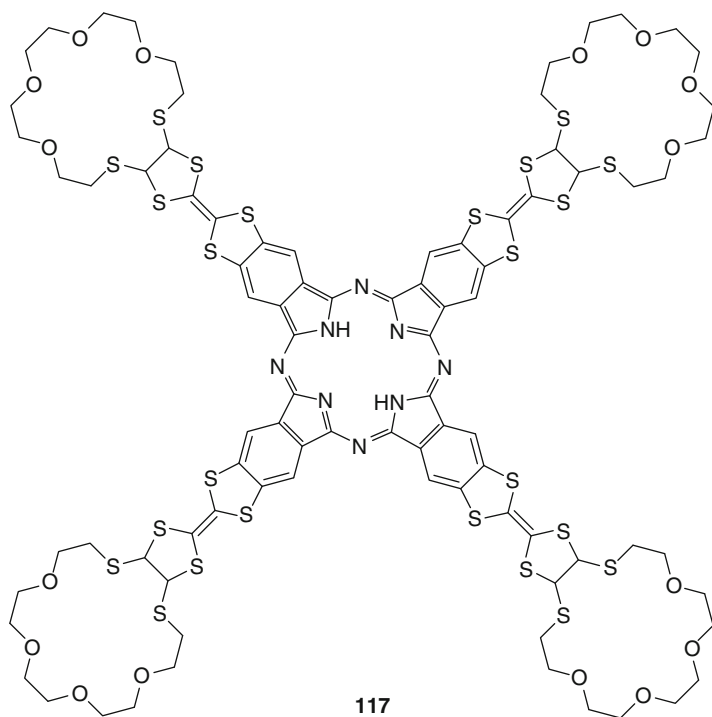


116a	M = 2H	Cr 255 N _D 298 I
116b	M = Zn(II)	Cr 254 N _D 289 I
116c	M = Ni(II)	Cr 293 N _D 298 I

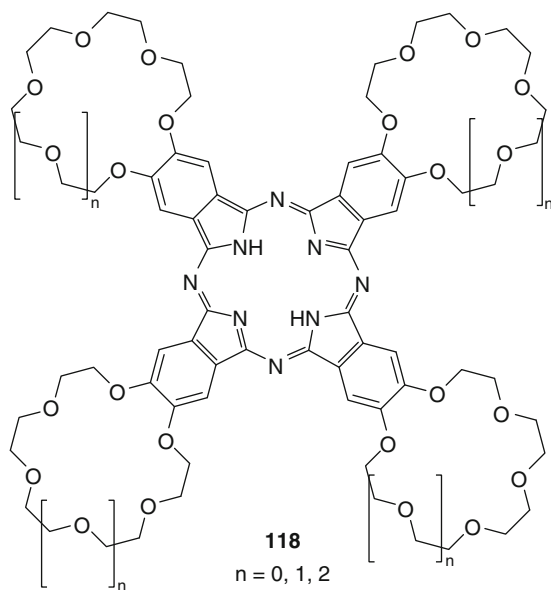
Scheme 63 Liquid crystalline crown ether phthalocyanine **116** without peripheral alkyl chains

and stabilization. Shortening one bridging chain (**119b**) increases the melting and clearing temperature. Lengthening of the linking chain (**119c**) lowers the phase transition temperatures. Compound **119c**, a constitutional isomer of **119a**, contains one longer and one shorter polyether chain. As expected, this “desymmetrization” leads to a depression of the melting and clearing point and the smectic phase range. The mesophase type, namely smectic E and smectic A [136], remains unchanged upon variation of the spacer chains.

Tschierske anticipated that the mesophase type and range is not only dependent on the spacer chains but also on the mesogenic units within the macrocycle. Cyclophane derivatives **120a–d** (Scheme 67) were synthesized and examined [136]. Indeed, the calamitic units have a strong impact on the mesomorphic properties. Phenyl benzoates **120a,b** exhibit nematic phases with significantly lower phase transition temperatures as compared with biphenylophane derivatives **119**. Compared with open-chain analogs, the mesophase stabilizing effect of

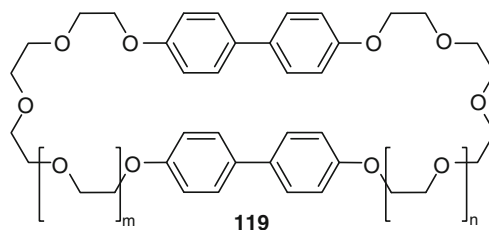


Scheme 64 Crown ether phthalocyanine **117** with redox-active tetrathiafulvalene groups

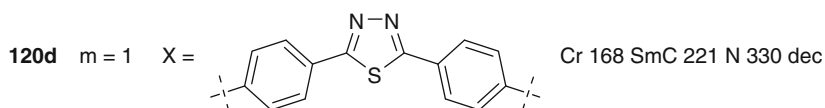
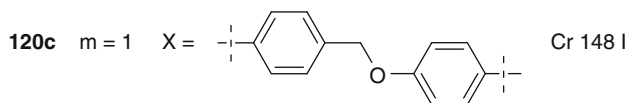
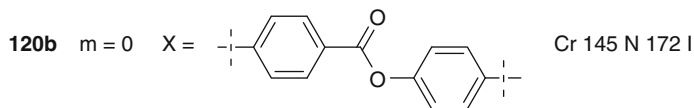
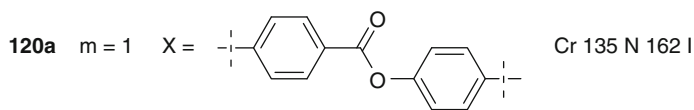
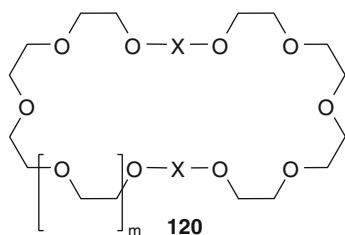


Scheme 65 Crown ether phthalocyanines **118** as sensor materials for NO_2

Scheme 66 Liquid crystalline biphenylophane derivatives **119**

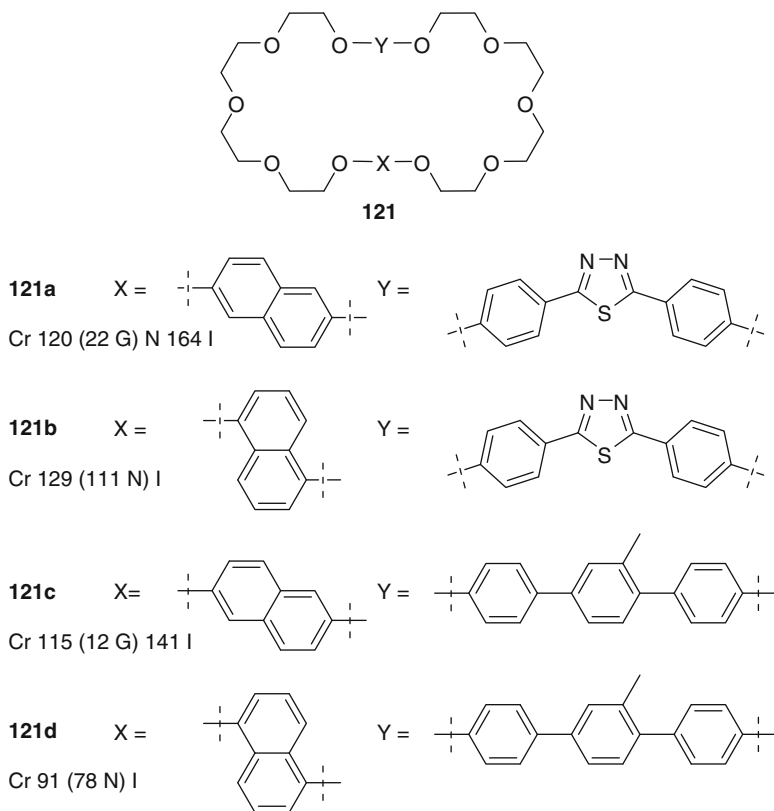


119a	$m = n = 1$	Cr 193 SmE 196 SmA 209 I
119b	$m = 0, n = 1$	Cr 212 SmE (212) SmA 217 I
119c	$m = 0, n = 2$	Cr 182 SmE 185 SmA 189 I
119d	$m = 1, n = 2$	Cr 173 SmE 176 SmA 186 I
119e	$m = n = 2$	Cr 156 SmE 161 SmA 167 I



Scheme 67 Liquid crystalline cyclophane derivatives **120**

cyclization could also be observed. The replacement of the carboxylic acid groups by the flexible oxymethylene group in **120c** lead to the loss of mesogeneity. Introducing a thiadiazole group can be a powerful tool for the induction of smectic C phases. As expected, **120d** exhibits a smectic C phase, followed by a nematic



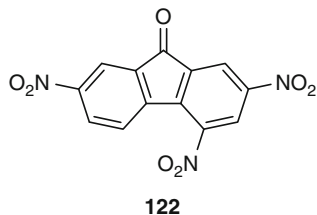
Scheme 68 Unsymmetrical substituted cyclophane derivatives **121**

phase at 221 °C. Clearing could not be observed due to decomposition above 330 °C.

The introduction of suitable mesogenic building blocks into macrocycles will generally have an enormous effect on the stability of mesophases. The reason results from the restricted flexibility of the linked calamitic units.

Tschierske also investigated derivatives **121** (Scheme 68) with different aromatic units in the macrocycle [137]. Besides the conventional thermotropic mesogens *p*-terphenyl or 2,5-diphenyl-1,3,4-thiadiazole, the non-mesomorphic naphthalene ring was included. The thiadiazoles are interesting compounds for electron-transfer interaction and for the templated synthesis of rotaxanes and catenanes. Despite the presence of the non-mesogenic naphthalenes, **121a–d** exhibit nematic phases with high clearing temperatures. The stability of the phases is dependent on the substitution pattern of the naphthalene unit. The 2,6-derivatives **121a,c** display higher mesophase stabilities than the corresponding 1,5-substituted derivatives **121b,d**. The nematic phases of **121a,c** can be supercooled and freeze in a nematic glassy state at 22 and 12 °C, respectively. For **121b,d** monotropic phases

Scheme 69 2,4,7-
Trinitrofluorenone **122**

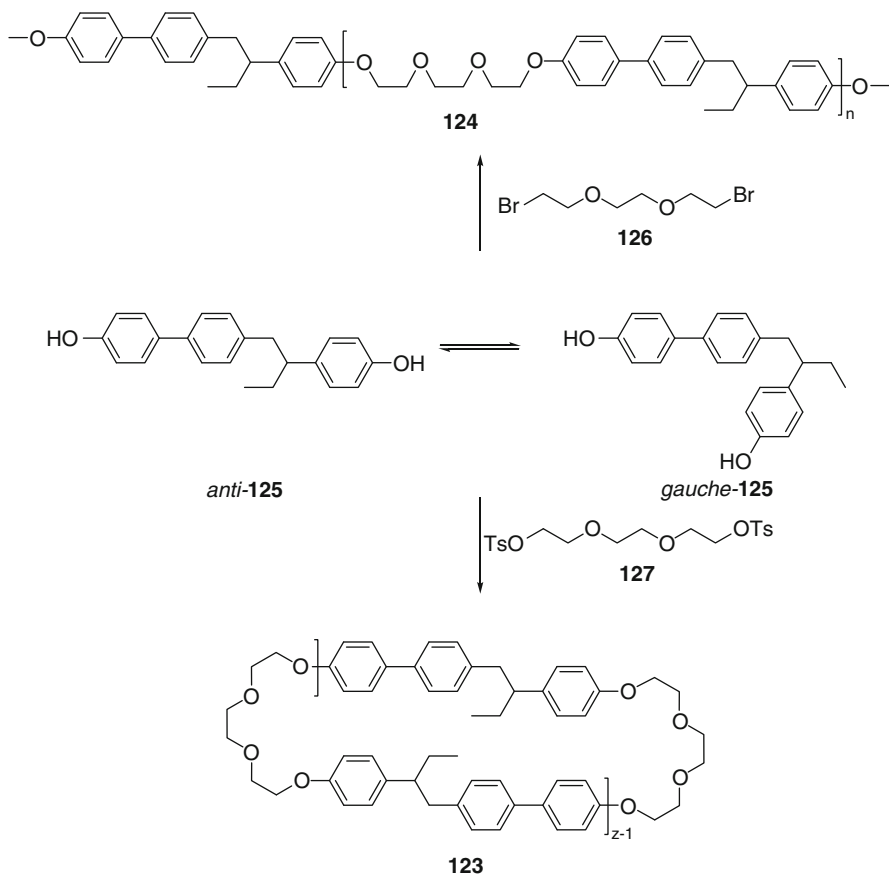


were found that did not show the nematic glassy state. Therefore, **121a,c** were the first glass-forming liquid crystalline cyclophanes.

Due to the electron-donating ability of naphthalene, compound **121a** was mixed with the electron acceptor 2,4,7-trinitrofluorenone **122** (TNF, Scheme 69) [137]. Upon mixing, a deep red color was observed. Under the POM, focal conic fan textures were observed, indicating a smectic A phase. While small amounts of TNF destabilize the nematic phase, larger amounts of it (~20 mol%) induce the smectic A phase. The attractive electron-acceptor/electron-donor interactions force the individual molecules to adopt a positional order which results in smectic A layers. Mixing of **121b–d** with TNF resulted in the same color but no smectic phases were induced. The reason can be seen in the twisted *p*-terphenyl structure and the 1,5-substitution pattern on the naphthalene ring.

Comparison of macrocyclic liquid crystals **123** based on triethylene glycol and 1-(4-hydroxy-4'-biphenyl)-2-(4-hydroxyphenyl)butane with varied degree of polymerization with their open-chain analogs **124** (Scheme 70) showed that macrocyclization overrides the established polymer effect in the formation and stabilization of liquid crystalline phases [138]. Contrary to what was thought in the past, the cyclic – and not the linear – architecture is the most powerful way to design molecular and macromolecular liquid crystals. It was found that for higher numbers of *z*, the *anti* conformer is found more often than the *gauche* counterpart. First, on increasing *z*, the cyclic **123** evolve from amorphous to liquid crystalline and back to amorphous. Second, an odd-even dependence of the isotropization temperature as a function of the ring size (i.e., the degree of polymerization) is observed. This is surprising because one would expect an odd-even effect with respect to the spacer chain length – not to the degree of polymerization. The main difference between the odd and even series of *z* in **123** is that in the odd series there is permanently one unit of **125** in the fold of the ring, resulting in a lower rigidity. The presence of the **125** unit in the fold is responsible for the odd-even effect which is not encountered in the linear liquid crystalline polymers **124**. This unusual behavior can lead to a design of nematic crown ethers with a predetermined placement of binding sites.

Crown ether binaphthyl derivatives **128–131** (Scheme 71) were synthesized and investigated by Akagi [139]. Compounds **128–131** were used to induce chiral nematic phases (N*) in liquid crystals. It was found that the helical twisting power increased with decreasing ring size. Helical polyacetylenes were synthesized in the N* phases. It was found that the interdistance between the fibril bundles of the helical polyacetylene was equal to the half-helical pitch of the N* liquid



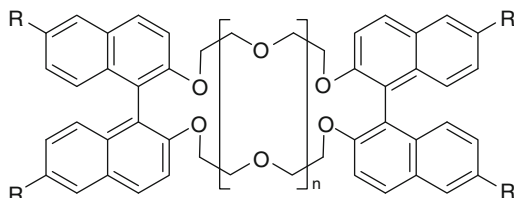
Scheme 70 Cyclic (**123**) vs linear (**124**) liquid crystalline polymers

crystal and the screw direction of the fibrils was opposite to that of the N* liquid crystal. Chiral dopants are promising in gaining control over the screwed structure of polyacetylenes.

2.8 Metallomesogens

The term “metallomesogen” is often used when a (transition) metal is complexed (by coordinative bonds between the *crown heteroatoms* and the metal center) by a crown ether. These compounds were discussed in the previous sections as “complexed crown ethers” (instead of “metallomesogens”) together with their uncomplexed precursors. In this section, mesogens with a covalent bond between

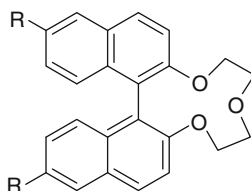
Scheme 71 Axial chiral crown-like binaphthyl derivatives **128–131**



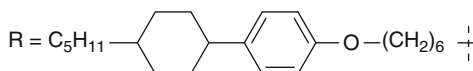
R-**128**, *S*-**129** $n = 1$

R-**129**, *S*-**129** $n = 2$

R-**130**, *S*-**130** $n = 3$



R-**131**

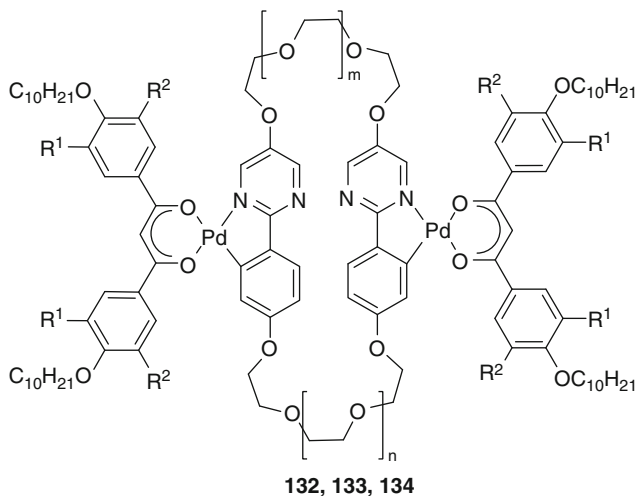


the metal and a *carbon atom that is not part of the crown ether macrocycle* will be discussed.

Tschierske synthesized the “butterfly” mesogens **132–134** (Scheme 72, Table 9). These compounds are based on a macrocyclic crown-like *para*-cyclophane ring containing two 2-phenylpyrimidine units. *Ortho*-palladation and subsequent treatment with substituted half-disks like β -diketones gave the desired dinuclear palladium complexes with 4 (**132**), 8 (**133**), and 12 (**134**) peripheral alkyl chains [127].

All uncomplexed *para*-cyclophanes show monotropic nematic phases upon cooling. For complex **132** with four alkyl chains, a fan-like texture was observed which corresponds to a smectic A phase (Table 9). Compound **134b** shows a mosaic-like texture (Fig. 20) typical for columnar mesophases. The columnar hexagonal phase could be unambiguously confirmed by temperature-dependent X-ray experiments as in the small angle regime of an aligned sample of **134b** a regular hexagon could be detected (Fig. 21).

Surprisingly, **133** with eight alkyl chains was not liquid crystalline (Table 9). With increasing number of alkyl chains a transition from a lamellar to a columnar organization of the molecules takes place. Due to the planar geometry around the Pd(II) centers linked by the macrocycle it is reasonable to assume that the molecules self-assemble in columnar phases. However, a certain number of chains are necessary to surround the molecules completely and to obtain columnar phases.



Scheme 72 *Ortho*-palladated “butterfly” mesogens **132–134**

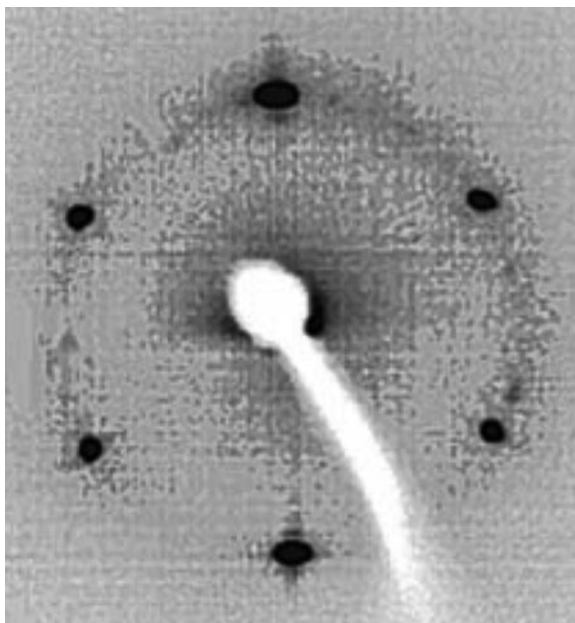
Table 9 Mesomorphic properties of **132–134**

Compound	<i>m</i>	<i>n</i>	R ¹	R ²	Phase transitions
132	3	1	H	H	Cr 197 SmA 207 I
133	3	1	OC ₁₀ H ₂₁	H	Cr 137 I
134a	3	1	OC ₁₀ H ₂₁	OC ₁₀ H ₂₁	Cr 110 Col _h 178 I
134b	1	2	OC ₁₀ H ₂₁	OC ₁₀ H ₂₁	Cr 108 Col _h 211 I
134c	1	3	OC ₁₀ H ₂₁	OC ₁₀ H ₂₁	Cr 110 Col _h 208 I



Fig. 20 Polarized light optical micrograph of the Col_h phase of **134b** at 103 °C. Reproduced by permission of The Royal Society of Chemistry from [127]

Fig. 21 Small-angle X-ray diffraction pattern of an aligned sample of **134b** at 110 °C. Reproduced by permission of The Royal Society of Chemistry from [127]



If this is not possible, the columnar order gets lost (**133**) or smectic layers are favored (**132**).

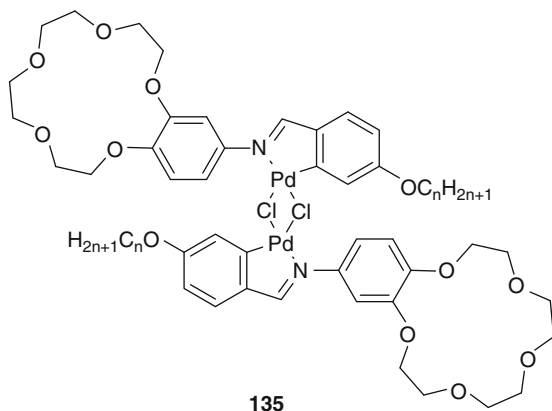
With an increasing number of linking polyether chains, the melting and clearing points increase (Table 9) as expected due to the increased rigidity of the molecules. Compounds **132**, **134** are interesting for further research and might open new possibilities to build well-defined structures containing transition metals and ion channels in close proximity to each other embedded in insulating surroundings.

Espinet synthesized imine-substituted benzo[15]crown-5 ethers which were not liquid crystalline. After orthopalladation and anion exchange, dinuclear chloride-bridged complexes **135** (Scheme 73) were obtained [140]. The dinuclear complexes exhibit enantiotropic smectic A phases. The smectic phase ranges of the series increase with increasing chain length in a range of 3 K (**135a**) to 62 K (**135b**). A problem of **135** is the high clearing temperature; the compounds start to decompose after three heating cycles.

In order to obtain mesophases with lower clearing temperatures and broader phases, the number of side chains was increased and the symmetry decreased by exchanging one ligand with a substituted β -diketone carrying two dodecyl chains [140]. The desired effect could be observed: the isotropization temperatures were significantly broadened and the mesophases gained in stability (37 K for **136a**, 65 K for **136b**, Scheme 74).

The mesogenic behavior of KClO_4 complexes was also studied, but none of the complexes $\text{KClO}_4\cdot\mathbf{135}$ and $\text{KClO}_4\cdot\mathbf{136}$ were liquid crystalline and melted accompanied by decomposition [140].

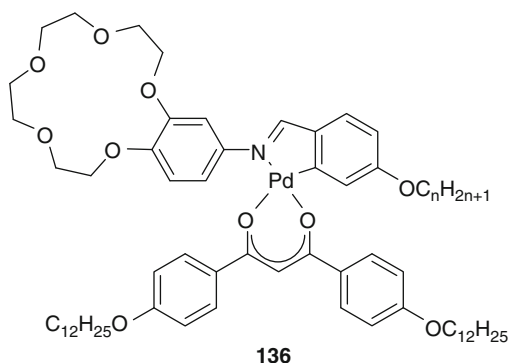
Scheme 73 Liquid crystalline Pd-organic compounds **135**



135a $n = 4$ Cr 220 SmA 223 I

135b $n = 12$ Cr 170 SmA 232 I

Scheme 74 Unsymmetrical Pd complexes **136** with improved mesogenic properties



136a $n = 4$ Cr 86 SmA 123 I

136b $n = 12$ Cr 70 SmA 135 I

Similar *ortho*-palladated complexes **137**, **138** (Scheme 75) were presented by Espinet and Coco [141].

All the Pd complexes show mesomorphic behavior. Although one might expect a columnar arrangement, due to the presence of the high number of alkyl chains in the periphery, enantiotropic smectic C phases were observed for **137a** and **138a** (Table 10) as deduced from POM and X-ray results. Complexes **137b** and **138b**, in contrast, show monotropic behavior (Table 10). The present phase could not be identified unambiguously. Complexation with KClO_4 produces an important change in the mesomorphic properties. Compared with the parent complexes, the potassium adducts have increased clearing temperatures and mesophase ranges (Table 10). Also, all potassium complexes are enantiotropic liquid crystals. Complexation makes the molecules more polar, the crown ethers become more

Scheme 75 Palladated complex **137**, **138** containing two dibenzo[18]crown-6 units

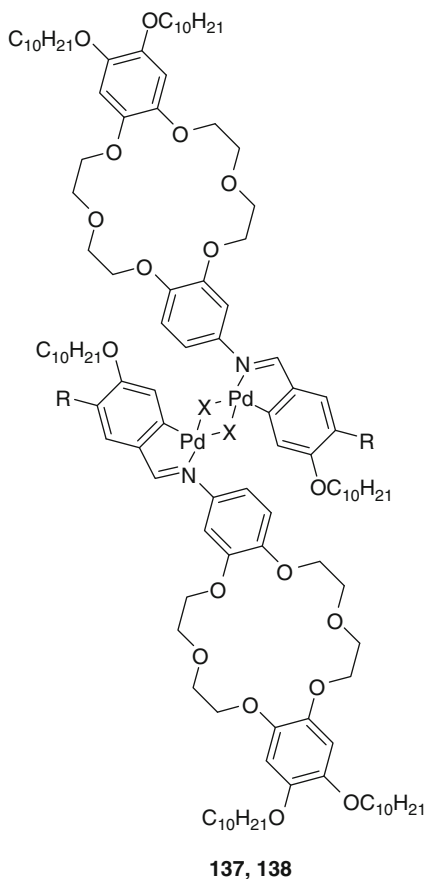
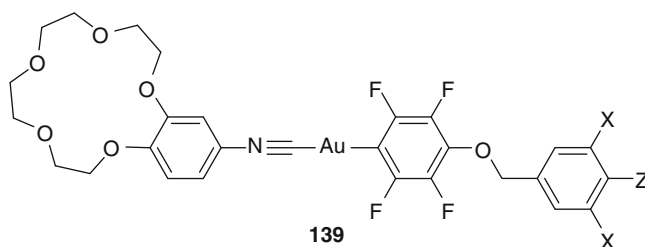


Table 10 Mesomorphic properties of **137, 138**

Compound	R	X	Phase transitions
137a	H	OAc	Cr 108 SmC 122 I
$\text{KClO}_4 \cdot \mathbf{137a}$	H	OAc	G 82 SmC 193 I
137b	$\text{OC}_{10}\text{H}_{21}$	OAc	I 77 M_X 44 G
$\text{KClO}_4 \cdot \mathbf{137b}$	$\text{OC}_{10}\text{H}_{21}$	OAc	Cr 94 M_X 147 I
138a	H	Cl	Cr 109 SmC 200 I
$\text{KClO}_4 \cdot \mathbf{138a}$	H	Cl	G 85 SmC 179 I
138b	$\text{OC}_{10}\text{H}_{21}$	Cl	I 139 M_X 90 Cr
$\text{KClO}_4 \cdot \mathbf{138b}$	$\text{OC}_{10}\text{H}_{21}$	Cl	G 110 M_X 207 I

rigid and, probably, the molecule gains in width. Combined with the improved microsegregation, the increased transition temperatures and phase stability ranges were explained.

Espinat also investigated liquid crystalline gold(I) complexes (Scheme 76) of crown ether isocyanides **139** [142].



Scheme 76 Liquid crystalline Au(I) isocyanide complexes **139**

Table 11 Liquid crystalline properties of **xx**

Compound	X	Z	Phase transitions
139a	H	OC ₁₀ H ₂₁	I 37 SmC 2 G
139b	H	OC ₁₂ H ₂₅	I 42 SmC
139c	OC ₁₀ H ₂₁	OC ₁₀ H ₂₁	I 55 SmC
139d	OC ₁₂ H ₂₅	OC ₁₂ H ₂₅	I 17 M _X 15 Cr

Complexes **139** exhibit monotropic liquid crystalline phases upon cooling from the isotropic phase (Table 11). Complexation with KClO₄ destroys the liquid crystalline properties. In the solid state as well as in the mesophase, and even in the isotropic liquid at moderate temperatures, the complexes show luminescence (which is surprising and has been rarely observed) which is visible with the naked eye for **139b,d** under a UV-vis chromatography lamp at 298 K. The luminescence properties make **139** interesting for use as sensors or light-emitting diodes.

In summary, metallomesogens of crown ethers are interesting compounds that combine a variety of properties: (1) appropriate metal centers can show luminescence, (2) all properties can be tuned by the addition of alkaline metal salts to the crown ether, and (3) ordered, liquid crystalline phases are possible. With these hybrid materials, interesting applications can be foreseen in the near future.

3 Concluding Remarks

In the last few sections we have shown that liquid crystalline crown ethers are very versatile compounds. In this relatively young field of research, a huge variety of compounds has already been synthesized and studied.

When synthesizing a liquid crystalline crown ether, one has many building blocks readily at hand. The type of crown ether can be chosen from a variety of commercially available or simple to synthesize structures and many mesogenic side groups ranging from rod- to taper- and disc-shaped moieties are accessible. It is possible to create molecules with more than one crown or more than one mesogenic group. Other functionalities, such as dyes or phthalocyanines, can also be part of the mesogen. The final products can be complexed with a variety of main group,

transition, or rare earth metal salts leading to a change of the mesogenic properties. According to the mesogen and the chosen salt, mesophases can be induced, stabilized, or disfavoured. This gives the possibility of fine-tuning liquid crystalline properties “on demand” by an external stimulus (salt complexation) while leaving the molecular structure itself unchanged.

Interesting properties and applications have been reported so far. Liquid crystalline crowns can be used as sensors for salts or even chirality. Luminescence can be observed when choosing appropriate metals for complexation. Supramolecular structures such as channels and wires are readily available. Combined with polymerizable side groups, matrix- or membrane-bound supramolecular structures can be obtained.

The huge versatility of the molecular structures combined with the unique properties makes liquid crystalline crowns interesting compounds for future research. Combination of selective ion complexation, ion conductivity, or even electric conductivity within the substituents gives rise to materials for use in biological or electronic devices. However, much has to be done to develop such systems and to understand fully the properties of liquid crystalline crowns.

References

1. Frängsmyr T (1992) Nobel lectures in chemistry 1981–1990. World Scientific, Singapore
2. Lehn JM (1995) Supramolecular chemistry: concepts and perspectives. Wiley-VCH, Weinheim
3. Lehn JM (1996) Comprehensive supramolecular chemistry. Pergamon, Oxford
4. Cram D (1997) Container molecules and their guests. Royal Society of Chemistry, Cambridge
5. Lehn JM, Malthête J, Levelut AM (1985) *J Chem Soc Chem Commun* 1794–1796
6. He GX, Wada F, Kikukawa K, Matsuda T (1987) *J Chem Soc Chem Commun* 1294–1296
7. He GX, Wada F, Kikukawa K, Shinkai S, Matsuda T (1990) *J Org Chem* 55:541–548
8. Akopova OB (2006) *J Struct Chem* 47:120–129
9. Blake AJ, Bruce DW, Fallis IA, Parsons S, Richtzenhain H, Ross SA, Schröder M (1996) *Philos Trans R Soc London, Ser A* 354:395–414
10. Boden N, Movaghar B (1998) Handbook of liquid crystals. Wiley-VCH, Weinheim
11. Gennes PGD, Prost J (1995) The physics of liquid crystals. Oxford University Press, Oxford
12. Brown G (1971) A review of the structure and physical properties of liquid crystals. Butterworths, London
13. Laschat S, Baro A, Steinke N, Giesselmann F, Hägele C, Scalia G, Judele R, Kapatsina E, Sauer S, Schreivogel A, Tosoni M (2007) *Angew Chem* 119:4916–4973; *Angew Chem Int Ed* 46:4832–4887
14. Pedersen CJ (1967) *J Am Chem Soc* 89:7017–7036
15. Pedersen CJ (1970) *J Am Chem Soc* 92:391–394
16. Pedersen CJ (1988) *Angew Chem* 100:1053–1059
17. Pedersen CJ (1988) *Science* 241:536–540
18. Bradshaw J (1997) *J Inclusion Phenom Macrocyclic Chem* 29:221–246
19. Patai S (1980) Chemistry of ethers, crown ethers, hydroxyl groups and their sulphur analogues. Wiley, Chichester

20. Tsukanov AV, Dubonosov AD, Bren VA, Minkin VI (2008) *Chem Heterocycl Comp* 44:899–923
21. Minkin VI, Dubonosov AD, Bren VA, Tsukanov AV (2008) *Arkivoc* IV:90–102
22. Kralj M, Tušek-Božić L, Frkanec L (2008) *ChemMedChem* 3:1478–1492
23. Grigoras M, Stafie L (2010) *Supramolecular Chem* 22:237–248
24. Walkowiak W, Kozłowski CA (2009) *Desalination* 240:186–197
25. Urs MSR, Surendranath V (1983) *Mol Cryst Liq Cryst* 99:279–284
26. Gallardo H, Silva FC (1987) *J Chem Soc Perkin Trans 2* 319–321
27. He GX, Wada F, Kikukawa K, Shinkai S, Matsuda T (1990) *J Org Chem* 55:548–554
28. Shinkai S, Shimamoto K, Manabe O, Sisido M (1989) *Makromol Chem Rapid Commun* 10:361–366
29. Shinkai S, Nishi T, Ikeda A, Matsuda T, Shimamoto K, Manabe O (1990) *J Chem Soc Chem Commun* 303–304
30. He Y, Xie M, Li L, Liao L (1997) *Mol Cryst Liq Cryst* 304:165–169
31. Jiang Q, Li L, Xie M, Ran J (1997) *Mol Cryst Liq Cryst* 302:1311–1319
32. Leblanc K, Berdague P, Bayle J, Judeinstein P, Rault J (2000) *Chem Commun* 1291–1292
33. Blake AJ, Bruce DW, Danks JP, Fallis IA, Guillon D, Ross SA, Richtzenhain H, Schröder M (2001) *J Mater Chem* 11:1011–1018
34. Percec V, Rodenhouse R (1989) *Macromolecules* 22:4408–4412
35. Ungar G, Percec V, Rodenhouse R (1991) *Macromolecules* 24:1996–2002
36. Hsiue G, Wen J, Hsu C (1991) *Makromol Chem* 192:2243–2254
37. Rodenhouse R, Percec V (1991) *Polym Bull* 25:47–54
38. Rodenhouse R, Percec V (1991) *Makromol Chem* 192:1873–1879
39. Percec V, Rodenhouse R (1991) *J Polym Sci Part A Polym Chem* 29:15–28
40. Percec V, Johansson G, Rodenhouse R (1992) *Macromolecules* 25:2563–2565
41. Percec V, Johansson G (1993) *J Mater Chem* 3:83–96
42. Shibaev V, Medvedev A, Bobrovsky A (2008) *J Polym Sci Part A Polym Chem* 46:6532–6541
43. Shinkai S, Minami T, Kusano Y, Manabe O (1983) *J Am Chem Soc* 105:1851–1856
44. Shinkai S, Ogawa T, Kusano Y, Manabe O, Kikukawa K, Goto T, Matsuda T (1982) *J Am Chem Soc* 104:1960–1967
45. Shinkai S, Ikeda A, Matsuda T, Shinkai S (1991) *J Chem Soc Chem Commun* 339–341
46. Shinkai S, Nishi T, Matsuda T (1991) *Chem Lett* 437–440
47. Vögtle F, Knops P (1991) *Angew Chem* 103:972–974; *Angew Chem Int Ed* 30:958–960
48. Kimura K, Kawai Y, Oosaki S, Yajima S, Yoshioka Y, Sakurai Y (2002) *Anal Chem* 74:5544–5549
49. Oosaki S, Yajima S, Kimura K (2007) *Anal Sci* 23:963–967
50. Feng R, Tian Y, Chen H, Huang Z, Zeng Z (2010) *Electrophoresis* 31:1975–1982
51. Schröter JA, Tschierske C, Wittenberg M, Wendorf JH (1997) *Angew Chem* 109:1160–1163; *Angew Chem Int Ed* 36:1119–1121
52. Plehnert R, Schröter JA, Tschierske C (1998) *J Mater Chem* 8:2611–2626
53. Plehnert R, Schröter JA, Tschierske C (1998) *Langmuir* 14:5245–5249
54. Tschierske C (1998) *J Mater Chem* 8:1485–1508
55. Kaller M, Tussetschläger S, Fischer P, Deck C, Baro A, Giesselmann F, Laschat S (2009) *Chem Eur J* 15:9530–9542
56. Leblanc K, Berdague P, Judeinstein P, Bayle JP, Guermouche MH (2001) *Liq Cryst* 28:265–269
57. Sinha N, Ramanathan KV, Leblanc K, Judeinstein P, Bayle JP (2002) *Liq Cryst* 29:449–457
58. Ziesel R, Camerel F, Donnio B (2009) *Chem Rec* 9:1–23
59. Rodenhouse R, Percec V, Feiring AE (1990) *J Polym Sci Part C Polym Lett* 28:345–355
60. Xie M, Peng M, Jiang Q, Hu Z, Wang X (1996) *Liq Cryst* 21:461–467
61. Pannell KH, Yee W, Lewandos GS, Hambrick DC (1977) *J Am Chem Soc* 99:1457–1461
62. Zhang S, He K, Zheng S, Tang S, Zhang X, Li Z (2004) *Chin J Chem* 22:395–399

63. Parikh VB, Menon SK (2008) *Mol Cryst Liq Cryst* 482:71–83
64. Xie M, Qin J, Hong F, Wang L (1991) *Mol Cryst Liq Cryst* 209:309–318
65. Heiney PA, Stetzer MR, Mindyuk OY, DiMasi E, McGhie AR, Liu H, Smith ABI (1999) *J Phys Chem B* 103:6206–6214
66. Xie M, Liu S, Liu G, Li L, Jiang Q (1996) *Liq Cryst* 21:313–316
67. Tuffin RP, Toyne KJ, Goodby JW (1995) *J Mater Chem* 5:2093–2104
68. Tuffin RP, Toyne KJ, Goodby JW (1996) *J Mater Chem* 6:1271–1282
69. Neve F, Ghedini M, Levelut A, Francescangeli O (1994) *Chem Mater* 6:70–76
70. Neve F, Ghedini M (1994) *J Incl Phenom Macrocycl Chem* 15:259–272
71. Belarbi Z, Sirlin C, Simon J, Andre JJ (1989) *J Phys Chem* 93:8105–8110
72. Miwa H, Kobayashi N, Ban K, Ohta K (1999) *Bull Chem Soc Jpn* 72:2719–2728
73. Ban K, Nishizawa K, Ohta K, van de Craats AM, Warman JM, Yamamoto I, Shirai H (2001) *J Mater Chem* 11:321–331
74. Qi M, Liu G (2003) *ChemPhysChem* 4:605–608
75. Nakai T, Ban K, Ohta K, Kimura M (2002) *J Mater Chem* 12:844–850
76. Qi M, Liu G (2003) *J Phys Chem B* 107:7640–7646
77. Binnemans K, Sleven J, De Feyter S, De Schryver FC, Donnio B, Guillon D (2003) *Chem Mater* 15:3930–3938
78. Suarez S, Mamula O, Scopelliti R, Donnio B, Guillon D, Terazzi E, Piguet C, Bünzli JG (2005) *New J Chem* 29:1323–1334
79. Suárez S, Imbert D, Gummy F, Piguet C, Bünzli JG (2004) *Chem Mater* 16:3257–3266
80. Suárez S, Mamula O, Imbert D, Piguet C, Bünzli JG (2003) *Chem Commun* 1226–1227
81. Blake AJ, Bruce DW, Fallis IA, Parsons S, Schröder M (1994) *J Chem Soc Chem Commun* 2471–2473
82. Richtzenhain H, Blake AJ, Bruce DW, Fallis IA, Li W, Schröder M (2001) *Chem Commun* 2580–2581
83. Percec V, Rodenhouse R (1989) *Macromolecules* 22:2043–2047
84. Percec V, Johansson G, Heck J, Ungar G, Batty SV (1993) *J Chem Soc Perkin Trans 1* 1411–1420
85. Johansson G, Percec V, Ungar G, Abramic D (1994) *J Chem Soc Perkin Trans 1* 447–459
86. Ungar G, Batty SV, Percec V, Heck J, Johansson G (1994) *Adv Mater Opt Electron* 4:303–313
87. Tomazos D, Out G, Heck JA, Johansson G, Perce V, Möller M (1994) *Liq Cryst* 16:509–527
88. Percec V, Heck J, Johansson G, Tomazos D, Kawasumi M, Ungar G (1994) *J Macromol Sci A* 31:1031–1070
89. Percec V, Heck J, Johansson G, Tomazos D, Kawasumi M, Chu P, Ungar G (1994) *Mol Cryst Liq Cryst* 254:137–196
90. Percec V, Johansson G, Ungar G, Zhou J (1996) *J Am Chem Soc* 118:9855–9866
91. Jung H, Kim SO, Hudson SD, Percec V (2002) *Appl Phys Lett* 80:395–397
92. Percec V, Cho W, Ungar G, Yeardley DJP (2002) *Chem Eur J* 8:2011–2025
93. Gitsov I, Ivanova PT (2000) *Chem Commun* 269–270
94. Steinke N, Frey W, Baro A, Laschat S, Drees C, Nimitz M, Hägele C, Giesselmann F (2006) *Chem Eur J* 12:1026–1035
95. Steinke N, Jahr M, Lehmann M, Baro A, Frey W, Tussetschläger S, Sauer S, Laschat S (2009) *J Mater Chem* 19:645–654
96. Steinke N (2007) *Neuartige columnare Flüssigkristalle mit Kronenether-Einheit als zentralem Baustein*. Mensch & Buch Verlag, Berlin
97. Beginn U, Zipp G, Möller M (2000) *Chem Eur J* 6:2016–2023
98. Beginn U, Zipp G, Möller M (2000) *Adv Mater* 12:510–513
99. Beginn U, Zipp G, Mourran A, Walther P, Möller M (2000) *Adv Mater* 12:513–516
100. Beginn U, Zipp G, Moller M, Johansson G, Percec V (1997) *Macromol Chem Phys* 198:2839–2852
101. Percec V, Zipp G, Johansson G, Beginn U, Moeller M (1997) *Macromol Chem Phys* 198:265–277

102. Beginn U, Zipp G, Möller M (2000) *J Polym Sci Part A Polym Chem* 38:631–640
103. Malthête J, Poupinet D, Vilanove R, Lehn J (1989) *J Chem Soc Chem Commun* 1016–1019
104. Mertesdorf C, Ringsdorf H (1989) *Liq Cryst* 5:1757–1772
105. Lattermann G (1989) *Liq Cryst* 6:619–625
106. Lattermann G (1990) *Mol Cryst Liq Cryst* 182:299–311
107. Lattermann G, Schmidt S, Gallot B (1992) *J Chem Soc Chem Commun* 1091–1092
108. Tatarsky D, Banerjee K, Ford WT (1990) *Chem Mater* 2:138–141
109. Idziak SHJ, Maliszewskij NC, Heiney PA, McCauley JP, Sprengeler PA, Smith AB (1991) *J Am Chem Soc* 113:7666–7672
110. Malthête J, Levelut A, Lehn JM (1992) *J Chem Soc Chem Commun* 1434–1436
111. Mori A, Yamamoto E, Kubo K, Ujiie S, Baumeister U, Tschierske C (2010) *Liq Cryst* 37:1059–1065
112. Liebmann A, Mertesdorf C, Plesniviy T, Ringsdorf H, Wendorff JH (1991) *Angew Chem* 103:1358–1361; *Angew Chem Int Ed* 30:1375–1377
113. Lattermann G, Schmidt S, Kleppinger R, Wendorff JH (1992) *Adv Mater* 4:30–33
114. Schmidt S, Lattermann G, Kleppinger R, Wendorff J (1994) *Liq Cryst* 16:693–702
115. Mertesdorf C, Ringsdorf H, Stumpe J (1991) *Liq Cryst* 9:337–357
116. Hirose T, Tanaka S, Aoki Y, Nohira H (2000) *Chem Lett* 1290–1291
117. Yan J, Tang R, Zhang B, Zhu X, Xi F, Li Z, Chen E (2009) *Macromolecules* 42:8451–8459
118. Kaller M, Staffeld P, Haug R, Frey W, Giesselmann F, Laschat S (2011) *Liq Cryst* 38:531–553
119. Schultz A, Laschat S, Saipa A, Giesselmann F, Nitz M, Schulte JL, Baro A, Miehllich B (2004) *Adv Funct Mater* 14:163–168
120. Kaller M, Deck C, Meister A, Hause G, Baro A, Laschat S (2010) *Chem Eur J* 16:6326–6337
121. Steinke N, Kaller M, Nitz M, Baro A, Laschat S (2010) *Liq Cryst* 37:1139–1149
122. Li J, He Z, Gopee H, Cammidge AN (2010) *Org Lett* 12:472–475
123. van Nostrum CF, Picken SJ, Nolte RJM (1994) *Angew Chem* 106:2298–2300; *Angew Chem Int Ed* 33:2173–2175
124. van Nostrum CF, Picken SJ, Schouten A, Nolte RJM (1995) *J Am Chem Soc* 117:9957–9965
125. van der Pol JF, Neeleman E, Zwikker JW, Nolte RJM, Drenth W, Aerts J, Visser R, Picken SJ (1989) *Liq Cryst* 6:577–592
126. Nolte RJM (2006) *Liq Cryst* 33:1373–1377
127. Hegmann T, Neumann B, Kain J, Diele S, Tschierske C (2000) *J Mater Chem* 10:2244–2248
128. Engelkamp H, Middelbeek S, Nolte RJM (1999) *Science* 284:785–788
129. Samorí P, Engelkamp H, de Witte P, Rowan AE, Nolte RJM, Rabe JP (2001) *Angew Chem* 113:2410–2412; *Angew Chem Int Ed* 40:2348–2350
130. Boamfa M, Christianen P, Engelkamp H, Nolte R, Maan J (2004) *Adv Funct Mater* 14:261–265
131. Yilmaz F, Atilla D, Ahsen V (2004) *Polyhedron* 23:1931–1937
132. Akopova OB, Logacheva NM, Baulin VE, Tsivadze AY (2008) *Russ J Gen Chem* 78:2118–2124
133. Wang R, Liu W, Chen Y, Zuo J, You X (2009) *Dyes Pigm* 81:40–44
134. Wright JD, Roisin P, Rigby G, Nolte RJ, Cook MJ, Thorpe SC (1993) *Sens Actuators B Chem* 13:276–280
135. Ashton PR, Joachimi D, Spencer N, Stoddart JF, Tschierske C, White AJP, Williams DJ, Zab K (1994) *Angew Chem* 106:1563–1566; *Angew Chem Int Ed* 33:1503–1506
136. Joachimi D, Ashton P, Sauer C, Spencer N, Tschierske C, Zab K (1996) *Liq Cryst* 20:337–348
137. Neumann B, Joachimi D, Tschierske C (1997) *Adv Mater* 9:241–244
138. Percec V, Turkaly PJ, Asandei AD (1997) *Macromolecules* 30:943–952
139. Akagi K, Guo S, Mori T, Goh M, Piao G, Kyotani M (2005) *J Am Chem Soc* 127:14647–14654
140. Arias J, Bardají M, Espinet P (2006) *J Organomet Chem* 691:4990–4999
141. Coco S, Cordovilla C, Espinet P, Gallani J, Guillon D, Donnio B (2008) *Eur J Inorg Chem* 1210–1218
142. Arias J, Bardají M, Espinet P (2008) *Inorg Chem* 47:3559–3567

Star-Shaped Mesogens – Hekates: The Most Basic Star Structure with Three Branches

Matthias Lehmann

Abstract The chapter introduces and defines the term star-shaped mesogens as a highly symmetric subgroup of multipodes. Hekates, the three arm stars, are in the focus of the other sections. Flexible, semi-flexible and shape-persistent mesogens can be distinguished. The chapter presents various modes of self-assembly which account for nanosegregation and space-filling. Recent examples are semi-flexible structures which fold to *E*-shaped conformers followed by self-organisation in columnar 2D and 3D and micellar cubic structures. Hekates are mesogens that will allow the design of complex mesomorphic and functional materials in the future.

Keywords Folding · Hekates · Liquid crystals · Multipodes · Nanosegregation · Phase engineering · Space-filling · Star-shaped mesogens

Contents

1	Introduction to Star-Shaped Mesogens	194
2	Hekates: Basic Stars with Three Arms	196
2.1	Flexible Hekates (Subgroup (i))	197
2.2	The Shape-Persistent Hekates (Subgroup (iii))	199
2.3	The Semi-Flexible Hekates (Subgroup (ii))	206
2.4	Supermolecules: Hekates Formed by Supramolecular Interactions	217
2.5	Summary and Outlook	218
	References	220

M. Lehmann (✉)

Institute of Organic Chemistry, University of Würzburg, Am Hubland, 97074 Würzburg, Germany
e-mail: Matthias.Lehmann@uni-wuerzburg.de

1 Introduction to Star-Shaped Mesogens

Molecules constructed from multifunctional cores to which linear scaffolds – the arms – are attached are often called star-shaped. In geometry star-shaped objects can be constructed in a plane (2D) by stellation of regular convex polygons and in three dimensions (3D) by stellation of convex polyhedra. This procedure provides concave objects called regular star polygons or regular star polyhedra, because of their asterisk-like topology [1]. However, regarding molecular topology, these geometrical definitions would exclude the most common structures considered to be star-shaped – molecules with three and four arms in a plane based on triangles and squares and four and eight arms in space based on tetrahedra and cubes. Thus here star-shaped molecules are defined as structures in which n ($n > 2$) arms are attached symmetrically to a multifunctional core. In the ideal case the core extends the arms to the vertices of polygons or polyhedra. Consequently, for 2D objects the arms point to the vertices of a triangle, square, pentagon or hexagon, and for 3D objects to the vertices of a tetrahedron, octahedron or a cube. Figure 1 collects most common examples of different cores – an inventory which is not comprehensive. Moreover, some cores are included in which the arms point to the vertices of a trigonal pyramid (E–J) or other pyramidal arrangements such as in core S and U, which is a configuration in 3D space of lower symmetry. However, we would also like to include molecules with these cores to the family of star-shaped molecules, when linear arms are attached. Star-shaped mesogens are generated when mesogenic or promesogenic arms are linked to the central core. Thereby true mesogens can be bound end-on or side-on via a flexible spacer – in general a conveniently long aliphatic chain – to form a flexible mesogenic oligomer (i) (Fig. 2). Such molecules are also called polypedes [3], polypedals [4], or multipodes. These names originate from the Latin word “pedis” or Greek word “pode” meaning foot. Since multipodes comprise all molecules with several “feet”, i.e. also molecules with arms that are non-symmetrically arranged in space, star-shaped mesogens with flexible spacer belong to the family of multipodes, but not all of them are star-shaped. In star-shaped structures the mesogenic or promesogenic scaffolds can be attached directly to the core without spacers and generate a star-shaped “supermesogen”. Such large mesogens can consist of a semi-flexible (ii) and a shape-persistent scaffold (iii) (Fig. 2). Both the flexibility of the arm and the self-assembly of the core and the arms may be achieved by covalent or supra-molecular bonds. Strictly, regular, i.e. symmetric star-shaped mesogens should consist of n identical arms. Stars with n similar arms of different length or different substitution are called non-symmetric star-shaped mesogens. Note that in this definition, the arm scaffolds should be similar to each other. The term similarity is however not well defined, and thus the latter is a rather open definition.

Since such molecules either lack shape anisotropy or high polarisability and constitute molecules of unusual shape with voids between their arms, this family of mesogens is considered to be non-conventional. In the last decades several reviews summarised most of the unconventional mesogens including the small subgroup of

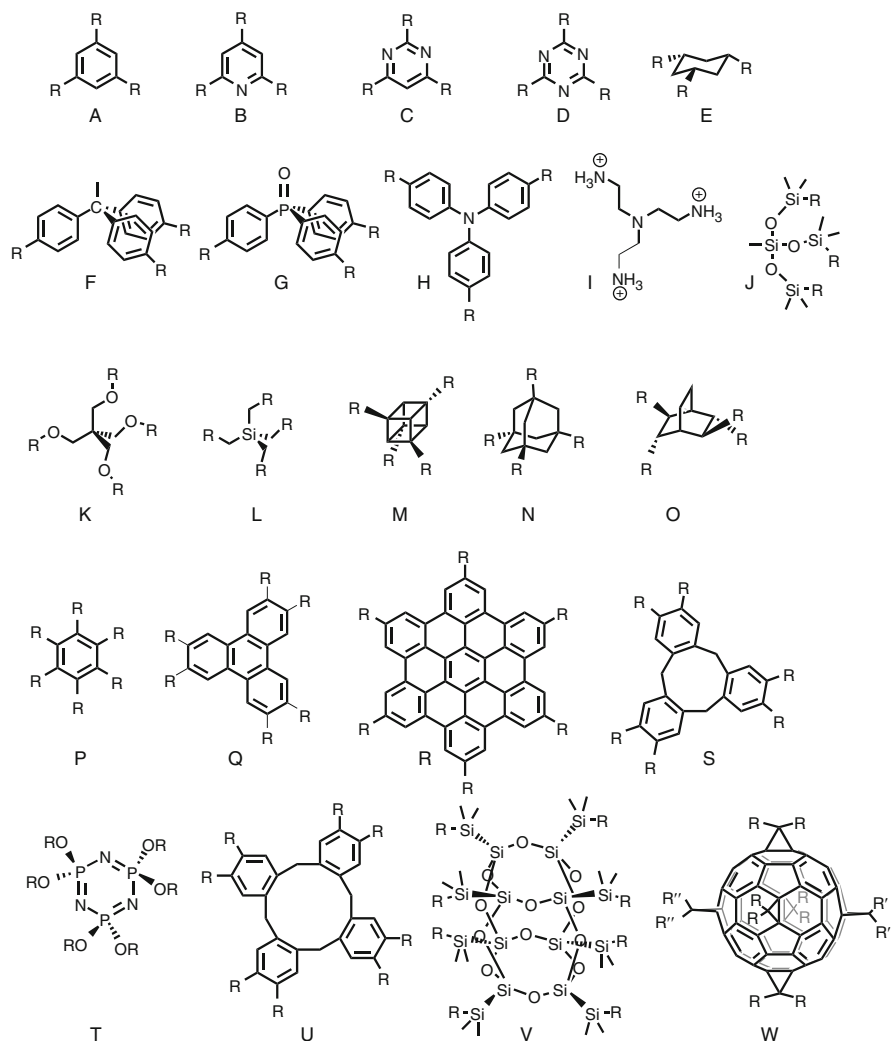


Fig. 1 Cores of star-shaped mesogens. Mesogens point to the vertices of a triangle (A–D), a trigonal pyramid (E–J), a tetrahedron (K–N) or a distorted tetrahedron (O), a hexagon (P, R), a truncated triangle (Q, S), a trigonal prism (T), a truncated square (U), a cube (V) and a distorted icosahedron (W)

stars [1, 3, 5–11]. The present chapter will not comprehensively review the field but will elaborate the main features of star-shaped mesogens, i.e. parameters of self-assembly comprising nanosegregation, folding, packing, supramolecular interactions; incorporation of guests and functionality. The chapter will focus on the stars with three arms, which we call “Hekates” owing to their very special properties and large voids between the arms. However, molecules with four and

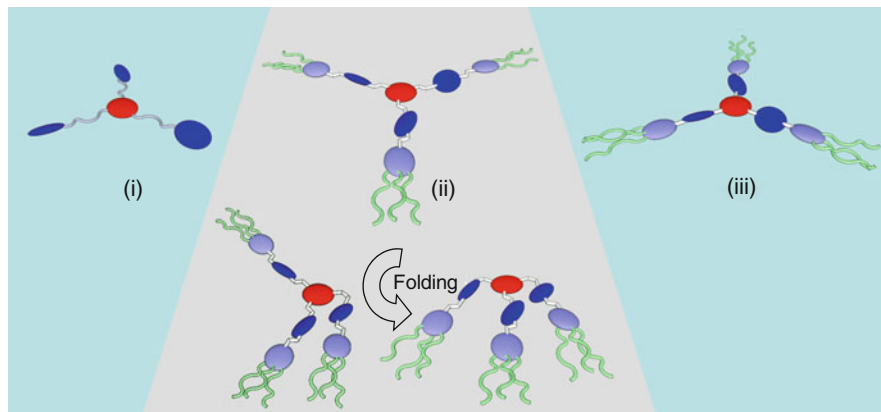


Fig. 2 Classification of star-shaped three arm mesogens. Flexible (*subgroup (i)*), semi-flexible (*subgroup (ii)*) and shape-persistent (*subgroup (iii)*) star-shaped molecules. Folding of star-shaped semi-flexible molecules to λ - and E -shaped mesogens [2]. Copyright Wiley-VCH Verlag GmbH & Co. KGaA. Reproduced with permission

six arms or stars with polycondensed aromatic cores are highly attractive with respect to their application in organic electronics and some examples are cited at the end of the chapter.

2 Hekates: Basic Stars with Three Arms

The simplest star-shaped mesogens with three arms are called Hekates. Their cores may be the centre of a triangle (Fig. 1A–D) or the top of a trigonal pyramid (Fig. 1E–J). The term “Hekates”¹ has been suggested for this mesogen family in order to distinguish them from other mesogenic trimers, e.g. linear trimers or irregular tripodes [9]. Moreover, Hekates possess an outstanding molecular structure owing to the empty spaces between the individual arms. The latter must be filled when these molecules assemble in thermotropic liquid crystals and this can be achieved by various self-assembly modes depending on the class of Hekates. Three subgroups can be classified and are illustrated schematically in Fig. 2. Subgroup (i) consists of Hekates with mesogenic groups linked via flexible spacers, subgroup (ii)

¹ Hekate is the name of a popular Greek goddess, also known as the goddess of the three ways and the connection of the three ways. She was represented as a triple-form figure owing to her threefold power in heaven, earth and underworld [12–15]. Since star mesogens with three arms are rather special, due to the large void space between their arms and thus should be distinguished from star mesogens with four or more arms, we suggest to introduce this more specific name “Hekates” for the star mesogens with three arms described in this section.

contains molecules with semi-flexible arms and in subgroup (iii) the mesogens are shape-persistent.

2.1 Flexible Hekates (Subgroup (i))

Many star mesogens of subgroup (i) are known and for the large majority the attached mesogens dominate the mesomorphic properties, since the flexible spacers allow any suitable folding. Thus calamitic mesogens induce lamellar or nematic phase behaviour and discotic units assist columnar mesomorphism (for some examples of flexible trimers see [16–21]). Note that the mode of self-assembly is significantly different to star-polymers and ABC star block copolymers [8, 22–24]. In the latter polymers the flexible chains fold and aggregate to larger domains. The three different domains are interconnected at one point and thus generate complex mesophases with a tiling according to the degree of polymerisation of the individual arms [8]. A small version of such a system was realised in an ABC star-shaped molecule, with a semi-perfluorinated, an aliphatic and an oligoethylenoxy chain [25]. This amphiphilic molecule forms columnar mesophases with a 12.6.4 tiling in mixtures with 10–25% water. Note that a polymeric ABC star was found to form quasicrystalline order [23, 26]. It remains to be a challenge to find such quasicrystalline materials also among low molar mass star mesogens. The self-organisation of the Hekates with mesogens attached by a flexible spacer distinguishes them from the star polymer assembly. The spacers only link the mesogens; however the formation and type of mesophase is dominated by the mesogenic unit and not by the nanosegregation of the spacer. Nevertheless, the length of the spacer plays a crucial role in the mesophase formation. A short spacer may prevent the mesogenic units from the appropriate accommodation in the LC phase. Recent examples are given by Zhang et al. based on the phloroglucinol core (Compounds **1**, Fig. 3) [27]. The arms **2** ($n \geq 4$) consisting of a cholesterol derivative all reveal cholesteric mesophases (N^* , e.g. **2b**). If attached to the phloroglucinol core (**1**), the temperature interval of the cholesteric phase widens significantly, which is a typical feature of such oligomers. However, the mesogens **1a** and **2a** with the shortest linker does not exhibit mesomorphism. Another feature of such oligomers becomes evident when a different *p*-alkoxybenzoyloxyphenyl group is attached via flexible spacers to the phloroglucinol (compounds **3a–c**) [28]. The star-shaped trimers **3** do not only form the same mesophase types over a much wider temperature interval than arms **4** but also freeze into low temperature glass phases. The latter is commonly observed for star-shaped mesogens and is of great interest when anisotropic photonic materials are sought [29]. Recently, the tripod **5** with lateral attached nematogens were reported for which the formation of the long and intensely sought thermotropic biaxial nematic phase of low molar mass mesogens was claimed based on polarised IR studies [30]. Here the lateral attachment of the mesogens via spacers hinders the rotation about the molecule's long axis and thus

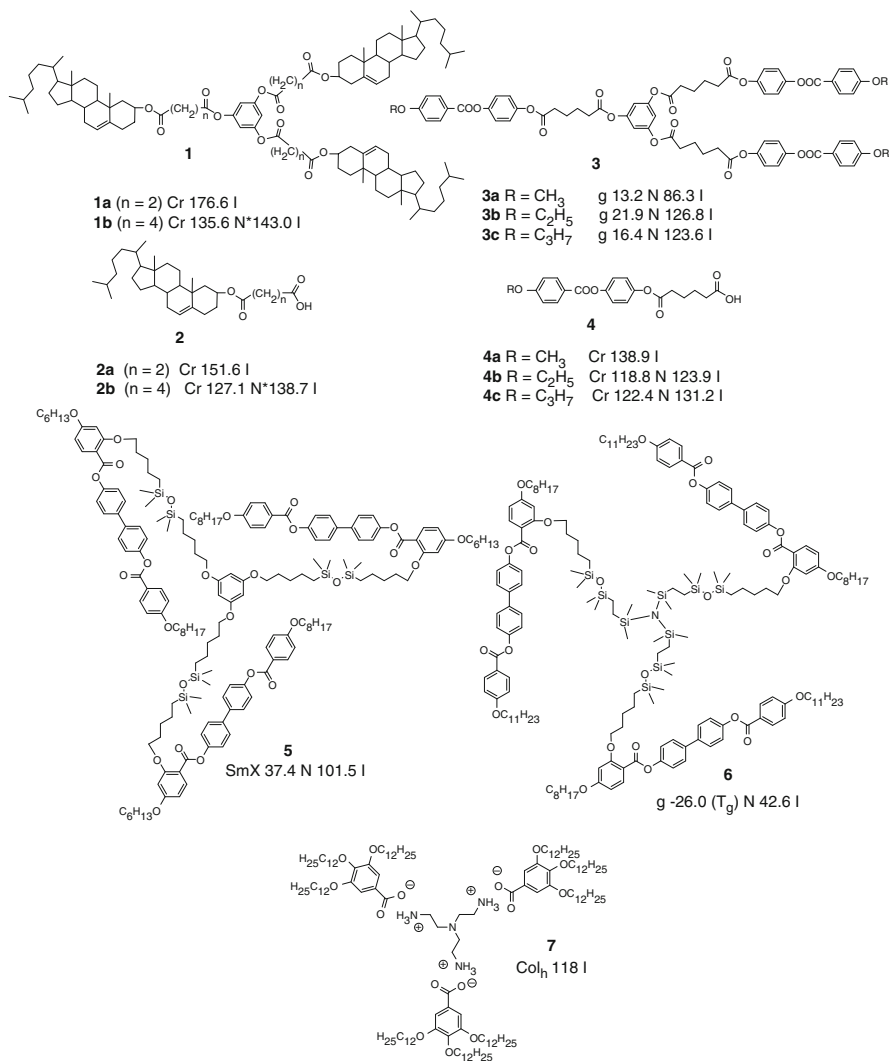


Fig. 3 Hekates with flexible spacers. Compounds **1**, **2**: Thermotropic properties as a function of spacer length. Compounds **3**, **4**: LC properties with unchanging spacer length and variable peripheral chains. Compounds **5**, **6**: Nematogens claimed to form biaxial nematic phases. *Cr* crystal, *g* glass, *N* nematic, *N** cholesteric, *SmX* unidentified smectic phase, *Col_h* columnar hexagonal phase. All temperature are given in °C

should promote a biaxial ordering. The related azasiloxane derivative **6** self-assembles only in a uniaxial phase with mesogens decoupled from the core evidenced by dielectric spectroscopy [31]. An interesting case of this class of Hekates is the supramolecular mesogen **7** in which the promesogenic gallic acid derivatives are bound by ionic interactions to flexible spacers which connect the

ammonium groups with the nitrogen core [32]. Such mesogens organise in columnar stacks. Very attractive Hekates for application in organic electronics contain larger condensed aromatic, disc-shaped mesogens stacking in columnar phases [21, 33, 34].

2.2 *The Shape-Persistent Hekates (Subgroup (iii))*

In the shape-persistent subgroup (iii) the arms may consist of, e.g. oligophenylene, oligothiophene, oligo(phenyleneethynylene) or oligo(phenylenevinylene) scaffolds. All these building blocks are not rigid since a considerable number of conformers by rotation about the single bonds can be formed. However, in contrast to subgroups (i) and (ii) the overall linear shape of the arms remains. As a consequence the space between the arms cannot be compensated by folding as it is the case for the flexible (i) or the semi-flexible (ii) classes (see next section) of Hekates. Therefore, LC properties for stars with long arms would not be expected.

Oligophenylene derivatives are evidently the most shape-persistent scaffolds. However, liquid crystals in the subgroup (iii) on the basis of 1,3,5-triphenylbenzene are not known. The design of mesogens with six and nine flexible chains did not succeed in obtaining mesophases [35]; however, they were used as doping agents to induce chiral mesophases. The non-mesomorphic properties in neat materials may be rationalised by non-planar conformers and the low tendency of the relatively small 1,3,5-triphenylbenzene unit for nanosegregation. Oligothiophene stars have been prepared revealing liquid crystalline properties only for the more extended derivatives **8c**, **9** (Fig. 4) [36, 37]. The LC phases are identified by their textures and are only monotropic, indicating that their stacking in fluid phases by nanosegregation is unfavourable. Note that these authors highlight the improved processability of their star materials for thin film production compared with linear conjugated derivatives. Thiophene Hekates **8–9** are endcapped with decyl chains (position 5 of the terminal thiophene). Other thiophene derivatives (Fig. 4, compound **10**) follow a different design in order to increase solubility in organic solvents [38, 39]. In these derivatives, for which in some cases waxy solids are reported, butyl chains are attached to the 3,4-position of the thiophene repeating units. In principle such a design may induce nematic liquid crystalline properties as is the case for stilbene based stars discussed below. Nevertheless, in the present case such phases were not reported. It appears that in such rather rigid scaffolds space-filling and nanosegregation are not optimised to obtain enantiotropic mesomorphism. Similar results were obtained for oxadiazole derivatives **11a,b** with three peripheral chains for which the monotropic columnar phases has been discovered depending on the length of the peripheral chains [40]. Disk-shaped compound **11c** with three flexible alkoxy chains assembled as expected in an enantiotropic columnar phase over a wide temperature range [41]. An extended scaffold **12** with six peripheral chains revealed an enantiotropic columnar phase, too [42], whereas derivative **13** with only one alkoxy chain per arm showed only a discotic nematic phase at elevated temperatures [43]. Note that

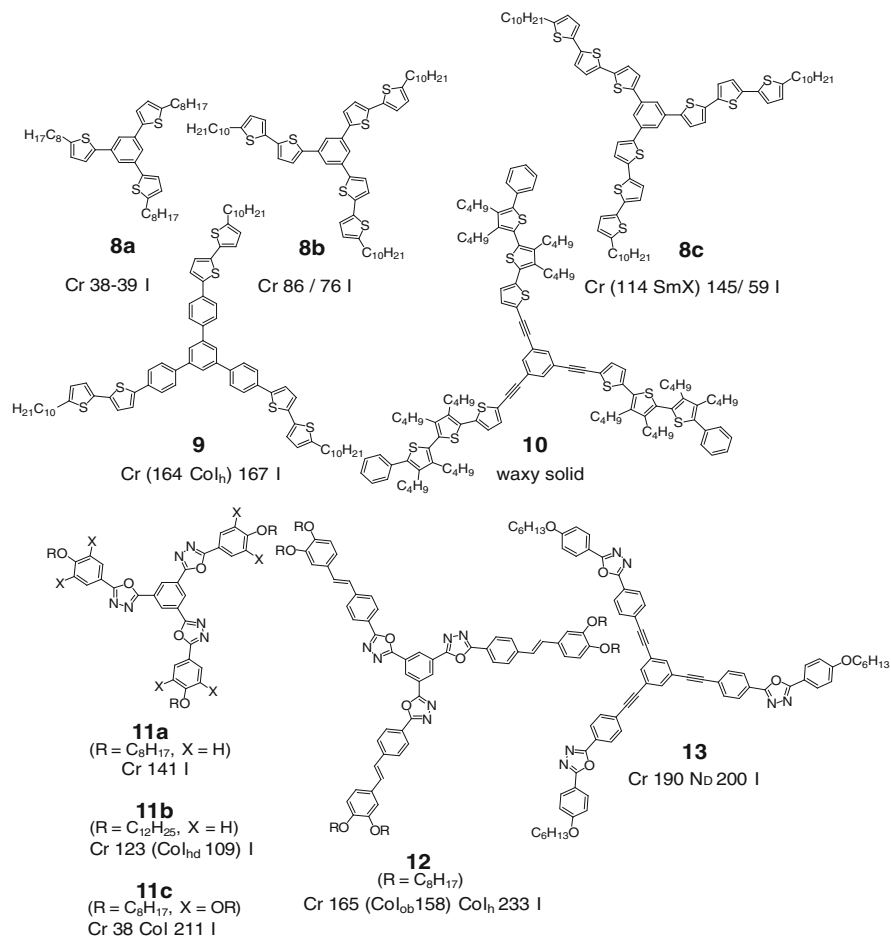


Fig. 4 Hekates with shape-persistent oligothiophene and oxadiazole arms. Only the endcapped molecules with extended arms revealed LC phases. *Col_{ob}* columnar oblique phase, *N_D* discotic nematic phase. All transition temperatures are given in °C

the aggregation of compounds **12** are sufficiently strong to form gels in non-polar solvents consisting of columnar fibres.

Figure 5 shows some structures based on oligo(phenyleneethynylene) arms. The small molecule **14** [44] with peripheral oligo(ethyleneoxy) chains can be regarded as a disc in which the flexible chains can fill the space between columns and arms. In the crowded mesogens **15** of Nuckolls et al. the free volume between arms is filled by the flexible chains and the columnar phase is stabilised by hydrogen bonding [45, 46]. This structure can be regarded as non-conventional discotic mesogen. Hekates **16** with internal alkoxy chains has been prepared; however, no liquid crystal properties have been reported [47].

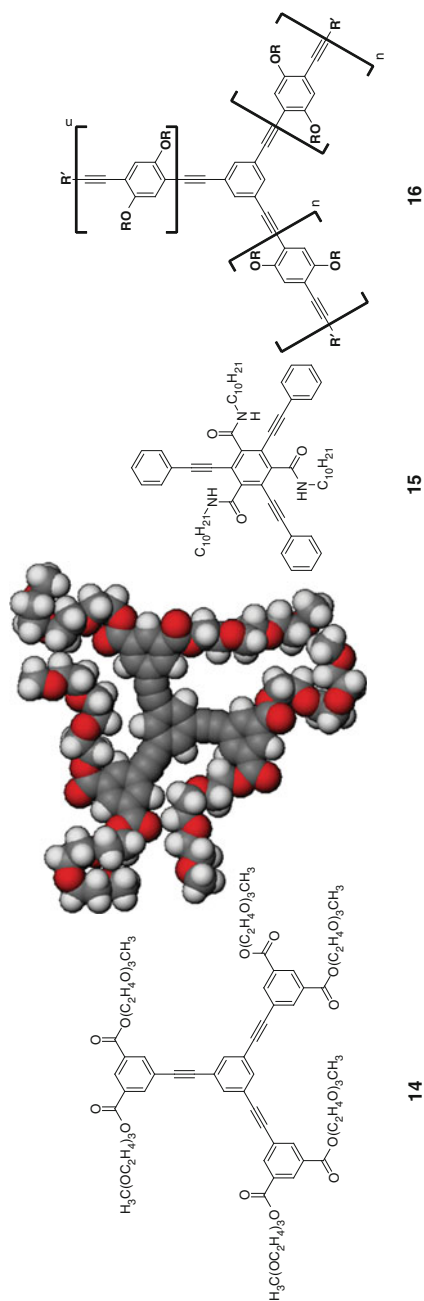


Fig. 5 Shape-persistent Hekates based on oligo(phenyleneethynylene) scaffolds. Compounds **14** and **15** form columnar mesophases. For stars **16** ($\text{R}' = \text{H}$ or fullerene, $\text{R} = \text{C}_{10}\text{H}_{21}$) thermotropic properties have not been published

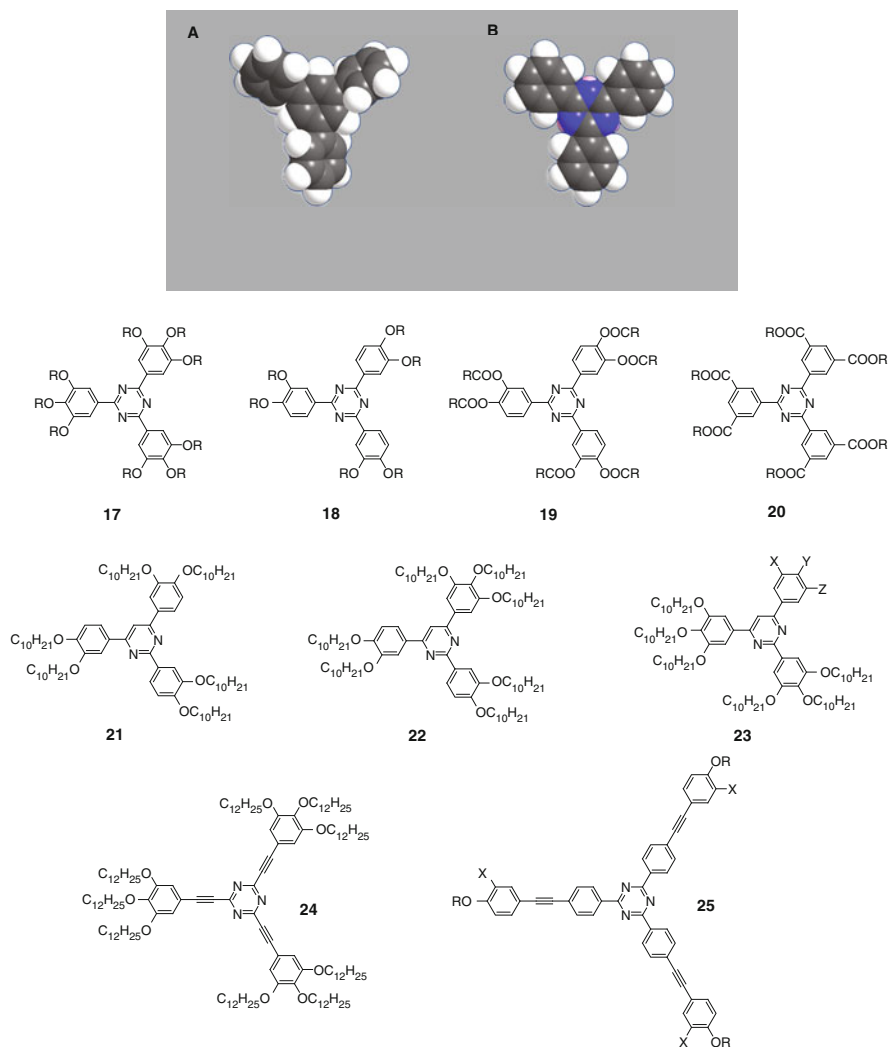


Fig. 6 Hekates with a pyrimidine or triazine core. In contrast to the non-planar triphenylbenzene **A** the triphenyltriazine core **B** can adopt a flat conformation owing to the reduced steric and the attractive interaction between hydrogens and the lone-pair of the nitrogens [48]

As pointed out earlier, the triphenylbenzene unit (Fig. 6, **A**) is non planar owing to steric interactions between *ortho* hydrogens. The *ortho* hydrogens are not present in the triazine core (Fig. 6, **B**) and thus this building block is able to adopt a planar structure, which is probably assisted by weak interactions between the hydrogens and the lone-pair of the nitrogens [48]. The flat structure is most likely the reason why many triphenyltriazine derivatives **17–20** are reported to be liquid crystalline depending only on the number, type and length of peripheral chains. Compounds **18** form only fibrous crystals with nonyloxy and decyloxy chains [49], whereas

nine decyl chains in **17** induce a very stable columnar hexagonal phase from 36 °C to 145 °C [50]. The methyl groups in a chiral 3,7-dimethyloctyl chain substituted star **17** reduce significantly the clearing temperature to 56 °C and the phase symmetry is rectangular. Two ester linking groups as in mesogen **19** lead only to monotropic discotic nematic phases below 58 °C for hexanoyl, heptanoyl and octanoyl chains [49]. Interestingly, when the direction of the carboxy group is reversed as in **20**, in which the 3,5-positions are substituted (R = pentyl), a very stable columnar hexagonal phase is revealed between 105 °C and 211 °C [48]. A dependence of mesophase formation on the number and length of peripheral chains is also observed for triphenylpyrimidine derivatives **21–23** [51]. Whereas the symmetric molecule **21** with six flexible chains did not show any liquid crystal phases similar to the related triazine derivatives, non-symmetric derivatives and molecules with six or more alkoxy chains (**22**, **23**) form hexagonal columnar LC phases. The most stable ones have been obtained for eight and nine decyloxy chains. Most probably this thermotropic behaviour is related to nanosegregation of aliphatic chains and the aromatic interior which is mediated by the type of linking unit and length and number of aliphatic chains. Similarly, compound **24** with phenylethynyl arms is a discotic mesogen self-assembling in a columnar mesophase [52].

Hekates **25**, with more extended arms, also reveal hexagonal columnar phases. With X = OR, only mesogens with decyl and undecyl chains show liquid crystal properties within a small temperature interval of approximately 12 °C [53]. Much higher mesophase stability is evolved by molecules with only one alkoxy chain per arm (X = H) [54]. This is rather surprising, since the related smaller triphenyl-triazine with three alkoxy chains only exhibit crystalline phases [55] and columnar phases are stabilised only with seven to nine alkoxy chains in the series of pyrimidine and triazine derivatives. It would be expected, that three alkoxy chains are not sufficient to fill efficiently space around a column of derivative **25**, but may rather form a nematic phase as for comparable mesogens **13** (see Fig. 4) or assemble in lamellae. Indeed, **25** with decyl and dodecyl chains are reported to reveal at low temperature unknown smectic phases and surprisingly at higher temperature hexagonal columnar phases. Molecules with longer chains only show the columnar phase. Unfortunately, no structural studies have been published in order to disclose a model for their stacking.

The most comprehensive studies on shape-persistent Hekates have been performed on stilbenoid star-shaped molecules. Structures and mesomorphic properties are collected in Table 1. Core building blocks with only one repeating unit per arm and one flexible chain **26a,b**, **28a–d**, **30a** did not show any liquid crystal properties [56–58]. In the series of two chain derivatives **28e**, **30b,c** the formation of mesophases depend on the core [57–59]. The electron deficient triazine and the dicyanopyridine building block induced obviously columnar mesophases. The pyridine derivative **30b** showed only a crystalline phase [58]. In the series of nine chain stars **26c–g** [60–62] and **28f–n** [57], the compounds formed columnar phases depending on the chain length of the peripheral chains. Propyloxy chains are too short but hexyloxy and dodecyloxy chains are sufficient for the formation of liquid crystal phases by nanosegregation [60–62]. This can be rationalised by a dense

Table 1 Thermotropic properties of stilbenoid stars

		26a, b $m = 6, 12$
		26c-e $n = 0-2, m = 12$
		26f, g $n = 0-1, m = 6$
		26h, i $n = 0-1, m = 3$
		27a-b $n = 1-2, E = \text{CHO}, R = \text{C}_3\text{H}_7$
		27c $n = 1, E = \text{CN}, R = \text{C}_6\text{H}_{13}$
		27d $n = 1, E = \text{H}, R = \text{C}_6\text{H}_{13}$
		27e $E = \text{CHO}, R = \text{C}_3\text{H}_7$
		28a-d $n = 0, m = 6, 7, 8, 12, R' = R'' = \text{H}$
		28e $n = 0, m = 8, R' = \text{H}, R'' = \text{OC}_m\text{H}_{2m+1}$
		28f-j $n = 0, m = 6, 8, 10, 12, 16$
		28k $n = 0, m = 10$ (3, 7-dimethyloctyl)
		28l-n $n = 1-3, m = 6$
		29a $E = \text{H}, R = \text{C}_6\text{H}_{13}$
		29b $E = \text{CN}, R = \text{C}_6\text{H}_{13}$
		30a $X = \text{H}, m = 12$
		30b $X = \text{H}, m = 12$
		30c $X = \text{CN}, m = 10$
		30d $X = \text{H}, m = 12$

Compound	Thermotropic behaviour [T ($^{\circ}\text{C}$)] ^a	Ref
26c ($n = 0$)	Cr 38 Col _{hd} 75 I	[60, 61]
26d ($n = 1$)	g 21 (T _g) Col _{hd} 108 I	[62]
26e ($n = 2$)	g 55 (T _g) Col _{hd} 199 I	[62]
26f ($n = 1$)	g -15 (T _g) Col _{hd} 74 I	[62]
26g ($n = 2$)	g 21 (T _g) L _D 129 I	[62]
26h ($n = 1$)	Cr 189 I	[62]
26i ($n = 2$)	Cr 216 I	[62]
27a ($n = 1$)	g 140 (T _g) N _D 260 I ^b	[70]
27b ($n = 2$)	g 246 (T _g) N _D 296 I ^b	[70]
27c ($n = 1$)	Cr 209 N _D 232 I	[71]
27d ($n = 1$)	g 2 (T _g) N _D 114 N _D 126 I	[71]
27e	g 140 (T _g) N 226 I ^b	[70]
28e ($n = 0$)	Cr 75 Col 82 I	[57]
28f ($n = 0$)	Cr (helical columns) 63 Col _{hd} 110 I	[57]
28g ($n = 0$)	Cr 32 Col _{hd} 86 I	[57]
28h ($n = 0$)	Cr -57 Col _{hd} 79 I	[57]
28i ($n = 0$)	Cr 3 Col _{hd} 88 I	[57]
28j ($n = 0$)	Cr 49 Col _{hd} 77 I	[57]
28k ($n = 0$)	Col _{hd} 37 I	[57]
28l ($n = 1$)	Col 96 I ^b	[64]
28m ($n = 2$)	Col 233 I ^b	[64]

(continued)

Table 1 (continued)

Compound	Thermotropic behaviour [T ($^{\circ}\text{C}$)] ^a	Ref
28n ($n = 3$)	Col >300 I ^b	[64]
29a	g 95 (T_g) N_{col} 107 I	[71]
29b	g 210 (T_g) N_{col} 236 I	[71]
30a	Cr 43 I	[58]
30b	Cr 69 I	[58]
30c	Cr (X 63) 81 Col_h 134 I	[59]
30d	oil at rt	[58]

^aValues given for the second heating cycle at a heating rate of $10^{\circ}\text{C}/\text{min}$

^bData obtained from polarised optical microscopy; T_g are approximate values, determined at temperatures when the phase was no longer shearable. *Cr* crystalline phase, *g* glassy phase, *Col* columnar phase, *Col_{hd}* columnar hexagonal disordered phase, *N* nematic, *N_D* nematic discotic, *N_{Col}* nematic columnar, *L_D* lamellar discotic, *I* isotropic phase

packing and a disc-like shape for the zeroth generation stars ($n = 0$). The discotic nature of the mesogens is substantiated by a comprehensive ^2H solid state NMR study of selectively deuterated derivatives of **26c** showing that, besides some flexibility of the stilbenoid scaffold, the molecules rotate about the columnar axis similar to discotic triphenylene derivatives [63]. It is surprising that the pyridyl derivative **30d** appeared to be only an oily material at ambient temperature [58]. Obviously the destabilisation by the negative charge at the nitrogen outweighs the stabilisation by the dipole moment of the core, since the space-filling and nanosegregation of the aliphatic chains is expected to be the same when compared with **26c**. Interestingly, even the Hekates with longer stilbenoid arms, **26d,e,g** ($n = 1,2$) [62] and **28n-1** ($n = 1-3$) [64], self-assemble in columnar LC structures. In the series of benzene core derivatives **26d,e**, X-ray scattering revealed a column diameter comparable with the diameter of the star molecules [62, 65]. In principle, star-shaped conformers should not be favourable for mesophase formation, since the increasing void with increasing length of the branches between individual arms does a priori not assist self-assembly in condensed phases. The reason for this prediction is the fact that nanosegregation and space-filling are enormously important for self-assembling molecules and this is difficult to fulfil simultaneously for such molecular structures. Therefore it is hard to imagine how such shape-persistent stilbenoid molecules with increasing number of repeating units ($n > 0$) can stack in columns with a reasonable density for liquid crystalline organic materials of approximately $1\text{ g}/\text{cm}^3$. Such a density can only be obtained for molecules **26** with $n = 1$ and 2, if two or more mesogens pack within a columnar slice with a height of 0.45 nm. Even for a non-coplanar packing of the molecules there are at least two cross points where segments must approach closer than the sum of Van der Waals radii; thus these interactions will be repulsive. A force-field simulation revealed that indeed the molecules can stack in a columnar structure with two molecules in such a columnar slice; however, the individual molecules are rotationally and translationally displaced [65]. The stilbenoid scaffolds are shape-persistent, but owing to the flat energy potential for the rotation about the single

bonds between phenyl rings and double bonds [66], the mesogens possess sufficient flexibility to avoid extreme steric interactions at the intermolecular cross points and thus they can accommodate in a columnar liquid crystalline structures of reasonable density. With respect to this model, the columnar stacking of Yamamotos mesogens **25** or Gallardos stars **11a,b** is highly surprising – first because the mesogens with phenyleneethynylene arms are less flexible to prevent steric repulsion at cross points and second because one long lateral alkoxy chain is usually not sufficient to induce columnar mesomorphism (compare with compounds **26a,b** and **28a–d**). A related mesogen **13** (see Fig. 4) formed for example only a nematic phase with chains of intermediate lengths. It is important to note that void space between arms of Hekates can be filled in phases with nanosegregated structures by different strategies. First, molecules can change their shape and fold like the one in subgroup (i) in order to nanosegregate the different molecular parts in soft phases. Second, mesogens may slightly change the conformation to avoid steric repulsion but maintain the overall shape and realise nanosegregated molecular segments in mesophases, as shown for extended stilbenoid stars **26d,e**. Third, molecules may crystallise and fill free space between the arms of the star either by the chains of neighbouring star molecule or by small guest molecules [67]. Fourth, the stacking of stars in dense columns may be realised by helical arrangements [57, 68]. The remaining grooves which are created by the helix formation can then be filled by the flexible aliphatic chains of neighbouring helices. The latter two possibilities are found in rather highly viscous mesophases [68] or crystals [57]. Recently it has been claimed on the basis of a theoretical study that the columnar LC phase of oxadiazole **11b** is formed by interdigitated columns [69]. This model focuses, however, mainly on electrostatic interactions of the conjugated cores and do not consider nanosegregation, packing and the fluid nature of the liquid crystalline phases. If molecules rotate about the columnar axes as shown for the stilbenoid stars **26c**, then such an interdigitated structure is no longer feasible.

In a different design of mesogens the alkoxy chains are shifted from a terminal to an internal position of the arms as in compounds **27** and **29** (see Table 1). As a consequence the aromatic scaffold can no longer nanosegregate from the aliphatic building blocks and nematic phases are generated [70, 71]. Note that for the triazine derivatives the transition enthalpies ΔH_{N-I} are extremely high for nematic phases, suggesting that at these transitions a columnar nematic phase is clearing in which presumably the columnar aggregates are disassembling, too.

2.3 *The Semi-Flexible Hekates (Subgroup (ii))*

The last subgroup in the series of Hekates, subgroup (ii), possesses linkers such as carboxy or methylene groups between the more rigid arm segments. As a consequence, conformers of different shapes can be envisaged. A few of the conformers are suitable to stack densely in condensed soft phases by nanosegregation of their different segments. Borderline cases are, for example, mesogens **31** and **32** (Fig. 7).

In mesogens **31** shape-persistent arms are attached via a semi-flexible linker to the core [72, 73]. Similar to the shape-persistent Hekates, they formed only monotropic phases with peripheral flexible alkoxy chains. A structural model was not presented; however from the given X-ray data it can be assumed that these mesogens stack in a two-dimensional ordered rectangular phase. The much smaller parameters of the unit cell compared with the diameter of the molecule indicate that even a folded conformer may play a role in mesophase formation.² Mesogens **32** were tailor-made to self-assemble their arms via intramolecular hydrogen bonding to shape-persistent entities. The semi-flexible linkers to the core allow the formation of propeller-shaped star mesogens stacking in helical columns [74–76]. Other semi-flexible triamides **33** self-assemble by intermolecular hydrogen bondings to helical columns [75–77]. For the latter two examples the mesogens behave analogous to some of the shape-persistent mesogens.

Other semi-flexible molecules realise a different mode of self-assembly. Among the most intensely studied systems are oligobenzoates with three identical, and two and three different arms **34–36** (Fig. 8) [9, 78]. The convergent synthesis allows the introduction of three different arms based on an ABC core unit [79]. The arms are usually obtained by a divergent synthesis, in which repeating units are attached to the peripheral gallic acid derivative. The applied repeating units consist of benzoic (RB) and naphthoic (RN) acid derivatives (Table 2). Table 2 summarises the thermotropic properties of these types of mesogens. A wide range of phases from highly ordered 3D columnar, 2D columnar, lamellar to cubic micellar were observed. For most of the mesogens the periphery consists of dodecyloxy chains and only the change in the benzoate scaffold modified the mesophase structure. Note that all symmetric mesogens **34** and **37** form columnar structures – at low temperature these columnar structures possess a 3D order – at higher temperature they transform to a regular hexagonal columnar phase [78, 80]. A 3D structure of a liquid crystalline columnar phase is rather unusual and its origin will be discussed below. The transition temperatures increase typically with the increasing size of the mesogens (see **34a–d**). The clearing temperatures depend mainly on the number of repeating units; the symmetry of the molecules has no major influence. For example, molecules with six repeating units, **34b**, **35b** and **36b**, possess clearing temperatures at 98 °C, 98 °C and 84 °C. Nevertheless, their phases (Col_{orth}, Col_{hd} and Cub) can be tuned simply by changing the number of repeating units per individual arm, although the size of the nanosegregated blocks do not change by this procedure [81]. The reason for this behaviour is most probably the folding of the benzoate scaffold [78, 81]. In principle, oligobenzoates can form conformers by rotation about single bonds between the aromatic and the carboxy groups.

²Note that in the original publications the interpretation of the X-ray results is not correct. Instead of a hexagonal phase the given X-ray data point to a rectangular phase with much smaller parameters compared to the molecular diameter. For the molecule with octyloxy chains the dimension of the column would be about 4.0 nm compared to a diameter of 5.2 nm for the molecule.

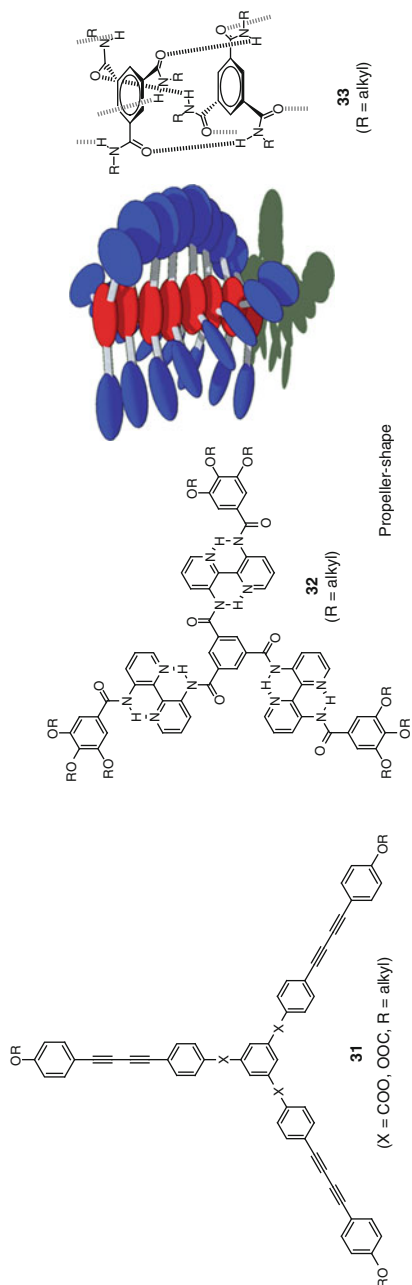


Fig. 7 Semi-flexible mesogens of subgroup (ii) – borderline cases

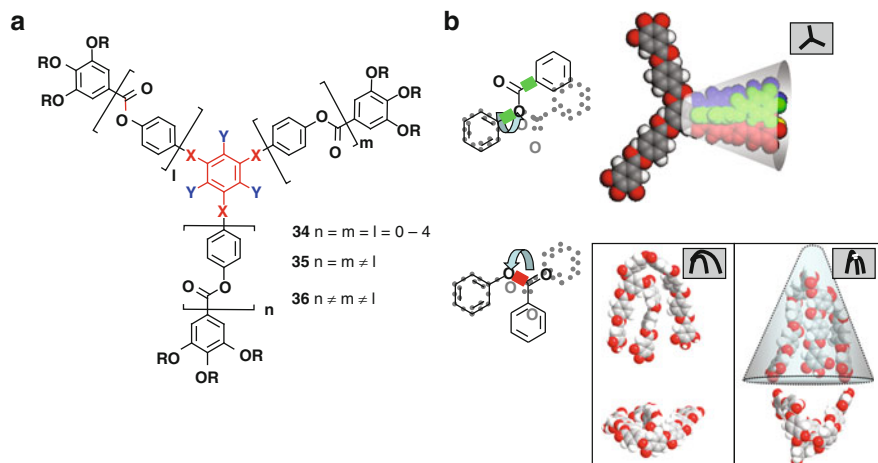


Fig. 8 General structure of semi-flexible oligobenzoate Hekates **34–36**. (a) These stars may consist of three identical arms (**34**), two (**35**) or three (**36**) different arms. Thereby the length (n, m, l), the peripheral chains (R', R'', R'''), the linking groups X (OOC, COO, CONH) to the core and the substituents Y (H, I) can be adjusted. (b) Borderline conformers – star-shaped, E -shaped and cone-shaped conformers – for a non-symmetric oligobenzoate scaffold ($X = \text{OOC}$). They can be created by rotation about the $\text{C}-\text{O}$ single bond within the carboxy linking group to the core

Such rotations move the arms on a cone as illustrated in Fig. 8b and the star-shaped topology remains. The rotation about the single bond within the carboxy group changes significantly the shape of the mesogens. Hundreds of possible conformers with slightly different shape can be envisaged [82]. While efficient packing and nanosegregation are important for the formation of liquid crystalline phases, only a few conformers appear to be applicable. Such conformers may be star-shaped, λ -shaped, T -shaped or E -shaped. Indeed, star-shaped conformers are the most stable in vacuum, when intermolecular interactions and intramolecular Van der Waals interactions are not considered [82]. Mesogens with short chains were observed to crystallise as star-shaped molecules from acetone [83]. However, it is hard to explain how star-shaped molecules can efficiently pack in mobile, liquid crystalline columnar phases with nanosegregated molecular segments, especially when the columnar diameter is much smaller than the diameter of a star-shaped oligobenzoate. The work of Yu et al. showed clearly that only stars with dodecyloxy chains reveal liquid crystal properties – shorter chains did not induce mesophases, which is evidence for nanosegregation as the driving force [84]. But how do the mesogens pack? Unfortunately, the mesophases did not allow the recording of a real image of the structure, and thus analysis relies on indirect evidence. Detailed studies were performed on the soft crystal phase of compound **34a** [78]. The column in the rectangular cell has dimensions of $a/2 = 38.6 \text{ \AA}$ and $b = 35.6 \text{ \AA}$, thus they are much smaller than the diameter of a single star-mesogen of approximately 55.2 \AA . In c -direction the column has an extension of 34 \AA .

Table 2 Thermotropic properties of Hekates based on oligobenzoate scaffolds

34 a-d	$n = m = l = 0 - 4$	
35 a, b	$n = 0, m = l = 1, 3$	
36 a, b, c	$n \neq m \neq l$	
$R = C_{12}H_{25}, X = OOC, Y = H$		
37a-d	$n = m = l = 1$	
38a, b	$n = m = l = 1, A = C = E = -$ $B = RN; D, F = RB, R^1 = C_{12}H_{25}, C_4H_8C_8F_{17}$	
39a	$n = 0, m = l = 1, A = C = -, B = RN, D = RB$	
39b	$n = 0, m = l = 1, C = -, B = RN, A = D = RB$	
$R^2, R^3 = C_{12}H_{25}$		
Compound	Thermotropic behaviour [T (°C)]^a	Ref
34a (n, m, l = 1, 1, 1)	Cr _{borh} (g 20 (T _g) Col _{hd} 53) 55 I	[78]
34b (n, m, l = 2, 2, 2)	Col _{borh} 79 Col _{hd} 98 I	[78]
34c (n, m, l = 3, 3, 3)	Col _{borh} 170 Col _{hd} 172 I	[78]
34d (n, m, l = 4, 4, 4)	Col _{borh} 241 Col _{hd} 251 I	[78]
35a (n, m, l = 0, 1, 1)	Col _{hd} 36 I	[81]
35b (n, m, l = 0, 3, 3)	g 38 (T _g) Cub (<i>Im3m</i>) 98 I	[81]
36a (n, m, l = 0, 1, 2)	Cub (<i>Im3m</i>) 51 I	[81]
36b (n, m, l = 1, 2, 3)	Col _{hd} 84 I	[81]
36c (n, m, l = 1, 2, 4)	Col _{hd} 45 Cub (<i>Im3m</i>) 128 I	[81]
37a (n, m, l = 1, 1, 1)	Col _{hd} 93 I	[80]
A, C, E = -; B, D, F = RN		
37b (n, m, l = 1, 1, 1)	Col _{bsorh} 122 Col _{hd} 146 I	[80]
A, C, E = RB; B, D, F = RN		
37c (n, m, l = 1, 1, 1)	Col _{borh} 94 Col _{hd} 137 I	[80]
A, C, E = RN; B, D, F = RB		
38a (n, m, l = 1, 1, 1)	Col _{hd} 65 I	[96]
A, C, E = -; B = RN, D, F = RB, R ¹ = C ₁₂ H ₂₅		
38b (n, m, l = 1, 1, 1)	Col _{rd} (<i>p2mg</i>) 152 SmA 190 I	[96]
A, C, E = -; B = RN, D, F = RB, R ¹ = C ₄ H ₈ C ₈ F ₁₇		

(continued)

Table 2 (continued)

Compound	Thermotropic behaviour [T ($^{\circ}\text{C}$)] ^a	Ref
39a (n, m, l = 0, 1, 1) B = RN; A, D = RB, C = –	Col _{hd} 43 I	[96]
39b (n, m, l = 0, 1, 1) B = RN, D = RB, A, C = –	Cub 61 I	[96]

Col_{hd} columnar hexagonal phase, *Col_{borh}* columnar body-centred orthorhombic phase, *Col_{bsorh}* columnar base centred orthorhombic phase, *Cub* cubic phase, *SmA* smectic A phase, *I* isotropic phase

Density measurements revealed that the unit cell contain 11–12 molecules. If star-shaped mesogens would stack on top of each other with a distance of 4.4 Å, then the column would achieve a height of 48.4–52.8 Å. Thus 12 Hekates can be accommodated in a stack of 34 Å in height only if molecules do not all overlap with each other and therefore the mesogens need to be inclined with respect to the columnar axis (see Fig. 10b). This leads to a model of five or six pairs of *E*-shaped molecules helically stacked on top of each other, which yield a double helix. Such a helix has an undulated morphology. This consequently explains why a soft columnar phase can achieve a 3D order. The helical organisation is substantiated by a high resolution AFM image [85]. It is further confirmed by an investigation of a naphthalene containing star **37b**, which was doped by a derivative with chiral peripheral chains showing a strong CD signal only in the low temperature phase [80]. All solid state NMR results on the soft crystal phase of **34a** point to a phase of folded, *E*-shaped conformers: (1) the whole molecule performs only librational motions instead of large angle motions as expected for a molecule not having the centre of gravity at the centre of the column; (2) the π -shift distribution in a double quantum experiment is only observed for the aromatic hydrogens, not for the aliphatic protons, pointing to nanosegregation; (3) cross peaks between aromatic and aliphatic protons in the same experiment demonstrate that aliphatic protons are permanently close to aromatic protons [78]. The latter is naturally the case in *E*-shaped conformers and in helical packings, since then the grooves of the helix presenting the aromatic parts are filled by aliphatic chains. Columnar orthorhombic soft crystals or liquid crystals which are base- or body-centred develop upon cooling from the more disordered hexagonal phase (see **34**, **37b,c** in Table 2) by inclination and helix formation. Indications for this process can be observed by optical microscopy (Fig. 9). The texture of the hexagonal phase is a smooth pseudo-focal conic texture of low birefringence typically found for columnar phases [86]. The texture of the highly ordered columnar phase is almost identical, but shows a higher birefringence and a fine structure even in the dark branches of the Maltese cross, pointing to undulation of the columns. The columnar structure remains during this process, evidenced by a detailed AFM study [87]. During the relatively slow phase transition the texture often disappears completely, which may be explained by the incoming inclination of the molecules vs the columnar axis. Consequently the phase changes from an optical negative (Col_h) to

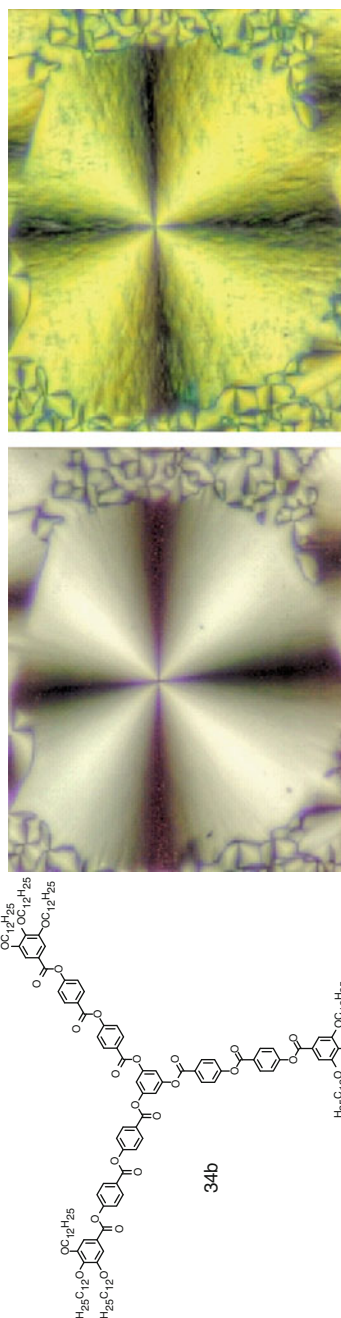


Fig. 9 Textures of the columnar phases of compound **34b**. Pseudo-focal conic texture at 92 °C of the Col_{hd} phase (*bottom*) and at 74 °C in the body-centred orthorhombic columnar phase (*top*). In order to increase the dynamic range of the photographs various photos with different exposure times have been superimposed. The black Maltese cross is perfectly dark in the centre for the Col_{hd}. In the low temperature phase undulation of the columns produces birefringence in the dark branches

an optical positive phase (Col_{borh} , Col_{bsorh}) and in the transition the indicatrix, describing the optical properties of the material, is isotropic³.

The columnar phases of oligobenzoate Hekates are most probably formed from *E*-shaped conformers which pack disordered in hexagonal columnar phases and for symmetric mesogens they can tilt and aggregate in highly ordered helical arrangements to form the 3D columnar structures (see Fig. 10a, b). Indications

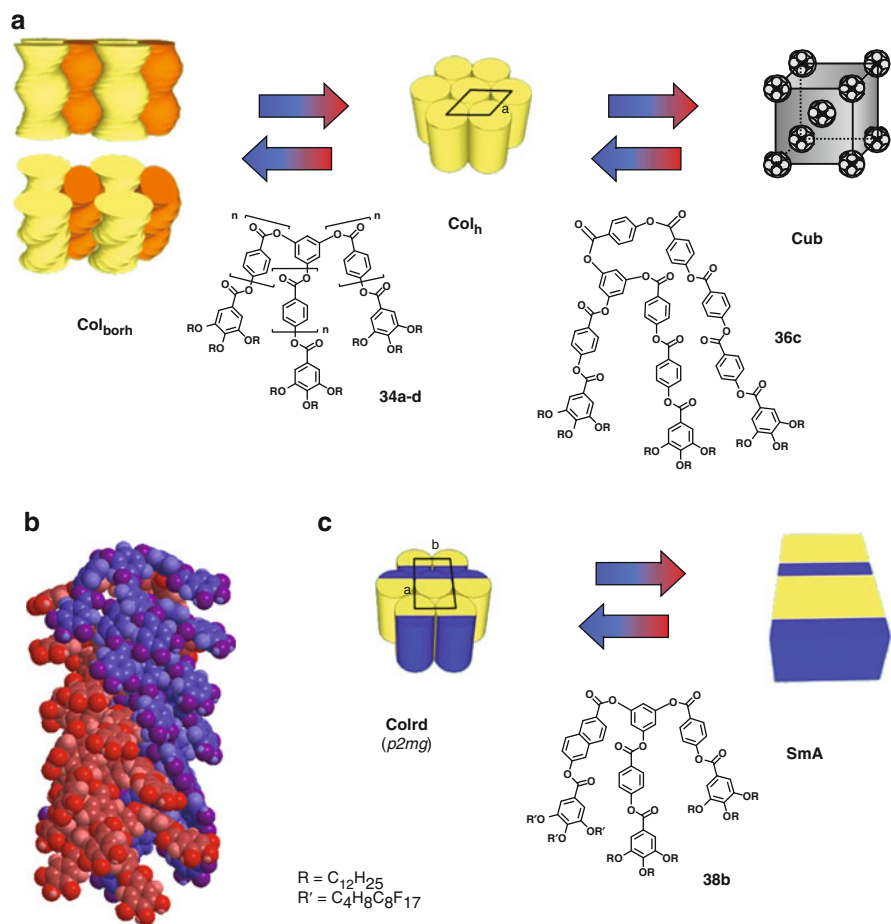


Fig. 10 Different LC structures formed from C_3 -symmetric or non- C_3 -symmetric oligobenzoate Hekates. (a) 3D ordered mesophases based on an undulated columnar topology of helical stacks as proposed for *E*-shaped oligobenzoates **34a–d** in the soft crystal and thermotropic LC phases (left) and their transition to the hexagonal phase (Col_h). Formation of the micellar cubic mesophase in the series of folded non-symmetric mesogens (e.g. **36c**) and the transformation to the hexagonal phase (right). (b) Model of the helical packing of *E*-shaped oligobenzoate scaffolds of **34a**. (c) 2D columnar mesophase (Col_{rd} rectangular columnar) in the rare plane group $p2mg$ and the transition to the lamellar structure (SmA) for a mesogen **38b** containing semi-perfluorinated chains. Copyright Wiley-VCH Verlag GmbH & Co. KGaA. Reproduced with permission from reference [2]

³ Tschierske, personal communication. The experimental verification is in progress.

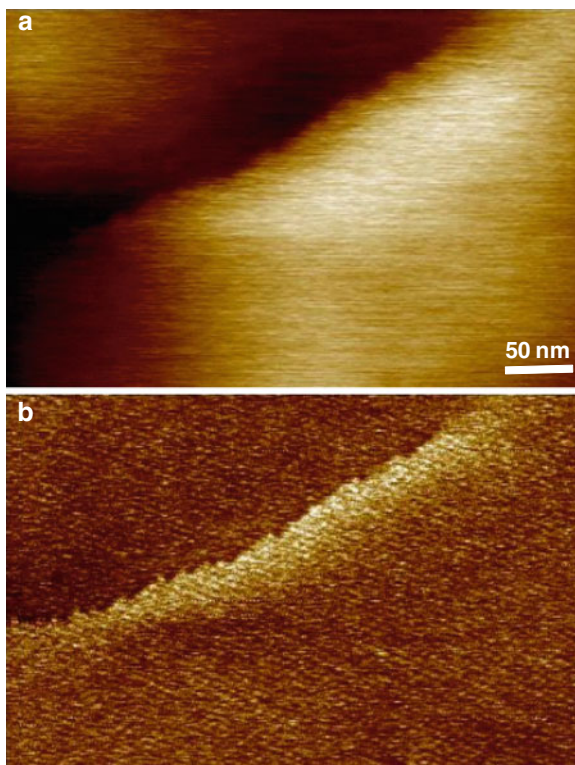
for folding of mesogens were obtained even for a compound with an iodine at the central benzene unit ($X = \text{OOC}$, $Y = \text{I}$) and with a more rigid trimesic acid core ($X = \text{COO}$, $Y = \text{H}$) [78]. Evidence for *E*-shaped conformers in the mesophases has been obtained still for compounds in which the peripheral carboxy groups are substituted by amides, which were supposed to stabilise aggregation of star-conformers by hydrogen bonding in solution [88]. Non-symmetric mesogens in which the length of the arms do not differ strongly, such as in **35a**, **36b**, **c**, **38a** and **39a** form only the Col_{hd} phases. As shown in Fig. 8 for the benzoate scaffold of **36c**, almost flat *E*-like conformers can still be obtained by folding of these mesogens.

A recent report claimed that oligobenzoates with only one peripheral alkoxy chain per arm organise in columnar phases, too [89]. The authors report mesogens with trimesic acid, phloroglucinol, 1,3-dihydroxybenzoic acid and 1,3,5-(3-hydroxyphenyl) benzene as core and dodecyloxy chains at the periphery. The elongated arms consisted of a 4-alkoxyphenylcarbonyloxyphenyl unit linked either by a carboxy or an oxycarbonyl group to the core. All semi-flexible mesogens showed columnar mesophases based on observation by optical microscopy and DSC studies; however no transition enthalpies were given which would help to substantiate the findings. This family of extended oligobenzoates was probably not investigated for a long time since similar shape-persistent mesogens failed to give mesomorphic materials. Based on the concept of folding, it is therefore not surprising that such mesogens can find a way to self-assemble in columnar structures. The negative result that the molecule with the larger shape-persistent triphenylbenzene core did not reveal a liquid crystal phase supports a model in which folding to *E*-shaped conformers plays an important role. The authors of that report suggested a model based on star-conformers with no further solid evidence. We believe that all the results can be better explained by *E*-shaped conformers. Unfortunately, no X-ray results were published, which would help to substantiate a model. Interestingly, earlier described mesogens with six or seven dodecyloxy chains did not show any mesomorphism [90].

New strong evidence for folding of the oligobenzoates has been obtained when the non-symmetric mesogens forming cubic phases have been studied in detail by GISAXS and high resolution AFM [91]. The results confirm micellar cubic mesophases in an $Im3m$ space group. It has been demonstrated that even isolated micelles preserve their integrity. As shown in Figure 11b, single micelles can be imaged by AFM at a one-layer step of the material. Such small micelles cannot assemble from flat star-shaped molecules. In models of different systems cone-shaped conformers were proposed as building blocks of a sphere [92–94], and it seems that in general a cone-shaped mesogen is mandatory for a micellar dense packing. Indeed slight rearrangement of the *E*-conformer in the third dimension provides a cone-shaped conformer of semi-flexible Hekates and force-field simulations support this model [91]. The cubic phase of the same mesogen **36c** transforms slowly to a columnar phase at lower temperature. This is possible via the change of the conformer from a cone-shape to an *E*-shape and does not afford strong conformational adjustments.

Indeed, for semi-flexible triarm oligobenzoate stars, Hekates of subgroup (ii), an enormous number of results point to folded *E*-shaped, cone-shaped or at least

Fig. 11 AFM micrograph of the (110) surface of the cubic phase of compound **36c** showing a one-layer step. (a) Height image. (b) Phase image. Lighter regions in (a) are raised. Imaged at 55 °C [91]. Reproduced by permission of The Royal Society of Chemistry



similar conformers self-assembling in dense soft structures. The driving force can be identified as the tendency to fill space efficiently and optimising intermolecular interactions by packing and by nanosegregation of peripheral chains and the more polar benzoate core. It is interesting to note that if one arm is removed, folding is no longer observed. The resulting banana mesogens aggregate in lamellar phases and do not need to change their conformation significantly for nanosegregation [95].

Incorporation of naphthalene chromophores afforded materials with relatively high charge carrier mobilities, evidenced by the pulse radiolysis time resolved microwave conductivity technique (PR-TRMC) [80]. This is a consequence of the aggregation of the naphthalene units in the middle of the column which has been shown by the enormous bathochromic shift of the emission maximum in fluorescence spectra. In order to tailor more complex functional materials, chromophores should be positioned by simple attachment of different incompatible peripheral chains at the arm with the chromophore. This has been accomplished in mesogen **38b** with semi-perfluorinated peripheral chains and compared to a mesogen with the same core but only aliphatic chains at its periphery [96]. Owing to the semi-perfluorinated chains at the arm with the naphthalene chromophore, a rarely observed rectangular phase with $p2mg$ symmetry was revealed. In this phase, perfluorinated chains segregate together with the linked chromophores from the rest of the *E*-shaped molecules (Fig. 10c). The all-alkyl chain derivative **38a**

only assemble in a hexagonal phase in which the chromophores can be supposed to be statistically distributed. This concept has been further developed and three incompatible peripheral chains have been introduced. It seems that by cooling from the isotropic phase an SmA phase formed similar to compound **38b**. The semi-perfluorinated chains segregate⁴ – the other chains obviously mix and consequently induce the formation of a smectic phase. Columns assembled along these layers upon cooling and a rectangular mesophase with $p2mg$ symmetry was generated. Further cooling leads to a unit cell change which is assumed to be based on nanosegregation of the alkyl and oligoethylenoxy chains [88]. The facile alignment of lamellar phases parallel with surfaces at high temperature can be used to create planar aligned columns, which could be interesting for the fabrication of field effect transistors.

Neat melamine Hekates **40** are a further interesting class of compounds. Depending on the number of side chains they either exist as star-shaped or λ -shaped conformers [99–103]. The disk-shaped star mesogens accommodate in columns when they are decorated with nine alkoxy chains. With three and six long alkoxy chains space cannot be efficiently filled and the mesogens fold to λ -shaped conformers which aggregate in dimers via intermolecular H-bonds. Such dimers self-assemble subsequently in columnar and lamellar mesophases. However, in the LC phase the void between the arms can be compensated not only by folding but also by incorporation of hydrogen bond donors such as carboxylic acids in host–guest complexes (Fig. 12). For the three and six chain derivatives of **40** a folding to λ -conformers has been proposed to create sufficient void to host various carboxylic acid derivatives with different steric demands. With few exceptions, they all reveal columnar mesomorphism. Note that even the star-shaped melamine with nine alkoxy chains can still provide enough space to accept benzoic acids with one, two and three alkoxy chains; however, steric more demanding, further branched carboxylic acids do not result in complexes [99]. Guests with chiral tails induce helical packing along the columns [104]. Janietz and co-worker recently provided carboxylic acids with two or three semi-perfluorinated chains as H-bonding guests. The melamine Hekates afforded Janus-type complexes **42** (Fig. 12) self-assembling in complex columnar hexagonal structures [105]. Melamine Hekates can also be formed by supramolecular interactions starting from a monoalkyl substituted melamine. The arms can be attached simply by hydrogen

⁴The segregation of perfluorinated segments is generally explained by the fluorophobic effect and not by an especially attractive interaction of perfluorinated alkyl chains. The dispersion interaction between small perfluorinated molecules has been shown to be larger than the non-fluorinated alkyl chains [97]; however, they decrease and become smaller than that of the alkyl chains for longer chain lengths owing to the larger intermolecular distance of perfluorinated aliphatic building blocks (see for more details [98]). In the present case the columnar phase of the all alkyl chain derivative **38a** clears at 65 °C whereas the derivative with one semi-perfluorinated arm **38b** shows a transition only at 152 °C to a SmA phase and the clearing temperature at 190 °C. This is difficult to explain by only an underlying phlorophobic effect; thus dispersion forces may play an important role here too.

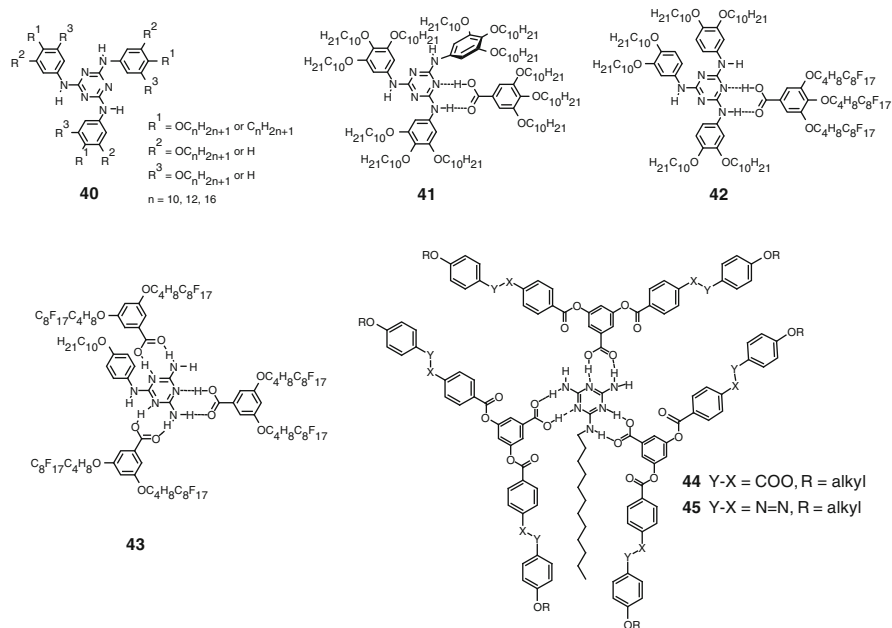


Fig. 12 Neat melamine Hekates **40**, their 1:1 host–guest complexes **41**, **42** and the 1:3 aggregates of a melamine core with three arms **43** and **44**. The disk-shaped aggregates **41** stack in a Col_{rd} phase [99]. The Janus-type Hekate **42** arrange in a Col_h phase with hexagonal superstructure of the nanosegregated semi-perfluorinated chains [105]. The supramolecular Hekate discs **43–45** self-assemble by hydrogen bonding of the three arms around a melamine core

bonding [106]. The disk-shaped, closed hydrogen-bonded aggregates **43** were built from a 1:3 mixture of core and perfluorinated arms. Propeller-shaped aggregates **44** resulted when banana shaped arms were complexed to the melamine core [107]. Chiral tails induced helical columnar arrangements [107, 108]. Helicity can also be controlled by photochemical processes using circular polarised light, when azo groups are incorporated in the arms as in compound **45** [109]. The last examples can be regarded as six arm stars. However, the morphology reminds one more of Hekates with three arms.

2.4 Supramolecules: Hekates Formed by Supramolecular Interactions

As discussed in the last section, some Hekates cannot only accept guests in LC phases but may also be entirely assembled by hydrogen bonding around a non-mesomorphic core (see compounds **44** and **45**, Fig. 12). The flexible mesogen **7** (Fig. 3) is another example of a Hekate supermolecule formed by ionic interactions.

Figure 13 highlights some further examples of Hekate supermolecules which are assembled via hydrogen bonding. Compounds **46** were reported to form nematic columnar phases with $R = C_nH_{2n+1}$ ($n = 4-9$) [110]. For longer chains columnar phases were found. It is remarkable that only one long alkoxy chain per arm is sufficient to generate columnar mesomorphism, e.g. decyloxy chains in **46b**. A model has not been proposed. However, the a parameter of the hexagonal phase amounts to 51.7 Å and is thus comparable to the diameter of the star molecule with the alkyl chains in all-antiperiplanar conformations. If the density is estimated to be about 1 g/cm³ then five molecules must form a columnar slice 4.2 Å in height. Consequently, five rather linear λ -type mesogens, i.e. folded hydrogen-bonded supermolecules, must assemble side by side in a disk-like aggregate, similar to phasmidic mesogens. Note that an analogous mixture with trimesic acid as a hydrogen bond donor core did not reveal mesomorphism (see compound **47** in Fig. 13) [111]. Most probably the trimesic acid forms more stable crystals upon cooling of the liquid mixture and thus is no longer available for heterogeneous complex formation. A small disk-shaped H-bond acceptor was used to create a rigid supramolecular Hekate **48** [112]. This compound with polymerisable peripheral chains formed a hexagonal columnar lattice. The small disc-shaped templates could be removed after polymerization, thus generating a material with nano-channels.

These few examples show that Hekates of all subgroups (i)–(iii) can be formed by supramolecular interactions, too, which make their synthesis even more versatile. The only obvious limitation of the supramolecular approach is that the individual components should not themselves form H-bonded networks or crystallise and thus precipitate from the mixture. This may be the reason that not many Hekate LC supermolecules are known presently.

2.5 Summary and Outlook

All these examples show that the structure of Hekates can be synthetically well controlled by tuning the nature of the arms, the core and the interacting guest molecules and functions can be implemented. Hekates combine various advantages over monomers and linear oligomers: (1) their versatile synthesis with different arms and a library of accessible cores; (2) their often high temperature glass transitions and thus rather stable glassy LC room temperature phases; (3) their good solubility; and (4) the possibility to incorporate guest molecules. All these features can be advantageously exploited to generate materials for application [9]. An example is the guest–host property that has been used in the supramolecular Hekate **48** to form a material with nano-channels showing high permeability for nitrogen and applicable for molecular recognition, separation or catalysis purposes [112]. Compound **45** is a photoswitchable material which opens the possibility to write chiral information in an LC phase [110]. Kato reported an ion responsive Hekate with a triphenylphosphine oxide core. The structure of such a material could be simply switched from a columnar to cubic micellar phase by addition of

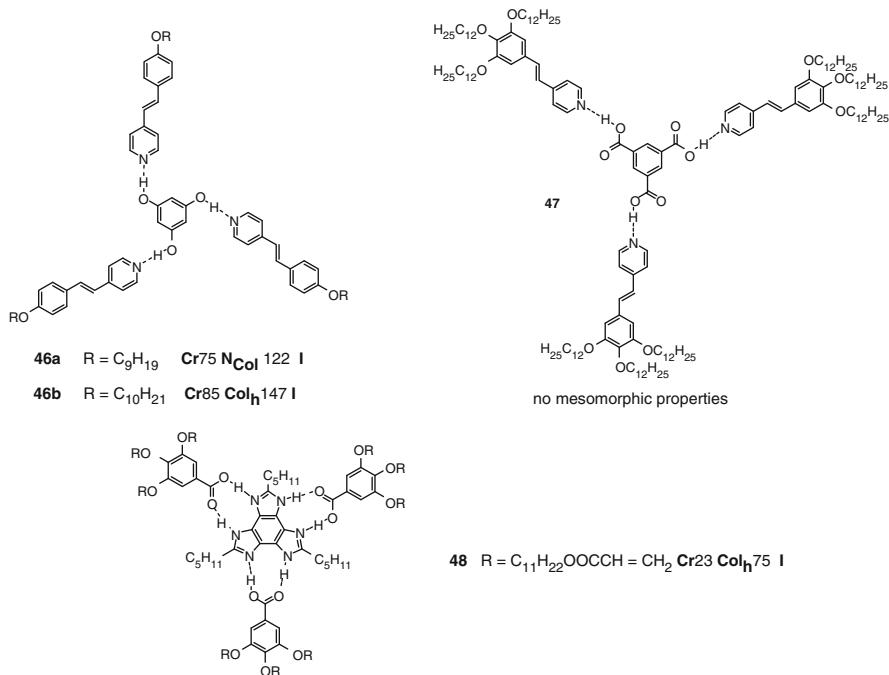


Fig. 13 Hekates formed by supramolecular interactions of different building blocks

different metal ions [113]. Owing to the good solubility and glass forming properties Hekates may be used in opto-electronic devices [114] or, if conjugated arms or chromophores are incorporated, they may be applied in organic electronics [11, 37, 80].

In the future this field will certainly evolve in order to gain the structural control of functional units in more complex materials on the nanoscale. The driving forces which can be synthetically programmed are nanosegregation and space-filling and these parameters depend strongly, of course, on molecular conformations. Already today numerous other more complex star-shaped molecules are known. Tetrahedral semi-flexible oligobenzoates based on pentaerythritol with an a priori 3D molecular structure are, for example, able to generate columnar phases because they can fold and pack efficiently, similar to the benzoate Hekates [6]. Rigid tetrahedral molecules only exist as crystalline materials, since folding is not possible and thus nanosegregation and space-filling cannot be accomplished [115]. Six-arm functional stars are of great interest owing to their strong aggregation properties in neat materials and solution [116]. In such structures, which are crowded benzene derivatives, the void space available in Hekates for folding and guest hosting is occupied by the three additional arms. Many different examples of liquid crystalline stars with large discotic arms and cores [33, 117–119] and high numbers of arms [119–121] can be mentioned as prototypes for future functional materials

based on the star LC concept. Although their detailed discussion is outside the scope of the present chapter, they show that the field of complex LC structures based on star-shaped molecular design is developing promisingly towards functional soft materials.

References

1. Wenninger MJ (1971) Polyhedron models. Cambridge University Press, New York
2. Lehmann M (2009) Star mesogens (Hekates) – tailor-made molecules for programming supramolecular functionality. *Chem Eur J* 15:3628–3651
3. Donnio B, Guillon D (2006) *Adv Polym Sci* 201:45–155
4. Goodby JW, Saez IM, Cowling SJ, Görtz V, Draper M, Hall AW, Sia S, Cosquer G, Lee S-E, Raynes EP (2008) *Angew Chem Int Ed* 47:2754–2787
5. Demus D (2001) *Mol Cryst Liq Cryst* 364:25–91
6. Tschierske C (2001) *J Mater Chem* 11:2647–2671
7. Tschierske C (1998) *J Mater Chem* 8:1485–1508
8. Tschierske C (2007) *Chem Soc Rev* 36:1930–1970, A review about tilings comprising ABC star blockcopolymers
9. Lehmann M (2009) *Chem Eur J* 15:3638–3651
10. Lehmann M, Jahr M (2011) Mesogens and mesophases. In: Andrews D, Scholes G, Wiederrecht G (eds) *Comprehensive nanoscience and technology*, vol 5. Elsevier, Amsterdam, pp 277–357
11. Detert H, Lehmann M, Meier H (2010) *Materials* 3:3218–3330
12. Halsey WD, Johnston B (eds) (1988) *Collier's encyclopedia*, vol 12. Macmillan Educational Company, New York
13. Burkert W (1985) Greek religion. Harvard University Press, Cambridge
14. Roscher WH (ed) (1993) Ausführliches Lexikon der griechischen und römischen Mythologie. I.2: 1885 ff, Georg Olms, Hildesheim
15. Binder W (1874) Dr. Vollmer's Wörterbuch der Mythologie aller Völker, 3rd edn. Hoffmann's, Stuttgart
16. Mehl GH, Thornton AJ, Goodby JW (1999) *Mol Cryst Liq Cryst* 332:455–461
17. Göring P, Pelzl G, Diele S, Delavier P, Siemensmeyer K, Eitzbach KH (1995) *Liq Cryst* 19:629–635
18. Kumar S, Manickman M (1999) *Liq Cryst* 26:939–941
19. Wilson L (1994) *Liq Cryst* 18:1005–1014
20. Chen SH, Shi H, Conger BM, Mastrangelo JC, Tsutsui T (1996) *Adv Mater* 8:998–1001
21. Paraschiv I, Giesbers M, van Lagen B, Grozema FC, Abellon RD, Siebbeles LDA, Marcellis ATM, Zuilhof H, Sudhölter EJR (2006) *Chem Mater* 18:968–974
22. Abetz V, Jiang S (2004) *e-Polymers* 054
23. Hückstädt H, Göpfert A, Abetz V (2000) *Macromol Chem Phys* 201:296–307
24. Ungar G, Tschierske C, Abetz V, Holyst R, Bates MA, Liu F, Prehm M, Kieffer R, Zeng X, Walker M, Glettnner B, Zywockinski A (2011) *Adv Funct Mater* 21:1296–1323
25. de Campo L, Varslot T, Moghaddam MJ, Kirkensgaard JJK, Mortensen K, Hyde ST (2011) *Phys Chem Chem Phys* 13:3139–3152
26. Hayashida K, Dotera T, Takano A, Matsushita Y (2007) *Phys Rev Lett* 98:195502
27. Yao D-S, Zhang B-Y, Zhang W-W, Tian M (2008) *J Mol Struct* 881:83–89
28. Zhang B-Y, Yao D-S, Meng F-B, Li Y-H (2005) *J Mol Struct* 741:135–140
29. Chen SH, Mastrangelo JC, Shi H, Bashir-Hashemi A, Li J, Gelber N (1995) *Macromolecules* 28:7775–7778
30. Kocot A, Vij V (2010) *Liq Cryst* 37:653–667

31. Tajber L, Kocot A, Vij JK, Merkel K, Zalewska-Rejda J, Mehl GH, Elsässer R, Goodby JW, Veith M (2002) *Macromolecules* 35:8601–8608
32. Katoh M, Uehara S, Kohmoto S, Kishikawa K (2006) *Chem Lett* 35:322–323
33. Zelcer A, Donnio B, Bourgoigne C, Cukiernik FD, Guillon D (2007) *Chem Mater* 19:1992–2006
34. Kumar S (2005) *Liq Cryst* 32:1089–1113
35. Frackowiak E, Scherowsky G (1997) *Z Naturforsch B Chem Sci* 52:1539–1543
36. Kotha S, Kashinath D, Lahiri K, Sunoj R B (2004) *Eur J Org Chem* 4003–4013
37. Ponomarenko SA, Kirchmeyer S, Elschner A, Huisman B-H, Karbach A, Drechsler D (2003) *Adv Funct Mater* 13:591–596
38. Narita T, Takase M, Nishinaga T, Iyoda M, Kamada K, Ohta K (2010) *Chem Eur J* 16:12108–12113
39. Pappenfus TM, Mann KR (2002) *Org Lett* 4:3043–3046
40. Christiano R (2005) Pereira de Oliveira Santos D M, Gallardo H. *Liq Cryst* 32:7–14
41. Zhang Y-D, Jespersen KG, Kempe M, Kornfield JA, Barlow S, Kippelen B, Marder SR (2003) *Langmuir* 19:6534–6536
42. Varghese S, Kumar NSS, Krishna A, Rao DSS, Prasad SK, Das S (2009) *Adv Funct Mater* 19:2064–2073
43. Kim BG, Kim S, Park SY (2001) *Tetrahedron Lett* 42:2697–2699
44. Pesak DJ, Moore JS (1997) *Angew Chem Int Ed* 36:1636–1639; *Angew Chem* 109:1709–1712
45. Bushey M, Nguyen T, Nuckolls C (2003) *J Am Chem Soc* 125:8264–8269
46. Nuckolls C (2004) *J Am Chem Soc* 126:5234–5242
47. Zhao Y, Shirai Y, Slepko AD, Cheng L, Alemany LB, Sasaki T, Hegmann FA, Tour JM (2005) *Chem Eur J* 11:3643–3658
48. Bock H, Babeau A, Seguy I, Jolinat P, Destruel P (2002) *Chem Phys Chem* 6:532–535
49. Bock HR, Anderson S, Fujita Y, Hudson AJ, Rorison JM, Weaver M (1999) UK Patent GB2336839
50. Lee H, Kim D, Lee H-K, Qiu W, Oh N-K, Zin W-C, Kim K (2004) *Tetrahedron Lett* 45:1019–1022
51. Lin YC, Kai CK, Chang Y-C, Liu K-T (2002) *Liq Cryst* 29:237–242
52. Pieterse K, Lauritsen A, Schenning APHJ, Vekemans JAJM, Meijer EW (2003) *Chem Eur J* 9:5597–5604
53. Lee CH, Yamamoto T (2001) *Tetrahedron Lett* 42:3993–3996
54. Lee CH, Yamamoto T (2002) *Mol Cryst Liq Cryst* 378:13–21
55. Kotha S, Kashinath D, Lopus M, Panda D (2009) *Ind J Chem* 48B: 1766–1770
56. Zerban G, Meier H (1993) *Z Naturforsch* 48b:171–184
57. Holst HC, Pakula T, Meier H (2004) *Tetrahedron* 60:6765–6775
58. Lifka T, Oehlhof A, Meier H (2008) *J Heterocycl Chem* 45:935–937
59. Attias A-J, Cavalli C, Donnio B, Guillon D, Hapiot P, Malthête J (2002) *Chem Mater* 14:375–384
60. Meier H, Lehmann M, Kolb U (2000) *Chem Eur J* 6:2462–2469
61. Meier H, Lehmann M (1998) *Angew Chem Int Ed* 37:643–645; *Angew Chem* 110:666–669
62. Lehmann M, Schartel B, Hennecke M, Meier H (1999) *Tetrahedron* 55:13377–13394
63. Lehmann M, Fischbach I, Spiess HW, Meier H (2004) *J Am Chem Soc* 126:772–784
64. Meier H, Holst HC, Oehlhof A (2003) *Eur J Org Chem* 4173–4180
65. Rumpf N, Lehmann M (2009) *Book of Abstracts. Topical Meeting on Liquid Crystals, Stuttgart*
66. Meier H (1992) *Angew Chem Int Ed* 31:1399–1420; *Angew Chem* 104:1425–1576
67. Meier H, Karpouk E, Lehmann M, Schollmeyer D, Enkelmann V (2003) *Z Naturforsch B* 58:775–781
68. Lehmann M, Köhn C, Meier H, Renker S, Oehlhof A (2006) *J Mater Chem* 16:441–451
69. Gihm SH, Kim BG, Kim S, Seo J, Park SY, Park CR (2010) *J Mol Struct* 984:371–375

70. Lehmann M (1995) Synthese und Untersuchung von stilbenoiden Sternstrukturen. Diplomarbeit, University of Mainz
71. Meier H, Lehmann M, Holst HC, Schwöppe D (2004) *Tetrahedron* 60:6881–6888
72. Chang JC, Yeon JR, Chin YS, Han MJ, Hong S-K (2000) *Chem Mater* 12:1076–1082
73. Chang JC, Baik JH, Lee CB, Han MJ, Hong S-K (1997) *J Am Chem Soc* 119:3197–3198
74. Palmans ARA, Vekemans JAJM, Fischer H, Hikmet RA, Meijer EW (1997) *Chem Eur J* 3:300–307
75. Brunsveld L, Folmer BJB, Meijer EW, Sijbesma RP (2001) *Chem Rev* 101:4071–4097
76. Brunsveld L, Schenning APHJ, Broeren MAC, Janssen HM, Vekemans JAJM, Meijer EW (2000) *Chem Lett* 292–293
77. van Gorp JJ, Vekemans JAJM, Meijer EW (2003) *Mol Cryst Liq Cryst* 397:191–205
78. Lehmann M, Jahr M, Donnio B, Graf R, Gemming S, Popov I (2008) *Chem Eur J* 14:3562–3576
79. Lehmann M, Jahr M (2006) *Org Lett* 8:721–723
80. Lehmann M, Jahr M, Grozema FC, Abellon RD, Siebbeles LDA, Müller M (2008) *Adv Mater* 20:4414–4418
81. Lehmann M, Jahr M (2008) *Chem Mater* 20:5453–5456
82. Gemming S, Lehmann M, Seifert G (2005) *Z Metallkd* 96:988–997
83. Lehmann M, Jahr M, Ruffer T, Lang H (2007) *Z Naturforschung* 62b:988–994
84. Yu LJ, Cho C-C (2004) *Mol Cryst Liq Cryst* 411:313–318
85. Ivanov DA, Gearba RI, Anokhin D, Magonov S, Lehmann M (2006) *PMSE Preprints* 94:655–656
86. Oswald P, Pieranski P (2006) *Smectic and columnar liquid crystals*. Taylor & Francis, Boca Raton
87. Gearba RI, Bondar A, Lehmann M, Goderis B, Bras W, Koch MHJ, Ivanov DA (2005) *Adv Mater* 17:671–676
88. Jahr M (2011) *Neue sternförmige Mesogene: Strukturbildung und Chromophore*. Dissertation, Chemnitz University of Technology
89. Stackhouse PJ, Wilson A, Lacey D, Hird M (2010) *Liq Cryst* 37:1191–1203
90. Lehmann M, Gearba RI, Ivanov DA, Koch MHJ (2004) *Mol Cryst Liq Cryst* 311:397–406
91. Weber CHM, Liu F, Zheng X-B, Ungar G, Mullin N, Hobbs JK, Jahr M, Lehmann M (2010) *Soft Matter* 6:5227–5246
92. Yeardley DJP, Ungar G, Percec V, Holerca NM, Johansson G (2000) *J Am Chem Soc* 122:1684–1689
93. Duan H, Hudson SD, Ungar G, Holerca MN, Percec V (2001) *Chem Eur J* 7:4134–4141
94. Donnio B, Garcia-Vazquez P, Gallani J-L, Guillon D, Terazzi E (2007) *Adv Mater* 19:3534–3539
95. Tschierske C, Photinos D (2010) *J Mater Chem* 20:4263–4294
96. Lehmann M, Jahr M, Gutmann J (2008) *J Mater Chem* 18:2995–3003
97. Tsuzuki S et al (2002) *J Chem Phys* 116:3309–3315
98. Tschierske C (2011) Fluorinated liquid crystals: design of soft nanostructures and increased complexity of self-assembly by perfluorinated segments. *Top Curr Chem*. doi:10.1007/128_2011_267
99. Barberá J, Puig L, Serrano J-L, Sierra T (2004) *Chem Mater* 16:3308–3317
100. Janietz D (1998) *J Mater Chem* 8:265–274
101. Goldmann D, Janietz D, Schmidt C, Wendorff J H (2000) *Angew Chem Int Ed* 39: 1851–1854
102. Goldmann D, Janietz D, Schmidt C, Wendorff J H (2004) *J Mater Chem* 14:1521–1525
103. Goldmann D, Janietz D, Schmidt C, Wendorff JH (1998) *Liq Cryst* 25:711–719
104. Barberá J, Puig L, Romero P, Serrano J-L, Sierra T (2005) *Chem Mater* 17:3763–3771
105. Kohlmeier A, Janietz D (2007) *Liq Cryst* 34:289–294
106. Kohlmeier A, Nordsieck A, Janietz D (2009) *Chem Mater* 21:491–498
107. Barberá J, Puig L, Romero P, Serrano J-L, Sierra T (2006) *J Am Chem Soc* 128:4487–4492

108. Vieira AA, Gallardo H, Barberá J, Romero P, Serrano J-L, Sierra T (2011) *J Mater Chem* 21:5916–5922
109. Vera F, Tejedor RM, Romero P, Barberá J, Ros MB, Serrano J-L, Sierra T (2007) *Angew Chem Int Ed* 46:1873–1877
110. Lee JH, Hwang SH, Jang I, Lee SJ, Yoo SH, Jho JY, Park S-Y (2005) *Tetrahedron Lett* 46:7143–7146
111. Kleppinger R, Lillya CP, Yang C (1997) *J Am Chem Soc* 119:4097–4102
112. Lee H-K, Lee H, Ko YH, Chang YJ, Oh N-K, Zin W-C, Kim K (2001) *Angew Chem Int Ed* 40:2669–2671
113. Hatano T, Kato T (2006) *Chem Commun* 1277–1279
114. Kim C, Marshall K, Wallace JU, Ou JJ, Chen SH (2008) *Chem Mater* 20:5859–5868
115. Pegenau A, Hegemann T, Tschierske C, Diele S (1999) *Chem Eur J* 5:1643–1660
116. Tomović Z, van Dongen J, George SJ, Xu H, Pisula W, Leclère P, Smulders MM, De Feyter S, Meijer EW, Schenning AP (2007) *J Am Chem Soc* 129:16190–16196
117. Zhi L, Wu J, Müllen K (2005) *Org Lett* 7:5761–5764
118. Graafe A, Janietz D (2005) *Chem Mater* 17:4979–4984
119. Kimura M, Narikawa H, Ohta K, Hanabusa K, Shirai H, Kobayashi N (2002) *Chem Mater* 14:2711–2717
120. Chuard T, Deschenaux R, Hirsch A, Schönberger H (1999) *Chem Comm* 2103–2104
121. Felder-Flesch D, Rubnicki L, Bourgogne C, Donnio B, Guillon D (2006) *J Mater Chem* 16:304–309
122. Miao J, Zhu M (2010) *J Phys Chem B* 114:1879–1887

DNA-Based Soft Phases

Tommaso Bellini, Roberto Cerbino, and Giuliano Zanchetta

Abstract This chapter reviews the state-of-the-art in the study of molecular or colloidal systems whose mutual interactions are mediated by DNA molecules. In the last decade, the robust current knowledge of DNA interactions has enabled an impressive growth of self-assembled DNA-based structures that depend crucially on the properties of DNA–DNA interactions. In many cases, structures are built on design by exploiting the programmable selectivity of DNA interactions and the modularity of their strength. The study of DNA-based materials is definitely an emerging field in condensed matter physics, nanotechnology, and material science. This chapter will consider both systems that are entirely constructed by DNA and hybrid systems in which latex or metal colloidal particles are coated by DNA strands. We will confine our discussion to systems in which DNA-mediated interactions promote the formation of “phases,” that is structures extending on length scales much larger than the building blocks. Their self-assembly typically involves a large number of interacting particles and often features hierarchical stages of structuring. Because of the possibility of fine-tuning the geometry and strength of the DNA-mediated interactions, these systems are characterized by a wide variety of patterns of self-assembly, ranging from amorphous, to liquid crystalline, to crystalline in one, two, or three dimensions.

Keywords Colloids · DNA · Gels · Glasses · Liquid crystals · Pairing · Self-assembly · Stacking

T. Bellini (✉), R. Cerbino, and G. Zanchetta
Dipartimento di Chimica, Biochimica e Biotecnologie per la Medicina, Università degli Studi di Milano, Via F.lli Cervi 93, 20090 Milano, Italy
e-mail: tommaso.bellini@unimi.it

Contents

1	Fundamental Interactions in DNA	226
1.1	Thermodynamic Stability of the Double Helix	228
1.2	DNA Melting Temperature	230
1.3	Pairing vs Stacking Forces	232
1.4	Ionic Strength Dependence	233
1.5	Chiral Inter-helical Interactions	234
2	All-DNA Superstructures	236
2.1	DNA Liquid Crystals	236
2.2	DNA Crystals	243
2.3	DNA Origami	254
2.4	Linear Aggregates	256
2.5	Hydrogels	258
3	Self-Assembly of DNA-Coated Colloids	262
3.1	DNA-Coated Particles and Their Interactions	264
3.2	Soft Phases Made of DNA-Coated Colloids	270
3.3	A New DNA-Mediated Phase: The Patchy Paradigm and the Empty Liquids	274
4	Conclusions	276
	References	276

1 Fundamental Interactions in DNA

DNA, deoxyribonucleic acid, the most celebrated molecule of life, is a polymer that usually associates in pairs to form the famous double helix, in which the two strands are wound around each other. DNA is a polynucleotide that is a chain of repeated basic units (nucleotides) comprised of a sugar deoxyribose, a nitrogen base (nucleobase), and a phosphate group. There are four types of nucleotides in DNA, which only differ in the nucleobase: adenine (A), guanine (G), cytosine (C), and thymine (T). Each polynucleotide is hence characterized by a specific nucleobase sequence, conventionally written in the direction from the 5'-end to the 3'-end of the sugar phosphate backbone. The double helix is shaped as a spiral “staircase” whose steps are the individual nucleotides. The right-handedness of the helix is a consequence of the chirality conformation of the sugar moiety. The sugar-phosphate backbones of the two DNA strands are antiparallel with the 3' terminal of one strand connected to the 5' terminal of the other (see Fig. 1). In the most common structure, the B-form, the bases remain on average perpendicular to the molecule axis. Helix periodicity is ~ 10 base pairs, equivalent to ~ 3.4 nm, while the diameter of the bare DNA is ~ 2 nm [1].

The sequence of nucleobases is what gives DNA its capacity of carrying the genetic information and this is why it is crucial that the nucleotides form covalent bond chains. By contrast, the two strands are held together by weak interactions to allow for the zipping and unzipping of the double helix, the critical step involved in the “reading” of the sequence during transcription and replication of DNA in the cell. Indeed, the biological role of DNA is rooted in the physical properties of its molecular structure. The solubility, flexibility, and mutual

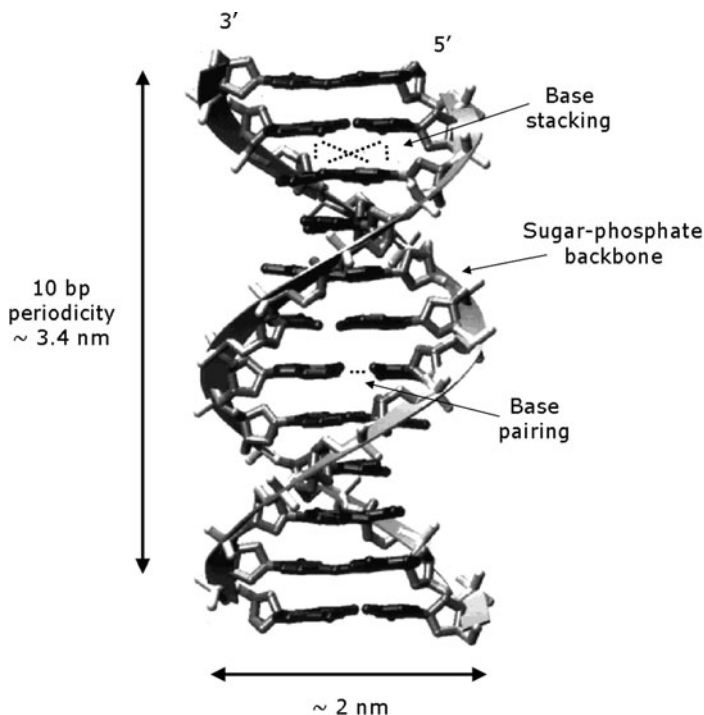


Fig. 1 The double helix structure of DNA in its B-form, with its relevant dimensions and the main interactions

interactions of DNA strands are key to its capacity to encode and transfer biological information. The very shape of the double helix is the result of a subtle balance of molecular constraints and interaction forces, all playing a role in the biological processes. Double helices are held together by a combination of two main intermolecular forces: the so-called base pairing and base stacking forces. These forces control the selectivity of the binding process, by which the binding energy depends on the degree of complementarity of the nucleobase sequences along the two polymers.

When instead assemblies of helices are taken into account, it is well known that for many aspects DNA duplexes in solution can be treated as a charged anisotropic particle [2]. Accordingly, steric, electrostatic, and Van der Waals interactions, together with the mechanical properties of the helix (bending and torsional rigidity), play a major role in the formation of DNA mesophases. In addition, all these different kinds of interactions combine in a subtle and still poorly understood way to generate other forces relevant for the case of DNA. A notable example is the helix-specific, chiral interaction, whose importance for DNA assemblies will be discussed below.

1.1 Thermodynamic Stability of the Double Helix

Base pairing originates from the formation of hydrogen (H) bonds between pairs of nucleotides. The strength of the interaction is maximum when the sequences match according to the Watson–Crick (WC) complementary couples, i.e., A \leftrightarrow T (two H bonds) and C \leftrightarrow G (three H bonds). The energy associated with the formation of the double helix (“hybridization”) depends on the length of the nucleic acid polymer and on the quality of the WC matching, vanishing for pairs of sequences with poor complementarity. Despite the fact that the conceptual description of the pairing of complementary bases is simple, the quantitative evaluation of the energy involved is complicated because, when unpaired, the nucleobases form H-bonds with water.

Base stacking forces, instead, act to pull the aromatic hydrocarbon plates of the nucleobases into contact with each other. It is believed that this is due to the hydrophobic nature of the base surfaces whose exposure to water tends to be minimized. Stacking is much less selective than pairing and its strength mainly depends on the overlap between the aromatic plates. Nevertheless, as better detailed below, stacking forces are the main sources of stability of the double helix, while pairing provides the necessary specificity of the bonds. When combined with the constraint of the sugar-phosphate backbone, the stacking forces result in the twist of a base pair relative to the neighboring ones of $\sim 36^\circ$.

The possibility of predicting a priori the interaction strength between two or more nucleotides sequences, together with the availability of the highly developed chemical machinery to synthesize sequences on design, makes nucleic acids very appealing to design molecular and supramolecular structures mutually interacting in a controlled way. The number of experimental systems constructed in this way is rapidly growing and this is at the same time the cause and the consequence of the large amount of quantitative thermodynamic studies on the thermal stability of double helices. In the past, experimental results obtained at various concentrations have been analyzed in the attempt to extract the amplitude of pairing and stacking forces. However, since pairing and stacking always act together in determining the DNA structure, it is hard to separate their contributions. Hence, thermodynamic studies of DNA are typically focused on determining the combined value of stacking and pairing in the overall Gibbs free energy G . Here the interest is in the free energy difference $\Delta G = G_D - G_U$, where G_D and G_U refer to duplexes and unbound strands, respectively. It is generally found that the formation of a DNA duplex involves variations of both enthalpy (ΔH) and entropy (ΔS), where $\Delta G = \Delta H - T\Delta S$. The large body of observations has enabled the formulation of simplified approximate strategies to express ΔG given the two sequences involved.

The most commonly adopted approach, the “nearest neighbor” (NN) model, is based on a very simple idea: since pairing and stacking always act together, the minimum entity which contains both effects is a quadruplet formed by two consecutive nucleotides on one strand and the corresponding nucleotides on the other strand. An example is given in Fig. 2, where the rectangles outline three such quadruplets. Note that the quadruplets overlap. The rationale of this approach is that

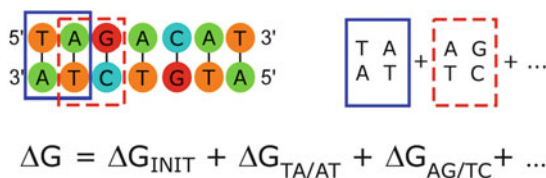


Fig. 2 Schematic diagram of the NN approach to the calculation of free energy of hybridization of a DNA sequence. The free energy is obtained as the sum of the free energies associated to each quartet along the sequence, plus an initiation entropy penalty

the simple counting of G–C and A–T contacts does not account for the helix stability, since it neglects the fundamental stacking contribution occurring between paired bases. Stacking is instead captured by this modular splitting of the helix. Accordingly, the free energy of each quadruplet, ΔG_Q , is expressed as a combination of the contribution from base pairing, ΔG_P , and from base stacking, ΔG_S as $\Delta G_Q = \Delta G_S + \frac{1}{2}(\Delta G_{P1} + \Delta G_{P2})$. The subscripts 1 and 2 indicate the two base pairs of which the quadruplet is made of, e.g., T–A and A–T in the first quadruplet of Fig. 2. In the case of the sequence in Fig. 2, we have seven nucleotides per strand and six different quadruplets in total. If we consider only WC pairing, each of them belongs to a list of the ten different possible quadruplets: AA/TT, AT/TA, TA/AT, CA/GT, GT/CA, CT/GA, GA/CT, CG/GC, GC/CG, and GG/CC, for which the hybridization free energy ΔG_Q is tabulated together with the corresponding contributions in terms of enthalpy ΔH_Q and entropy ΔS_Q . Quite clearly, the NN model neglects contribution arising from non-local (beyond nearest neighbors) interactions along the helix. A detailed description of the NN approach to the calculation of the DNA binding is beyond the aim of the present review chapter and can be found in the current literature (see, for example, [3] and references therein). This simplified introduction is aimed at offering a simple tool for a rough quantification of the free energy involved in the double helix formation.

On this basis, the total free energy involved in the formation of the double helix can be estimated by $\Delta G = \sum \Delta G_Q + \Delta G_{\text{INIT}}$, where the summation is on all the quadruplets of the sequence and ΔG_{INIT} is an “initiation” free energy discussed below. The analysis of the database in [3] indicates that ΔG_Q significantly promotes the formation of the double helix only when the quadruplet is formed by two WC pairs. When averaged over all the possible combinations of WC pairs, $\langle \Delta G_Q \rangle \sim -1.4$ kcal/mol (conventionally calculated at $T = 37^\circ\text{C}$, and corresponding to $\sim 2.3 k_B T$). The related average enthalpic and entropic contributions are $\langle \Delta H_Q \rangle \sim -8.3$ kcal/mol and $\langle \Delta S_Q \rangle \sim -22.3$ cal/(mol K). These values have been determined in solutions with an ionic strength of 1 M NaCl. If we limit the averaging to the three possible quadruplets involving only G and C we obtain $\langle \Delta G_Q \rangle \sim -2.1$ kcal/mol; for the four quadruplets that contain all the four bases A, T, C, and G, one has $\langle \Delta G_Q \rangle \sim -1.4$ kcal/mol; finally, if only A and T are present on the quadruplet an average over the three possible choices provides $\langle \Delta G_Q \rangle \sim -0.8$ kcal/mol. Pairing errors in one of the two couples lead, on average, to an

increased free energy: $\langle \Delta G_Q \rangle \sim 0.4$ kcal/mol. Here again the value depends on the specific error: the improper pair G–G is the most energetically favored among the non-WC pairs, while errors involving C have the most unfavorable effects on the duplexes.

All the values reported above are obtained by using the data in [3], extracted from experiments of duplex thermal unzipping. It is worth noting that alternative analyses of different datasets obtained in similar conditions yield significantly different data in the average values [4, 5]. For instance, in [6] the average thermodynamic parameters of the double helix are found to be $\langle \Delta G_Q \rangle \sim -1.4$ kcal/mol (at $T = 25^\circ\text{C}$), $\langle \Delta H_Q \rangle \sim -10$ kcal/mol, and $\langle \Delta S_Q \rangle \sim -29$ cal/(mol K).

In [3] the “initiation” free energy is reported to be equal to $\Delta G_{\text{INIT}} \sim 2.0$ kcal/mol (at $T = 37^\circ\text{C}$), which splits into $\Delta H_{\text{INIT}} \sim 0.2$ kcal/mol and $\Delta S_{\text{INIT}} \sim -5.7$ cal/(mol K). The meaning and the value of ΔG_{INIT} have been recently investigated in detail [6]. ΔG_{INIT} represents the free energy cost involved in constraining the two strands in the conformational space available to them when they are bonded. In other words, it expresses the free energy cost for nucleating the double helix in the absence of the contributions from pairing and stacking. ΔG_{INIT} is therefore mainly entropic, although some enthalpic contribution is also present because of long-range aspecific interactions, mainly electrostatic. In the same reference a new estimate of ΔG_{INIT} is determined by extrapolating ΔG for the vanishing number N of nucleotides. It is found that $\Delta G_{\text{INIT}} \sim 3.7$ kcal/mol (at 25°C). The difference with respect to the value in [3] points once more to the need and timeliness for further improvement in the measurements and modeling of the energetics of DNA double helices.

1.2 DNA Melting Temperature

Despite the lack of precision in determining the various contributions yielding the actual free energy of the DNA helices, the overall values of ΔG , ΔH , and ΔS for each given sequence can be experimentally determined with good accuracy through melting experiments. As T is increased, the weak non-covalent bonds break and the double helices become unstable and denatured. The melting temperature T_m is defined as the temperature where, for half of the double helices, the two strands have unbound and split, i.e., where $\Delta G = 0$. Such a transition can be monitored by optical (absorbance, fluorescence) or calorimetric methods. An example is reported in Fig. 3, where the UV absorbance and the corresponding fraction of single strands are plotted as a function of the temperature T . T_m is determined as the middle point of single strands to double helix transition.

Experiments indicate that for a fixed ionic strength T_m is very sensitive to the number N of base nucleotides for short oligomers, while for long double helices it reaches a saturated, yet rather high, value (see Fig. 4). For 1 M NaCl, T_m ranges from $T_m \approx 20\text{--}25^\circ\text{C}$ for $N = 6$, to $T_m \approx 80\text{--}90^\circ\text{C}$ for $N > 25$. This behavior can be reproduced fairly well by combining the thermodynamic parameters introduced

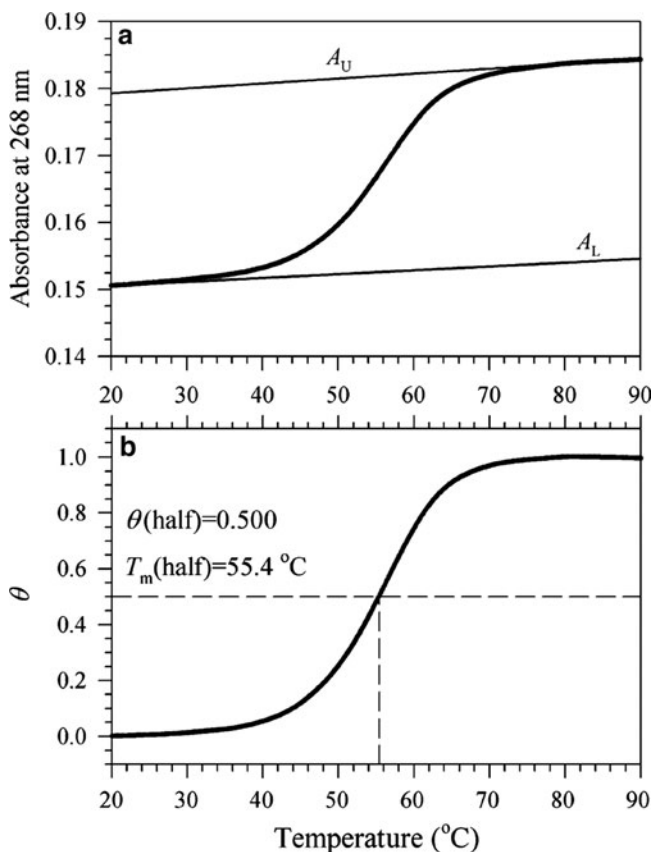


Fig. 3 Thermal denaturation transition of a DNA helix. (a) UV absorbance increases with temperature, following the unstacking of bases, following a sigmoidal shape. A_D and A_U are lower and upper baselines, also slightly dependent on temperature. (b) Fraction of single strands θ extracted from data in (a), which defines the melting temperature corresponding to $\theta = 0.5$. Adapted with permission from [7]

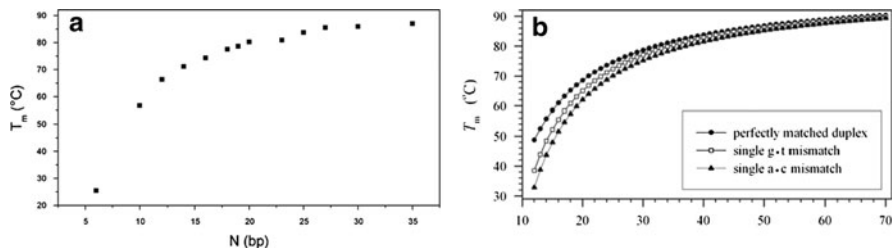


Fig. 4 Dependence of DNA melting temperature T_m on duplex length N . (a) Experimental data from [6], obtained for $[\text{Na}^+] = 1 \text{ M}$. The saturation is already approached for $N = 35$. (b) Calculated behavior for the same conditions of (a), based on NN parameters. Reproduced with permission from [8]

above for the double helix formation [7, 8]: $T_m = (\Delta H_{\text{INIT}} + (N - 1)\Delta H_Q) / (\Delta S_{\text{INIT}} + (N - 1)\Delta S_Q)$. In the limit of large N , the melting temperature saturates to $T_m \approx \Delta H_Q / \Delta S_Q$.

The free energy holding the DNA double helices together is typically very large with respect to the thermal energy. From the values given above one can easily verify that at room temperature, in 1 M NaCl, the binding energy of a fully hybridized 6mer is of the order of $10 k_B T$, growing to about $20 k_B T$ for a 10mer and to $45 k_B T$ for a 20mer, the energy approximately scaling linearly with N . It could thus appear somehow surprising that T_m remains in such a limited interval of values. This result is due to the subtle interplay and compensation of a large enthalpic binding contribution and a large entropic penalty, the two effects almost canceling each other when ΔG_Q is considered. This partial cancellation produces a large binding energy that vanishes rapidly as the temperature is increased.

1.3 Pairing vs Stacking Forces

Despite the many decades of studies on the DNA structure and properties, deconvolving base pairing and base stacking is still a matter of investigation. Rather recently, this distinction has been achieved by studying a system of helices with a broken phosphate–sugar bond in one of the complementary strands by Frank-Kamenetskii and co-workers [9]. They could resolve these two contributions by measuring the ratio of double helices adopting the straight conformation that preserve both pairing and stacking, to helices bent at the nick, where one stacking contribution to free energy is lost. The outcome is rather surprising since it differs from the most conventional concepts on this matter. As shown in Fig. 5, the free energy involved in pairing is either negligible (in the case of C–G bonding), or even positive, i.e., unfavorable for A–T pairs, and it appears to involve almost no entropic contribution, as visible from its independence on T . Pairing energy of

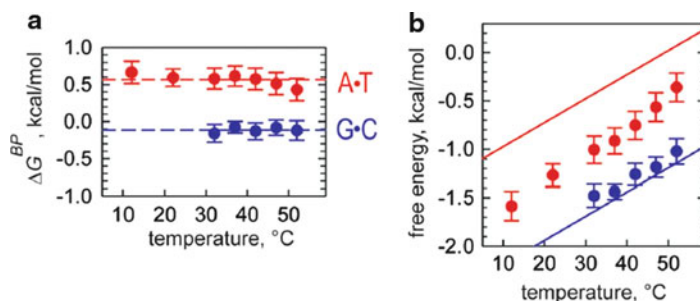


Fig. 5 Base pairing and base stacking free energy contributions to the helix thermal stability, as obtained from experiments with nicked duplexes. (a) Pairing shows negligible or even unfavorable effect on free energy, while stacking (b) gives favorable contribution with strong dependence on T , revealing both enthalpic and entropic effects. Adapted with permission from [9]

non-WC pairs is yet more unfavorable. Base stacking instead always promotes the duplex formation. The analysis in [9] yields, for C–G pairs, $\Delta H_S \sim -8.9$ kcal/mol and $\Delta S_S \sim -24$ cal/(mol K), and, for A–T pairs, $\Delta H_S \sim -8.3$ kcal/mol and $\Delta S_S \sim -24$ cal/(mol K). These numbers yield values for ΔG_Q in fair agreement with those given above.

The picture emerging from this analysis is that the double helix is held together by base stacking forces, while base pairing acts to enforce the correct WC pairing, providing a free energy penalty for erroneous pairings.

The quantification of the base stacking energy contributes to a better understanding of its physical origin. A systematic study in [10] has explored the correlation of stacking forces with various properties of the natural nucleobases and of non-natural base substituents, which include electric dipole, polarizability, and stacked area. On the basis of a strong correlation between stacking energy and surface (roughly $\Delta G \sim 1.8$ kcal/nm²mol), and no correlation with other molecular parameters, the authors conclude that the solvation-driven hydrophobic effect is the largest factor in determining the base stacking forces.

Further insight into this complicated matter can be obtained with difficulty. Hydrophobic forces have a complex dependence on the solute size [11–13]. The solubilization of small hydrophobic solute molecules bears an entropic cost (the entropy variation for introducing a solute molecule in water is negative) but has an almost negligible enthalpic effect. In this limit, the solubilization free energy grows with the molecular volume of the solute and the aggregation of solute molecules is promoted by an entropic increase. As the size of the solute molecules grows above 1 nm, a different regime sets in. The solubilization energy becomes a function of the solute surface and it is given by negative enthalpic and positive entropic contributions. This is the “macroscopic” regime, where solubilization of hydrophobic bodies is mainly determined by the interface tension. Water–benzene interface tension yields a free energy per unit surface $\Delta G/S \sim -55$ mJ/m² + 0.07 T mJ/m²K, [174] the second term expressing its temperature dependence. If we attempt to apply this argument to the nucleobase (each pair having a surface size ~ 80 Å²) we obtain $\Delta G \sim (-12 + 0.016 T)$ kcal/mol, rather similar to the free energy of DNA stacking. The estimate of ΔG via using the water–benzene interface tension, though simplifying, enables one to appreciate that the explanation of base stacking as a mainly hydrophobic effect is in fact plausible.

1.4 Ionic Strength Dependence

A DNA strand bears a negative charge for each phosphate group in a wide range of pH values and the bare double helix thus has a high linear charge density of approximately $-6 e^-/\text{nm}$. Although in electrolyte solutions the screening of counterions can significantly reduce the effective charge density [14], the electrostatic repulsion plays a significant role in the stability of the DNA helix. This is apparent from the strong dependence of the melting temperature on ionic strength [3, 15]: for

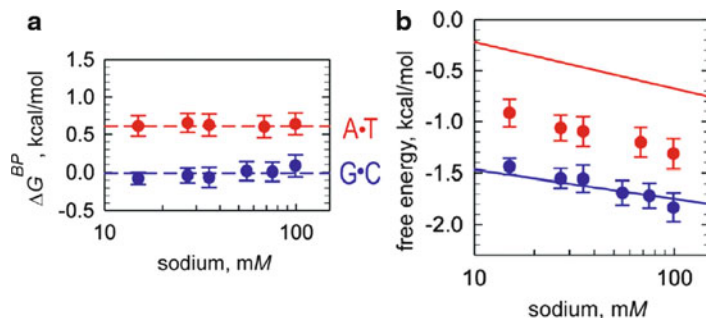


Fig. 6 Dependence of the DNA hybridization free energy on ionic strength. Base-pairing (a) is small and salt-independent, while base-stacking (b) is the main part of the interaction. Adapted with permission from [9]

a 12mer, T_m is reduced by nearly 30°C upon changing the added sodium from 1 M to 50 mM. For monovalent ions, the overall ionic effect on free energy is found to be proportional to the number of phosphate groups on the helix. In [3] and earlier works, the salt dependence is assumed to come only from the entropic contribution, while enthalpy would be salt-independent [16]. However, later measurements [6] have reported that both ΔH and ΔS increase (their absolute values decrease) with increasing ionic strength and thus both contribute to the observed free energy increase.

With the same experimental system described above, Frank-Kamenetskii and co-workers have also examined how the two components of the quadruplet free energy, base pairing and base stacking, respond to salt [9]. They report that the base pairing contribution would not be affected by ionic strength, while stacking would (see Fig. 6). However, among the factors determining base stacking, primarily hydrophobicity and electrostatic attraction between partial charges across the nucleotides, it is not easy to discriminate which is mainly responsible for explaining the influence of the ionic strength on the DNA energetics [9].

For practical purposes, within the NN frame the ionic strength dependence can be taken into account in the estimate of the free energy and of the melting temperature by using empirical equations with numerical prefactors. Such equations display a leading logarithmic dependence on salt concentration which reproduces the experimental observations well and allows simple and reliable calculations [3, 15].

1.5 Chiral Inter-helical Interactions

The high charge density of DNA helices also has implications on inter-helical interactions. While at long distances duplexes sense each other as homogeneously charged rods, at increasing concentrations the helical pattern of charges on the backbone introduces a handedness asymmetry in the interaction. This asymmetry can originate twisted arrangements in liquid crystalline and other condensed phases

and may ultimately be related to the DNA packing strategies within viral capsids [17] and to some biological processes *in vivo* [18].

The overall electrostatic interaction is complex, as it obviously involves repulsion between negative phosphates on different molecules, but also helix-specific terms, depending on the mutual azimuthal orientation and twist angle of duplexes, which may result in net attraction because of counterions adsorbed in the grooves (see Fig. 7a). The most complete and celebrated theory devoted to the topic has been developed over the last decade by Kornyshev and Leikin [18, 19]. They describe the helices as clean cylinders with helical lines of charge accounting for phosphate groups and adsorbed counterions. At long distances, since the helices are free to rotate along their principal axis, the asymmetry arising from the molecule handedness is “washed out” and the net repulsion prevails. At lower spacing, the so-called “electrostatic zipper” can set in (Fig. 7a): helices try to accommodate their negative backbones close to positive (or less negative) grooves of neighboring duplexes, which minimizes repulsion and determines significant azimuthal correlations among the molecules. However, since the system of azimuthally locked helices is frustrated, the optimal alignment can change with the inter-axial distance and can result in a net twist of both handednesses.

Electrostatic interactions are not the only chiral forces at play. At high packing fractions, relevant to experimental systems described below, steric hindrance effects come into play. The helical shape of the sugar phosphate backbone and the geometrical details of minor and major grooves are likely to play an important role in determining interactions between neighboring helices. The combination of steric and electrostatic factors was systematically considered by Tombolato and Ferrarini [14]. They model the helices as cylinders decorated with protruding charged spheres having a steric volume (see Fig. 7b) and study the resulting competing effects: electrostatic repulsion is maximized in the most sterically

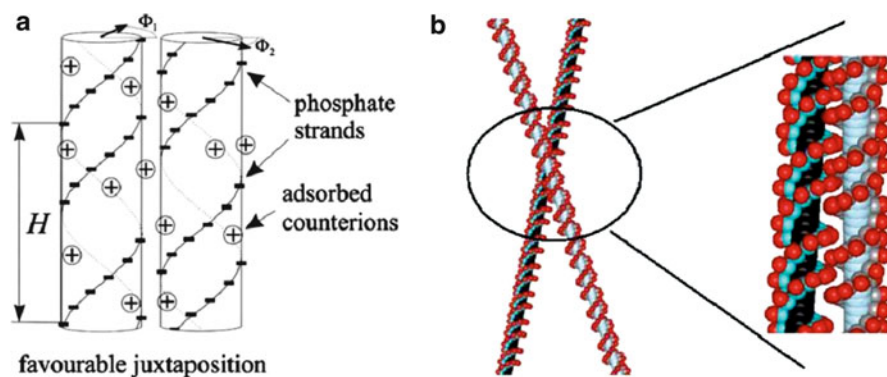


Fig. 7 Schematic view of the different approaches used to model the chiral interactions between DNA double helices. **(a)** DNA duplexes are viewed as clean cylinders with charged helical patterns of negative phosphates and positive adsorbed counterions. Reproduced with permission from [18]. **(b)** Duplexes interact via steric interlocking of backbone and grooves and through electrostatic repulsion of the phosphate groups. Reproduced with permission from [14]

avored configurations where charges of equal sign lie at close distance. Which contribution to chiral strength dominates depends on the mean-interhelical distance. We will later describe a situation where chiral interactions determine the macroscopic ordering of DNA helices, the liquid crystalline cholesteric phase.

2 All-DNA Superstructures

The modularity and selectivity of DNA–DNA interactions provide, in principle, a remarkably flexible tool for the design of assemblies with controlled structure and mutual interactions. In practice, this is made possible by the ability to synthesize chemically oligonucleotides of given sequences. DNA synthesis is typically performed on solid-phase substrates with phosphoramidite chemistry, developed in the 1980s [20], and enables producing oligomers of length up to more than 100 base pairs in milligram quantities. This possibility, together with the knowledge and capacity to master DNA–DNA interaction strength, has produced a remarkable blooming of research results.

In this part we are going to focus on systems entirely made of DNA, so designed to yield a two-stage interaction process. First, strongly bound aggregates are formed by exploiting WC pairing. In the simplest cases, this first step involves the formation of standard linear double helices. In other cases, sequences are such as to produce multi-strand aggregates, locally structured as double helices, but globally developing in more complex shapes. These aggregates can then mutually interact in a variety of ways. Depending on the design of the assembly, the interactions can be limited to steric and electrostatic, or they may involve WC pairing between unpaired bases of different aggregates or stacking interactions between clean-cut double-helix terminals. In almost all the observations reviewed here, sequences have been selected so as to separate well the two ranges of energies: stronger energies involved in the formation of the aggregates and weaker energies controlling their mutual interactions.

2.1 DNA Liquid Crystals

Liquid crystals (LC) are fluid phases characterized by a partial orientational and positional ordering, and are thus normally classified as mesophases, in between the isotropic liquid state and the crystalline packing. Initially viewed as an odd form of collective ordering of a very limited set of organic molecules, LCs are nowadays recognized as a common form of self-organization of soft and biological matter. This trend has also been followed by the study of LC ordering of DNA. DNA LCs were first observed *in vitro* with long double strands; later they were recognized as the *in vivo* packing mechanism of some organisms, and quite recently they started being considered as a common ordering for DNA oligomers.

2.1.1 Long DNA

Early studies carried out between the 1950s and the 1960s identified mesophase behavior of long DNA chains of biological origin *in vitro* [21, 22]. Shortly thereafter Bouligand started a systematic analysis of the textures of various biological specimens obtained through optical and electronic microscopy, in particular of the chromosomes of *Dinoflagellates* (primitive unicellular algae) finding evidence of LC arrangement of highly concentrated DNA *in vivo* [23]. LC order of DNA was also found in other chromosomes, bacteria, viruses, and sperm heads, where its concentration reaches extremely high values, up to 800 mg/mL, suggesting a correlation between LC packing and biological activity [24, 25], in particular with respect to protection from external stress or damage [26].

DNA LC phases have been extensively studied by using more easily controllable experimental systems, namely DNA double strands obtained through enzymatic cut of nucleosomal DNA, providing a nearly monodispersed ensemble of $N \sim 150$ semi-rigid rods, or through sonication, which yields average lengths N between 10^2 and 10^4 bp (contour length L between 30 nm and 3 μm) with relatively narrow distributions.

Two main mesophases were identified:

1. A *cholesteric, or chiral nematic (N^*) phase*. This is a positionally disordered fluid in which the constituent molecules align on average their axes along a common direction called the nematic director. Being the DNA helices chiral, the orientational order develops an additional macro-helical superstructure with the twist axis perpendicular to the local director. The phase thus consists of local nematic “layers” continuously twisted with respect to each other, with periodicity $p/2$ (where p is the cholesteric pitch; see Fig. 8a) [27, 28]. For 150-bp helices, the N^* phase appears at a concentration around 150 mg/mL in 100 mM monovalent salt conditions. This LC phase is easily observed in polarized optical microscopy. Since the N^* pitch extends to tens of micrometers (that is, across

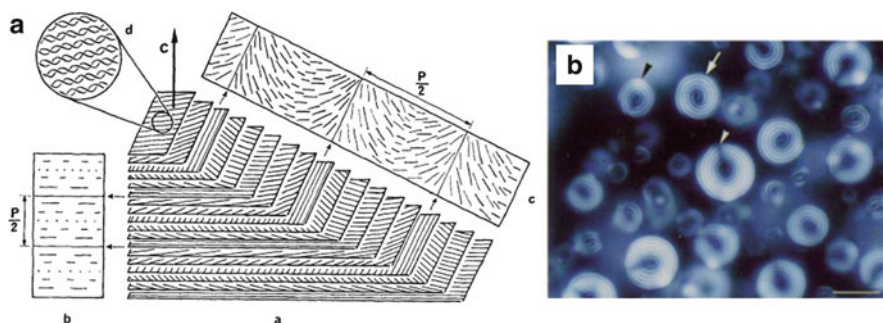


Fig. 8 (a) Schematic representation of the structure of the chiral nematic phase of DNA, showing continuously twisting nematic layers, giving rise to a $p/2$ periodicity easily observable in the side view on the left. (b) N^* droplets observed in polarized microscopy. The bright and dark stripes correspond to $p/2$ (size bar is 10 μm). Adapted with permission from [27]

more than 10^4 molecules), the optical anisotropy of DNA bases leads to characteristic textures such as the droplet in Fig. 8b, where the stripes correspond to the macrohelical periodicity of the N^* ordering.

2. A *columnar (COL) phase*, in which parallel DNA helices align on a 2D lattice (see Fig. 9a) but remain free to slide relative to each other in the orthogonal direction. The continuous bending of the columns gives rise to the so-called developable domains, shown in Fig. 9b. The nature of the phase and its hexagonal packing symmetry were demonstrated by a combination of polarized microscopy, X-ray diffraction, and freeze fracture electron microscopy experiments [29, 30]. The COL phase is observed for concentrations higher than 400 mg/mL.

Experimental evidence was reported for the existence of various additional phases: a pre-cholesteric order in the form of a network of double-twisted cylinders, analogous to the thermotropic blue phases [27], a hexatic phase that replaces the hexagonal columnar in very long DNA fragments [31], and a structure with orthorhombic symmetry appearing in the transition to crystalline order [27].

The appearance of a DNA nematic phase follows from its basic rod-like shape and its rigidity when in helical conformation. While single-stranded DNA is extremely flexible, with a polymer persistence length as short as 2 nm [32], when paired into the double helix it becomes a rather stiff object, with persistence length around 50 nm (that is, ~ 150 base pairs) [33]. According to the classic argument by Onsager [34] based on excluded volume interactions, elongated semi-flexible repulsive rods at sufficiently high concentration are expected to develop orientational order. The nematic order becomes favored because the loss of orientational

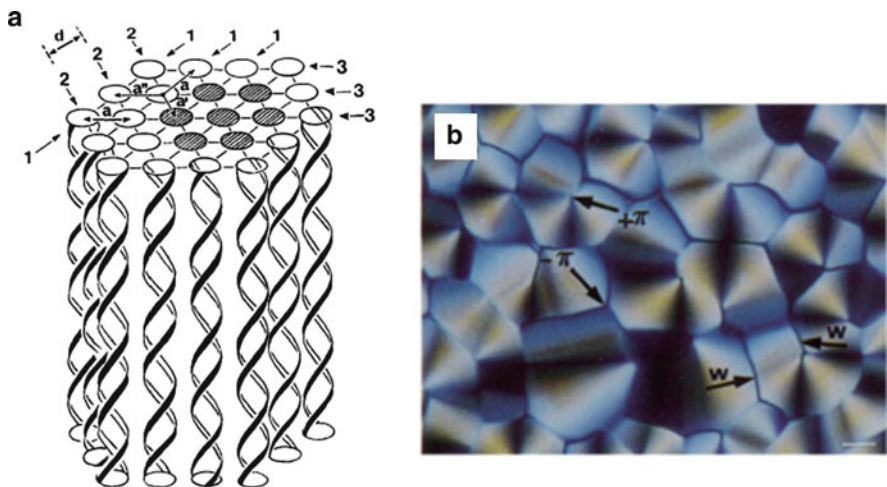


Fig. 9 (a) Sketch of the structure of the hexagonal columnar phase of DNA, showing parallel molecules hexagonally packed in the plane perpendicular to their axis. “ a ” and “ d ” are the lattice parameters. (b) COL developable domains observed in polarized microscopy. “ w ” indicates defect walls between differently oriented domains, while “ $\pm\pi$ ” stands for point defect around which DNA molecules continuously bend (*size bar* is 10 μm). Adapted with permission from [27]

entropy is more than compensated by the increased positional entropy. Despite its polydispersity, flexibility, and electrostatic repulsion, DNA proved to be a good test-bench for the Onsager prediction [34]: once the effective diameter D is properly rescaled to include repulsive interactions (in turn depending on the ionic strength), the critical volume fraction for nematic ordering is found to match Onsager's prediction, $\varphi_{\text{IN}} \approx 4D/L$ [35], where L is the length of the double helix (see Fig. 10).

In a hard-rod system, at sufficiently high volume fraction a transition is usually expected from the nematic to the smectic A phase [37], a lamellar phase with layers perpendicular to the nematic director. However, as elegantly demonstrated by Livolant [29], in DNA the smectic phase is replaced by columnar ordering; this behavior can easily be explained on the basis of strand flexibility [38] or length polydispersity [39], both favoring the COL phase over smectic.

High concentration, however, is not the only means to obtain LC phases of DNA in aqueous solutions. DNA has been found to collapse upon adding in the solutions various condensing agents, which introduce effective attractive interhelical interactions. This is what happens with alcohols and other solvents, which reduce DNA solubility [40], or with multivalent cations like spermidine, spermine, and cobalt hexamine, which are thought to establish correlated counterion fluctuations with

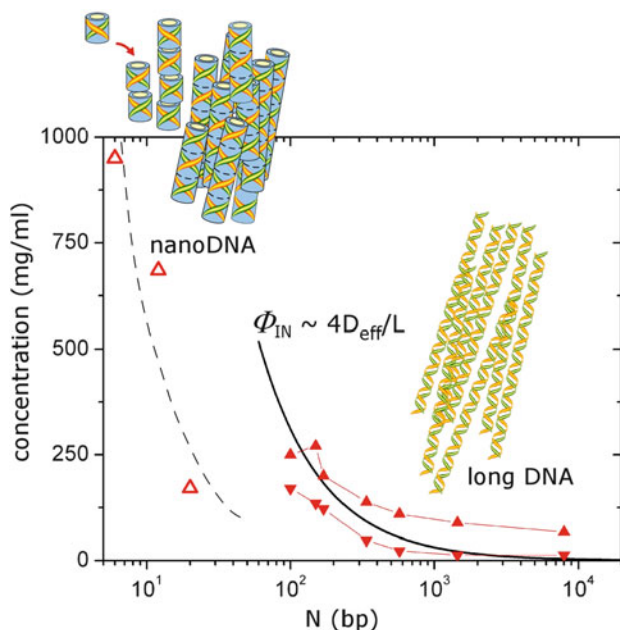


Fig. 10 Phase behavior of DNA molecules of different lengths. Helices longer than 100 bp (*filled triangles*) display isotropic-to-nematic transition at concentrations reasonably well described by Onsager theory once the diameter is rescaled for electrostatic repulsion (*continuous black line*). In contrast, short DNA strands lack the necessary anisotropy to spontaneously align and their critical concentrations (*open triangles*) imply end-to-end stacking into longer aggregates. The *dashed line* is a guide to the eye. Long DNA and nanoDNA data are from [35] and [36], respectively

a resulting net attraction between DNA molecules [41]. The most common structure of the resulting aggregates is that of a toroid of hexagonally packed DNA, similar to that observed within virus capsids [42], but the addition of non-adsorbing polymers reproduces the formation of the same mesophases described above for concentrated solutions [2]. Similar behavior is observed for multivalent ions in the case of 150-bp strands [41].

2.1.2 Short DNA

According to the Onsager theory and to computer simulations of the behavior of hard spherocylinders [37], in the absence of additional interactions no LC ordering is predicted for rods with $L/D < 4$, and therefore DNA double helices with a number of base pairs $N < 24$ would lack the anisotropy to display mesophase behavior at any concentration (Fig. 10).

However, rather unexpectedly, LC ordering has recently been found in concentrated aqueous solutions of DNA self-complementary sequences with N as low as 6 bp (“nano-DNA”, nDNA), which pair into helices with aspect ratio well below the Onsager limit [36]. The LC phases exhibited by nDNA are the same as those observed in long DNA, N^* and hexagonal COL, although they are found at higher concentration, e.g., around 750 mg/mL for the N^* of the self-complementary 12mer. The formation of LC phases of nDNA is a consequence of pairing and stacking interactions.

The first observation of LC in nDNA involved the use of self-complementary sequences. When these kinds of oligomers pair, they form blunt-ended double helices (Fig. 11a). The terminal bases of different duplexes tend to stack to avoid exposure to water, leading to an attractive interaction that acts to hold them together when their flat aromatic faces are in contact. These end-to-end interactions induce reversible linear aggregation of the oligonucleotides into effectively long chains, a process somewhat analogous to the “living polymerization” of surfactants into rod-like micelles (Fig. 11b; see [43] and references therein). When the physically bound, but chemically nicked, chains reach an axial ratio and concentration large enough to enter the Onsager regime, the solution orders into the N^* phase, and, upon further increasing the concentration, into the COL phase (Fig. 11c). The free-energy change associated with the stacking of duplexes, as estimated from the nDNA phase diagram, $\Delta G_{BS} \sim 4-6 k_B T$, is similar to that expected for base stacking within helices [9]. The freedom of stacked duplexes to rotate around their axis may enable the system to find a better stacking condition (larger stacked surface) than the normal quadruplets within double helices. This fact could indeed explain why the free energy involved in stacked duplexes exceeds that for stacking within helices.

The stacking of nucleobases has been found to be involved in several DNA self-assembly processes, promoting the formation of DNA–DNA and DNA–protein complexes in vivo [44, 45], driving end-to-end interactions of DNA double- and triple-helices in semi-dilute solutions [46], or determining the geometry of DNA

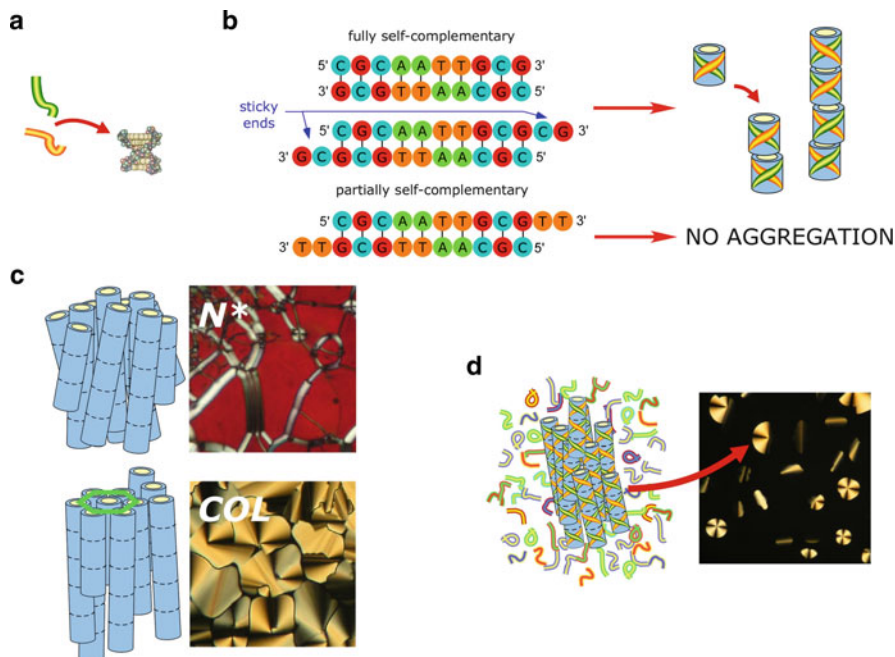


Fig. 11 Schematic representation of short DNA self-assembly stages. **(a)** Pairing of complementary strands yield double helices. **(b)** Blunt-ended or sticky-ended helices stack and form linear aggregates, while helices with unpaired dangling ends cannot aggregate. **(c)** Helices capable of linear aggregation display N^* and COL LC phases. **(d)** Complementary sequences segregate from mixtures of unpaired sequences through the nucleation of LC domains

oligonucleotide crystals [47, 48]. Stacking is also at the origin of the self-assembly processes leading to linear aggregation and LC ordering in solutions of guanosine quartets [49]. We note that in both nDNA and G-quartets the self-assembly is triggered by pairing events: G monomers and DNA single strands have only a weak propensity to stack, but the formation of H-bonds enormously reduces the water solubility of the molecules because of the enlarged hydrophobic surface, and promotes aggregation and ordering.

Since nDNA linear aggregation is critically dependent on stacking interactions, it is easily disrupted by the addition of unpaired bases to one terminal of the self-complementary sequence, which is found to suppress LC formation [36]. However, if such single stranded sequences dangling at the end of the nDNA double helix are designed to be complementary to each other (“sticky ends”), the linear aggregation and LC order are restored [50]. An example of sticky end is given by the self-complementary sequence CG in Fig. 11a. Sticky overhangs of different length or sequence and hence different interaction strength can determine very different LC stability. The study of the N^* and COL phase boundary thus provides a new direct route to evaluate the strength and the temperature dependence of the stacking and pairing forces [50]. Sticky ends were also recently proposed as an effective driving

mechanism to aggregate short DNA strands into longer polymers that are more easily condensed into DNA particles, as a valuable method of oligonucleotide delivery in gene therapy [51].

The experimental observations of nDNA LC have also renewed the interest in theoretically modeling systems where reversible linear aggregation and LC ordering are cooperatively correlated [43]. This is also the case for chromonics, flat hydrophobic molecules, mainly dyes, with soluble moieties at their edges [52].

The investigation of mixtures of nDNA in which only some of the sequences formed double helices, while others remained in the solution as single strands, led to the recognition of yet another force acting to promote DNA self-assembly. The system was found to undergo phase separation via the nucleation of liquid crystalline domains rich in helices coexisting with an isotropic background rich in single strands, as shown in Fig. 11d [53]. The main mechanism driving the phase separation is the difference of flexibility between double- and single-strands. Because of the phase separation, single strands act as an osmolyte, increasing the local concentration of duplexes above the value required for LC ordering. This behavior is analogous to protein crystallization promoted by dissolving PEG in the protein solution: in that case depletion-type entropic forces develop because of the mismatch between the flexibility of PEG and the rigid structure of proteins in their native state. In the case of DNA the spontaneous partitioning between complementary and unpaired sequences depends on the combination of the entropic depletion-type interactions and the free energy gain from the end-to-end stacking and LC ordering of duplexes [53]. This becomes evident when sequences have a terminal group interfering with the stacking: in this case neither LC formation nor demixing of complementary sequences is observed.

2.1.3 Chirality of the nDNA N^* Phase

LC phases observed in long DNA strands are substantially the same as those obtained in nDNA, as can be directly visualized by a contact experiment: two drops of long and short DNA solutions, when put in contact on a microscope slide, display a continuous LC texture along the gradient of the two components, without abrupt changes or defects [36]. Further optical microscopy and X-ray diffraction experiments demonstrated that most of the properties of the LC phases made of long DNA are shared by the corresponding phases of discontinuous aggregates of nDNA. Very recently it was recognized that significant differences between the two systems can be found by studying the chiral properties of the N^* phase [54].

Long DNA N^* shows characteristic pitch values between 2 and 4 μm [27]. Its concentration dependence is non-monotonic, with pitch first decreasing and then rising upon increasing concentration. The N^* pitch is also found to depend on ionic strength and temperature: it decreases (leading to a higher twist value between nematic layers) with increasing ionic strength [55], while it increases by increasing temperature [56]. These trends are basically captured within the frame of

Kornyshev–Leikin (KL) and Tombolato–Ferrarini (TF) models [14, 19] introduced above as the result of competing interactions.

An easily recognized difference of nDNA N^* with respect to longer DNA is that generally shorter pitch values are found, well within the visible range for some short sequences, so that distinctive colored textures are generated by selective reflection of incident light, as apparent in Fig. 11c [54].

A more striking difference concerns the handedness of the phase. Long DNA helices always yield a left-handed N^* phase [27]. The apparently simple issue of establishing how the chirality of a helical molecule like DNA propagates into the handedness of its supramolecular order, is actually quite a complex task [57]. On the experimental side, it is known that other right-handed helices like guanosine oligomer quadruplexes order in a right-handed N^* [58]. As for the theoretical modeling, the chiral behavior of long DNA is correctly predicted by the TF model, while it is missed in the KL one, although within the latter model the azimuthal frustration of helices, with two different arrangements minimizing free energy, may support the possibility of a left-handed phase [19].

In nDNA, where a wide set of sequences with N between 8 and 20 bp were explored, both right- and left-handed N^* arrangements are found [54]. The handedness appears to be strongly dependent on several parameters, reflecting small changes in the detailed helix–helix interactions: (1) oligonucleotide length: strands with $N > 12$ reproduce long DNA behavior, while shorter oligos can yield both right- and left-handed N^* phases; (2) the mode of terminal interaction: only blunt-ended helices can produce right-handed N^* , while sticky-ended helices, which yield polymers with a continuous helical pattern, always behave like long DNA; (3) oligomer sequence: 12mers differing by two bases can yield opposite handedness of the phase; (4) concentration: oligomers whose N^* phases appear in highly concentrated solution order in right-handed fashion. This last observation indicates that, at high concentrations, steric interactions, which favor right twist, may prevail over electrostatics, a phenomenon consistent with the TF model. Intriguingly, the critical concentration for handedness inversion corresponds to inter-helical distances close to the helical pitch. Although a complete understanding of these phenomena is still to come, the whole body of observations suggests that the inter-helical distance is the main factor determining the handedness of the phase. All the other factors listed above affect the N^* handedness by influencing the concentration (and hence the mean inter-helical distance) at which the N^* phase is found.

2.2 DNA Crystals

The same inter-duplex interactions that lead to liquid crystallization of DNA oligomeric double helices – stacking of blunt ends and pairing and stacking of sticky ends – can be exploited to produce other DNA-based materials having either crystalline symmetry or amorphous structure. These are typically obtained by the association of building blocks resulting from the aggregation of DNA stands whose

sequences are chosen to guide specific three-dimensional combination as in the example shown in Fig. 12a. In this case, four DNA strands, each with $N = 63$, are designed so that each has partial complementarity with the other three. The matching of 20-base stretches of the four sequences leads to the formation of a tetrahedral structure [59]. The structure is rather rigid since each edge is formed by a double helix. Such helical arrangement also brings about the need to determine the edge length on the basis of the helical pitch, since the orientation of the paired strands as edges merge into a vertex can interfere with their hybridization. DNA nano-polyhedra were first obtained in 1991 by Chen and Seeman [61]. Inspired by their seminal work, many other experiments were performed, aimed at designing various DNA structures [59, 62, 63]. These studies have played an important role in understanding how to control multi-strand complex hybridization and to develop constructs of potential interest in the field of molecular motors and drug delivery, as reviewed in [60, 64]. In analogy to the liquid crystallization of interacting oligomeric DNA double strands, aggregates of multiple DNA oligomers can be designed so as to seed the growth of crystals or other macroscopically organized phases.

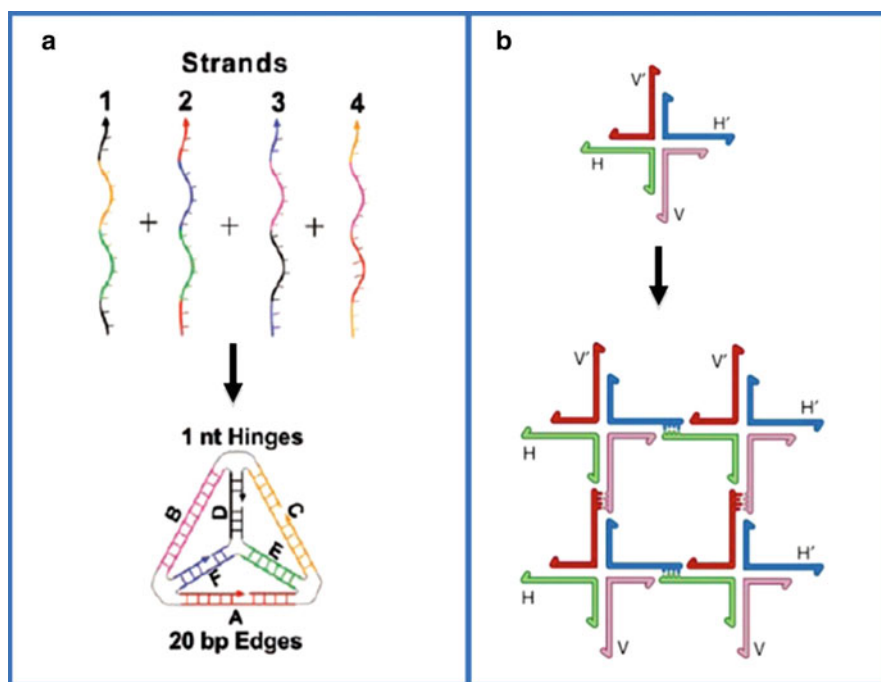


Fig. 12 (a) Design principle for DNA tetrahedra, composed of four oligonucleotides with complementary segments to form each edge. These are identified by colors. Reproduced with permission from [59]. (b) Concept drawing of star-like junctions formed by four oligos, having terminal unpaired tracts, complementary two-by-two. Accordingly, V can only bind to V' and H to H' , thus enabling units to assemble into two-dimensional crystals. Adapted with permission from [60]

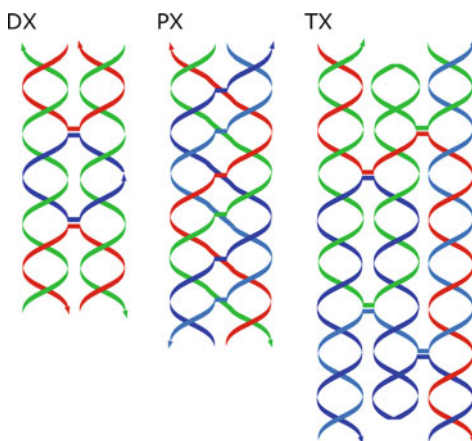
A simple sketch of mutually interacting DNA structures is given in Fig. 12b, in which star-like constructs are formed by the aggregation of four strands, each partially complementary to two other strands. This yields the formation of DNA stars with four arms, each made by a DNA double helix. Moreover, sequences are such that arms terminate with an overhang of a few unpaired bases, chosen so as to stick with the tips of other arms. In this way, structures of unlimited sizes can in principle be generated.

2.2.1 Two-Dimensional Crystals

DNA stars with three to eight arms have been produced and characterized [65]. While they indeed enable the formation of large aggregates, the spatial arrangement of the arms is rather flexible [66], not allowing the development of crystalline order. Hence, specific effort was put on trying to make more strongly interlaced constructs that would ensure a better-defined position – and possibly orientation – of the mutual links. Two basic solutions have been proposed, in some cases employed in combination. One is to build polygons (especially triangles) with sticky vertices. For example, three segments of DNA double helix lead to a more rigid structure if arranged as a triangle rather than if assembled in a star-like structure, in which bonds cannot constrain helices to remain at given reciprocal angles. The other solution is to link together two or more parallel double helices. This is obtained by the “double crossover” (DX) and its variants as shown in Fig. 13 [67]. As evident in the figure, the sequences have to be designed so that the strands swap between helices in the specific places where the DNA backbone chains are closest. DX motifs have been shown to be about twice as stiff as standard duplex DNA [68] and are thus interesting as building elements of stable structures.

With these strategies, various large two-dimensional periodic aggregates have been obtained. They can be classified in two main groups: planar structures built

Fig. 13 Use of strand exchange between helices to create DNA inter-helical crossover motifs. The double-crossover (DX) structure is formed by three different sequences with complementary segments (arrows indicate 3' terminals). The PX structure is one of the various possible variations of the crossover structure, involving four strands. Four sequences can also produce triple-crossover (TX) motifs



assembling tiles in which helices are constrained to run at given angles and structures in which helices are all parallel.

Two-dimensional lattices have been obtained by interacting triangular tiles. One way to do this is reported in [69], where the authors assemble triangles with edges made of $N = 30$ base pairs and two sticky groups of length $N = 4$ per vertex. Two different groups of triangles were built, having different dangling sequences at the vertices so that triangles of each group would interact only with triangles of the other group (see Fig. 14a, b). The two sets of triangles have been prepared separately by annealing five different DNA sequences for each set. Upon mixing, triangles aggregate in the hexagonal lattice in Fig. 14c–e.

A similar kind of triangular unit was proposed by Mao and coworkers [70] (see Fig. 15a). Here only one species of triangle was produced, with sticky ends chosen so that each vertex would join with either one or two other triangles as in Fig. 15b, leading to the formation of two-dimensional lattices (Fig. 15c, d). This approach and that previously described [69] do not yield extended structures, possibly because of intrinsic curvature and/or excessive flexibility. To overcome these limitations, stiffer structures based on DX-type junctions were considered.

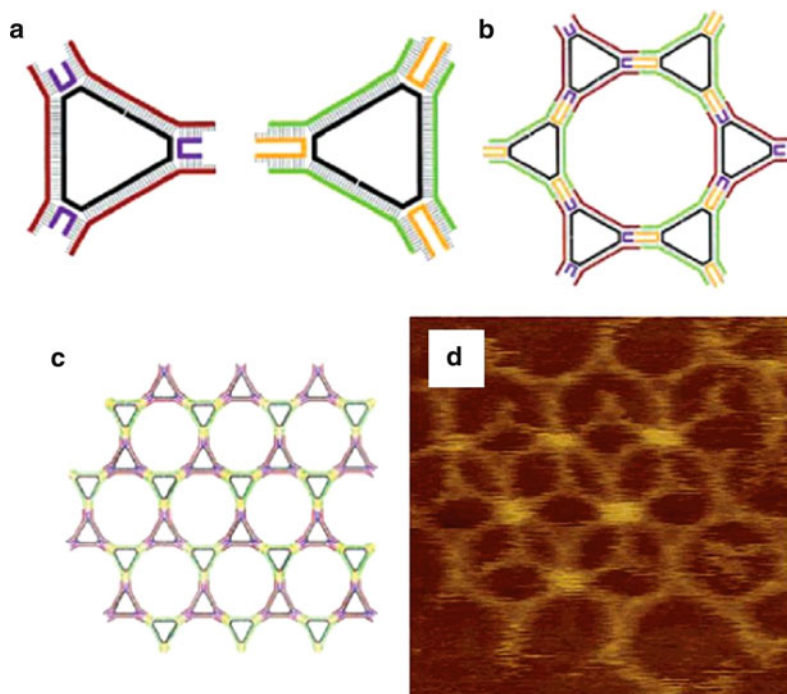


Fig. 14 Interacting triangular tiles. (a) Sequences are designed so to assemble in two different triangular tiles with complementary sticky ends. (b) Six connected triangles form hexagonal units, which (c) create a two-dimensional crystal. (d) AFM image (edge size is 133 nm) of two overlapped hexagonal tilings. Adapted with permission from [69]

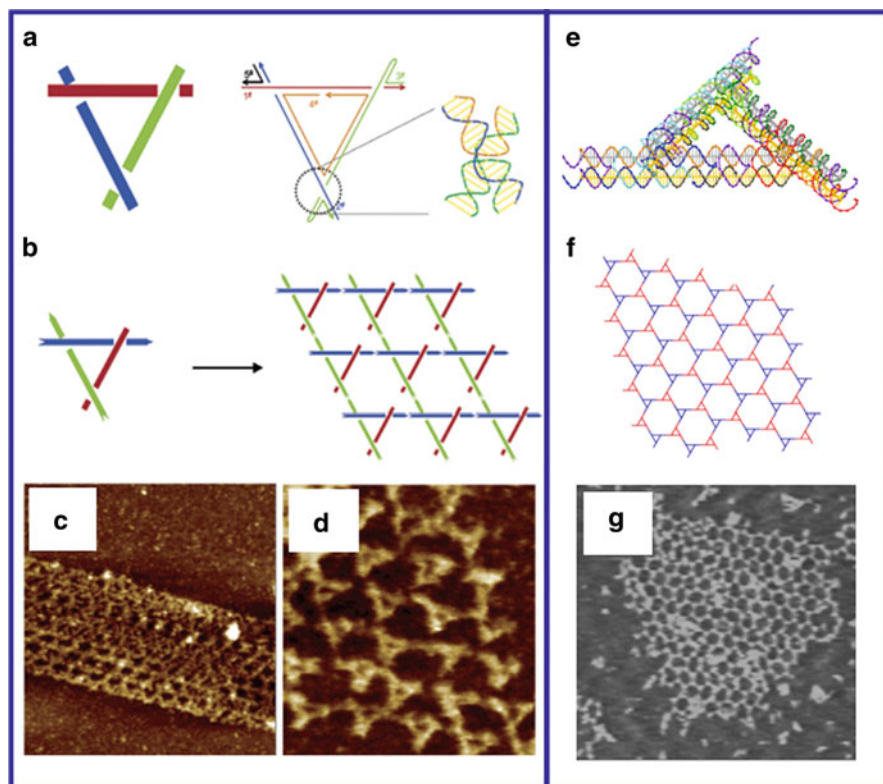


Fig. 15 (a) Sketch of the assembly of a DNA triangular motif from the combination of three duplexes. Some of the vertices have sticky ends yielding (b) two-dimensional assembly of triangles. (c, d) AFM images of the triangular tiling. Image size is 600 nm (c) and 200 nm (d). Adapted with permission from [70]. (e) Assembly of a triangle resulting from three DX structures. (f) Two species of tiles are connected, creating hexagonal cells. (g) AFM image of the pseudo-hexagonal trigonal array (image size is 1.22 μm). Adapted with permission from [71]

A first attempt was to use triangles having edges made by DX structures, as in Fig. 15e [71]. The mixing of two kinds of triangle, having the same structure but different choices of dangling ends, gives rise to hexagonal lattices (Fig. 15f) detectable by AFM (Fig. 15g).

Much larger planar periodic structures have been obtained by symmetrised interactions of DX-type sticky DNA stars. Figure 16a, d shows three-arm [72] and four-arm [73] DNA stars constructed by paired double helices both with $N = 22$ long arms and $N = 4$ long sticky terminals. These structures are symmetric for, respectively, threefold and fourfold rotations but they are not mirror-symmetric. The lack of mirror symmetry favors deviations of the constructs from perfect flatness: the center of the star may not be in the same plane as the arm tips. For this reason, in both cases the DNA constructs have been designed so that their arms stick end-to-end in such a way that each star interacts only with stars turned upside

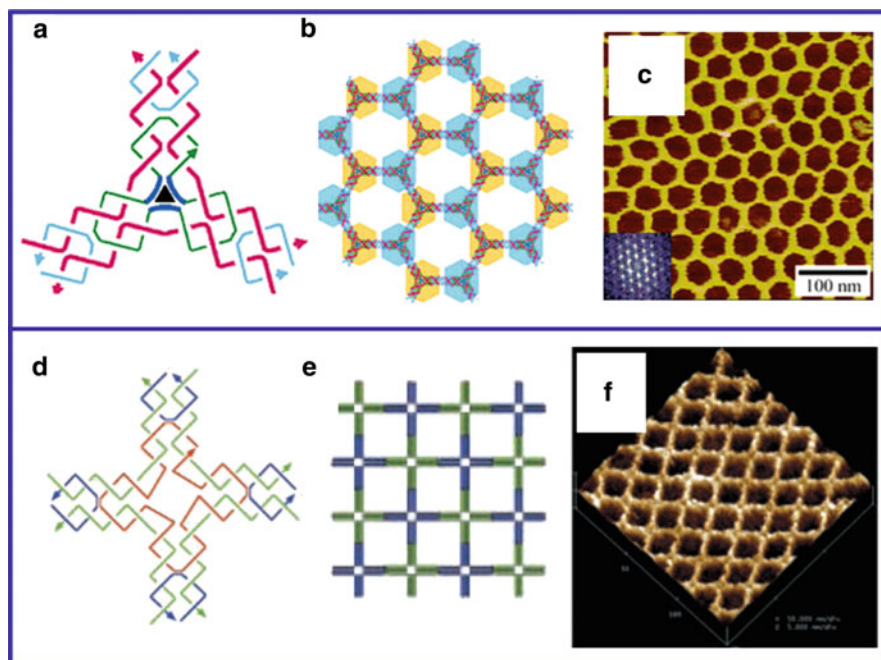


Fig. 16 (a) Three-point-star DNA motif with sticky ends, formed by seven sequences. (b) Two families of such motifs can bind and yield a two-dimensional array. (c) AFM imaging of the structure in (b); the *inset* shows the associated Fourier pattern. Adapted with permission from [72]. (d) DNA 4×4 tile structure (nine sequences); two different tiles can produce a square lattice (e). (f) AFM surface plot of the structure in (e), edge size is 150 nm. Adapted with permission from [73]

down. This generates planar aggregates of DNA stars with alternate orientation, as marked by colors in Fig. 16b, e. Such a regular flipping of the aggregated units ensures perfect planarity, which appears to be the key element to produce macroscopically the large two-dimensional crystals obtained by this approach ([72] reports crystal leaflets up to 1 mm in size). This notion is explicitly demonstrated in [73], where it is shown that aggregates of equally oriented four-arm stars have a curvature that prevents them growing unlimitedly. In this case they form instead ribbon-type crystallites, such as that in Fig. 15e.

Yet another DNA design leading to the formation of two-dimensional crystals is proposed in [74] through the assembly of bundles of six double helices of length $N = 76$ held together by DX joints. The aggregate resembles a hexagonal prism (top view in Fig. 17a, colors indicate different strands). Double helices terminate with sticky ends of length $N = 8$, designed so as to produce aggregation of the bundles according to various geometries. Two-dimensional lattices (as in the AFM image in Fig. 17b) are obtained by mixing two sets of six-helix bundles. In each, two helices have blunt terminals, while the other four have sticky sequences that

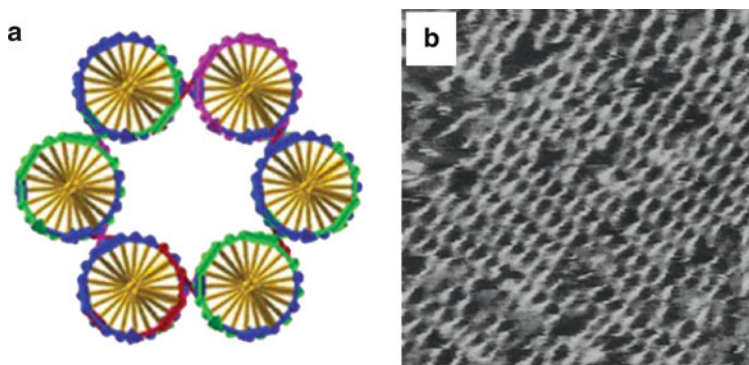


Fig. 17 (a) Six-helix bundle consisting of six helices connected by double crossovers; the strands shared by different helices are identified by colors. (b) AFM image of two-dimensional hexagonal arrangement of bundles (edge size is 324 nm). Adapted with permission from [74]

promote the adhesion of each bundle to four other bundles of the other set, in a similar way to the scheme in Fig. 18a.

A markedly different approach in obtaining two-dimensional lattices is to exploit directly the double crossover structure in Fig. 13 and its variants as first proposed by Fu and Seeman [67] and developed by Winfree et al. [75] to obtain crystals. For this, the two parallel helices of the DX structures need to terminate with sticky ends that ensure end-to-end aggregation in a translated-type pattern. This is schematized in Fig. 18a where each rectangle represents the two paired double-helices in the DX structure while the colors at the terminals identify the interacting sticky ends, one for each helix terminal. The structure in this scheme is obtained by mixing two DX tiles (A and B), each 36 base pairs long, with $N = 5$ sticky terminals [75]. Of course, care needs to be taken to design the DX terminals so that they properly match in helical phase and strand orientation. The resulting structure is a periodic two-dimensional lattice, made identifiable by AFM (see Fig. 18b) by adopting for one of the tiles a modified DX structure (“DX + J”) that contains an additional hairpin loop protruding on one side of the structure. Overall, the lattice is formed by parallel double helices, joined longitudinally through sticky ends and transversely by crossover links.

Natural extensions of this concept involve replacing DX structures with the analogous, but sturdier, “triple crossover” (TX) tiles (see Fig. 13) [77] and double double-crossover [76], amounting to four connected parallel double helices, shown in Fig. 18c. The way these last structures can be assembled is shown in Fig. 18d, e. Many variants and developments of these structures have been proposed, involving the combination of tiles with various length and terminals, tiles of different morphology, and tiles linked to additional groups, including proteins and nanoparticles [75–77].

By devising variants of the DX tile structure, Schulman and Winfree exploited the programmable interactions of DNA to study the nucleation and growth process of two-dimensional structures [78]. Indeed, a simple inspection of Fig. 18a clarifies

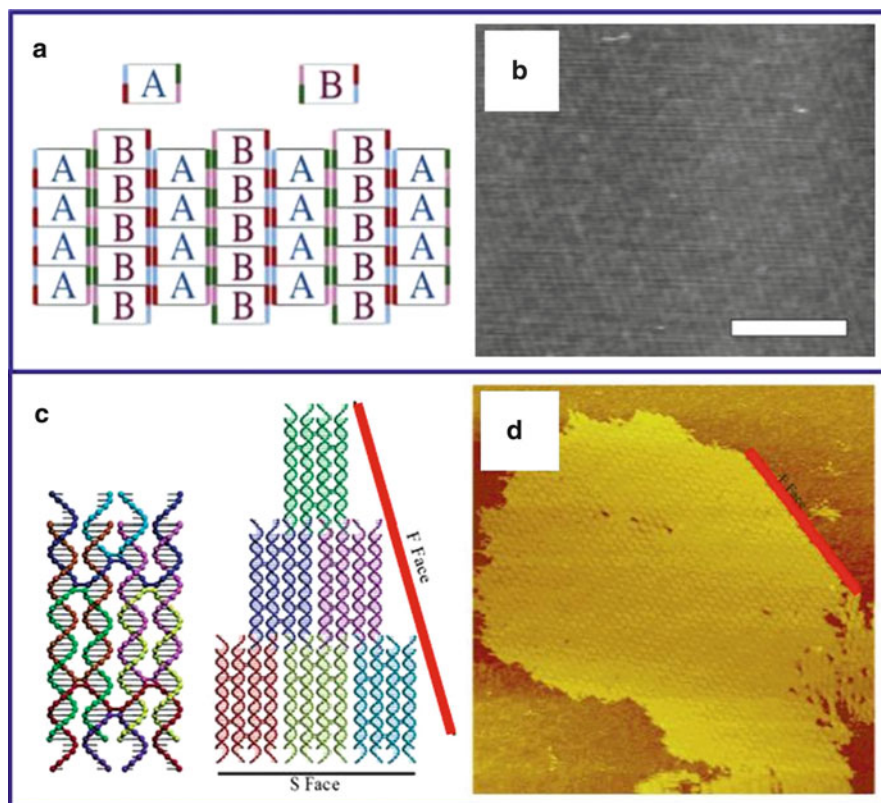


Fig. 18 (a) Tiles with colored edges are formed by DNA helices connected through double crossover motifs and interacting through sticky ends. The pairing rules determine a two-dimensional striped lattice, as observed in AFM imaging (b). *Scale bar* is 300 nm. Adapted with permission from [75]. (c) Double double crossover yields tiles with four parallel helices, which connect through sticky-ends. (d) This tiling can be imaged with AFM (image size 600 nm), where the *red line* highlights the stepped edge in (c). Adapted with permission from [76]

that growth implies the addition of tiles to the growing nucleus through the formation of either one or two sticky end bonds. In the kinetic study in [78] the set of tiles and the geometry were chosen so that nucleation would imply singly bonded tiles, while growth would proceed by addition of doubly bonding tiles. By separating the two stages, nucleation and growth rates were studied as a function of nucleus size.

An alternative way to build tiles for the assembly of two-dimensional crystals is by means of the “scaffolding” of short sequences along a longer one that acts as a guide to their positioning. The first example of this strategy is in [79] where sequences having length in the range $N = 260\text{--}330$ strands (orange line in Fig. 19a) interact with typically 15 shorter sequences (black lines) forming tiles as reported in the figure. The assembly is held together by the double crossover DX construct and

features some hairpin-type folding. The tile is schematized in Fig. 19b, d, the red axis representing the scaffolding sequence. The tile has the shape of a long double helix with five satellite double helix segments. Hairpins are drawn as black dots,

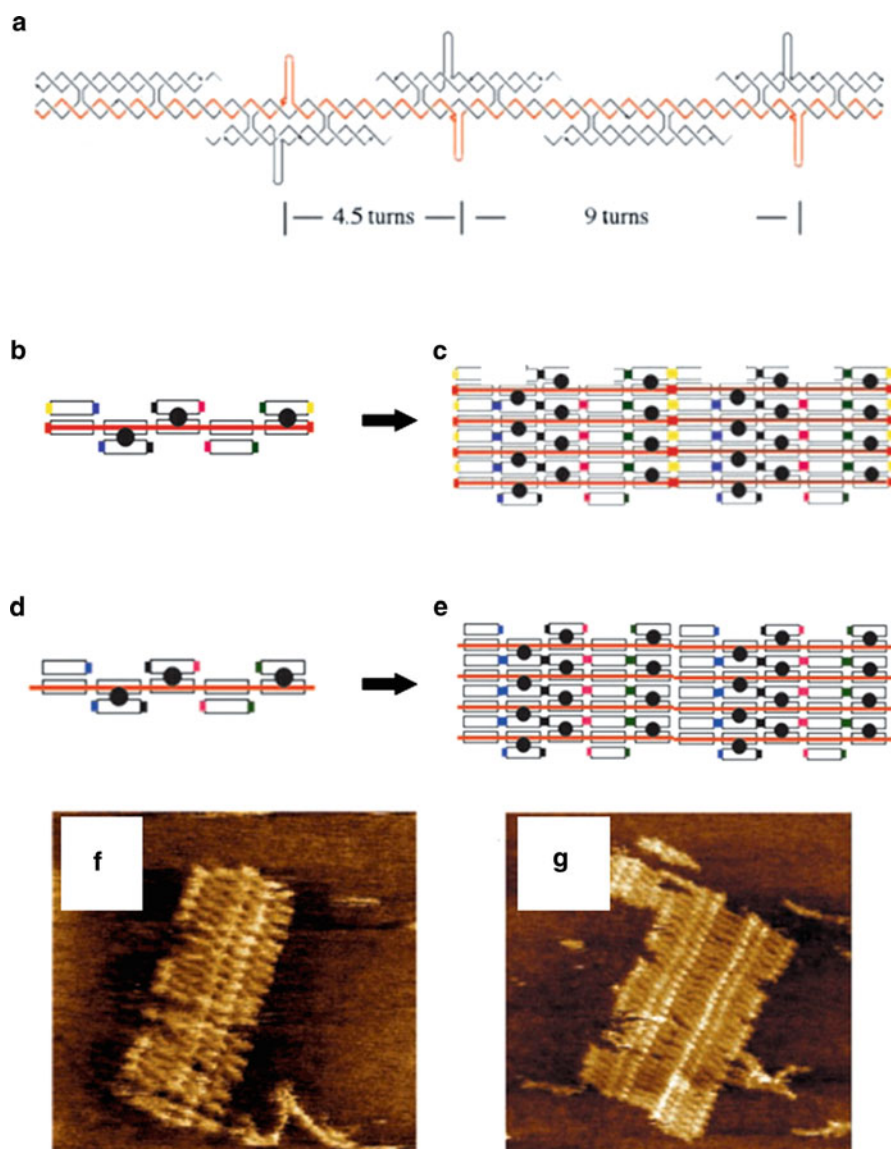


Fig. 19 (a) Tile structure proposed in [79], with a scaffold sequence (*red*) connected to shorter satellite strands through WC pairing and DX, with or without protruding hairpins. (b, d) Schematic illustration of the tile in (a), with *black dots* representing hairpins and *colored caps* representing sticky ends. The tiles form layers through sticky end pairing and can aggregate end-to-end, either through sticky ends (c) or blunt-end stacking (e). (f, g) AFM images corresponding respectively to (c) and (e). Image size is 250 nm (f) and 400 nm (g). Adapted with permission from [79]

and sticky-end termination as colored caps. Tiles aggregate side–side because of their perfect complementary shape and because of the sticky-end interactions between the satellite double helices. They also aggregate end-to-end both when they are terminated by sticky-ends (Fig. 19b) and when they end by blunt-ends (Fig. 19d). The aggregates are inspected by AFM (Fig. 19f, g). One interesting advantage of this scaffolding approach is that the relative concentration of long and short strands is immaterial since the folding is guided by the interactions between long and short strands, while interactions between the oligomers are negligible. Although tiling can proceed with no limits, the size of 2D crystals formed in this way has never been found to exceed a few micrometers.

2.2.2 Three-Dimensional Crystals

The two-dimensional lattices so far discussed are all based on the same mechanism of staged assembly: building blocks made of DNA oligomers, internally stabilized by stronger bonds, mutually aggregate because of weaker interactions, and assemble into ordered patterns. In spite of the effort of devising sequences that would give rise to three-dimensional crystals along this same pathway, the first extended three-dimensional crystal produced was the outcome of a serendipitous event and involves a type of folding that does not follow the paradigm above. Indeed, solutions of 13-mers GGACAGATGGGAG crystallize in a rather unpredictable structure [80]: a layered crystal having hexagonal symmetry, made of stacked layers of parallel helices, each layer stacked with a 120° rotation with respect to the one below (see sketch in Fig. 20a). Layers are held together by unusual crossover-type arrangement of the strands in the helices. Once interpreted, this structure has been reproduced in longer strands, leading to less dense hexagonal packing. This has been done by mixing two sequences ($N = 24$ and $N = 11$) that effectively add one full helical turn between the inter-helical contact points [81] (Fig. 20b). Crystals obtained in this way have sizes up to a fraction of a millimeter (Fig. 20c). The larger pores, large enough to be permeated by proteins, make this class of crystals interesting for applications in molecular separation.

There is an additional element of interest in this class of three-dimensional crystals. A simple analysis of the $N = 13$ sequence given above (rich in G and A) indicates that any resulting self-assembled structure cannot involve WC pairing of all bases. Indeed, the full analysis of the crystal structure in [80] reveals that the helices are in large part due to non-WC pairing. This finding clarifies that, in DNA self-assembly, the free energy penalty resulting from non-WC pairing may be overcome by the overall benefit of stacking. This awareness is important for the whole DNA-based soft matter science here reviewed: the rational design typically implemented to control DNA secondary structures enables access to only a fraction of the immensely rich variety of potentially realizable DNA oligomers.

Extended three-dimensional crystals based on the rational design of staged DNA self-assembly have been obtained only recently [82]. This goal was achieved by using, as building elements, triangles with double sticky ends as shown in Fig. 20d.

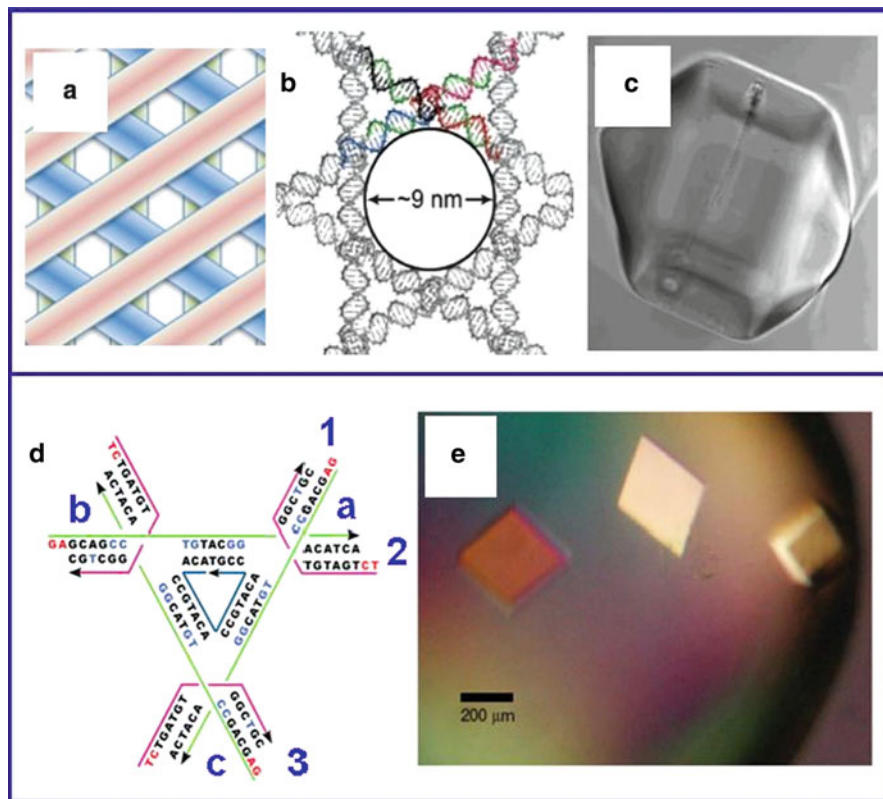


Fig. 20 (a) Stacked layers of parallel helices, with a 120° twist between adjacent layers, result in a sieve-like pattern with hexagonal symmetry. (b) A similar structure is obtained by inter-connected DNA strands and replicated into millimeter-sized crystals, as shown in the optical microscopy image in (c). Adapted with permission from [81]. (d) Design of a triangle from seven strands. The relative position of helices (1, 2, 3) at the vertices (*a*, *b*, *c*) is discussed in the text. Sticky ends mediate the aggregation of tiles into macroscopic rhombohedral crystals, shown in the optical microscopy image in (e). Adapted with permission from [82]

The basic design of these structures is similar to those used in [69] (see Fig. 14). The differences are, however, quite relevant. In this case the triangles are constructed so that the three double helices cross each other while not being on the same plane: in vertex A (see Fig. 20d) helix 1 is above helix 2, in vertex B helix 2 is above helix 3 and in vertex C helix 3 is above helix 1. The resulting angle between the 3' ends of the three helices is about 105° . This structure has been obtained in triangles of various sizes, the distance between vertices ranging from $N = 7$ to $N = 28$. The total length of each helix is such as to match an integer number of helical twists, while their sticky groups (short, $N = 2$) are chosen so as to promote the adhesion of triangles oriented in the same way along the three directions, resulting in a three-dimensional extension of the two-dimensional structure in [70] (see Fig. 15). In this way, extended all-DNA crystals are obtained (Fig. 20e).

The results in [82] also indicate how strongly the three-dimensional crystallization depends on the symmetry of the aggregating units. The terminals of the internal DNA strand (blue in Fig. 20d) inevitably produce an asymmetry in the aggregate since one of the three helices forming the triangles necessarily has a chemical discontinuity (between the 3' and the 5' ends of the internal strand). Since the sequences in the internal triangle are all equal, such a nick is equally distributed in the three directions, a situation that somehow compensates the asymmetry. If this compensation is eliminated by choosing different sequences in the internal triangle, the resulting crystal size is severely reduced.

2.3 DNA Origami

The construction of DNA nanostructures guided by scaffolding has recently gained a further extension that yielded to the so-called “scaffolded DNA origami,” reviewed in [83]. The concept is that the localized interactions of short sequences to specific position of a long DNA strand can be exploited to make the long strand fold in a controlled way into sophisticated structures. Indeed, the intrinsic selectivity of DNA pairing enables designing oligomers that locally hybridize to selected stretches of quite long sequences. This enlightens the power of DNA design to control nanofabrication. The structures obtained in this way are typically not thought to constitute the elements of a macroscopic aggregation, and thus lay somehow outside the scope of this review. The emphasis in this new form of DNA nanotechnology is instead on the amazingly precise control of size and shape of the structures.

A first realization of this concept was achieved by using an $N = 1,700$ long synthetic DNA strand so designed to interact partly with itself and partly with a set of oligomers [63]. The rational design of the sequences succeeded in guiding the folding of the long strand into an octahedron. The structure obtained in this way is quite robust, since each edge is formed by two parallel helices, joined together via a DX crossover. DNA origami was later perfected by the impressive work of Paul Rothemund [84], who managed to guide the folding of an $N = 7,176$ sequence taken from the genome of a bacteriophage. The selected sequence (“M13mp18” from the phage M13) was well known and carefully sequenced. The folding was obtained by the presence of carefully designed oligomers having length in the range $N = 26\text{--}40$ that “stapled” together various positions of the phage DNA sequence, as sketched in Fig. 21a. A specific realization of this concept is presented in Fig. 21b, c, where the long DNA strand is depicted in black while the staples are colored. Locally, the structure is always that of a B-type double helix, formed by the hybridization of the long sequence with the oligomers. To build the star structure in Fig. 21b, c, just one of the many structures obtained in this way, 244 different oligomeric sequences were mixed with the phage DNA.

The precise control of molecular arrangement in the DNA scaffolding, where each nucleobase has its well-defined position inside the origami, makes this DNA

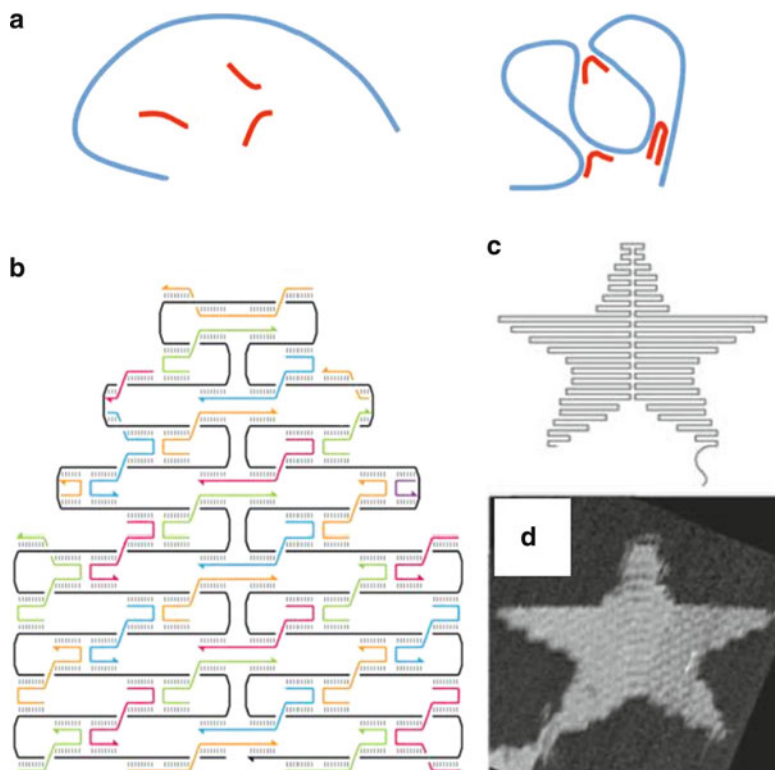


Fig. 21 (a) Sketch of the basic idea of DNA origami: a long strand is “stapled” by oligonucleotides complementary to specific tracts along its sequence and is folded into designed shapes (b), as complex as a star (c). (d) AFM image of the experimental realization of (c) (edge size is 165 μm). Adapted with permission from [84]

folding technology a powerful platform for the patterning of molecules with nanometer precision. This concept has been developed by different research groups that have used the origami as a template for the spatial organization of various kinds of receptors [85–89], viruses [90], and nanoparticles [91–93]. Their effective localization at a specific position in the DNA template was confirmed by surface analysis by AFM, TEM, and SEM.

The strategy for folding long DNA into designed origami has also been recently extended to the construction of three-dimensional structures [62, 94–96]. As in the two-dimensional case, assembly of long DNA strands is guided by staples to form a variety of full and empty three-dimensional shapes. In some cases, these structures are designed so as to be able, with the aid of additional oligomeric linkers, to assemble mutually [62]. This adds to the DNA origami the potential of being used as elemental units for the construction of three-dimensional smart materials.

2.4 Linear Aggregates

Despite their simplicity, the linear aggregates obtained from DNA oligonucleotides through binding of double helices – via blunt-end stacking or sticky ends – display a rich phenomenology, as described in the part devoted to LCs. However, in the last few years a growing body of work has dealt with more refined one-dimensional structures developed as hollow tubes or bundles made of interconnected DNA strands, with diameters ranging from tens to hundreds of nanometers and up to tens of micrometers in length. Such structures present tunable properties and appear as promising candidates for various applications, such as, for instance, scaffolds for nanowires [73] or for ordered arrays of quantum dots [97], for guiding controlled spacing of colloids for photonics [98], and as drug nano-carriers [99].

Tubes are generally obtained by taking advantage of the know-how developed in 2D crystals and can be regarded as planar tile arrays “welded” upon themselves on one edge, which favors elongation at unbound edges. Indeed, the very first demonstration of linear aggregates from DNA strands was obtained by Seeman in 1998 [100], with rigid double crossover molecules connected to rigid triangles also made of DNA helices. The combination of such elements yields long straight chains, whose symmetry (triangles either on the same side or alternating on both sides) is determined by the length of the connecting DX molecules: depending on the number – or fractions – of turns separating different crossovers, different positions along the helix “staircase” and thus different angles between the connected structures are obtained (see Fig. 22).

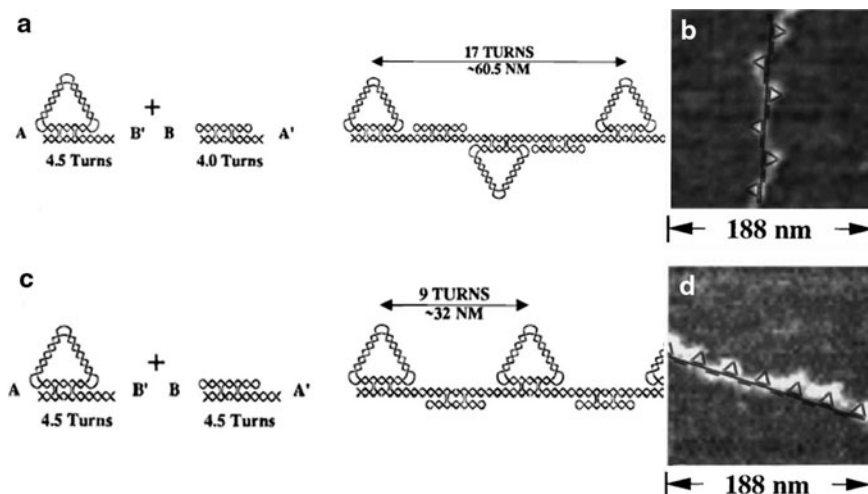


Fig. 22 Linear aggregates obtained by combining double crossover structures and triangles also made of double helices. Depending on the length of the connecting strands, the resulting straight aggregates present triangles with alternated orientation (a) or on the same side (c); (b, d) show AFM evidence for the geometric arrangement. Adapted from [100]

Various structures of DNA tubes have been devised based on the main building blocks exploited in 2D crystals: four-arm junctions [73] and different kinds of DX [68] and TX tiles [101]. The spontaneous curvature of DNA constructs is in this case exploited rather than minimized or compensated as in 2D crystals. Specifically, the curvature is the consequence of the symmetry of the different tiles and of the nature, the number, and the spatial arrangement of the crossover points, whose ultimate origin is an implementation of the approach proposed in [100] and shown in Fig. 22 (see [102] for a detailed discussion).

Alternatively, specific DNA motifs with encoded curvature have been designed, as the six-helix bundle already described above [74] (see Fig. 17). The dimensionality of the aggregates built in this way can be tuned by modifying the number and the sequence of sticky ends connecting the helices. Specifically, one-dimensional structures are obtained when the sticky ends on the two terminals of each helix are complementary to each other so as to ensure linear growth. Aggregates obtained in this way reach lengths of several micrometers. This strategy also allows one to tune easily the number of helices forming the tube. Bundles of 3 [103] and 12 helices [104] have been reported.

A different method yet to tune the diameter of DNA nanotubes relies on an interesting idea first exploited in [105]: a single oligonucleotide ($N = 52$) composed of four different self-complementary segments serves as the building block for a DX tile, and can thus fold into long tubes like those obtained from the multi-stranded structures previously described (see Fig. 23). Since a single sequence is required, this approach offers simplified design and minimizes errors and structural distortions. Furthermore, by only changing the relative size of the sequence segments it can be specialized to produce tiles with different widths, yielding tubes with circumferences between 4 and 20 helices [106].

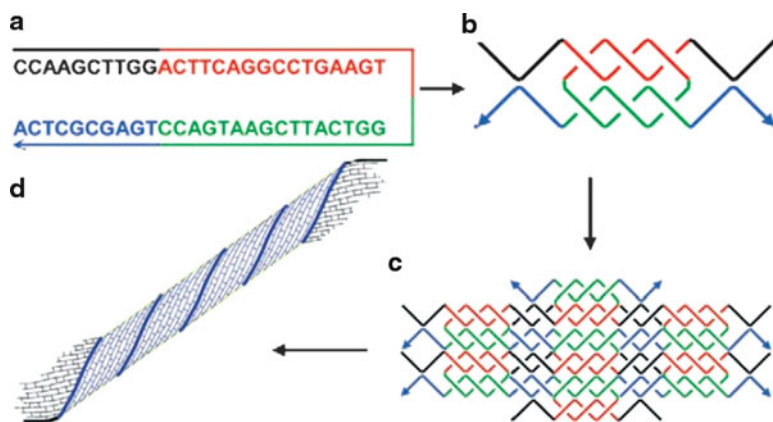


Fig. 23 Schematic illustration of the formation of a nanotube from a single sequence composed of four self-complementary segments (shown in different colors in (a)); the strand forms DX tiles (b) which then assemble into folded sheets (c, d). Adapted from [105]

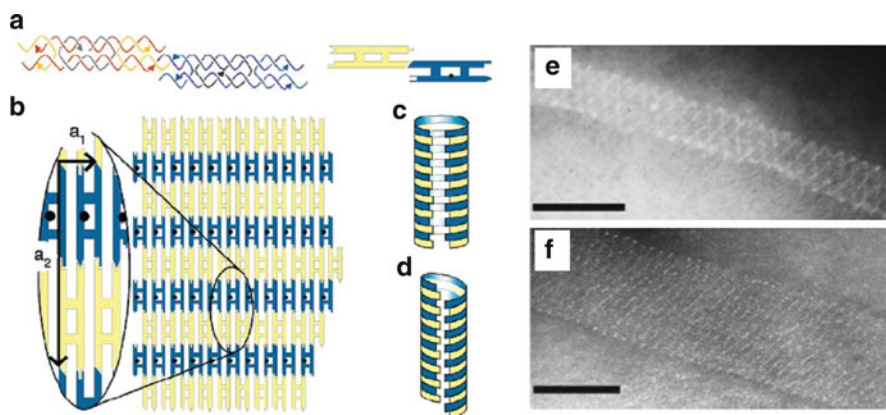


Fig. 24 Schematic diagram of the formation of tubes from two different DX tiles (*yellow and blue* in (a)), assembling through sticky ends, represented as complementary shapes. The resulting sheets (b), labeled with biotin (*black dots*), can fold in register, yielding achiral tubes (c), or with shifted bonds, giving rise to helical tubes (d). The TEM images in (e, f), with scale bar 200 nm, show zigzag arrangement of biotin (*bright dots*), indicative of chiral structures. Adapted from [108]

Various other parameters have also been explored in one-dimensional structures. (1) Geometry – triangular and square modules have been generated by attaching DNA strands to synthetic organic molecules that act as vertices, each module being connected with others by single or double strands [107]. (2) Length – aggregates have been tuned by using the module structure described in [107] as a template and capping sequences to control their growth into monodispersed structures, with obvious interest for applications [98]. (3) Persistence length, which is typically 100 times larger than in a single DNA double helix and can thus be tuned by modifying crossover position and bundle diameter [102]. (4) Chirality, obtained either by folding a tube with a shift along neighboring edges (see Fig. 24) [108], or by promoting left or right-handed twisted conformations in bundles through differentiated crossover distances, which exert positive or negative strain [109].

2.5 Hydrogels

DNA hydrogels are amorphous water-swollen cross-linked DNA networks typically extending over macroscopic volumes. DNA gels are being investigated in the attempt to exploit the richness of the DNA behavior to create a biocompatible, easily assembled material having some degree of mechanical strength. Besides their interest in fundamental material science, DNA hydrogels have potential application in drug delivery, cell culture, and tissue engineering.

It has been shown that semi-dilute solutions of long DNA without any additional linkage have significant viscoelastic behavior [110]. This is shown in Fig. 25, where

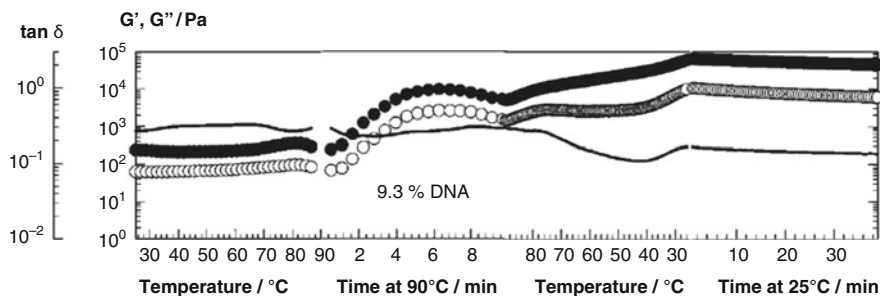


Fig. 25 Viscoelastic behavior of a semi-dilute solution of DNA. Elastic modulus (G' , filled symbols) and viscous modulus (G'' , open symbols) are plotted, together with their ratio $G''/G' = \tan \delta$ (solid curve), for a 93 mg/mL DNA solution subjected to a heating-cooling cycle. The entanglement of DNA helices and, at high temperature, of single strands causes the almost monotonous increase of the dynamic moduli. Reproduced with permission from [110]

the elastic and viscous shear moduli, together with the associated loss factor, are shown for a 93 mg/mL solution of double-stranded DNA sodium salt from salmon testes, having a length of approximately $N = 2,000$ base pairs. In particular, the figure shows the evolution of the rheological properties as the sample is heated above melting and cooled back. Both melting and renaturation bring about an increase, by one order of magnitude, of the viscoelastic moduli. The first increase is explained by the growth of entanglement associated with the denaturation and hence with the increase in number of filaments and their flexibility. The second increase is due instead to the formation of cross bonds between DNA stands. This is visually represented in the upper cartoon in Fig. 26. As the solution is heated, double strands melt. Upon cooling the random local complementarity and following hybridization between stretches of various strands induces the formation of a viscoelastic cross-linked network.

Various authors have studied DNA hydrogels where the cross-linking is provided by chemical covalent bonding of the DNA strands through the use of ligating agents. One common strategy is the use of glycol diglycidyl ether (EGDE) that provides links between the amino groups on the nucleotide bases to form a three-dimensional DNA network. EDGE-DNA gels have been studied as a relevant example of discontinuous transition from swollen (good solvent) to collapsed (bad solvent) as the quality of the solvent is gradually changed [111]. The transition was produced by adding acetone to the solution: at about 60 vol.% acetone the DNA hydrogel suddenly collapses to a volume about 1/15 of that in the swollen state. Similar, but less marked transition is found upon increasing the concentration of divalent calcium cations [112, 113], of spermidine, a trivalent cation [114], and of cationic surfactant [115, 116]. This multivalent cation induced collapse is interpreted as a result of the association of DNA double strands that follows their charge neutralization [112].

The viscoelastic properties of EDGE-DNA hydrogels were studied as a function of the density of DNA and chemical cross linker and as a function of temperature

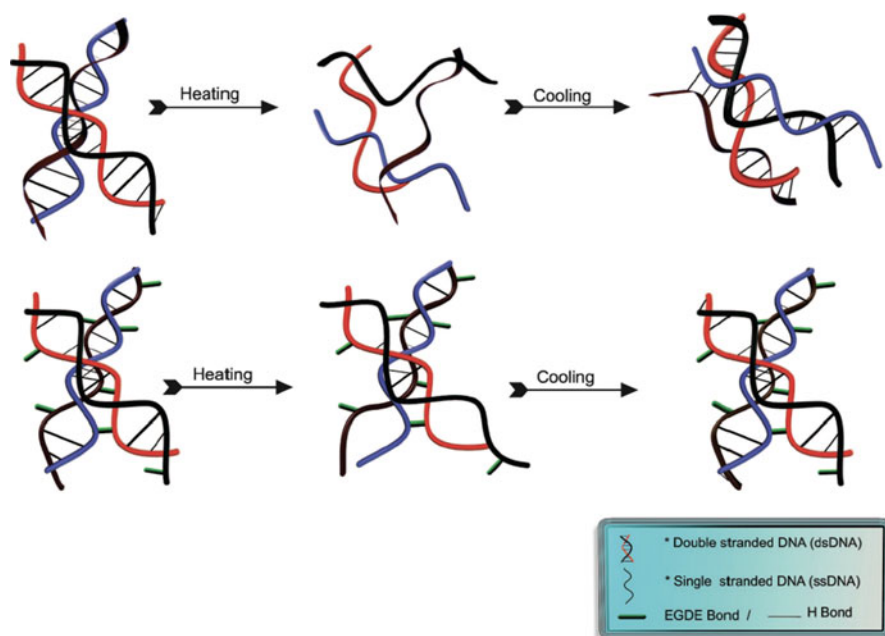


Fig. 26 Cartoon illustration of the temperature effect on conformational changes of DNA in solutions (*up*) and in gels (*down*). The *green pendants* represent cross-linker molecules named EGDE. Reproduced with permission from [110]

[117]. Freshly prepared chemically cross-linked DNA hydrogels are stiffer than unreacted DNA solutions, but their stiffness doesn't grow as much through denaturation–renaturation cycles. At high cross-link density, the thermal cycle does not affect the viscoelastic properties at all. This can be interpreted as described in the lower cartoon of Fig. 26: the cross-linking doesn't allow enough conformational variations to the DNA chains to find matching sequences in other strands. Overall, EDGE-DNA hydrogels, in the explored ranges of variables, don't reach the stiffness provided in thermally cycled DNA. The behavior of chemically cross-linked DNA is reviewed in [118].

A somehow reversed situation is obtained when DNA provides reversible cross-linking in hybrid hydrogels formed by oligonucleotides bound to synthetic chains, typically polyacrylamide or closely related water-soluble polymers. This structure was first proposed by [119], and later developed by various groups [120–122]. DNA oligomers are bound to the main chain polymer as side-chains. Cross-linking is provided by DNA hybridization, either directly, if the oligos are mutually complementary, or by virtue of linker DNA sequences that have subsequences complementary to the side chains so as to bind them in pairs. DNA-mediated cross-linking is attractive because the intrinsic reversibility of DNA–DNA interactions can thus be exploited. This can be done either using temperature as the control parameter, or by competition, i.e., by adding DNA strands that are perfectly complementary

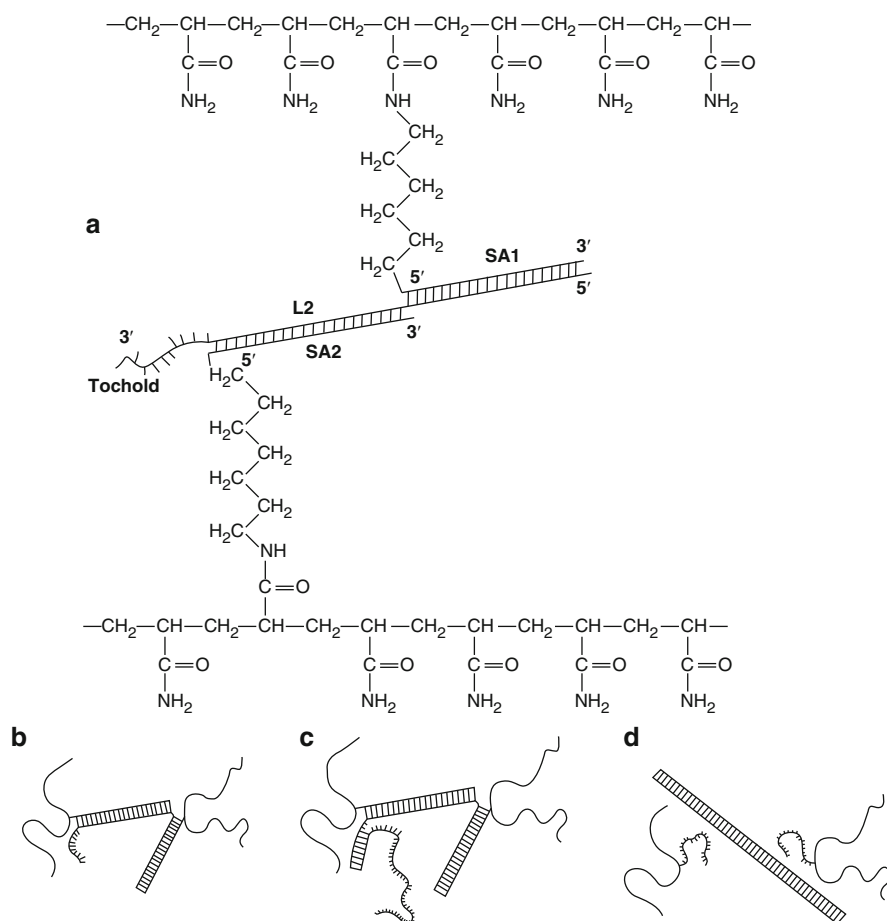


Fig. 27 (a) Chemical structure of a polyacrylamide hydrogel, with DNA side chains providing cross-linking (b). As competing sequences are introduced, they first hybridize with a “toehold” overhanging sequence (c) to replace gradually the DNA linker (d), thus unbinding the network. Adapted with permission from [120]

to the linker DNA sequences so as to oust it from the bond with the side-chains. The mechanism enabling this process is described in Fig. 27.

This approach enables one to control the stiffness of the hydrogel [120, 121]. The microscopic structure of this class of hybrid DNA–polyacrylamide hydrogel, and its change following the dissolution of reversible cross-linking, have been investigated by tracking the diffusion of quantum dots in microscopy experiments [122]. It has been found that quantum dots are trapped in the hydrogel network even when their size is smaller than the nominal mesh size of the network. In agreement with expectations, as the DNA–polyacrylamide chains unbind, quantum dots recover free diffusion.

A different approach to the construction of all-DNA hydrogel involves the use of sticky star-like aggregates of the type previously described in the context of periodic structures [123, 124]. The process of hydrogel formation is described in Fig. 28. Three types of building units have been employed, differing in valence and geometry. Arms are $N = 18\text{--}21$ long, while the sticky overhangs are all equal and self-complementary 4-mers. Oligomer solutions, having concentrations of the order of 10 mg/mL, assemble into an amorphous network, which is stabilized by enzymatic ligation. The resulting structure can swell by further hydration up to volumes one to four times larger than the original. Hydrogels prepared in this way have good shape memory: they can be dried and re-wetted to gain back the shape they had when ligated. The mechanical properties and the microscopic structure of the hydrogel depend on the geometry of their building blocks. Hydrogel built from four-arms stars have the largest tensile modulus and the largest swelling capacity. Fig. 28c,d shows the morphology of such hydrogels as obtained by confocal microscopy (Fig. 28c) and by AFM (Fig. 28d). The emerging picture is of a rather regular local arrangement of the building blocks (see Fig. 28d) that gives rise to a bushy-type structure at larger length scales.

3 Self-Assembly of DNA-Coated Colloids

Colloidal science is one of the first areas where the potential of biological interactions for realizing highly specific, thermally reversible bonds with tunable strength was realized. In particular, starting from the pioneering work of Mirkin et al. [125] and Alivisatos et al. [126], DNA has been extensively used to tailor the interactions between colloidal particles for the realization of effectively programmable *building blocks* devoted to the *self-assembly* of large structures. The success of DNA-based molecular interactions for self-assembly of colloidal particles is not surprising. The already numerous possibilities represented by natural and synthetic colloids have been explored in depth during the last few decades and much work was done both in terms of basic science and applications. Nowadays, colloidal scientists know how to obtain stable colloidal dispersions and avoid or drive externally the aggregation of the individual constituents. DNA-coated particles offer a change of perspective: the key concept is to combine the collective nature of colloidal phenomena such as aggregation or flocculation with the peculiar properties of DNA-based molecular interactions to obtain the bottom-up spontaneous fabrication of complex materials with the desired features. Such a fabrication takes place on the nano- and micro-scale by using the predictable, controlled, and engineered aggregation of small elementary building blocks. Of course, the bottom-up nature of the self-assembly can also take advantage of the use of external templates or agents (electric, magnetic, or thermal fields) to realize *directed self-assembly*. In this section we describe the basic ingredients of the self-assembly of DNA-coated colloids, with particular attention to the possible soft materials and phases arising from the use of the intriguing combination of concepts from colloidal science and biology.

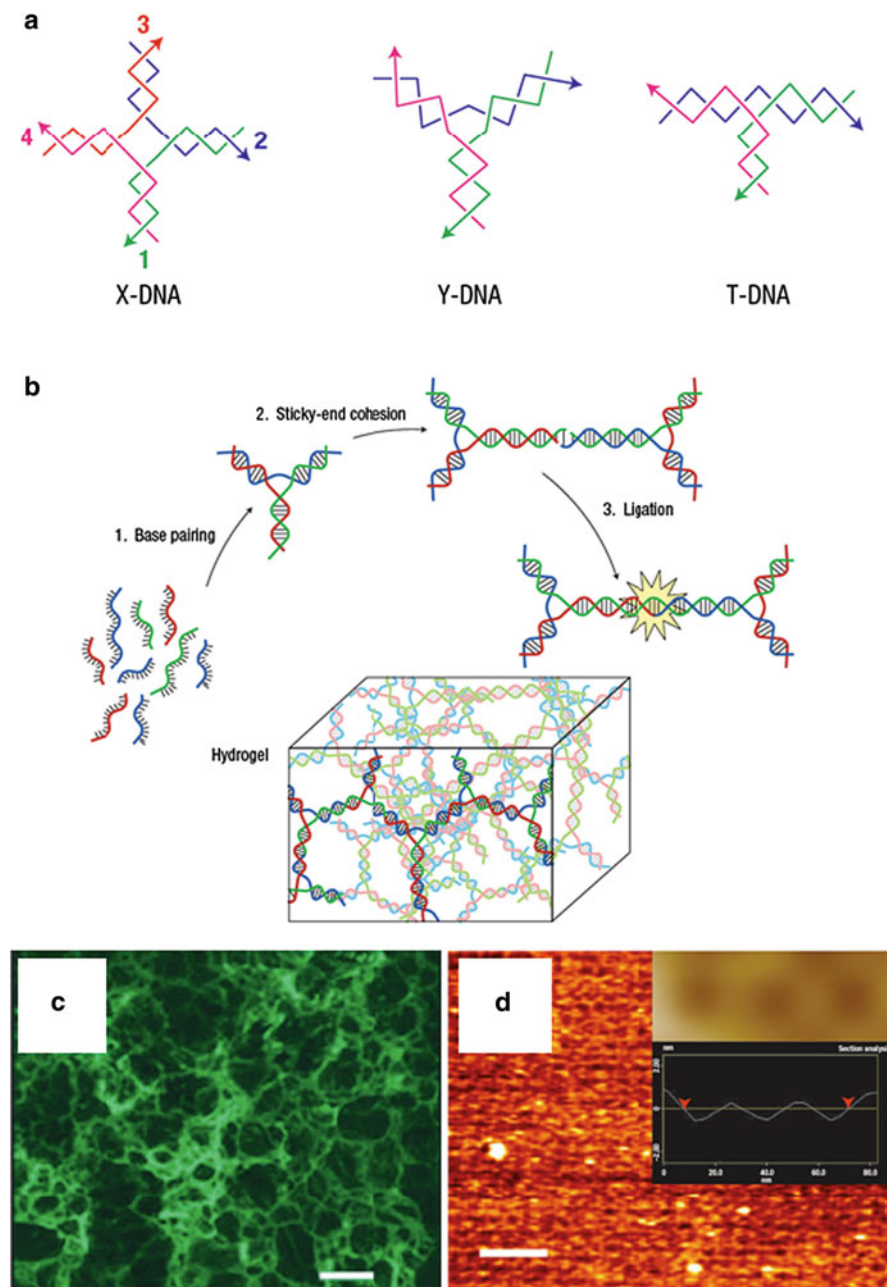


Fig. 28 (a) Various branched DNA structures with sticky ends. (b) Schematic representation of the aggregation of branched monomers and of their ligation into hydrogel networks. (c) Confocal microscopy image of swollen DNA hydrogel obtained from X-DNA structure in (a). Scale bar is 200 μm . (d) AFM image of X-DNA gel (scale bar is 200 nm). The inset shows an enlarged portion of the image with hydrogel pores visible. (a, c, d) reproduced with permission from [123], (b) from [124]

3.1 DNA-Coated Particles and Their Interactions

Size is a key parameter for DNA-functionalized particles in that it dictates the strategy needed to achieve the desired particle functionalization.

For small, nano-sized colloids the state-of-the-art is the method introduced in [125], which is suitable to be used with metallic nanoparticles (mainly gold). In [125] oligonucleotides functionalized with alkane thiols at their 3' termini are mixed with the gold nanoparticles and incubated for a few hours. During the incubation covalent Au–S bonds fix the oligonucleotides on the particle surfaces. This operation produces nanoparticles coated with single strands of DNA (ssDNA) that can be designed at will. In the original recipe two different kinds of particles are created, covered with the non-complementary sequences TTTGCTGA and TACCGTTG that we will label a and b, respectively. While bare gold particles do aggregate at moderately high salt concentration (0.1 M NaCl) or at high temperatures, the DNA-coated nanoparticles exhibit stability against these two agents, thanks to the steric repulsion induced by the ssDNA oligomers. Reversible self-assembly is obtained by adding suitable linkers between the two kinds of nanoparticles. The linkers are oligonucleotide duplexes with “sticky ends” a' and b' that are complementary to both sequences. In [125] this is achieved by employing as a' and b' the sequences 5'-AAACGACTCTAGCGCGTATA and 5'-ATGGCAACTATACGCGCTAG, respectively (the underlined 12-base pairs overlap and the remaining 8-base pairs are the sticky ends). Of course, the choice of the specific strands to be attached on the particle surface can be different and, in a quite general fashion, one can obtain a thermoreversible assembly as depicted in Fig. 29 [127].

As far as larger particles – in the micron range – are concerned, the functionalization is based on a few successful strategies which depend on the properties of the desired bond. If a covalent bonding is required, the commonly used strategy makes use of carboxyl-functionalized colloidal particles and water-soluble carbodiimide chemistry [128–131]. On the surface of the particles 1-ethyl-3-(3-dimethylaminopropyl)carbodiimide functional groups are attached. This group is water soluble and is a good carboxyl activating agent for the coupling of primary amines to yield amide bonds. If amino-labeled DNA is added in solution, it attaches covalently to the

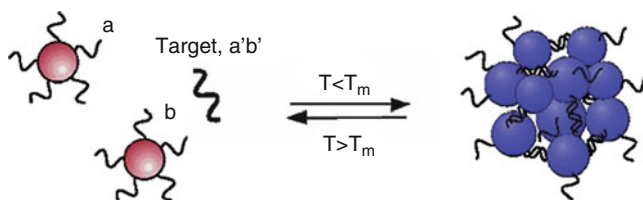


Fig. 29 Two families of gold nanoparticles are functionalized with different non-complementary DNA sequences a and b. The strands are designed to recognize a single target sequence a'b', which then assembles the particles into clusters. Reproduced with permission from [127]

particle surface by means of an amide bond. This procedure is difficult and sometimes the easier avidin–biotin binding is exploited [132, 133]. In that case, neutravidin coated particles are mixed in solution with DNA with biotin terminals attached. The non-covalent avidin–biotin bond is one of the strongest biological interactions known but, in comparison with the covalent bonding described above, it allows one to obtain a lower surface density coverage. More recently, a third functionalization strategy was devised, which is based on trapping a water-soluble, functionalized polymer surfactant on the particle surface via swelling with an organic solvent followed by deswelling [134]. The surfactant is a triblock copolymer adsorbed on the particle surface. Swelling of the particle is induced by addition of an organic solvent and it favors the penetration of the hydrophobic block of the copolymer in the particle bulk. The solvent is then removed by heating. As a result the particles deswell and the triblock polymers stay well attached to the particles surface with the hydrophilic blocks exposed to the outer environment. If the triblock copolymer is suitably designed, DNA can be attached, obtaining thereby the DNA coated colloids.

In most of the cases the interaction of micron-sized particles is not mediated by a linker sequence [135]. Usually the particles are directly covered with complementary sequences that bypass the need of having a third component in solution. This approach is illustrated in Fig. 30 where a few key aspects of the functionalization strategy chosen in [136, 137] are stressed.

The micron-sized particles in Fig. 30 are of two different kinds. Both particles are covered with $N = 61$ oligomers, attached via a short poly(ethylene glycol) spacer to a biotin group linked to the 50th base, and hybridized from its 50 end to a 49-nucleotide complementary strand (CS). As a result, a rigid 15 nm long double-stranded “rod” with a flexible single-stranded end of 11 bases is obtained. Three types of 11-base-ends were used: two were complementary “sticky” sequences (S/S’), the other was a non-sticky thymine-only sequence (N). The presence of the sterically stabilizing polymer and of the non-sticky ends can be understood by looking at a simple model of the interactions in DNA-coated particle systems.

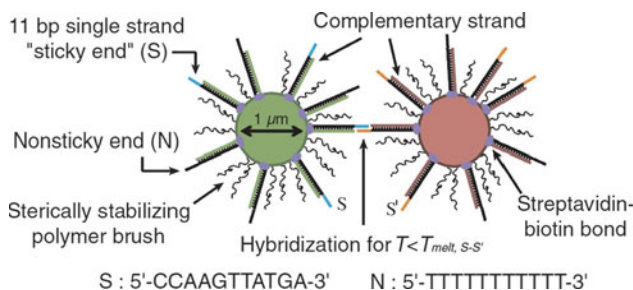


Fig. 30 Schematic representation – not to scale – of micron-sized colloidal particles coated with DNA strands with interacting sticky ends. Double helices bound to colloids form a 15-nm-thick coating which contributes to particle stability together with polymer brushes. Each helix ends with an 11-based dangling strand, either non-interacting (N) or complementary to the tails on the second type of particle (S, S’). Reproduced with permission from [136]

In [138] the interactions between two particles are supposed to consist of three parts: an attractive part U_{DNA} , due to interparticle DNA hybridization, a steric and/or electrostatic repulsive term U_{rep} , and a strong attractive van der Waals contribution U_{vdW} , acting at short distances. It is clear that the van der Waals term is responsible for the irreversibility, while a clever combination of the other two terms is needed to obtain a secondary minimum in the total potential $U_{\text{tot}} = U_{\text{DNA}} + U_{\text{rep}} + U_{\text{vdW}}$, well outside the van der Waals region. The mechanism is described in Fig. 31. For temperatures much higher than the melting temperature T_m of the strands, $U_{\text{DNA}} = 0$ and U_{tot} is always positive (see Fig. 31c, d). For smaller temperatures, if $2L$ is the length of the hybridized DNA and d is the separation between two particles surfaces, one has that U_{DNA} is non-zero only for $d < 2L$. In that region, U_{DNA} is negative (attraction) and increases linearly with d . The slope increases with larger particle radius R_0 , smaller T , and larger surface density of strands on the particle. If the stabilizing contribution from U_{rep} is too small the particles might get too close to each other and the van der Waals potential may lead to irreversible aggregation (Fig. 31c). To avoid this irreversible bonding one can increase U_{rep} either by adding steric stabilizers on the particle surface or by reducing U_{DNA} . As mentioned above, at a fixed temperature and radius this can be done only by decreasing the surface density of the DNA strands. In [138] the adopted choice was to increase U_{rep} by addition of copolymer stabilizers. In

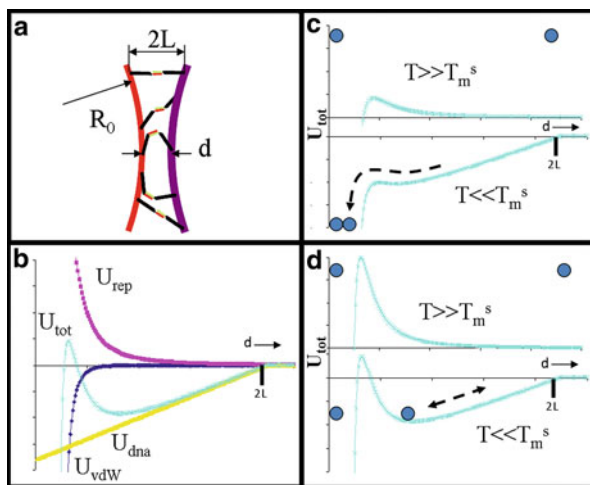


Fig. 31 Overall interaction energy between two DNA-coated colloids. (a) Sketch of the interacting surfaces of two spheres of radius R_0 separated by d . The maximum length of hybridized strands is $2L$. (b) Total interaction energy as a function of d . It is the sum of the attractive U_{DNA} from the binding of accessible DNA strands, the repulsive U_{rep} from electrostatics and/or polymer steric effect, and the van der Waals attraction U_{vdW} . (c) For weak, short-range U_{rep} , particles which are unbound at high temperatures are irreversibly trapped in the van der Waals well after DNA hybridization at low temperatures. (d) For strong, medium-range U_{rep} , DNA binding produces a secondary minimum of reversible aggregation. Reproduced with permission from [138]

that case (Fig. 31d), by decreasing the temperature a potential barrier remains that prevents irreversible aggregation by facilitating reversible aggregation at larger distances in the secondary minimum. This means that, by increasing again the temperature above T_m , DNA dehybridizes and the particles disperse thermally because of the repulsive barrier at small distances.

Varying the fraction χ of sticky-ends on the colloidal surface allows for a fine tuning of the interactions as shown in [136, 137]. By examining the same sequences used for the sticky-ends in a solution without the particles, a rather broad melting curve (width is about 20°) is measured, which is represented as a blue line in Fig. 32. The hybridization free energy of DNA in solution $\Delta F_{\text{DNA}}^0 = \Delta H_{\text{DNA}}^0 - T\Delta S_{\text{DNA}}^0$, shown as a solid red line in Fig. 32, is determined from the concentration dependence of the melting curve of the sticky-ends in solution [139]. For $T < T_0 = \Delta H_{\text{DNA}}^0 / \Delta S_{\text{DNA}}^0$, attraction sets in and the fraction of non-hybridized strands decreases with T . At the melting temperature T_m the singlet fraction equals 50%. Theoretical modeling and experiments show that the melting curve of the particles covered with the strands bearing the same sticky ends is much narrower (width is about 1°) and depends on the sticky-end fraction χ . At high DNA coverage of the particles, decreasing χ induces a shift of the melting/dissociation temperature toward a lower temperature that approaches T'_0 for $\chi = 1$ but does not result in a significant change in the width of the transition (see Fig. 32). This temperature shift can be associated with a shift of the free energy (dashed red line in Fig. 32) which is caused by a configurational entropy cost paid by the DNA at the particle surface.

A different strategy to tailor the interparticle interaction is based on the use of palindromic sticky ends that allow the interactions of single strands with themselves or with neighboring strands on the same colloidal particle [140]. In this way the formation of loops and hairpins at the particle surface is possible, which gives in

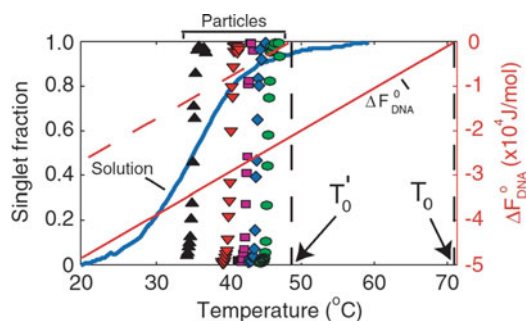


Fig. 32 Unbound particle fraction as a function of temperature for colloids interacting through DNA sticky-end pairing. Experimental data for various sticky end fraction (*symbols*) are compared with the melting curve for the same sticky end sequence in solution (*blue line*), much broader. The *red line* shows the hybridization free energy of DNA in solution (*right axis*), while the *dashed red line* shows the effect of an entropy correction (see discussion in the text). Reproduced with permission from [136]

situ control over the interparticle binding strength and association kinetics. Quite interestingly, the attraction between particles can be finely tuned and even switched off, providing thereby a useful means to obtain switchable, self protected interactions. A pictorial representation of this approach is presented in Fig. 33.

The key idea in [140] is that, even though the binding energy of structures such as loops or hairpins are smaller than the interparticle association energies, a fast temperature quench can favor the formation of the loops and hairpins inside the DNA coatings. This is possible if such structures form over times that are smaller than the typical time of diffusive encounter of the particles. Of course, this is easier for smaller particle concentrations as shown in Fig. 34.

If the temperature is lowered quickly, neighboring sticky ends at the same particle can connect before they can form bonds between different particles. However, if two particles with already formed loops or hairpins are held together for a longer time (for example by means of an optical tweezer) they can still stick together because for long times the bond with larger binding energy dominates. In addition, if the temperature is raised above the melting temperature of the loops and hairpins the particles can still bind together, providing thereby a very nice demonstration of a switchable self-protected attraction between DNA-coated colloidal particles.

As a final remark for this section we note that for nano-particles, for which U_{DNA} is roughly two orders of magnitude smaller than for micro-particles, a subtle control of the balance between the different terms in U_{tot} may seem more difficult. Nevertheless, reversible assembly may easily be obtained with nanoparticles [127,

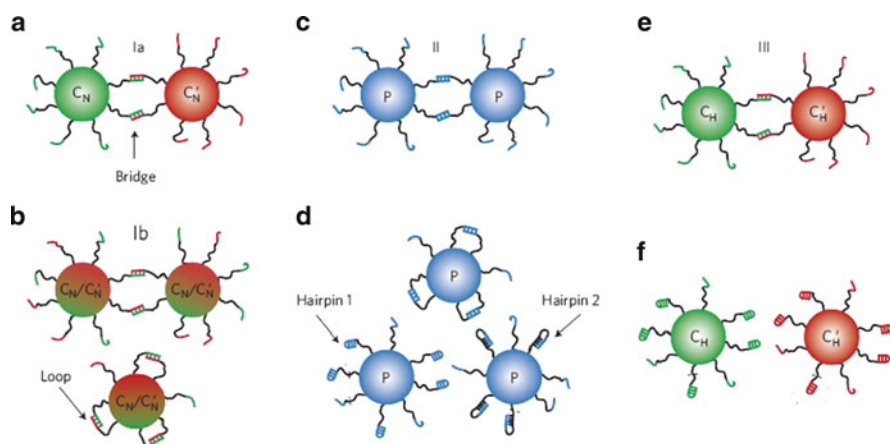


Fig. 33 Various types of colloid DNA-mediated interactions, either conventional or self-protected – switched off – through intra-particle hybridization. (a, b) Normal, hairpin-free pair of complementary sticky ends, either grafted to separate beads (a) or mixed on the same bead (b). (c, d) Self-complementary sticky ends. Besides self-protective loops as in (b), this sequence can form two hairpin structures: the sticky end sequence can fold on itself (1), or it can bind to the backbone (2). (e, f) As in (a), but each of the sticky ends can fold into a protective hairpin. Adapted with permission from [140]

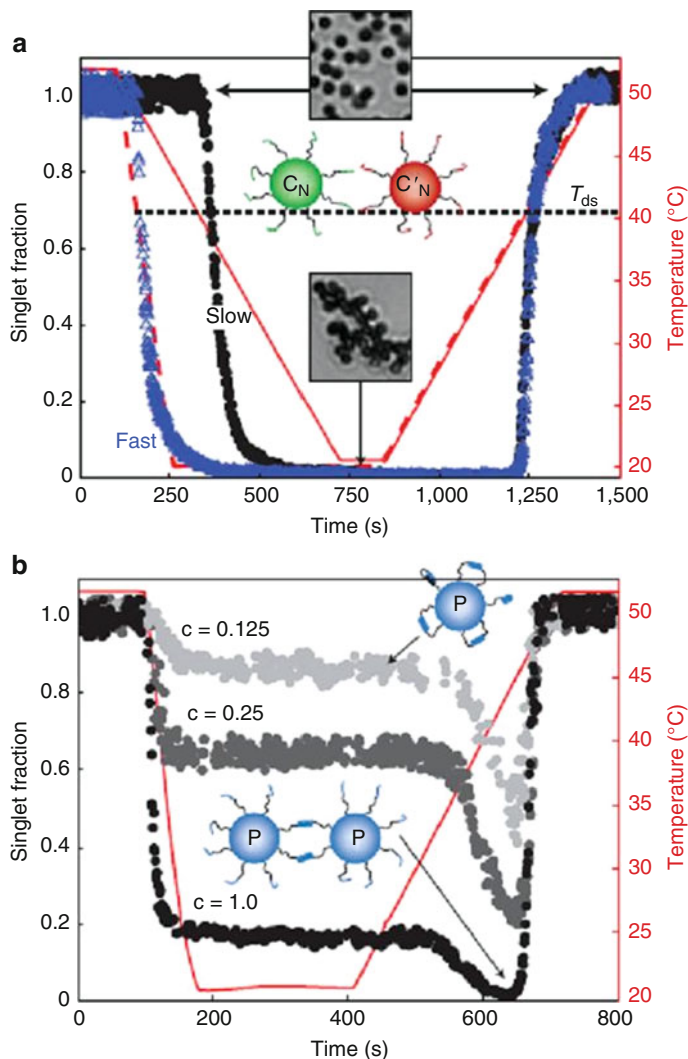


Fig. 34 Kinetics of association and dissociation for conventional and self-protected interactions. (a) Conventional scheme (Fig. 33a). Red lines and right axis represent temperature as a function of the elapsed time, while symbols and the left axis are the corresponding particle singlet fraction at fast (blue) or slow (black) temperature quench. The insets show microscopy images of isolated or aggregated particles. (b) Self-protected scheme (Fig. 33c). Particle singlet fraction as a function of time at fixed temperature profile (red line), but at different overall particle concentrations: for dilute colloids, intra-particle hybridization prevents aggregation, while at higher c the inter-particle diffusion competes with hairpin formation. Adapted with permission from [140]

[141, 142] as well as with small DNA-coated clusters [143], even though micron-sized colloids are very often preferred because they can be easily studied with optical microscopy and light scattering.

3.2 *Soft Phases Made of DNA-Coated Colloids*

It is almost 15 years since the original proof of the principle that DNA oligonucleotides can be attached to nanoparticles and used for the self-assembly of larger structures [125, 126]. With the previously described rich portfolio of building-blocks and switchable forces available for the investigators, much work has been devoted to the assembly of larger structures, as mirrored by the more than 3,300 citations collected during this period by [125, 126]. These two works originated a very wide area of research, whose full review is beyond the aim of the present chapter. A quite broad coverage of the subject can be found in recent reviews [144–146], whereas here we will give a self-contained introduction to the topic.

One of the points of interest in the use of DNA-coated particles is related to the possibility of realizing materials ordered on a length-scale much larger than the size of the particles. It is well known that colloidal particles can form colloidal crystals during sedimentation or drying. In the presence of a purely repulsive interaction the particles crystallize above a given volume fraction because of the limited free volume available. Repulsion favors crystallization because the particles do not lock on to each other and are free to move and to find the best configuration in space. However, this phenomenon leads to a lattice of hexagonally close-packed layers, whose symmetry is not suitable for photonic crystals or other optoelectronics applications.

The use of DNA-coated particles introduces a finer control on the interaction potential and suggests this method as a very promising step to produce metamaterials with novel electronic, magnetic, plasmonic, and photonic properties [147–150]. Highly specific biosensors, efficient solar panels, light sources and detectors, and invisibility cloaks are a few dream applications that might come as a byproduct of the research on the self-assembly of DNA-coated colloidal particles. However, despite the fervent theoretical and experimental activity, we are still far away from such challenging achievements, even though recent results brought us much closer to the aim. Indeed, only in 2008 two groups achieved simultaneously the crystallization of DNA-coated nanoparticles, revealing that both body-centered cubic (bcc) and face-centered cubic (fcc) lattices can be obtained as a result of the assembly [141, 142]. One year later Xiong et al. drew the first experimental phase diagram by means of X-ray scattering experiments [151]. They employed DNA-functionalized nanoparticles interacting via a DNA linker, as described in the previous section. Both the linker length and the number of linkers per particle determine the interparticle interactions and are found to influence the phase state. The experimental phase diagram shows that the ordered phase (crystal) exists only in a limited range of linker lengths and that the number of linkers determines the onset of crystallization. In addition, bcc and fcc crystals of octahedral-shaped colloids homogeneously coated with DNA were obtained by changing the length of the DNA linkers. Longer and more flexible DNA linkers promote fcc ordering against the tendency of the system to orient octahedra so as to have parallel faces.

Very recently the crystallization of non-spherical nanoparticles into ordered arrangements has been observed that had not been seen with spherical particles. Thanks to the high density of DNA on the particle solid faces, hexagonal packing of nanorods, and columnar stacking of nanoprisms, fcc crystals of rhombic dodecahedrons were observed in [152] (see Fig. 35).

As far as crystallization of DNA-coated microparticles is concerned, it is quite interesting to note that the first success was achieved in 2005 when small hexagonal crystals were eventually observed in addition to the more ubiquitous fractal aggregates, which are much easier to obtain [153]. This success could be obtained only by using the swelling/deswelling functionalization strategy that allowed high control of the functionalized surface property. However, these crystals could not be made larger than a few micrometers (see Fig. 36), a limitation that was also made evident by successive work [154, 155].

What emerges, at least at the micron scale, is that DNA hybridization is too effective in gluing the particles when they touch each other. This is not advantageous for crystallization that benefits from a certain freedom of motion of the particles to find the configuration of minimum free energy. The work with micron-sized particles points out that only by working very close to the melting temperature of DNA, where the bonding is weak and reversible, is it possible to achieve crystallization, eventually by thermally cycling the sample to favor local rearrangements of the particles' positions. Additional work in this direction is very important because micron-sized building blocks have just the right length scale

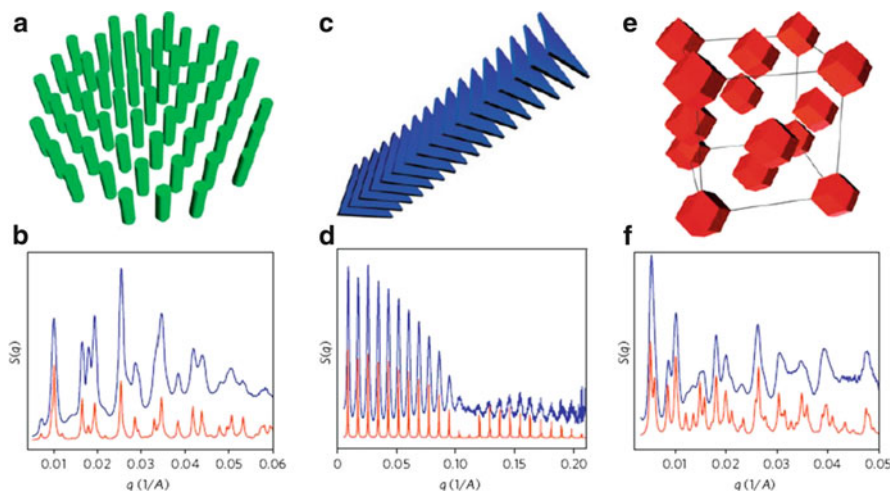


Fig. 35 Crystallization of non-spherical particles homogeneously coated with DNA. (a, b) Schematic of a hexagonal close-packed 2D layer in assemblies of gold nanorods and corresponding structure factor $S(q)$ obtained from SAXS measurements (blue line) and simulations (red line). (c, d) Schematic of 1D columnar assembly of gold triangular nanoprisms and corresponding SAXS patterns. (e, f) Schematic of the 3D fcc assembly of gold rhombic dodecahedra (the lines indicate the fcc unit cell) and corresponding SAXS patterns. Adapted with permission from [152]

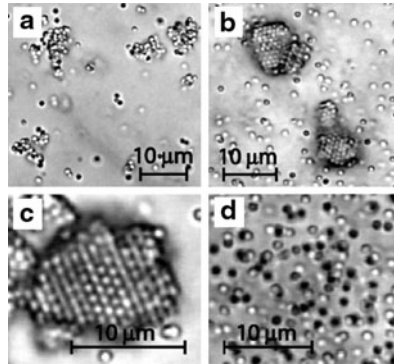


Fig. 36 Self-assembly of DNA-coated colloids observed in optical microscopy. (a) Fractal-like aggregates of microspheres with 14,000 DNA molecules per each sphere. (b, c) Similar colloids with 3,700 DNA/sphere form small crystals. (d) Upon heating by only 2°C, the crystallites and the aggregates both melt into monomers. Adapted with permission from [153]

for photonic applications and the bottom-up self assembly of photonic crystals would have a huge technological impact. Directed self assembly approaches are excellent candidates for bringing in additional ingredients to achieve such a challenging task [146].

In one-dimension (1D), chains of nano- and micro-particles have been obtained with normal and directed self-assembly. Apart from being of obvious interest for realizing three-dimensional (3D) systems by starting from 1D assembled building blocks, this kind of structure is interesting per se for at least two reasons. From one side it is appealing to obtain chains of metal nanoparticles close enough to favor the transport of electrons as electric nanowires. Moreover, as suggested in [140, 156, 157], such structures could be used for the large scale equivalent of the DNA replication mechanisms and could be used as templates for the exponential replication of specific 1D particles sequences. We report in Fig. 37 the results of experiments described in [157] with micron-sized DNA-coated particles with self-protected interactions that we have already described above. Particle chains are formed by means of a magnetic field and according to the rapidity of the quench rate different behaviors are reported (see the figure legend for details).

A last notable example is represented by a templated self-assembly of metallic nanoparticles by using DNA as a scaffold. This leads to the formation of extended, close-packed, ligand-stabilized metal nanoparticle structures, including long chains of nanoparticles [158].

Concerning 2D structures, a very interesting procedure employs a combination of DNA-surface patterning and DNA-coated colloids for the sequence-specific reversible self-assembly of well-ordered 2D colloidal arrays (see for example [159–162]). Similar results were obtained with the above-mentioned DNA-origami [163]. Another strategy consists of building up 2D structures by using three-armed DNA motifs where one of the three arms binds one particle, and the other two are used for building the 2D structure [164]. We report in Fig. 38 the results of such experiments.

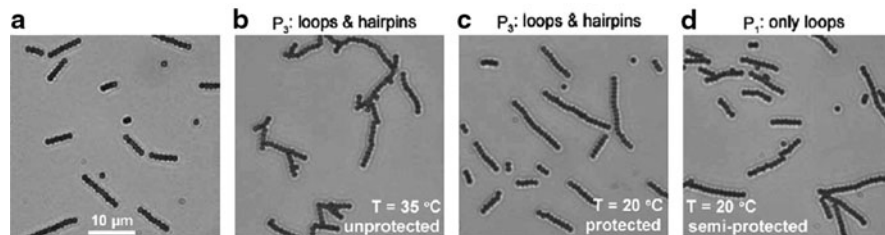


Fig. 37 Linear chain formation of DNA-coated paramagnetic polystyrene colloids with the different self-protection schemes displayed in Fig. 33. By using an external magnetic field, DNA-functionalized particles were brought together into linear chains, after which the temperature was lowered below the association temperature for beads, and the field turned off. (a) Representative microscopy picture of the resulting chain structures immediately after switching off the magnetic field. (b–d) Chains after 1 h at the specified temperature for particles functionalized with sticky end sequences able to form both loops and hairpins (b, c) or only loops (d). The degree of aggregation of chains in (d) is intermediate between the unprotected, branched chains in (b) and the perfectly linear, protected chains in (c). Adapted with permission from [157]

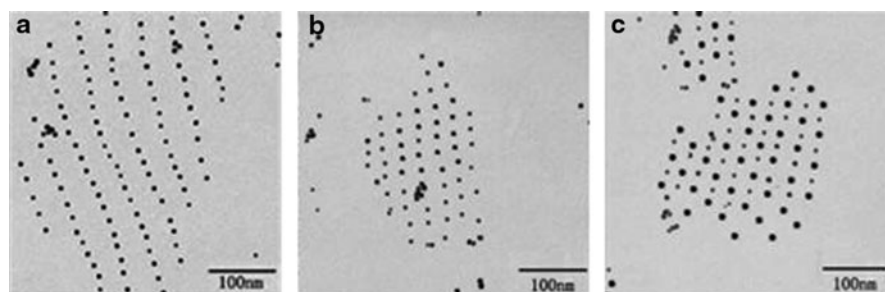
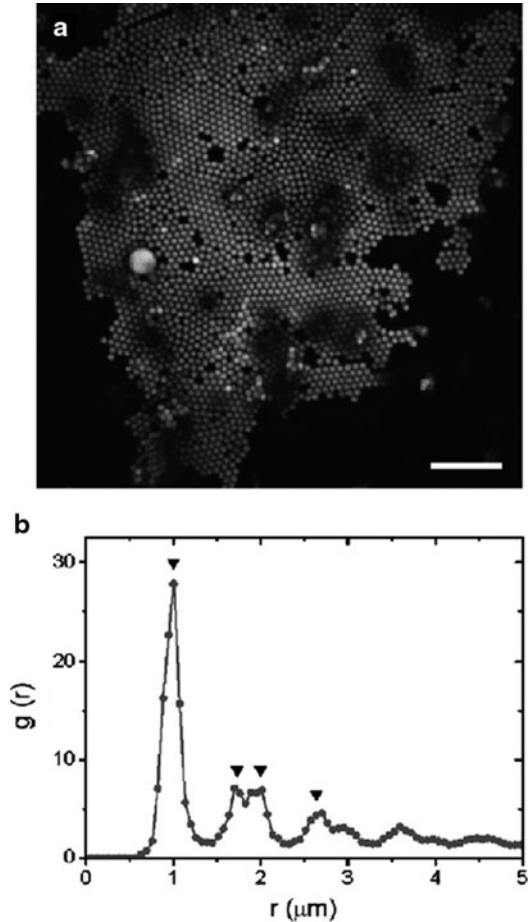


Fig. 38 Transmission electron micrographs of gold nanoparticles organized in 2D arrays through binding of two types of three-branched DNA motifs. (a) Array where only one tile contains 5 nm particles. The resulting arrangement has two different characteristic length scales. (b) Array where both tiles contain 5-nm particles, yielding an equally spaced pattern. (c) Array where one tile contains a 5-nm particle and the other tile contains a 10-nm particle. The pattern of alternating smaller and bigger spheres mimics the rhombic pattern of the tile array. Adapted with permission from [164]

The last system that we would like to mention in our non-exhaustive review is the so-called flying colloidal carpet [165], shown in (Fig. 39). Such a structure is obtained with micron-sized colloids coated with double-stranded λ -phage DNA. λ -DNA is quite long with a contour length of 16 μm . These colloids can bind to a rigid plane surface via hybridization of ssDNA on the particles to complementary ssDNA on the surface, with the long dsDNAs acting as spacers. A weak electrostatic attraction brings the colloids close to the surface and 2D crystals are formed that float several microns away from the surface itself. It is worth noting that if short dsDNA is used as spacer the resulting structure is amorphous rather than crystalline, stressing thereby the importance of the length of the dsDNA. Colloidal flying carpets could be used to make novel colloidal structures (Fig. 39).

Fig. 39 Aggregation of colloids coated with long DNA strands above a “sticky” surface leads to “flying carpets,” floating 2D crystals. **(a)** Confocal microscopy image of a flying carpet (*scale bar is 10 μm*). **(b)** Pair correlation function of the structure depicted in **(a)**. The observed peaks match those expected for a perfect hexagonal crystal (*black triangles*). Reproduced with permission from [165]

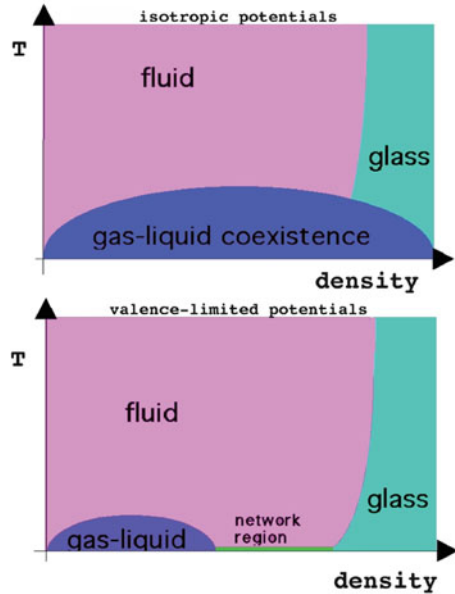


3.3 A New DNA-Mediated Phase: The Patchy Paradigm and the Empty Liquids

In most of the cases, one is interested in having a relatively high DNA coverage of the particle surface. However, very recently some interest arose as to whether DNA functionalization could be used to achieve a completely different aim: the realization of colloidal particles with a limited number of active spots, so to break the spherical symmetry of the interaction potential. Within this limit a strong directionality of the bonds is introduced, which mimics the chemical valence of molecules at much longer length-scales [166, 167].

Small valence systems exhibit a peculiar phase diagram when the valence is significantly smaller than 12, the average number of nearest neighbors in the liquid state of a hard sphere system. Reducing the valence makes it possible to obtain

Fig. 40 Schematic phase diagram of the disordered phases for particles interacting with isotropic potentials (*upper panel*) and limited valence potentials (*lower panel*). In the first, standard case, the glass line hits the gas–liquid spinodal at large densities. In the limited valence case, the shrunk gas–liquid coexistence region leaves a new region in which a stable network with saturated bonding can develop. Reproduced with permission from [167]



states where all the particle bonding possibilities are saturated without requiring large local densities. A simplified, schematic phase diagram for the traditional isotropic case and for a limited valence potential is shown in Fig. 40. It can be noted that the width of the gas–liquid coexistence curve shrinks on decreasing valence and disconnects from the glass line. This implies that, if crystallization can be avoided, it is possible to reach low temperature states in a homogeneous, equilibrium condition, without any phase separation (network region in the lower panel of Fig. 40). If this pathway is selected and the low temperature state is reached, the system undergoes a dynamical arrest at low density, which is caused by the formation of a network with long-lived bonds and not by packing as in glasses. In contrast with the arrested phase-separation mechanism outlined in [168], small valence colloidal systems allow for a continuous equilibrium dynamic arrest, which may produce an ideal gel [167].

As of today, the experimental realization of an intelligently designed patchy particle is still missing and the only proof of the existence of an empty liquid and of an equilibrium gel has been just recently provided in [169], which relies on the uncontrollable, native patchiness of a Laponite disk. Quite curiously, one of the first systems proposed and studied by theoreticians for the realization of this new arrested state of matter is a collection of micron sized particles where the limited valence is obtained by grafting a reduced number of single strands of DNA on the particle surface [170–173]. To our knowledge this system has not yet been realized even though the progresses in the realization of DNA-coated colloids suggest that the wait will probably be not too long.

4 Conclusions

The detailed knowledge of the properties of DNA and the accessibility to its synthesis have opened a whole new area of investigation. The wide variety of structures described in this chapter witnesses the relevance that DNA-based structures are acquiring in various fields of materials science. Indeed, the control of the interactions between DNA strands and double helices has enabled the accurate design of nanostructures and the tuning of their mutual interaction, yielding all the basic forms of condensed matter: liquid crystals, gels, and crystals of various dimensionality. A remarkable feature of these DNA-based materials is that they are obtained through hierarchical stages of self-assembly, with a fine control on the geometrical properties, on the valence, and on the strength of the interactions within and between building blocks.

The rich variety of DNA structures shown in this review chapter is the result of the combination of knowledge developed in more than one area of research: biochemistry, soft matter, statistical physics, and crystallography. We believe that this constant exchange of ideas and methods among different disciplines is a key requisite for maintaining in future years the same rate of scientific discovery and of development of novel technological strategies at the nanoscale.

Acknowledgments We acknowledge useful discussions with A.S. Benight, N.A. Clark, and F. Sciortino. We thank S. Biffi for critical reading of the manuscript and all the colleagues who gave their permission to reproduce copyrighted material.

References

1. Calladine CR, Drew H, Luisi B, Travers A (2004) *Understanding DNA: the molecule and how it works*. Academic, New York
2. Podgornik R, Strey HH, Parsegian VA (1998) *Curr Opin Colloid Interface Sci* 3:534–539
3. SantaLucia J, Hicks D (2004) *Annu Rev Biophys Biomol Struct* 33:415–440
4. Breslauer KJ (1986) *Proc Natl Acad Sci USA* 83:3746–3750
5. Sugimoto N, Nakano S, Yoneyama M, Honda K (1996) *Nucleic Acids Res* 24:4501–4505
6. Manyanga F, Horne MT, Brewood GP et al (2009) *J Phys Chem B* 113:2556–2563
7. Owczarzy R (2005) *Biophys Chem* 117:207–215
8. You Y, Moreira BG, Behlke MA et al (2006) *Nucleic Acids Res* 34:e60
9. Yakovchuk P, Protozanova E, Frank-Kamenetskii MD (2006) *Nucleic Acids Res* 34:564–574
10. Guckian KM, Schweitzer BA, Ren RX-F et al (2000) *J Am Chem Soc* 122:2213–2222
11. Chandler D (2005) *Nature* 437:640–647
12. Ball P (2008) *Chem Rev* 108:74–108
13. Ashbaugh HS (2009) *Chem Phys Lett* 477:109–111
14. Tombolato F, Ferrarini A (2005) *J Chem Phys* 122:54908
15. Owczarzy R, You Y, Moreira BG et al (2004) *Biochemistry* 43:3537–3554
16. SantaLucia J (1998) *Proc Natl Acad Sci USA* 95:1460–1465
17. Marenduzzo D, Orlandini E, Stasiak A et al (2009) *Proc Natl Acad Sci USA* 106:22269–22274

18. Kornyshev AA (2010) *Phys Chem Chem Phys* 12:12352–12378
19. Kornyshev A, Lee D, Leikin S et al (2007) *Rev Mod Phys* 79:943–996
20. Caruthers MH (1985) *Science* 230:281–285
21. Luzzati V, Nicolaieff A (1959) *J Mol Biol* 1:127–133
22. Robinson C (1961) *Tetrahedron* 13:219–234
23. Bouligand Y (1972) *Tissue Cell* 4:189–217
24. Livolant F (1991) *Physica A* 176:117–137
25. Chow MH, Yan KTH, Bennett MJ et al (2010) *Eukaryot Cell* 9:1577–1587
26. Minsky A, Shimoni E, Frenkiel-Krispin D (2002) *Nat Rev Mol Cell Biol* 3:50–60
27. Livolant F, Leforestier A (1996) *Prog Polym Sci* 21:1115–1164
28. Strzelecka T, Davidson MW, Rill RL (1988) *Nature* 331:457–460
29. Livolant F, Levelut AM, Doucet J et al (1989) *Nature* 339:724–726
30. Zanchetta G, Cerbino R (2010) *J Phys Condens Matter* 22:323102
31. Strey H, Wang J, Podgornik R et al (2000) *Phys Rev Lett* 84:3105–3108
32. Tinland B, Pluen A, Sturm J et al (1997) *Macromolecules* 30:5763–5765
33. Lu Y, Weers B, Stellwagen NC (2002) *Biopolymers* 61:261–275
34. Onsager L (1949) *Ann NY Acad Sci* 51:627–659
35. Merchant K, Rill RL (1997) *Biophys J* 73:3154–3163
36. Nakata M, Zanchetta G, Chapman BD et al (2007) *Science* 318:1276–1279
37. Bolhuis P, Frenkel D (1997) *J Chem Phys* 106:666
38. Selinger JV, Bruinsma RF (1991) *Phys Rev A* 43:2922–2931
39. Bohle AM, Holyst R, Vilgis T (1996) *Phys Rev Lett* 76:1396–1399
40. Piskur J, Rupprecht A (1995) *FEBS Lett* 375:174–178
41. Pelta JJ, Durand D, Doucet J et al (1996) *Biophys J* 71:48–63
42. Hud NV, Downing KH (2001) *Proc Natl Acad Sci USA* 98:14925–14930
43. Kuriabova T, Betterton MD, Glaser MA (2010) *J Mater Chem* 20:10366
44. Redinbo MR, Stewart L, Kuhn P et al (1998) *Science* 279:1504–1513
45. Davey CA, Sargent DF, Luger K et al (2002) *J Mol Biol* 319:1097–1113
46. Li L, Pabit SA, Lamb JS et al (2008) *Appl Phys Lett* 92:223901–2239013
47. Wing R, Drew H, Takano T et al (1980) *Nature* 287:755–758
48. Campos L, Valls N, Urpí L et al (2006) *Biophys J* 91:892–903
49. Davis JT, Spada GP (2007) *Chem Soc Rev* 36:296–313
50. Zanchetta G, Nakata M, Buscaglia M et al (2008) *J Phys Condens Matter* 20:494214
51. Sarkar T, Conwell CC, Harvey LC et al (2005) *Nucleic Acids Res* 33:143–151
52. Collings PJ, Dickinson AJ, Smith EC (2010) *Liq Cryst* 37:701–710
53. Zanchetta G, Nakata M, Buscaglia M et al (2008) *Proc Natl Acad Sci USA* 105:1111–1117
54. Zanchetta G, Giavazzi F, Nakata M et al (2010) *Proc Natl Acad Sci USA* 107:17497–17502
55. Stanley CB, Hong H, Strey HH (2005) *Biophys J* 89:2552–2557
56. Van Winkle DH, Davidson MW, Chen WX et al (1990) *Macromolecules* 23:4140–4148
57. Cherstvy AG (2008) *J Phys Chem B* 112:12585–12595
58. Proni G, Gottarelli G, Mariani P et al (2000) *Chem Eur J* 6:3249–3253
59. Goodman RP, Schaap IAT, Tardin CF et al (2005) *Science* 310:1661–1665
60. Seeman NC (2003) *Nature* 421:427–431
61. Chen JH, Seeman NC (1991) *Nature* 350:631–633
62. Douglas SM, Dietz H, Liedl T et al (2009) *Nature* 459:414–418
63. Shih WM, Quispe JD, Joyce GF (2004) *Nature* 427:618–621
64. Seeman NC (2010) *Annu Rev Biochem* 79:65–87
65. Wang Y, Mueller JE, Kemper B et al (1991) *Biochemistry* 30:5667–5674
66. Ma RI, Kallenbach NR, Sheardy RD et al (1986) *Nucleic Acids Res* 14:9745–9753
67. Fu TJ, Seeman NC (1993) *Biochemistry* 32:3211–3220
68. Sa-Ardyen P, Vologodskii AV, Seeman NC (2003) *Biophys J* 84:3829–3837
69. Chelyapov N, Brun Y, Gopalkrishnan M et al (2004) *J Am Chem Soc* 126:13924–13925
70. Liu D, Wang M, Deng Z et al (2004) *J Am Chem Soc* 126:2324–2325

71. Ding B, Sha R, Seeman NC (2004) *J Am Chem Soc* 126:10230–10231
72. He Y, Chen Y, Liu H et al (2005) *J Am Chem Soc* 127:12202–12203
73. Yan H, Park SH, Finkelstein G et al (2003) *Science* 301:1882–1884
74. Mathieu F, Liao S, Kopatsch J et al (2005) *Nano Lett* 5:661–665
75. Winfree E, Liu F, Wenzler LA et al (1998) *Nature* 394:539–544
76. Reishus D, Shaw B, Brun Y et al (2005) *J Am Chem Soc* 127:17590–17591
77. LaBean TH, Yan H, Kopatsch J et al (2000) *J Am Chem Soc* 122:1848–1860
78. Schulman R, Winfree E (2007) *Proc Natl Acad Sci USA* 104:15236–15241
79. Yan H, LaBean TH, Feng L et al (2003) *Proc Natl Acad Sci USA* 100:8103–8108
80. Paukstelis PJ, Nowakowski J, Birktoft JJ et al (2004) *Chem Biol* 11:1119–1126
81. Paukstelis PJ (2006) *J Am Chem Soc* 128:6794–6795
82. Zheng J, Birktoft JJ, Chen Y et al (2009) *Nature* 461:74–77
83. Nangreave J, Han D, Liu Y et al (2010) *Curr Opin Chem Biol* 14:608–615
84. Rothmund PWK (2006) *Nature* 440:297–302
85. Ke Y, Lindsay S, Chang Y et al (2008) *Science* 319:180–183
86. Kuzyk A, Laitinen KT, Törmä P (2009) *Nanotechnology* 20:235305
87. Rinker S, Ke Y, Liu Y et al (2008) *Nat Nanotech* 3:418–422
88. Kuzuya A, Kimura M, Numajiri K et al (2009) *ChemBioChem* 10:1811–1815
89. Voigt NV, Tørring T, Rotaru A et al (2010) *Nat Nanotech* 5:200–203
90. Stephanopoulos N, Liu M, Tong GJ et al (2010) *Nano Lett* 10:2714–2720
91. Maune HT, Han S-P, Barish RD et al (2010) *Nat Nanotech* 5:61–66
92. Ding B, Deng Z, Yan H et al (2010) *J Am Chem Soc* 132:3248–3249
93. Pal S, Deng Z, Ding B et al (2010) *Angew Chem Int Ed* 49:2700–2704
94. Ke Y, Douglas SM, Liu M et al (2009) *J Am Chem Soc* 131:15903–15908
95. Andersen ES, Dong M, Nielsen MM et al (2009) *Nature* 459:73–76
96. Kuzuya A, Komiyama M (2009) *Chem Commun* 4182–4184
97. Bui H, Onodera C, Kidwell C et al (2010) *Nano Lett* 10:3367–3372
98. Lo PK, Altvater F, Sleiman HF (2010) *J Am Chem Soc* 132:10212–10214
99. Ko S, Liu H, Chen Y et al (2008) *Biomacromolecules* 9:3039–3043
100. Yang X, Wenzler LA, Qi J et al (1998) *J Am Chem Soc* 120:9779–9786
101. Liu D, Park SH, Reif JH et al (2004) *Proc Natl Acad Sci USA* 101:717–722
102. Rothmund PWK, Ekani-Nkodo A, Papadakis N et al (2004) *J Am Chem Soc* 126:16344–16352
103. Park SH, Barish R, Li H et al (2005) *Nano Lett* 5:693–696
104. Ke Y, Liu Y, Zhang J et al (2006) *J Am Chem Soc* 128:4414–4421
105. Liu H, Chen Y, He Y et al (2006) *Angew Chem Int Ed* 45:1942–1945
106. Yin P, Hariadi RF, Sahu S et al (2008) *Science* 321:824–826
107. Aldaye FA, Lo PK, Karam P et al (2009) *Nat Nanotech* 4:349–352
108. Mitchell JC, Harris JR, Malo J et al (2004) *J Am Chem Soc* 126:16342–16343
109. Dietz H, Douglas SM, Shih WM (2009) *Science* 325:725–730
110. Topuz F, Okay O (2008) *Macromolecules* 41:8847–8854
111. Amiya T, Tanaka T (1987) *Macromolecules* 20:1162–1164
112. Horkay F, Basser PJ (2004) *Biomacromolecules* 5:232–237
113. Horkay F, Basser PJ, Hecht A-M et al (2007) *Macromol Symp* 256:80–87
114. Mayama H, Nakai T, Takushi E et al (2007) *J Chem Phys* 127:034901
115. Costa D, Hansson P, Schneider S et al (2006) *Biomacromolecules* 7:1090–1095
116. Costa D, Miguel MG, Lindman B (2007) *J Phys Chem B* 111:10886–10896
117. Topuz F, Okay O (2009) *Biomacromolecules* 10:2652–2661
118. Costa D, Miguel MG, Lindman B (2010) *Adv Colloid Interface Sci* 158:21–31
119. Nagahara S, Matsuda T (1996) *Polym Gels Netw* 4:111–127
120. Lin DC, Yurke B, Langrana NA (2004) *J Biomech Eng* 126:104
121. Lin DC, Yurke B, Langrana NA (2005) *J Mater Res* 20:1456–1464
122. Liedl T, Dietz H, Yurke B et al (2007) *Small* 3:1688–1693

123. Um SH, Lee JB, Park N et al (2006) *Nat Mater* 5:797–801
124. LaBean T (2006) *Nat Mater* 5:767–768
125. Mirkin CA, Letsinger RL, Mucic RC et al (1996) *Nature* 382:607–609
126. Alivisatos AP, Johnsson KP, Peng X et al (1996) *Nature* 382:609–611
127. Jin R, Wu G, Li Z et al (2003) *J Am Chem Soc* 125:1643–1654
128. Grabarek Z, Gergely J (1990) *Anal Biochem* 185:131–135
129. Brinkley M (1992) *Bioconjug Chem* 3:2–13
130. Nakajima N, Ikada Y (1995) *Bioconjug Chem* 6:123–130
131. Tobiesen FA, Michielsen S (2002) *J Polym Sci Part A: Polym Chem* 40:719–728
132. Huang SC, Stump MD, Weiss R et al (1996) *Anal Biochem* 237:115–122
133. Leckband DE, Schmitt FJ, Israelachvili JN et al (1994) *Biochemistry* 33:4611–4624
134. Kim AJ, Manoharan VN, Crocker JC (2005) *J Am Chem Soc* 127:1592–1593
135. Rogers PH, Michel E, Bauer CA et al (2005) *Langmuir* 21:5562–5569
136. Dreyfus R, Leunissen M, Sha R et al (2009) *Phys Rev Lett* 102:048301
137. Dreyfus R, Leunissen ME, Sha R et al (2010) *Phys Rev E* 81:041404
138. Valignat M-P, Theodoly O, Crocker JC et al (2005) *Proc Natl Acad Sci USA* 102:4225–4229
139. Lytton-Jean AKR, Mirkin CA (2005) *J Am Chem Soc* 127:12754–12755
140. Leunissen ME, Dreyfus R, Cheong FC et al (2009) *Nat Mater* 8:590–595
141. Nykypanchuk D, Maye MM, van der Lelie D et al (2008) *Nature* 451:549–552
142. Park SY, Lytton-Jean AKR, Lee B et al (2008) *Nature* 451:553–556
143. Kim J-Y, Lee J-S (2009) *Nano Lett* 9:4564–4569
144. Niemeyer CM, Simon U (2005) *Eur J Inorg Chem* 2005:3641–3655
145. Geerts N, Eiser E (2010) *Soft Matter* 6:4647
146. Grzelczak M, Vermant J, Furst EM et al (2010) *ACS Nano* 4:3591–3605
147. Redl FX, Cho K-S, Murray CB et al (2003) *Nature* 423:968–971
148. Linden S, Enkrich C, Wegener M et al (2004) *Science* 306:1351–1353
149. Urban JJ, Talapin DV, Shevchenko EV et al (2007) *Nat Mater* 6:115–121
150. Lee J, Hernandez P, Lee J et al (2007) *Nat Mater* 6:291–295
151. Xiong H, van der Lelie D, Gang O (2009) *Phys Rev Lett* 102:015504
152. Jones MR, Macfarlane RJ, Lee B et al (2010) *Nat Mater* 9:913–917
153. Biancaniello P, Kim A, Crocker J (2005) *Phys Rev Lett* 94:058302
154. Kim AJ, Biancaniello PL, Crocker JC (2006) *Langmuir* 22:1991–2001
155. Kim AJ, Scarlett R, Biancaniello PL et al (2009) *Nat Mater* 8:52–55
156. Leunissen ME, Dreyfus R, Sha R et al (2009) *Soft Matter* 5:2422
157. Leunissen ME, Dreyfus R, Sha R et al (2010) *J Am Chem Soc* 132:1903–1913
158. Warner MG, Hutchison JE (2003) *Nat Mater* 2:272–277
159. Niemeyer CM, Ceyhan B, Noyong M et al (2003) *Biochem Biophys Res Commun* 311:995–999
160. Pinto YY, Le JD, Seeman NC et al (2005) *Nano Lett* 5:2399–2402
161. Noyong M, Ceyhan B, Niemeyer CM et al (2006) *Colloid Polym Sci* 284:1265–1273
162. Shyr MHS, Wernette DP, Wiltzius P et al (2008) *J Am Chem Soc* 130:8234–8240
163. Sharma J, Chhabra R, Andersen CS et al (2008) *J Am Chem Soc* 130:7820–7821
164. Zheng J, Constantinou PE, Micheel C et al (2006) *Nano Lett* 6:1502–1504
165. Geerts N, Eiser E (2009) *Soft Matter* 6:664–669
166. Bianchi E, Largo J, Tartaglia P et al (2006) *Phys Rev Lett* 97:168301
167. Sciortino F (2008) *Eur Phys J B* 64:505–509
168. Lu PJ, Zaccarelli E, Ciulla F et al (2008) *Nature* 453:499–503
169. Ruzicka B, Zaccarelli E, Zulian L et al (2011) *Nat Mater* 10:566–569
170. Starr FW, Sciortino F (2006) *J Phys Condens Matter* 18:L347–L353
171. Largo J, Starr FW, Sciortino F (2007) *Langmuir* 23:5896–5905
172. Hsu C, Sciortino F, Starr F (2010) *Phys Rev Lett* 105:055502
173. Dai W, Hsu CW, Sciortino F et al (2010) *Langmuir* 26:3601–3608
174. Motomura K., Hidemi I., Ikeda N., Aratono M. (1988) *J. Coll. Interface Sci.* 126: 26–36

Polar and Apolar Columnar Phases Made of Bent-Core Mesogens

N. Vaupotič, D. Pociecha, and E. Gorecka

Abstract Structural studies of two-dimensionally ordered phases made of bent-core mesogens are presented, with the emphasis on the X-ray studies of the columnar phases built of smectic layer fragments. We present the evidence for two types of packing of layer fragments: the B1-type structures where the layers are broken into blocks arranged into the orthogonal body centered lattice and the B1rev-type structures made of slightly deformed layers, where the primitive crystallographic unit cell is in general oblique. In some cases two-dimensional structures made of bilayers are observed. Bilayers are characteristic for the general tilt phases, which possess a longitudinal polarization component, in the direction perpendicular to the smectic layer fragment. We also outline the theoretical model predicting and describing the observed structures and present a model which enables the calculation of the electron density maps from the X-ray diffraction data.

Keywords Liquid crystals · Bent-core mesogens · Polar properties · X-ray structure studies

N. Vaupotič

Faculty of Natural Sciences and Mathematics, Institute of Physics, University of Maribor, Koroška
160, 2000 Maribor, Slovenia

Jozef Stefan Institute, Jamova 39, 1000 Ljubljana, Slovenia

D. Pociecha and E. Gorecka (✉)

Department of Chemistry, University of Warsaw, Al. Zwirki i Wigury 101, 02-089 Warsaw,
Poland

e-mail: gorecka@chem.uw.edu.pl

Contents

1	Introduction	282
2	Structural Studies of 2D Phases	284
3	Theoretical Considerations	293
3.1	Modeling the Layer and Director Structure in 2D Phases	293
3.2	Modeling of the Electron Density Distribution	297
4	Conclusions	299
	References	300

1 Introduction

Among complex mesogenic molecules there are multiple intermolecular interactions. One would expect that such interactions should lead to unusual, complex phase structures and properties of the system. In reality it is often the opposite: even molecules combining several very different chemical units can form simple layered (smectic) or columnar phases. Regarding this, compounds made of bent-core molecules are really exceptional. A rather simple modification of the mesogenic core, that is bending it by approximately 120° , made a huge impact on the structure of the liquid crystalline phases formed. Due to the nonlinear shape, these molecules experience an anisotropic potential for rotation around the long molecular axis. When the energy barrier is comparable to kT the rotation becomes hindered. As a result the transverse dipole moments correlate their directions and smectic layers became electrically polarized (Fig. 1). Bent-core molecules are the first group of non-chiral mesogens for which polar properties were reported [1]. Until their discovery the ferroelectric and antiferroelectric properties were inherent to the smectic or columnar phases made of chiral molecules (see for example [2]). In rod-like liquid crystals the polar order is the secondary order parameter which occurs only in the tilted smectic phases where the symmetry of the phase is sufficiently low to allow for the existence of polarization; moreover, ferroelectric order is obtained only for the synclinic arrangement of molecules in the consecutive

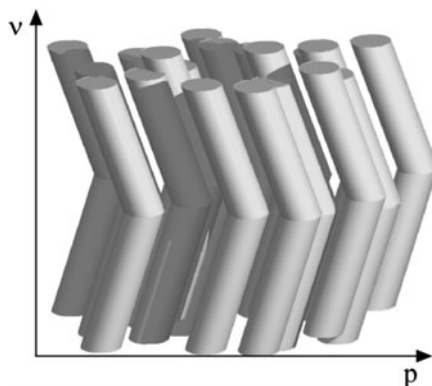


Fig. 1 Due to their strongly bent shape and the excluded volume effects bent-core molecules tend to form polar layers. \mathbf{v} is the layer normal and \mathbf{p} the electric polarization

layers, while antiferroelectric phase has to be antclinic. In contrast, for the bent-core materials, the polar and the tilt orders are decoupled and ferroelectric properties can appear for non-tilted as well as tilted smectics. Moreover, tilt-polarization decoupling allows for the ferroelectric antclinic and antiferroelectric synclinic phases, never observed in the rod-like systems.

The bent-core mesogens are also unusual because of their ability to form a variety of two-dimensional (2D) density modulated structures. Such phases are only rarely encountered if the building blocks are rod-like molecules, as the formation of 2D structures requires special molecular architecture. So far two groups of rod-like molecules exhibiting 2D structures have been identified: molecules having a strong longitudinal dipole moment [3] and molecules having multiple terminal chains (polycatenars) [4].

Molecules having strong longitudinal dipole moments are able to form dimers. Since the dimer length is slightly different than twice the single molecular length the frustration occurs in the smectic phase that is relieved by a periodic variation of the dipole moment direction inside the smectic layer [5]. This leads to the periodic density modulation inside the layer and results in a 2D structure (Fig. 2). Such modulated phases were given the common name “*smectic antiphases*.”

Polycatenars form a “broken-layer” type 2D density modulated phases because of the mismatch between the cross-section areas required for the terminal chains and for the mesogenic core. For such compounds layers become locally bent to provide more space for tails and, since the bending of layers is finite, this leads to

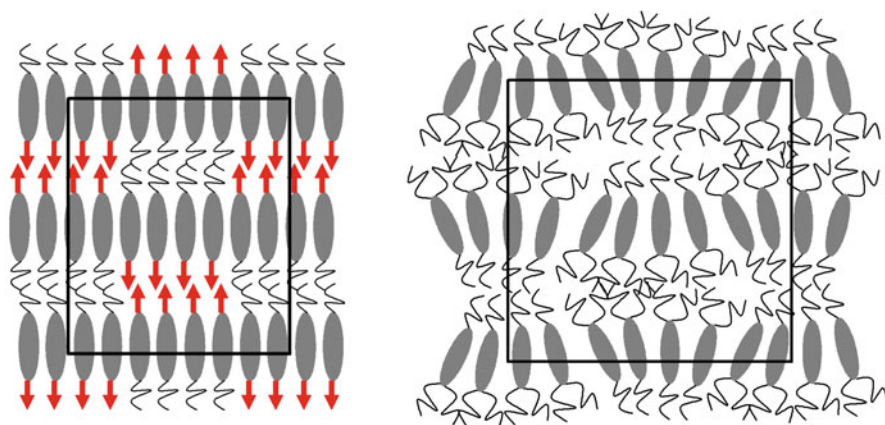


Fig. 2 *Left:* The basic 2D structure in the rod-like liquid crystals made by strongly polar molecules (the dipole moment directions are represented by *arrows*). The asymmetric rod-like molecules tend to form double layer structures in order to compensate dipole moments. Since the thickness of a double layer is smaller than twice the thickness of a single layer the resulting stress in the system is relieved by the in-layer modulation. *Right:* 2D structures in polycatenar rod-like liquid crystals. The ribbon like structure is formed by the asymmetric polycatenar molecules. To accommodate the additional alkyl chains layers become slightly bent. Both structures possess the body centered crystallographic unit cell

the formation of blocks that are arranged into a body centered lattice in order to fill the space efficiently (Fig. 2).

It seems that, in contrast to the rod-like molecules, in the case of the bent-core molecules there are no special molecular prerequisites for the formation of 2D structures; they are frequent and found for symmetric as well as asymmetric molecules, for molecules with strong and weak dipole moments – multiple terminal chains are also not required (see for example [6]).

In the following sections we shall focus on the structure and properties of the two-dimensional phases formed by the bent-core liquid crystals. In Sect. 2 we describe the structure studies by the X-ray diffraction (XRD) method, optical studies, and the response of different structures to the external electric field. In Sect. 3 we give theoretical models of the director and layer structure in 2D modulated phases and discuss how to reconstruct electron density maps from XRD data.

2 Structural Studies of 2D Phases

XRD is a fundamental method to obtain information on the electron density distribution of a phase [7]. Positions of XRD signals reflect the size and shape of the crystallographic unit cell, while the signal intensities give information on the electron density within the crystallographic unit cell. If the electron density distribution is known, the XRD pattern can be unambiguously obtained by the Fourier transform of the density function. However, the reverse procedure, i.e., the reconstruction of electron density distribution from XRD data is not straightforward, as the Fourier components are generally complex numbers, for which only modulus but not phase can be determined from the XRD experiment. In Sect. 3 we will describe how the phase problem can be overcome and the electron density reconstructed from XRD measurements. In the following paragraphs we focus only on the results of XRD measurements and description of possible 2D structures.

In general, 2D density modulated structures of bent-core molecules can be viewed as built of fragments of smectic layers (blocks). Two types of XRD patterns were found for such phases (Fig. 3). Both show a diffused high angle signal signifying the liquid like order within the smectic blocks. The main difference between them is the appearance or lack of the signal related to the size of the block along the layer fragment. This suggests that the phases have considerably different block boundaries. The appearance of the signal related to the width of the block shows that blocks are connected by the area where the electron density differs from the density inside the block (Fig. 3b). In the literature this type of phase is often referred to as the B1rev-type [8]. The lack of signal related to the width of the blocks shows that the average density along the direction of the block is not modulated, which means that blocks are attached to each other and the block boundary is created by a lateral shift of identical blocks (Fig. 3a). This type of phase is often referred to as the B1-type [9]. Materials showing the B1 and B1rev

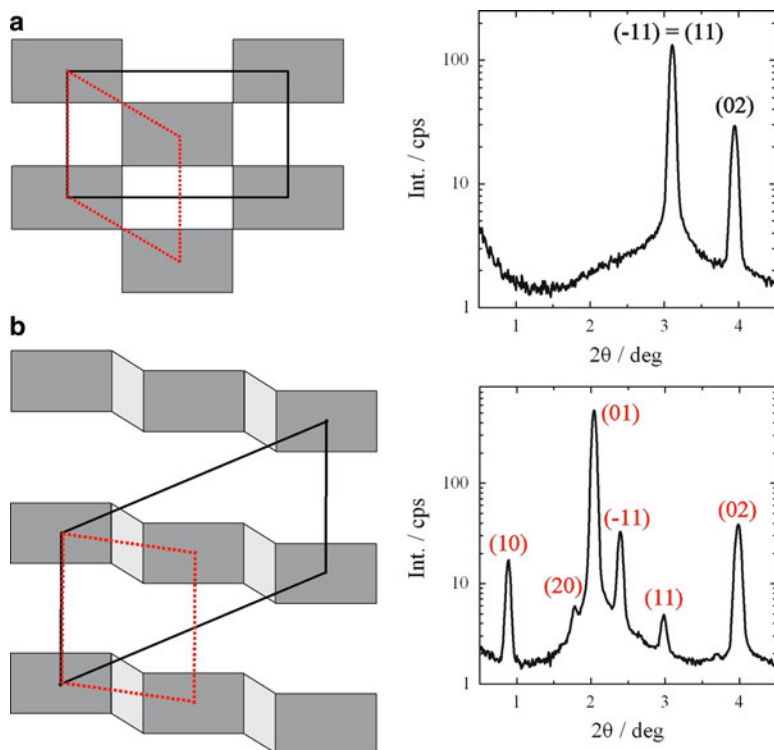


Fig. 3 *Left*: Schematic models of 2D modulated structures; *dark regions* are filled with the aromatic parts of molecules. The possible choices of the primitive (*dotted red*) and the body centered (*solid black*) crystallographic unit cells are shown for both phases. *Right*: The corresponding XRD patterns. (a) B1-type phase: the layer fragments are only displaced and there are no connecting regions of different density. XRD signals are indexed assuming the body centered unit cell. (b) B1rev-type phase: layer fragments are connected by defects in which the electron density is lower than in the blocks. XRD Miller indices are given assuming the primitive unit cell. Note that the position of the main, most intensive signal in the X-ray pattern of the B1 and B1rev phase is much different despite the similar sizes of the blocks

phases are not miscible in the temperature range where the modulated phases are observed.

The X-ray pattern of the B1-type phase is simple (Fig. 3a). It usually shows only two low angle signals, one of them corresponding to half the layer thickness, which suggests that blocks are arranged into a body centered lattice. It is quite striking that for this phase the body centered cell is always orthogonal. The X-ray pattern of the B1rev-type is richer; it consists of several signals, the most intensive one being related to the layer thickness. In systems in which the B1rev phase appears below or above the lamellar phase, the main signal intensity and its position are only slightly affected by the phase transition [10, 11]. In addition, from the orientation of signals in the X-ray pattern it can be deduced that neither the average layer normal nor the orientation of the long molecular axis changes significantly at the transition point.

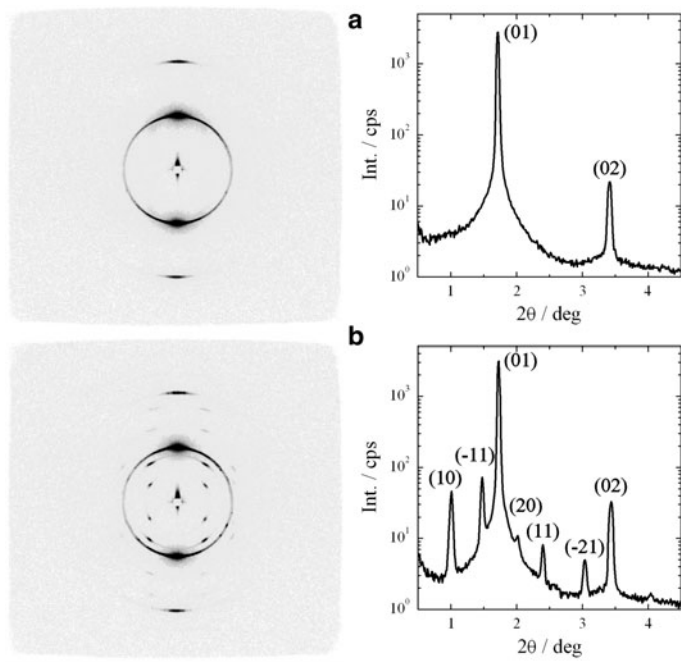


Fig. 4 Changes in the low angle XRD pattern when the 2D phase is formed below the lamellar structure. XRD of the (a) lamellar and (b) B1rev structure and the corresponding intensities vs 2θ , obtained by the integration of the 2D pattern over the azimuthal angle. The Miller indices of signals for the B1rev phase are given assuming the primitive cell. Note that the position of the main, most intensive signal is not affected by the phase transition

The transition from the lamellar to the 2D density modulated structure is signified only by a sudden appearance of a few additional, weak signals related to the in-plane density modulations (Fig. 4). Thus one can conclude that the 2D structure is made of weakly deformed layers in which defects appear due to a small displacement of molecules. The primitive unit cell describing the structure of such deformed layers can be rectangular or oblique depending on how the defects are arranged in the consecutive layers. For most of the materials the oblique unit cell is observed, signified by the splitting of the (hk) and $(-hk)$ signals (Fig. 4). In rare cases when the defects are positioned exactly one above another, the inclination angle of the cell locks to 90° (Fig. 5).

While the positions of XRD signals give unambiguous information about the crystallographic lattice, the intensities of the signals can also provide information about the size, shape, and inclination of the molecular blocks filling the crystallographic unit cell. While it seems that in the B1 phase the smectic layer fragments (blocks) are oriented along the body centered crystallographic unit sides, from the information acquired by analyzing the signal intensities one can conclude that in the B1rev phase the blocks are oriented at an arbitrary angle with respect to the

Fig. 5 The typical XRD pattern for the structure with the orthogonal primitive unit cell is characterized by the perpendicular mutual positions of the (10) and (01) signals

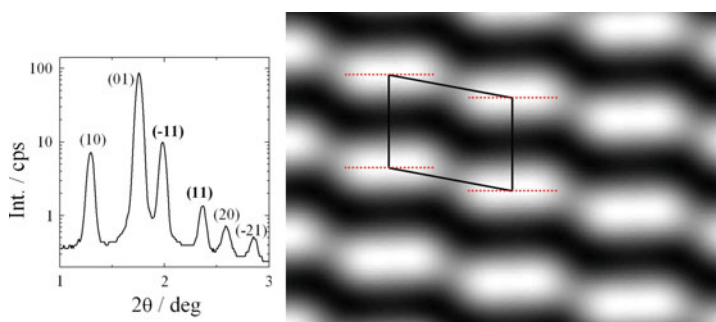
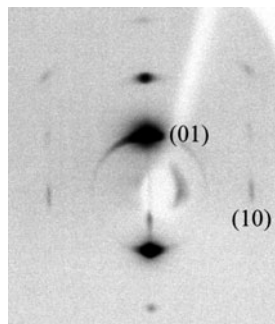


Fig. 6 In the case of the oblique unit cell the intensity of the (-11) signal in the XRD pattern is usually higher than the intensity of the (11) signal (*left*). This indicates that the layer fragments in the crystallographic unit cell are inclined toward the shorter diagonal [the crystallographic plane (-11)] of the primitive unit cell (*right*). The electron density map was reconstructed from the X-ray data (see Sect. 3); *bright regions* are filled by the aromatic parts of molecules while the *dark regions* are filled by the alkyl chains. *Dotted lines* show midplanes of the blocks

crystallographic unit cell (Fig. 6). Because the blocks are tilted the whole structure can be viewed as smectic layer “stairs.” In the oblique primitive unit cell (defined by $\gamma > 90^\circ$) it is quite common that the inclination of blocks is toward the shorter diagonal of the cell. The inclination of blocks is mainly defined by the ratio between the (11) and (-11) signal intensities, and the intensity of the (-11) signal is usually considerably higher than the intensity of the (11) signal (Fig. 6).

It should be stressed that the crystallographic unit cell angle is not directly related to the inclination of molecular long axis inside the layer fragments. There are known examples of the B1rev phase with an orthogonal crystallographic unit cell in which molecules are tilted inside the blocks [12] as well as the oblique crystallographic unit cell made of layers in which molecules are not tilted [8]. The average local orientation of the molecules can be described by the average orientation of the long molecular axis (this we call the nematic director) and by the average orientation of the molecular tips (the polar director) – see Fig. 7. The angle θ by which the nematic director is tilted with respect to the local smectic layer normal

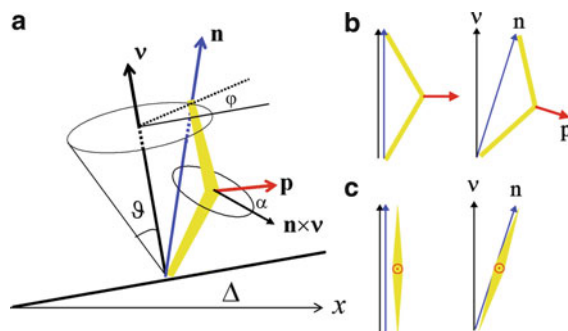


Fig. 7 (a) The average local orientation of molecules inside the layer fragment is described by the nematic director \mathbf{n} – average orientation of long molecular axes and the polar director \mathbf{p} – average direction of the molecular tips. θ is the angle between the layer normal \mathbf{v} , and the nematic director, α is the angle between the tilt plane and the polar director, and the azimuthal angle φ determines the position of the nematic director on the tilt cone, defined by the angle θ . Orientation of the smectic layer (departure from the planar layer alignment) is denoted by the angle Δ . The general orientation of molecules in the layer is obtained by combination of the leaning – rotation around axis perpendicular to polarization direction (b) and tilting – rotation around polarization direction (c)

(the tilt angle) can be obtained by optical measurements, as for smectic phases, by observing the texture of a sample placed between crossed polarizers. For samples exhibiting a fan texture with circular domains, the tilt can be deduced by determining the angle by which the extinction brushes are inclined from the polarizing directions. Alternatively, for well aligned samples the molecular tilt can be deduced from the angle by which the sample has to be rotated under crossed polarizers to obtain the light extinctions in the opposite tilt domains (Fig. 8).

For phases made of tilted molecules, measurements show that the inclination of the unit cell can be higher or smaller than the molecular tilt. This is not surprising since the crystallographic unit cell is defined by complex interactions between the deformed layers.

The B1 and B1rev phases also have different responses to the external electric field. In the ground state both phases are antiferroelectric. This is confirmed by the lack of the SHG activity [13] and a low dielectric response, as expected for the phase with compensated polarization. The B1 phase is usually not susceptible to the electric field; neither clear current peak nor optical changes are visible upon applying a square or triangular wavefunction voltage [14]. At sufficiently high field, transition to the lamellar smectic phase is sometimes observed [15]. On the other hand, the B1-rev phase in most cases gives a single current peak upon applying a triangular wave voltage due to the slow switching. The optical response to the electric field is usually complex; the switching can occur with or without changes of light extinction directions, depending on the material and on the experimental conditions, such as temperature, the frequency of the field, and the applied wavefunction [16, 17]. In the first case molecules rotate on the tilt cone in the layer fragments, in the latter rotation occurs around the long molecular axis without

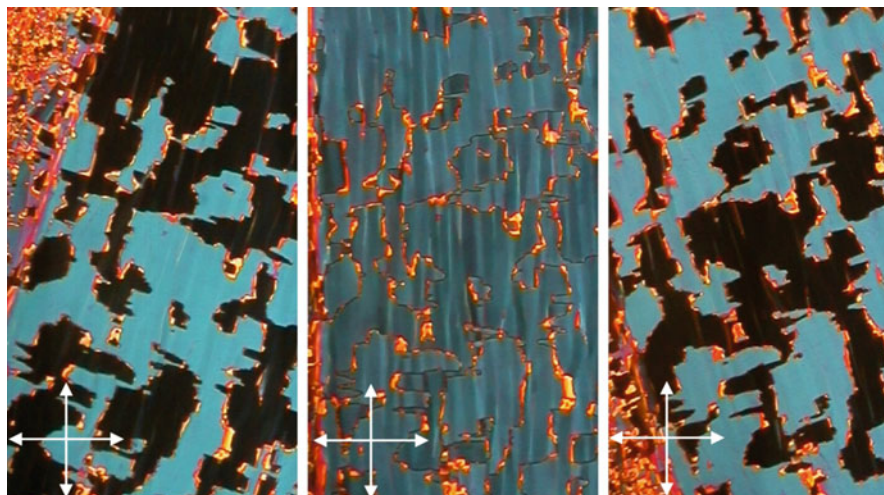


Fig. 8 Texture of the B1rev phase made of layer fragments in which molecules are tilted with respect to the local layer normal. In order to get light extinction in the domains with opposite tilt the sample has to be rotated against crossed polarizer and analyzer. The angle by which the sample is rotated shows the inclination of molecules from the local layer normal (for the material shown the tilt angle is approximately 19°)

changing the azimuthal position of molecules on the tilt cone, which is accompanied by only a small birefringence change. As will be explained in the theoretical section, the difference in the type of switching might be due to the width of blocks and thus constraints of molecular motions by defects. In some cases, as for the B1 phase, a sufficiently high electric field induces phase transition to the lamellar phase [18]. It is worth mentioning that dielectric response is also usually different for the B1 and the B1rev-type modulated phases. In the B1rev phase the dielectric response is typically stronger than in the B1 phase, although weaker than in the lamellar antiferroelectric smectic phase [19]. In the polar smectic phase the low frequency mode is attributed to the collective fluctuations of polar order. In the antiferroelectric phase, which is the most frequently observed tilted polar smectic phase made of bent-core molecules, the low frequency mode is related to thermal distortion of the antiparallel arrangement of dipole moments in the consecutive layers [20]. For systems in which defects appear in the layers it can be expected that such fluctuations are additionally suppressed by interactions with the block boundaries. As a result the amplitude of the dielectric response decreases and its relaxation frequency shifts to higher values compared to the lamellar antiferroelectric phase.

Summarizing the information from the optical, electrooptical, and dielectric measurements we can draw several structures which are consistent with the crystallographic data but differ in the tilt and polarization distribution (Fig. 9). There is no direct method which would enable one to determine unambiguously which structure is correct, and we are left with some freedom for speculation. It seems

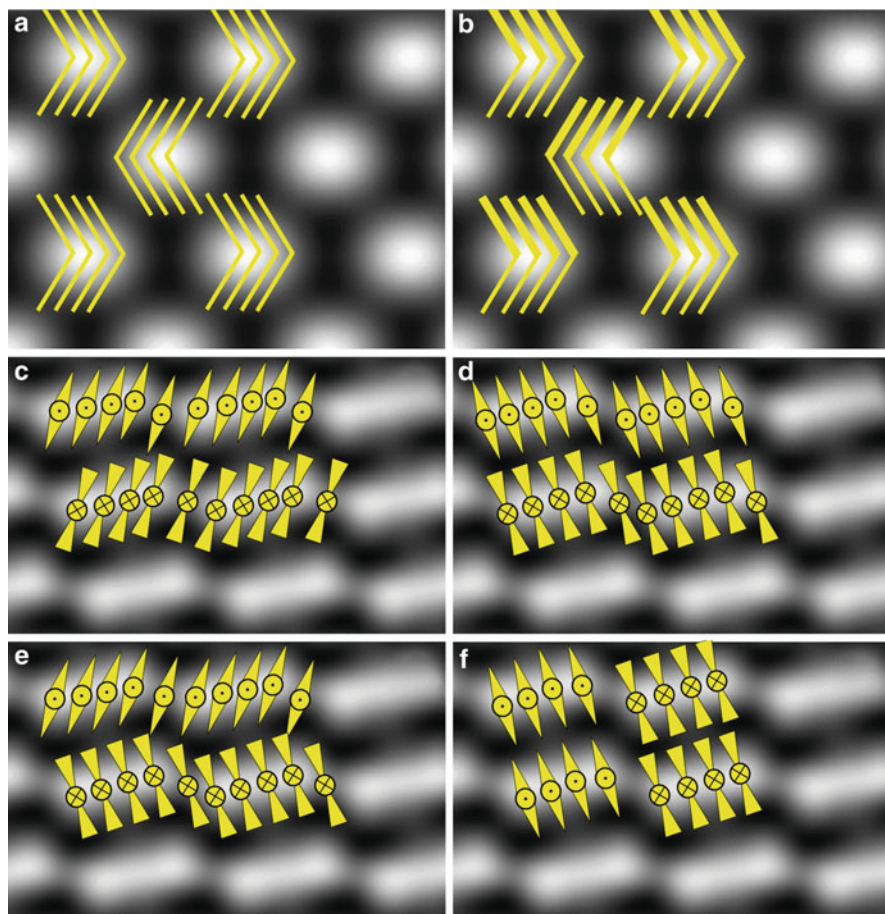


Fig. 9 Few possible combinations of tilt and polarization for B1 and B1rev phases. In B1 phase molecules are (a) not tilted or (b) tilted in the blocks. The tilt is denoted by one part of the molecule being thicker. This is a part that is tilted out of the paper plane. B1rev structures can be made of the deformed synclinic, antiferroelectric layers with the tilt in the defect region connecting the blocks (c) lower or (d) higher than in the block itself or from (e) the anticlinic antiferroelectric deformed layers or from (f) the synclinic layers where polarization alternates in the neighboring blocks of the same layer

that the orthogonal body centered cell of the B1 phase is filled by layer fragments with the polarization vectors being in the plane of the 2D density modulation, in which molecules can be tilted or not (Fig. 9a, b). Such a structure is consistent with the low susceptibility of the phase to the electric field, as the switching would require significant rebuilding of the structure by either changing the block boundaries and/or inducing the state with the polarization vectors perpendicular to the modulation plane; both changes would be energetically costly for such a system. In the B1rev phase we assume that polarization vectors are perpendicular to

the density modulation plane. The X-ray studies clearly show that the B1rev phase is built from layer fragments (blocks) connected by defect regions. In systems made of only weakly deformed layers it is expected that the layer fragments connected by defects are of the same polarity (Fig. 9c–e). Upon going through the defect region the tilt of the molecules can be larger (Fig. 9d) or smaller (Fig. 9c) than in the block itself. As will be explained in the theoretical section (Sect. 3), the second possibility is energetically more favorable for the system. Moreover, it seems that the B1rev phase should have a synclinic structure of the deformed layers, as the anticlinic structure (Fig. 9e) would require alternation of higher or lower tilt in the defect regions of the neighboring layers. If the neighboring blocks are strongly vertically shifted with respect to each other, the opposite polarity of blocks should be considered (Fig. 9f) [21].

So far we have discussed 2D density modulated phases that are formed by deformation or breaking of the layers. However, there are also 2D phases with more subtle electron density modulations. In some cases additional peaks observed in the XRD pattern (Fig. 10) are related to a double layer periodicity in the structure. As double layer periodicity was observed in the bent-core liquid crystals formed by the asymmetric as well as symmetric molecules [22–25] it should be assumed that the mechanism leading to bilayers must be different from that of the pairing of longitudinal dipole moments of molecules from the neighboring layers, which is valid for “*smectic antiphases*” made by asymmetric rod-like molecules.

The experimental observations could be consistently explained if the general tilt structure (SmC_G) inside the layers is assumed. For most bent-core smectics the polar vector is perpendicular to the tilt plane, defined by the layer normal and averaged long axis direction, just as polarization in the ferroelectric rod-like liquid crystalline systems. However, since in the bent-core liquid crystals the polar order is decoupled from the tilt order, the polar director can in general have any direction in space; thus it can also have a non-zero component along the layer normal. This can be achieved by a combination of tilting (rotation around the polar director) and leaning (rotation around the direction perpendicular to the polar director) of

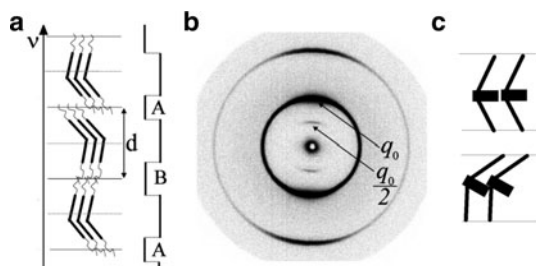


Fig. 10 (a) Double layer periodicity in the structure appears due to the alternating leaning direction in the consecutive layers, which makes layer boundaries A and B slightly different. (b) As a result a subharmonic signal at $q_0/2$, related to the double layer periodicity, is detected in the XRD pattern. $q_0 = 2\pi/d$ reflects the single layer thickness. (c) Leaning might lead to better packing of molecules having bulky central parts

molecules (Fig. 7) in the smectic layer. If in the consecutive layers leaning of molecules alternates, i.e., banana tips are slightly above and below the layer midplane, then the density across the layers will have a double layer periodicity visible in XRD as a weak subharmonic of the main “lamellar” signal (Fig. 10).

Additionally, due to the competition between the density modulation associated with the monolayer and the bilayer periodicity resulting from the general tilt structure, the mass centers (banana tips) can change the positions periodically along the layer, being below or above the geometrical center of the layer (Fig. 11). This leads to the 2D density modulated structures. In this case the inclination of the crystallographic unit cell is directly related to the tilt of molecules, as one of the of crystallographic unit cell sides is defined by the orientation of the long molecular axis. In the case of the synclinically tilted molecules in the consecutive layers the inclination of the oblique body centered crystallographic unit cell is the same as the tilt angle deduced from the optical measurements, while for the anticlinically tilted molecules in the consecutive layers a rectangular body centered crystallographic unit cell is detected. For some materials rich polymorphism of the SmC_G -type modulated phases is observed that involves the synclinc modulated, anticlinic modulated and bilayer general tilt smectic phases [24].

Since the B1rev phase is made of smectic layer fragments the following question arises: can the layer fragments have the SmC_G structure? The answer is “yes.” In some compounds the B1rev phase consists of bilayers which become deformed and

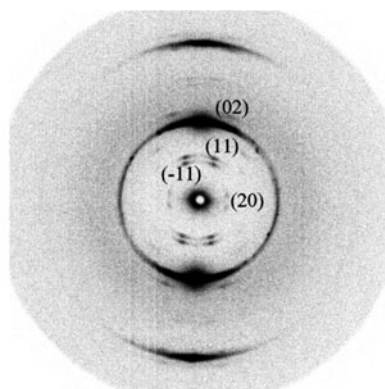
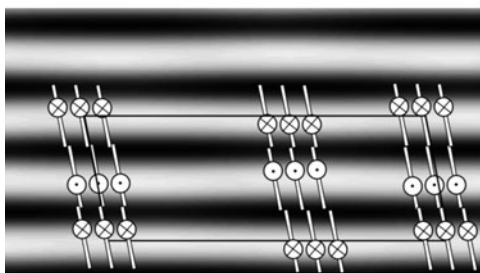


Fig. 11 XRD pattern of modulated SmC_G general tilt structure with the synclinc tilt of molecules in the neighboring layers. The pattern corresponds to a structure with the body center oblique crystallographic unit cell; note that for this phase the tilt of the unit cell is correlated to the tilt of the molecules



even a transition between the monolayer B1rev to bilayer B1rev phase is observed as one of the crystallographic unit cell sides doubles at the transition point. But surprisingly it seems that both modulation types, breaking of layers and changing of leaning direction along layers, can become incommensurate and can co-exist in the same temperature window [24].

At the end of this paragraph it has to be mentioned that, in addition to the phases discussed in this section, the other columnar structures are also possible for bent-core molecules. In the case of the bent-core molecules having multiple terminal chains the hexagonal columnar phase was found, in which the column cross section is made by three to four molecules forming a disc with the aromatic part inside the disc and alkyl chains outside (see the review papers [26, 27] and the references therein). The large curvature of the aromatic-alkyl interface enables the accommodation of the multiple terminal chains. For phases made of flat discs a non-polar structure is observed, because the dipole moments in each disc are compensated. However, for some polycatenar bent-core systems the transition to the axially polar phase is observed upon lowering the temperature. In the polar phase the flat disc is deformed into a conical shape with the non-compensated dipole moment. The phase transition seems to be continuous, accompanied by a pronounced softening of the dielectric response and birefringence changes [28, 29].

3 Theoretical Considerations

3.1 Modeling the Layer and Director Structure in 2D Phases

The question is what might be the driving force for layer deformation and why for so many bent core systems homogenous layers are not energetically favorable? In 2003 the Boulder group suggested that the mechanism might be similar to those observed for polycatenars, i.e., the mismatch between the area required for the packing of molecular cores and tails that eventually leads to splay of polarization [30, 31]. When molecules are tilted the splay can be obtained by rotation of molecules on the tilt cone or by rotation of molecules around the long molecular axis.

In this section we present a model [32, 33] which predicts that regions of favorable splay are connected by regions of unfavorable splay in which layers are inclined to reduce the molecular tilt. Unfavorable splay occurs on a smaller tilt cone and as a result the energy penalty in the unfavorable splay regions is reduced. The local increase of the layer thickness due to the smaller tilt angle leads to the bending of layers and as a result to the formation of undulated layers or fragmented layer structure.

The layer and director structure in the bent-core liquid crystal phases can be studied by the Landau–de Gennes type model [32, 34, 35]. The layer and director structure is such that the free energy ($F = \int f dV$) has the minimum value. The free energy density (f) is written in terms of:

- The nematic director \mathbf{n} , which describes the local average orientation of the molecular long axes
- The polar director \mathbf{p} , which describes the local average orientation of the molecular tips
- The smectic order parameter ψ which describes the spatial variation of density due to the layered structure

The free energy density is written as a sum of the nematic-type contribution (f_n), the general smectic contribution (f_s), the energy due to the polarization self-interaction (f_p), and the term specific for the bent-core systems (f_{bc}):

$$f = f_n + f_s + f_p + f_{bc}. \quad (1)$$

The nematic free energy density describes the energy associated with the spatial variation in the nematic director:

$$f_n = \frac{1}{2} K_n \left[(\nabla \cdot \mathbf{n})^2 + (\nabla \times \mathbf{n})^2 \right], \quad (2)$$

where K_n is the elastic constant and the equality of the elastic constants for the bend, splay, and twist deformation was assumed. The smectic contribution is

$$f_s = c_{||} |(\mathbf{n} \cdot \nabla - iq_0) \psi|^2 + c_{\perp}(T) |\mathbf{n} \times \nabla \psi|^2 + D |(\mathbf{n} \times \nabla)^2 \psi|^2. \quad (3)$$

The smectic order parameter

$$\psi = |\psi| \exp\{iqz + u(x)\} \quad (4)$$

describes the layer formation and thus the sinusoidal density modulation along the smectic layer normal defined by

$$v = \frac{\nabla \psi}{|\nabla \psi|}. \quad (5)$$

By adding the function $u(x)$ to the phase factor in (4) one can describe departures from the planar (lamellar, one-dimensional) layer arrangement, which is characteristic for the 2D structures. The first term in (3) is the smectic layer compressibility energy. It is zero when layers are of the equilibrium thickness. If $c_{\perp}(T) > 0$, the second term in (3) requires the director to be along the smectic layer normal (the smectic-A phase). If $c_{\perp}(T) < 0$, this term would prefer the director to lie in the smectic plane. So the last term in (3) is needed to stabilize a finite tilt of the director with respect to the smectic layer normal. In addition this term gives the energy penalty for the spatial variation of the smectic layer normal.

As an example, let us consider the one-dimensional lamellar structure of layers and the molecules being arranged with their long molecular axis in the direction of

the smectic layer normal (smectic-A phase). In such a structure the nematic director is $\mathbf{n} = (0, 0, 1)$, the smectic order parameter is $\psi = |\psi| \exp\{iq_0z\}$, $d_0 = 2\pi/q_0$ is the equilibrium smectic layer thickness, and $\nabla\psi/|\nabla\psi| = (0, 0, 1)$ gives the direction of the smectic layer normal \mathbf{v} .

The polarization self-interaction energy density is

$$f_p = \frac{P_0^2 p_x^2}{2\epsilon\epsilon_0}, \quad (6)$$

where P_0 is the local value of polarization and $P_0 p_x$ is its x -component. We call $\mathbf{p} = (p_x, p_y, p_z)$ the polar director and note that $|\mathbf{p}| = 1$. The simple expression (6) for the polarization self-interaction energy is possible only if polarization direction is a function of one variable (in our case x) only.

The free energy density terms introduced so far are all used in the description of the smectic phases made by rod-like molecules, the electrostatic term (6) being characteristic for the ferroelectric liquid crystals made of chiral rod-like molecules. To describe phases made by bent-core molecules one has to add symmetry allowed terms which include the divergence of the polar director (polarization splay) and coupling of the polar director to the nematic director and the smectic layer normal:

$$f_{bc} = \tilde{K}_p(\nabla \cdot \mathbf{p})|\mathbf{n} \times \nabla\psi|^2 + \frac{1}{2}K_p(\nabla \cdot \mathbf{p})^2 + K_{np}^{(1)}(\mathbf{p} \times (\mathbf{n} \times \nabla\psi))^2 + K_{np}^{(2)}(\mathbf{p} \times (\mathbf{n} \times \nabla\psi))^4. \quad (7)$$

The first term in (7) describes the coupling between the polarization splay and tilt of the molecules with respect to the smectic layer normal. This coupling is responsible for the chiral symmetry breakdown in phases where bent-core molecules are tilted with respect to the smectic layer normal [32, 36]. The second term in (7) stabilizes a finite polarization splay. The third term with positive parameter $K_{np}^{(1)}$ describes the preferred orientation of the molecular tips in the direction perpendicular to the tilt plane (the plane defined by the nematic director and the smectic layer normal). However, if $K_{np}^{(1)}$ is negative, this term prefers the molecular tips to lie in the tilt plane. The last term in (7) stabilizes some general orientation (α) of the polar director (see Fig. 7) which leads to a general tilt (SmC_G) structure.

The stability analysis [32] of the lamellar (one-dimensional) structure shows that it is stable only for weak coupling between the splay of polarization and molecular tilt. When \tilde{K}_p is larger than some critical value, layers start to undulate.

Let us first consider the case where the preferred orientation of the polar director is perpendicular to the tilt plane ($K_{np}^{(1)} > 0$). The spatial variation of the layer normal and the nematic and polar directors is shown in Fig. 12. We see that regions of favorable splay (called blocks or layer fragments in Sect. 2) are intersected by regions of unfavorable splay (defects, walls). In the region of favorable splay the smectic layer is flat. In the defects regions the tilt angle decreases to reduce energy

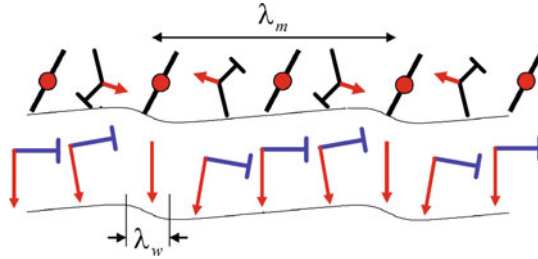


Fig. 12 Layer and director structure in 2D phases which occur due to the preference of the system to polarization splay. *Upper line*: side view on the layer; *lower line*: top view on the layer. *Red arrows* show the polar director. *Blue nails* show the projection of the nematic director to the smectic plane. There is no blue nail in the centre of the wall, meaning that the cone angle is reduced to zero

penalty related to the unfavorable polarization splay. The increase in the smectic layer thickness is coupled to the change in the smectic layer orientation (2) and as a result the smectic layer undulates. The width of the block (λ_m) with respect to the width of the wall (λ_w) depends on the ratio among the constants in the free energy density. Depending on the width of the wall compared to the width of the block one can call the phase either columnar or layer undulated.

The model predicts that for the typical elastic parameters the polarization splay is small, just a few degrees. This was also confirmed experimentally as only a small change of birefringence under the electric field is detected for the B1rev phase. The electric field eliminates the spontaneous splay by aligning the dipole moments along the electric field direction.

Let us now consider the case of $K_{np}^{(1)}$ in (7) being negative. The term with $K_{np}^{(1)}$ alone would now require the molecular tips to lie in the tilt plane. So the last term in (7) is needed to stabilize a finite angle between the polar director and the tilt plane. As shown in Fig. 10 the system can profit by the orientation of the polar director towards the tilt plane since this can lead to a better packing of the bulky molecular cores.

Numerical results show that the reduction of the cone angle in the region of the unfavorable splay is smaller in the general tilt structure than in the structure with polarization being perpendicular to the tilt plane. The cone angle reduction is coupled to the undulation of layers. So in the general tilt structure the undulation is less pronounced than in the regular B1rev phase (Fig. 13), as was indeed observed experimentally [25].

Finally we consider the switching by an external electric field. We assume planar layers within one layer fragment (block) and a constant tilt angle. This assumption is confirmed by the numerical calculations, which predict that the cone angle variation and the layer reorientation occur only inside the wall connecting the layer fragments of the preferred uniform splay (Fig. 12). The walls can be approximated by surfaces on which the director position is strongly anchored. The free energy density can then be expressed only by the angle φ which determines the director position on the cone

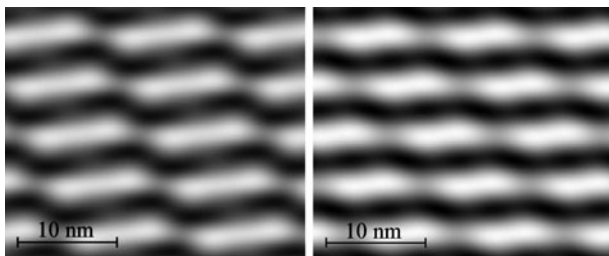


Fig. 13 In the general tilt structure stronger lamellarization is predicted by the theoretical model and also observed experimentally. *Left*: the layer structure in the B1rev-type phase; *right*: the lamellar structure in the higher temperature general tilt structure

and the angle α which gives the orientation of the molecular tip. To model the time response of both angles across the layer fragment upon the application of the external field we use the simplest possible approach by the Landau–Khalatnik equations:

$$\frac{\partial f}{\partial \alpha} - \frac{d}{dx} \frac{\partial f}{\partial \alpha_x} + \gamma_1 \frac{\partial \alpha}{\partial t} = 0 \quad (8)$$

and

$$\frac{\partial f}{\partial \varphi} - \frac{d}{dx} \frac{\partial f}{\partial \varphi_x} + \gamma_2 \frac{\partial \varphi}{\partial t} = 0, \quad (9)$$

where α_x and φ_x are the first order derivatives of α and φ over x and γ_1 and γ_2 are viscosities for the rotation around the long molecular axis and the rotation around the cone, respectively (Fig. 14). Numerical results show that the type of rotation (around the long molecular axis or around the cone) depends on the width of the layer fragment [16]. In the case of small blocks, rotation around the long molecular axis can be expected, for large blocks the rotation on the tilt cone should be preferred. Both types of switching were observed experimentally [16, 17, 37].

3.2 Modeling of the Electron Density Distribution

As already explained at the beginning of Sect. 2, XRD is a fundamental method to obtain information on the electron density structure of the phase. The electron density distribution is the Fourier transform of the structure factor. However, in XRD experiments squares of modulus of Fourier components are recorded, while the information about the phase of the Fourier components is lost. For the centrosymmetric structure the possible phase values are reduced to 0 and π . The amplitudes of the Fourier components can thus be taken as real numbers, positive or negative. With n detected peaks (usually less than ten in the case of B1 or B1 rev phases) this

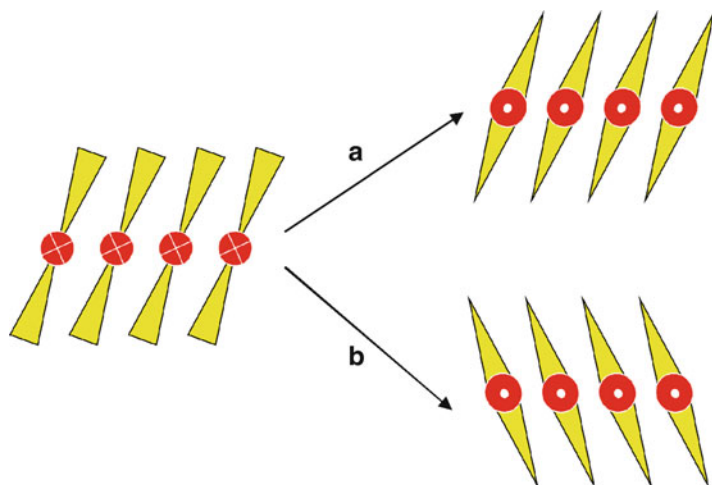


Fig. 14 Switching by an external electric field can be achieved in two ways. (a) Rotation around the long molecular axis leads to a switch in structural chirality. (b) Rotation around the cone does not change the chirality of the structure

means that one should test 2^n possible electron density maps obtained by reverse Fourier transform. Some of them can be discarded immediately since they appear unphysical; however, there is still a large ambiguity to choose among several maps which might look quite sensible. To avoid this ambiguity we have developed a simple model to determine the phases of Fourier components [38].

The electron density maps, $\rho_{\text{exp}}(x,z)$, are obtained from the experimentally measured peak intensities $I_{h,k}$ as

$$\rho(x,z) = \sum_{h,k} \sqrt{I_{h,k}} \cos(\vec{q}_{h,k} \cdot \vec{r} + \phi_{h,k}), \quad (10)$$

where $\vec{q}_{h,k}$ is the wave vector and $\phi_{h,k}$ is the phase which cannot be obtained from the measurements. The wave vector $\vec{q}_{h,k}$ in the reciprocal space is

$$\vec{q}_{h,k} = h\vec{q}_a + k\vec{q}_b = \left\{ \frac{2h\pi}{a}, -\frac{2h\pi}{a \tan \delta} + \frac{2k\pi}{b \sin \delta} \right\}, \quad (11)$$

where a and b are the dimensions of the crystallographic unit cell and δ is the crystallographic unit cell angle (Fig. 15).

To be able to predict the phases $\phi_{h,k}$ a model with a parallelogram as a structural motif of the crystallographic unit cell is used (Fig. 15). Keeping the same crystallographic unit cell and rotating the blocks allows for an easy prediction of the XRD pattern for a variety of structures. For the considered crystallographic unit cell with a base at the position $\vec{r}_b = (\vec{a} + \vec{b})/2$ the structure factor is

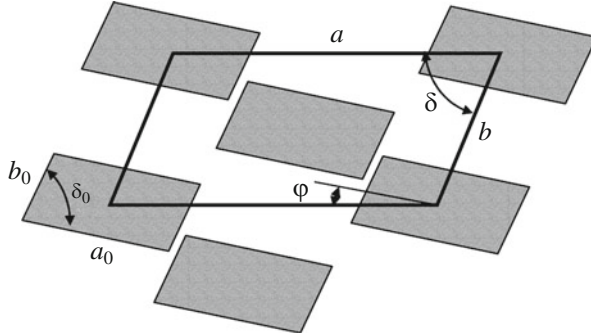


Fig. 15 The block model used to calculate the phases of the Fourier components. The crystallographic unit cell parameters a , b , and δ are found from XRD measurements. The block parameters a_0 , b_0 , δ_0 , and φ are chosen such that the best agreement is obtained between the experimental measurements and the theoretical model regarding the signal intensities

$$F(h, k) = f_B \left(1 + \exp\left\{i\vec{q} \cdot \vec{r}_b\right\} \right) = f_B (1 + \exp\{i\pi(h + k)\}), \tag{12}$$

where h and k are integer numbers and f_B is the Fourier transform of the motif:

$$f_B = \int_S \exp\left\{i\vec{q} \cdot \vec{r}\right\} dx dz, \tag{13}$$

where the integration runs over the surface S of the block. In order to have f_B as a real number the origin of the coordinate system is set in the center of the block. The sign of f_B then defines the 0 or π phase required in (10).

The parameters a , b , and δ are obtained by XRD measurements. The parameters defining the dimensions and the orientations of the motif are taken such that the theoretically obtained ratios between different peak intensities approximately fit the experimental measurements. In such a way the phases of the Fourier components are determined. Not all the phases can be obtained unambiguously, but in the cases that we have studied we ended up with at most four possibilities to be tested. In these cases the experimental and theoretical maps were drawn for all the possible sign combinations, and the map which gave the best fit between the theory and the experiment was chosen.

4 Conclusions

Bent-core liquid crystals are especially interesting materials for basic research as in these systems the polar and tilt order are decoupled and polarization splay seems to be an inherent property of the system. Both effects lead to a variety of structures with unusual properties, e.g., formation of the 2D density modulated phases built of the smectic layers fragments. We have presented the current knowledge

related to the structural studies of such phases. The information about the electron density distribution was obtained from X-ray diffraction studies while the molecular arrangement inside the layer fragments was deduced from optical studies and from the response to the external electric field. We have shown that there are in general two types of layer fragment arrangement in 2D structures. In the B1-type phase the crystallographic unit cell is always orthogonal body centered and made of blocks vertically shifted by half of their thickness. Lack of signal related to block width in the XRD pattern of the B1-type phase shows that there are no defect regions of different electron density between the blocks. The B1rev-type structure is made of deformed layers in such a way that in most cases defects in the layers are arranged to form oblique primitive cells and rarely orthogonal primitive cells. The electron density maps obtained from X-ray diffraction measurements show that in the B1rev-type phases the layer fragments are connected by defect regions where the electron density is lower than in the blocks. The layer fragments are in general inclined with respect to the crystallographic unit cell. However, the inclination angle is not consistent with the molecular tilt inside the layer fragments. The molecular arrangement inside the blocks is such that the polarization splays across the block. Theoretical modeling shows that coupling between the splay of polarization and the tilt of the molecular long axis leads to the chiral symmetry breaking and acts as the driving mechanism for the formation of two dimensional structures.

We have also shown the existence of 2D phases due to more subtle electron density changes. In some cases additional peaks are observed in the XRD pattern, signifying a double layer periodicity in the system, which can be accounted for if a general orientation of the polar director is allowed. If the polar director is not perpendicular to the tilt plane there exists a component of polarization in the direction of the smectic layer normal (longitudinal polarization). By double layer periodicity the system escapes from the polar structure and in addition achieves better packing of the molecular cores and molecular tails.

Acknowledgments The work presented was supported by the Slovenian Research Agency through the research program P1-0055 and by the Polish-Slovenian bilateral projects BI-PL/08-09-015 and BI-PL/10-11-010.

References

1. Niori T, Sekine T, Watanabe J, Takezoe H (1996) Distinct ferroelectric smectic liquid crystals consisting of banana shaped achiral molecules. *J Mater Chem* 6:1231–1233
2. Takezoe H, Górecka E, Čepič M (2010) Antiferroelectric liquid crystals: interplay of simplicity and complexity. *Rev Mod Phys* 82:897–937
3. Sigaud G, Hardouin F, Achard MF, Levelut AM (1981) A new type of smectic A phase with long range modulation in the layers. *J Phys (Paris)* 42:107–111
4. Fazio D, Mongin C, Donnio B, Galerne Y, Guillon D, Bruce DW (2001) Bending and shaping: cubics, calamitics and columnars. *J Mater Chem* 11:2852–2863
5. Prost J, Barois P (1983) Polymorphism in polar mesogens. *J Chim Phys* 80:65–81

6. Redy RA, Tschierske C (2006) Bent-core liquid crystals: polar order, superstructural chirality and spontaneous desymmetrisation in soft matter systems. *J Mater Chem* 16:907–961
7. Als-Nielsen J, McMorrow D (2001) Elements of modern X-ray physics. Wiley, Chichester
8. Szydłowska J, Mieczkowski J, Matraszek J, Bruce DW, Górecka E, Pocięcha D, Guillon D (2003) Bent-core liquid crystals forming two- and three-dimensional modulated structures. *Phys Rev E* 67:031702-1–031702-5
9. Watanabe J, Niori T, Sekine T, Takezoe H (1998) Frustrated structure induced on ferroelectric smectic phases in banana-shaped molecular system. *Jpn J Appl Lett* 37:L139–L142
10. Shreenivasa Murthy HN, Bodyagin M, Diele S, Baumeister U, Peřlž G, Weissflog W (2006) Reentrant SmCP_A phases: unusual polymorphism variant SmA–SmC_SPA–Col_{ob}–SmC_SPA observed in new bent-core mesogens. *J Mater Chem* 16:1634–1643
11. Coleman DA, Jones CD, Nakata M, Clark NA, Walba DM, Weissflog W, Fodor-Csorba K, Watanabe J, Novotna V, Hamplova V (2008) Polarization splay as the origin of modulation in the B1 and B7 smectic phases of bent-core molecules. *Phys Rev E* 77:021703
12. Mieczkowski J, Pocięcha D, Górecka E, to be published
13. Shimbo Y, Górecka E, Pocięcha D, Araoka F, Goto M, Takanishi Y, Ishikawa K, Mieczkowski J, Gomola K, Takezoe H (2006) Electric-field-induced polar biaxial order in a nontilted smectic phase of an asymmetric bent-core liquid crystal. *Phys Rev Lett* 97:113901
14. Wang L-Y, Chiang I-H, Yang P-J, Li W-S, Chao I-T, Lin H-C (2009) Configuration effects of H-bonded sites and rigid core lengths on H-bonded banana-shaped liquid crystalline supramolecules consisting of symmetric trimers and asymmetric heterodimers. *J Phys Chem B* 113:14648–14660
15. Ortega J, de la Fuente MR, Etxebarria J, Folcia CL, Diez S, Gallastegui JA, Gimeno N, Ros MB, Perez-Jubindo MA (2004) Electric-field-induced B1–B2 transition in bent-core mesogens. *Phys Rev E* 69:011703
16. Górecka E, Vaupotič N, Pocięcha D, Čepič M, Mieczkowski J (2005) Switching mechanisms in polar columnar mesophases made of bent-core molecules. *Chemphyschem* 6:1087–1093
17. Zhang Y, Baumeister U, Tschierske C, O’Callaghan MJ, Walker C (2010) Achiral bent-core molecules with a series of linear or branched carbosilane termini: dark conglomerate phases, supramolecular chirality and macroscopic polar order. *Chem Mater* 22:2869–2884
18. Nakata M, Link DR, Takanishi Y, Takahashi Y, Thisayukta J, Niwano H, Coleman DA, Watanabe J, Iida A, Clark NA, Takezoe H (2005) Electric-field-induced transition between the polarization-modulated and ferroelectric smectic- $C_S P_F^*$ liquid crystalline states studied using microbeam X-ray diffraction. *Phys Rev E* 71:011705
19. Gimeno N, Barbera J, Serrano JL, Ros MB, de la Fuente MR, Alosa I, Folcia CL (2009) Terminal chains as a tool to modulate the properties of bent-core liquid crystals. *Chem Mater* 21:4620–4630
20. Pocięcha D, Górecka E, Čepič M, Vaupotič N, Gomola K, Mieczkowski J (2005) Paraelectric-antiferroelectric phase transition in achiral liquid crystals. *Phys Rev E* 72:060701R
21. Zhang Y, O’Callaghan MJ, Baumeister U, Tschierske C (2008) Bent-core mesogens with branched carbosilane termini: flipping suprastructural chirality without reversing polarity. *Angew Chem Int Ed* 47:6892–6896
22. Pocięcha D, Vaupotič N, Górecka E, Mieczkowski J, Gomola K (2008) 2-D density-modulated structures in asymmetric bent-core liquid crystals. *J Mater Chem* 18:881–885
23. Bedel JP, Rouillon JC, Marcerou JP, Nguyen HT, Achard MF (2004) Evidence for different polymorphisms with and without an external electric field in a series of bent-shaped molecules. *Phys Rev E* 69:061702
24. Górecka E, Pocięcha D, Vaupotič N, Čepič M, Gomola K, Mieczkowski J (2008) Modulated general tilt structures in bent-core liquid crystals. *J Mater Chem* 18:3044–3049
25. Vaupotič N, Pocięcha D, Čepič M, Gomola K, Mieczkowski J, Górecka E (2009) Evidence for general tilt columnar liquid crystalline phase. *Soft Matter* 5:2281–2285

26. Takezoe H, Kishikawa K, Gorecka E (2006) Switchable columnar phases. *J Mater Chem* 16:2412–2416
27. Takezoe H, Takanishi Y (2006) Bent-core liquid crystals: their mysterious and attractive world. *Jpn J Appl Phys* 45:597–625
28. Gorecka E, Pocięcha D, Mieczkowski J, Matraszek J, Guillon D, Donnio B (2004) Axially polar columnar phase made of polycatenar bent-shaped molecules. *J Am Chem Soc* 126:15946–15947
29. Gorecka E, Pocięcha D, Matraszek J, Mieczkowski J, Shimbo Y, Takanishi Y, Takezoe H (2006) Polar order in columnar phase made of polycatenar bent-core molecules. *Phys Rev E* 73:031704
30. Coleman DA et al (2003) Polarization-modulated smectic liquid crystal phases. *Science* 301:1204–1211
31. Bailey C, Jakli A (2007) Role of molecular shape on bent-core liquid crystal structures. *Phys Rev Lett* 99:207801
32. Vaupotič N, Čopič M (2005) Polarization modulation instability in liquid crystals with spontaneous chiral symmetry breaking. *Phys Rev E* 72:031701-1–031701-4
33. Vaupotič N, Čopič M, Górecka E, Pocięcha D (2007) Modulated structures in bent-core liquid crystals: two faces of one phase. *Phys Rev Lett* 98:247802-1–247802-4
34. de Gennes PG (1972) An analogy between superconductors and smectics-A. *Solid State Commun* 10:753–756
35. Lubensky TC, Renn SR (1990) Twist-grain-boundary phases near the nematic smectic-A smectic-C point in liquid crystals. *Phys Rev A* 41:4392–4401
36. Link DR, Natale G, Shao R, MacLennan JE, Clark NA, Körblová E, Walba DM (1997) Spontaneous formation of macroscopic chiral domains in a fluid smectic phase of achiral molecules. *Science* 278:1924–1927
37. Nakata M, Shao RF, MacLennan JE, Weissflog W, Clark NA (2006) Electric-field-induced chirality flipping in smectic liquid crystals: the role of anisotropic viscosity. *Phys Rev Lett* 96:067802-1–067802-4
38. Górecka E, Vaupotič N, Pocięcha D (2007) Electron density modulations in columnar banana phases. *Chem Mater* 19:3027–3031

Spontaneous Achiral Symmetry Breaking in Liquid Crystalline Phases

H. Takezoe

Abstract It is well known that spontaneous deracemization or spontaneous chiral resolution occasionally occurs when racemic molecules are crystallized. However, it is not easy to believe such phenomenon will occur when forming liquid crystal phases. Spontaneous chiral domain formation is introduced, when molecules form particular liquid crystal phases. Such molecules possess no chiral carbon but may have axial chirality. However, the potential barrier between two chiral states is low enough to allow mutual transformation even at room temperature. Therefore the systems are essentially not racemic but nonchiral or achiral. First, enhanced chirality by doping chiral nematic liquid crystals with nonchiral molecules is described. Emphasis is made on ester molecules for their anomalous behavior. Second, spontaneous chiral resolution is discussed. Three examples with rod-, bent-, and disk-shaped molecules are shown to give such phenomena. Particular attention will be paid to controlling enantiomeric excess (*ee*). Actually, almost 100% *ee* was obtained by applying some external chiral stimuli. This is very noteworthy in the sense that we can create chiral molecules (chiral field) without using any chiral species.

Keywords Axial chirality · Bent-core molecule · Chirality · Chirality control · Deracemization

Contents

1	Introduction	304
2	Enhanced Chirality by Nonchiral Molecules	306
2.1	Experimental Observation of Enhanced Chirality in Chiral Phases by Achiral Bent-Shaped Molecules	306
2.2	Theoretical Consideration	307

H. Takezoe

Department of Organic and Polymeric Materials, Tokyo Institute of Technology, 2-12-1,
O-okayama, Meguro-ku, Tokyo 152-8552, Japan
e-mail: takezoe.h.aa@m.titech.ac.jp

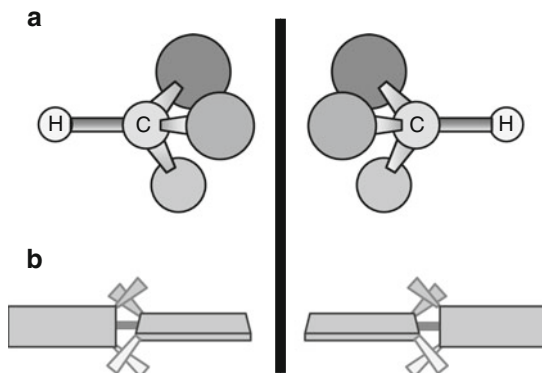
2.3	Stabilization of Blue Phase by Bent-Core Molecules	309
2.4	Experimental Observation of Enhanced Chirality in Chiral Phases by Achiral Ester Molecules	310
3	Spontaneous Deracemization in Mesogenic Systems	312
3.1	Historical View	312
3.2	Spontaneous Deracemization in Bent-Shaped Mesogens	312
3.3	Spontaneous Deracemization in Rod-Shaped Mesogens	316
3.4	Spontaneous Deracemization in Disk-Shaped Mesogens	318
3.5	Enhanced Twisting Power by Doping B4 Phase with Rod-Like Molecules	319
3.6	Controlling Enantiomeric Excess by Chiral Stimuli	323
4	Conclusions	324
	References	326

1 Introduction

Chirality has been one of the most topical subjects in chemistry since the famous historical experiment by Louis Pasteur [1]. He found that a tartaric acid salt forms two kinds of crystals which are mirror images of each other. Solutions of these crystals give opposite optical activity, indicating the existence of two different types of molecules with mirror images. Chirality in a liquid crystal (LC) is particularly unique [2] since molecules form macroscopic helical structures. They usually appear as cholesteric (chiral nematic) and chiral smectic C phases (N^* and SmC^* phases); the former shows a simple one-dimensional helical structure with the helical axis perpendicular to the local director and the latter also shows a simple one-dimensional helical structure, where the local director is tilted from the layer normal and precesses from layer to layer with the helical axis perpendicular to the smectic layer. In some particular cases, more complicated helical structures emerge, i.e., a three-dimensional helical network is formed in blue phases (BPs), a different kind of one-dimensional helical structure is formed in twist grain boundary (TGB) phases, where the helical axis is parallel to the smectic layer, and chiral disk-like molecules form even intracolumnar helix along the column axis. Such structures are realized in chiral LC systems or by introducing *chiral* molecules to *nonchiral* LC systems. Particularly, BPs and TGB generally emerge in highly chiral systems.

There are two different kinds of sources of molecular chirality; central chirality and axial chirality (Fig. 1). Central chirality is due to the existence of chiral carbon, whereas axial chirality originates from twisted structures of molecules, between which a sufficiently high energy barrier exists, preventing the chiral conformational interconversion in ambient conditions. Surprisingly, however, the introduction of *nonchiral* molecules to *chiral* liquid crystalline environments sometimes enhances the chirality of the systems [3–5]. This means that inherently nonchiral molecules act as chiral molecules in chiral environments. This occurs in the following way. Molecules with axial chirality behave as nonchiral molecules when the potential barrier is low enough for chiral conformational interconversion. But when such

Fig. 1 Two origins of chirality. (a) Central chirality. (b) Axial chirality



molecules are located in chiral circumstance, one of the chiral conformers is stabilized and otherwise nonchiral molecules become chiral.

Essentially, the origin of spontaneous chiral resolution is the same as the previous example. When molecules with the same chiral conformation form small chiral domains due to packing entropy effects, the same chiral conformation of molecules is stabilized when they approach the chiral domain. Thus both chiral domains with different chiral conformations grow, resulting in spontaneous chiral resolution [6–8]. Chirality enhancement occurs even in such chiral domains. For instance, chirality in both segregated chiral domains is enhanced by doping nonchiral bent-shaped molecules (BSMs) with nonchiral rod-shaped molecules (RSMs), as observed by circular dichroism (CD) or optical rotatory power (ORP) [9].

Chirality in LCs has become more attractive, since BSMs started to provide many chirality related topics. First Link et al. [10] pointed out the chirality induced by tilting of BSMs. They defined layer chirality by three axes, i.e., bent (or polarization), tilt, and layer normal directions, in the tilted smectic B2 phase. Another striking observation was apparent bright and dark domains by decrossing polarizer and analyzer, which correspond to two chiral domains [6, 11–13], as observed in B4 [14], B7 [15], and dark conglomerate [16] phases (see for example Fig. 2) [11]. The chirality in the latter case mainly originates from axial chirality, as evidenced by polarized IR spectroscopy [17] and NMR spectroscopy [18, 19], but seems to be strongly correlated with the layer chirality [20]. In this chapter axial chirality plays a major role. The spontaneous chiral domain formation mentioned above is an LC analog of Pasteur's experiment. The ratio of sizes of the two chiral domains is 1:1 (racemic). Of particular interest in this case is that the ratio can be controlled by external chiral stimuli to make optical enantiomers; almost 100% enantiomeric excess (*ee*) can be achieved [21, 22]. This is possible only if the energy barrier between two chiral conformations is not too high.

In this chapter very unusual phenomena are described, i.e., (1) chirality enhanced by achiral or nonchiral molecules, (2) spontaneous chiral resolution in apparently nonchiral molecular systems composed of rod-, bent-, or disk-shaped

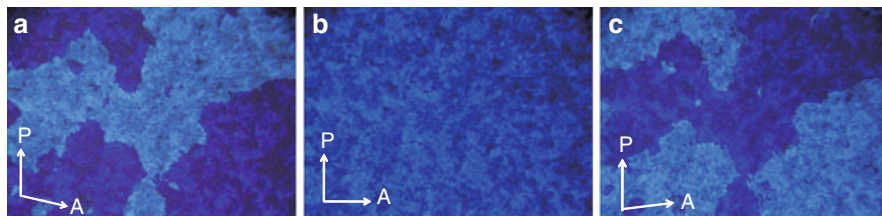


Fig. 2 Polarizing optical micrographs in the B4 phase of bent-core LC. Under crossed polarizers, texture with bluish color is observable (*middle*). By decreasing polarizers, two brighter and darker domains are observable (*right and left*). The brightness is interchanged by decreasing polarizers to counter senses [11]

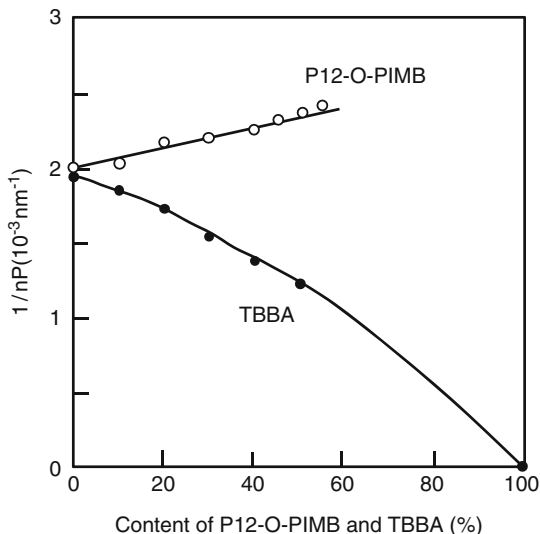
molecules, and (3) chirality control by external chiral stimuli. Particular attention is paid to BSMs and molecules with ester linkage(s).

2 Enhanced Chirality by Nonchiral Molecules

2.1 Experimental Observation of Enhanced Chirality in Chiral Phases by Achiral Bent-Shaped Molecules

The first surprising result was reported by Thisayukta et al. [3]. They used three BSMs, which are so chosen that all have common side wings connected to different central cores by ester linkage, but show different banana phases. Here one example using P-12-O-PIMB is shown (see Fig. 17 for homolog P-8-O-PIMB). The N* host used is cholesteryl 4-formylbenzoate, which also has an ester linkage between cholesterol and phenyl group. The N* compound was doped with nonchiral P-12-O-PIMB, and the optical pitch nP was measured as a function of reduced temperature $T_i - T$, where T_i is the isotropization temperature for the pure N* and four mixtures with 10, 20, 40, and 50% P-12-O-PIMB. Here n and P are an average refractive index and a structural helical pitch, respectively. The result is shown in Fig. 3 and is quite unusual. Namely, the optical pitch at the same $T_i - T$ becomes shorter with increasing P-12-O-PIMB content, although the temperature range of the N* phase becomes lower and narrower. In other words, the twisting power proportional to $1/nP$ becomes larger with increasing nonchiral dopant content. The result is surprising since doping of the chiral system with achiral molecules has otherwise always resulted in a “diluted” chirality and consequently in an increase of the pitch length. The results are qualitatively the same for two other BSMs, which show different phase sequences from that of P-12-O-PIMB. As a control experiment, a classical rod-like molecule TBBA was also used. The result is also shown in Fig. 3. In contrast to BSMs, the introduction of rod-like molecules elongates the helical pitch of N*, as can be expected.

Fig. 3 Inverse structural pitch ($1/nP$) as a function of dopant ratio. Bent-shaped molecule P12-O-PIMB enhances the twisting power, which is proportional to $1/nP$, whereas rod-shaped molecule TBBA gives just a dilution effect; the helical pitch increases



A similar phenomenon was also found in SmC^* and antiferroelectric or anticlinic SmC_A^* , and was even more conspicuous [4]. We found shortening of helical pitches both in the SmC^* and SmC_A^* phases in all mixtures of one of four hosts showing SmC^* and/or SmC_A^* and one of three nonchiral BSMs. Figure 4 shows the result for one of the mixtures. Because of the steric effect of bend shape of the dopant, the SmC_A^* phase is stabilized, resulting in a wider temperature range [23]. It is obvious that the helical pitch becomes shorter even at very low doping rate, 1% and 3%. The inverse pitch almost linearly increases with fraction of dopant. In other words, the twisting power increases by doping nonchiral molecules.

2.2 Theoretical Consideration

Let us consider an N^* phase doped with BSMs, where BSMs interact with chiral host molecules. The interaction energy between left-handed bent-core conformation and the chiral host molecule U_{LH} is different from that between right-handed bent-core conformation and the same chiral host molecule U_{RH} . The nonzero difference $\Delta U = U_{\text{LH}} - U_{\text{RH}}$ induces finite ee in BSMs, resulting in increased chiral molecules in the system. At the same time, we have to consider the dilution effect.

The distortion of free energy of the N^* phase is expressed as

$$F_d = \lambda(n \text{ curl } n) + \frac{1}{2} K_{22}(n \text{ curl } n)^2, \quad (1)$$

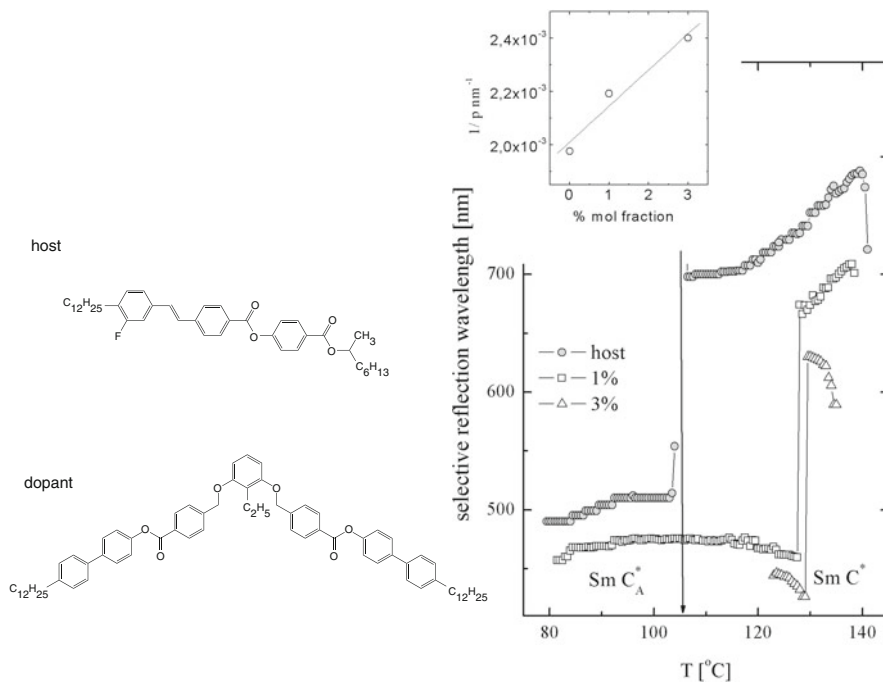


Fig. 4 Selective reflection wavelength (optical pitch) as a function of temperature for three samples; host material showing SmC* and SmC_A* without dopant, with 1% and 3% dopant. The chemical structures of the rod-shaped host and the bent-shaped dopant molecules are also shown. As shown in *inset*, inverse pitch increases almost linearly with dopant content [4]

where the coefficient λ is determined by molecular chirality, i.e., the number of chiral molecules. Minimizing the distortion energy leads to the N* pitch p ,

$$\frac{2\pi}{p} = \frac{\lambda}{K_{22}}. \quad (2)$$

In the present system, N* phase doped with BSMs, λ can be expressed as [24]

$$\lambda = \lambda_0 - x_b \lambda_d + (x_L - x_R) \lambda_b, \quad (3)$$

where λ_0 is the λ in the pure N* phase, and x_L , x_R , and $x_b = x_L + x_R$ are the molar fraction of left-handed, right-handed, and total bent-core conformers in the N* solvent. The second and third terms represent dilution and enhanced chirality effects, respectively. If the third term is predominant and has opposite sign to the second term, as in the present condition, chirality enhancement occurs by introducing nonchiral BSMs to the N* phase. The induced $ee \Delta\alpha$ can be determined by minimizing the free energy ΔF :

$$\Delta F(x_L, x_R) = kT\rho_0 x_L \ln x_L + kT\rho_0 x_R \ln x_R + \rho_0^2 x_L U_{LH} + \rho_0^2 x_R U_{RH} \quad (4)$$

which is obtained under the assumption that x_L and x_R are small and the interaction between BSMs is negligible,

$$\Delta x = x_b \tanh\left(\frac{\rho_0 \Delta U}{2kT}\right). \quad (5)$$

Substitution of (5) into (2) and (3) yields the expression for the inverse pitch:

$$\frac{2\pi}{p} = \frac{\lambda_0 + x_b \left[\lambda_b \tanh\left(\frac{\rho_0 \Delta U}{2kT}\right) - \lambda_d \right]}{K_{22}}. \quad (6)$$

This result indicates that the pitch becomes smaller with increasing content of BSMs if $\lambda_b \tanh(\rho_0 \Delta U / 2kT) > \lambda_d$, namely the dilution effect is much smaller than the helical twisting power of BSMs. In the above discussion, we have neglected the effect of BSMs on the elastic constant K_{22} . The effect on K_{22} has not been reported, whereas it has been experimentally shown that K_{33} in bent-core nematogens is remarkably small compared with that in rod-like nematogens [25].

The enhanced chirality by doping SmC* with BSMs can be explained qualitatively in the same way as in the N* phase. However, the situation is more complicated in SmC* because of spontaneous polarization and flexoelectric effect, and (3) must be replaced by an equation including such effects. Actually, the contribution of flexoelectric effect has been discussed by Gorecka et al. [4]. The other important effect is caused by the fact that the BSMs are in the tilted smectic phase. As mentioned above, the tilt of BSMs induces chirality as observed in the B2 phase.

Finally, the difference of chirality enhancement in the N* and SmC* phases should be mentioned. As shown in Sect. 2.1, enhancement rate in SmC* is about one order of magnitude larger than that in N*. In the SmC* chirality enhancement is attributed to two effects: (1) the interaction between bent-core and chiral host molecules and (2) the coupling between ee , tilt, and spontaneous polarization. The latter effect is absent in the N* phase and is an additional effect in SmC*. Moreover, the chiral discrimination parameter ΔU is expected to be larger in SmC* than in N* because of a confined geometry, i.e., smectic layer.

2.3 Stabilization of Blue Phase by Bent-Core Molecules

Enhanced chirality has also been observed in the induction and stabilization of BPs. The first related experiment was made by Nakata et al. [26]. It is known that BPs emerge between the isotropic and N* phases only in highly chiral systems. For instance, we cannot have any BPs in a commercial NLC ZLI-2293 with chiral dopant MLC6248 at least up to 25%, but instead only the N* phase emerges. By doping such N* phases with BSMs, BP emerges and expands with increasing

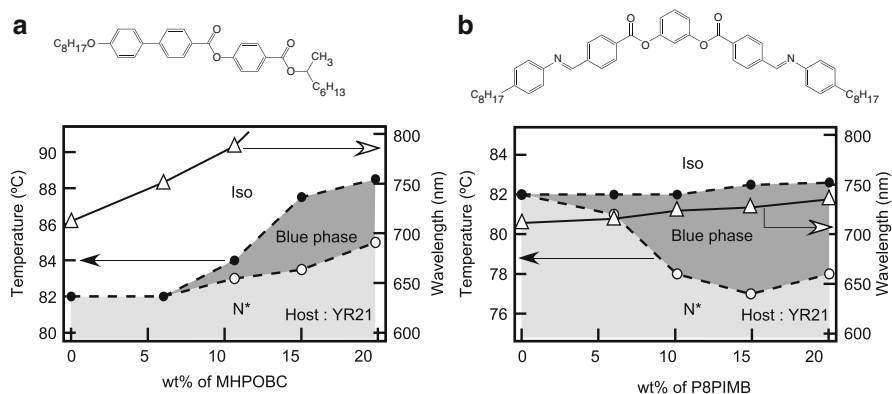


Fig. 5 Induction of the blue phase by doping a N* material with (a) a rod-shaped molecule MHPOBC and (b) a bent-shaped molecule P8-PIMB. In both cases, the blue phase is induced above the N* phase. The bent-shape of the antiferroelectric molecule is responsible for the blue phase induction in (a), since the doping of a real rod-shaped molecule (TBBA) does not induce the blue phase [26]

content of BSMs, as shown in Fig. 5. We assigned the origin of the BP induction to enhanced chirality by BSM and/or the change of elastic constant. More recently, Alexander and Yeomans showed theoretically that the cubic BP is remarkably stabilized when K_{33} is smaller than K_{11} [27]. Recently, Hur et al. also investigated the relationship between the elastic constants of host nematic LCs (NLCs) and the thermal stability of BP1 [28]. By adding BSMs to a conventional NLC, we could gradually increase (decrease) the elastic constant K_{11} (K_{33}) of host NLCs. We confirmed experimentally that the thermal stability of BP strongly depends on the ratio of the elastic constants K_{11} and K_{33} of the host NLCs; the stability increases with decreasing K_{33}/K_{11} , being consistent with the theoretical prediction by Alexander and Yeomans [27].

Stabilization of BP consisting of bent-core N with chiral dopant was also investigated [29–31]. One of the most dramatic results is that BPIII is easily induced by adding a very small amount of chiral dopant such as 1% [29]. The BPIII temperature range was more than 20°. If BSMs show the N phase at room temperature, the BPIII phase over 20° including room temperature is easily realized [30]. Since BSMs have low K_{33} compared with K_{11} [25, 32], the effect of elastic constant on the BP stabilization is confirmed [28].

2.4 Experimental Observation of Enhanced Chirality in Chiral Phases by Achiral Ester Molecules

It was found that enhanced chirality is achieved by doping CLCs with ester molecules instead of BSMs. The same doping experiment on CLCs was

performed [5] using ester molecules as dopant. As shown in Fig. 6, the helical pitch of N^* becomes short by adding ester molecules. In contrast, dilution effect (pitch elongation) was observed by adding nonester rod-like molecules. According to potential calculation [33], the potential barrier between two axially chiral conformations is very low (ca. 0.2 kcal/mol) in ester molecules. Because of nonzero ΔU , one of the potential minima could be removed. Then the ester molecules behave as chiral molecules in the N^* phase. On the other hand, nonester molecules have their potential barrier of ca. 1.5 kcal/mol between two chiral conformers. Nonzero ΔU may induce unbalanced potential minima. However, if the difference is small, the molecules act as nonchiral molecules, since the potential barrier is comparable to the thermal energy. In this way, only dilution effect is effective.

The above observation suggests a unique feature of ester molecules, which tend to induce chirality in LC systems. Actually it is known that molecules are strongly bent at an ester linkage to form P- and M-conformers. Moreover, molecules are bent at the ester linkage. Yan et al. concluded that the system with bent molecules and chiral molecules results in macroscopic chiral aggregation using simulation [34].

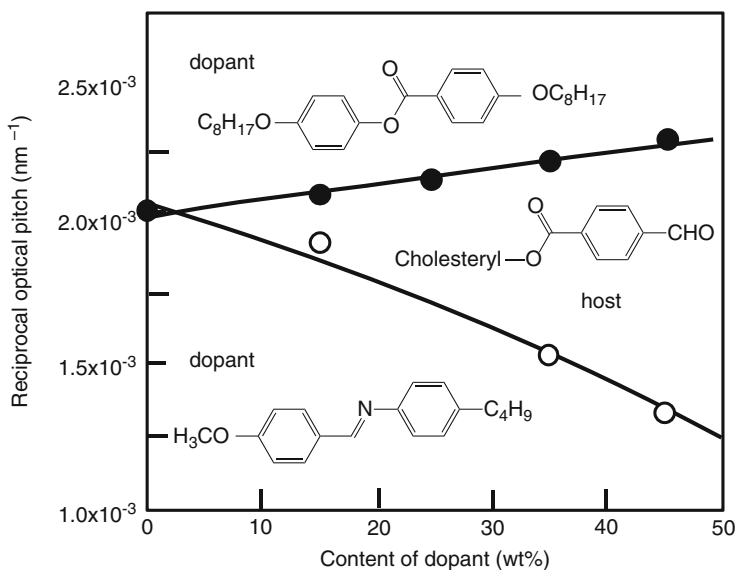


Fig. 6 Reciprocal optical pitch as a function of dopant content. Host material is a cholesterol derivative used in the enhanced chirality in N^* with bent-core molecules [5]

3 Spontaneous Deracemization in Mesogenic Systems

3.1 *Historical View*

As described in the Introduction, Pasteur showed beautifully that racemic molecules resolve spontaneously into chiral forms when they crystallize. We call them conglomerates, in which molecules form condensates comprised of only one enantiomer. The condensation into conglomerates can now be observed not only in crystals but in monolayers, fibers, and supramolecules self-assembled in solution [35]. The researches became possible because of the development of microscopic observation techniques at the nanometer scale. However, in crystals we still do not know what kinds of molecules show spontaneous resolution. Hence, observation of chiral resolution in soft matter may provide important information on the general question.

As for monolayers, chiral resolution was observed on water (Langmuir film) [36], graphite [37], and Au(111) surfaces [38]. Even nonchiral LC molecules such as cyanobiphenyl [39] and triphenylene derivatives [40] form enantiomeric domains on graphite surfaces. As shown in Fig. 7, however, molecules themselves are not of chiral conformation, but the 2D crystal packing motif is chiral. Chiral resolution from racemic mixtures of ferroelectric LCs was also observed in monolayers on graphite, proved by scanning tunneling microscopy [41]. Racemic compounds form two chiral 2D domains, while enantiomers form a unique 2D structure. All these examples are essentially in the crystalline state, although not in 3D crystals. Even in Langmuir films, monolayers are crystallized by surface pressure.

A conglomerate in real liquid crystalline phases was first observed in the smectic phase of a rod-shaped mesogen with two stereogenic centers in its tail [42]. We used a racemic mixture which was supposed not to electrically switch. Evidence for conglomerate formation was provided by clear electro-optic switching and texture observation under a polarizing microscope; domains with stripes, which themselves display fine stripes. These stripes are tilted in two different directions with respect to the primary stripes. This is a still very rare example now that fluid soft matter is known to resolve spontaneously into a three-dimensional conglomerate.

After this observation several authors report chirality nature or chiral resolution in racemic molecular systems [43]. However it should be pointed out that small amounts of the enantiomer may provide erroneous results, as pointed out by Walba et al. [44]. Careful experiments are indispensable.

3.2 *Spontaneous Deracemization in Bent-Shaped Mesogens*

As briefly mentioned in the Introduction, the extensive flow of chirality-related topics has been initiated by the discovery of polar switching in bent-core mesogens [11, 45]. Among the first banana smectic phases B1–B8, at least the B2 [10], B4 [14], and B7 [15] phases can be chiral. The chirality in the B2 phase was

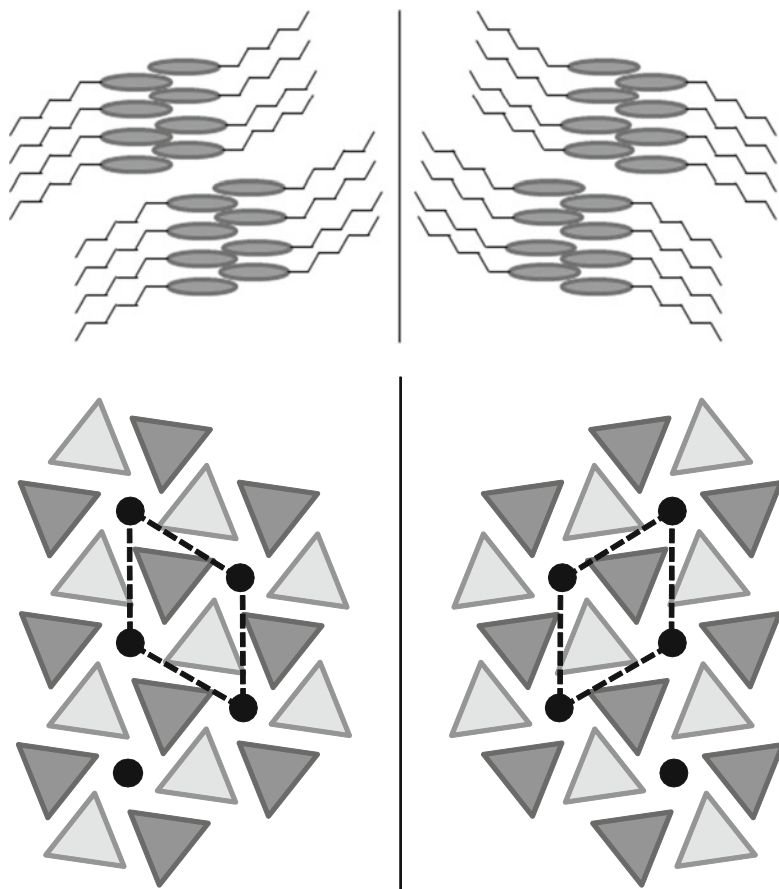


Fig. 7 Chiral packing of rod- and disk-shaped molecules in 2D crystal lattice

demonstrated by Link et al. [10]. This is a smectic phase with tilted molecules with respect to the layer. The chirality is defined by three axes – polarization (bent-direction) b , molecular long axis n , and layer normal z – as shown in Fig. 8. Because of interlayer chiral and polar correlations, four structures are possible: SmC_SP_F , SmC_SP_A , SmC_AP_F , and SmC_AP_A , where subscripts S and A to C (clincity or tilt) stand for synclincic and anticlincic, and subscripts F and A to P (polarity) stand for ferroelectric and antiferroelectric, respectively. The first and last ones are chiral, while the other two are racemic. Let us think about an electric-field induced transition from SmC_AP_A to SmC_SP_F . The transition is associated with optical axis rotation, where the rotational sense is opposite in two conglomerates (white and gray) as shown in Fig. 9. In this way, the chiral resolution can be easily identified.

In some cases, chiral resolution can be recognized by helical structure formation. A variety of helical filaments and fibers can be observed in the B7 phase, as shown in Fig. 10. The B7 phase is identified to be a polarization-modulated phase and the internal helical polarization modulation is responsible for the helix [15]. In contrast,

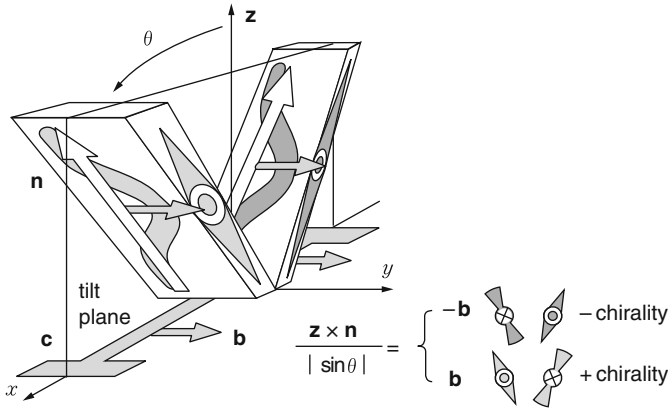
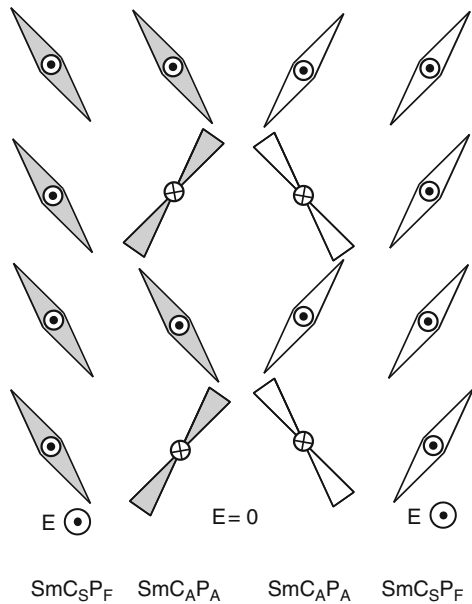


Fig. 8 Definition of layer chirality in the bent-core tilted smectic phase

Fig. 9 Two chiral forms of the $SmC_A P_A$ phase (gray and white molecules). By applying an upward field, transition to $SmC_S P_F$ occurs via opposite rotations of the optical axis



any helical structures cannot be seen optically in the B4 phase, although two chiral domains are clearly observable by decrossing polarizers (see Fig. 2). At the first stage, this phase was ascribed to a kind of twist-grain-boundary phase, since it is chiral and the layer X-ray diffraction gives a ring pattern [46]. Recently using freeze-fractured transmission electron microscopy (FFTEM), Hough et al. unambiguously observed helical nanofilaments, as shown in Fig. 11 [14]. In this case, tilt of bent-core molecules with respect to the layer is also believed to be a cause of chiral (helical) structure. As will be mentioned in Sect. 3.5, the chiral domains consisting of helical nanofilaments give remarkable optical activity, and also serve as a template for helical superstructure, when rod-shaped nematic LCs are mixed with B4 [9].

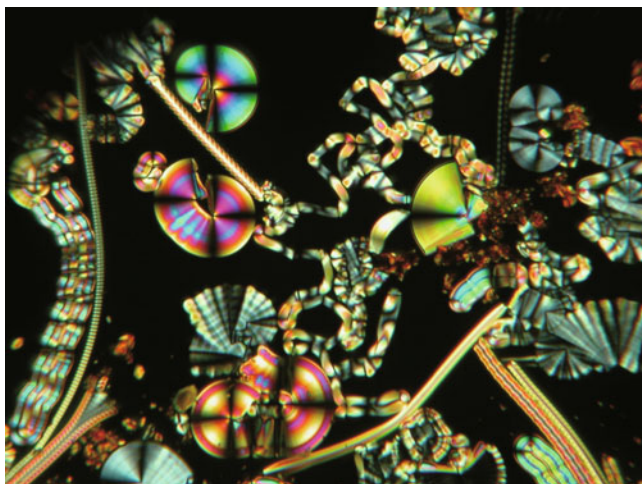


Fig. 10 Texture of the B7 phase. Variety of helical fibrils can be observed

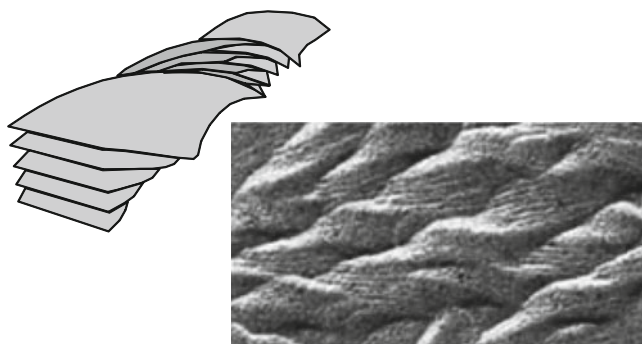


Fig. 11 Model structure of a helical nanofilament (*upper left*) and FFTEM image (*lower right*) of the B4 phase [14]

In addition, the so-called dark conglomerate (DC) phase [16] shows strong chirality, although this phase is optically isotropic and only has a short-range fully translational and orientational order. These short-range orders originate from deformed layer structures, i.e., sponge-like organization of molecules, which make the phase low birefringent. However, long-range chirality transfer occurs by chiral coupling among tilt, polarization, and the layer deformation as in the B2 phase. Here layer continuity plays a key role for the long-range chirality transfer. The DC phase usually exhibits chiral resolution of several hundred microns. However, the achiral domain is also possible like in the B2 phase [47]. Because of fluidity and polarity, this phase is transformed to the B2 phase by applying a sufficiently strong electric field. In some compounds, either DC or B7 phase emerges due to sample thermal history.

3.3 Spontaneous Deracemization in Rod-Shaped Mesogens

In 2005, Kajitani et al. reported a striking observation: rod shaped mesogens show spontaneous deracemization using the same ester molecules shown in Fig. 6 [48]. Soon after this report, however, Walba et al. claimed that the observation must be a surface effect [49]. We repeated the same experiments as they did and concluded that spontaneous deracemization does not occur in this particular compound, but may occur in other compounds. However, since ester molecules seem to have some particular feature in chirality as described in Sect. 2.4, we continued to search for compounds showing chiral resolution and found two homologous series of achiral ester molecules that do [50].

The molecules used are shown in Fig. 12: two types of simple rod-shaped molecules possessing alkyl and semifluoroalkyl terminated phenylene ester structures. These molecules show conventional smectic phases such as SmA and SmB. Figure 13 shows a typical circular dichroism (CD) spectrum, which was observed in different positions of a sandwich cell of 1–8 at room temperature [50]. The repeated measurements at different positions gave positive and negative CD signals in equal probabilities. We also confirmed that the introduction of a small amount of chiral dopant biases the CD signals to either the positive or the negative side depending on the handedness of the chiral molecules. The temperature dependence of the CD measurements indicated that no CD signals were observed in the isotropic and SmA phase. The CD signals started to appear in the SmB phase and

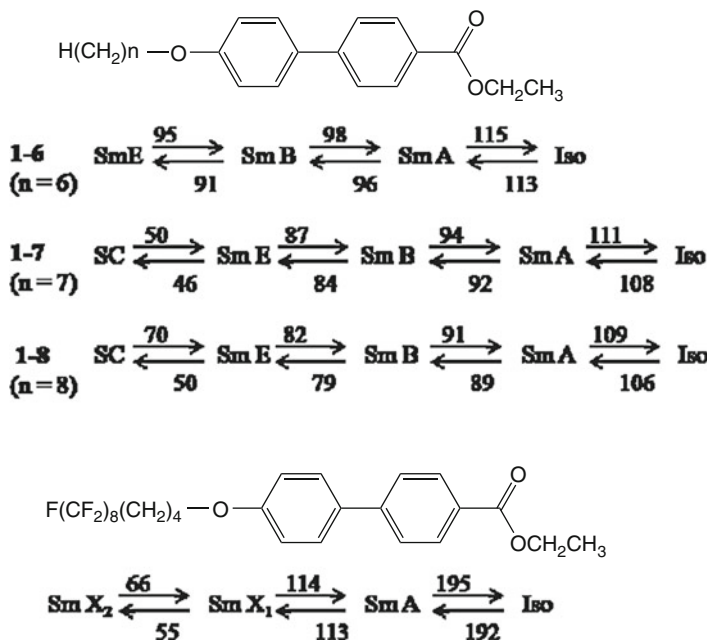
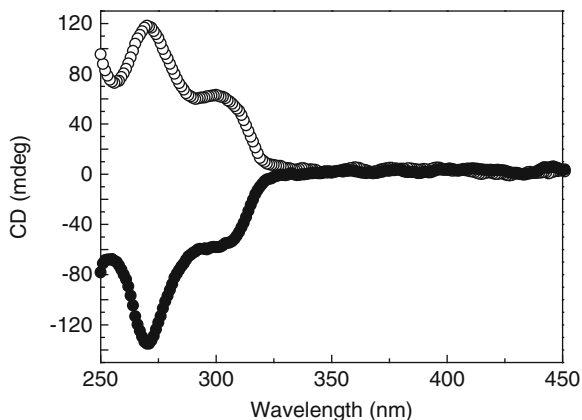


Fig. 12 Chemical structures of ester molecules used for deracemization experiment [50]

Fig. 13 CD spectra in two different positions of sample 1–8 [50]



increased with lowering temperature through the SmE and soft crystal (SC) phases. The negligible effect of birefringence was confirmed by rotating the cell about the cell surface normal.

To remove the possible surface effect on chirality we also performed CD measurement using free-standing films. We observed almost identical CD spectra to those observed in sandwiched cells. The CD experiments were also made using nonester pyrimidine derivatives. Although these compounds show different phase sequences, we observed no meaningful CD signal. Thus we can conclude that ester moieties in the rod-shaped LCs play a significant role in the spontaneous chiral induction process. Actually, according to VCD measurements, we always observed strong VCD signals at 1,291 and 1,709 cm^{-1} , which correspond to ester C–O and C=O, respectively. In order to find the stable conformations, density functional theory calculations were performed. Then potential barriers between chiral conformers were calculated by changing the dihedral angle at the biphenyl linkage between the two aromatic rings. The potential barriers for interconversion of the enantiomers is found to be ~ 1.76 kcal/mol, higher than the thermal energy (~ 0.6 kcal/mol) at room temperature. Hence both conformers can take chiral forms that are responsible for the enantiomeric separation process in the present systems.

Theory suggests the induced formation of chirality from achiral molecules is caused by a collective tilting from the molecular layer normal of the superstructure formed from dimerically interacting molecules [51]. Since ester molecules are bent at the ester carbonyl group [52] and are chiral, this chiral bent conformation appears to be an important feature that gives rise to the chiral properties of LCs. Recently, Yan et al. succeeded in simulating the formation of self-assembled chiral superstructures by using rigid achiral bent-shaped molecules [33]. The proposed superstructure, i.e., one molecular arm is parallel to the layer normal and the other arm is tilted from the normal, is similar to our system. It is important to note that chiral dopant is necessary to form chiral structure in Yan's simulation, but the ester molecules themselves act as chiral molecules when they are aggregated in our system.

3.4 Spontaneous Deracemization in Disk-Shaped Mesogens

Extensive studies have been conducted to investigate the formation of chiral columns or helical superstructures in chiral and nonchiral disk- [53], star- [54, 55], and board-shaped [56] molecules. However, spontaneous deracemization has never been unambiguously demonstrated in discotic columnar phases consisting of nonchiral or racemic molecules. We recently observed clear evidence showing chiral resolution in a disk-like molecules with a dibenzo[*g,p*]chrysene core [57].

The molecule used exhibits only one columnar mesophase. The compound is paste-like at room temperature and is not a crystalline phase. Although the chemical structure shown in Fig. 14 is apparently flat, the most stable conformations are twisted ones because of the steric repulsion between hydrogen atoms by quantum chemical calculations, as shown in Fig. 15. The top and side views of the molecule are shown in Fig. 15a, b, respectively. The modeled side view is also shown by solid and broken lines representing the proximal and distal wings, respectively. Calculated relative potential energy (Fig. 15c) indicates the existence of a metastable state with a conformation shown in the figure. The chiral exchange of this aromatic core occurs by two steps through an achiral metastable state. The energy barrier between chiral conformations (41.1 kJ/mol) is much greater than the thermal energy at room temperature. However, it is still too small to isolate the chiral conformation, so this aromatic core is still macroscopically achiral.

For CD measurements, we fabricated thin (500 nm) cells. By slowly cooling such cells from the isotropic phase, large single domains could be obtained. As shown in Fig. 16, CD peaks appear in a wavelength range corresponding to the absorption peaks attributable to an aromatic core. The sign of the CD signal changes randomly in repeated experiments after heating the cells to the isotropic phase. VCD measurements were also conducted. In addition to C–C stretching of an aromatic ring ($1,500\text{ cm}^{-1}$), strong signals were observed due to C=O stretching of an ester ($1,760\text{ cm}^{-1}$) and C–O–C stretching of an ester ($1,260$ and $1,150\text{ cm}^{-1}$). Thus a nonflat aromatic core is evident from the signal in C–C stretching. In addition, chiral transfer from the core to achiral terminal alkyl chains is clearly recognized.

For such deracemization to occur, formation of chirality must occur in two steps: (1) only molecules with the same chirality stack in one column and (2) only

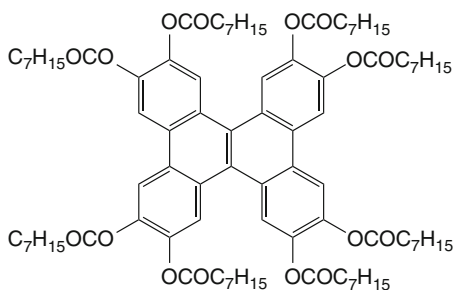


Fig. 14 Disk-like molecules with a dibenzo[*g,p*]chrysene core used for the deracemization experiment

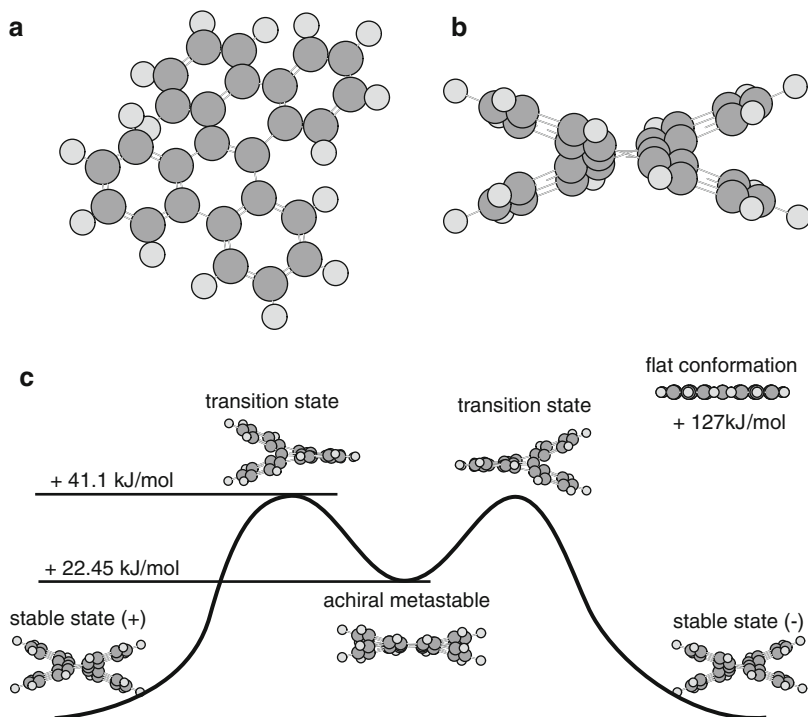


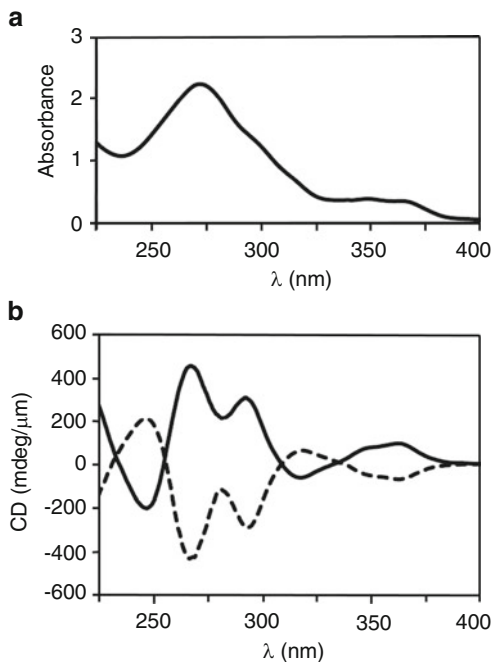
Fig. 15 (a) Top and (b) side views of the disk-shaped molecule. (c) Relative potential energy between two chiral structures via a metastable structure

columns with the same chirality are resolved into macroscopic chiral domains. Chiral column formation (1) is the result of close packing of chiral molecules with a twisted conformation. However, chiral domain formation (2) is not easy because of the existence of alkyl chains. It is important to note that molecules with longer ($-\text{OCOC}_{15}\text{H}_{31}$) terminal alkyl chains do not exhibit the deracemization phenomenon. Thus, rather shorter terminal chains are necessary so as not to block the chiral interactions between central column cores for macroscopic chiral domain formation.

3.5 *Enhanced Twisting Power by Doping B4 Phase with Rod-Like Molecules*

As nonchiral molecules enhance the chirality of chiral phases, as described in Sects. 2.1 and 2.4, the chirality of spontaneously resolved chiral domains can also be enhanced by adding nonchiral rod-shaped molecules. We introduce such an example observed in mixtures of bent- (P8-O-PIMB) and rod-shaped molecules

Fig. 16 (a) UV-vis absorption spectrum of the disk-shaped molecule. (b) CD spectra from two chiral conformers [57]



(5CB) [9]. The enhancement occurs in both chiral domains, although the dopant is nonchiral. The phase diagram with chemical structures of the two components are shown in Fig. 17. The B2 and B3 phases readily disappear by the introduction of a small amount of 5CB, and the B4 phase is stabilized. In the mixtures with more than 50 wt% 5CB, we observe a new phase transition at an almost constant temperature of 32 °C, corresponding to the Iso-N transition of 5CB. This transition point can be detectable by DSC [58] and texture observation, but not by X-ray analysis [59]. Based on the experimental fact of no layer structure changes, we can infer that P8-O-PIMB and 5CB molecules are nanosegregated. Namely helical nanofilaments are in the isotropic and nematic sea of 5CB in the B4 and lower phases, respectively. Hereafter we call these phases B4/Iso and B4/N phases, respectively.

In order to see how isotropic and nematic 5CBs behave, careful CD measurements were performed using thin cells, which makes accurate measurements possible in the UV absorption range. Because of different absorption wavelengths of P8-O-PIMB and 5CB molecules, we can even identify the origin of the CD signal. In the B4/Iso phase, the magnitude of the CD signal linearly decreases with increasing 5CB content. However, the situation drastically changes in the B4/N phase. Figure 18 shows CD intensity as a function of temperature in four mixtures. In the mixture with 30% 5CB, signal intensity monotonically and slightly increases with decreasing temperature. The increasing rate becomes slightly larger in the B4/N phase compared with the B4/Iso phase in the mixture with 50% 5CB, in which the transition from B4/N to B4/Iso is a supercritical point [58]. In the mixtures with 60 and 70% 5CB, we observe a remarkable increase in the

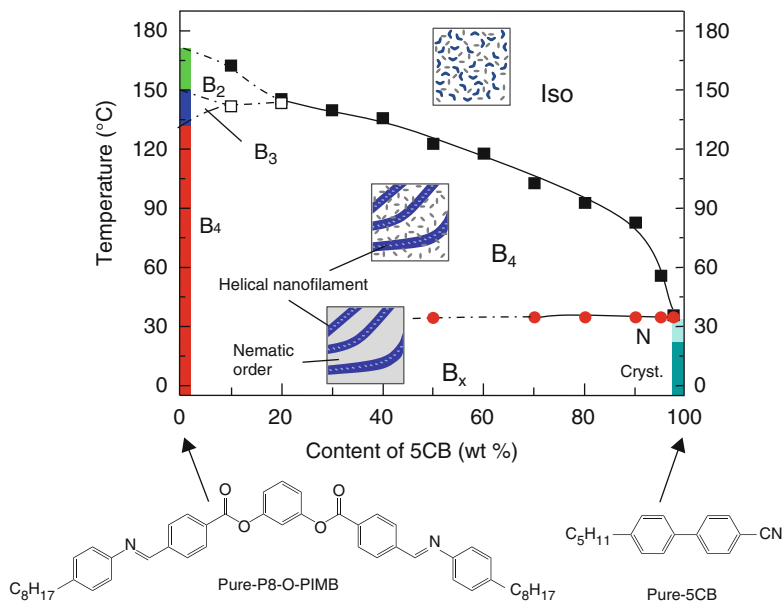
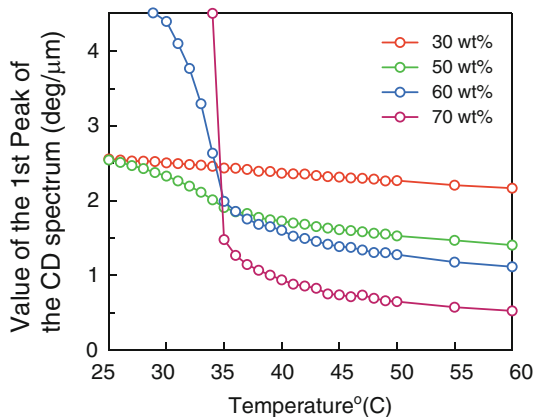


Fig. 17 Phase diagram of a binary mixture of bent- (P8-O-PIMB) and rod-shaped (5CB) molecules. Cartoon showing the phase structures are also shown. In the B₄/Iso and B₄/N phases, 5CB molecules are in the isotropic and nematic phases [9]

Fig. 18 CD intensity at the low energy CD peak as a function of temperature for mixtures of various mixing ratios. Note remarkable change in CD at the B₄/Iso and B₄/N phase boundary in the mixtures with large 5CB contents [9]



B₄/N phase. Particularly in 70% 5CB, the CD signal becomes undetectably high (more than 4°/μm) just below the B₄/Iso–B₄/N transition.

The following three possible models, as illustrated in Fig. 19, are suggested. We know P8-O-PIMB molecules form helical nanofilaments. If 5CB molecules align parallel to the grooves of the filaments, we can expect helical structure of 5CB shown in Fig. 19a, b. If we assume that nanofilaments align rather parallel to each other (Fig. 19a), 5CB molecules form a twisted nematic structure. But this is not always

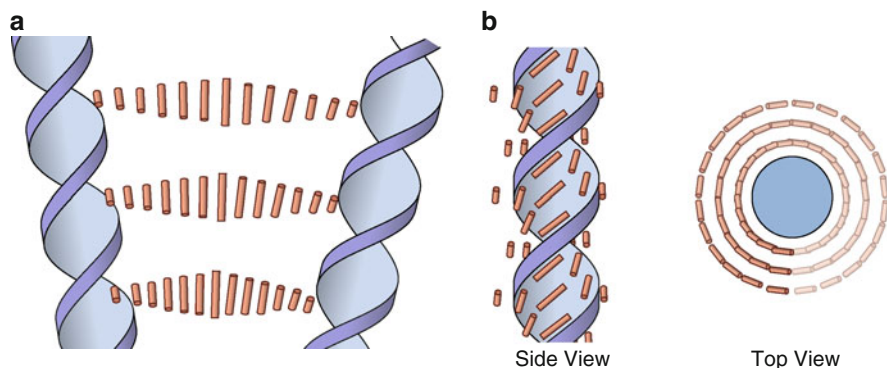


Fig. 19 Possible model to show enhanced optical activity by nonchiral 5CB molecules. (a) 5CB molecules form twisted nematic structure between helical nanofilaments. (b) 5CB molecules form superhelical structure around a helical nanofilament [9]

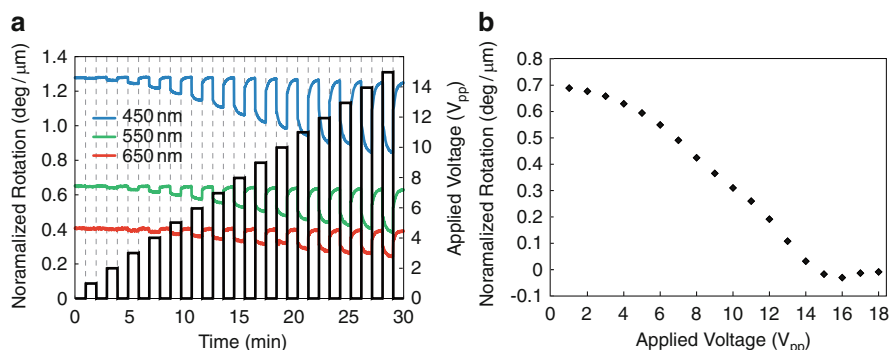


Fig. 20 (a) Performance of a device, which can control optical rotator power by applying elevated electric field. (b) Optical rotation as a function of electric field strength [60]

the case. If we consider an isolated nanofilament (Fig. 19b), 5CB molecules can form a superhelical structure around the nanofilament. Because of the long-range orientational order in the nematic phase, this superhelical structure grows very large. Another idea is that the helical nanofilaments act as chiral dopants in the nematic phase. In any event, the CD signal or optical activity increases sharply because of chiral structure formation of 5CB molecules in the B4/N phase.

This large optical activity can be used as a device with electric-field-controllable optical activity. The device performance using a mixture with 90% 5CB is shown in Fig. 20 [60]. By applying an electric field, 5CB molecules reorient toward the field direction, resulting in nonchiral N phase and rotatory power becoming almost zero. Here the contribution of the helical nanofilaments to the optical activity is very low in the transparent wavelength region.

3.6 Controlling Enantiomeric Excess by Chiral Stimuli

Spontaneous resolved two chiral domains are formed in equal probability. In other words, enantiomeric excess (ee) is zero. We now ask whether ee can be controlled or not. The answer is yes. Several methods used in bent-shaped mesogenic phases will be introduced. The direct method is of course an addition of chiral dopant. Actually this has been shown to be a viable method [6, 61]. Use of chiral surface is also effective [62]. By using polyimide with chiral side chains at both substrate surfaces, imbalance of two chiral domains (10% ee) has been achieved. Another method using macroscopic helical structure was demonstrated by Jakli et al. [63]. They used a nonchiral polymer network, which was formed in the N* phase. After the polymerization, N* compounds were washed out, then bent-core mesogens were introduced. Because of the polymer helical fibers, bent-core mesogen shows a chiral domain.

More effective methods without using any chiral molecular species were demonstrated. The first uses circularly polarized light (CPL) irradiation [21]. A large ee of almost 100% was induced during the cooling process from Sm_CA to a B4-like phase of a bent-core dimer (Fig. 21, top) under CPL irradiation. As shown in Fig. 21, a single chiral domain of almost 100% ee was obtained. By using right- and left-handed CPL irradiation, opposite chiral domains can be stabilized.

To confirm the importance of ester linkage for chiral formation, we conducted vibrational circular dichroism (VCD) measurements [64]. FT-IR spectrum of this molecule shows many C=O, O–C–O related peaks in addition to peaks of N=N and phenyl and CH₂ vibrational modes, as shown in Fig. 22a. It is noted that strong VCD signals are observed in C=O and O–C–O vibrations, as shown in Fig. 22b. This implies that ester linkage is strongly related to the chiral structure.

Another effective method without using chiral species is based on twisted nematic cell geometry [22]. The molecule used (Fig. 23, top) has the N phase above the B4-like phase, so that the conventional rubbing method can be used to obtain well aligned cells. Actually a good twisted nematic (TN) cell was obtained. After slowly cooling the TN cell to the B4-like phase, a large imbalance in two chiral domains was obtained. We examined the optical activity as a function of twist angle α using CD measurements. When $\alpha = 0^\circ$, we can easily observe two domains of elongated shape along the rubbing direction with equal areas. As shown in Fig. 23, CD intensity drastically increased between cells with $\alpha = 40^\circ$ and 60° . Above 60° , the CD is saturated. That means we have almost 100% ee in this condition, as is also clear by POM observation under decrossed polarizers. If we use opposite twist, the opposite chiral domain with 100% ee is obtained.

In this way, the above two methods are very effective to control ee and choose one of the chiral domains. It is noted that both methods use no chiral molecular species. Instead, CPL and twist cell geometry are used as chiral stimuli, which act as a symmetry-degeneracy-breaking field. This field triggers and accelerates a preferential formation of one of the two possible chiral conglomerates, which is fixed in a B4-like phase. The monochiral films obtained by achiral molecules open

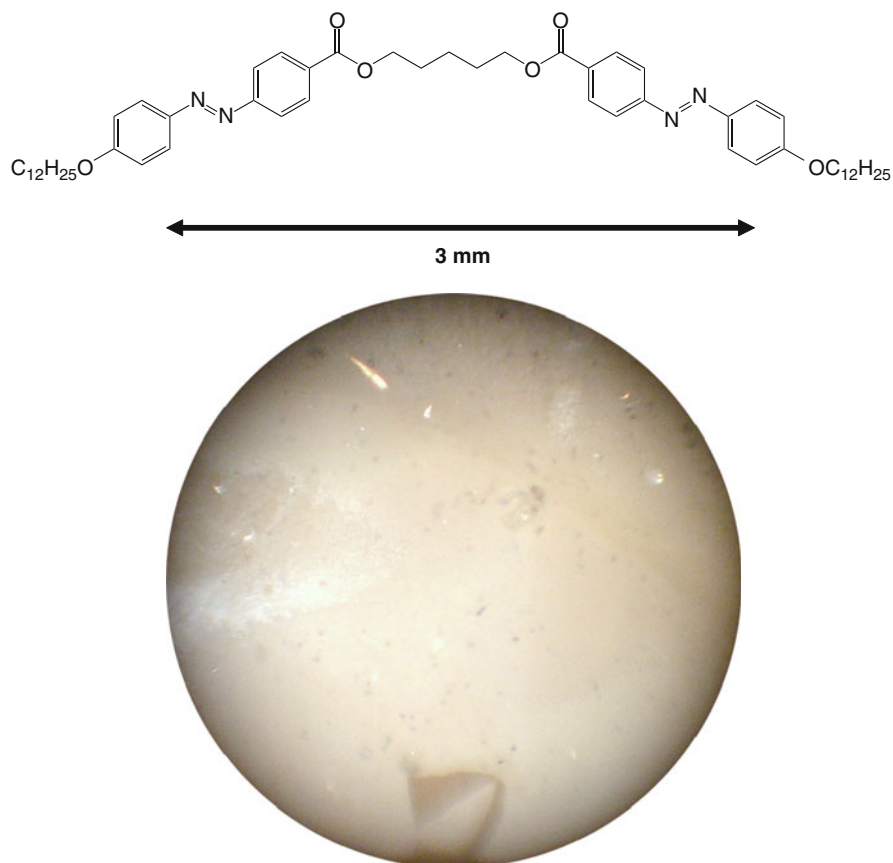


Fig. 21 Chirality control by circularly polarized light. The molecules used are bent-shaped twin dimer shown in the top, which has azo-linkages at both arms and shows SmC_A to B4-like phase. By CPL irradiation, almost 100% ee is obtained. In the photo taken between decrossed polarizers, only a very tiny darker domain can be seen in the lower region in a 3-mm domain [21]

up the possibility for a wide range of practical applications such as chiral separation and enzyme adsorption through chiral molecular recognition.

4 Conclusions

In this chapter, chirality-related topics driven by achiral molecules are described. Such studies have been accelerated by the revolutionary observation of chirality in nonchiral BSMs. They include spontaneous chiral resolution in several banana phases, and enhanced chirality by doping chiral host with achiral BSMs. These works triggered similar works in rod-shaped and even disk-shaped LCs, as

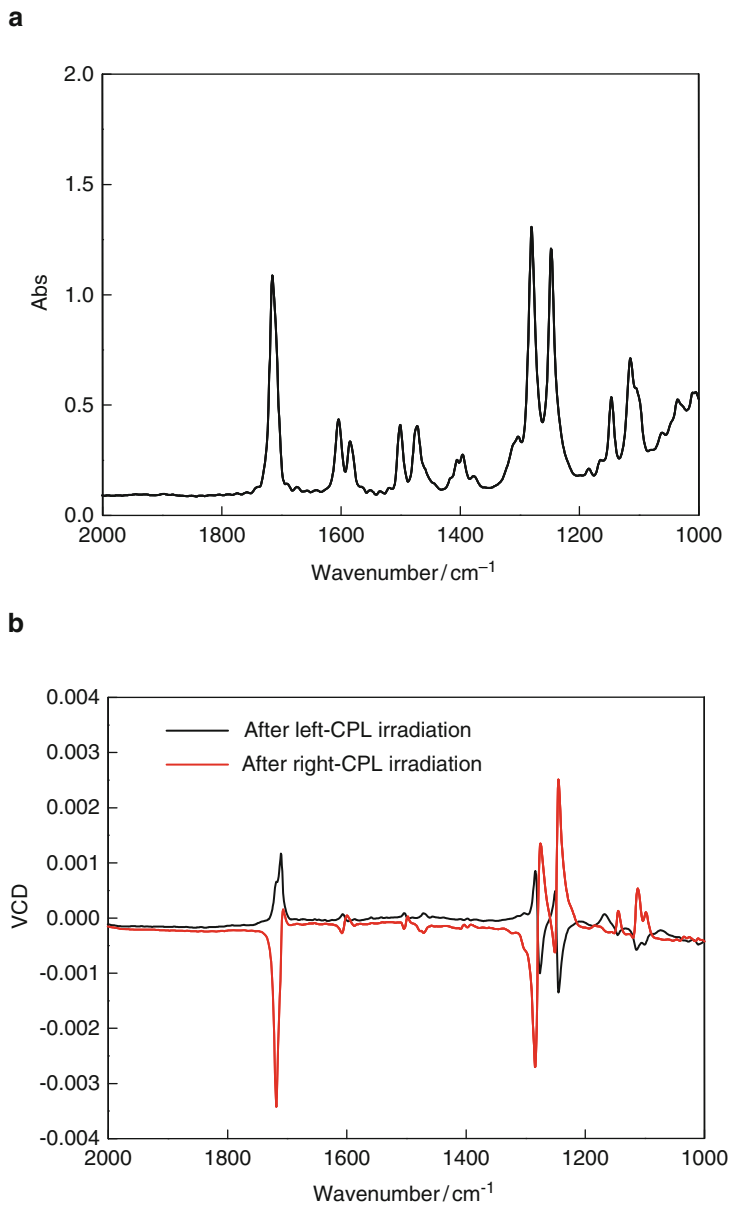


Fig. 22 (a) IR absorption spectra of a bent-shaped twin dimer. (b) Vibrational CD spectra in two chiral domains stabilized by right- and left-CPL [64]

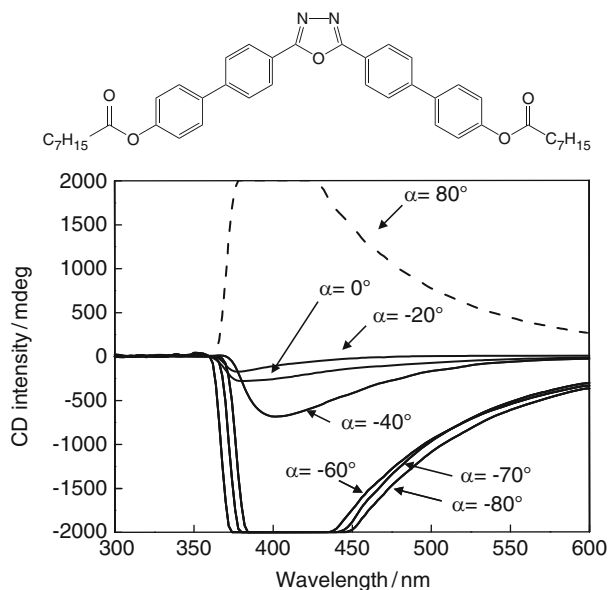


Fig. 23 Controlled chirality by twisted nematic geometry. (a) Chemical structure of the molecule used for the experiment. The molecule shows N and B4-like phases. (b) CD spectra for cells with various twisting angles [22]

mentioned in the text. When achiral bent-shaped molecules form both conglomerates, achiral rod-shaped molecules enhance chirality in both conglomerates. This means that achiral molecules act as chiral molecules corresponding to chiral circumstances.

Many other reports have been published, demonstrating spontaneous deracemization in N [65, 66], SmA [67], and other phases [68]. In most cases the existence of conglomerates was concluded by direct chiral domain observations by decrossing polarizers. To confirm deracemization unambiguously, additional methods have to be applied. In some cases, an electric field promotes deracemization [69]. Because of time and ability, I have particularly focused on my own works. I am sure that there are many other important works which could not even be cited in this chapter. I hope to write again on the subject, next time including comprehensive works related to chirality in LCs.

References

1. Pasteur L (1848) Recherches sur les relations qui peuvent exister entre la forme cristalline et la composition chimique, et le sens de la polarisation rotatoire. *Ann Chim Phys* 24:442–459
2. Kitzerow H-S, Bahr C (2001) Chirality in liquid crystals. Springer, New York

3. Thisayukta J, Niwano H, Takezoe H, Watanabe J (2002) Enhancement of twisting power in the chiral nematic phase by introducing achiral banana-shaped molecules. *J Am Chem Soc* 124:3354–3358
4. Gorecka E, Cepic M, Mieczkowski J, Nakata M, Takezoe H, Zeks B (2003) Enhanced chirality by adding achiral molecules into the chiral system. *Phys Rev E* 67:061794-1-5
5. Choi S-W, Fukuda K, Nakahara S, Kishikawa K, Takanishi Y, Ishikawa K, Watanabe J, Takezoe H (2006) Amplification of twisting power in chiral mesophase by introducing achiral rod-like compound with ester group. *Chem Lett* 35:896–897
6. Thisayukta J, Nakayama Y, Kawauchi S, Takezoe H, Watanabe J (2000) Distinct formation of a chiral smectic phase in achiral banana-shaped molecules with a central core based on a 2,7-dihydroxynaphthalene unit. *J Am Chem Soc* 122:7441–7448
7. Jeong HS, Tanaka S, Yoon DK, Choi S-W, Kim YH, Kawauchi S, Araoka F, Takezoe H, Jung H-T (2009) Spontaneous chirality induction and enantiomer separation in liquid crystals composed of achiral rod-shaped 4-arylbenzoate esters. *J Am Chem Soc* 131:15055–15060
8. Nagayama H, Varshney SK, Goto M, Araoka F, Prasad V, Takezoe H (2010) Spontaneous deracemization of disk-like molecules in the columnar phase. *Angew Chem Int Ed* 49:445–448
9. Otani T, Araoka F, Ishikawa K, Takezoe H (2009) Enhanced optical activity by achiral rod-like molecules nano-segregated in the B₄ structure of achiral bent-core molecules. *J Am Chem Soc* 131:12368–12372
10. Link DR, Natale G, Shao R, MacLennan JE, Clark NA, Korblova E, Walba DM (1997) Spontaneous formation of macroscopic chiral domains in fluid smectic phase of achiral molecules. *Science* 278:1924–1927
11. Takezoe H, Takanishi Y (2006) Bent-core liquid crystals: their mysterious and attractive world. *Jpn J Appl Phys* 45:597–625
12. Heppke G, Parghi DD, Sawade H (2000) Novel sulphur-containing banana-shaped liquid crystal molecules. *Liq Cryst* 27:313–320
13. Pelzl G, Diele S, Jakli A, Lischka Ch, Wirth I, Weissflog W (1999) Helical superstructures in a novel smectic mesophase formed by achiral banana-shaped molecules. *Liq Cryst* 26:135–139
14. Hough E, Jung HT, Kruerke D, Heberling MS, Nakata M, Jones CD, Chen D, Link DR, Zasadzinski J, Heppke G, Rabe JP, Stocker W, Korblova E, Walba DM, Glaser MA, Clark NA (2009) Helical nanofilament phases. *Science* 325:456–460
15. Coleman DA, Femsler J, Chattham N, Nakata M, Takanishi Y, Korblova E, Link DR, Shao R-F, Jang WG, MacLennan JE, Mondainn-Monval O, Boyer C, Weissflog W, Pelzl G, Chien L-C, Zasadzinski J, Watanabe J, Walba DM, Takezoe H, Clark NA (2003) Polarization-modulated smectic liquid crystal phases. *Science* 301:1204–1211
16. Hough LE, Spannuth M, Nakata M, Coleman DA, Jones CD, Dantlgraber G, Tschierske C, Watanabe J, Korblova E, Walba DM, MacLennan JE, Glaser MA, Clark NA (2009) Chiral isotropic liquids from achiral molecules. *Science* 325:452–456
17. Zennyoji M, Takanishi Y, Ishikawa K, Thisayukta J, Watanabe J, Takezoe H (2001) Molecular chirality due to twisted conformation in a bent-shaped liquid crystal studied by polarized FT-IR spectroscopy. *Mol Cryst Liq Cryst* 366:2545–2553
18. Kurosu H, Kawasaki M, Hirose M, Yamada M, Kang S, Thisayukta J, Sone M, Takezoe H (2004) Solid-state C-13 NMR study of chiral twisted conformation attributable to chirality in smectic phases of achiral banana-shaped molecules. *J Phys Chem A* 108:4674–4678
19. Xu JD, Dong RY, Domenici V, Fodor-Csorba K, Veracini CA (2006) C-13 and H-2 NMR study of structure and dynamics in banana B-2 phase of a bent-core mesogen. *J Phys Chem B* 110:9434–9441
20. Niwano H, Nakata M, Thisayukta J, Link DR, Takezoe H, Watanabe J (2004) Chiral memory on transition between the B₂ and B₄ phases in achiral banana-shaped molecular system. *J Phys Chem B* 108:14889–14896
21. Choi S-W, Izumi T, Hoshino Y, Takanishi Y, Ishikawa K, Watanabe J, Takezoe H (2006) Circular-polarization-induced enantiomeric excess in an achiral bent-shaped liquid crystal. *Angew Chem Int Ed* 45:1382–1385

22. Choi SW, Kang S, Takanishi Y, Ishikawa K, Watanabe J, Takezoe H (2006) Intrinsic chirality in a bent-core mesogen induced by extrinsic chiral structures. *Angew Chem Int Ed* 45:6503–6506
23. Gorecka E, Nakata M, Mieczkowski J, Takanishi Y, Ishikawa K, Watanabe J, Takezoe H, Eichhorn SH, Swager TM (2000) Induced antiferroelectric smectic-CA* phase by doping ferroelectric-C* phase with bent-shaped molecules. *Phys Rev Lett* 85:2526–2529
24. Earl DJ, Osipov MA, Takezoe H, Takanishi Y, Wilson MR (2005) Induced and spontaneous deracemization in bent-core liquid crystal phases and in other phases doped with bent-core molecules. *Phys Rev E* 71:021706-1-11
25. Sathyanarayana P, Mathew M, Sastry VSS, Kundu B, Le KV, Takezoe H, Dhara S (2010) Splay bend elasticity of a bent-core nematic liquid crystal. *Phys Rev E (Rapid)* 81:010702(R)-1-4
26. Nakata M, Takanishi Y, Watanabe J, Takezoe H (2003) Blue phases induced by doping chiral nematic liquid crystals with non-chiral molecules. *Phys Rev E* 68:041710-1-6
27. Alexander GP, Yeomans JM (2006) Stabilizing the blue phases. *Phys Rev E* 74:061706-1-9
28. Hur S-T, Gim M-J, Yoo H-J, Choi S-W, Takezoe H (2011) Enhanced thermal stability of liquid crystalline blue phase I with decreasing bend and splay elastic constant ratio K_{33}/K_{11} . *Soft Matter*, in press (DOI: 10.1039/c1sm06046e)
29. Taushanoff S, Le KV, Williams J, Twieg RJ, Sadashiva BK, Takezoe H, Jáklí A (2010) Stable amorphous blue phase of bent-core nematic liquid crystals doped with a chiral material. *J Mater Chem* 20:5893–5898
30. Le KV, Aya S, Sasaki Y, Choi H, Araoka F, Ema K, Mieczkowski J, Jakli A, Ishikawa K, Takezoe H (2011) Liquid crystalline amorphous blue phase and its large electrooptical Kerr effect. *J Mater Chem* 21:2855–2857
31. Lee M, Hur S-T, Higuchi H, Song K, Choi S-W, Kikuchi H (2010) Liquid crystalline blue phase I observed for a bent-core molecule and its electro-optical performance. *J Mater Chem* 20:5813–5816
32. Kundu B, Pratibha R, Madhusudana NV (2007) Anomalous temperature dependence of elastic constants in the nematic phase of binary mixtures made of rodlike and bent-core molecules. *Phys Rev Lett* 99:247802-1-4
33. Kawauchi S, Choi S-W, Fukuda K, Kishikawa K, Watanabe J, Takezoe H (2007) Why achiral rodlike compound with ester group amplifies chiral power in chiral mesophase. *Chem Lett* 36:750–751
34. Yan F, Hixson CA, Earl DJ (2008) Self-assembled chiral superstructures composed of rigid achiral molecules and molecular scale chiral induction by dopants. *Phys Rev Lett* 101:157801-1-4
35. Perez-Garcia L, Amabilino DB (2002) Spontaneous resolution under supramolecular control. *Chem Soc Rev* 31:342–356
36. Weissbuch I, Kuzmenko I, Berfeld M, Leiserowitz L, Lahav M (2000) Stereochemical studies on chiral systems in two dimensions. *J Phys Org Chem* 13:426–434
37. De Feyter S, Gesquiere A, Wurst K, Amabilino DB, Veciana J, De Schryver FC (2001) Homo- and heterochiral supramolecular tapes from achiral, enantiopure, and racemic promesogenic formamidst: expression of molecular chirality in two and three dimensions. *Angew Chem Int Ed* 40:3217–3220
38. Huang T, Hu Z, Zhao A, Wang H, Wang B, Yang J, Hou JG (2007) Quasi chiral phase separation in a two-dimensional orientationally disordered system: 6-nitrospiropyran on Au (111). *J Am Chem Soc* 129:3857–3862
39. Smith DPE (1991) Defects in alkylcyanobiphenyl molecular-crystals studied by scanning tunneling microscopy. *J Vac Sci Technol B* 9:1119–1125
40. Charra F, Cousty J (1998) Surface-induced chirality in a self-assembled monolayer of discotic liquid crystal. *Phys Rev Lett* 80:1682–1685
41. Walba DM, Stevens F, Clark NA, Parks DC (1996) Detecting molecular chirality by scanning tunneling microscopy. *Acc Chem Res* 29:591–597

42. Takanishi Y, Takezoe H, Suzuki Y, Kobayashi I, Yajima T, Terada M, Mikami K (1999) Spontaneous enantiomeric resolution in a fluid smectic phase of a racemate. *Angew Chem Int Ed* 38:2354–2356
43. Cowling SJ, Hall AW, Goodby JW (2005) Electro-optic response in a racemic smectic C liquid crystal. *Adv Mater* 17:1077–1080
44. Walba DM, Dyer DJ, Rego JA, Tiessink-Trotter J, Shao R, Clark NA (2004) Chirality detection with FLCs – a comment. *Ferroelectrics* 309:121–124
45. Niori T, Sekine T, Watanabe J, Takezoe H (1996) Distinct ferroelectric smectic liquid crystals consisting of banana shaped achiral molecules. *J Mater Chem* 6:1231–1233
46. Thisayukta J, Takezoe H, Watanabe J (2001) Study on helical structure of the B4 phase formed from achiral banana-shaped molecule. *Jpn J Appl Phys* 40:3277–3287
47. Keith C, Dantlgraber G, Reddy RA, Baumeister U, Prehm M, Hahn H, Lang H, Tschierske C (2007) The influence of shape and size of silyl units on the properties of bent-core liquid crystals – from dimmers via oligomers and dendrimers to polymers. *J Mater Chem* 17:3796–3805
48. Kajitani T, Masu H, Kohmoto S, Yamamoto M, Yamaguchi K, Kishikawa K (2005) Generation of a chiral mesophase by achiral molecules: absolute chiral induction in the smectic C phase of 4-octyloxyphenyl 4-octyloxybenzoate. *J Am Chem Soc* 127:1124–1125
49. Walba DM, Korblova E, Huang C-C, Shao R, Nakata M, Clark NA (2006) Reflection symmetry breaking in achiral rod-shaped smectic liquid crystals? *J Am Chem Soc* 128:5318–5319
50. Jeong HS, Tanaka S, Yoon DK, Choi S-W, Kim YH, Kawauchi S, Araoka F, Takezoe H, Jung H-T (2006) Spontaneous chirality induction and enantiomer separation in liquid crystals composed of achiral rod-shaped 4-arylbenzoate esters. *J Am Chem Soc* 131:15055–15060
51. Pang JH, Clark NA (1994) Observation of a chiral-symmetry-breaking twist-bend instability in achiral freely suspended liquid-crystal films. *Phys Rev Lett* 73:2332–2335
52. Miyachi K, Matsushima J, Ishikawa K, Takezoe H, Fukuda A (1995) Spontaneous polarization parallel to the tilt plane in the antiferroelectric chiral smectic-C_A phase of liquid-crystals as observed by polarized infrared-spectroscopy. *Phys Rev E* 52:R2153–R2156
53. Vera F, Serrano JL, Sierra T (2009) Twists in mesomorphic columnar supramolecular assemblies. *Chem Soc Rev* 38:781–796
54. Lehmann M, Jahr M, Donnio B, Graf R, Gemming S, Popov I (2008) Star-shaped oligobenzoates: non-conventional mesogens forming columnar helical mesophases. *Chem Eur J* 14:3562–3576
55. Lehmann M, Jahr M, Grozema FC, Abellon RD, Siebbeles LDA, Muller M (2008) Columnar mesophases with 3D order from new functional nonconventional star-shaped mesogens. *Adv Mater* 20:4414–4418
56. Barbera J, Cavero E, Lehmann M, Serrano J-L, Sierra T, Vazquez JT (2003) Supramolecular helical stacking of metallomesogens derived from enantiopure and racemic polycatenar oxazolines. *J Am Chem Soc* 125:4527–4533
57. Nagayama H, Varshney SK, Goto M, Araoka F, Ishikawa K (2010) Spontaneous deracemization of disc-like molecules in the columnar phase. *Angew Chem Int Ed* 48:445–448
58. Takekoshi K, Ema K, Yao H, Takanishi Y, Watanabe J, Takezoe H (2006) Appearance of a liquid crystalline nematic-isotropic critical point in a mixture system of rod- and bent-shaped molecules. *Phys Rev Lett* 97:197801-1-4
59. Takanishi Y, Shin GJ, Jung JC, Choi S-W, Ishikawa K, Watanabe J, Takezoe H, Toledano P (2005) Observation of very large chiral domains in a liquid crystal phase formed by mixtures of achiral bent-core and rod molecules. *J Mater Chem* 15:4020–4024
60. Araoka F, Sugiyama G, Ishikawa K, Takezoe H (2011) Electric-field controllable optical activity in the nano-segregated system composed of rod- and bent-core liquid crystals. *Opt Mater Exp* 1:27–35
61. Thisayukta J, Niwano H, Takezoe H, Watanabe J (2001) Effect of chiral dopant on a helical Sm1 phase of banana-shaped N-n-O-PIMB molecules. *J Mater Chem* 11:2717–2721

62. Shiromo K, Sahade DA, Oda T, Nihira T, Takanishi Y, Ishikawa K, Takezoe H (2005) Finite enantiomeric excess nucleated in an achiral banana mesogen by chiral alignment surfaces. *Angew Chem Int Ed* 44:1948–1951
63. Jakli A, Nair GG, Lee CK, Su R, Chen LC (2001) Macroscopic chirality of a liquid crystal formed nonchiral molecules. *Phys Rev E* 63:061710-1-4.
64. Choi S-W, Kawauchi S, Tanaka S, Watanabe J, Takezoe H (2007) Vibrational circular dichroism spectroscopic study on circularly polarized light-induced chiral domains in the B4 phase of a bent mesogen. *Chem Lett* 36:1018–1019
65. Gortz V, Goodby JW (2005) Enantioselective segregation in achiral nematic liquid crystals. *Chem Commun* 2005:3262–3264
66. Prasang C, Whitwood AC, Bruce DW (2008) Spontaneous symmetry-breaking in halogen-bonded, bent-core liquid crystals: observation of a chemically driven Iso-N-N* phase sequence. *Chem Commun* 2008:2137–2139
67. Guo L, Dhara S, Sadashiba BK, Radhika S, Pratibha R, Shimbo Y, Araoka F, Ishikawa K, Takezoe H (2010) Polar switching in the smectic-A_dP_A phase composed of asymmetric bent-core molecules. *Phys Rev E* 81:011703-1-6
68. Miyake I, Takanishi Y, Rao NVS, Kr M, Ishikawa K, Takezoe H (2005) Novel chiral filament in an achiral W-shaped liquid crystalline compound. *J Mater Chem* 15:4688–4694
69. Kane A, Shao R-F, MacLennan JE, Wang L, Walba DM, Clark NA (2007) Electric-field-driven deracemization. *ChemPhysChem* 8:170–174

Nanoparticles in Liquid Crystals and Liquid Crystalline Nanoparticles

Oana Stamatoiu, Javad Mirzaei, Xiang Feng, and Torsten Hegmann

Abstract Combinations of liquid crystals and materials with unique features as well as properties at the nanoscale are reviewed. Particular attention is paid to recent developments, i.e., since 2007, in areas ranging from liquid crystal-nanoparticle dispersions to nanomaterials forming liquid crystalline phases after surface modification with mesogenic or promesogenic moieties. Experimental and synthetic approaches are summarized, design strategies compared, and potential as well as existing applications discussed. Finally, a critical outlook into the future of this fascinating field of liquid crystal research is provided.

Keywords Carbon nanotubes · Liquid crystals · Nanoclay · Nanocomposites · Nanoparticles · Nanorods · Self-assembly

Contents

1	Introduction	332
1.1	Synopsis	332
1.2	Nanomaterials: Critical Aspects Regarding Synthesis, Manipulation and Characterization	333
2	Nanoparticle-Doped Liquid Crystal Phases	347
2.1	Zero-Dimensional Nanoparticle Additives	347
2.2	One-Dimensional Nanoparticle Additives: Nanorods and Nanotubes	363
2.3	Two-Dimensional Nanoparticle Additives: Nanoclay	370
3	Liquid Crystalline Nanoparticles	371
4	Conclusion and Future Outlook	378
	References	380

1 Introduction

1.1 Synopsis

Nanomaterials are commonly defined as materials with morphological features on the nanoscale (commonly below 100 nm in one, two, or all three dimensions), but a more precise definition would limit the scope to only those materials showing unique properties different from individual atoms or molecules as well as the bulk as a result of their nanoscale dimensions.

Nanomaterials have revolutionized many fields of research such as engineering, physics, medicine, and chemistry, to name a few. The sheer endless variety of readily available, and nowadays almost routinely discovered, new nanomaterials with compositions featuring the majority of elements in the periodic table are the focus of many original research programs or already used in practical applications in areas as diverse as drug delivery, biomedical imaging, catalysis, functional coatings, optoelectronics, photovoltaic devices, and many other functional composites and blends. It is thus no surprise that many nanomaterials differing in size, shape, core material, and coating have found an entrance into the field of liquid crystals; from very fundamental studies on interactions of nanoparticles with liquid crystal phases to liquid crystal template syntheses of nanomaterials to nanoparticles as dopants for liquid crystals used in electro-optic devices.

Some fundamental aspects of liquid crystal nanoscience have already been summarized in earlier reviews, covering research published prior to 2007 [1, 2]. The current review will primarily focus on recent developments in the field dealing with the effects of nanomaterial dopants in liquid crystalline phases as well as with liquid crystalline nanomaterials (i.e., with the self-assembly of nanomaterials into ordered, yet fluid liquid crystalline superstructures) largely facilitated by the “decoration” or functionalization of nanomaterials with mesogenic (liquid crystalline) or pro-mesogenic units (usually, but not exclusively rigid rod- or disc-like structural motifs resembling common liquid crystal moieties). The main interest of the first research area, i.e., nanomaterials as dopants, lies with the manipulation and improvement of distinctive optical and electro-optic characteristics of liquid crystals used in optical device and display applications as well as the creation of metamaterials [3–7], for example for the use as negative refractive index materials. The second area of intensive research, i.e., liquid crystalline nanomaterials, is very attractive from the viewpoint of designing functional nanomaterials that can be aligned, manipulated, and reoriented by external stimuli such as temperature, light, electric or magnetic fields like common organic liquid crystals. The self-assembly of functional nanomaterials is often described as an important cornerstone of nanotechnology success [8–31]. A combination of the unique properties of materials at the nanoscale with the mobility and ordering (at different length scales and dimensions) of the liquid crystalline state would allow one to achieve this laudable goal. Potential benefits include such possibilities as self-healing of defects in macroscopic arrays (using the fluidity of liquid crystal

phases) and using well-established large-scale industrial manufacturing concepts, for example, for the production of large-panel liquid crystal displays (LCDs) [32–35].

At first, however, this review will provide the reader with a critical overview over the most commonly used nanomaterials. The emphasis here will be particularly on those aspects of their synthesis, manipulation, and characterization that are of significant importance for their use as dopants in liquid crystalline phases or as precursors for the formation of liquid crystalline superstructures including size and size-distribution, shape, chemical purity, post-synthesis surface modifications, stability of capping monolayers, and overall thermal as well as chemical stability.

1.2 Nanomaterials: Critical Aspects Regarding Synthesis, Manipulation and Characterization

The simplest way to classify nanomaterials used in combination with liquid crystal materials or the liquid crystalline state is by using their shape. Three “shape families” of nanomaterials have emerged as the most popular, and sorted from the highest to the lowest frequency of appearance in published studies; these are zero-dimensional (quasi-spherical) nanoparticles, one-dimensional (rod or wire-like) nanomaterials such as nanorods, nanotubes, or nanowires, and two-dimensional (disc-like) nanomaterials such as nanosheets, nanoplatelets, or nanodiscs.

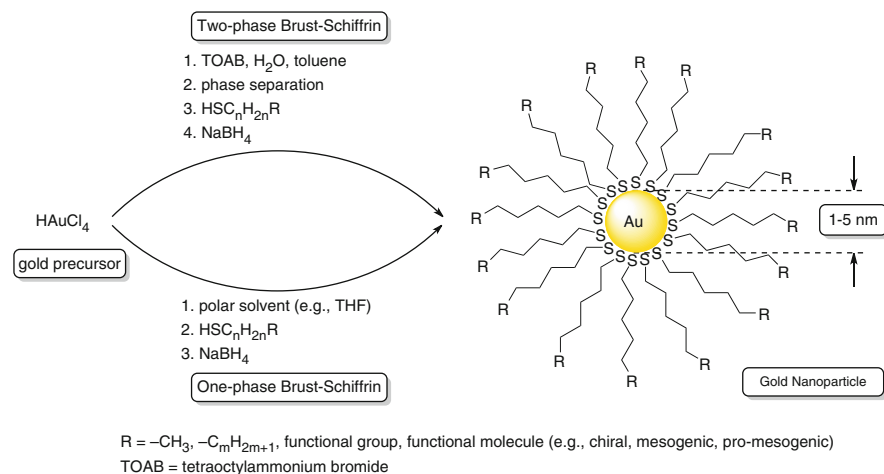
The aforementioned frequency of the use of these nanomaterial shapes is best attributed to two factors: (1) the ease with which these nanoparticle shapes can be synthesized in the laboratory and (2) the availability of these nanomaterials from commercial sources. It cannot be the aim of this review to cover all of the different nanomaterials used so far, but some of the most commonly investigated will be introduced in more detail. For zero-dimensional nanoparticles, emphasis will be put on metallic nanoparticles (mainly gold), semiconductor quantum dots, as well as magnetic (different iron oxides) and ferroelectric nanoparticles. In the area of one-dimensional nanomaterials, metal and semiconductor nanorods and nanowires as well as carbon nanotubes will be briefly discussed, and for two-dimensional nanomaterials only nanoclay. Finally, researchers active in the field are advised to seek further information about these and other nanomaterials in the following, very insightful review articles [16, 36–45].

1.2.1 Zero-Dimensional Metal Nanoparticles

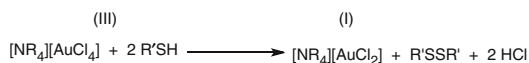
Most of the work dealing either with the assembly of metal nanoparticles or with metal nanoparticles as additives in liquid crystals has been carried out using nanoparticles with gold cores. Such gold nanoparticles display unusual and unique size-dependent chemical and physical properties; their surface can be passivated in

situ or via place exchange reactions with molecules ranging from simple alkanethiols, phosphines, and amines to more complex molecular structures including dendrimers, polymers, and peptides. Less attention has so far been paid to other metals such as silver, copper, palladium, or platinum. However, the preparation of some of the latter is possible in principle, and often done, using similar methods as described here for nanoparticles with gold cores. Gold nanoparticles can be produced by a number of different methods including sonochemical syntheses [46, 47], syntheses using ionic liquids [48–56], and many others. Each method claims a certain advantage in terms of being a green or surfactant-free method, or a method with good size-control, etc., but the majority of research groups to date use one of the two revolutionary methods developed by Brust and Schiffrin in the mid-1990s. The so-called one- [57] and two-phase Brust–Schiffrin reactions [58] providing thiol-capped gold nanoparticles or monolayer-protected clusters allow for a reasonable control over size and size-distribution, and can be carried out using a great variety of functionalized thiols [59–62], given that they survive the reductive power of sodium borohydride (NaBH_4) in the final step of the reaction. The mechanisms of these reactions have been debated in the literature for many years, and recent work by Lennox et al. using ^1H NMR spectroscopy now shows that the Au(I) thiolate polymer intermediate, often presumed, is not formed prior to the reductive step with NaBH_4 in both the one- and two-phase Brust–Schiffrin method (see Scheme 1) [63].

Other, commonly pursued approaches to obtain functionalized gold nanoparticles make use of one of the following techniques: (I) the so-called place



via:



Scheme 1 The one- and two-phase Brust–Schiffrin method for the synthesis of thiol-capped gold nanoparticles, and the first step of the reaction prior to the reduction step with NaBH_4 [63]

exchange reaction (often thiol-for-thiol exchange) on the nanoparticle surface [64, 65], (2) post-synthetic modifications (e.g., using a reactive R group on the nanoparticle corona as in Scheme 1), or (3) via a displacement of weaker ligands or weaker surface protective agents with functional, stronger binding ligands (e.g., a thiol-for-dimethylaminopyridine [66, 67] or a thiol-for-triphenylphosphine exchange providing access to gold nanoparticles with low polydispersity indices [68]).

A complete and accurate characterization of the size and size distribution of metal nanoparticles (prepared as described with any of the methods listed above) should always include at least one imaging and one bulk method. In most cases, imaging of metal nanoparticles with a size ranging from 1 to 10 nm requires transmission electron microscopy (TEM). The two-dimensional projection of three-dimensional nanoparticles in TEM, however, can lead to misinterpretations. TEM, in principle, provides some information on the particle size and size distribution and generally sufficient information about the particle shape (either a specific shape or a combination of different polyhedral shapes) on a limited sample volume. Therefore, bulk methods such as powder X-ray diffraction (using the Scherrer formula to determine particle/domain size and size distribution – often a reasonable approximation), dynamic light scattering (DLS), UV/vis spectrophotometry (using Mie theory at least for larger metal nanoparticles), or small angle X-ray scattering (SAXS) [69] should be used and compared with the TEM image analysis results.

Unfortunately, reproducibility issues, chemical purity, as well as homogeneity of nanoparticle samples frequently studied by groups active in the field are often overlooked. Batches of nanoparticles prepared in different laboratories or at different times, even following widely accepted, published procedures are not necessarily identical in terms of purity, size, or size distribution.

It should be standard for each newly prepared batch of nanoparticles to characterize all chemical as well as physical properties, and report all data necessary to prove unequivocally purity and size/size distribution including, but not limited to, ^1H NMR (absence of free, non-bound ligands, ammonium salts, or other impurities/reagents) and elemental analysis and/or inductively coupled plasma spectroscopy, ICP-OES/MS (providing information about purity as well as monolayer coverage in conjunction with size information provided by TEM, X-ray diffraction/scattering or DLS).

Additional factors complicating the matter arise from the chemical and thermal (in)stability of metal nanoparticles as well as from the proposed mobility of surface bound capping agents (usually thiols). The chemical stability or instability of thiol-capped metal nanoparticles towards oxidation (i.e., oxidation of surface-bound thiols in air or in the presence of other oxidants) [70], towards halides [71], and towards alkaline metal ions has been studied by a number of groups [72] using TEM, UV-vis, NMR, as well as X-ray photoelectron spectroscopy (XPS) [73], and this collective work highlights the importance of determining nanoparticle purity.

The thermal stability of metal nanoparticles (for the most part nanoparticles used in liquid crystal phases with high phase transition temperatures or nanoparticles decorated with functional molecules) should also be of significant importance,

particularly in view of the use of these composites in technological applications. Both thermogravimetric analysis (TGA) data [74] and temperature-dependent XPS studies frequently reveal that most thiols with an alkyl chain length longer than C6 start to or completely desorb (forming dithiols) from the gold nanoparticle surface at temperatures above 160°C; thiols with shorter chain length desorb at even lower temperatures (between 90°C and 140°C for C3–C5) [75]. However, radiation damage through continued exposure with X-rays during these XPS experiments was potentially a source of error in these studies. Hence, TGA data suggesting higher temperatures for thiol desorption from the nanoparticle surface could be more accurate [69, 76]. Nevertheless, sintering of gold nanoparticles is often observed for particle sizes below 4 nm as shown by Brust and co-workers, rapidly (10 min) at elevated temperatures (e.g., 250°C) but also appreciably at room temperature, an effect known as coarsening [74].

Using electron paramagnetic resonance (EPR) spectroscopy on gold nanoparticles passivated with spin labels, Chechik et al. and a number of other groups also demonstrated that thiol ligands on gold nanoparticle surfaces are mobile [77–79]. Although this lateral diffusion is slow at room temperature and may even take several hours at elevated temperatures (~90 °C) [77], the chance for segregation of thiol ligands on the surface of so-called mixed monolayer-capped nanoparticles (different ligands simultaneously cap the surface of the nanoparticle) [80–83] is given, and may even have been beneficial for some of the discovered effects. Last, but not least, gold nanoparticles capped with hydrophobic ligands are difficult to size-separate (ideally into batches consisting of so-called magic-numbered clusters) using techniques such as gel electrophoresis or diafiltration [84–86].

1.2.2 Zero-Dimensional Semiconductor Quantum Dots

Quantum dots are another class of zero-dimensional nanoparticles. The variety of quantum dots based on II–VI, III–V, and IV–VI semiconductor materials is far greater than for metal nanoparticles owing to the different possible elemental compositions such as CdS, CdSe, CdTe, ZnS, ZnSe, PbS, and many others including core-shell [43, 87–93] and alloy-type quantum dots [94] including elements such as In, Hg [95], As [96], and several lanthanides [97]. This list is far from complete. Thus, the discussion of quantum dots will be limited to hydrophobic quantum dots capped mainly with aliphatic amines and thiols, which are likely of more interest with respect to liquid crystal research and applications due to their anticipated better dispersibility in liquid crystal phases composed of rod- or disc-like molecules featuring flexible alkyl chains. Our group has recently demonstrated that this is by no means a strict rule. Thioglycolic acid-capped CdTe quantum dots, which disperse best in water or alcohol/water mixtures, also disperse well in reasonably non-polar nematic liquid crystals with two terminal hydrocarbon chains (see below) [98]. However, most current investigations focus on quantum dots protected with hydrophobic hydrocarbon monolayers.

Numerous hydrophilic as well as hydrophobic quantum dots are now commercially available as suspensions in organic or aqueous solvents, yet for a specific coating motif or quantum dot size researchers have the choice between organometallic syntheses commonly based on a high-temperature thermolysis [99] of a precursor or sol-gel type aqueous phase syntheses [100].

Quantum dots used in liquid crystal systems (ranging in size from a few to tens of nanometers) are usually from the II–VI group, and include CdS, CdSe, and CdTe capped with trioctylphosphine/trioctylphosphine oxide (TOP/TOPO) [101–103], CdS as well as CdTe stabilized with thiols [104], and CdSe protected with amines [105].

Depending on the kind of synthesis, these quantum dots can be prepared or size separated into batches covering almost the entire visible spectral range from 400 to 750 nm with, in part, high photoluminescence quantum efficiencies (some stable in air [106], others not [107]). Weller et al. reported on a very efficient synthesis for hydrophilic, thiol-capped CdTe quantum dots [108, 109], which can be transformed to lipophilic, alkanethiol-stabilized CdTe quantum dots using a place exchange reaction similar to that for metal nanoparticles described above [110]. A related strategy has also been successfully employed to produce hydrophobic or otherwise functionalized CdS [111] or CdSe quantum dots [112] (Fig. 1).

A complete and satisfactory characterization of quantum dots prepared by any of these methods requires many of the same techniques listed for metal nanoparticles described already (see above). In addition to critical electronic properties, photoluminescence spectroscopy is an extremely valuable tool to obtain preliminary information on size and size distribution of quantum dots, which can in many cases (i.e., for larger sizes and quasi-spherical shapes) be estimated from λ_{\max} and the full width at half maximum (fwhm) of the absorption or emission peak using approximations such as Brus' model or the hyperbolic band model [113].

A major concern for the use of these quantum dots in liquid crystal applications is their stability. Weller et al. using NMR spectroscopy, UV-vis spectrophotometry, and analytical ultracentrifugation (AUC) showed that thiol-stabilized cadmium chalcogenide quantum dots are unstable at low particle concentrations ($<10 \mu\text{M}$ in DMF), i.e., even the covalently bound thiols desorb from the quantum dot surface

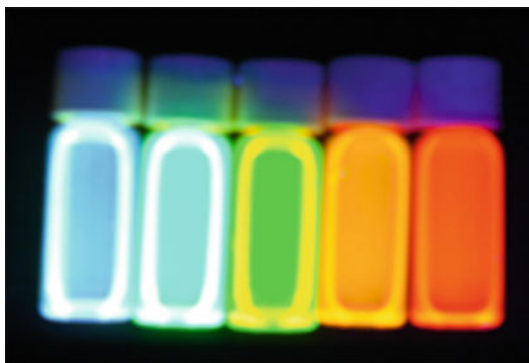


Fig. 1 A series of hexadecylamine-stabilized CdSe quantum dots (sizes range from 2.5 on the *far left* to 5.2 nm on the *far right*) excited at $\lambda_{\text{exc}} = 366 \text{ nm}$ (image provided by B. Kinkead)

and the particles decay (reducing particle size) with time and at elevated temperatures [104]. Similar studies including place exchange reactions have also shown related effects for amine-stabilized [114] as well as TOP/TOPO-capped CdS and CdSe quantum dots [115]. Hence, research groups studying quantum dots in liquid crystals are encouraged to examine the effect of low quantum dot concentrations in mixtures over time as well as changes in the particle size after thermal treatments, for example during sample preparation or in liquid crystal hosts with phase transition temperatures well above ambient. Here, silica coatings or surface silanization could be used as possible solutions to enhance the stability of such quantum dots [116–118].

1.2.3 Zero-Dimensional Magnetic Nanoparticles

Magnetic nanoparticles, for many apparent reasons such as the creation of magnetic nanoparticle superlattices or the design of magnetically controllable, optical liquid crystal devices, have also been of significant interest to the liquid crystal community. The reorientation of nematic liquid crystal molecules by an applied magnetic field, i.e., a Fréedericksz transition [119, 120], has been known for a long time, and some of the very early work on magnetic nanoparticle-doped nematic liquid crystals (so-called ferronematics) dates back to experiments performed by Brochard and de Gennes in 1970 using 7CB doped with magnetic nanoparticles featuring a 10 nm core [121].

The formation of magnetic nanoparticles is known for a variety of elements and elemental compositions including Fe, Co, CoFe, FePt, $Zn_{1-x}Fe_xO$, and others, but the vast majority of studies on magnetic nanoparticles, from medical applications to the liquid crystal composites discussed here, focus on commonly superparamagnetic iron oxide nanoparticles, i.e., magnetite (Fe_3O_4) or maghemite ($\gamma-Fe_2O_3$).

There are numerous methods of preparing magnetic iron oxide nanoparticles including co-precipitation (see below), non-aqueous and aqueous sol-gel [122], microemulsion, hydrothermal/solvothermal [123], as well as sonochemical processes [124]. In general, the co-precipitation method by Massart is widely used for its simplicity with the final product typically comprised of nanoparticles in the size regime from around 7 to 30 nm in diameter with both magnetite (Fe_3O_4) and maghemite ($\gamma-Fe_2O_3$) phases. However this method provides only access to iron oxide nanoparticles dispersible in aqueous media [125].

To overcome this restriction, a number of high temperature syntheses were developed over the past decade that follow a thermal decomposition of an organo-metallic iron species such as iron(III) acetylacetonate (acac) or iron pentacarbonyl in an organic solvent [126]. Sun et al. reported an organic phase synthesis of monodisperse magnetite nanoparticles starting from $Fe(acac)_3$. The precursor, $Fe(acac)_3$ in phenyl ether, in the presence of 1,2-hexanediol, oleic acid, and oleylamine, is refluxed at 265°C to yield magnetite nanoparticles with an average diameter of 4 nm [127]. Larger nanoparticles with a diameter of 8, 12, and 16 nm, respectively, were synthesized from these 4 nm particles in the presence of a

varying concentration of the precursor $\text{Fe}(\text{acac})_3$ (a seed mediated growth procedure). Many reports yielding reasonably monodisperse iron oxide nanoparticles follow such high temperature decomposition protocols starting from iron(III) precursors such as iron(III) oleate [128–130]. Post-synthetic modification of the nanoparticle surfaces with mesogenic or pro-mesogenic molecules is commonly achieved by a partial place exchange with functional molecules featuring carboxylate or phosphonate groups [131–133].

A full characterization of iron oxide nanoparticles requires most of the techniques listed for the other two classes of zero-dimensional nanomaterials discussed in the previous two sections including electron microscopy (scanning and transmission, SEM and TEM), powder XRD, SAXS-WAXS (as an alternative), or DLS. Fourier transform infrared (FT-IR) spectroscopy is often used for this class of nanoparticles to establish the chemical link (bonding) between iron sites on the nanoparticle surface and the capping ligands as well as to gain a basic idea of the iron oxide phase (maghemite vs magnetite) [131]. Due to peak broadening in powder XRD as well as selected area electron diffraction (SAED) experiments (from TEM), particularly on smaller iron oxide nanoparticles (core below 10–15 nm in diameter), the exact composition is difficult to determine with these techniques. Hence, transmission Mössbauer spectroscopy would here be the method of choice to determine the phase or ratio between different iron oxides (or eventually hydroxide or mixed oxide/hydroxide) phases [134–139]. The magnetic properties of iron oxide nanoparticles are usually characterized using a vibrating sample magnetometer (VSM), a superconducting quantum interference device (SQUID) magnetometer, or a combination of both measurement principles. Finally, the thermal stability should be tested using TGA and/or differential thermal analysis (DTA).

1.2.4 Quasi-Zero-Dimensional Ferroelectric Nanoparticles

The last type of quasi-spherical (i.e., zero-dimensional) nanoparticles discussed here in more detail is ferroelectric nanoparticles. Ferroelectric nanoparticles are of significant interest in liquid crystal research because of the potential coupling of their ferroelectric, piezo-electric and dielectric properties, in particular to thermotropic nematic liquid crystal phases. The most commonly investigated ferroelectric nanoparticles in liquid crystals are based on BaTiO_3 and $\text{Sn}_2\text{P}_2\text{S}_6$ [140–144]. However, potential applications of such particles in non-volatile memories, capacitors, or actuators have seen a surge in the creation of many different ferroelectric nanoparticles with compositions including PbTiO_3 [145] and $\text{Pb}(\text{Zr}_{1-x}\text{Ti}_x)\text{O}_3$ [146], to $\text{SrBi}_2\text{Ta}_2\text{O}_9$ [147], to $\text{Ba}_{0.6}\text{Sr}_{0.4}\text{TiO}_3$ [148], and several others. The choice of the synthesis method here is of particular significance as only some methods yield true single ferroelectric domain nanoparticles; others yield only ferroelectric multi-domains [149]. Methods known to produce ferroelectric nanoparticles such as those listed above include several high-temperature protocols (commonly using autoclaves) [150], biosyntheses including template syntheses

[151, 152], as well as sol-gel [153, 154], molten hydrates salt [155], and grinding methods [156]. A key problem with some of these particles is the colloidal stability, which appears to depend on the nanoparticle core size as well as the degree of coverage with surfactant molecules; for BaTiO_3 and $\text{Sn}_2\text{P}_2\text{S}_6$ often oleic acid [144, 156]. Sizes for BaTiO_3 nanoparticles produced by grinding in a ball mill commonly range from 8 to 30 nm [156], but much larger sizes were reported for $\text{Sn}_2\text{P}_2\text{S}_6$, often close to 1 μm [144]. A careful look at the published work suggests that the characterization of these nanoparticles is sometimes insufficient. While TEM analysis was frequently used to determine the size and size distribution, data on the chemical purity, i.e., the complete removal of free, non-bound surfactant molecules is often not provided. In much the same way, evidence for a complete coverage with surfactant molecules would be essential to avoid long-term aggregation of the nanoparticles in liquid crystal phases, and should be performed in analogy to metal nanoparticles or semiconductor quantum dots using techniques described earlier in this review such as elemental analysis in conjunction with TEM or SEM imaging.

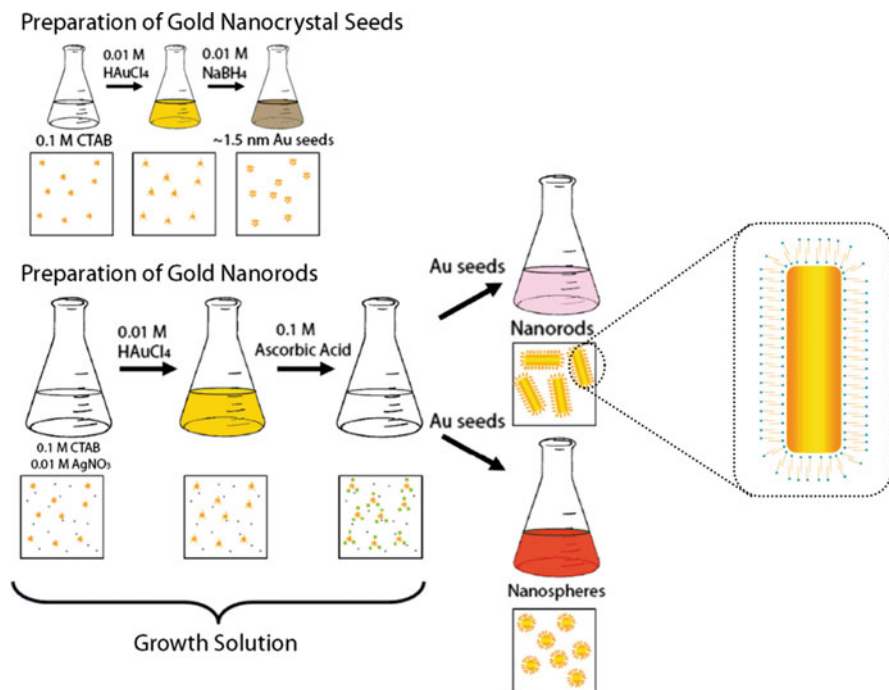
1.2.5 One-Dimensional Metal and Semiconductor Nanorods

Similar to zero-dimensional metal nanoparticles, most of the work on one-dimensional metal nanostructures focuses almost exclusively on gold nanorods. The high interest in anisometric gold nanoclusters arises from their unique optical and electronic properties that can be easily tuned through small changes in size, structure (e.g., the position, width, and intensity of the absorption band due to the longitudinal surface plasmon resonance is strongly influenced by the shell as well as the aspect ratio of the nanorods), shape (e.g., needle, round capped cylinder, or dog bone), and the inter-particle distance [157].

Gold nanorods (GNRs) can be produced with reasonable yields through several approaches such as template-based methods [158, 159], electrochemical methods [160, 161], or via seed-mediated wet chemistry methods. Due to their simplicity and the ease of nanorod size and shape control, the latter, seed-mediated growth methods in the presence or absence of Ag^+ ions are commonly preferred [162–165].

Typically, this method consists of three independent steps: (1) the preparation of surfactant-capped gold nanoparticle seeds (generally ranging in diameter from 1.5 to 5 nm) by reducing HAuCl_4 using NaBH_4 (see above), (2) the preparation of a growth solution via the reduction of HAuCl_4 using a milder reducing agent such as ascorbic acid (both steps in the presence of cetyltrimethylammonium bromide (CTAB) as a stabilizing surfactant, and finally (3) an addition of the gold nanoparticle seeds prepared in the first step to the growth solution (see Scheme 2).

The resulting GNRs are coated with a CTAB bilayer that prevents aggregation and facilitates the formation of relatively stable nanorod suspensions in aqueous solution. Smith et al. recently showed that very small amounts of iodide present as an impurity in CTAB samples purchased from different chemical suppliers have a dramatic influence on nanorod growth. In some cases, nanorods did not

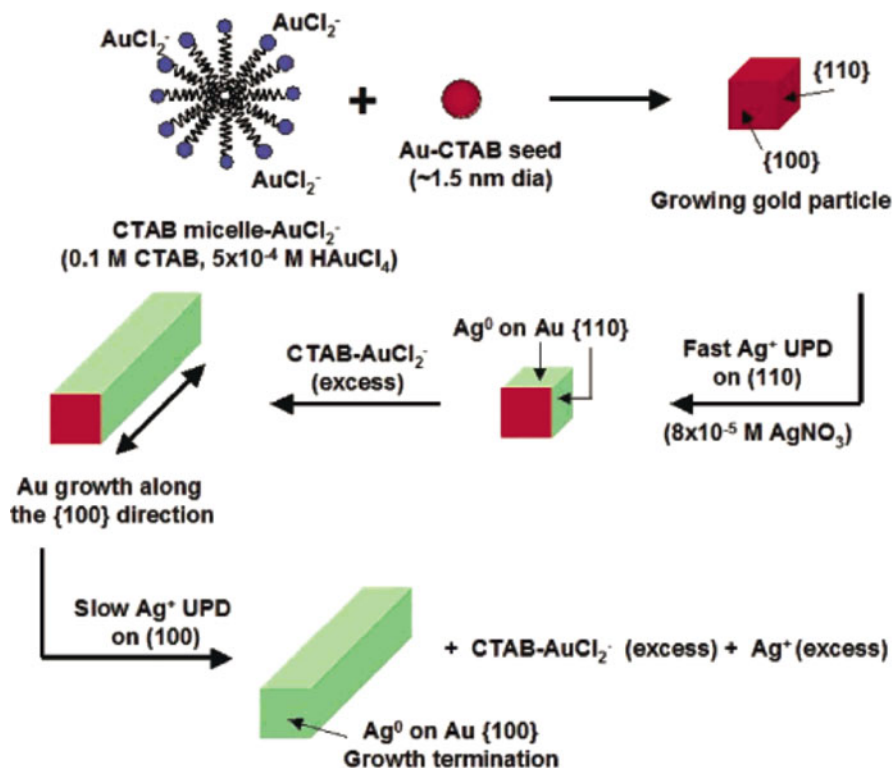


Scheme 2 Schematic of a seed-mediated, surfactant-assisted gold nanorod synthesis. The *small black dots* represent Ag^+ ions, the *orange stars* are CTAB molecules forming micelles, the *yellow circles* and *green squares* are AuCl_4^- and AuCl_2^- , respectively, forming complexes with the CTAB micelles. Freshly-prepared gold nanoparticle seeds are injected into the growth solution in the final step of the nanorod synthesis [166]. (Copyright © 2008, American Chemical Society)

form at all; only quasi-spherical nanoparticles were observed if the concentration of the iodide impurity was greater than 50 ppm [166, 167].

Both yield and quality of the gold nanorods are significantly increased if silver ions are present in the growth solution. The presence of Ag^+ leads to 99% gold nanorod formation and allows efficient control over the aspect ratio ranging from 1.5 to 4.5 with a maximum nanorod length of about 100 nm. It is worth mentioning that the smallest seeds give higher yields of nanorods, and that the best yield and size homogeneity is achieved when a one-step colloidal synthesis method is followed [168, 169].

To obtain higher nanorod aspect ratios and lengths in the presence of Ag^+ ions, a co-surfactant is required; benzyldimethylhexadecylammonium chloride for nanorods with aspect ratios up to 10 [164] or Pluronic F-127 for aspect ratios up to 20 [165]. The average length of the nanorods can be increased continuously by adding new amounts of growth solution. However, for longer nanorods or nanowires (i.e., aspect ratios above 80) the synthesis should be performed in the absence of Ag^+ ions.



Scheme 3 Nanorod growth mechanism in the presence of Ag⁺ ions [170]. (Copyright © 2006, American Chemical Society)

According to the Ag under-potential deposition mechanism [170], AuCl₂⁻ ions on the CTAB micelles diffuse to the CTAB-capped seed spheres by electric field interactions and thus break the spheres symmetry into different facets. CTAB binding and Ag⁺ deposition are faster onto the {110} facet than onto the {100} end facet, which results in preferential particle growth along the (110) direction until the complete deposition of silver ions on the {100} end facet has occurred (see Scheme 3). There are pros and cons for each of the proposed mechanisms of gold nanorod growth, either in the presence or in the absence of Ag⁺ ions, but it is commonly accepted that gold nanorods synthesized via the Ag⁺-assisted methodology are crystallographically different from those obtained in the absence of Ag⁺ ions [164, 171–173].

Reports on other syntheses performed at elevated temperature revealed that the nanorod length decreases with increasing temperature, but also that the width remained constant [169]. By decreasing the reaction temperature, the aspect ratio of the resulting nanorods significantly increases due to a decrease of the nanorod diameter, which was explained by a confinement of the growth in diameter at lower temperatures [174, 175].

A major drawback of seed-mediated growth methods is often the occurrence of a significant fraction of nanospheres and other shapes forming during the growth step, which can be difficult to separate from the desired nanorods. The most common purification technique relies on several rounds of centrifugation followed by supernatant removal. An efficient purification method, yielding single-size nanorods from a mixture of rods, spheres, and plates, seems to be a surfactant assisted organization of concentrated dispersions of nanorods forming ordered liquid crystalline phases, which can then be precipitated out of solution [176]. Even assuming that during centrifugation the heaviest nanoparticles sediment first could be too simple, recent work by Sharma et al. showed that the sedimentation behavior of gold nanorods depends more strongly on the nanorods' diameter than on their total weight or aspect ratio, demonstrating that the key factor for the sedimentation is the ratio of the Svedberg coefficients of the nanorods [174].

Unlike for zero-dimensional gold nanoparticles, no direct synthesis producing functionalized nanorods has been demonstrated. Thus, coating exchanges become tremendously important for enhancing the dispersion of GNRs, for example in organic solvents. The stability of the CTAB bilayer capping the nanorods is often difficult to overcome, and further optimization of coating exchange reactions appears to be a difficult task that still requires significant improvements [177].

To date, the vast majority of work deals with hydrophilic GNRs functionalized by electrostatic attraction of CTAB molecules, anionic polyelectrolytes, or covalent binding of hydrophilic thiols. Hydrophobic GNRs are mainly produced by depositing octadecyl-trimethoxysilane as a coating agent onto the nanorod surface either in the presence [178, 179] or absence of a silica shell [180].

Reports on the preparation of GNRs with hydrophobic thiol coatings are comparatively rare [181]. Surface modification using thiols commonly leads to preferential reactions at the facet of the short axis on the nanorod, but not on the entire nanorod surface [182]. For the same reason, thiol-for-CTAB exchanges typically require several rounds of ligand exchange for a near complete hydrophobization [183, 184]. From our own experience, CTAB replacement with polyethylene glycol thiols (PEG-SH) acting as a steric barrier stabilizing the nanorods, followed by a PEG-SH-functionalized thiol exchange, appears to be suitable method producing the best results and concurrently offering flexibility in ligand customization.

Ligand exchange can easily be monitored by surface characterization techniques (XPS, ζ -potential, and TGA) or common spectroscopic methods (i.e., ^1H NMR, FT-IR, UV-vis-NIR), amongst which UV-vis-NIR spectrophotometry deserves special attention due to the two surface plasmon resonance bands present in the vis-NIR region of the absorption spectrum. The transversal contribution band usually appears around 520 nm and undergoes small variations with different factors, while the position of the longitudinal band in the NIR is strongly influenced by the aspect ratio of the nanorods and the refractive index of the medium/coating [179]. Since the surface plasmon resonance bands are sensitive to the GNR organization and orientation, UV-vis-NIR spectrophotometry ("normal" or polarized) is also a very valuable tool for investigating the alignment or self-organization of GNRs as well as detecting nanorod aggregation.

Readers interested in more specific details about synthesis strategies, mechanisms of nanorod formation, characterization, or factors influencing the morphology of noble metal nanorods are referred to a comprehensive review by Sau and Rogach [185]. Reviews by Kijima and Zhang et al. will provide additional, detailed information on the synthesis of other one-dimensional metal nanostructures (including nanowires and nanotubes) [186, 187].

Semiconductor nanoparticles with a rod-like morphology are another striking class of one-dimensional nanomaterials attracting significant attention over the past decade due to their usefulness in electronics, optoelectronics and sensor devices [188–190]. As a result of their shape anisotropy, semiconductor nanowires and nanorods possess unique optical and electronic properties such as advantageous directional capabilities in transporting electronic carriers in comparison to related zero- or two-dimensional nanomaterials [191, 192]. To adjust these capabilities, semiconductor nanorods have been fabricated using various approaches with core materials ranging from Si, ZnO, and ZnS to CdS and CdSe to TiO₂ and SnO₂ [193–200].

The vapor-liquid-solid (VLS) process [193] is a common approach for growing nanorods from the vapor phase, which requires high operating temperatures (around 500°C) [201] and a metal catalyst such as Au, Cu, or Ni [202]. Colloidal synthetic methods have also been used with great success for producing semiconductor nanorods [200, 203]. The key point of these methods is the separation of nucleation and growth steps, which is commonly achieved using hot-injection [204] or heat-up protocols [133] that generate homogeneous nucleation and facilitate uniform growth of nanorods.

Li and co-workers, for example, developed a solvothermal synthesis [196] using stable inorganic precursors such as nitrates and chlorides instead of the toxic and unstable organometallic precursors normally involved in solvothermal synthetic methods [200, 205]. In this way, they obtained CdS, ZnS, and ZnS/Mn semiconductor nanorods with controllable aspect ratios from the reaction of stable inorganic salts and thioacetamide using octadecylamine or oleylamine as capping agents. Template-based syntheses were also demonstrated to be facile and versatile techniques for producing nanorods with controlled morphology [198, 200]. Templates such as nanoporous membranes (“hard” templates) as well as micelles (“soft” templates) [206] are employed as scaffolds for guiding the growth of nanorods by filling holes or covering inner faces of the templates with a precursor. It is worth mentioning that liquid crystals have been employed as templates as well [207–210], and that liquid crystals were found to play a key role for the stabilization of nanorods during some synthesis procedures [211].

1.2.6 One-Dimensional Carbon Nanomaterials: Carbon Nanotubes

Carbon nanotubes (CNTs) have emerged as one of the most interesting nanomaterials during the past decade [212]. The unique structural, mechanical, electrical, and thermal properties [213, 214] of these long hollow cylinders, along

with an extremely high aspect ratio, make CNTs a key component for a wide range of novel applications in new materials and devices ranging from polymer nanocomposites with enhanced mechanical strength to nanoscale electronic and optoelectronic devices [215–220]. There are two main types of CNTs with high structural perfection: (1) single-walled carbon nanotubes (SWCNTs) with a typical diameter of the order of one nanometer and (2) multi-walled carbon nanotubes (MWCNTs) composed of several concentric nanotube cylinders ranging in overall outer diameter from 1.4 to 100 nm. A SWCNT can be visualized as a single sp^2 -hybridized graphene sheet rolled into a seamless tube closed with a hemispherical fullerene cap at each end. The combination of a hollow structure, small diameter, and high aspect ratio makes SWCNT an unusual one-dimensional material with a very low mass density [221] and an extremely high specific surface area [222]. SWCNTs and MWCNTs are usually made by carbon-arc discharge, laser ablation of carbon, or chemical vapor deposition, typically on catalytic particles [223].

CNTs, like liquid crystals, are anisotropic; in other words, their properties are direction-dependent. Therefore, the control of the orientation and predetermined direction of a microscopic single tube is crucial in order to achieve significant control of the CNTs properties in a macroscopic scale and then manipulate the obtained alignment via an external field. Several studies have shown enhanced performances of aligned CNTs in various potential applications [224–230].

However, despite the plethora of possible applications, only a limited number of practical uses have been realized to date. Critical issues such as difficulties in their manipulation and handling mainly due to their strong van der Waals forces causing bundling and aggregation, lack of uniformity of physical dimensions, poor solubility, and control of purity limit the applicability of CNTs [231, 232]. To overcome the solubility problem and achieve aligned CNT arrays, several in-growth [233, 234] and post-growth methods for dispersion and orientation of CNTs have been investigated. Post-growth methods for assembling CNTs into ordered structures are currently receiving considerable attention with reports of experiments using a.c. [235] or d.c. [236, 237] electric or magnetic fields [238–240], as well as methods relying on external forces such as flow [241, 242] or Langmuir–Blodgett films [243]. In addition, there is extensive research on the liquid crystal phase formation of CNTs with the main focus on dispersions in aqueous media [244–247], in superacids [248, 249], or using DNA [250]. Preparation of aligned SWCNT composite membranes via the suspension of CNTs in a gellan gum-based biopolymer [251] or fabrication of self-assembled systems by dispersion of MWCNTs in a nematic liquid crystalline system formed from hydrogen bonding between *D*-(-)-tartaric acid and undecyloxy benzoic acid [252] are two other interesting examples amid the post-growth alignment methods. Theoretical studies of lyotropic or thermotropic nematic liquid crystal phase behavior of anisotropic CNTs have been reported as well [253–255]. Overall, the post-growth alignment methods have shown more attractive results than in-growth methods in terms of controlling the density and shape of CNTs. Nevertheless, no method can be considered versatile, fulfilling large scale and good quality alignment and dispersion. A very interesting approach to solving the dispersion and alignment

problems simultaneously has been the use of liquid crystalline materials. The fluidity of liquid crystals and more importantly their self-organization ability are advantageous for CNTs as a potential solvent with superiority in uniform large-scale alignment. Not surprising, liquid crystal applications have benefited from the presence of CNTs as well (see below).

1.2.7 Two-Dimensional Nanomaterials: Nanodiscs and Clay

Two-dimensional, disc-shaped nanomaterials are the last class of nanomaterials to be discussed in more detail. Though a great variety of nanodiscs, nanosheets and nanoplatelets based on metals [256], metal oxides [257–260], graphene [261], or semiconductors [262] are frequently described in the literature, the vast majority of studies in liquid crystal systems dealt with some form of nanoclay.

Prominent exceptions are studies on the liquid crystal phase formation and self-assembly of two-dimensional disc- or sheet-like nanomaterials such as the organization of nanodiscs or nanoplatelets into nematic, smectic, or columnar morphologies [263–270] (see Fig. 2 for an example of the self-assembly of nanoclay in aqueous suspensions) or the synthesis of CuCl nanoplatelets from ionic liquid crystal precursors as described by Taubert and co-workers [271–273].

The most common nanoclay materials used either in pure form or organically-modified (i.e., coated with an appropriate surfactant or polymer) are montmorillonite (MMT – a monoclinic smectite; with a chemical formula $(\text{Na,Ca})_{0.3}(\text{Al,Mg})_2\text{Si}_4\text{O}_{10}(\text{OH})_2 \cdot n\text{H}_2\text{O}$), beidellite ($\text{Na}_{0.5}\text{Al}_2(\text{Si}_{3.5}\text{Al}_{0.5})\text{O}_{10}(\text{OH})_2 \cdot n\text{H}_2\text{O}$), synthetic laponite RD ($\text{Na}_{0.7}(\text{Si}_8\text{Mg}_{5.5}\text{Li}_{0.4})\text{O}_{20}(\text{OH})_4$), or hectorite ($\text{Na}_{0.3}(\text{Mg,Li})_3\text{Si}_4\text{O}_{10}(\text{OH})_2$).

The characterization of these natural or synthetic nanoclay materials is just as critical as for the nanomaterials discussed in the previous sections and should

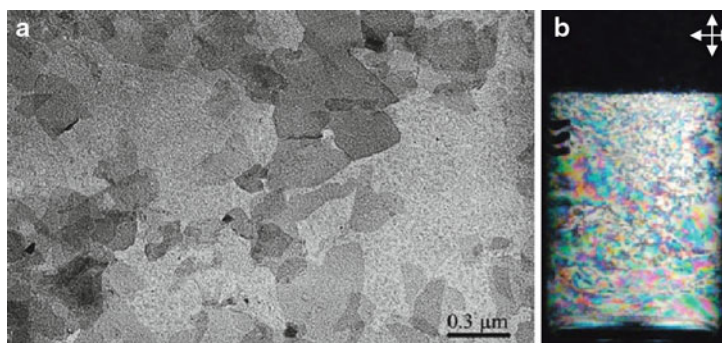


Fig. 2 (a) Transmission electron microscopy (TEM) image of a disc-like beidellite clay sample (sizes of the platelets range from 69 to 480 nm in diameter), and (b) lyotropic nematic phase of an aqueous suspension of the same beidellite sample at an ionic strength of $10^{-4} \text{ mol L}^{-1}$ ($\phi = 0.5\%$) observed between crossed polarizers [263]. (Copyright © 2009, American Chemical Society)

include SEM, TEM, or SAXS to determine size, size distribution as well as shape (SEM, TEM), and X-ray diffraction (often to ensure complete exfoliation by sonication [274]). Organically modified clays (or organoclays) should undergo FT-IR studies to confirm surface functionalization (e.g., the exchange of clay sodium ions with ammonium ions of ammonium-based surfactants), and TGA for thermal stability (i.e., non-bound surfactants or surfactant release, which is often overlooked) [275–277].

Several other nanomaterials (e.g., silica nanoparticles) have been studied predominantly as dopants for nematic or smectic liquid crystal phases [278–287], but we decided to limit the discussion above to the major types receiving significantly more attention over the last few years.

2 Nanoparticle-Doped Liquid Crystal Phases

Having laid down the basic foundation by introducing some of the most widely used nanomaterials in liquid crystal nanoscience including major synthesis and characterization methods, the following section will now focus on the use of these nanomaterials as additives or dopants for liquid crystalline systems. The discussion will focus on a number of key examples that we believe will highlight the emergence of nanomaterials as a viable class of dopants for improving the properties and characteristics of liquid crystalline systems used in optical devices and display applications. Hence, the vast majority of examples will deal with nanoparticle-doped nematic as well as smectic liquid crystal phases, both achiral and chiral, but will also cover advances using other liquid crystal phases such as blue phases. In the light of earlier work, recent examples (starting from 2006) will be used to summarize both beneficial and detrimental optical, thermal, alignment, and electro-optic effects observed when nanoparticles are suspended in liquid crystal host phases. We will not touch on the synthesis of nanomaterials using liquid crystal phases as templates, but present major breakthroughs in the assembly and alignment of nanomaterials in liquid crystals.

2.1 *Zero-Dimensional Nanoparticle Additives*

2.1.1 **Zero-Dimensional Nanoparticle Additives in the Nematic Phase**

The nematic phase has unquestionably been the “go-to” phase to study and understand the major driving forces that govern interactions between suspended, quasi-spherical nanoparticles and liquid crystal molecules or mixtures. We credit this to three important factors: (1) early experimental studies [288, 289] based on the foundation of de Gennes’ very early work on ferronematics [121], (2) the availability of nematic liquid crystals including room temperature and wide temperature

range nematics, and (3) the use of nematic liquid crystals in leading, large panel liquid crystal display modes such as in-plane [290–292] and fringe-field switching [293] as well as multi-domain and patterned vertical alignment [33, 294, 295].

Before delving into examples of nanoparticle-doped nematic liquid crystals, we have to introduce two important concepts which determine to some extent the faith of quasi-spherical nanoparticles in nematic liquid crystals. The first concept deals with surface anchoring of nematic liquid crystal molecules on the nanoparticle surfaces as well as the anchoring energy, and the second is the influence of the critical nanoparticle radius. Both are inherently connected to one another, and both will prove to be of significant importance in several nanoparticle-doped nematic systems. Two principle surface anchoring conditions can be distinguished, planar and vertical (homeotropic) anchoring (Fig. 3).

Both parameters, anchoring and particles radius, have an important impact on the aggregation of phase-separated particles as well as on the local distortion of the liquid crystal ordering (i.e., the induction of defects around the nanoparticle). Lavrentovich et al. formulated, qualitatively, when particles will aggregate in regions with the highest liquid crystal distortions [296]. The change in the free energy caused by introducing a spherical particle with the radius R_P in a distorted liquid crystal is given by

$$\Delta E = -E_V + \Delta E_S + E_{ind}, \quad (1)$$

where E_V is the elastic energy of the excluded volume V_P ,

$$E_V \equiv \frac{1}{2}K \int_{V_P} \frac{\partial n_i}{\partial x_j} \frac{\partial n_i}{\partial x_j} dV_P \cong \frac{2}{3}\pi K \frac{R_P^3}{\xi^2} A^2, \quad (2)$$

and ΔE_S the difference in the anchoring energy at the particle surface for homogeneous and distorted director fields. E_{ind} is the elastic energy of the additional distortions induced by the particle, K is the average Frank elastic constant, A is the amplitude, and ξ is the characteristic length of director distortions. In a uniform aligned nematic liquid crystal, no preferable site for nanoparticle aggregation

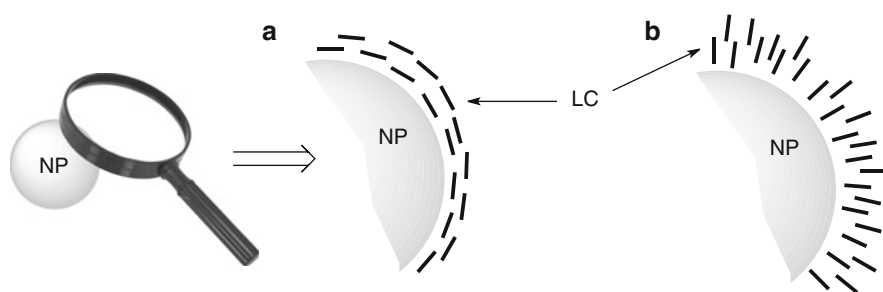


Fig. 3 Principle anchoring conditions of nematic liquid crystals at nanoparticle surfaces: (a) planar anchoring, and (b) vertical (or homeotropic) anchoring

would exist in the plane of the sandwiched liquid crystal cell. In a distorted liquid crystal, however, elimination of the volume term R_P^3 leads to a decrease in the elastic energy by E_V . From (2) it becomes evident that the energy gain scales with the strength of the distortion, A/ξ , and from (1) that the other two terms, ΔE_S and E_{ind} , depend on whether R_P is smaller or larger than the length $L_P = K/W_P$, where W_P is the anchoring coefficient at the particle/nematic interface. Hence, the critical radius, R_P , for distortions of the nematic director by quasi-spherical particles or particle aggregation for most systems falls roughly between 100 nm and 10 μm [296]. Based on this qualitative treatment, smaller particles should be “invisible” in an aligned nematic environment given that they can, experimentally, be well dispersed in the nematic host. Preparation procedures to obtain well-dispersed nanoparticle suspensions in nematics often make use of an organic solvent, which is first used to dissolve or disperse both components (nanoparticles and nematic liquid crystal) and, after mixing of these solutions, carefully evaporated in different ways; either under vacuum or by heating under a stream of inert gas. Also often successful is a rapid thermal quench, i.e., rapid cooling from the isotropic to the nematic phase, to keep the nanoparticles, which are in general better dispersible in the isotropic liquid phase, from aggregating in the nematic phase. Nevertheless, a number of interesting and applicable effects have been described for aggregated (segregated) nanoparticles in nematic hosts (see below).

Most reports over the past 4 years have dealt with the manipulation of display-related parameters such as electro-optic response and alignment, but increasingly also with thermal effects, pattern formation, nanoparticle-liquid crystal compatibility (i.e., enhancing the stability of dispersions), and to some degree with nanoparticle organization.

Some important observations, which should apply de facto to many nematic systems containing dispersed nanoparticles, particularly those with metal or semiconductor cores, were reported in 2006 by Prasad et al. [297]. The authors found that gold nanoparticles stabilized with dodecanethiol decreased the isotropic to nematic phase transition of 4-pentyl-4'-cyanobiphenyl (5CB) almost linearly with increasing nanoparticle concentration (x_{NP}) and increased the overall conductivity of these mixtures by about two orders of magnitude. However, the anisotropy of the electric conductivity ($\Delta\sigma = \sigma_{\parallel} - \sigma_{\perp}$) measured at 10^4 Hz decreased with increasing x_{NP} .

Their measurements revealed no significant change of the dielectric anisotropy at the same reduced temperatures ($T_{Iso/N} - T$), which our group was able to confirm in related experiments using mixtures of 5CB doped with hexanethiol-capped gold nanoparticles [298].

However, we found higher values for the electrical resistance, slightly higher threshold voltages (V_{th}) in 5CB, but lower V_{th} in 8CB. In contrast to Prasad's work [297], which did not provide size or size distribution data for their gold nanoparticles synthesized via the two-phase Brust-Schiffirin method [58], we observed the induction of homeotropic alignment in 5CB as well as 8CB doped with alkanethiol-protected gold nanoparticles (1.6–2.1 nm in diameter), prepared using a modified one-phase method (see above) [299], for a number of indium tin

oxide (ITO)-coated glass cells with unidirectional rubbed polyimide alignment layers normally favoring planar alignment of the molecules [298, 300]. In addition, Prasad et al. also proposed that a local anchoring of the liquid crystal molecules to the nanoparticle surface, which might extend to substantial distances into the bulk, could explain the occurrence of two, rather close peaks for the isotropic to nematic phase transition observed on cooling in DSC experiments and the two-step change in the dielectric data [297].

The concept of local perturbations of the director around nanoparticles, often linked to homeotropic anchoring to the nanoparticle surface, is a concept often brought forward in discussions of thermal, optical and electro-optic properties of nanoparticle-doped nematic liquid crystals, which adds a slightly different perspective to the “invisibility” of smaller particles in aligned nematics. This appears to be of particular relevance for particles coated with either hydrocarbon chains or pro-mesogenic as well as mesogenic units.

Toshima and co-workers prepared a series of monometallic Ag and Pd as well as bimetallic Ag–Pd nanoparticles coated with 5CB with an average diameter of 1.4–3.6 nm, which reduced the phase transition temperature of the 5CB host by a maximum of 1.2°C for the monometallic Ag particles (the smallest in the series being 1.4 nm in diameter), induced a frequency modulation response, and a nonlinear (with respect to an increasing amount of Ag) increase of the threshold voltage (Fig. 4a). The authors argue that an electronic charge-transfer (Coulomb attraction and repulsion) from the bimetallic nanoparticle surface via the cyano group of the 5CB capping molecules might be responsible for the observed electro-optic effects, particularly if these interactions extend into the bulk via homeotropically anchored 5CB host molecules (Fig. 4b) [301].

Protecting the surface of metal nanoparticles with a monolayer of (or a mixed monolayer containing) pro-mesogenic and mesogenic units has been described in the past by a number of groups. Kobayashi et al., though mostly for twisted (chiral) nematic systems, which will be discussed in more detail in the next section, demonstrated a number of exciting effects including frequency modulation response of tunable birefringence mode twisted nematic LCDs and faster response times particularly for Ag and Pd nanoparticles capped with cyanobiphenyl moieties (with a metal core diameter ranging from 2 to 4 nm; see **1** in Fig. 5) [302–309]. However, a detailed characterization, other than the size and size distribution obtained by TEM image analysis, using NMR or TGA of some of these nanoparticles, was unfortunately not always provided.

Zubarev and Link et al. have recently described the formation of highly stable dispersions of metal nanoparticles capped with pro-mesogenic ligands. In a two-step process, 4-sulfanylphenyl-4-[4-(octyloxy)phenyl]benzoate-capped, mixed monolayer gold nanoparticles with fairly narrow size distribution (around 6 nm in diameter) were prepared first by a partial ligand exchange of decanethiol with 4-mercaptophenol followed by an esterification of the phenolic hydroxy groups with 4'-octyloxybiphenyl-4-carboxylic acid (**2** in Fig. 5) [310]. The authors propose an enhanced solubility of these nanoparticles with respect to decanethiol-capped gold nanoparticles in the same nematic host (here 5CB) based on the absence of

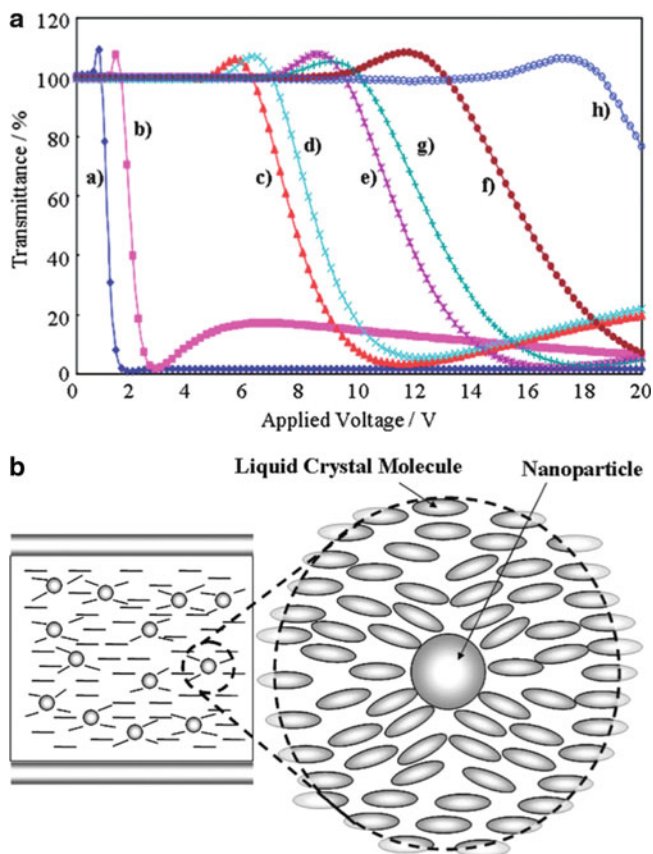


Fig. 4 (a) Applied voltage vs. transmission (V - T) curves of in twisted cells at 100 Hz and 25°C. a) Pure 5CB, b) 5CB-capped Pd, c) 5CB-capped Ag-Pd (1/9), d) 5CB-capped Ag-Pd (1/4), e) 5CB-capped Ag-Pd (1/1), f) 5CB-capped Ag-Pd (4/1), g) 5CB-capped Ag-Pd (9/1), and h) 5CB-capped Ag. (b) Cartoon of a liquid crystal cell filled with 5CB-sol containing metal nanoparticles. A self-assembly property of liquid crystal is speculatively perturbed by nanoparticles in the liquid crystal medium [301]. (Copyright © 2008, American Chemical Society)

peak broadening and a bathochromic (red) shift of the surface plasmon resonance (SPR) band of 8 nm for the nanoparticles in 5CB vs isotropic methylene chloride. The same effect was also reported earlier by Park et al. as well as Stroud and co-workers based on experimental data as well as calculations using Mie scattering theory and discrete dipole approximations [311, 312]. The calculated maximum solubility was estimated to be 0.2 wt% based on the optical density at the surface plasmon resonance maximum, and then verified experimentally. At the maximum soluble nanoparticle concentration of 0.2 wt%, the nematic-to-isotropic phase transition temperature decreased only slightly (0.4°C), which is consistent with earlier reports (see above). Finally, the threshold voltage (V_{th}) also decreased by about 0.2 V [310].

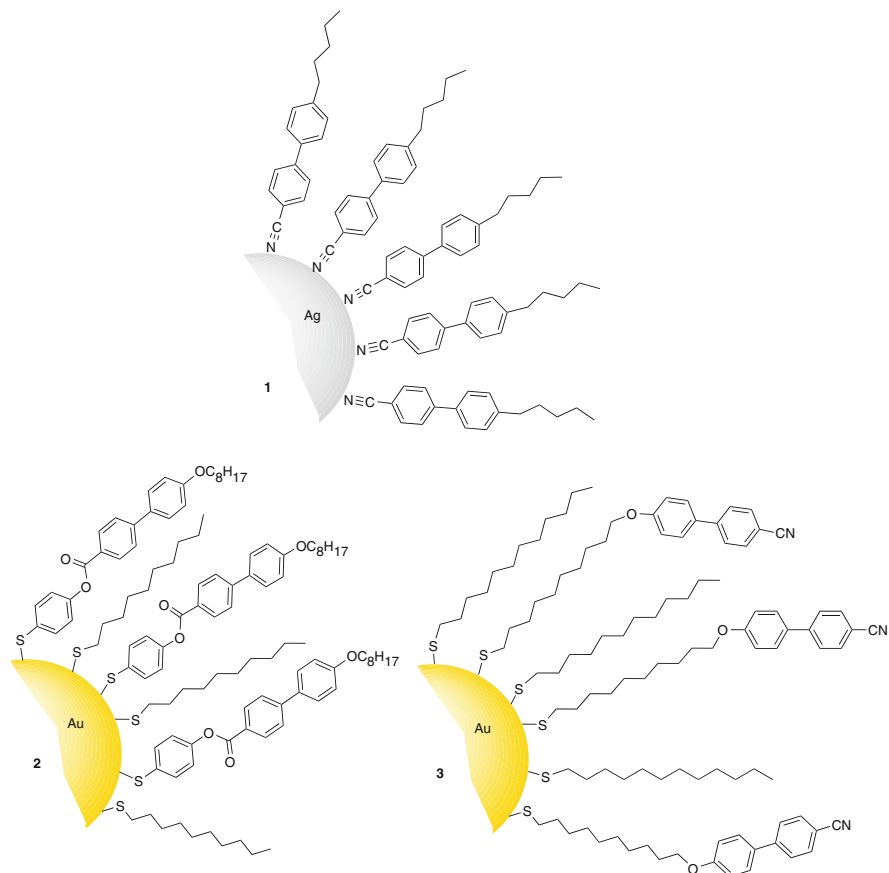


Fig. 5 Metal nanoparticles capped with mesogenic and pro-mesogenic units: **1** [301, 306, 313, 314], **2** [310], and **3** [298]

Quite surprisingly, our group recently showed that capping metal nanoparticles with mesogenic units does not always result in a better solubility in nematic hosts [298]. In this study, we demonstrated that alkanethiol-capped gold nanoparticles were more soluble in 5CB and 8CB (forming stable suspensions) than mixed monolayer-capped gold nanoparticles featuring alkanethiols of varying chain length (C_6 or C_{12}) as well as 4'-(10-mercaptodecyloxy)biphenyl-4-carbonitril – a nematic cyanobiphenyl-based thiol: Cr 62 N 72.5 Iso (**3** in Fig. 5). Both types of nanoparticles, homogeneously-capped with alkanethiols and mixed monolayer-capped with nematic liquid crystals, were initially well dispersed in both CB hosts at concentrations reaching up to 5 wt%. However, all dispersions containing mixed monolayer (liquid crystal)-capped gold nanoparticles clearly lacked the required long-term stability, which could easily be recognized by the settling (precipitation) of the nanoparticles in both nematic hosts over a period of less than 12 h [298].

Yoshida et al. recently disclosed an alternative method that allowed them to produce stable suspensions of gold nanoparticles (1–2 nm in diameter) in nematic liquid crystals [315]. They used a simple sputter deposition process, which allowed them to prepare thin liquid crystal films of well-dispersed gold nanoparticles in both 5CB and E47 (available from Merck) with a nanoparticle size depending on the used nematic liquid crystal. Unfortunately, the authors did not provide any details on whether the nanoparticles were capped with a ligand or bare, non-coated particles, which makes it difficult to assess and compare the reported thermal as well as electro-optic data. However, very similar effects were found as a result of nanoparticle doping, including lower nematic-to-isotropic phase transition temperatures compared to the used pure nematics as well as 10% lower threshold voltages at nanoparticle concentrations below 1 wt% [315].

BaTiO₃ particles are another very attractive and intensively studied type of nanoparticles in nematic liquid crystals. Cook et al. reported on an asymmetric Fréedericksz transition, where doping nematic TL205 with single domain ferroelectric BaTiO₃ nanoparticles (9 nm in diameter) reduced or increased the threshold voltage by 0.8 V depending on the polarity of the applied voltage [149].

Blach and co-workers also observed a lower Fréedericksz transition threshold voltage (V_{th}) for 5CB doped with rather large BaTiO₃ particles (150 nm in diameter) [316], which is surprising considering an earlier report by West and Reznikov et al., who found no such reduction of V_{th} using smaller, chemically similar nanoparticles [317].

In addition to lowering V_{th} , ferroelectric nanoparticles such as BaTiO₃ or Sn₂P₂S₆ [144, 156, 318–323] have also been shown to increase the nematic-to-isotropic phase transition temperature ($T_{N/iso}$) and the order parameter of the nematic host [142, 320, 324–326], which are thought to have their origin in a coupling of the electric dipole moment of the particles with the orientational order of the surrounding nematic molecules (Fig. 6).

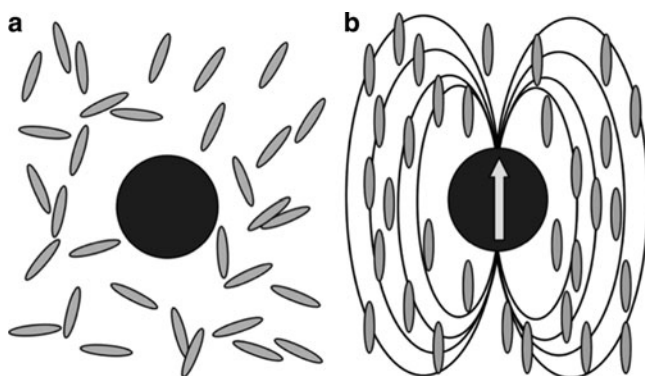


Fig. 6 (a) Cartoon of a nanoparticle with no electric dipole moment in the isotropic phase. (b) Cartoon of a ferroelectric nanoparticle with electric dipole moment, which produces an electric field that interacts with orientational order of the nematic phase [327]. (Copyright © 2009, American Physical Society)

Lopatina and Selinger recently presented a theory for the statistical mechanics of ferroelectric nanoparticles in liquid crystals, which explicitly shows that the presence of such nanoparticles not only increases the sensitivity to applied electric fields in the isotropic liquid phase (maybe also a possible explanation for lower values for V_{th} in the nematic phase) but also $T_{N/Iso}$ [327]. Another computational study also supported many of the experimentally observed effects. Using molecular dynamics simulations, Pereira et al. concluded that interactions between permanent dipoles of the ferroelectric nanoparticles and liquid crystals are not sufficient to produce the experimentally found shift in $T_{N/Iso}$ and that additional long-range interactions between field-induced dipoles of nematic liquid crystal molecules are required for such stabilization of the nematic phase [328].

In addition, Glaser and co-workers reported earlier on the behavior of spherical nanoparticles, focusing first on the isotropic nematogen matrix [329] and later on the nematic phase itself [330]. In the isotropic phase, the nematogens show the tendency for frustrated planar anchoring, which results in long-range reduction of the orientational ordering compared to the pure isotropic phase. The local orientational order and weakly long-range repulsive interactions between nanoparticles were found to depend on the size of the suspended nanoparticles [329]. Glaser et al. confirmed experimental observations that spherical nanoparticles are generally better “soluble” in the isotropic than in the nematic phase. Finally, nematic matrix induced intermediate-range repulsion interactions between nanoparticles and nematic molecules in the isotropic phase were also described for the case of homeotropic anchoring, but particle–particle interactions not only led to suppression of repulsion but to nanoparticle aggregation [330].

Beneficial electro-optic effects have also been reported for semiconductor quantum dots doped into nematic liquid crystals. Khoo and Mallouck et al. published one of the earlier reports on suspensions of quantum dots in nematic liquid crystals [331]. This work, however, focused on CdSe nanorods and will be discussed in a later section on two-dimensional nanomaterials in liquid crystals.

Kitzerow et al. recently demonstrated that temperature-induced phase transitions (Iso-N) and electric field-induced reorientation of a nematic liquid crystal (5CB in this case) can be used to tune photonic modes of a microdisc resonator, in which embedded InAs quantum dots serve as emitters feeding the optical modes of the GaAs-based photonic cavity [332].

Tong and Zhao presented an interesting concept of using the electric field response of a chiral nematic liquid crystal containing either a self-assembled physical network or a covalently cross-linked polymer to modulate the photoluminescence intensity of CdSe/ZnS core-shell quantum dots [333]. To avoid aggregation in these networks, the authors used rather low concentrations of the quantum dots (0.02 or 0.2 wt%), which might explain why altered electro-optic properties were not observed. Zhang et al., for example, found lower threshold voltages in 5CB doped with CdS quantum dots (by up to 25% in twisted nematic cells) [334].

Our group also reported on mixtures of a nematic 2-phenyl-pyrimidine derivative (Felix-2900-03) containing either hexadecylamine-capped CdSe (ranging in size from 2.5 to 5.2 nm) or thioglycolic acid-capped CdTe quantum dots (3.2–4.0 nm in

diameter). Quantum dots of each series were effective in reducing V_{th} as well as the splay elastic constant (K_{11}) in anti-parallel cells. Interestingly, the smallest quantum dot (CdSe, 2.5 nm in diameter) showing the least aggregation tendency in Felix-2900-03 (even at 5 wt%), showed the largest effect (lowest V_{th}) [98].

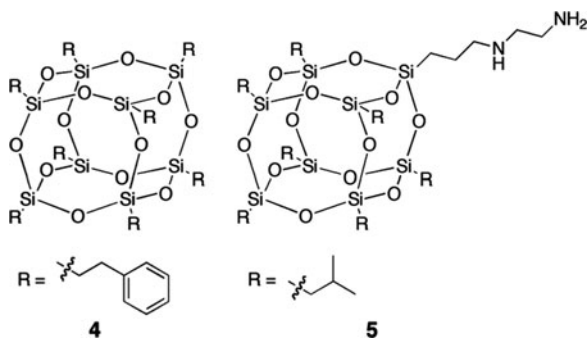
When combined with available data on insulating nanoparticles such as ZnO, TiO₂, and Si₃N₄ in nematic liquid crystals [335], one can conclude that most metallic, semiconducting, ferroelectric as well as insulating nanoparticles can be used to tune and improve the electro-optic characteristics of nematic liquid crystals without the need for additional chemical synthesis. A reduction of the operating or threshold voltage, which is not observed for all systems [336], is likely the most prominent and promising feature related to applications in display devices, but the causes for this reduction in V_{th} are as diverse as the colloids used in these studies. Nanoparticle aggregation, segregation at interfaces, intrinsic properties of the nanoparticle core material, and influential effects of the capping monolayer have been shown to impact the electro-optic properties of the nematic host.

Moreover, segregation of nanoparticles at liquid crystal/substrate interfaces is also an effective way to promote or alter the alignment of thin nematic liquid crystal films. Depending on their concentration, size, and nature, several types of nanoparticles have been shown to induce homeotropic alignment as well as defects and remarkable defect patterns.

Hwang et al. and Liao et al. have shown that nanoparticle analogs such as polyhedral oligomeric silsesquioxanes (POSS) can be used to induce homeotropic alignment, particularly in ITO/glass cells without alignment layers and in so-called hybrid aligned nematic (HAN) cells. In one experiment, phenethyl POSS or aminoethyl-aminopropylisobutyl-POSS (**4** and **5** in Fig. 7, available from Aldrich) were first dispersed in E7 ($\Delta\epsilon = 14.5$) or MLC6882 ($\Delta\epsilon = -3.1$) [337, 338], then segregated to both interfaces, and induced homeotropic alignment (Fig. 8).

Tuning of the pre-tilt angle at the interface was also demonstrated by doping commonly used polyimide alignment layers with POSS nanoparticles [339]. In addition, the fabrication of a tunable liquid crystal flat microlens was achieved by placing a drop of a nematic liquid crystal doped with POSS nanoparticles onto a substrate inducing planar alignment (local HAN mode) [340]. Simultaneously, Takatoh and co-workers extended this concept to a series of metal oxide

Fig. 7 Examples of polyhedral oligomeric silsesquioxane (POSS) nanoparticles used to induce homeotropic alignment in nematic liquid crystals



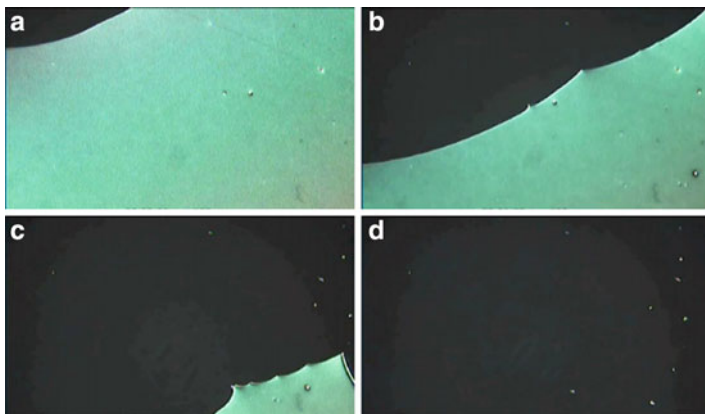


Fig. 8 The dynamic process of POSS-induced vertical alignment in an LC cell observed with a POM (observation area of 1.5×1.0 mm: (a) during filling of the cell, (b) 1 min later, (c) 2 min later, and (d) 3 min later [337]. (Copyright © 2009, IOP Publishing Ltd)

nanoparticles such as BaTiO_3 , MgO , CaCO_3 , and TiO_2 with sizes ranging from 10 to 200 nm in diameter. They found an enhancement of the contrast ratio, but with respect to liquid crystal alignment, only minor changes in the pre-tilt angle [341]. Theoretical work such as Cheung and Allen's studies using classical density functional theory may here provide further insight into the underlying interactions between nanoparticles and surfaces in nanoparticle-doped nematic liquid crystals [342, 343].

Masutani et al. have shown that nanoparticles can be embedded into polymer-dispersed liquid crystal (PDLC) matrices and reduce the viewing angle dependency of a gain reflector as well as metallic glare [344]. Also Huang et al. demonstrated that silica nanoparticles (Aerosil[®]R812 with 7 nm diameter, Degussa-Huls), which are negatively charged, migrate to the planar side of a HAN cell after driving the cell with a d.c. pulse voltage and induce homeotropic alignment (a memory mode). The authors of the latter, in principle, achieved a dual mode device with a memory mode after applying a d.c. pulse and a dynamic mode with lower response times when the same cell is driven with an a.c. pulse [345].

Recently, Chen and co-workers also presented a combination of photo- and nanoparticle-induced alignment, where the homeotropic alignment induced by POSS nanoparticles can be changed into planar alignment by adsorption of a photo-excited azo-dye [346–348].

Considering all of the above, it should in theory also be possible to combine useful electro-optic effects with nanoparticle-induced alignment. Our group has shown that gold nanoparticles as well as quantum dots capped primarily with hydrocarbon chains (thiols for gold nanoparticles and amines for CdSe quantum dots) can induce homeotropic alignment in thin nematic films sandwiched between plain glass, ITO-coated glass, as well as cells coated with polyimide alignment layers. In addition to induced homeotropic alignment, we regularly observed the

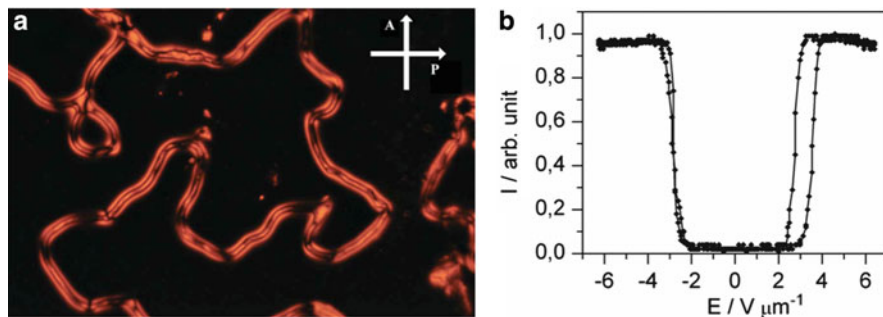


Fig. 9 (a) POM image of a liquid crystal dispersion consisting of 3 wt% gold nanoparticles (diameter: 5.4 nm) capped with dodecylthiol dispersed in Felix-2900-03 (obtained using monochromatic light, $\lambda = 589$ nm, and crossed polarizers) [350]. (Copyright © 2010, Taylor & Francis) (b) Electro-optic characteristics of Felix-2900-03 doped with 5 wt% of dodecylthiol-capped Au-nanoparticles (diameter: 1.9 nm) inducing homeotropic alignment. The frequency of the applied a.c. voltage is 0.01 Hz, and the measurement was performed with monochromatic light ($\lambda = 579$ nm) [352]. (Reproduced by permission of The Royal Society of Chemistry)

simultaneous formation of birefringent stripes and patterns thereof (Fig. 9a), which we first thought originated from the aggregation of the nanoparticles in these birefringent stripe domains [349]. Thorough two- and three-dimensional imaging studies using fluorescence confocal polarizing microscopy (FCPM) later showed that these birefringent stripes are not walls spanning the entire liquid crystal films and that they are located at the top liquid crystal-substrate interface. FCPM also helped us to determine the director fields in and around these stripes [350] as well as clarify that the nanoparticles, which primarily reside at both liquid crystal-substrate interfaces, are responsible for the induced homeotropic alignment at these substrates [351].

A more detailed study of the alignment inducing effects of gold nanoparticles capped with alkyl thiolates (ranging in size from 1.6 to 5.4 nm in diameter) revealed that preloading the cells' polyimide alignment layers with nanoparticles, similar to the approaches described above, produced cells with almost defect-free homeotropic alignment. Additionally, we were able to observe that the change from the initial, substrate-induced planar alignment to the nanoparticle-induced homeotropic alignment was not only temperature-dependent but also thermally reversible (i.e., the alignment transition was observed at the same temperature on heating and cooling several degrees below $T_{\text{iso/N}}$) [353]. Finally, we also found that this contrast inversion is causing an instability, which in turn leads to the formation of convection rolls [354–362], providing the basis for the earlier reported dual alignment and frequency dependent, dual electro-optic switching mode [300, 363] in these nanoparticle-doped nematic liquid crystal systems (the transmission vs applied voltage plot for the 0.01 Hz low frequency switching mode is shown in Fig. 9b) [352].

2.1.2 Zero-Dimensional Nanoparticle Additives in the Chiral Nematic Phase

Several exciting phenomena described for non-chiral nematic systems were also reported for nanoparticle-doped chiral nematic liquid crystals. We mentioned the work of Kobayashi et al., who, most notably, demonstrated a frequency modulation twisted nematic (FM-TN) mode and fast switching characteristics using metal nanoparticles as dopants [301–307, 313, 314].

Guo et al. demonstrated an interesting concept based on composites consisting of magnetite (Fe_3O_4) nanoparticles either bare (around 50 nm in diameter) or coated with oleic acid (smaller in diameter). The exact size and size distribution was unfortunately not disclosed, and neither was the exact nature of the iron or iron oxide surface states (no Mössbauer spectroscopy data). Nevertheless, the authors showed that the oleic acid-protected magnetite nanoparticles formed more homogeneous dispersions in comparison to the bare magnetite particles, and that composites of magnetite nanoparticles capped with oleic acid and additionally modified with a chiral dopant can eventually be developed into flexible and magnetically addressable/erasable color optical devices (or so-called M-paper, see Fig. 10) [364].

Our group pursued another approach of combining the properties of nanoparticles with chiral nematic liquid crystal phases. The idea was to decorate gold nanoparticles with chiral molecules known to be strong inducers of chiral nematic phases. To realize the idea, we prepared a series of alkylthiol-capped gold nanoparticles, either pure monolayer or mixed monolayer, with all or about every second of the alkylthiols end-functionalized with (*S*)-naproxen (e.g., **6** in Fig. 11) [349].

Using circular dichroism (CD) spectropolarimetry experiments, we demonstrated that these nanoparticles induce chiral nematic liquid crystal phases in non-chiral nematic hosts such as 5CB not only more effectively in comparison to the pure organic chiral dopant (more intense CD signals at lower overall chiral dopant loading) but also with the opposite helical sense [365]. In addition, these nanoparticles provided new insights into the different mechanisms discussed for chiral ligand-capped gold nanoparticle chirality as well as place-exchange reactions (thiol-for-thiol exchanges) on gold nanoparticle surfaces [366].

2.1.3 Zero-Dimensional Nanoparticle Additives in Smectic Phases

In comparison to nematic liquid crystals, examples of smectic liquid crystals doped with quasi-spherical nanoparticles became more elusive over the last few years. This is surprising especially considering recent work by Smalyukh et al., who found that nanoscale dispersion (based on *N*-vinyl-2-pyrrolidone-capped gold nanoparticles with 14 nm diameter) in a thermotropic smectic liquid crystal (8CB) are potentially much more stable than dispersions of nanoparticles in nematics [367].

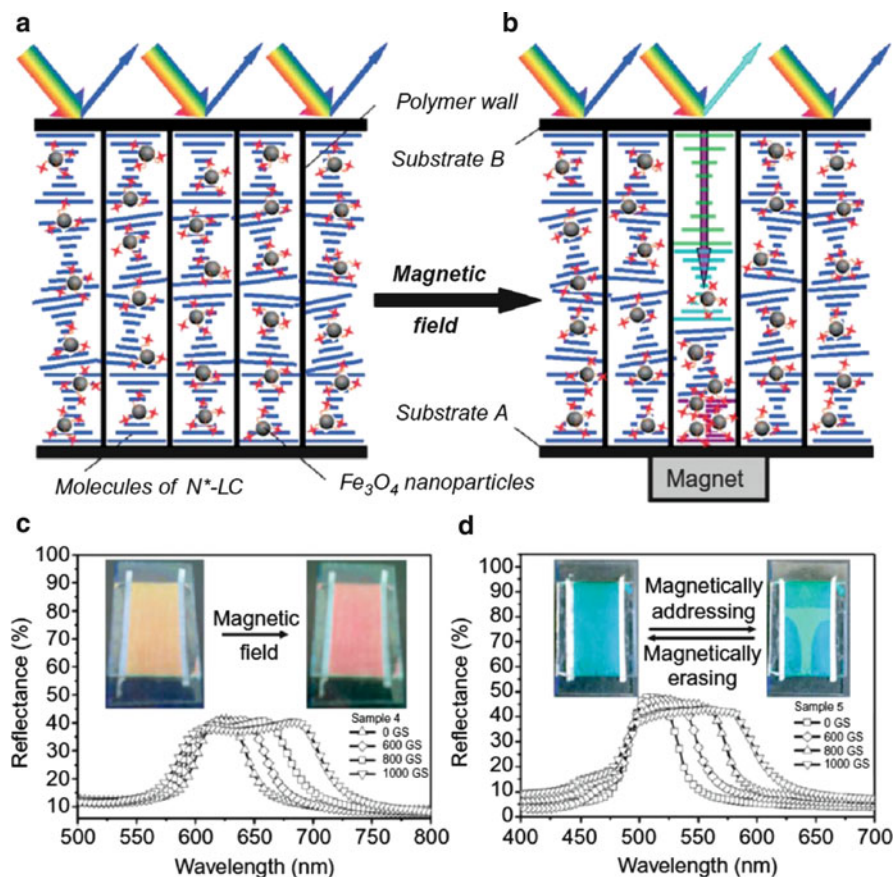


Fig. 10 (a, b) Schematic mechanism demonstrated for a reflective color M-paper with magnetically controllable characteristics. (c, d) The intensity of magnetic field dependence on the reflection spectra of chiral nematic mixtures doped with magnetite nanoparticles that are surface modified with oleic acid and a chiral pyridine-based dopant, as well as photographs of both formulations before and after a magnetic field of 1,000 GS was applied (see photograph insets above) [364]. (Copyright © 2010, Taylor & Francis)

Earlier work on nanoparticle-doped chiral smectic-A (SmA^*) and chiral smectic-C (SmC^*) phases including some intriguing electro-optic effects in ferroelectric SmC^* phases were summarized in two earlier reviews [1, 2].

Hydrophilic and hydrophobic AerosilTM particles forming gels and networks in nematic and smectic liquid crystal phases received continuous attention over the past two decades or so. Nounesis et al., for example, investigated both hydrophilic AerosilTM 300 and hydrophobic AerosilTM R812 (both with a diameter of approximately 7 nm, Degussa Corp.) in three different SmA - $SmC^{(*)}$ materials (two chiral materials with an SmA - $SmC^{(*)}$ and one achiral SmA - SmC compound). Using high-resolution calorimetric and small angle X-ray diffraction experiments, the authors

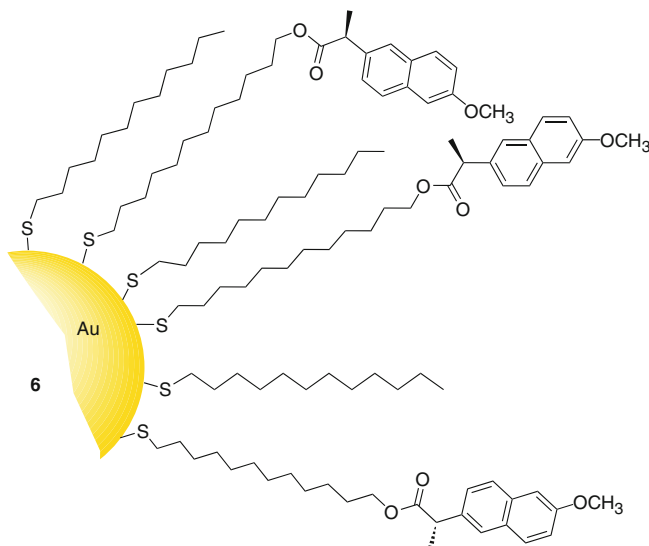


Fig. 11 Mixed monolayer alkythiol-capped gold nanoparticle end-functionalized with (*S*)-naproxen chiral dopant moieties [349, 365, 366]

confirmed that the layer thickness in the SmA phase monotonically decreased with an increasing concentration of the AerosilTM particles, and that this effect was more pronounced for the achiral liquid crystal host. In both composites based on chiral hosts, the layer shrinkage exhibited a pronounced crossover where the AerosilTM network shows its concentration-dependent soft-stiff transition. The authors suggested that the layer shrinkage is coupled to an aerosil-induced tilt of the LC molecules with respect to the layer planes [368]. A related study on reentrant nematic behavior in mixtures of 8OCB/6OCB showed that the gel formed by doping with AerosilTM 300 particles preserved the reentrant behavior but destroyed the long-range order of the SmA phase [369].

Martínez-Miranda et al. investigated the effects of different coatings on the surface of magnetic Fe_xCo_y nanoparticles (2 and 11 nm in diameter) in the SmA phase of 8CB, and showed that the nature of the coating had an immense effect on the reorientation of the liquid crystal molecules in response to an applied magnetic field [370].

Dispersions of nanoparticles in ferroelectric liquid crystals (FLCs) predominantly focused on induced or altered electro-optic effects, but also on the alignment of FLCs. Raina and co-workers reported on a gradual decrease of the dielectric permittivity, ϵ , by doping with SiO₂ nanoparticles at frequencies up to 1 kHz and a rather minor increase of ϵ as well as an increase in optical transmission at frequencies above 2 kHz [279]. Liang et al. used BaTiO₃ nanoparticles (31 nm in diameter after grinding commercially available 90 nm nanoparticles; Aldrich) and showed, perhaps expectably, a twofold increase in the spontaneous polarization

(P_S) and a nanoparticle concentration-dependent increase in the dielectric permittivity [371].

An opportunity to induce homeotropic alignment in various ferroelectric liquid crystal mixtures was demonstrated by Kumar et al. using co-polymer nanoparticles of polybenzene and anthracene (size not disclosed). The authors showed that an increasing concentration of the polymeric nanoparticles resulted in an increase of P_S (at least at concentrations of about 10 wt%), but also an increase of the rotational viscosity (η) and the response time (τ_R) [372, 373]. Biradar and co-workers earlier reported on dispersions in FLCs using gold nanoparticles prepared by citrate reduction (approximately 10–15 nm in diameter). However, citrate-capped gold nanoparticles are negatively charged and not particularly stable, which leads to questions on the cause for the observed memory effects [374, 375], and the observation of enhanced photoluminescence attributed to a coupling of the localized surface plasmon polaritons to the surrounding FLC molecules [376].

Finally, the groups of Biradar and Huang both found an increase in the optical contrast (contrast ratio) in FLC mixtures doped with ZnO nanoparticles, and ascribed this effect to dipolar interactions between nanoparticles and FLC molecules [377, 378].

2.1.4 Zero-Dimensional Nanoparticle Additives in Blue Phases

In the past, blue phases largely remained a subject of scientific curiosity, because for many years the rather limited temperature range (commonly from 0.5 to 2°C) severely restricted further scientific exploration as well as practical use of these intriguing phases. Early work on blue phases primarily focused on new materials [379–392], their response to electric fields [393–406], the shape of blue phase crystals grown for example under an applied electric field [407–409], as well as lasing in blue phases [410].

With the discovery of wide temperature range blue phases in liquid crystal bimesogens (or terminal twins) by Coles et al. [411] and polymer-stabilized blue phases by Kikuchi et al. [412], blue phases are currently experiencing a renaissance [413, 414]. Now, wide temperature range blue phases (including room temperature) are sought after and being developed for use in display applications [415–422], for lasing [423, 424], and for tunable photonic band gap materials [425, 426].

It was really only a matter of time until researchers in the field started doping blue phases with quasi-spherical nanoparticles. This area is very much in its infancy, but the few recent reports already show some promising results. Yoshida et al., for example, reported on an expansion of the temperature range of cholesteric blue phases from 0.5 to 5°C by doping blue phases with gold nanoparticles (average diameter of 3.7 nm) as well as a decrease in the clearing point of approximately 13°C [427]. A similar effect was also observed by Kutnjak et al. for CdSe quantum dots simultaneously capped with oleyl amine and TOP (diameter of the core: 3.5 nm) in CE8 (Merck) and CE6 (BDH). The authors found that particularly blue phase III was stabilized in these mixtures, blue phase II destabilized, and

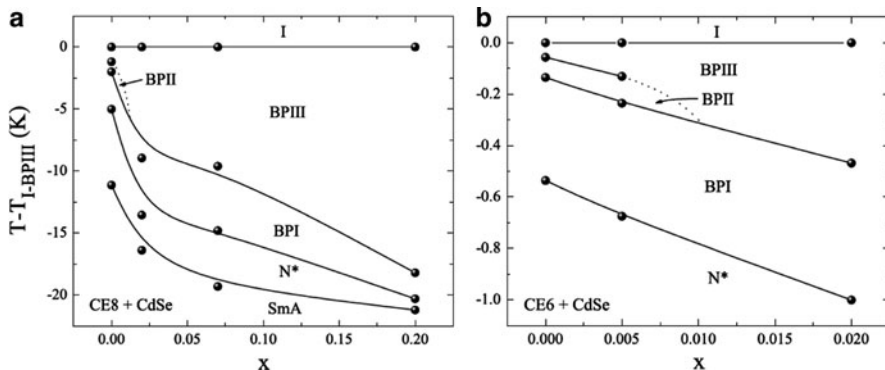


Fig. 12 (a) Reduced temperature $T - T_{Iso/BP}$ vs x_{CdSe} phase diagram for CE8 + CdSe mixtures obtained from cooling runs by a.c. colorimetry. T_{I-BP} was found to be a weak function of x . (b) $T - T_{Iso/BP}$ vs x_{CdSe} plot for CE6 + CdSe mixtures obtained from heating runs by adiabatic scanning calorimetry. For clarity the data in both diagrams are plotted vs the T_{I-BP} [428]. (Copyright © 2010, The American Physical Society)

blue phase I remained more or less unaffected in CE8 and was slightly stabilized in CE6 at lower quantum dot loadings (Fig. 12) [428].

Both groups claimed that the mechanism of nanoparticle stabilization of blue phases is similar to that reported for polymer stabilized blue phases [412], with the nanoparticles accumulating or being trapped in the lattice disclinations, which finds support from numerical modeling of colloidal particles in blue phases recently described by Žumer and co-workers [429].

2.1.5 Zero-Dimensional Nanoparticle Additives in Columnar Phases

Surprisingly, columnar liquid crystal phases have not yet received much attention as host materials for nanoparticles. Columnar liquid crystal phases often show high charge-carrier mobilities and generation efficiencies, making them prime candidates for organic photovoltaics [430–433], and these applicable features could potentially be altered, even enhanced, by the addition of small quantities of metal, semiconductor or other nanoparticles. Problems for the creation of such composites could be related to the higher viscosity of some columnar phases (compared to nematics), a lower dispersibility in columnar phases as a result thereof, and the general shape mismatch between quasi-spherical nanoparticles and disc-like molecules stacking to form columns.

Kumar et al. nevertheless succeeded in creating stable suspensions of hexanethiol-capped gold nanoparticles (1.6 nm core diameter) and gold nanoparticles capped with a 10CB thiol (similar to nanoparticle 3 in Fig. 5) in a lyotropic hexagonal columnar phase (H1 phase formed by a 42:58 w/w Triton X-100/water system) as well as an inverse hexagonal columnar phase (H2 phase formed by AOT). Both types of nanoparticles were shown to stabilize the H1 phase

(increase in clearing point) and increase the ordering of the phase (additional $\sqrt{7}$ peaks in SAXS experiments). Similarly, the H2 phase of AOT shows an increase in ordering after nanoparticle doping. In all cases, the nanoparticles are thought to reside outside of the columnar core, dispersed between the columns, with the column dimensions remaining virtually constant [434].

The same research group also reported on dispersions of gold nanoparticles capped with triphenylene-based discotic liquid crystals in a hexagonal columnar triphenylene host, and found that doping the columnar phase with these nanoparticles enhanced the electrical conductivity by several orders of magnitude [435, 436]. Holt and co-workers confirmed these results by demonstrating a similarly significant increase (10^6) in electrical conductivity in the same hexagonal columnar liquid crystal doped with methylbenzene thiol-protected gold nanoparticles (diameter of the core: 2.7 nm). The authors show that nanoparticle aggregation and formation of smaller chain-like aggregates may be responsible for this conductivity enhancement [437].

2.2 *One-Dimensional Nanoparticle Additives: Nanorods and Nanotubes*

2.2.1 **Metal Nanorods**

The past decade has witnessed an increasing interest in possible applications of nanorods, nanotubes, and nanowires as nonlinear optical (NLO) materials, photo-sensors [438], photo-induced memory devices, and in numerous other technologically important applications. The need to obtain ordered and assembled architectures of nanorods has led to the development of new methodologies for organizing these anisotropic building blocks. Two main strategies have been traditionally followed: (1) embedding metal nanorods in a polymer film and subsequently warming up and stretching the composite film (with the nanorods tending to align in a preferred direction given by the elongation of the polymer molecules) [439, 440] and (2) alignment and assembly approaches utilizing nanorod surface chemistry.

Doping nanorods into liquid crystals may represent an alternative means through which long-range nanorod alignment could be accomplished. Moreover, alignment on substrates and reorientation of liquid crystal molecules in response to an applied electric or magnetic field would offer the possibility to obtain tunable metamaterials. In practice, however, this has proven to be a difficult task, mainly due to problems associated with preparing thermotropic LC mixtures with well dispersed GNRs [441].

Here, a paper by Smalyukh et al. stands out, which reports on nanorod alignment using likely more suitable lyotropic liquid crystals [6]. The authors demonstrated spontaneous, long-range orientational ordering of CTAB-capped GNRs dispersed in lyotropic nematic and hexagonal columnar liquid crystalline phases formed by

the CTAB/benzyl alcohol/water ternary system. The alignment was achieved in bulk samples with an area of about 1 in^2 and thicknesses ranging from several micrometers to millimeters. Freeze-fracture TEM images corresponding to different fracture planes containing the director show unidirectional alignment of well dispersed GNRs. The nanorods follow the orientation of the director of the anisotropic fluids and are separated by distances comparable with their length. Similar to common nematics, no correlation of the nanorods' centers of mass was observed. The two-dimensional orientational order parameter was estimated to be 0.86–0.91 (based on these TEM images), while the three-dimensional ordering was deduced from polarized extinction spectra recorded for different angles between the linear polarizer and the director. The authors calculated a three-dimensional order parameter of a shear-aligned columnar hexagonal sample to be about 0.46. This relatively low value is due to the imperfect alignment of the director at the millimeter scale, where micron-sized domains with slightly misaligned director orientations were clearly visible. Using dark-field microscopy it was shown that within these microdomains the local order is higher and that the order parameter values are consistent with those deduced from TEM images. In addition, if a magnetic field is applied to a nematic sample annealed from its isotropic phase, both the rod-like micelles and the suspended nanorods orient along the external magnetic field and preserve this uniform alignment after the field is turned off. Polarized surface plasmon resonance (SPR) spectra of these magnetically aligned samples revealed that the GNRs were imposed to follow the director of the liquid crystal, and that the orientation of GNRs in the nematic phase can be controlled by magnetic fields.

Interested in the electronic effects of GNR on nematic liquid crystals, Prasad et al. studied the electro-optic properties of GNR/8CB suspensions [442]. The authors found that the introduction of rod-like colloidal gold particles into the nematic fluid: (1) did not destabilize the mesophase, (2) enhanced the dielectric anisotropy by about 14%, and (3) dramatically increased the elasticity anisotropy. Furthermore, the electrical conductivity was raised by more than three orders of magnitude after GNR doping, with both σ_{\parallel} and σ_{\perp} increasing. However, unlike quasi-spherical gold nanoparticles, probably because of their anisometric shape, the introduced GNRs did not significantly change the anisotropy of the conductivity.

Electro-optic effects induced by doping liquid crystals with one-dimensional metal nanoparticles were not only investigated in standard electro-optic test cells, but also in costume-made cells consisting of a thin layer of liquid crystal either deposited onto a thin film of alumina with embedded GNRs [443], or using rubbed polyimide alignment layers modified with solution-cast GNR [444]. In both cases, surface plasmon resonance frequencies of the GNR integrated into these liquid crystal cells could be electrically controlled.

Finally, magnetic nanowires and other submicrometer-scale anisometric particles can also be manipulated and organized via controlled spatial variations in the alignment of nematic liquid crystals. Leheny and co-workers, for example, measured the elastic forces imposed on anisotropic Ni nanowires suspended in a nematic liquid crystal (here 5CB, Fig. 13a), and showed that by applying a magnetic field the nanowire reorients and distorts the director in the adjacent area [445, 446].

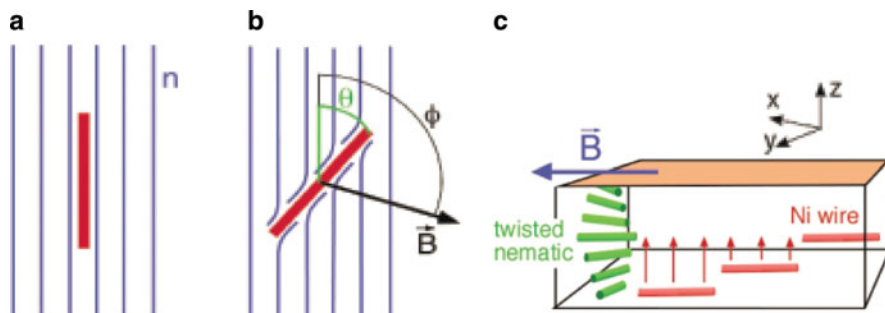


Fig. 13 Schematic representation of the orientation-dependent elastic torque on a nickel nanowire with longitudinal anchoring in 5CB: (a) in equilibrium, and (b) in the presence of a magnetic field. (c) Levitation of the nanowire in a twisted nematic cell [446]. (Copyright © 2004, American Association for the Advancement of Science)

The wire comes to rest at an angle θ when the magnetic torque and elastic torque balance (see Fig. 13b).

For a wire that rotates away from $\theta = 0$ near a plate, the longitudinal anchoring of the liquid crystal at the surface of the wire and the planar alignment induced by the rubbed polyimide layer that covers the glass slides will introduce a twist in the director between the underside of the wire and the plate, leading to a repulsive force between them. When the applied magnetic field positions the wire along the director, the elastic energy becomes a function of the wire's height within the film, leading to a levitating force on a wire resting on the bottom substrate (see Fig. 13c). Thus, by varying the direction of an external magnetic field, one can control the alignment of a magnetic nanowire within the nematic film, and this can be converted to a translational force on the wire when the nematic order varies.

2.2.2 Semiconductor Nanorods

One-dimensional semiconductor nanorods, because of their unique electronic, optical, and mechanical properties, are attractive dopants for liquid crystals. Hence, composites of these two distinctive materials undoubtedly have great potential for applications in electronic and optical devices.

Chen et al. reported on a general approach by which the polarization of the emission from semiconductor nanorods can be manipulated by an external bias. In their device, the composite of a nematic liquid crystal mixture (E7, Merck) and nanorods (CdS) filled into an ITO-coated cell with an optimized concentration of one CdS nanorod per 10^{10} LC molecules was used to achieve the highest polarization ratio of the suspended nanorods [447, 448]. The nematic liquid crystal in this system acts as a solvent and media whose direction of alignment can be tuned by an applied electric field. Hence, the orientation of the CdS nanorods can be fine-tuned by an external bias because of the anchoring force between the liquid crystal

molecules and the nanorods. This unique property of fine-tunable emission anisotropy opens up new possibilities of applications in smart optoelectronic devices.

Interactions between nanorods and liquid crystals were also used to modify electro-optic properties of liquid crystals. Several groups reported lower threshold voltages in nematic liquid crystals doped with nanorods [449–452]. Acharya et al. reported on a blend of ultra-narrow ZnS nanorods (1.2 nm in diameter and 4.0 nm in length) in a nematic liquid crystal mixture (ZLI-4792), and found that the long-range ordering of the blend was enhanced due to a favorable energetic configuration as a result of the refractive index compatibility of the liquid crystal and the octadecylamine surfactant coating the nanorods [449, 450]. In addition, the electro-optic properties of this blend were enhanced due to the effective dielectric anisotropy derived from the strong inherent dipole moment (~ 37 D) of these ultra-small nanorods. As a result, the threshold voltage of the blend was reduced by up to 10% in comparison to the pristine liquid crystal, and the optical response time was improved to 4 ms from 33 ms for the neat liquid crystal mixture.

On a side note, Ouskova and co-workers also reported that the composite of magnetic β -Fe₂O₃ nanorods in 5CB showed lower threshold voltages than pure 5CB, and that the sensitivity of the nematic liquid crystal to external magnetic fields was increased in the presence of such magnetic nanorods [451]. Finally, several groups interested in the macroscopic organization and orientation of nanorods also reported on the formation of a lyotropic liquid crystal phase induced by the self-assembly of polymer-coated semiconductor nanorods [453–457], which might be used to improve the device performance, for example, of solar cells.

2.2.3 Carbon Nanotubes

The self-organization of both thermotropic and lyotropic liquid crystals make these ordered fluids remarkable media for the dispersion and organization (alignment) of CNTs. This subject has been the focus of a recent excellent review by Scalia [231], theoretical work on anchoring at the liquid crystal/CNT interface by Popa-Nita and Kralj [458], and a number of earlier experimental reports on liquid crystal/CNT composites demonstrating that liquid crystal orientational order can be transferred to dispersed CNTs, which is commonly illustrated using polarized Raman spectroscopy [459–462].

From this collective work it becomes obvious that CNTs integrate into liquid crystal matrices and are capable of inducing detectable effects on the electro-optic properties of liquid crystals, even at very low concentrations, which could be very attractive for display applications. Accordingly, one extremely important issue is the quality of CNT dispersion in liquid crystals. To probe this, i.e., minimizing aggregation and increasing the long-term stability of dispersions, Lagerwall et al. systematically studied several CNT mixtures using a number of pure and multi-component liquid crystals [463]. The authors showed that there is not only a structural dependence (choice of liquid crystal host) on the quality of these dispersions and the maximum CNT concentration, but also that some mechanical

aspects like stirring and the duration of sonication in the dispersion process are rather critical. Their results suggest that liquid crystals with longer alkyl chains and less aromatic content as well as multi-component nematic mixtures (due to lower solvation entropy) are better in solubilizing CNTs.

Lagerwall and Tschierske et al. also showed that the addition of polyphilic liquid crystalline molecules acting as dispersion promoters is a viable and very promising approach for stabilizing CNT in liquid crystal/CNT dispersions [464]. In this work, rationally-designed polyphilic molecules were synthesized featuring three distinct sub-units; a rod-like mesogenic cyanobiphenyl core that is compatible with the liquid crystal host, flexible hydrocarbon or ethylene oxide spacers, and terphenyl, anthracene, or pyrene anchor groups interacting with the CNTs via π - π stacking (Fig. 14).

Another interesting approach for organizing CNTs using liquid crystals was reported by Kimura and co-workers [465]. The authors synthesized π -conjugated oligo(phenylene vinylene) (OPV) liquid crystals featuring terminal cyanobiphenyl moieties (Fig. 15), and demonstrated the formation of stable supramolecular complexes with SWCNTs through strong π - π interactions between the sidewall of the tubes and the phenylene vinylene segments. These OPV units can also wrap around the SWCNTs imparting excellent solubility in organic solvents. In addition, it was found that precipitates from such dispersions exhibit thermotropic liquid

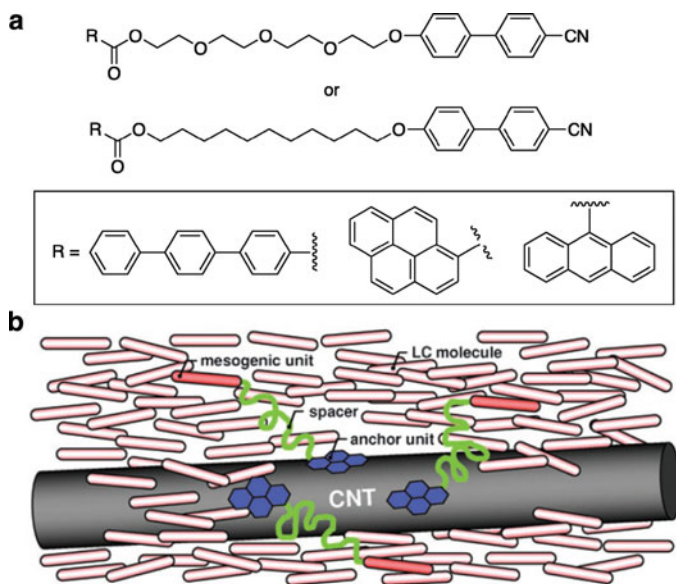


Fig. 14 (a) Chemical structures of the polyphilic dispersion-promoter molecules. (b) Tailor-designed polyphilic molecules promoting CNT dispersion in the nematic host. Pyrene anchoring group (blue), mesogenic CB unit (dark red), flexible hydrocarbon or ethylene oxide spacer (green), and liquid crystal host (light red) [464]. (Reproduced by permission of The Royal Society of Chemistry)

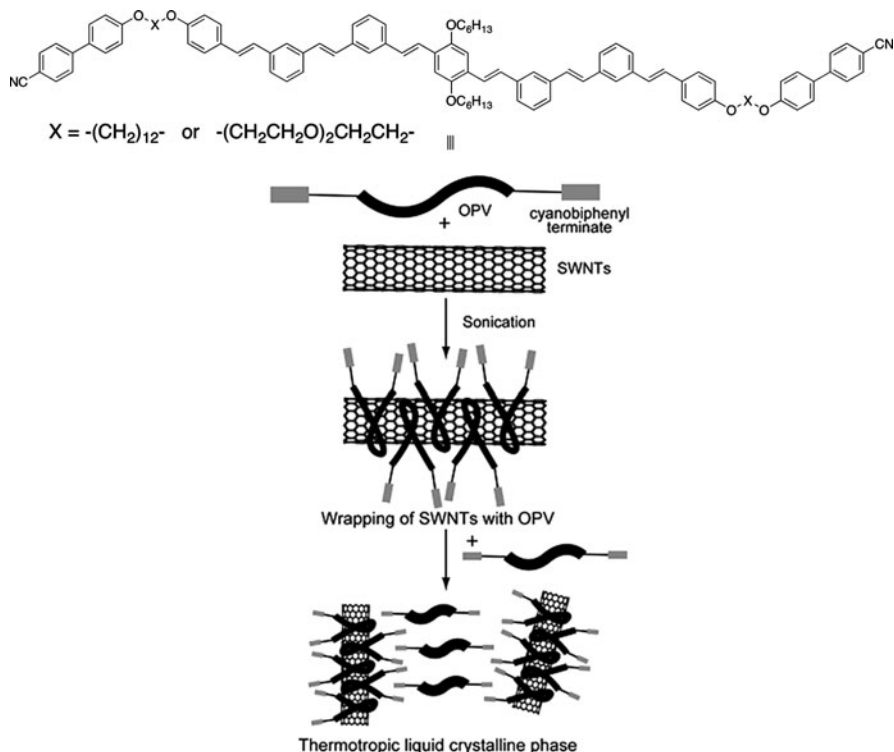


Fig. 15 Schematic illustration of the self-organizing processes for the composite of liquid crystalline OPV oligomers and SWCNTs [465]. (Reproduced by permission of The Royal Society of Chemistry)

crystalline phase behavior. This result is quite significant since the dispersion of SWCNTs within these custom-made liquid-crystalline hosts not only promotes good solubility but also provides new opportunities for dynamically changing the orientation of SWCNTs within the composites.

Different characterization methods like scanning probe microscopy techniques, optical microscopy, elastic light scattering, resonant Raman spectroscopy, and absorption spectroscopy (visible and IR) for monitoring the quality CNT-liquid crystal dispersions along with appropriate sample preparation for each characterization method have also been discussed [466]. Interestingly, the concentration of commercially available, functionalized SWCNTs in an equilibrated liquid crystal solution (supernatant of a filtered liquid crystal/CNT mixture after settling for 2 weeks) was estimated to be around 10^{-9} wt%, showing that these commercial samples are far from ideal liquid crystal/CNT dispersions with an adequate concentration of nanotubes [466].

Several other groups reported interesting combinations of experimental and theoretical results on the alignment and electro-optic response of CNTs in thermotropic nematic liquid crystals [467–469]. However, lyotropic liquid crystals should

also be considered potential platforms for CNT dispersion and alignment. First, many surfactants that are versatile dispersants for CNTs [470] can form lyotropic liquid crystalline phases and, second, successful CNT dispersion and alignment in aqueous media can open new doors for biological applications [471]. Sodium dodecyl sulfate (SDS) – the most common surfactant for dispersing and aligning CNTs – in its nematic liquid crystal phase either with disc- or rod-shaped micelles – can be used to disperse commercial HiPCO SWCNTs (from a high-pressure CO conversion process) without any optically visible bundling [472, 473]. The advantage of using surfactants (and lyotropic liquid crystal phases formed by these molecules) is their inherent excellent ability to keep CNTs well dispersed, efficiently counteracting the strong tendency of CNTs to aggregate into disordered bundles, together with macroscopically uniform alignment.

In addition to nematic lyotropic phases, integration of SWCNTs in a hexagonal lyotropic liquid crystal phase has been successfully demonstrated [474–477]. Regev et al. using small angle X-ray scattering experiments indicated that SWCNTs can indeed be integrated into such liquid crystal phases, as manifested by an increase of the lattice parameter at CNT concentrations up to 0.15 wt%, which the authors associate with a swelling induced by the incorporation of SWCNTs within the cylinders of the hexagonal phase. Above 0.15 wt%, a decrease of the lattice parameter was regarded as an indication of slow phase separation [474].

Further work by Lagerwall et al. showed that a combination of cationic and anionic surfactants forming a hexagonal columnar lyotropic liquid crystal phase not only generates well-dispersed, macroscopically aligned suspension of unsupported CNTs with a 20-fold increase in nanotube concentration but also allows the transfer of liquid crystal-dispersed CNTs to solid substrates and provides access to aligned thin filaments, which could both prove to be excellent ways for handling and processing CNTs [475, 476]. This approach may well open up new ways towards easy and cheap fabrication of devices requiring CNTs deposited on substrates and aligned along selected directions. Recently, anisotropic CNTs films were also fabricated from lyotropic liquid crystal polymers using either *p*-sulfo-phenylene terephthalamide [478] or polymerizable dodecyldimethyl-ammonium ethyl methacrylate as surfactant molecules [479]. Hence, research on CNT alignment using liquid crystals is thriving.

Likewise, there are numerous studies targeting mainly the improvement of electro-optic properties of liquid crystals by incorporating CNTs. The preparation, characterization, and analysis of electro-optic properties of liquid crystal/CNT dispersions featuring widely used nematic liquid crystals was disclosed in several recent reports [480–484], and have been reviewed by Lee et al. [485]. For example, CNTs induced a frequency and concentration-dependent dielectric permittivity in 5CB [486]. Basu et al. reported on the significant impact of CNTs on the isotropic to nematic phase transition in CNT-doped liquid crystals [487]. The same group also demonstrated a dramatic improvement in the nematic ordering and an increase of the dielectric anisotropy ($\Delta\epsilon$) in 5CB even in the isotropic phase, and attributed these effects to an enhancement in the orientational order parameter, S , promoted by a strong anchoring between 5CB molecules and the CNTs as a result of π - π

stacking [488, 489]. In addition, ionic properties of liquid crystal/CNT dispersions [490], CNT-induced chirality [491], and an irreversible electro-optic response (i.e., electro-optic memory effects) were all subjects of recent studies on liquid crystal/CNT suspension [492–494].

Haase and co-workers investigated electro-optic and dielectric properties of ferroelectric liquid crystals doped with chiral CNTs [495, 496]. The performance of the doped liquid crystal mixture was greatly affected even by a small concentration of CNTs. The experimental results were explained by two effects: (1) the spontaneous polarization of the ferroelectric liquid crystal is screened by the π -electron system of the CNT and (2) the CNT π -electrons trap ionic impurities, resulting in a significant modification of the internal electric field within liquid crystal test cells.

Another example of a dispersion of SWCNTs in a multi-component antiferroelectric smectic-C* liquid crystal mixture was shown by Lagerwall and Dabrowski et al. [497]. In this study, SWCNTs caused the appearance of a single-layer SmC* phase between the SmA phase and the crystalline state in comparison to the non-doped sample exhibiting an SmA and two specific intermediate phases, an SmC* $_{\beta}$ and an SmC* $_{\gamma}$ phase.

Finally, dispersions of MWCNT in chiral nematic liquid crystals were studied as well. These experiments suggested no change in the helical twisting characteristics of the chiral nematic phase. However, the MWCNTs were thought to disrupt the translational order in the SmA phase (decrease of the SmA-N* phase transition) yet follow the twist of the nematic director in the chiral nematic phase [498].

2.3 Two-Dimensional Nanoparticle Additives: Nanoclay

Suspensions of organically modified clay (for the various types see Sect. 1.2.7) in liquid crystal phases almost exclusively focus on the nematic host 5CB. These studies commonly use calorimetric measurements, small and wide angle X-ray diffraction, as well as optical and electro-optic analysis to study the exfoliation (dispersion in the nematic host and penetration of nematic molecules between clay sheets), aggregation, and induced electro-optic effects. Earlier work by Pizzey et al. laid down some of the groundwork for later studies. They showed that laponite clay stabilized with a quaternary ammonium surfactant forms fairly stable suspensions in 5CB consisting of freely tumbling discs that do not tend to aggregate. Claytone[®] AF, however, formed stacks of discs in the same liquid crystal host [499, 500]. Related optical microscopy and small angle X-ray scattering inspections by van Duijneveldt and co-workers also revealed that there is a noticeable difference in how certain clays behave in 5CB as a nematic host with respect to their dispersion or aggregation tendency [501, 502].

Series of studies by Huang et al. as well as Puchkovska and co-workers concentrated on electro-optic effects induced by the addition of organoclays to 5CB. Puchkovska et al. reported on electro-optic contrast and memory effects as a

result of van der Waals interactions between the two components as well as interface orientational effects [503–505], and Huang et al. concluded that the effective trapping of impurity ion charges that enhances the nematic molecular order is the underlying cause for these observed electro-optic effects [274, 506–508]. Optical transparency and memory effects (i.e., a residual transparency after the electric field is switched off) were also described for polymer-dispersed liquid crystal (PDLC) devices containing organically modified clays [509]. Finally, Lee et al. succeeded in the creation of holographic PDLC devices consisting of either pristine or organically modified montmorillonite clay [510, 511].

One can certainly expect more work in the area of organoclay-doped liquid crystals in the near future. The hope is that these studies will not be limited to polar 5CB as a host material only, which is not necessarily an ideal host, but explore other nematic systems and other liquid crystal phases.

3 Liquid Crystalline Nanoparticles

The final section of this review will provide an overview of recent work on the design of liquid crystalline nanoparticles accomplished by protecting the surface of nanomaterials with mesogenic or pro-mesogenic capping agents. We will limit the discussion to metal and metal oxide nanomaterials (Au, TiO₂, and Fe₂O₃). The spontaneous self-assembly of pristine nanoparticles (nanorods and nanodiscs), i.e., those not capped with liquid crystal functionalities, were summarized in Sect. 1.2.7 and in an earlier review [1]. Carbon-based liquid crystalline nanomaterials such as fullerenes and fullerodendrimers [512–531], graphene [532], or carbon nanotubes [246, 247, 254] have also been the focus of extensive research over the last few years, and a number of design concepts for creating liquid crystalline fullerenes, for example, have been effectively applied to metal and metal oxide nanoparticles (see below).

For thermotropic liquid crystalline nanoparticles three basic design concepts seem to show the most promising roads to success. In all cases, quasi-spherical metal or metal oxide nanoparticles were decorated with calamitic mesogenic or pro-mesogenic ligands either in an end-on fashion with the functional group binding to the nanoparticle at the terminal end of the molecule or a side-on fashion using rod-like mesogens with a chemical functionality binding to the nanoparticle surface at the end of a lateral hydrocarbon chain. Finally, dendrons bearing mesogenic units at the termini were used, binding to the nanoparticle with a functional group at the focal point (7–9 in Fig. 16).

In 2003, Sugimoto and Kanie published what appears to be the first claim on the formation of nematic-like one-dimensional ordering in liquid crystal-nanoparticle hybrid materials. Different shapes of TiO₂ nanoparticles were hybridized with two structurally different rod-like liquid crystal amines (one based on a cyanobiphenyl and a second with a fluorinated cyclohexylbiphenyl core), but only the combination of spindle-like TiO₂ nanorods (with an aspect ratio greater than 10) with the

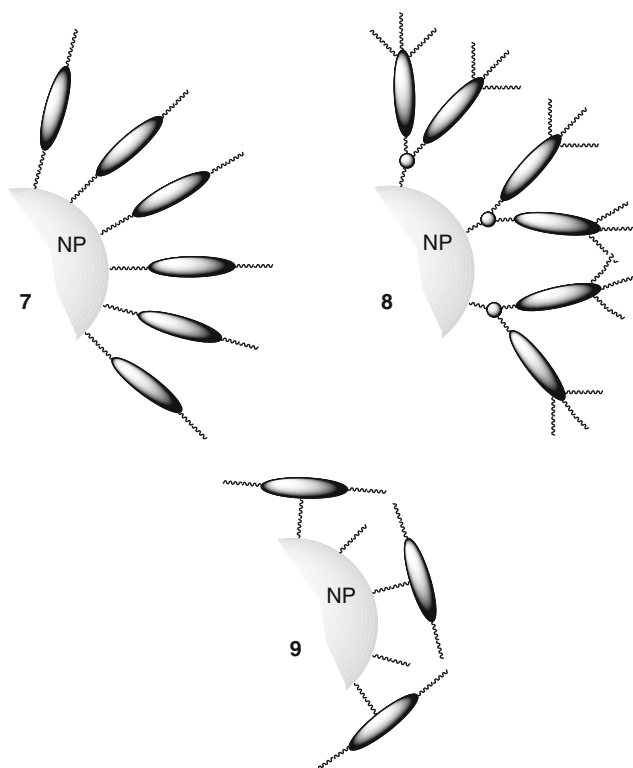


Fig. 16 2D-cartoons of quasi-spherical nanoparticles protected with mesogenic or pro-mesogenic capping agents giving rise to liquid crystalline quasi-spherical nanoparticles. The three major approaches include the decoration: with calamitic molecules in an end-on fashion (7), with dendrons featuring calamitic or polycatenar moieties at the termini (8), and with laterally substituted calamitic molecules in a side-on fashion (9). The concept shown for the quasi-spherical nanoparticle 7 was also successfully used for spindle-like nanoparticles [533, 534]

terphenyl amine derivative showed birefringent textures (reminiscent of a nematic phase) and nematic-type ordering in small angle X-ray diffraction experiments (see 10 in Fig. 17). The TiO_2 nanospindles are likely simultaneously capped with both the liquid crystalline cyclohexylbiphenyl amine and ethylenediamine (the reagent used to control the nanoparticle shape). Unfortunately, no sufficient analysis to estimate the ratio of the two capping ligands on the nanoparticle surface was provided (or to show whether the nanoparticle is coated entirely with the liquid crystal amine) [533]. Kanie and Muramatsu later extended these studies to hematite ($\alpha\text{-Fe}_2\text{O}_3$) nanoparticles with shapes ranging from spindle-like to cuboidal to hexagonal platelets. This time, the capping liquid crystal molecules were end-functionalized with phosphate groups to enable binding to the iron oxide nanoparticle surface, and again only the non-cyanobiphenyl-based liquid crystal phosphate ligand (11 in Fig. 17) gave rise to nematic-like organization for the spindle-like nanoparticles and a simple cubic liquid crystal morphology for cuboidal

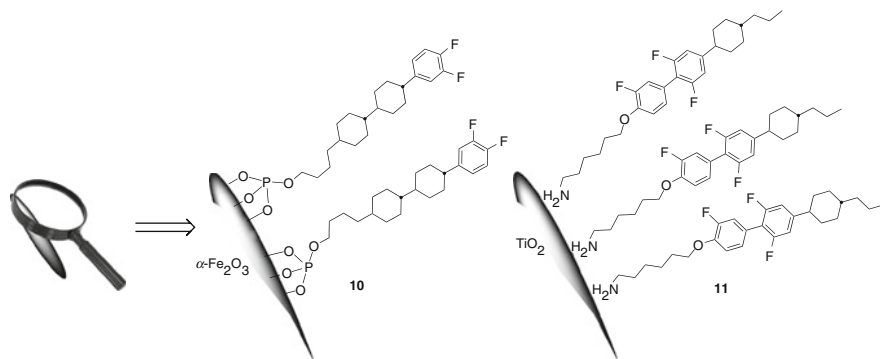


Fig. 17 Spindle-like hematite (**10**) [534] and anatase (**11**) [533] nanoparticles coated with calamitic liquid crystals

nanoparticles. However, the exact surface composition (i.e., how many liquid crystal ligands are on the nanoparticle surface) is not known since phosphate (KH_2PO_4) was also used in the nanoparticle synthesis [534]. Generally, the shape of the nanoparticle and the type of liquid crystal ligand used in both studies appeared to play the most crucial roles in the formation of liquid crystal superstructures.

Quasi-spherical gold nanoparticles decorated with mesogenic rod-like as well as pro-mesogenic discotic thiol ligands showed remarkable self-assembly properties but no apparent formation of identifiable liquid crystal phase behavior. Ikeda and co-workers described the formation of a “mesoscopic” phase (perhaps a nematic phase) for gold nanoparticles (diameter: 3.0 nm) capped with a monotropic nematic cyclohexylphenoxy thiol derivative [535]. Later, Kim et al. showed that gold nanoparticles (2.7 nm in diameter) capped exclusively with cyanobiphenyl thiol ligands [536] (similar to **3** [298] in Fig. 5) formed one-dimensional string-like nanoparticle aggregates using TEM and SAXS investigations [537]. Similarly, Miyake and co-workers used a triphenylene thiol derivative to cap gold nanoparticles ranging in diameter from 2.4 to 3.0 nm, and showed using TEM that these nanoparticles form beautiful quasi-hexagonal or linear arrays with a varying degree of π - π stacking between triphenylene units of neighboring particles depending on the ratio between methanol and toluene used to drop-cast these nanoparticles on TEM grids (**12** in Fig. 18) [538].

John and Ajayan et al. were able to take a related approach even one step further. Using glass-forming chiral liquid crystals (featuring SmC^* , SmA , TGBA^* , and N^* phases), the authors effectively demonstrated not only the single-step (no additional reducing or stabilizing agents), shape-selective synthesis of gold nanoparticles (spherical, rod-like and triangular-shaped) using only the liquid crystals as reducing agents, but also the creation of hierarchically ordered gold nanoparticles at multiple length scales [539].

Cseh and Mehl at last showed that quasi-spherical gold nanoparticles are capable of forming genuine liquid crystalline phases. The approach they used was to decorate gold nanoparticles (1.6–2 nm in diameter) with a mixed monolayer of

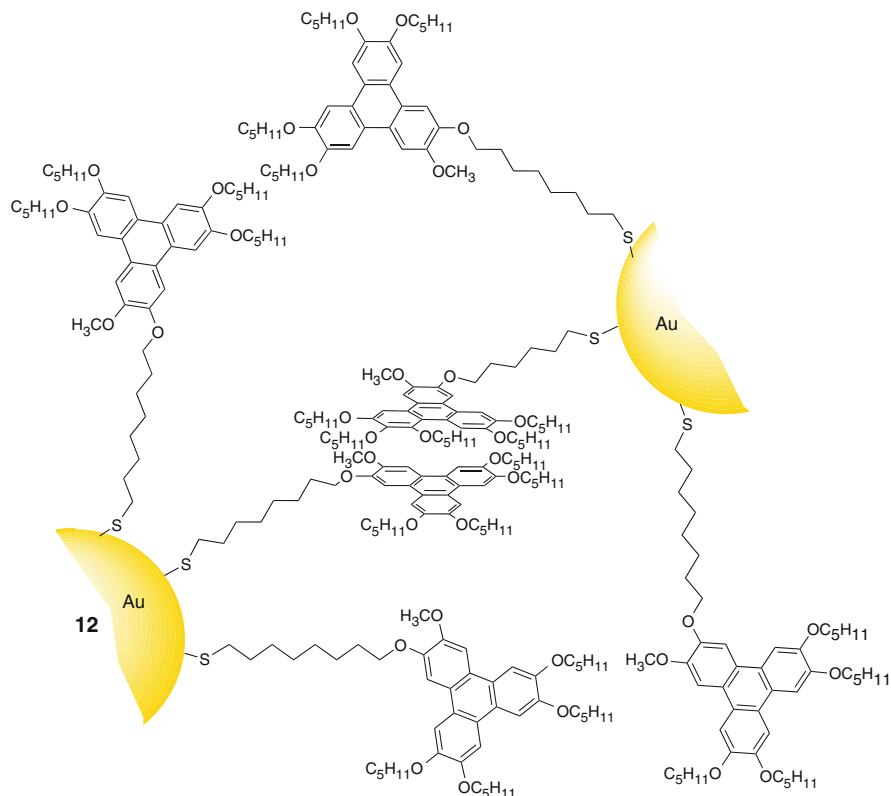


Fig. 18 Gold nanoparticles capped with triphenylene thiols forming linear arrays due to full π - π -stacking of triphenylenes attached to adjacent gold nanoparticles. Adapted from Fig. 2c in [538]

thiols (ratio $\sim 1:1$), i.e., an alkanethiol (length of the hydrocarbon chain either C6 or C12) and a lateral substituted rod-like nematic thiol in a side-on fashion as shown in cartoon **9** in Fig. 16 (see **13** and **14** in Fig. 19) [540, 541].

Preliminary investigations of the liquid crystal phase behavior of these gold nanoparticles initially revealed an enantiotropic nematic phase (based on polarized light optical microscopy and thermal analysis) as well as some pattern formation of the gold nanoparticles in TEM experiments [540, 541].

In depth X-ray diffraction and TEM experiments on these systems by Ungar et al. recently showed that the metal nanoparticles form gold strings that pack in rhombohedral (**14**) or hexagonal and rectangular columnar lattices (**13**) surrounded by a nematic continuum formed by the rod-like mesogenic groups – stunning examples of highly ordered nanoparticle superlattices (Fig. 20) [542].

Finally, Donnio et al. showed that capping gold nanoparticles with an alkyl thiol (dodecanethiol) as well as a second generation dendron, providing mixed monolayer-capped gold nanoparticles (**15** in Fig. 21), results in the formation of a

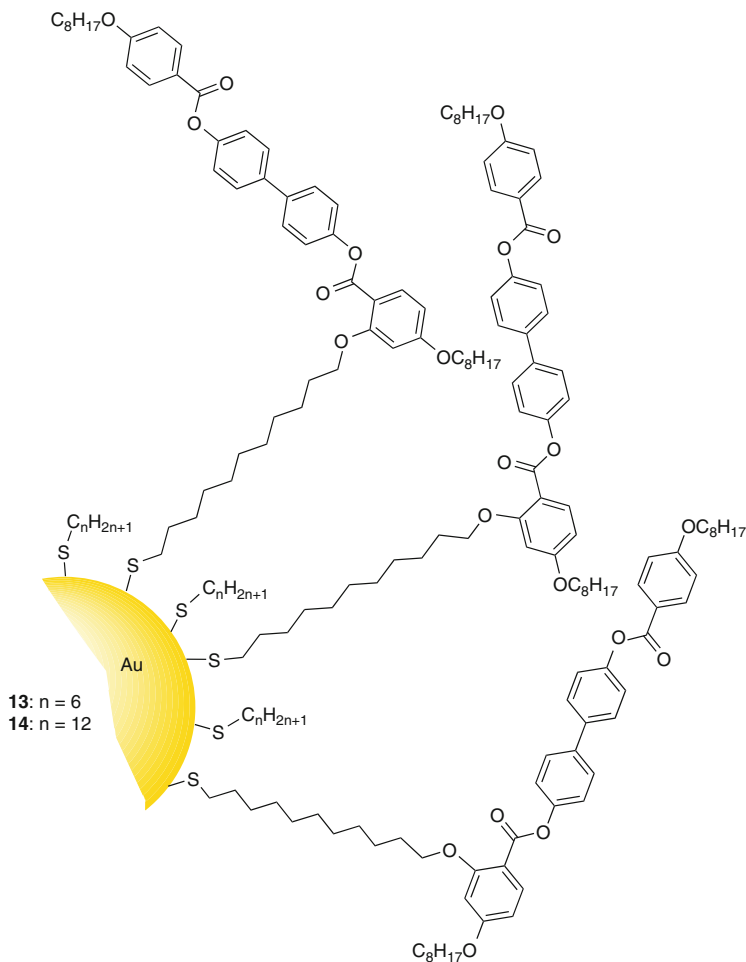


Fig. 19 Gold nanoparticles **13** and **14** capped with a mixed monolayer of hexanethiol (**13**) or dedecanethiol (**14**) and a lateral substituted nematic liquid crystal thiol in a side-on fashion (thiol ratio: $\sim 1:1$) [540, 541]

body-centered cubic phase with $Im\bar{3}m$ symmetry, which also displayed pattern formation after drop-casting on TEM grids and ferromagnetic properties from 1.8 to 380 K with a remanent magnetization ranging from $0.27 \mu_B$ to $0.14 \mu_B$, respectively [543]. Recently, the authors investigated the magnetic properties of these dendronized nanoparticles in more detail, and ascribed the observed magnetic effects to the existence of a spin glass-like behavior that is coupled to the liquid crystal order parameter of the mesomorphic gold nanoparticles [544].

Initial attempts to replicate the idea of using dendronized liquid crystal ligands to induce mesophase formation in magnetic nanoparticles failed for core-shell

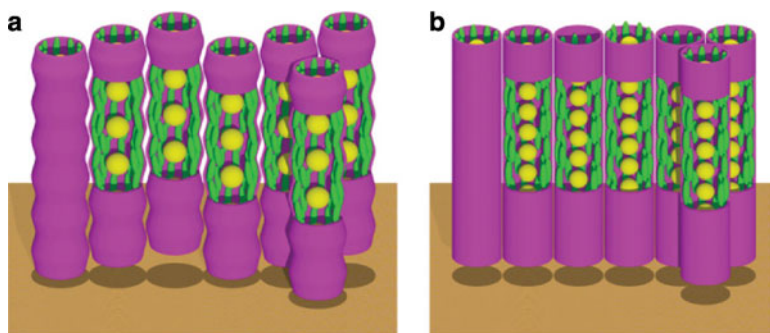


Fig. 20 Schematic models of the gold nanoparticle strings: (a) rhombohedral phase of **14** and (b) hexagonal columnar phase of **13**. Gold nanoparticles are in yellow, mesogens in green [542]. (Copyright © Wiley-VCH Verlag GmbH & Co. KGaA, reproduced with permission)

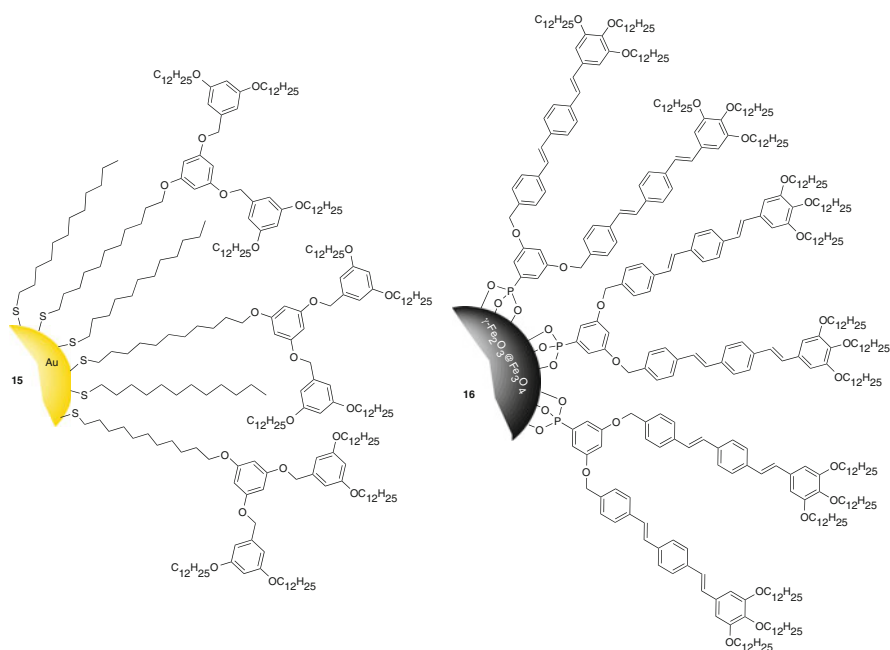


Fig. 21 Nanoparticles decorated with dendronized ligands: gold nanoparticles forming a cubic phase (**15**) [543], and non-mesogenic $\gamma\text{-Fe}_2\text{O}_3@Fe_3O_4$ core-shell nanoparticles (**16**) [131, 545]

magnetite/maghemite nanoparticles ($\gamma\text{-Fe}_2\text{O}_3@Fe_3O_4$) with an average diameter of 39 nm despite the use of mesomorphic oligo(phenylene vinylene)-based dendrons forming broad hexagonal columnar liquid crystal phases (**16** in Fig. 21). Nevertheless, these particles, where the lack of liquid crystal phase formation was attributed to the mismatch in size between the nanoparticle core and the much smaller liquid

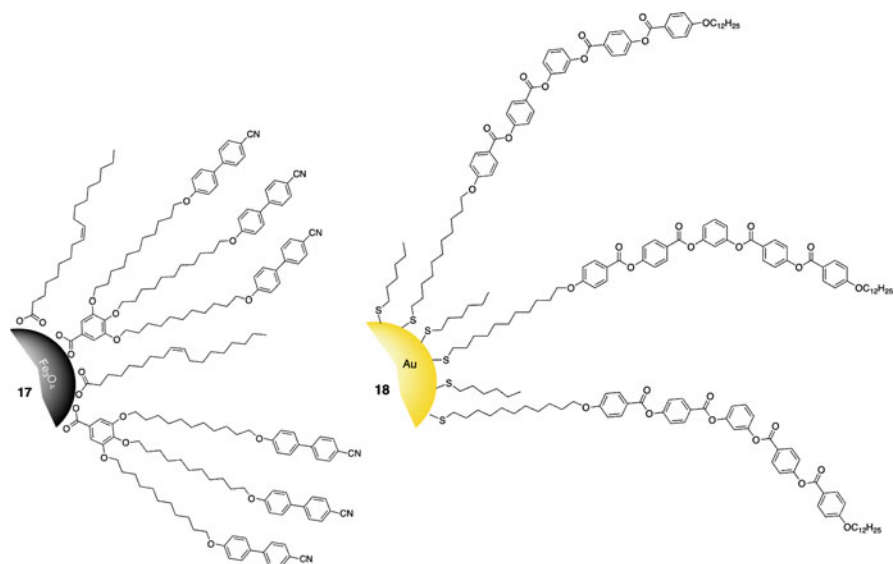


Fig. 22 Nanoparticles decorated with pro-mesogenic dendronized or bent-core liquid crystal ligands: nematic Fe_3O_4 mixed monolayer nanoparticles capped with dendronized cyanobiphenyl ligands and oleic acid (**17**) [132], and mixed monolayer, non-mesogenic gold nanoparticles decorated with bent-core liquid crystal and hexane thiolates (**18**) [547]

crystal ligands, show interesting magnetic as well as luminescent properties, which could be extremely useful for applications in data storage or biomedical imaging [131, 545]. Drastically reducing the size of the magnetic iron oxide nanoparticle cores to an average of 3.3 nm in diameter using Hyeon's thermal decomposition methodology [133], and using cyanobiphenyl-based pro-mesogenic dendrons together with non-mesogenic oleic acid ligands (**17** in Fig. 22), the same group succeeded in creating mesomorphic magnetic iron oxide nanoparticles with room temperature nematic phase behavior [132].

Deschenaux et al. were likely first to use this combination of mesomorphic cyanobiphenyl-based dendrons, both mixed and homogeneous monolayer fashion, on gold nanoparticles with average sizes of 1.2 or 1.7 nm in diameter, but found no liquid crystal phase formation in the bulk aside from the pattern formation on TEM grids resembling a layer-like organization of the gold nanoparticles [546].

Finally, our group reported on gold nanoparticles decorated with bent-core liquid crystals showing pattern formation on TEM grids after slow solvent evaporation (**18** in Fig. 22). These particles showed interesting self-assembly effects in different bent-core liquid crystal hosts (SmCP_A and Col_r) and slightly improved electro-optic effects such as shorter response time, τ , and unaltered spontaneous polarization in the SmCP_A host, but no mesophase formation [547].

4 Conclusion and Future Outlook

The field of liquid crystal nanoscience has experienced tremendous growth over the past decade. Research on nanoparticle-doped liquid crystals makes use of a wide variety of nanoparticles differing in size, shape, core material, and coating (Fig. 23).

The most significant progress has been made for nanoparticle-doped nematic phases, both chiral and achiral, and the observed alignment and electro-optic effects bode well for the use of such liquid crystal nanocomposites in electro-optic applications. Smectic liquid crystal phases have yet to see a major breakthrough, but initial results in the area of nanoparticle-doped ferroelectric liquid crystals are promising. Blue phases will surely see a surge of research over the next few years based on the increasing interest in blue phase mode displays, and if stable nanoparticle-doped blue phase composites can be created that show both wide temperature ranges and lower operating voltages (here Kerr effect) frequently observed for nanoparticle-doped nematic liquid crystal composites (Fréedericksz effect).

Many possible combinations of nanoparticle core material, shape, and surface functionality have not yet been examined independent of the liquid crystal host phase, and more focused structure/size/shape-property relationship studies are needed to draw comprehensive conclusions about nanoparticle-induced effects. Such studies would ideally start with truly monodisperse (so-called magic-numbered or magic-sized) nanoparticles and vary only one parameter at the time (e.g., the hydrocarbon chain length of the capping ligand). Many unique effects were also only reported for a very limited number of liquid crystal hosts. Not surprisingly, 5CB is still the nematic liquid crystal used in the majority of investigations, but progress in terms of applications of liquid crystal nanocomposites will only be made if the observed effects could either be generalized for many liquid crystal hosts or tailored for hosts used in specific applications.

The long-term stability of the nanomaterials used as well as the liquid crystal composites containing these are also very critical points that will need to be addressed with future research. Likewise, a complete characterization of all nanoparticles used is essential given the plethora of possible dissimilarities from one batch to another including size, size distribution, surface coverage, thermal stability, and ligand distribution on the nanoparticle surface (for mixed monolayer-capped nanoparticles), to name but a few.

Finally, an area that will most likely see an explosive growth over the next few years is the self-assembly of nanoparticles covered with mesogenic and pro-mesogenic capping agents. A number of different approaches have been summarized in this review, and the formation of nematic, smectic-like, cubic, and columnar phases and/or superstructures have been demonstrated. Once more, the possibilities to produce such metamaterials using nanoparticles and liquid crystal motifs are endless, and future research will surely discover other, in part, more complex phase morphologies as well as uniquely tunable nanoscale properties as a result of liquid crystal phase formation.

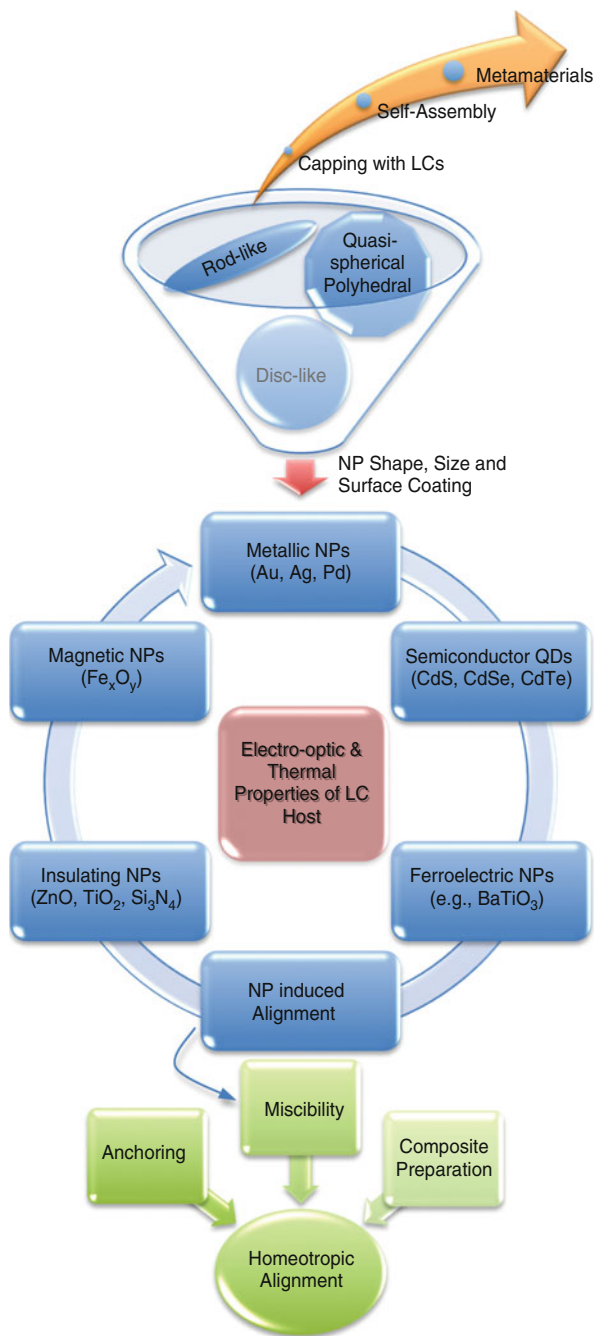


Fig. 23 A graphical summary of liquid crystal nanoscience summarized in this review. This chart shows the link between nanoparticles (their size, shape, and coating) and liquid crystals, effects induced in liquid crystal phases, as well as nanoparticle mesomorphism (*NP* nanoparticle, *LC* liquid crystal, *QD* quantum dot)

References

1. Hegmann T, Qi H, Marx VM (2007) *J Inorg Organomet Polym Mater* 17:483
2. Qi H, Hegmann T (2008) *J Mater Chem* 18:3288
3. Agarwal A, Lilly GD, Govorov AO, Kotov NA (2008) *J Phys Chem C* 112:18314
4. Sanchez-Iglesias A, Grzelczak M, Rodriguez-Gonzalez B, Alvarez-Puebla RA, Liz-Marzan LM, Kotov NA (2009) *Langmuir* 25:11431
5. Kretzers IKJ, Parker RJ, Olkhov RV, Shaw AM (2009) *J Phys Chem C* 113:5514
6. Liu QK, Cui YX, Gardner D, Li X, He SL, Smalyukh II (2010) *Nano Lett* 10:1347
7. Lin MH, Chen HY, Gwo S (2010) *J Am Chem Soc* 132:11259
8. Srivastava S, Kotov NA (2009) *Soft Matter* 5:1146
9. Kiehl RA (2007) Nanomaterials synthesis, interfacing, and integrating in devices, circuits, and systems II 6768:Z7680
10. Chen Y, Zhang YM, Liu Y (2010) *Chem Commun* 46:5622
11. Grzelczak M, Vermant J, Furst EM, Liz-Marzan LM (2010) *ACS Nano* 4:3591
12. Moth-Poulsen K, Bjornholm T (2010) *Chimia* 64:404
13. Ernenwein D, Ghosh P, Rotello V, Chmielewski J (2010) *J Mater Chem* 20:5608
14. Born P, Murray E, Kraus T (2010) *J Phys Chem Solids* 71:95
15. Barick KC, Bahadur D (2010) *J Nanosci Nanotechnol* 10:668
16. Hu T, Gao Y, Wang ZL, Tang ZY (2009) *Front Phys China* 4:487
17. Shibu ES, Muhammed MAH, Kimura K, Pradeep T (2009) *Nano Res* 2:220
18. Aldaye FA, Sleiman HF (2009) *Pure Appl Chem* 81:2157
19. Khan SJ, Pierce F, Sorensen CM, Chakrabarti A (2009) *Langmuir* 25:13861
20. Bishop KJM, Wilmer CE, Soh S, Grzybowski BA (2009) *Small* 5:1600
21. Lu ZD, Goebel J, Ge JP, Yin YD (2009) *J Mater Chem* 19:4597
22. Mangold MA, Weiss C, Calame M, Holleitner AW (2009) *Appl Phys Lett* 94:161104
23. Yi CQ, Liu DD, Yang MS (2009) *Curr Nanosci* 5:75
24. Chattopadhyay S, Mukherjee R, Datta A, Saha A, Sharma A, Kulkarni GU (2009) *J Nanosci Nanotechnol* 9:190
25. Goodby JW, Bates M, Saez IM, Gorecka E, Kitzerow HS, Guillon D, Donnio B, Serrano JL, Deschenaux R (2009) Polymer-based smart materials – processes, properties and application 1134:261
26. Min YJ, Akbulut M, Kristiansen K, Golan Y, Israelachvili J (2008) *Nat Mater* 7:527
27. Marsh DH, Rance GA, Whitby RJ, Giustiniano F, Khlobystov AN (2008) *J Mater Chem* 18:2249
28. Hansen CR, Westerlund F, Moth-Poulsen K, Ravindranath R, Valiyaveetil S, Bjornholm T (2008) *Langmuir* 24:3905
29. Verdes C, Chantrell RW, Satoh A, Harrell JW, Nikles D (2006) *J Magn Magn Mater* 304:27
30. Farrell D, Cheng Y, Kan S, Sachan M, Ding Y, Majetich SA, Yang L (2005) *J Phys Conf Ser* 17:185
31. Bethell D, Schiffrin DJ, Kiely C, Brust M, Fink J (2001) Hyper-structured molecules II – chemistry, physics and applications: 179
32. Hong H, Shin H, Chung I (2007) *J Disp Technol* 3:361
33. Lyu JJ, Sohn J, Kim HY, Lee SH (2007) *J Disp Technol* 3:404
34. Hoogboom J, Rasing T, Rowan AE, Nolte RJM (2006) *J Mater Chem* 16:1305
35. Kawamoto H (2002) *Proc IEEE* 90:460
36. Scharl W (2010) *Nanoscale* 2:829
37. Cademartiri L, Ozin GA (2010) *Philos Trans Royal Soc A* 368:4229
38. Gaponik N, Hickey SG, Dorfs D, Rogach AL, Eychmuller A (2010) *Small* 6:1364
39. Ma QA, Su XG (2010) *Analyst* 135:1867
40. Nune SK, Gunda P, Thallapally PK, Lin YY, Forrest ML, Berkland CJ (2009) *Expert Opin Drug Del* 6:1175
41. Peng XH, Chen JY, Misewich JA, Wong SS (2009) *Chem Soc Rev* 38:1076

42. Galian RE, de la Guardia M (2009) *Trac-Trend Anal Chem* 28:279
43. Reiss P, Protiere M, Li L (2009) *Small* 5:154
44. Khanna VK (2008) *Defence Sci J* 58:608
45. Stroyuk AL, Shvalagin VV, Raevskaya AE, Kryukov AI, Kuchmii SY (2008) *Theor Exp Chem* 44:205
46. Shchukin DG, Radziuk D, Mohwald H (2010) *Annu Rev Mater Res* 40:345
47. Sakai T, Enomoto H, Torigoe K, Sakai H, Abe M (2009) *Colloid Surface A* 347:18
48. Bai XT, Li XW, Zheng LQ (2010) *Langmuir* 26:12209
49. Safavi A, Zeinali S (2010) *Colloid Surface A* 362:121
50. Ballarin B, Cassani MC, Tonelli D, Boanini E, Albonetti S, Blosi M, Gazzano M (2010) *J Phys Chem C* 114:9693
51. Obliosca JM, Arellano IHJ, Huang MH, Arco SD (2010) *Mater Lett* 64:1109
52. Akiyama T, Ibata C, Fujihara H (2010) *Heterocycles* 80:925
53. Khare V, Li ZH, Manton A, Ayi AA, Sonkaria S, Voelkl A, Thunemann AF, Taubert A (2010) *J Mater Chem* 20:1332
54. Okazaki K, Kiyama T, Suzuki T, Kuwabata S, Torimoto T (2009) *Chem Lett* 38:330
55. Zhang H, Cui H (2009) *Langmuir* 25:2604
56. Pringle JM, Winther-Jensen O, Lynam C, Wallace GG, Forsyth M, MacFarlane DR (2008) *Adv Funct Mater* 18:2031
57. Brust M, Fink J, Bethell D, Schiffrin DJ, Kiely C (1995) *J Chem Soc Chem Commun* 1655
58. Brust M, Walker M, Bethell D, Schiffrin DJ, Whyman R (1994) *J Chem Soc Chem Commun* 801
59. Brust M, Bethell D, Kiely CJ, Schiffrin DJ (1998) *Langmuir* 14:5425
60. Bethell D, Brust M, Schiffrin DJ, Kiely C (1996) *J Electroanal Chem* 409:137
61. Brust M, Bethell D, Schiffrin DJ, Kiely CJ (1995) *Adv Mater* 7:795
62. Rowe MP, Plass KE, Kim K, Kurdak C, Zellers ET, Matzger AJ (2004) *Chem Mater* 16:3513
63. Goulet PJG, Lennox RB (2010) *J Am Chem Soc* 132:9582
64. Kassam A, Bremner G, Clark B, Ulibarri G, Lennox RB (2006) *J Am Chem Soc* 128:3476
65. Zachary M, Chechik V (2007) *Angew Chem Int Ed* 46:3304
66. Rucareanu S, Gandubert VJ, Lennox RB (2006) *Chem Mater* 18:4674
67. Gandubert VJ, Lennox RB (2005) *Langmuir* 21:6532
68. Weare WW, Reed SM, Warner MG, Hutchison JE (2000) *J Am Chem Soc* 122:12890
69. Terrill RH, Postlethwaite TA, Chen CH, Poon CD, Terzis A, Chen AD, Hutchison JE, Clark MR, Wignall G, Londono JD, Superfine R, Falvo M, Johnson CS, Samulski ET, Murray RW (1995) *J Am Chem Soc* 117:12537
70. Hou WB, Dasog M, Scott RWJ (2009) *Langmuir* 25:12954
71. Dasog M, Scott RWJ (2007) *Langmuir* 23:3381
72. Shon YS, Chuc S, Voundi P (2009) *Colloid Surface A* 352:12
73. Joseph Y, Besnard I, Rosenberger M, Guse B, Nothofer HG, Wessels JM, Wild U, Knop-Gericke A, Su DS, Schlögl R, Yasuda A, Vossmeier T (2003) *J Phys Chem B* 107:7406
74. Ristau R, Tiruvalam R, Clasen PL, Gorskowski EP, Harmer MP, Kiely CJ, Hussain I, Brust M (2009) *Gold Bull* 42:133
75. Butner M, Belsler T, Oelhafen P (2005) *J Phys Chem B* 109:5464
76. Corbierre MK, Cameron NS, Lennox RB (2004) *Langmuir* 20:2867
77. Ionita P, Volkov A, Jeschke G, Chechik V (2008) *Anal Chem* 80:95
78. Lucarini M, Pasquato L (2010) *Nanoscale* 2:668
79. Gentilini C, Franchi P, Mileo E, Polizzi S, Lucarini M, Pasquato L (2009) *Angew Chem Int Ed* 48:3060
80. Chow E, Gengenbach TR, Wieczorek L, Raguse B (2010) *Sens Actuators B Chem* 143:704
81. Wang GF, Park HY, Lipert RJ (2009) *Anal Chem* 81:9643
82. Dass A, Stevenson A, Dubay GR, Tracy JB, Murray RW (2008) *J Am Chem Soc* 130:5940
83. Dass A, Holt K, Parker JF, Feldberg SW, Murray RW (2008) *J Phys Chem C* 112:20276

84. Sweeney SF, Woehrlé GH, Hutchison JE (2006) *J Am Chem Soc* 128:3190
85. Pellegrino T, Sperling RA, Alivisatos AP, Parak WJ (2007) *J Biomed Biotechnol* 26796
86. Kitaev V (2008) *J Mater Chem* 18:4745
87. Bang J, Park J, Lee JH, Won N, Nam J, Lim J, Chang BY, Lee HJ, Chon B, Shin J, Park JB, Choi JH, Cho K, Park SM, Joo T, Kim S (2010) *Chem Mater* 22:233
88. Zhang WJ, Chen GJ, Wang J, Ye BC, Zhong XH (2009) *Inorg Chem* 48:9723
89. Yang YA, Chen O, Angerhofer A, Cao YC (2009) *Chem-Eur J* 15:3186
90. Yang HW, Luan WL, Wan Z, Tu ST, Yuan WK, Wang ZM (2009) *Cryst Growth Des* 9:4807
91. Law WC, Yong KT, Roy I, Ding H, Hu R, Zhao WW, Prasad PN (2009) *Small* 5:1302
92. Bhattacharyya S, Estrin Y, Moshe O, Rich DH, Soloviyov LA, Gedanken A (2009) *ACS Nano* 3:1864
93. Sharma M, Gupta D, Kaushik D, Sharma AB, Pandey RK (2008) *J Nanosci Nanotechnol* 8:3949
94. Regulacio MD, Han MY (2010) *Acc Chem Res* 43:621
95. Lan GY, Lin YW, Lin ZH, Chang HT (2010) *J Nanopart Res* 12:1377
96. Zhang JB, Zhang DL (2010) *Crystengcomm* 12:591
97. Petoud S (2009) *Chimia* 63:745
98. Kinkead B, Hegmann T (2010) *J Mater Chem* 20:448
99. Tang AW, Qu SC, Li K, Hou YB, Teng F, Cao J, Wang YS, Wang ZG (2010) *Nanotechnology* 21:285602
100. Wang Y, Hou YB, Tang AW, Feng B, Li Y, Teng F (2008) *Acta Phys-Chim Sin* 24:296
101. Wang FD, Tang R, Buhro WE (2008) *Nano Lett* 8:3521
102. Sharma SN, Kumar U, Kumari K, Vankar VD, Kakkar R, Kumar V (2007) *Proceedings of the 2007 International Workshop on the Physics of Semiconductor Devices: IWPSD-2007*, p 843
103. Sudeep PK, Emrick T (2009) *ACS Nano* 3:4105
104. Dollefeld H, Hoppe K, Kolny J, Schilling K, Weller H, Eychmüller A (2002) *Phys Chem Chem Phys* 4:4747
105. Hwang S, Choi Y, Jeong S, Jung H, Kim CG, Chung TM, Ryu BH (2010) *Jpn J Appl Phys* 49:05EA03
106. Rockenberger J, Troger L, Rogach AL, Tischer M, Grundmann M, Eychmüller A, Weller H (1998) *J Chem Phys* 108:7807
107. Talapin DV, Haubold S, Rogach AL, Kornowski A, Haase M, Weller H (2001) *J Phys Chem B* 105:2260
108. Gaponik N, Talapin DV, Rogach AL, Hoppe K, Shevchenko EV, Kornowski A, Eychmüller A, Weller H (2002) *J Phys Chem B* 106:7177
109. Rogach AL, Katsikas L, Kornowski A, Su DS, Eychmüller A, Weller H (1996) *Ber Bunsen Phys Chem* 100:1772
110. Gaponik N, Talapin DV, Rogach AL, Eychmüller A, Weller H (2002) *Nano Lett* 2:803
111. Resch U, Eychmüller A, Haase M, Weller H (1992) *Langmuir* 8:2215
112. Liu IS, Lo HH, Chien CT, Lin YY, Chen CW, Chen YF, Su WF, Liou SC (2008) *J Mater Chem* 18:675
113. Pejova B, Grozdanov I (2005) *Mater Chem Phys* 90:35
114. Foos EE, Wilkinson J, Makinen AJ, Watkins NJ, Kafafi ZH, Long JP (2006) *Chem Mater* 18:2886
115. Wang XS, Dykstra TE, Salvador MR, Manners I, Scholes GD, Winnik MA (2004) *J Am Chem Soc* 126:7784
116. Zhou L, Gao C, Hu XZ, Xu WJ (2010) *ACS Appl Mater Interfaces* 2:1211
117. Li H, Shih WY, Shih WH (2007) *Nanotechnology* 18
118. Jana NR, Earhart C, Ying JY (2007) *Chem Mater* 19:5074
119. Deuling HJ, Buka A, Janossy I (1976) *J Phys-Paris* 37:965
120. Freedericksz V, Zolina V (1933) *Trans Faraday Soc* 29:919
121. Brochard F, Gennes PGD (1970) *J Phys-Paris* 31:691
122. Bilecka I, Djerdj I, Niederberger M (2008) *Chem Commun* 886

123. Sun SH, Zeng H, Robinson DB, Raoux S, Rice PM, Wang SX, Li GX (2004) *J Am Chem Soc* 126:273
124. Kim EH, Lee HS, Kwak BK, Kim BK (2005) *J Magn Magn Mater* 289:328
125. Massart R (1981) *IEEE Trans Magn* 17:1247
126. Hyeon T, Lee SS, Park J, Chung Y, Bin Na H (2001) *J Am Chem Soc* 123:12798
127. Sun SH, Zeng H (2002) *J Am Chem Soc* 124:8204
128. Ge JP, Hu YX, Biasini M, Dong CL, Guo JH, Beyermann WP, Yin YD (2007) *Chem-Eur J* 13:7153
129. Ge JP, Hu YX, Biasini M, Beyermann WP, Yin YD (2007) *Angew Chem Int Ed* 46:4342
130. Figuerola A, Fiore A, Di Corato R, Falqui A, Giannini C, Micotti E, Lascialfari A, Corti M, Cingolani R, Pellegrino T, Cozzoli PD, Manna L (2008) *J Am Chem Soc* 130:1477
131. Buathong S, Ung D, Daou TJ, Ulhaq-Bouillet C, Pourroy G, Guillon D, Ivanova L, Bernhardt I, Begin-Colin S, Donnio B (2009) *J Phys Chem C* 113:12201
132. Demortiere A, Buathong S, Pichon BP, Panissod P, Guillon D, Begin-Colin S, Donnio B (2010) *Small* 6:1341
133. Park J, An KJ, Hwang YS, Park JG, Noh HJ, Kim JY, Park JH, Hwang NM, Hyeon T (2004) *Nat Mater* 3:891
134. Gorski CA, Scherer MM (2010) *Am Mineral* 95:1017
135. Wang J, Wu HY, Yang CQ, Lin YL (2008) *Mater Charact* 59:1716
136. Morais PC (2008) *Hyperfine Interact* 181:1
137. Santos JG, Silveira LB, Oliveira AC, Garg VK, Lacava BM, Tedesco AC, Morais PC (2007) *Hyperfine Interact* 175:71
138. Rebbouh L, Hermann RP, Grandjean F, Hyeon T, An K, Amato A, Long GJ (2007) *Phys Rev B* 76:174422
139. Marchetti SG, Mercader RC (2003) *Hyperfine Interact* 148:275
140. Kurochkin O, Buchnev O, Iljin A, Park SK, Kwon SB, Grabar O, Reznikov Y (2009) *J Opt A-Pure Appl Opt* 11:024003
141. Glushchenko A, Buchnev O, Iljin A, Kurochkin O, Reznikov Y (2007) *SID Int Symp Dig Tec*, vol XXXVIII, 38:1086
142. Buchnev E, Dyadyusha A, Kaczmarek M, Reshetnyak V, Reznikov Y (2007) *J Opt Soc Am B* 24:1512
143. Buchnev O, Glushchenko A, Reznikov Y, Reshetnyak V, Tereshchenko O, West J (2003) *Nonlinear optics of liquid and photorefractive crystals* 5257:7
144. Ouskova E, Buchnev O, Reshetnyak V, Reznikov Y, Kresse H (2003) *Liq Cryst* 30:1235
145. Erdem E, Matthes A, Bottcher R, Glasel HJ, Hartmann E (2008) *J Nanosci Nanotechnol* 8:702
146. Ram S, Mishra A (2006) *Mod Phys Lett B* 20:159
147. Ke H, Jia DC, Wang W, Zhou Y (2007) *Sol St Phen* 121–123:843
148. Mornet S, Elissalde C, Hornebecq V, Bidault O, Duguet E, Brisson A, Maglione M (2005) *Chem Mater* 17:4530
149. Cook G, Reshetnyak VY, Ziolo RF, Basun SA, Banerjee PP, Evans DR (2010) *Opt Express* 18:17339
150. Ram S, Jana A, Kundu TK (2007) *J Appl Phys* 102:054107
151. Jha AK, Prasad K (2010) *Colloid Surface B* 75:330
152. Bansal V, Poddar P, Ahmad A, Sastry M (2006) *J Am Chem Soc* 128:11958
153. Johann F, Jungk T, Lisinski S, Hoffmann A, Ratke L, Soergel E (2010) *Appl Phys Lett* 96:139901
154. Johann F, Jungk T, Lisinski S, Hoffmann A, Ratke L, Soergel E (2009) *Appl Phys Lett* 95:202901
155. Tian XL, Li JA, Chen K, Han JA, Pan SL, Wang YJ, Fan XY, Li F, Zhou ZX (2010) *Cryst Growth Des* 10:3990
156. Atkuri H, Cook G, Evans DR, Cheon CI, Glushchenko A, Reshetnyak V, Reznikov Y, West J, Zhang K (2009) *J Opt A-Pure Appl Opt* 11:024006

157. Huang XH, Neretina S, El-Sayed MA (2009) *Adv Mater* 21:4880
158. Martin CR (1996) *Chem Mater* 8:1739
159. Hurst SJ, Payne EK, Qin LD, Mirkin CA (2006) *Angew Chem Int Ed* 45:2672
160. Chang SS, Shih CW, Chen CD, Lai WC, Wang CRC (1999) *Langmuir* 15:701
161. El-Sayed MA (2001) *Acc Chem Res* 34:257
162. Jana NR, Gearheart L, Murphy CJ (2001) *J Phys Chem B* 105:4065
163. Murphy CJ, San TK, Gole AM, Orendorff CJ, Gao JX, Gou L, Hunyadi SE, Li T (2005) *J Phys Chem B* 109:13857
164. Nikoobakht B, El-Sayed MA (2003) *Chem Mater* 15:1957
165. Iqbal M, Chung YI, Tae G (2007) *J Mater Chem* 17:335
166. Smith DK, Korgel BA (2008) *Langmuir* 24:644
167. Smith DK, Miller NR, Korgel BA (2009) *Langmuir* 25:9518
168. Jana NR (2005) *Small* 1:875
169. Zijlstra P, Bullen C, Chon JWM, Gu M (2006) *J Phys Chem B* 110:19315
170. Orendorff CJ, Murphy CJ (2006) *J Phys Chem B* 110:3990
171. Liu MZ, Guyot-Sionnest P (2005) *J Phys Chem B* 109:22192
172. Perez-Juste J, Liz-Marzan LM, Carnie S, Chan DYC, Mulvaney P (2004) *Adv Funct Mater* 14:571
173. Chen HM, Liu RS (2006) *J Chin Chem Soc-Taip* 53:1343
174. Sharma V, Park K, Srinivasarao M (2009) *Mater Sci Eng R Rep* 65:1
175. Park HJ, Ah CS, Kim WJ, Choi IS, Lee KP, Yun WS (2006) *J Vac Sci Technol A* 24:1323
176. Jana NR (2003) *Chem Commun* 1950
177. Mitamura K, Imae T (2009) *Plasmonics* 4:23
178. Pastoriza-Santos I, Perez-Juste J, Liz-Marzan LM (2006) *Chem Mater* 18:2465
179. Wu CL, Xu QH (2009) *Langmuir* 25:9441
180. Mitamura K, Imae T, Saito N, Takai O (2007) *J Phys Chem B* 111:8891
181. El Khoury JM, Zhou XL, Qu LT, Dai LM, Urbas A, Li Q (2009) *Chem Commun* 2109
182. Mitamura K, Imae T, Saito N, Takai O (2009) *Compos Interface* 16:377
183. Wijaya A, Hamad-Schifferli K (2008) *Langmuir* 24:9966
184. Pierrat S, Zins I, Breivogel A, Sonnichsen C (2007) *Nano Lett* 7:259
185. Sau TK, Rogach AL (2010) *Adv Mater* 22:1781
186. Kijima T (2010) *Top Appl Phys* 117:215
187. Yan GQ, Wang L, Zhang L (2010) *Rev Adv Mater Sci* 24:10
188. Wang ZL (2003) *Nanowires and nanobelts: materials, properties and devices*. Kluwer, Dordrecht
189. Nalwa HS (2000) *Handbook of nanostructured materials and nanotechnology*. Academic Press, San Diego
190. Klabunde KJ (2001) *Nanoscale materials in chemistry*. Wiley, New York
191. Bockrath M, Cobden DH, Lu J, Rinzler AG, Smalley RE, Balents L, McEuen PL (1999) *Nature* 397:598
192. Yao Z, Postma HWC, Balents L, Dekker C (1999) *Nature* 402:273
193. Yi GC, Wang CR, Park WI (2005) *Semicond Sci Technol* 20:S22
194. Thomas PJ, Christian P, Daniels S, Li Y, Wang YS, O'Brien P (2006) *Pure Appl Chem* 78:1651
195. Gu F, Wang SF, Cao HM, Li CZ (2008) *Nanotechnology* 19:095708
196. Li P, Wang LY, Wang L, Li YD (2008) *Chem-Eur J* 14:5951
197. Weintraub B, Zhou ZZ, Li YH, Deng YL (2010) *Nanoscale* 2:1573
198. Wu XJ, Zhu F, Mu C, Liang YQ, Xu LF, Chen QW, Chen RZ, Xu DS (2010) *Coord Chem Rev* 254:1135
199. Xi GC, Ye JH (2010) *Inorg Chem* 49:2302
200. Chun JY, Lee JW (2010) *Eur J Inorg Chem* 4251
201. Lyu SC, Zhang Y, Lee CJ, Ruh H, Lee HJ (2003) *Chem Mater* 15:3294
202. Ding Y, Gao PX, Wang ZL (2004) *J Am Chem Soc* 126:2066

203. Yu JH, Joo J, Park HM, Baik SI, Kim YW, Kim SC, Hyeon T (2005) *J Am Chem Soc* 127:5662
204. Jana NR, Peng XG (2003) *J Am Chem Soc* 125:14280
205. Li YD, Liao HW, Ding Y, Fan Y, Zhang Y, Qian YT (1999) *Inorg Chem* 38:1382
206. Lv RT, Cao CB, Zhai HZ, Wang DZ, Liu SY, Zhu HS (2004) *Solid State Commun* 130:241
207. Surendran G, Tokumoto MS, dos Santos EP, Remita H, Ramos L, Kooyman PJ, Santilli CV, Bourgaux C, Dieudonne P, Prouzet E (2005) *Chem Mater* 17:1505
208. Ding YH, Chen L, Guo R (2007) *Colloid Surface A* 295:85
209. Huang NM, Shahidan R, Khiew PS, Peter L, Kan CS (2004) *Colloid Surface A* 247:55
210. Zhang DB, Qi LM, Cheng HM, Ma JM (2002) *J Colloid Interface Sci* 246:413
211. Jia XT, He W, Zhang XD, Zhao HS, Li ZM, Feng YJ (2007) *Nanotechnology* 18
212. Iijima S (1991) *Nature* 354:56
213. Saito R, Dresselhaus G, Dresselhaus MS (1998) *Physical properties of carbon nanotubes*. Imperial College Press, London
214. Chae HG, Liu J, Kumar S (2006) *Materials carbon nanotubes properties and applications*. Taylor & Francis Group, Boca Raton
215. Lu W, Lieber CM (2007) *Nat Mater* 6:841
216. Peng H, Sun X (2009) *Chem Phys Lett* 471:103
217. Gao L, Zhou X, Ding Y (2007) *Chem Phys Lett* 434:297
218. Sgobba V, Guldi DM (2008) *J Mater Chem* 18:153
219. Yang W, Ratinaç K, Ringer S, Thordarson P, Gooding J, Braet F (2010) *Angew Chem Int Ed* 49:2114
220. Yan Y, Chan-Park M, Zhang Q (2007) *Small* 3:24
221. Ajayan PM (1999) *Chem Rev* 99:1787
222. Cinke M, Li J, Chen B, Cassell A, Delzeit L, Han J, Meyyappan M (2002) *Chem Phys Lett* 365:69
223. Ding RG, Lu GQ, Yan ZF, Wilson MA (2001) *J Nanosci Nanotechnol* 1:7
224. Kang SJ, Kocabas C, Ozel T, Shim M, Pimparkar N, Alam MA, Rotkin SV, Rogers JA (2007) *Nat Nanotechnol* 2:230
225. Ko H, Tsukruk VV (2006) *Nano Lett* 6:1443
226. Ahir SV, Terentjev EM (2005) *Nat Mater* 4:491
227. Zhang M, Fang SL, Zakhidov AA, Lee SB, Aliev AE, Williams CD, Atkinson KR, Baughman RH (2005) *Science* 309:1215
228. Du FM, Fischer JE, Winey KI (2005) *Phys Rev B* 72:121404
229. Ji Y, Huang YY, Rungsawang R, Terentjev EM (2010) *Adv Mater* 22:3436
230. Diaó P, Liu Z (2010) *Adv Mater* 22:1430
231. Scalia G (2010) *ChemPhysChem* 11:333
232. Itkis ME, Perea DE, Jung R, Niyogi S, Haddon RC (2005) *J Am Chem Soc* 127:3439
233. Murakami Y, Chiashi S, Miyauchi Y, Hu MH, Ogura M, Okubo T, Maruyama S (2004) *Chem Phys Lett* 385:298
234. Huang SM, Cai XY, Liu J (2003) *J Am Chem Soc* 125:5636
235. Chen XQ, Saito T, Yamada H, Matsushige K (2001) *Appl Phys Lett* 78:3714
236. Bubke K, Gnewuch H, Hempstead M, Hammer J, Green MLH (1997) *Appl Phys Lett* 71:1906
237. Kim S-K, Lee H, Tanaka H, Weiss PS (2008) *Langmuir* 24:12936
238. Fischer JE, Zhou W, Vavro J, Llaguno MC, Guthy C, Haggemueller R, Casavant MJ, Walters DE, Smalley RE (2003) *J Appl Phys* 93:2157
239. Shaver J, Parra-Vasquez ANG, Hansel S, Portugal O, Mielke CH, von Ortenberg M, Hauge RH, Pasquali M, Kono J (2008) *ACS Nano* 3:131
240. Steinert BW, Dean DR (2009) *Polymer* 50:898
241. Li S, Yan YH, Liu NY, Chan-Park MB, Zhang Q (2007) *Small* 3:616
242. Zhang QH, Vichchulada P, Cauble MA, Lay MD (2009) *J Mater Sci* 44:1206

243. Li XL, Zhang L, Wang XR, Shimoyama I, Sun XM, Seo WS, Dai HJ (2007) *J Am Chem Soc* 129:4890
244. Song WH, Kinloch IA, Windle AH (2003) *Science* 302:1363
245. Zhang SJ, Li QW, Kinloch IA, Windle AH (2010) *Langmuir* 26:2107
246. Lee HW, You W, Barman S, Hellstrom S, LeMieux MC, Oh JH, Liu S, Fujiwara T, Wang WM, Chen B, Jin YW, Kim JM, Bao ZA (2009) *Small* 5:1019
247. Zhang S, Kumar S (2008) *Small* 4:1270
248. Davis VA, Ericson LM, Parra-Vasquez ANG, Fan H, Wang YH, Prieto V, Longoria JA, Ramesh S, Saini RK, Kittrell C, Billups WE, Adams WW, Hauge RH, Smalley RE, Pasquali M (2004) *Macromolecules* 37:154
249. Green MJ, Parra-Vasquez ANG, Behabtu N, Pasquali M (2009) *J Chem Phys* 131:084901
250. Badaire S, Zakri C, Maugey M, Derre A, Barisci JN, Wallace G, Poulin P (2005) *Adv Mater* 17:1673
251. Lu L, Chen W (2010) *ACS Nano* 4:1042
252. Vijayakumar VN, Madhu MMLN (2010) *Phys B* 405:4418
253. Bravo-Sanchez M, Simmons TJ, Vidal MA (2010) *Carbon* 48:3531
254. Puech N, Grelet E, Poulin P, Blanc C, van der Schoot P (2010) *Phys Rev E* 82:020702
255. Zakri C (2007) *Liq Cryst Today* 16:1
256. Samson J, Varotto A, Nahirney PC, Toschi A, Piscopo I, Drain CM (2009) *ACS Nano* 3:339
257. Pan L, Xu M, Zhang ZD (2010) *Mater Chem Phys* 123:293
258. Yan HW, Hou JB, Fu ZP, Yang BF, Yang PH, Liu KP, Wen MW, Chen YJ, Fu SQ, Li FQ (2009) *Mater Res Bull* 44:1954
259. Polleux J, Pinna N, Antonietti M, Niederberger M (2005) *J Am Chem Soc* 127:15595
260. Wei XM, Zeng HC (2003) *J Phys Chem B* 107:2619
261. Ezawa M (2009) *New J Phys* 11:095005
262. Sigman MB, Ghezelbash A, Hanrath T, Saunders AE, Lee F, Korgel BA (2003) *J Am Chem Soc* 125:16050
263. Paineau E, Antonova K, Baravian C, Bihannic I, Davidson P, Dozov I, Imperor-Clerc M, Levitz P, Madsen A, Meneau F, Michot LJ (2009) *J Phys Chem B* 113:15858
264. Michot LJ, Bihannic I, Maddi S, Funari SS, Baravian C, Levitz P, Davidson P (2006) *Proc Natl Acad Sci U S A* 103:16101
265. Saunders AE, Ghezelbash A, Smilgies DM, Sigman MB, Korgel BA (2006) *Nano Lett* 6:2959
266. Brown ABD, Clarke SM, Rennie AR (1998) *Langmuir* 14:3129
267. van der Kooij FM, Kassapidou K, Lekkerkerker HNW (2000) *Nature* 406:868
268. Davidson P, Gabriel JCP (2005) *Curr Opin Colloid Interface Sci* 9:377
269. Gabriel JCP, Camerel F, Lemaire BJ, Desvaux H, Davidson P, Batail P (2001) *Nature* 413:504
270. Miyamoto N, Iijima H, Ohkubo H, Yamauchi Y (2010) *Chem Commun* 46:4166
271. Taubert A, Palivan C, Casse O, Gozzo F, Schmitt B (2007) *J Phys Chem C* 111:4077
272. Taubert A, Steiner P, Manton A (2005) *J Phys Chem B* 109:15542
273. Taubert A (2004) *Angew Chem Int Ed* 43:5380
274. Tsai TY, Huang YP, Chen HY, Lee W, Chang YM, Chin WK (2005) *Nanotechnology* 16:1053
275. Hoshino J, Limpanart S, Khunthong S, Osotchan T, Traiphol R, Sriksirin T (2010) *Mater Chem Phys* 123:706
276. Galimberti M, Martino M, Guenzi M, Leonardi G, Citterio A (2009) *E-Polymers* 056
277. Cui LL, Bara JE, Brun Y, Yoo Y, Yoon PJ, Paul DR (2009) *Polymer* 50:2492
278. Rozanski SA, Thoen J (2005) *J Non-Cryst Solids* 351:2802
279. Neeraj, Raina KK (2010) *Phase Transit* 83:615
280. Crucenau F, Liang D, Leheny RL, Iannacchione GS (2008) *Liq Cryst* 35:1061
281. Manaila-Maximean D, Bossis G, Metayer C, Giulieri F (2004) *Mol Cryst Liq Cryst* 417:711
282. Jin T, Finotello D (2004) *Phys Rev E* 69:041704
283. Ewiss MAZ, Nabil G, Stoll B, Herminghaus S (2003) *Liq Cryst* 30:1241

284. Mertelj A, Jakli A, Copic M (1999) *Mol Cryst Liq Cryst* 331:1941
285. Jakli A, Kali G, Rosta L (1997) *Physica B* 234:297
286. Almasy L, Jakli A, Rosta L, Pepy G (1997) *Physica B* 241:996
287. Guba G, Reznikov Y, Lopukhovich N, Ogenko V, Reshetnyak V, Yaroshchuk O (1994) *Mol Cryst Liq Cryst* 251:303
288. Morozov KI (2002) *Phys Rev E* 66:011704
289. Bena RE, Petrescu E (2002) *J Magn Magn Mater* 248:336
290. Ok CH, Kim BY, Oh BY, Kim YH, Lee KM, Park HG, Han JM, Seo DS, Lee DK, Hwang JY (2008) *Liq Cryst* 35:1373
291. Gwag JS, Sohn K, Kim YK, Kim JH (2008) *Opt Express* 16:12220
292. Tahata S, Yuuki A (2004) *Mol Cryst Liq Cryst* 419:13
293. Hwang JY, Kim SH, Choi SH, Kang HK, Choi JH, Ham MH, Myoung JM, Seo DS (2006) *Ferroelectrics* 344:435
294. Shin HK, Kim KH, Yoon TH, Kim JC (2008) *J Appl Phys* 104:084515
295. Lu RB, Nie XY, Wu ST (2008) *J Soc Inf Disp* 16:1139
296. Voloschenko D, Pishnyak OP, Shiyantovskii SV, Lavrentovich OD (2002) *Phys Rev E* 65:060701
297. Prasad SK, Sandhya KL, Nair GG, Hiremath US, Yelamaggad CV, Sampath S (2006) *Liq Cryst* 33:1121
298. Qi H, Kincaid B, Marx VM, Zhang HR, Hegmann T (2009) *ChemPhysChem* 10:1211
299. Choo H, Cutler E, Shon YS (2003) *Langmuir* 19:8555
300. Qi H, Kincaid B, Hegmann T (2008) *Adv Funct Mater* 18:212
301. Nishida N, Shiraishi Y, Kobayashi S, Toshima N (2008) *J Phys Chem C* 112:20284
302. Kobayashi S, Miyama T, Nishida N, Sakai Y, Shiraki H, Shiraishi Y, Toshima N (2006) *J Disp Technol* 2:121
303. Kobayashi S, Miyama T, Sakai Y, Shiraki H, Shiraishi Y, Toshima N (2005) *Proc SPIE - Emerging Liquid Crystal Technologies* 5741:7
304. Sakai Y, Nishida N, Shiraki H, Shiraishi Y, Miyama T, Toshima N, Kobayashi S (2005) *Mol Cryst Liq Cryst* 441:143
305. Shiraki H, Kundu S, Sakai Y, Masumi T, Shiraishi Y, Toshima N, Kobayashi S (2004) *Jpn J Appl Phys* 43:5425
306. Thisayukta J, Shiraki H, Sakai Y, Masumi T, Kundu S, Shiraishi Y, Toshima N, Kobayashi S (2004) *Jpn J Appl Phys* 43:5430
307. Miyama T, Thisayukta J, Shiraki H, Sakai Y, Shiraishi Y, Toshima N, Kobayashi S (2004) *Jpn J Appl Phys* 43:2580
308. Shiraishi Y, Sano S, Baba A, Kobayashi S, Toshima N (2002) *Kobunshi Ronbunshu* 59:753
309. Yoshikawa H, Maeda K, Shiraishi Y, Xu J, Shiraki H, Toshima N, Kobayashi S (2002) *Jpn J Appl Phys* 41:L1315
310. Khatua S, Manna P, Chang WS, Tcherniak A, Friedlander E, Zubarev ER, Link S (2010) *J Phys Chem C* 114:7251
311. Pratibha R, Park K, Smalyukh II, Park W (2009) *Opt Express* 17:19459
312. Park SY, Stroud D (2005) *Phys Rev Lett* 94:217401
313. Toko Y, Yokoyama S, Takigawa S, Nishino S, Toshima N, Kobayashi S (2007) *SID Int Symp Dig Tec*, vol XXXVIII, 38:158
314. Miyama T, Kundu S, Shiraki H, Sakai Y, Shiraishi Y, Toshima N, Kobayashi S (2004) *Proc SPIE - Liquid Crystal Materials, Devices, and Applications X and Projection Displays X* 5289:143
315. Yoshida H, Kawamoto K, Kubo H, Tsuda T, Fujii A, Kuwabata S, Ozaki M (2010) *Adv Mater* 22:622
316. Blach JF, Saitzek S, Legrand C, Dupont L, Henninot JF, Warengem M (2010) *J Appl Phys* 107:074102
317. Glushchenko A, Il Cheon C, West J, Li FH, Buyuktanir E, Reznikov Y, Buchnev A (2006) *Mol Cryst Liq Cryst* 453:227

318. Buchnev O, Ouskova E, Reznikov Y, Reshetnyak V, Kresse H, Grabar A (2004) *Mol Cryst Liq Cryst* 422:47
319. Kaczmarek M, Buchnev O, Nandhakumar I (2008) *Appl Phys Lett* 92:103307
320. West JL, Li FH, Zhang K, Atkuri H (2007) AD'07: Proc Asia Display 2007, vols 1 and 2, p 113
321. Reshetnyak VY, Shelestiuk SM, Sluckin TJ (2006) *Mol Cryst Liq Cryst* 454:201
322. Reznikov Y, Buchnev O, Glushchenko A, Reshetnyak V, Tereshchenko O, West J (2005) *Proc SPIE - Emerging Liquid Crystal Technologies* 5741:171
323. Reznikov Y, Buchnev O, Tereshchenko O, Reshetnyak V, Glushchenko A, West J (2003) *Appl Phys Lett* 82:1917
324. Li FH, Buchnev O, Il Cheon C, Glushchenko A, Reshetnyak V, Reznikov Y, Sluckin TJ, West JL (2006) *Phys Rev Lett* 97:147801
325. Glushchenko A, Il F, Cheon C, West J, Reznikov Y (2007) *Proc SPIE – Emerging Liquid Crystal Technologies II* 6487:T4870
326. Li FH, West J, Glushchenko A, Il Cheon C, Reznikov Y (2006) *J Soc Inf Disp* 14:523
327. Lopatina LM, Selinger JV (2009) *Phys Rev Lett* 102:197802
328. Pereira MSS, Canabarro AA, de Oliveira IN, Lyra ML, Mirantsev LV (2010) *Eur Phys J E* 31:81
329. Tian P, Smith GD, Glaser M (2006) *J Chem Phys* 124:161101
330. Xu JQ, Bedrov D, Smith GD, Glaser MA (2009) *Phys Rev E* 79:011704
331. Khoo IC, Williams YZ, Lewis B, Mallouk T (2006) *Mol Cryst Liq Cryst* 446:233
332. Piegdon KA, Declair S, Forstner J, Meier T, Matthias H, Urbanski M, Kitzerow HS, Reuter D, Wieck AD, Lorke A, Meier C (2010) *Opt Express* 18:7946
333. Tong X, Zhao Y (2007) *J Am Chem Soc* 129:6372
334. Zhang T, Zhong C, Xu J (2009) *Jpn J Appl Phys* 48:055002
335. Chen WT, Chen PS, Chao CY (2009) *Jpn J Appl Phys* 48:015006
336. Manohar R, Yadav SP, Srivastava AK, Misra AK, Pandey KK, Sharma PK, Pandey AC (2009) *Jpn J Appl Phys* 48:101501
337. Hwang SJ, Jeng SC, Yang CY, Kuo CW, Liao CC (2009) *J Phys D Appl Phys* 42:025102
338. Kuo CW, Jeng SC, Wang HL, Liao CC (2007) *Appl Phys Lett* 91:141103
339. Hwang SJ, Jeng SC, Hsieh IM (2010) *Opt Express* 18:16507
340. Hwang SJ, Shieh YM, Lin KR, Jeng SC, Yu HH, Liao CC (2008) 2008 IEEE Photonicsglobal@Singapore (IPGC), vols 1 and 2, p 230
341. Akimoto M, Kundu S, Isomura K, Hirayama I, Kobayashi S, Takatoh K (2009) *Mol Cryst Liq Cryst* 508:1
342. Cheung DL, Allen MP (2008) *J Chem Phys* 129:114706
343. Cheung DL, Allen MP (2007) *Phys Rev E* 76:041706
344. Masutani A, Roberts T, Schuller B, Hollfelder N, Kilickiran P, Sakaigawa A, Nelles G, Yasuda A (2008) *J Soc Inf Disp* 16:137
345. Huang CY, Lai CC, Tseng YH, Yang T, Tien CJ, Lo KY (2008) *Appl Phys Lett* 92:221908
346. Lin TH, Chen WZ (2010) *Advances in Liquid Crystals* 428–429:276
347. Chen WZ, Tsai YT, Lin TH (2009) *Appl Phys Lett* 94:201114
348. Chen WZ, Tsai YT, Lin TH (2009) *Opt Lett* 34:2545
349. Qi H, Hegmann T (2006) *J Mater Chem* 16:4197
350. Urbanski M, Kinkead B, Hegmann T, Kitzerow HS (2010) *Liq Cryst* 37:1151
351. Kinkead B, Urbanski M, Qi H, Kitzerow HS, Hegmann T (2010) *Proc SPIE – Liquid Crystals XIV* 7775:77750C1
352. Urbanski M, Kinkead B, Qi H, Hegmann T, Kitzerow HS (2010) *Nanoscale* 2:1118
353. Qi H, Hegmann T (2009) *ACS Appl Mater Interfaces* 1:1731
354. Ahlers G, Dressel B, Oh J, Pesch W (2010) *J Fluid Mech* 642:15
355. Buka A, Eber N, Pesch W, Kramer L (2006) *Nato Sci Ser II Math* 218:55
356. Buka A, Dressel B, Kramer L, Pesch W (2004) *Chaos* 14:793

357. Buka A, Dressel B, Otowski W, Camara K, Toth-Katona T, Kramer L, Lindau J, Pelzl G, Pesch W (2002) *Phys Rev E* 66:051713
358. Huh JH, Hidaka Y, Yusuf Y, Eber N, Toth-Katona T, Buka A, Kai S (2001) *Mol Cryst Liq Cryst* 364:111
359. Eber N, Rossberg A, Buka A, Kramer L (2000) *Mol Cryst Liq Cryst* 351:161
360. Buka A, Toth P, Eber N, Kramer L (2000) *Phys Rep* 337:157
361. Rossberg AG, Eber N, Buka A, Kramer L (2000) *Phys Rev E* 61:R25
362. Brand HR, Fradin C, Finn PL, Pesch W, Cladis PE (1997) *Phys Lett A* 235:508
363. Qi H, Kinkead B, Hegmann T (2008) *Proc SPIE - Emerging Liquid Crystal Technologies III* 6911:91106
364. Hu W, Zhao HY, Shan LK, Song L, Cao H, Yang Z, Cheng ZH, Yan CZ, Li SJ, Yang HA, Guo L (2010) *Liq Cryst* 37:563
365. Qi H, O'Neil J, Hegmann T (2008) *J Mater Chem* 18:374
366. Qi H, Hegmann T (2008) *J Am Chem Soc* 130:14201
367. Pratiha R, Park W, Smalyukh II (2010) *J Appl Phys* 107:063511
368. Cordoyiannis G, Kralj S, Nounesis G, Kutnjak Z, Zumer S (2007) *Phys Rev E* 75:021702
369. Ramazanoglu M, Laroche S, Garland CW, Birgeneau RJ (2008) *Phys Rev E* 77:031702
370. Martinez-Miranda LJ, McCarthy K, Kurihara LK, Harry JJ, Noel A (2006) *Appl Phys Lett* 89:161917
371. Liang HH, Xiao YZ, Hsh FJ, Wu CC, Lee JY (2010) *Liq Cryst* 37:255
372. Kumar A, Silotia P, Biradar AM (2010) *J Appl Phys* 108:024107
373. Kumar A, Prakash J, Goel P, Khan T, Dhawan SK, Silotia P, Biradar AM (2009) *Europhys Lett* 88:26003
374. Prakash J, Choudhary A, Kumar A, Mehta DS, Biradar AM (2008) *Appl Phys Lett* 93:112904
375. Kaur S, Singh SP, Biradar AM, Choudhary A, Sreenivas K (2007) *Appl Phys Lett* 91:023120
376. Kumar A, Prakash J, Mehta DS, Biradar AM, Haase W (2009) *Appl Phys Lett* 95:023117
377. Joshi T, Kumar A, Prakash J, Biradar AM (2010) *Appl Phys Lett* 96:253109
378. Li LS, Huang JY (2009) *J Phys D Appl Phys* 42:125413
379. Heppke G, Krueker D, Lohning C, Lotzsch D, Moro D, Muller M, Sawade H (2000) *J Mater Chem* 10:2657
380. Seshadri T, Haupt HJ (1998) *Chem Commun* 735
381. Stegemeyer H, Schumacher M, Demikhov E (1993) *Liq Cryst* 15:933
382. Kitzerow HS, Schmid H, Ranft A, Heppke G, Hikmet RAM, Lub J (1993) *Liq Cryst* 14:911
383. Stegemeyer H, Onusseit H, Finkelmann H (1989) *Makromol Chem-Rapid* 10:571
384. Chanishvili AG, Chilaya GS, Elashvili ZM, Ivchenko SP, Khoshtaria DG, Vinokur KD (1986) *Mol Cryst Liq Cryst* 3:91
385. Marcus MA (1984) *Mol Cryst Liq Cryst* 102:207
386. Crooker PP (1983) *Mol Cryst Liq Cryst* 98:31
387. Kuczynski W, Bergmann K, Stegemeyer H (1980) *Mol Cryst Liq Cryst* 56:283
388. Pollmann P, Scherer G (1979) *Z Naturforsch A* 34:255
389. Bergmann K, Stegemeyer H (1979) *Z Naturforsch A* 34:251
390. Bergmann K, Stegemeyer H (1979) *Z Naturforsch A* 34:1031
391. Bergmann K, Pollmann P, Scherer G, Stegemeyer H (1979) *Z Naturforsch A* 34:253
392. Coates D, Gray GW (1973) *Phys Lett A* 45:115
393. Kitzerow HS, Crooker PP, Rand J, Xu J, Heppke G (1992) *J Phys II* 2:279
394. Stark H, Trebin HR (1991) *Phys Rev A* 44:2752
395. Yang DK, Crooker PP (1990) *Liq Cryst* 7:411
396. Kitzerow HS, Crooker PP, Kwok SL, Xu J, Heppke G (1990) *Phys Rev A* 42:3442
397. Kitzerow HS, Crooker PP, Kwok SL, Heppke G (1990) *J Phys-Paris* 51:1303
398. Porsch F, Stegemeyer H (1989) *Liq Cryst* 5:791
399. Heppke G, Jerome B, Kitzerow HS, Pieranski P (1989) *J Phys-Paris* 50:2991
400. Heppke G, Jerome B, Kitzerow HS, Pieranski P (1989) *J Phys-Paris* 50:549
401. Chen NR, Ho JT (1987) *Phys Rev A* 35:4886

402. Heppke G, Kitzerow HS, Krumrey M (1985) *Mol Cryst Liq Cryst* 1:117
403. Heppke G, Kitzerow HS, Krumrey M (1985) *Mol Cryst Liq Cryst* 2:59
404. Gerber PR (1985) *Mol Cryst Liq Cryst* 116:197
405. Stegemeyer H, Porsch E (1984) *Phys Rev A* 30:3369
406. Heppke G, Krumrey M, Oestreicher F (1983) *Mol Cryst Liq Cryst* 99:99
407. Pieranski P, Cladis PE, Barbetmassin R (1989) *Liq Cryst* 5:829
408. Pieranski P, Barbetmassin R, Cladis PE (1985) *Phys Rev A* 31:3912
409. Barbetmassin R, Cladis PE, Pieranski P (1984) *Phys Rev A* 30:1161
410. Cao WY, Munoz A, Palfy-Muhoray P, Taheri B (2002) *Nat Mater* 1:111
411. Coles HJ, Pivnenko MN (2005) *Nature* 436:997
412. Kikuchi H, Yokota M, Hisakado Y, Yang H, Kajiyama T (2002) *Nat Mater* 1:64
413. Kitzerow HS (2006) *ChemPhysChem* 7:63
414. Kitzerow HS (2010) *Ferroelectrics* 395:66
415. Rao LH, Ge ZB, Wu ST (2010) *Opt Express* 18:3143
416. Rao LH, Cheng HC, Wu ST (2010) *J Disp Technol* 6:287
417. Lu SY, Chien LC (2010) *Opt Lett* 35:562
418. Li Y, Jiao MZ, Wu ST (2010) *Opt Express* 18:16486
419. Lu SY, Chien LC (2009) 2009 SID International Symposium Digest of Technical Papers, vol XI, Books I–III, p 1193
420. Lu L, Hwang JY, Chien LC (2009) 2009 SID International Symposium Digest of Technical Papers, vol XL, Books I–III, p 1608
421. Iwata T, Suzuki K, Higuchi H, Kikuchi H (2009) *Liq Cryst* 36:947
422. Ge ZB, Rao LH, Gauza S, Wu ST (2009) *J Disp Technol* 5:250
423. Yokoyama S, Mashiko S, Kikuchi H, Uchida K, Nagamura T (2006) *Adv Mater* 18:48
424. Morris SM, Ford AD, Gillespie C, Pivnenko MN, Hadeler O, Coles HJ (2006) *J Soc Inf Disp* 14:565
425. Liu HY, Wang CT, Hsu CY, Lin TH, Liu JH (2010) *Appl Phys Lett* 96:121103
426. Coles HJ (2007) *Proc SPIE - Emerging Liquid Crystal Technologies II* 6487:M4870
427. Yoshida H, Tanaka Y, Kawamoto K, Kubo H, Tsuda T, Fujii A, Kuwabata S, Kikuchi H, Ozaki M (2009) *Appl Phys Express* 2:121501
428. Karatairi E, Rozic B, Kutnjak Z, Tzitzios V, Nounesis G, Cordoyiannis G, Thoen J, Glorieux C, Kralj S (2010) *Phys Rev E* 81:041703
429. Ravnik M, Alexander GP, Yeomans JM, Žumer S (2010) *Faraday Discuss* 144:159
430. Zhou XL, Kang SW, Kumar S, Li Q (2009) *Liq Cryst* 36:269
431. Li LF, Kang SW, Harden J, Sun QJ, Zhou XL, Dai LM, Jakli A, Kumar S, Li Q (2008) *Liq Cryst* 35:233
432. Hanna J (2005) *Opto-Electron Rev* 13:259
433. Bushby RJ, Lozman OR, Bunning JC, Donovan KJ, Kreouzis T, Scott K (2003) *Organic Photonic Materials and Devices V* 4991:222
434. Kumar PS, Pal SK, Kumar S, Lakshminarayanan V (2007) *Langmuir* 23:3445
435. Kumar S, Pal SK, Kumar PS, Lakshminarayanan V (2007) *Soft Matter* 3:896
436. Kumar S (2007) *Synth React Inorg Me* 37:327
437. Holt LA, Bushby RJ, Evans SD, Burgess A, Seeley G (2008) *J Appl Phys* 103:063712
438. Durr NJ, Larson T, Smith DK, Korgel BA, Sokolov K, Ben-Yakar A (2007) *Nano Lett* 7:941
439. Perez-Juste J, Rodriguez-Gonzalez B, Mulvaney P, Liz-Marzan LM (2005) *Adv Funct Mater* 15:1065
440. Wilson O, Wilson GJ, Mulvaney P (2002) *Adv Mater* 14:1000
441. Zhang SS, Leem G, Srisombat LO, Lee TR (2008) *J Am Chem Soc* 130:113
442. Sridevi S, Prasad SK, Nair GG, D'Britto V, Prasad BLV (2010) *Appl Phys Lett* 97:151913
443. Evans PR, Wurtz GA, Hendren WR, Atkinson R, Dickson W, Zayats AV, Pollard RJ (2007) *Appl Phys Lett* 91:043101
444. Chu KC, Chao CY, Chen YF, Wu YC, Chen CC (2006) *Appl Phys Lett* 89:103107
445. Lapointe CP, Reich DH, Leheny RL (2008) *Langmuir* 24:11175

446. Lapointe C, Hultgren A, Silevitch DM, Felton EJ, Reich DH, Leheny RL (2004) *Science* 303:652
447. Chen HS, Chen CW, Wang CH, Chu FC, Chao CY, Kang CC, Chou PT, Chen YF (2010) *J Phys Chem C* 114:7995
448. Wu KJ, Chu KC, Chao CY, Chen YF, Lai CW, Kang CC, Chen CY, Chou PT (2007) *Nano Lett* 7:1908
449. Acharya S, Kundu S, Hill JP, Richards GJ, Ariga K (2009) *Adv Mater* 21:989
450. Kundu S, Hill JP, Richards GJ, Ariga K, Khan AH, Thupakula U, Acharya S (2010) *ACS Appl Mater Interfaces* 2:2759
451. Ouskova E, Buluy O, Blanc C, Dietsch H, Mertelj A (2010) *Mol Cryst Liq Cryst* 104
452. Williams Y, Chan K, Park JH, Khoo IC, Lewis B, Mallouk TE (2005) *Proc SPIE - Liquid Crystals IX* 5936:593613
453. Zorn M, Meuer S, Tahir MN, Khalavka Y, Sonnichsen C, Tremel W, Zentel R (2008) *J Mater Chem* 18:3050
454. Meuer S, Fischer K, Mey I, Janshoff A, Schmidt M, Zentel R (2008) *Macromolecules* 41:7946
455. Zorn M, Zentel R (2008) *Macromol Rapid Commun* 29:922
456. Zorn M, Tahir MN, Bergmann B, Tremel W, Grigoriadis C, Floudas G, Zentel R (2010) *Macromol Rapid Commun* 31:1101
457. He LL, Zhang LX, Ye YS, Liang HJ (2010) *J Phys Chem B* 114:7189
458. Popa-Nita V, Kralj S (2010) *J Chem Phys* 132:024902
459. Scalia G, Lagerwall JPF, Schymura S, Haluska M, Giesselmann F, Roth S (2007) *Phys Status Solidi B* 244:4212
460. Lagerwall JPF, Scalia G (2008) *J Mater Chem* 18:2890
461. Dierking I, Scalia G, Morales P (2005) *J Appl Phys* 97:044309
462. Dierking I, Scalia G, Morales P, LeClere D (2004) *Adv Mater* 16:865
463. Schymura S, Kuehnast M, Lutz V, Jagiella S, Dettlaff-Weglikowska U, Roth S, Giesselmann F, Tschierske C, Scalia G, Lagerwall J (2010) *Adv Funct Mater* 20:3350
464. Kuehnast M, Tschierske C, Lagerwall J (2010) *Chem Commun* 46:6989
465. Kimura M, Miki N, Adachi N, Tatewaki Y, Ohta K, Shirai H (2009) *J Mater Chem* 19:1086
466. Trushkevych O, Collings N, Hasan T, Scardaci V, Ferrari AC, Wilkinson TD, Crossland WA, Milne WI, Geng J, Johnson BFG, Macaulay S (2008) *J Phys D: Appl Phys* 41:125106
467. Jeon SY, Park KA, Baik IS, Jeong SJ, Jeong SH, An KH, Lee SH, Lee YH (2007) *Nano* 2:41
468. van der Schoot P, Popa-Nita V, Kralj S (2008) *J Phys Chem B* 112:4512
469. Sureshkumar P, Srivastava AK, Jeong SJ, Kim M, Jo EM, Lee SH, Lee YH (2009) *J Nanosci Nanotechnol* 9:4741
470. Moore VC, Strano MS, Haroz EH, Hauge RH, Smalley RE, Schmidt J, Talmon Y (2003) *Nano Lett* 3:1379
471. Heister E, Lamprecht C, Neves V, Tilmaciu C, Datas L, Flahaut E, Soula B, Hinterdorfer P, Coley HM, Silva SRP, McFadden J (2010) *ACS Nano* 4:2615
472. Lagerwall JPF, Scalia G, Haluska M, Dettlaff-Weglikowska U, Giesselmann F, Roth S (2006) *Phys Status Solidi B* 243:3046
473. Lagerwall J, Scalia G, Haluska M, Dettlaff-Weglikowska U, Roth S, Giesselmann F (2007) *Adv Mater* 19:359
474. Weiss V, Thiruvengadathan R, Regev O (2006) *Langmuir* 22:854
475. Scalia G, von Buhler C, Hagele C, Roth S, Giesselmann F, Lagerwall JPF (2008) *Soft Matter* 4:570
476. Schymura S, Enz E, Roth S, Scalia G, Lagerwall JPF (2009) *Synth Metals* 159:2177
477. Xin X, Li H, Kalwarczyk E, Kelm A, Fialkowski M, Gorecka E, Pocięcha D, Hołyst R (2010) *Langmuir* 26:8821
478. Okano K, Noguchi I, Yamashita T (2010) *Macromolecules* (Washington, DC, U S) 43:5496
479. Kwon YS, Jung BM, Lee H, Chang JY (2010) *Macromolecules* 43:5376
480. Goncharuk AI, Lebovka NI, Lisetski LN, Minenko SS (2009) *J Phys D: Appl Phys* 42:165411

481. Chen HY, Lee W, Clark NA (2007) *Appl Phys Lett* 90:033510
482. Jeon SY, Shin SH, Jeong SJ, Lee SH, Jeong SH, Lee YH, Choi HC, Kim KJ (2007) *Appl Phys Lett* 90:121901
483. Lisetski LN, Minenko SS, Fedoryako AP, Lebovka NI (2009) *Phys E* 41:431
484. Zhao W, Wang J, He J, Zhang L, Wang X, Li R (2009) *Appl Surf Sci* 255:6589
485. Rahman M, Lee W (2009) *J Phys D: Appl Phys* 42:063001
486. Kovalchuk A, Dolgov L, Yaroshchuk O (2008) *Semicond Phys, Quantum Electron Optoelectron* 11:337
487. Basu R, Sigdel KP, Iannacchione GS (2009) *arXiv.org, e-Print Arch., Condens. Matter*, p 1
488. Basu R, Iannacchione GS (2010) *Phys Rev E* 81:051705
489. Basu R, Iannacchione GS (2009) *arXiv.org, e-Print Arch., Condens. Matter*, p 1
490. Liu H-H, Lee W (2010) *Appl Phys Lett* 97:173501
491. Basu R, Boccuzzi K, Ferjani S, Rosenblatt C (2010) *Appl Phys Lett* 97:121908
492. Dolgov L, Yaroshchuk O, Lebovka M (2008) *Mol Cryst Liq Cryst* 496:212
493. Dolgov LA, Lebovka NI, Yaroshchuk OV (2009) *Colloid J* 71:603
494. Basu R, Iannacchione GS (2009) *J Appl Phys* 106:124312
495. Arora P, Mikulko A, Podgornov F, Haase W (2009) *Mol Cryst Liq Cryst* 502:1
496. Podgornov FV, Suvorova AM, Lapanik AV, Haase W (2009) *Chem Phys Lett* 479:206
497. Lagerwall JPF, Dabrowski R, Scalia G (2007) *J Non-Cryst Solids* 353:4411
498. Lisetski LN, Minenko SS, Zhukov AV, Shtifanyuk PP, Lebovka NI (2009) *Mol Cryst Liq Cryst* 510:43
499. Pizzey C, Van Duijneveldt J, Klein S (2004) *Mol Cryst Liq Cryst* 409:51
500. Pizzey C, Klein S, Leach E, van Duijneveldt JS, Richardson RM (2004) *J Phys-Condens Mat* 16:2479
501. van Duijneveldt JS, Klein S, Leach E, Pizzey C, Richardson RM (2005) *J Phys Condens Matter* 17:2255
502. Zhang ZX, van Duijneveldt JS (2007) *Soft Matter* 3:596
503. Bezrodna T, Chashechnikova I, Nesprava V, Puchkovska G, Shaydyuk Y, Boyko Y, Baran J, Drozd M (2010) *Liq Cryst* 37:263
504. Chashechnikova I, Dolgov L, Gavrliko T, Puchkovska G, Shaydyuk Y, Lebovka N, Moraru V, Baran J, Ratajczak H (2005) *J Mol Struct* 744:563
505. Bezrodna T, Chashechnikova I, Dolgov L, Puchkovska G, Shaydyuk Y, Lebovka N, Moraru V, Baran J, Ratajczak H (2005) *Liq Cryst* 32:1005
506. Chang YM, Tsai TY, Huang YP, Chen WS, Lee W (2007) *Jpn J Appl Phys* 46:7368
507. Huang YP, Tsai TY, Lee W, Chin WK, Chang YM, Chen HY (2005) *Opt Express* 13:2058
508. Huang YP, Chen HY, Lee W, Tsai TY, Chin WK (2005) *Nanotechnology* 16:590
509. Jeong EH, Sun KR, Kang MC, Jeong HM, Kim BK (2010) *Express Polym Lett* 4:39
510. Huang YP, Chang YM, Tsai TY, Lee W (2009) *Mol Cryst Liq Cryst* 512:2013
511. Chang YM, Tsai TY, Huang YP, Cheng WS, Lee W (2009) *J Opt A-Pure Appl Opt* 11:024018
512. Kasdorf O, Kitzerow HS, Lenoble-Zwahlen J, Deschenaux R (2010) *Jpn J Appl Phys* 49:01AF01
513. Yevlampieva N, Beljaev N, Lavrenko P, Deschenaux R (2009) *Mol Cryst Liq Cryst* 506:34
514. Perez L, Lenoble J, Barbera J, de la Cruz P, Deschenaux R, Langa F (2008) *Chem Commun* 4590
515. Maringa N, Lenoble J, Donnio B, Guillon D, Deschenaux R (2008) *J Mater Chem* 18:1524
516. Frein S, Auzias M, Sondenecker A, Vieille-Petit L, Guintchin B, Maringa N, Suss-Fink G, Barbera J, Deschenaux R (2008) *Chem Mater* 20:1340
517. Lenoble J, Campidelli S, Maringa N, Donnio B, Guillon D, Yevlampieva N, Deschenaux R (2007) *J Am Chem Soc* 129:9941
518. Deschenaux R, Donnio B, Guillon D (2007) *New J Chem* 31:1064
519. Gottis S, Kopp C, Allard E, Deschenaux R (2007) *Helv Chim Acta* 90:957

520. Campidelli S, Brandmuller T, Hirsch A, Saez IM, Goodby JW, Deschenaux R (2006) *Chem Commun* 4282
521. Campidelli S, Vazquez E, Milic D, Lenoble J, Castellanos CA, Sarova G, Guldi DM, Deschenaux R, Prato M (2006) *J Org Chem* 71:7603
522. Lenoble J, Maringa N, Campidelli S, Donnio B, Guillon D, Deschenaux R (2006) *Org Lett* 8:1851
523. Campidelli S, Perez L, Rodriguez-Lopez J, Barbera J, Langa F, Deschenaux R (2006) *Tetrahedron* 62:2115
524. Allard E, Oswald F, Donnio B, Guillon D, Delgado JL, Langa F, Deschenaux R (2005) *Org Lett* 7:383
525. Yevlampieva NP, Lavrenko P, Dardel B, Deschenaux R (2003) *Abstr Pap Am Chem S* 225: U637
526. Campidelli S, Vazquez E, Milic D, Prato M, Barbera J, Guldi DM, Marcaccio M, Paolucci D, Paolucci F, Deschenaux R (2004) *J Mater Chem* 14:1266
527. Deschenaux R, Yevlampieva N, Dmitrieva T, Dardel B, Lavrenko P (2004) *Fuller Nanotub Car N* 12:193
528. Yevlampieva NP, Dardel B, Lavrenko P, Deschenaux R (2003) *Chem Phys Lett* 382:32
529. Guillon D, Nierengarten JF, Gallani JL, Eckert JF, Rio Y, Carreon MD, Dardel B, Deschenaux R (2003) *Macromol Symp* 192:63
530. Chuard T, Deschenaux R (2002) *J Mater Chem* 12:1944
531. Carano M, Chuard T, Deschenaux R, Even M, Marcaccio M, Paolucci F, Prato M, Roffia S (2002) *J Mater Chem* 12:829
532. Behabtu N, Lomeda JR, Green MJ, Higginbotham AL, Sinitskii A, Kosynkin DV, Tsentalovich D, Parra-Vasquez ANG, Schmidt J, Kesselman E, Cohen Y, Talmon Y, Tour JM, Pasquali M (2010) *Nat Nanotechnol* 5:406
533. Kanie K, Sugimoto T (2003) *J Am Chem Soc* 125:10518
534. Kanie K, Muramatsu A (2005) *J Am Chem Soc* 127:11578
535. Kanayama N, Tsutsumi O, Kanazawa A, Ikeda T (2001) *Chem Commun* 2640
536. Kumar S, Pal SK (2005) *Liq Cryst* 32:659
537. In I, Jun YW, Kim YJ, Kim SY (2005) *Chem Commun* 800
538. Yamada M, Shen ZR, Miyake M (2006) *Chem Commun* 2569
539. Mallia VA, Vemula PK, John G, Kumar A, Ajayan PM (2007) *Angew Chem Int Ed* 46:3269
540. Cseh L, Mehl GH (2007) *J Mater Chem* 17:311
541. Cseh L, Mehl GH (2006) *J Am Chem Soc* 128:13376
542. Zeng XB, Liu F, Fowler AG, Ungar G, Cseh L, Mehl GH, Macdonald JE (2009) *Adv Mater* 21:1746
543. Donnio B, Garcia-Vazquez P, Gallani JL, Guillon D, Terazzi E (2007) *Adv Mater* 19:3534
544. Donnio B, Derory A, Terazzi E, Drillon M, Guillon D, Gallani JL (2010) *Soft Matter* 6:965
545. Daou TJ, Greneche JM, Pourroy G, Buathong S, Derory A, Ulhaq-Bouillet C, Donnio B, Guillon D, Begin-Colin S (2008) *Chem Mater* 20:5869
546. Frein S, Boudon J, Vonlanthen M, Scharf T, Barbera J, Suss-Fink G, Burgi T, Deschenaux R (2008) *Helv Chim Acta* 91:2321
547. Marx VM, Girgis H, Heiney PA, Hegmann T (2008) *J Mater Chem* 18:2983

Stimuli-Responsive Photoluminescent Liquid Crystals

Shogo Yamane, Kana Tanabe, Yoshimitsu Sagara, and Takashi Kato

Abstract We describe mechanochromic and thermochromic photoluminescent liquid crystals. In particular, mechanochromic photoluminescent liquid crystals found recently, which are new stimuli-responsive materials are reported. For example, photoluminescent liquid crystals having bulky dendritic moieties with long alkyl chains change their photoluminescent colors by mechanical stimuli associated with isothermal phase transitions. The photoluminescent properties of molecular assemblies depend on their assembled structures. Therefore, controlling the structures of molecular assemblies with external stimuli leads to the development of stimuli-responsive luminescent materials. Mechanochromic photoluminescent properties are also observed for a photoluminescent metallomesogen and a liquid-crystalline polymer. We also show thermochromic photoluminescent liquid crystals based on origo-(*p*-phenylenevinylene) and anthracene moieties and a thermochromic photoluminescent metallocomplex.

Keywords Liquid crystal · Mechanical stimuli · Phase transition · Photoluminescence · Stimuli-responsive liquid crystal · Thermal stimuli

Contents

1	Introduction	396
2	Mechanochromic Photoluminescent Liquid Crystals	397
3	Thermochromic Photoluminescent Liquid Crystals	400
4	Conclusion	404
	References	404

Abbreviations

Col	Columnar
Cr	Crystalline
Cub	Cubic
G	Glassy
Iso	Isotropic
LC	Liquid-crystalline
N	Nematic
SmA	Smectic A

1 Introduction

Soft materials such as polymers, gels, and liquid crystals have attracted much attention because of their dynamic properties [1–21]. The development of new functional self-organized soft materials such as liquid crystals and physical gels having dynamic properties is of interest to obtain energy-saving and environmentally benign materials. Self-organization of LC molecules leads to various ordered functional nanostructures such as bicontinuous cubic, smectic, columnar, cubic phases (Fig. 1). Highly functional soft materials can be prepared using the process of self-organization into such nanostructures. For example, anisotropic ionic or electrical transporting properties are observed for these materials [13–16]. Photofunctional liquid crystals have been prepared by introducing photochromic [17] and photoluminescent [11, 13, 16, 18] moieties.

In general, the photoluminescent properties of molecular assemblies depend on their assembled structures [21]. Therefore, controlling the structures of molecular assemblies with external stimuli leads to the development of stimuli-responsive luminescent materials. Recently, some photoluminescent materials showing stimuli-responsive properties have been reported [11, 21–34]. However, the number of stimuli-responsive photoluminescent liquid crystals is still limited [11, 21, 28–34]. Here we focus on mechano- and thermochromic photoluminescent mesomorphic materials. As the first topic, we focus on LC materials that change their photoluminescent colors by mechanical and/or thermal stimuli. We then describe another

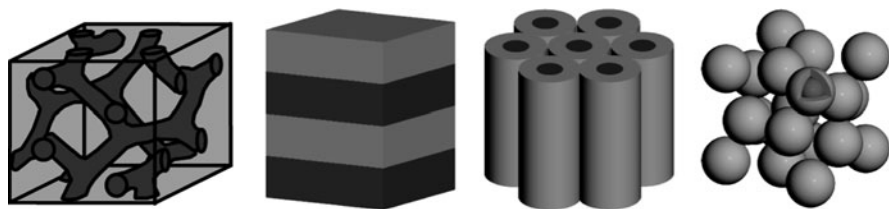


Fig. 1 Schematic illustrations of LC nanostructures: bicontinuous cubic, smectic, columnar and micellar cubic

type of photoluminescent liquid crystals changing their photoluminescent colors by thermal stimuli. These stimuli-responsive properties are achieved by controlling self-assembled structures of the photoluminescent π -conjugated moieties.

2 Mechanochromic Photoluminescent Liquid Crystals

As mentioned in the introduction section, the photoluminescent properties of molecular assemblies depend on the assembled structures of photoluminescent moieties [11, 21–34]. If assembled structures of photoluminescent moieties are changed by external stimuli, stimuli-responsive photoluminescent materials can be prepared. Recently, we have reported on anthracene, pyrene and naphthalene derivatives **1–3** having dendritic moieties which contain amide moieties to form intermolecular hydrogen bonds (Fig. 2) [28–30]. These dendritic moieties are known to be

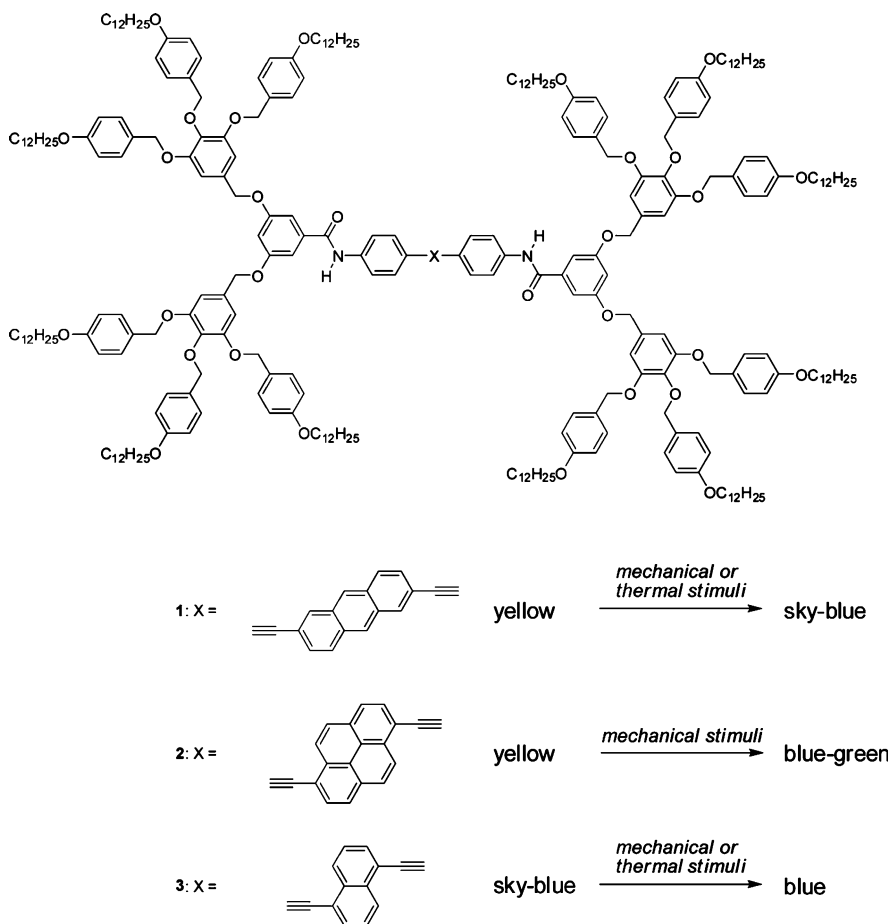


Fig. 2 Molecular structures of compounds **1–3** and observed mechanochromic photoluminescent behavior on the cubic–columnar liquid-crystalline phase transitions

Table 1 Liquid-crystalline properties of **1–3**

Compound	Sample preparation	Phase transition behavior ^a	Lattice parameter ^b
1	Rapid cooling ^c	Cr ₁ –15 Cub 168 Col 182 Iso	–
	Slow cooling ^c	Cr ₂ 63 Col 180 Iso	–
2	Cooling ^c	Cr ₁ –13 Cub 175 Iso	$a = 107.6 \text{ \AA}^d$
	Shearing ^c	Cr ₂ 44 Col 192 Iso	$a = 96.7 \text{ \AA}, b = 71.2 \text{ \AA}^f$
3	Rapid cooling ^c	Cr ₁ –13 Cub 128 Col 177 Iso	$a = 90.7 \text{ \AA}^d$
	Slow cooling ^c	Cr ₂ 15 Col 177 Iso	$a = 86.9 \text{ \AA}, b = 73.0 \text{ \AA}^f$

^aPeak temperatures (°C) determined by differential scanning calorimetry measurements on heating

^bDetermined by X-ray diffraction data

^cCooled from isotropic phase

^dMeasured in the cubic (*Pm3n*) phase

^eMechanically sheared in the cubic (*Pm3n*) phase

^fMeasured in the rectangular columnar (*P2/a*) phase

synthesized by convergent methods [35, 36]. The dendrons with long alkyl spacers at the periphery were reported to show a variety of LC structures [37, 38].

Compounds **1–3** exhibit mechano- and/or thermochromic photoluminescent properties accompanied by cubic–columnar LC phase transitions. Table 1 shows the LC properties of compounds **1–3**. Compounds **1** and **3** show cubic phases and columnar phases on rapid cooling and slow cooling, respectively. A columnar phase is not observed for compound **2** on cooling. The differential scanning calorimetry (DSC) measurements of compounds **1–3** show that the cubic phases of compounds **1–3** are metastable phases, while the columnar phases are stable. The X-ray diffraction patterns indicate that compounds **2** and **3** form *Pm3n* cubic phases and *P2/a* rectangular columnar phases.

Compounds **1–3** change their photoluminescent colors from yellow to sky-blue, from yellow to blue-green, and from sky-blue to blue on the cubic–columnar LC phase transitions, respectively. Figure 3 shows the absorption and emission spectra of compounds **1** and **3** in the chloroform solution states, cubic phases, and columnar phases. The absorption spectrum of compound **1** in chloroform (Fig. 3a, top) displays an absorption band between 360 and 430 nm with a well resolved vibronic structure, indicative of the monomeric state of compound **1**. On the other hand, compound **1** in the cubic phase shows the structureless absorption band in the 350–470 nm region, which suggests that ground-state interactions occur between adjacent luminophores in the cubic phase (Fig. 3a, middle). As for the photoluminescent spectra, a broad and structureless emission band in the longer wavelength region is observed in the cubic phase. It can be attributed to excimer formation of the emission cores in the cubic phase. The absorption spectrum of compound **1** in the columnar phase is red-shifted compared to that in the cubic phase. The red-shift can be ascribed to conformational change of the anthracene moiety of compound **1**, or the change of ground-state interaction between the chromophores (Fig. 3a, bottom). In the columnar phase, compound **1** shows the emission band with the maximum at 473 nm. The change in the emission spectra on the cubic–columnar phase transition corresponds to the change of the photoluminescent color from yellow to sky-blue by heating or shearing

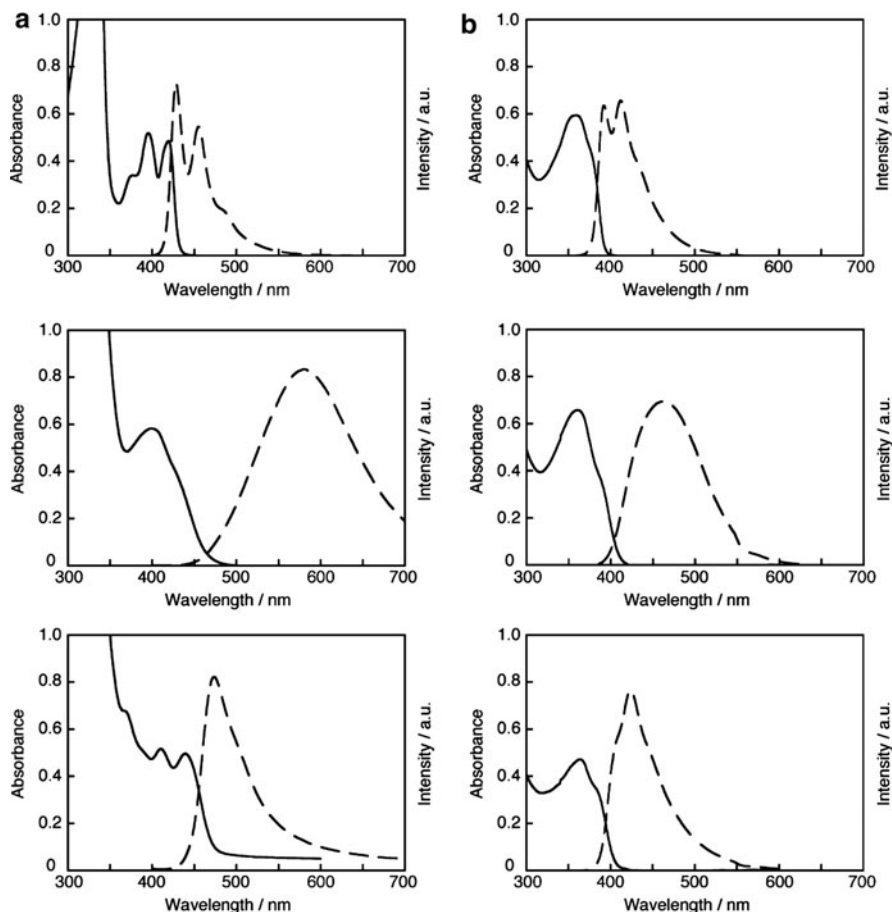


Fig. 3 UV-Vis absorption (solid line) and photoluminescence (dashed line) spectra of (a) **1** and (b) **3**. *Top*: in chloroform solutions; *middle*: in the cubic phases; *bottom*: in the columnar phases

in the condensed states. The yellow photoluminescence observed in the cubic phase is recovered by rapid cooling from the isotropic phase. Compounds **2** and **3** show the same trends as compound **1** (Fig. 3b), indicating that this dumbbell-shaped molecular design can be applied to various types of flat luminophores for development of stimuli-responsive photoluminescent liquid crystals.

Kozhevnikov, Bruce, and coworkers described an LC N,C,N-coordinated platinum(II) derivative **4** showing mechanochromic luminescence (Fig. 4) [31]. Compound **4** shows a hexagonal columnar phase up to 145 °C and another hexagonal columnar phase up to 220 °C. A pure film of compound **4** shows a red excimer-like emission at room temperature. Interestingly, the photoluminescent color of compound **4** changes from red to yellow by annealing at 110 °C and the yellow photoluminescence is preserved after cooling to room temperature. The red

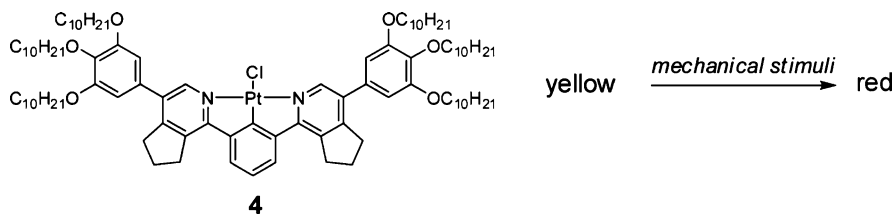


Fig. 4 Molecular structure of compound **4** and observed mechanochromic photoluminescent behavior before and after applying mechanical stimuli

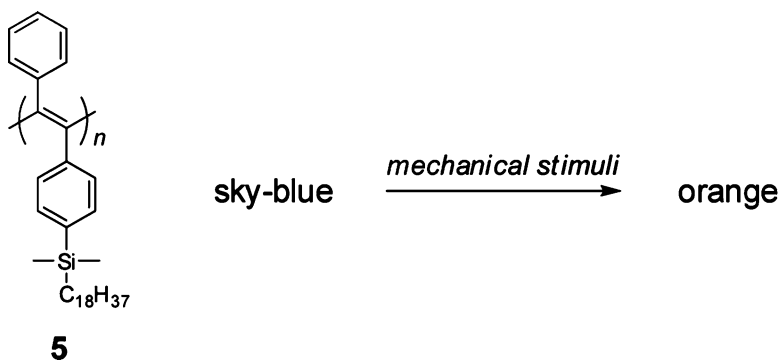


Fig. 5 Molecular structure of compound **5** and observed mechanochromic photoluminescent behavior before and after applying mechanical stimuli

photoluminescence can be recovered by mechanical stimuli and another heat-cool cycle leads to the yellow photoluminescence again.

Recently, Lee, Kwak, and coworkers have reported on mechanochromic photoluminescent LC polymer **5** (Fig. 5) [32]. This poly(diphenylacetylene) derivative has flexible dimethyloctadecylsilyl side chains. A solvent cast film made from toluene solution of compound **5** shows a smectic LC phase above 5 °C and phase transition to the isotropic phase is not observed until 200 °C. The cast film of compound **5** shows a blue emission. An orange emission can be observed when mechanical stimulus is induced to the cast film of compound **5**. In the emission spectra, an additional shoulder appears after the mechanical stimulus is induced. The longer wavelength component is attributed to forming intermolecular excimers. The sky blue emission is recovered by annealing of compound **5** in hexane.

3 Thermochromic Photoluminescent Liquid Crystals

Thermochromic photoluminescent liquid crystals have been reported recently as well as the mechanochromic photoluminescent liquid crystals. Weder and coworkers reported on oligo(*p*-phenylene vinylene) derivative **6** showing thermochromic

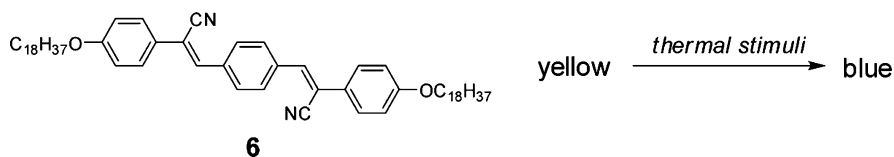


Fig. 6 Molecular structure of compound **6** and a change of its observed photoluminescent color on the nematic–smectic liquid-crystalline phase transition

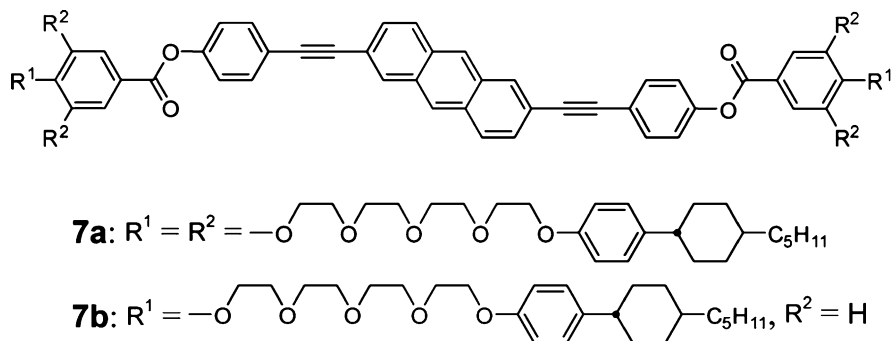


Fig. 7 Molecular structures of anthracene derivatives **7a** and **7b**

photoluminescent properties on the nematic–smectic phase transition [11] (Fig. 6). In addition, compound **6** also shows mechanochromic photoluminescent properties in the solid state. Compound **6** shows a yellow emission in the nematic phase and the photoluminescent color of compound **6** changes to blue on cooling to the smectic phase. This behavior can be ascribed to the change from excimer emission to monomeric emission.

We have recently reported that compound **7a** shows a smectic–smectic phase transition associated with the change of the photoluminescent color (Fig. 7) [33]. Compound **7a** has a 2,6-diethynylantracene group as a photoluminescent core. This molecule has fork-like mesogens which consist of tetra(ethylene oxide) and *p*-(4-*trans*-pentylcyclohexyl)phenyl moieties. A similar molecular design was previously applied to induce smectic liquid crystallinity for rotaxanes and catenanes [39–41].

The phase transition temperatures of compounds **7a** and **7b** are summarized in Table 2. Compound **7a** shows a highly viscous smectic (denoted as Sm1) phase, smectic (denoted as Sm2 and Sm3) phases with lower viscosity, and an SmA phase. On the other hand, compound **7b** shows a highly viscous smectic (denoted as Sm4) phase and a nematic phase.

The absorption and emission spectra of **7a** in the smectic phases and in chloroform solution are shown in Fig. 8. The absorption bands of **7a** in the Sm3 and SmA

Table 2 Phase transition behavior of compounds **7a** and **7b**

Compound	Phase transition behavior ^a
7a	G – 14 Sm1 83 Sm2 94 Sm3 104 SmA 132 Iso
7b	G – 26 Sm4 206 N ^b

^aPeak temperatures (°C) determined by differential scanning calorimetry measurements on heating

^bThermal decomposition occurred above 270 °C before reaching the isotropic state

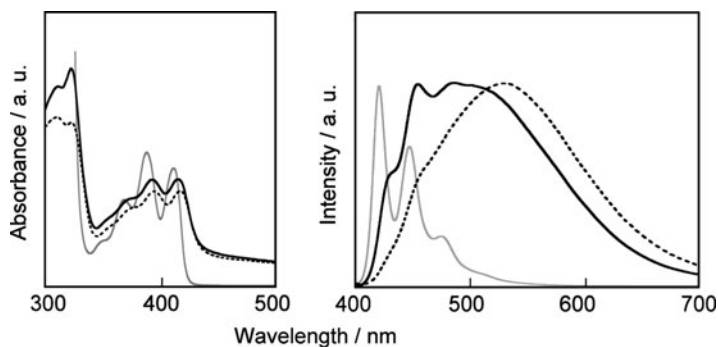


Fig. 8 Absorption (*left*) and emission (*right*) spectra of **7a** in chloroform solution (1×10^{-5} M, *gray line*), in the Sm3 phase at 98 °C (*black dotted line*) and in the SmA phase at 120 °C (*black solid line*)

phases are similar to that of **7a** in chloroform solution, indicating that no obvious ground-state interactions occur between the luminescent cores of **7a** in the two smectic phases. The emission spectrum for **7a** in the Sm3 phase differs from that for **7a** in the SmA phase. The broad and structureless band appears with the peak at 531 nm. It can be ascribed to excimer emission of the luminescent core of **7a**. In contrast, the emission peaks and shoulders are observed at the same positions as that of chloroform solution in addition to the excimer emission band in the SmA phase. These peaks and shoulders can be ascribed to the monomeric emission of **7a**. The change of the relative ratio of the monomeric emission is induced by the Sm3–SmA phase transition.

The X-ray diffraction (XRD) measurements for **7a** have been performed to examine the relationship between the photoluminescent properties and the self-assembled structures (Fig. 9). The XRD pattern of **7a** in the Sm3 phase shows several diffractions in the small angle region, corresponding to (100), (200), (300), (400), and (500) reflections. The layer spacing is similar to the molecular length calculated to be 82 Å. It is assumed that monolayer self-assembled structures are formed in the Sm3 phase (Fig. 9, top). In the SmA phase, only one peak appears at 38.2 Å in the diffraction pattern obtained at 120 °C. The layer spacing is less than half

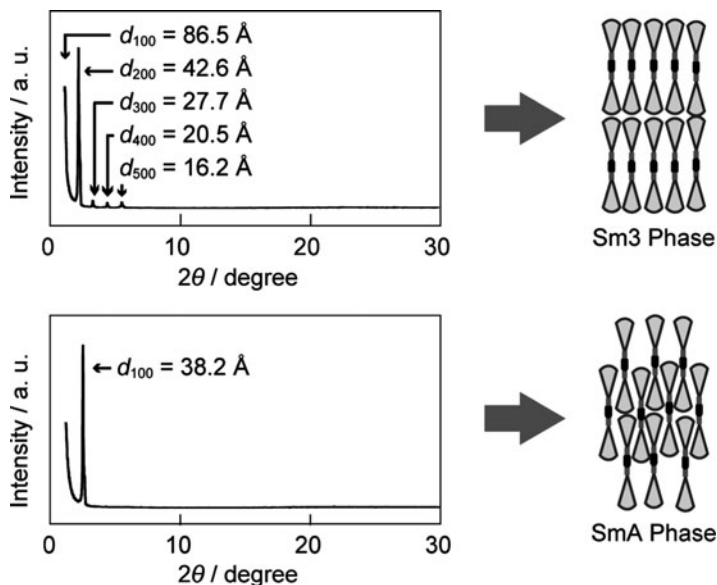


Fig. 9 X-ray diffraction patterns and schematic illustrations of the self-assembled structures of **7a** in the Sm3 phase at 98 °C (*top*) and in the SmA phase at 120 °C (*bottom*)

of the calculated molecular length, which suggests that compound **7a** forms interdigitated structures in the SmA phase (Fig. 9, bottom). The photoluminescent properties of **7a** significantly depend on its self-assembled structures. The photoluminescent cores of **7a** in the Sm3 phase are assumed to be closer than those in the SmA phase. Therefore, the excited luminescent cores form excimer with the adjacent luminescent core and the energy transfer may occur from most of the luminescent cores to the excimer sites [42, 43]. As a result, no monomeric emission is observed in the emission spectrum of **7a** in the Sm3 phase. On the other hand, luminescent cores in the SmA phase are separated by the terminal mesogenic groups. In this case, the deactivation of excited states with monomeric emission occurs before the excited cores form excimers or energy transfer occurs.

Copper(I) pyrazolate complex **8** was reported to show two phosphorescent properties depending on the cooling procedures to an ordered columnar phase from an isotropic phase by Aida and coworkers (Fig. 10) [34]. Compound **8** shows yellow phosphorescence after slow cooling with deliberate aging. On the other hand, red phosphorescence is observed by rapid cooling. A rewritable phosphorescent paper was prepared by using compound **8**.

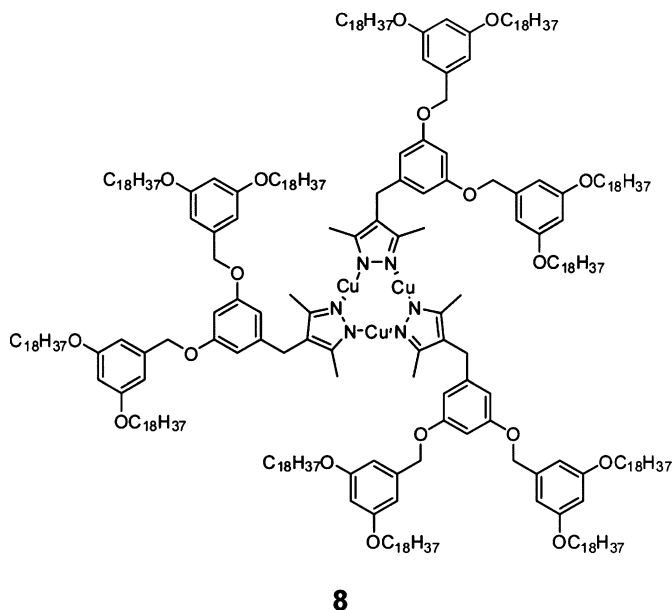


Fig. 10 Molecular structure of compound 8

4 Conclusion

The design and properties of stimuli-responsive photoluminescent LC materials are described. It is essential to control the interactions between luminescent cores to induce stimuli-responsive luminescent properties. These classes of anisotropic materials would be important for future photonic materials.

Acknowledgments We would like to thank the Japan Society of the Promotion of Science (JSPS) for financial support. Partial financial support from Grant-in-Aid for a Scientific Research on Innovative Areas of “Fusion Materials” (No. 2206) from the Ministry of Education, Culture, Sports, Science and Technology (MEXT) is gratefully acknowledged. S. Y., K. T., and Y. S. are grateful for financial support from the JSPS Research Fellowship for Young Scientists.

References

1. Ciferri A (ed) (2005) *Supramolecular polymers*, 2nd edn. London, Taylor and Francis
2. Urban MW (ed) (2011) *Handbook of stimuli-responsive materials*. Wiley-VCH, Weinheim
3. Demus D, Goodby JW, Gray GW, Spiess HW, Vill V (eds) (1998) *Handbook of liquid crystals*. Wiley-VCH, Weinheim
4. Kato T (ed) (2008) *Liquid crystalline functional assemblies and their supramolecular structures. Structure and bonding*, vol 96. Springer, Berlin
5. Kato T (2002) *Science* 295:2414
6. Kato T, Mizoshita N, Kishimoto K (2006) *Angew Chem Int Ed* 45:38
7. Tschierske C (2007) *Chem Soc Rev* 36:1930

8. Tschierske C (1998) *J Mater Chem* 8:1435
9. Saez IM, Goodby JW (2008) *Struct Bond* 128:1
10. Zhang H, Shiino S, Shishido A, Kanazawa A, Tsutsumi O, Shiono T, Ikeda T (2000) *Adv Mater* 12:1336
11. Kunzelman J, Kinami M, Crenshaw BR, Protasiewicz JD, Weder C (2008) *Adv Mater* 20:119
12. Zhu Z, Swager TM (2002) *J Am Chem Soc* 124:9670
13. Kato T, Yasuda T, Kamikawa Y, Yoshio M (2009) *Chem Commun* 729
14. Pisula W, Zorn M, Chang JY, Müllen K, Zentel R (2009) *Macromol Rapid Commun* 30:1179
15. Funahashi M, Shimura H, Yoshio M, Kato T (2008) *Struct Bond* 128:151
16. Yasuda T, Ooi H, Morita J, Akama Y, Minoura K, Funahashi M, Shimomura T, Kato T (2009) *Adv Funct Mater* 19:411
17. Natansohn A, Rochon P (2002) *Chem Rev* 102:4139
18. Kato T, Tanabe K (2009) *Chem Lett* 38:634
19. Thomas SW III, Joly GD, Swager TM (2007) *Chem Rev* 107:1339
20. Kato T, Hirai Y, Nakaso S, Moriyama M (2007) *Chem Soc Rev* 36:1857
21. Sagara Y, Kato T (2009) *Nat Chem* 1:605
22. Mutai T, Satou H, Araki K (2005) *Nat Mater* 4:685
23. Sagara Y, Mutai T, Yoshikawa I, Araki K (2007) *J Am Chem Soc* 129:1520
24. Yoon SJ, Chung JW, Gierschner J, Kim KS, Choi MG, Kim D, Park SY (2010) *J Am Chem Soc* 132:13675
25. Zhang G, Lu J, Sabat M, Fraser CL (2010) *J Am Chem Soc* 132:2160
26. Mizukami S, Houjou H, Sugaya K, Koyama E, Tokuhisa H, Sasaki T, Kanesato M (2005) *Chem Mater* 17:50
27. Ito H, Saito T, Oshima N, Kitamura N, Ishizaka S, Hinatsu Y, Wakeshima M, Kato M, Tsuge K, Sawamura M (2008) *J Am Chem Soc* 130:10044
28. Sagara Y, Kato T (2008) *Angew Chem Int Ed* 47:5175
29. Sagara Y, Yamane S, Mutai T, Araki K, Kato T (2009) *Adv Funct Mater* 19:1869
30. Sagara Y, Kato T (2011) *Supramol Chem* 23:310
31. Kozhevnikov VN, Donnio B, Bruce DW (2008) *Angew Chem Int Ed* 47:6286
32. Lee WE, Lee CL, Sakaguchi T, Fujiki M, Kwak G (2011) *Chem Commun* 47:3526
33. Yamane S, Sagara Y, Kato T (2009) *Chem Commun* 3597
34. Kishimura A, Yamashita T, Yamaguchi K, Aida T (2005) *Nat Mater* 4:546
35. Wooley KL, Hawker CJ, Fréchet JMJ (1993) *J Am Chem Soc* 115:11496
36. Tomalia DA, Fréchet JMJ (2002) *J Polym Sci A* 40:2719
37. Rosen BM, Wilson CJ, Wilson DA, Peterca M, Imam MR, Percec V (2009) *Chem Rev* 109:6275
38. Percec V, Cho WD, Ungar G, Yeardley DJP (2001) *J Am Chem Soc* 123:1302
39. Aprahamian I, Yasuda T, Saha S, Dichtel WR, Isoda K, Kato T, Stoddart JF (2007) *Angew Chem Int Ed* 46:4675
40. Yasuda T, Tanabe K, Tsuji T, Coti KK, Aprahamian I, Stoddart JF, Kato T (2010) *Chem Commun* 46:1224
41. Baranoff ED, Voignier J, Yasuda T, Heitz V, Sauvage JP, Kato T (2007) *Angew Chem Int Ed* 46:4680
42. Ajayaghosh A, Vijayakumar C, Praveen VK, Babu SS, Varghese R (2006) *J Am Chem Soc* 128:7174
43. Hulvat JF, Sofos M, Tajima K, Stupp SI (2005) *J Am Chem Soc* 127:366

Index

A

n-Alkanes, semiperfluorinated, 17
3,4-Alkylenedioxyppyroles, 91
Amphiphilicity, 5
Aromatics, perfluorinated, 92
Au(I) isocyanide, 188
Axial chirality, 303
Aza crown ethers, 110

B

Beidellite, 346
Bent-core mesogens, 280, 303
 perfluorinated segments, 81
Bent-shaped mesogens, deracemization, 312
Benzo[15]crown-5, 112
Benzo[18]crown-6, 112
Benzoic acids, RF-substituted, 28
Bicontinuous cubic phases, 8
Biphenyl benzoate, 83
Biphenyl bisbenzoates, 92
Biphenylophane, 179
Bis(perfluoropropylene oxide), 49
1,4-Bis(phenylethynyl)benzenes, 92
Blue phases, 361
Bolaamphiphiles, 66
Butterfly mesogens, 183

C

Carbon nanotubes, 331, 344, 366
Catenanes, 401
CdTe quantum dots, 336
Chain rigidity, 33
Chirality, 303
 control, 303
 enhanced, 306

Cholesteryl 4-formylbenzoate, 306
Cohesive energy density (CED), 13
Colloids, 225
Columnar phases, 5ff, 280, 362
Copper(I) pyrazolate, 403
Coronene diimides, 55
Crown compounds, 109
Crown ether-binaphthyl derivatives, 181
Crown ether-phthalocyanines, 175
Crown ethers, 26, 109
 mesogenic, 111
Crown thioethers, 141
Crystalline solid state, 5
Cubic mesophase, 1
Cyclophanes, 109
 crown-like, 176

D

Dark conglomerate (DC) phase, 315
Dendrimers, 1, 86
Deracemization, 303, 312
Diazacrowns, 133
Dibenzo[*g,p*]chrysene, 318
Dibenzo[18]crown-6, 165, 187
Dibenzo[30]crown-10, 166
Dimesogens, 83
Disk-shaped mesogens, deracemization, 318
Dithiaazacrown, 118
DNA, 225
 B-form, 227
 chiral inter-helical interactions, 234
 crystals, 243
 hydrogels, 258
 ionic strength dependence, 233
 linear aggregates, 256
 liquid crystals, 236

DNA (*cont.*)

- melting temperature, 230
- nanotubes, 257
- origami, 254
- superstructures, 236

DNA-coated colloids, self-assembly, 262

Double helix, 228

E

3,4-Ethylenedioxythiophenes, 91

F

Ferroelectric nanoparticles,
quasi-zero-dimensional, 339

Fluorenes, 91

Fluorescence confocal polarizing microscopy
(FCPM), 357

Fluorophobic effect, 15

Folding, 193

G

Gels, 225

Giant cylinder honeycombs, 69

Glasses, 225

Gold nanoparticles, 374

Gold nanorods, 340

Graphene, 346

H

Halogen bonding, 94

Hectorite, 346

Hekates, 193, 195

Hematite, 372

Hexa(cyclohexanebenzoyloxy)triphenylene,
174

Hexa-*peri*-hexabenzocoronenes, 55

Honeycombs, 64

Hybrid aligned nematic (HAN) cells, 355

I

Intercalation, 18

Interdigitation, 18

Iron(III) acetylacetonate, 338

Isotropic liquid state, 5

K

Kagome lattice, 79

L

Laminated phases, 70

Lanthanide-containing mesophases, 138

Laponite, 346

Layer frustration, 46

Lipophobicity, 31

Liquid crystal phases, nanoparticle-doped, 347

Liquid crystals, 1ff

discotic, 53

DNA, 236

fluorinated, 1, 10

photoluminescent, 397

polycatenar, 51

polyphilic, 60

rod-like, fluorinated chains, 36

self-assembly, 3

stimuli-responsive, 395

supramolecular, 94

M

Maghemite, 338, 376

Magnetic nanoparticles, 338

Magnetite, 338, 358, 376

Mechanical stimuli, 395

Melamine hekates, 216

Mesogens, bent-core, 280, 303

star-shaped, 193

Mesophases, 109

columnar, 1

Metal nanorods, 363

Metallomesogens, 1, 56, 109, 182

Methyl benzoates, 30

Micellar cubic phases, 7

Micro-segregation, 1, 5

Monoaza[15]crown-5, 173

Multipodes, 193

Multi-walled carbon nanotubes (MWCNTs),
345

N

Nanoclay, 331, 370

Nanocomposites, 331

Nanodiscs, 346

Nanoparticles, 331, 371

Nanorods, 331, 363

Nanosegregation, 5, 193

Nanotubes, 363

Naphthalene tetracarboxylic diimides, 55

Naproxen, 358

Nematic phase, 5

O

- Oligomesogens, 85
- Oligonucleotides, 20
- Oligo(phenylene vinylene) (OPV), 199, 367, 395, 400
- Orthoconic switching, 45

P

- Pairing, 225
- Pentaerythritol tetrabenzoates, 87
- Pentakis(phenylethynyl)phenoxy core, 54
- Perfluorinated molecules, 1
- Perfluoroalkanes, 12
- Perfluoro-*n*-hexane, 12
- Perylene diimides, 55
- Phase engineering, 193
- Phase transition, 395
- Phenyl benzoates, 177
- Photoluminescence, 395
- Phthalocyanines, 109, 171
- Polar properties, 280
- Poly(amido amine) (PAMAM), 88
- Polyamines, polysubstituted macrocyclic, 157
- Poly(benzyl ether) monodendrimers, 150
- Poly(diphenylacetylene), 400
- Polyethers, 26
- Polyfluorinated organic compounds, 1
- Polyhedral oligomeric silsesquioxanes (POSS), 355
- Polymer-dispersed liquid crystal (PDLC), 356, 371
- Polymers, 89, 109
- Polymethacrylates, 124
- Poly(phenylene ethylenes), 91
- Polyphiles, bent aromatic cores, 74
 - X-shaped, 75
- Polyphilicity, 33, 60
- Polyphilic molecules, 1, 9
- Polypropylene imine (PPI), 88
- Polysiloxane, crown-containing, 121
- Poly(thiophenes), 91
- Poly(vinylidene fluoride), 94
- P8-O-PIMB, 319
- P12-O-PIMB, 306
- Porphyrins, 56
- Pyromellitic diimides, 56

Q

- Quantum dots, 336

R

- R_F-R_H diblocks, 17
- Rod-bundle phases, 72
- Rod-like LCs, fluorinated chains, 36
- Rod-like mesogen, 112
- Rotaxanes, 401

S

- Salt effects, 109
- Scaffolded DNA origami, 254
- Self-assembly, 1, 225, 265
- Self-healing, 10
- Semiconductor nanoparticles, 344
- Semiconductor nanorods, 333, 344, 365
- Semiconductor quantum dots, 336, 340, 354
- Semiconductors, organic, 1, 56
- Semifluorinated thiophenes, 91
- Single-walled carbon nanotubes (SWCNTs), 345, 367
- Smectic antiphases, 283
- Smectic phases, 5, 22, 358
 - double layer, 37
- Space-filling, 193
- Stacking, 225
- Star-shaped mesogens, 193
- Stilbazole, 48
- Stilbenoid stars, 204
- Stimuli, external, 10
- Stimuli-responsive liquid crystal
- Substituent effects, 109
- Superconducting quantum interference device (SQUID) magnetometer, 339
- Supramolecular chemistry, 109

T

- Ternary amphiphiles, 61
- Tetrabromodibenzo[18]crown-6, 167
- Tetrathiafulvalene, 178
- Thermal stimuli, 395
- Thiaza crown ethers, 118
- Trinitrofluorenone, 181
- Trioctylphosphine/trioctylphosphine oxide (TOP/TOPO), 337
- T-shaped ternary amphiphiles, 64

U

- Upper critical solution temperature (UCST), 14

V

Vapor-liquid-solid (VLS) process, 344
Vibrating sample magnetometer (VSM), 339

X

X-ray structure, 280

Z

ZnS nanorods, 366